Understanding the Formation of Protective $FeCO_3$ on to Carbon Steel Pipelines during CO_2 Corrosion

By

Daniel Phillip Burkle

Submitted in accordance with the requirements for the degree of
Doctor of Philosophy

The University of Leeds
Institute of Functional Surfaces, iFS
School of Mechanical Engineering

April 2017

Publication Statement

The candidate confirms that the work submitted is his/her own, except where work which has formed part of jointly-authored publications has been included. The contribution of the candidate and the other authors to this work has been explicitly indicated below. The candidate confirms that appropriate credit has been given within the thesis where reference has been made to the work of others.

In all papers listed below, the primary author completed all experimental studies, evaluation of data and preparation of publications. All authors contributed to proof reading of the articles prior to publication.

Papers contributing to this thesis:

- Burkle, D, De Motte, R, Taleb, W, Kleppe, A, Comyn, T, Vargas, S, M, Neville, A, Barker, R. **Development of an electrochemically integrated SR-GIXRD flow cell to study $FeCO_3$ formation kinetics**. Review of Scientific Instruments, 2016. ISSN 0034-6748.
- Burkle, D, De Motte, R, Taleb, W, Kleppe, A, Comyn, T, Vargas, S, M, Neville, A, Barker, R. ***In-situ* SR-XRD study of $FeCO_3$ precipitation kinetics onto carbon steel in CO_2-containing environments: The influence of brine pH**. Submitted to Electrochemical Acta.

Acknowledgements

Firstly I would like to thank my primary academic supervisor, Professor Anne Neville for all of her supervision, continued support, enthusiasm, encouragement and advice throughout the course of this work. Anne has been amazing from start to finish and without her continued support, knowledge and passion for engineering, this work would not have been possible.

I am extremely grateful to my co-supervisor/colleague/friend Dr. Richard Barker for his invaluable daily advice, input and support in the lab and when writing my thesis and papers.

I would like to thank the Diamond Light Source for beam time (Beamline I15, reference EE12481-1), specifically Dr. Annette Kleppe and Allan Ross for their assistance before and during our visit. I would also like to thank everyone involved in the development of the flow cell, particularly Graham Brown and Mick Huggan for their expertise and assistance with the design, manufacture and testing of the flow cell. A further big thank you to everyone that helped and were involved in the synchrotron tests at Diamond, Rick, Mike, Wassim and especially Tim Comyn for his expertise in XRD and operating the Beamline and even more so for keeping us entertained/sane when pulling all-nighters to continue testing.

I would also like to express my sincere appreciation to BP for their technical guidance and financial sponsorship throughout the course of the PhD.

The support I received from my colleagues was tremendous and I wish to thank all my friends in the School of Mechanical Engineering, both past and present.

A big thanks goes to all of my family (Mum, Dad (I know you would be proud), Emma, Donna, Sam, Lee, all of my beautiful nephews (Taylor, Joshua, Jayden and Teddy), Victor, Christine and Christopher (my second family)) for believing in me and helping me cope with the stress of writing up!

Finally, a massive thank you to my amazing girlfriend Victoria for being so supportive during this PhD from start to finish (especially for providing all the meals that I didn’t have time to cook when writing up – without complaining (most of the time)).

Abstract

In the oil and gas industry, internal corrosion of carbon steel pipelines is commonly encountered during production and transportation of carbon dioxide (CO_2)-containing salt water and hydrocarbons. The growth of iron carbonate ($FeCO_3$) on the internal walls of carbon steel pipelines can reduce internal corrosion by blocking active sites on the steel surface and creating a diffusion barrier. Two of the key aspects to consider when predicting pipeline corrosion rates in CO_2 environments are the kinetics of film formation and level of protection afforded by the film under different operating conditions. This research focuses on understanding the factors governing the rate of precipitation, formation kinetics and protective properties of the $FeCO_3$ layer. This is an important step in order to take advantage of the positive attributes of $FeCO_3$ film formation and reduce the occurrence of localised corrosion attack.

An electrochemically-integrated Synchrotron Grazing Incidence X-Ray Diffraction (SR-XRD) flow cell for studying corrosion product formation on carbon steel in CO_2-containing brines typical of oil and gas production has been developed. The system is capable of generating flow velocities of up to 2 m/s at temperatures in excess of 80^{o}C during SR-XRD measurements of the steel surface, enabling flow to be maintained over the course of the experiment while diffraction patterns are being collected. The design of the flow cell is presented, along with electrochemical and diffraction pattern transients collected from the Diamond Light Source Synchrotron facility located in Oxford, UK. The flow cell is used to follow the nucleation and growth kinetics of $FeCO_3$ using SR-XRD linked to the simultaneous electrochemical responses of the steel surface which were collected in the form of Linear Polarisation Resistance (LPR) measurements to for *in-situ* corrosion rates. The results show that $FeCO_3$ nucleation could be detected consistently and well before its inhibitive effect on the general corrosion rate of the system. *In-situ* measurements are compared with *ex-situ* Scanning Electron Microscopy (SEM) observations showing the development of an $FeCO_3$ layer on the corroding steel surface over time confirming the *in-situ* interpretations. The results presented demonstrate that under the specific conditions evaluated, $FeCO_3$ was the only crystalline phase to form in the system, with no crystalline precursors being apparent.

Solution chemistry can be considered to be one of the most influential factors with regards to the kinetics, morphology and protection of the $FeCO_3$ film. The cell was used to follow the nucleation and growth kinetics of corrosion

products on X65 carbon steel surfaces in a CO_2-saturated 3.5 wt.% NaCl brine at 80°C and a flow rate of 0.1, 0.5 and 1 m/s over a range of solution pH values (6.3, 6.8 and 7) under different electrochemically controlled methods. The purpose of the work was to establish whether correlations exist between the kinetics of $FeCO_3$ formation, the quantity of film, and the level of protection facilitated and to identify the presence of any addition corrosion product phases or precursors. In all conditions tested in this work, $FeCO_3$ was identified as the only crystalline phase to form on the steel surface in all conditions and was detected in all tests well before its inhibitive effect on general corrosion rate was detected using electrochemistry. With increasing pH, the $FeCO_3$ precipitation rate and protectiveness increased, while the film thickness, crystallite size and induction time decreased.

A critical observation was that the quantity of $FeCO_3$ (measured from the *in-situ* diffraction data) on the steel surface is not a good indication of the protection of the film formed across different pH values. However, the results in this work have shown that at higher pH, larger portions of the surface become covered faster with thinner, more protective films consisting of smaller, dense and more compact crystals. *Ex-situ* SEM images are used to evaluate the surface coverage and size of the $FeCO_3$ crystals at various time intervals. The comparison between XRD main peak intensities and the surface coverage indicate a qualitative relationship between the two parameters at each pH, providing valuable information on the kinetics of films growth.

Table of Contents

List of Tables

List of Figures

List of Units, Chemicals, Symbols and Abbreviations

Units

A	ampere
Å	Angstrom
Bar	x10^5 Pascal
˚C	degrees Celsius
cm	centimetre
eV/s	Electron volt per second
g	grams
Hz	Hertz
J	Joule
K	Kelvin
kg/m^3	Kilogram per meter squared
kg/ms^{-1}	Kilogram per meters per second
kHz	Kilohertz
kV	Kilovolts
x k	1000 magnification
mA/cm^2	milliamp per centimetre squared
mm	millimetre
mm/year	millimetre per year
MPa	mega Pascal
m/s	meters per second
mol/L	moles per litre
mV/s	millivolts per second
nm	nanometre
Pa	Pascal

ppb	parts per billion
ppm	parts per million
ppt	parts per thousand
psi	pounders per square inch
µm	micrometre
V	volt
wt.%	Weight percent

Chemicals

Ag/AgCl	Silver/Sliver Chloride
C, Ca, Ca^{2+}	Carbon, Calcium, Calcium ion
$CaCO_3$	Calcium Carbonate
$Ca(Fe,Mg)CO_3$	Ankerite
CO_2, CO_3^{2-}	Carbon dioxide, carbonate ions
Cu	Copper
Cr^{3+}	Chromium ion
e^-	Negative electron
Fe, Fe^{2+}	Iron, Iron ion
Fe_3C	Cementite/Iron Carbide
$Fe_xCa_yCO_3$	Iron calcium carbonate
$FeCO_3$	Iron Carbonate (Siderite)
$Fe(OH)_2$	Geothite
$Fe_2(OH)_2CO_3$	Chukanovite
Fe_3O_4	Magnetite
HCO_3^-, H_2CO^3	Bicarbonates, carbonic acid
H^+, H_2S	Hydrogen ion, hydrogen sulfide
H_2O	Water
Mg, Mg^{2+}	Magnesium, magnesium ion

N_2	Nitrogen
NaCl	Sodium Chloride
$NaHCO_3$	Sodium bicarbonate
O_2	Oxygen
PMMA	Hollow poly-methyl methacrylate
POSS	Polyhedral Oligomeric Silsesquioxane
SiC	Silicon carbide

Symbols and Abbreviations

α	Charge transfer co-efficient
ΔG	Gibbs free-energy change
$\Delta G_{c(\text{hom})}$	Free energy for homogeneous nucleation
$\Delta G_{c(\text{het})}$	Free energy for heterogeneous nucleation
η	Overpotential
β_a	Anodic Tafel Gradient
β_c	Cathodic Tafel Gradient
η_a	Anodic overpotential
η_c	Cathodic overpotential
λ	Wavelength of the X-ray beam
θ	Incident angle of X-ray
Ø	Diameter
ρ	Density
μ	Fluid dynamic viscosity
σ	Driving force element
τ	Wall shear stress
γ	Interfacial tension
A	Inlet Area
$a_{products}$	Chemical reactivity of the products

$a_{reactants}$	Chemical reactivity of the reactants
ABS	Acrylonitrile Butadiene Styearene
AC	Alternate Current
ASTM	American Society for Testing Materials
B	Stern-Geary coefficient
BL	Boundary Layer
c	Equilibrium concentration
c	Speed of light
CE	Counter Electrode
C_f	Friction factor
CI	Corrosion Inhibitor
CR	Corrosion Rate
CRA	Corrosion Resistance Alloys
CS	Carbon Steel
Cu-Sn	Copper-Tin
D	Diffusion coefficient
DC	Direct Current
D_h	Hydraulic diameter
DLSSF	Diamond Light Source Synchrotron Facility
E	Measured cell potential
E^0	Standard cell potential
E_a	Activation Energy
$E_{applied}$	External power source
E_{corr}	Free corrosion potential
EDL	Electrical Double Layer
EEC	Electrochemical Equivalent Circuit
EIS	Electrochemical Impedance Spectroscopy
EOR	Enhanced Oil Recovery
F	Faraday’s constant

FILC	Flow Induced Localised Corrosion
FIB	Focused Ion Beam
$f(\theta)$	Surface factor
h	Plank's constant equal
HAADF	High Angle Annular Dark Field
i_0	Current density
i	Exchange current density
i_a	Anodic current
i_c	Cathodic current
i_{corr}	Corrosion current density
ICDD	International Centre for Diffraction Data
IHP	Inner Helmholtz Plane
J	Flux of material to/from the electrode surface
K	Equilibrium constant
k	Boltzmann constant
k_r	Kinetic constant
K_{sp}	Equilibrium constant for iron carbonate
LPR	Linear Polarisation Resistance
n	Number of the species present
NACE	National Association of Corrosion Engineers
OCP	Open Circuit Potential
OHP	Outer Helmholtz Plane
$P[A]$	Probability of nuclei that will grow
p_{CO_2}	Carbon dioxide partial pressure
pH	potential Hydrogen
PR_{FeCO_3}	Iron carbonate precipitation
P_{total}	Total pressure in system
Q	Flow rate
R	Ideal gas constant

RE	Reference Electrode
Re	Reynold's number
R_p	Polarisation Resistance
R_s	Solution Resistance
R_{ct}	Resistance Charge Transfer
R_{Nuc}	Rate of nucleation
SAED	Selected Area Electron Diffraction
S_R	Saturation Ratio
SEM	Scanning Electron Microscopy
ST	Scaling Tendency
SR-XRD	Synchrotron Radiation X-Ray Diffraction
SS_{FeCO_3}	Iron carbonate supersaturation
T	Temperature
TEM	Transmission Electron Microscopy
T_{ind}	Induction time
T_n	Nucleation time
T_g	Time for nucleus to grow to a detectable size
v	Flow velocity
V	Volume
WE	Working Electrode
XRD	X-ray Diffraction

Part I:
Introduction, Background and Literature Review

Chapter 1.
Introduction, Motivation of Study, Research Objectives and Thesis Structure

To fully understand the motivation behind this work, a literature review related to the current and previous research topics was grouped into the following key areas: Carbon dioxide (CO_2) corrosion, Iron Carbonate ($FeCO_3$) layer formation and *in-situ* flow cell designs.

1.1 Introduction

Safe and efficient recovery of hydrocarbons is of paramount importance in the oil and gas industry. One of the main obstacles to successful oil production is internal pipeline corrosion, which can cause catastrophic and unexpected failures, leakages, down-time and severe environmental damage. As the oil and gas is extracted and emerges from the geological formations they are accompanied by varying amounts of water and of corrosive gases. One of the main corrosive gas to exist in hydrocarbon production fluid is carbon dioxide (CO_2), which when dissolved into the aqueous phase can cause a number of corrosion mechanisms during transportation from upstream to downstream applications having significant impacts on the integrity of the inner walls of the carbon steel pipelines. Although such forms of aggressive corrosion mechanisms have been known and studied for over 100 years, aqueous CO_2 corrosion of carbon steel still represents a significant problem for the oil and gas industry. All transportation and production pipelines, many wells and much of the processing equipment in the oil and gas network both upstream and downstream are constructed out of carbon steel. Despite the fact that high cost Corrosion Resistant Alloys (CRAs) exist that are able to withstand internal corrosion, carbon steel is still the most cost effective construction material used in this industry during oil and gas production.

During oil and gas production and transportation, when CO_2 dissolves in the aqueous phase that is often produced along with crude petroleum, and creates a solution that is corrosive to the inner walls of pipeline steel, the precipitation of CO_2 corrosion product compounds can present a physical barrier at the surface interface between the steel and the environment. Iron carbonate ($FeCO_3$), is often the main corrosion product found in carbon steel pipelines. Favourable physical properties of $FeCO_3$ such as low porosity and strong adhesion to pipeline walls can limit the further rate of corrosion of the underlying steel. Thus, by having the ability to slow down corrosion, $FeCO_3$

can play a significant role in material sustainability [1, 4]. The natural formation of an $FeCO_3$ corrosion product on the inside of steel pipework is one of the most important factors governing the corrosion rate of the underlying steel; the rate of corrosion can be >100 times lower when $FeCO_3$ is present. If a dense and protective layer of $FeCO_3$ is formed, the corrosion rates can be reduced to levels well below 0.1 mm/year. Therefore, understanding the associated kinetics of formation protective $FeCO_3$ as well as the conditions conducive to its removal (mechanically or chemically) is of great interest to the oil and gas industry. $FeCO_3$ films with protective properties can form, but local breakdown of the protective $FeCO_3$ layer may result in rapid local attack, also known as mesa attack, especially at high flow rates. Mesa-attack is aggravated by the galvanic effect established between $FeCO_3$ layer and bare steel areas and may ultimately lead to costly equipment failure. Consequently, many operators are dependent on the properties of this corrosion product to assist in mitigating pipeline corrosion.

Typically, such aqueous CO_2-induced corrosion products are assumed to only consist of $FeCO_3$ [1]. However, in reality, the chemical composition of CO_2 corrosion products are more complex and depend on the operating conditions of the pipeline. Studies have shown that the exposure of a carbon steel sample to a CO_2-saturated brine solution can lead to the formation of alternative corrosion products consisting of iron-oxy carbonate ($Fe_2O_2CO_3$) and iron-hydroxide carbonate ($Fe_2(OH)_2CO_3$) phases [2], and can also include iron oxide (Fe_3O_4) [3], at solution temperatures lower than 50°C or greater than 150°C [4]. This iron oxide, magnetite, has been concluded to be the key towards offering enhanced corrosion resistance to the steel surface [5,6] to below 0.01 mm/year.

Despite the importance and extensive research in to the overall CO_2 corrosion mechanism, there are still a number of questions that remain unanswered relating to the formation of the $FeCO_3$, its removal and the level of protection offered.

1.2 Motivation of Study

The oil and gas industry is mainly divided into two parts: ‘upstream’ referring to the exploration and production of petroleum; and ‘downstream’ referring to the gathering, transportation, refining, purifying, processing and marketing of petroleum [7]. Upstream operators require excessive tonnes of material to construct the oil and gas network. Carbon steel has been the primary material of choice for many different large-scale structural applications because of its

ideal mechanical properties, acceptable general corrosion performance and relatively low capital expenditure. The work in this thesis is concerned with internal carbon steel corrosion issues in upstream oil and gas operations.

The transportation of produced natural gas is typically transported long distances of 10-20 km in up to 16” diameter pipelines downstream for post-processing, see Figure 1.1. A typical carbon steel pipeline transports on average 4 million m^3 natural gas/day; therefore a breakdown is extremely costly [8].

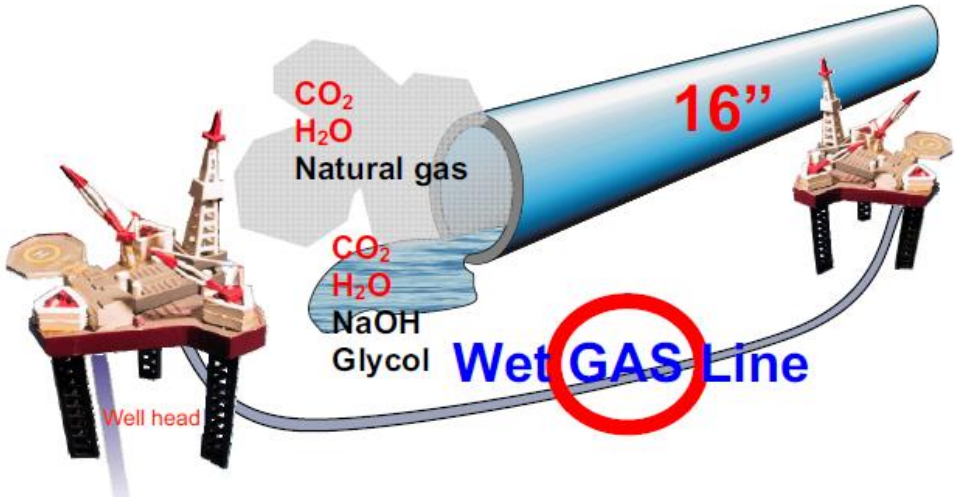

Figure 1.1. An overview of a gas transportation system [8].

The cost of equipment failure due to internal CO_2 corrosion is enormous, both in terms of direct costs such as: repair costs and lost production, as well as in indirect costs such as: environmental cost, impact on the downstream industries, etc. There are many challenges relating to cost-effective operational performance and asset integrity management. The ultimate goal for the industry is to maximise production with improved process safety to the environment. Corrosion can be severe and lead to catastrophic disasters. This is especially true during the production and transportation process in the oil and gas industry. Among the 50 major engineering failures in the oil and gas industry between 1977–2007, more than one third of the major failures were due to corrosion related processes [9]. The wide range of environmental conditions present in oil and gas production and transportation provides an overabundance of different degradation mechanisms causing failures that have resulted in downtime and maintenance, with corrosion being the most recurrent form of attack. An analysis of the types of petroleum industry related failures and corrosion related failures were published in Kermani *et al.* [10] and reproduced in Table1.1 and Table 1.2.

Table 1.1. Types of failures in the oil and gas industry [10]

Type of Failure (Oil and Gas Production)	Frequency (%)
Corrosion (all types)	**33**
Fatigue	18
Mechanical damage/ overload	14
Brittle fracture	9
Fabrication defects (excluding weld defects)	9
Welding defects	7
Others	10

Among the 33% of the corrosion related failures observed in the oil and gas industry in Table 1.1, CO_2 corrosion of carbon steels is the most common corrosive environment encountered in the production and transportation of oil and gas and makes up 28% of the overall corrosion failures (see Table 1.2). Extracted oilfield brines pass through the major components during production (wellheads, tubing strings, flowlines, transportation pipelines and risers) under variable temperatures (from 5°C to 300°C (downhole)) and pressures (0.1 MPa to 100 MPa (downhole)) [11-13] and the internal corrosion under these conditions can become quite problematic to the integrity of such components.

Table 1.2. Typical corrosion failures observed during oil and gas production [10].

Type of Corrosion Failure	Frequency (%)
CO_2 related	**28**
H_2S related	18
Preferential weld	18
Pitting	12
Erosion corrosion	9
Galvanic	6
Crevice	3
Impingement	3
Stress corrosion	3

To put the impact of corrosion related incidents into perspective, a real example of one of the most devastating corrosion incidents in modern day history is outlined below:

"In 2006, there was an oil spill in the Prudhoe Bay oil field that BP Alaska operated, originated from a small hole on the wall of one of the pipelines, which was attributed to corrosion (most likely localised corrosion). The amount of leakage was estimated to be over 5,000 barrels of crude oil which resulted in BP suffering a loss of $100 million to the pipeline and approximately a total of $320 million in government fines was inflicted due to the risk of endangering the safety of the environment and the public. It is estimated that in the five day leak, up to 267,000 US gallons of oil were spilled over 1.9 acres. BP had to pay a large penalty and the oil price increased after this incident, since the Prudhoe Bay oil field is a major oil supplier for North America [14]."

The impact of corrosion in this case was costly not only to the oil and gas industry and the operator, but more importantly the public and environment. This highlights the importance of managing corrosion effectively and efficiently. Research and development into corrosion mitigation techniques and further corrosion understanding can help reduce costs, environmental risks, and could improve the safety of operation.

Despite the importance and extensive research in to the overall CO_2 corrosion mechanism, there are still a number of questions that remain unanswered relating to the formation of the $FeCO_3$, its removal and the level of protection offered. In general, despite the complexity of $FeCO_3$ alone, there remains an incomplete understanding with regards the development of corrosion products during CO_2 corrosion, their chemical compositions, and the favourable/unfavourable effects that they impart upon underlying substrates. Therefore, it is critical that oil and gas companies are better informed of the processes governing not only the formation of $FeCO_3$ (and any other corrosion products that may form), but that they are aware of the consequences brought about by changes of the important factors that can remove and reduce the protectiveness of the $FeCO_3$ and cause severe localised corrosion, leading to unexpected failures, leakages, down-time and severe environment damage.

A precise knowledge of the growth stages and composition of the corrosion products to form that offer ultra-protective properties to the carbon steel surface during CO_2 corrosion is expected to allow the development of

enhanced corrosion prevention and control practices, and therefore is the focus of the present study.

1.3 Research Objectives

Some key questions of interest to both academia and industry are:

"What are the growth stages of the CO_2 corrosion products present on a carbon steel surface, prior to offering ultra-corrosion resistance?"

"What is the chemical composition of the ultra-protective corrosion product(s)?"

"What are the properties and important factors that lead to protection against corrosion? Why does the corrosion rate reduce? What is the driving force?".

In this light, the overall vision for this research project sets out to provide a comprehensive understanding of the near surface region of a corroding steel and the early kinetics of $FeCO_3$ film formation on a carbon steel surface in a CO_2 corrosive environment and the protectiveness offered. Explicitly, focusing on the growth kinetics and chemical composition of $FeCO_3$ formation (and any other phases that may form) and the degree of protectiveness offered through a unique, custom made flow cell, integrated with the ability to perform *in-situ* electrochemical measurements and collect real-time Synchrotron Radiation X-Ray Diffraction (SR-XRD) data simultaneously. The outcomes of this research will demonstrate a new methodology, enabling carbon steel CO_2 corrosion mechanisms to be related to the kinetics of $FeCO_3$ film formation. The focus is to help ensure and understand how CO_2 corrosion products can be exploited and maintained to utilise their protective properties. In order to achieve these goals, the following objectives are outlined and then broken down into three main frameworks in Figure 1.2:

1. Understand the effect of variation in the environmental factors, such as temperature, pH, supersaturation and CO_2 partial pressure, on the precipitation of $FeCO_3$ and the protectiveness offered through an extensive literature review.
2. Identify the key gaps in relation to $FeCO_3$ formation and develop a new methodology to fill the current gaps in the research available.
3. To determine the characterisation and chemical composition of the corrosion product(s) that offers ultra-protection to the underlying carbon steel (in the range of 0.01 mm/year).

4. Identify and follow the evolution of the phases formed in the early stages of CO_2 corrosion in real time to determine if the kinetics can be related to formation from the XRD patterns
5. Understand the kinetics and resulting electrochemistry during $FeCO_3$ formation.
6. To develop an understanding of the mechanism of $FeCO_3$ on steel under hydrodynamic conditions and as a function of different key influential parameters through an experimental approach.
7. To develop a flow cell that can enable *in-situ* measurements and XRD to be performed to study the $FeCO_3$ kinetics.

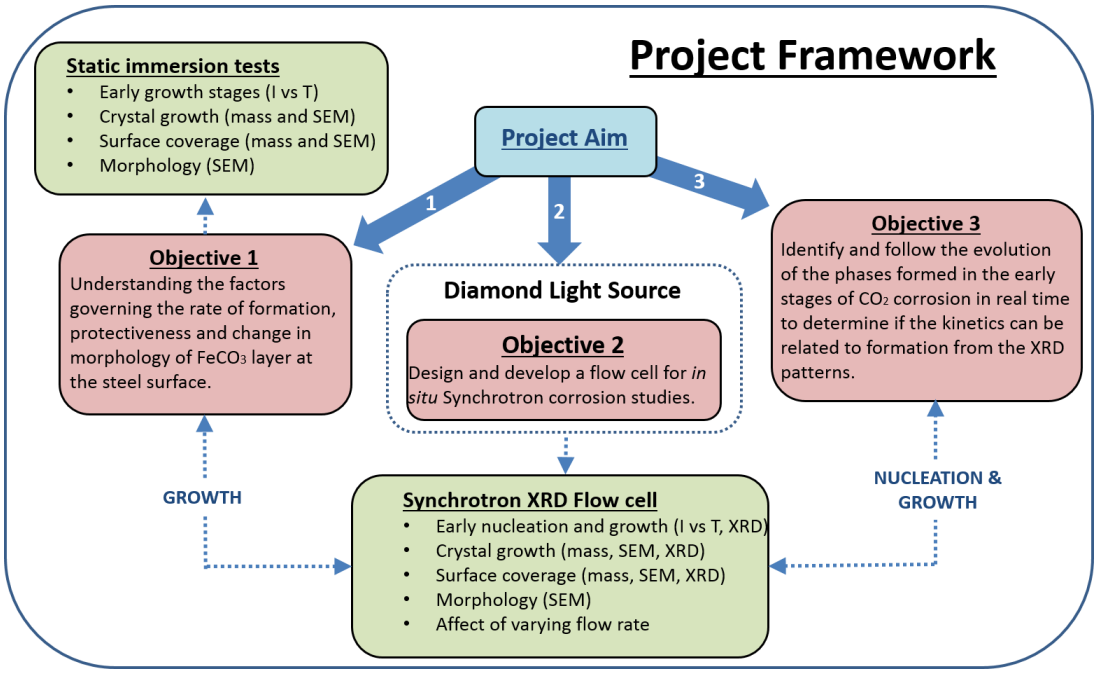

Figure 1.2. Schematic showing thesis objectives outline broken down into three main frameworks

1.4 Structure of Thesis

This work contributes to literature by providing further understanding of the early nucleation and growth kinetics of $FeCO_3$ on to the surface of X65 carbon steel in CO_2 corrosion through the use of a new designed, unique flow cell developed for *in-situ* SR-XRD studies. The work demonstrates the ability of flow cell to investigate the characteristics of the formation of $FeCO_3$ film formation and to provide information where experimental techniques have been limited previously. There are ten chapters in this thesis, including the current one.

Chapter 2 initially provides an introduction to CO_2 oilfield corrosion and **Chapter 3** provides a review of $FeCO_3$ formation in the oil and gas industry. Subsequent to this, in **Chapter 3**, a literature review is presented on a variety *in-situ* cell designs and presents some designs specifically designed to follow corrosion product formation in CO_2 conditions using synchrotron radiation. **Chapter 4** outlines the experimental techniques used in the work during the static immersion tests in order to define the ultra-protective layer formed and provides the physics behind their operation. **Chapter 5** presents the results from the static immersion experiments of X65 carbon steel in a CO_2-saturated deionised water solution (buffered to pH 6.8 with $NaHCO_3$), followed by *ex-situ* surface analyses as described in **Chapter 4** and outlines the limitations in the experimental techniques used in order to confidently determine the true nature of the corrosion products present. **Chapter 6** presents the design and development of the SR-XRD flow cell which addresses the current research gaps found in the literature and the limitations and uncertainty of the results in **Chapter 5**. The SR-XRD experimental methodologies are described and a selection of results are shown in order to validate the flow cells performance. **Chapters 7**, **8** and **9** detail the results of the Diamond Light Source Synchrotron (DLSS) experimental programme. **Chapter 7** focuses on the early kinetics of nucleation and growth of CO_2 corrosion products as a function of time and brine chemistry in a freely corroding flowing system comparing *in-situ* electrochemical observations with *in-situ* SR-XRD observations in real-time. **Chapter 8** explores how varying the system pH and flow affects the kinetics of the ultra-protective layer formed during anodic polarisation of the carbon steel surface. **Chapter 9** compares the kinetics of film growth under a freely corroding surface with a 'forced' corroding surface and assesses the capability of using *in-situ* SR-XRD to quantitatively determine the amount (in mass) of corrosion product to form on the carbon steel surface. **Chapter 9** also describes the mechanism of corrosion product formation in detail under the different operating conditions used throughout this work.

Conclusions are provided at the end of every 'results' chapter (5 to 8). However, **Chapter 10** provides a summary of the findings from the individual chapters, and proposes possible future directions of research and the relevance and impact this research has on industry and future academic studies

Chapter 2.
CO_2 Oilfield Corrosion Mechanisms: CO_2 Corrosion Background

2.1 Introduction to Oilfield Corrosion

The integrity of the vast amount of engineered systems and structures within the oil and gas network is of paramount importance during operation and production. Predicting if/when a metal component could fail is crucial. As previously mentioned, corrosion is the most common cause of equipment failure and downtime in the oil and gas industry. Corrosion is the destructive attack of a metal, a chemical effect, in particular, the metal dissolves/degrades over time due to surface electrochemical and chemical reactions brought about by the aqueous environment [15]. Corrosion is generally defined as:

"*The irreversible deterioration of a substance or its properties because of a reaction with its environment."*

Almost any aqueous environment can promote corrosion, which occurs under numerous complex conditions in oil and gas production, processing, and pipeline systems. Some of the known types of corrosion are electrochemical corrosion caused by electron transfer, cracking caused by tensile stress, flow assisted corrosion caused by fluid flow, fretting caused by friction and rubbing and high temperature corrosion caused by alloy melting. CO_2 corrosion is an electrochemical process which is discussed in detail within this study. This process is composed of three elements: an anode, a cathode, and an electrolyte. The anode is the site of the corroding metal, the electrolyte is the corrosive medium that enables the transfer of electrons from the anode to the cathode, and the cathode forms the electrical conductor in the cell that is not consumed in the corrosion process [16].

The nature and extent of the corrosion damage that may occur are functions of the concentration and particular combinations of these various corrosive constituents within the transportation pipeline, as well as of the operating conditions of the pipeline. Most corrosion occurs due to aqueous interactions with the metal surface because water is a solvent for the variety of corrosion products, salts, gases and oxidising agents, which can be damaging to a metal surface. Uninhibited carbon steel surfaces exposed to aqueous oilfield brines

can lead to severe internal corrosion and Figure 2.1 indicates some common internal corrosion issues that have resulted in down time in carbon steel pipelines during the transportation of oil and gas fluids. A variety of factors such as the environmental conditions, solution chemistry, types of fluid flow, fluid flow rates, corrosion product deposition and microbial activity influence the nature and rates of internal corrosion phenomena encountered in pipelines [8].

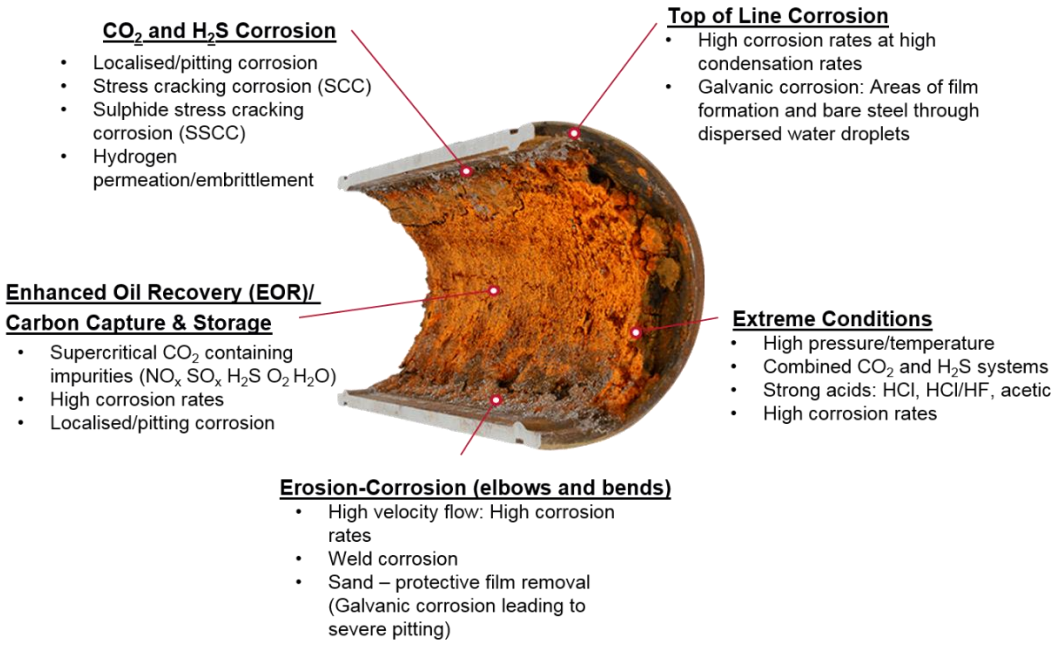

Figure 2.1. Common internal pipeline corrosion issues during oil and gas production and transportation.

Extracted oilfield brines pass through wellheads, tubing strings, flowlines and risers under variable conditions which are outlined in Table 2.1 [11–13].

High concentrations of CO_2 and H_2S accompany the extracted natural gas (methane) through the flowlines and approximately 33% of asset failures in the oil and gas industry are corrosion-related, and the majority of these are under CO_2 corrosive environments [17]. H_2S (sour) corrosion is caused by high amounts of H_2S gas dissolved in the aqueous phase and causes issues such as pitting, hydrogen embrittlement and stress-corrosion cracking [12, 18]. If the concentration of H_2S is low and the partial pressure is negligible, the production environment is CO_2-rich and described as CO_2 (sweet) corrosion [7] and will be the point of discussion beyond this point.

Table 2.1. Range of oilfield production operating conditions.

Solution chemistry	Condensed water, brines – pH 3 - 8
Types of fluid flow	Stagnant, laminar, turbulent, supersonic
Fluid flow rates	0, 0.1 – 10 m/s
Temperatures	- 5°C to 300°C (downhole)
Pressures	0.1 bar to 1000 bar (downhole)

2.2 Aqueous CO_2 Corrosion of Carbon Steel

Aqueous CO_2 corrosion of carbon steel is an electrochemical process involving the anodic dissolution of iron and the cathodic evolution of hydrogen. A number of processes including chemical reactions in the bulk, electrochemical reactions at the surface and transport of species to and from the bulk solution to the steel surface occur simultaneously in the overall CO_2 corrosion process. In the past few decades, corrosion has been recognised as a serious issue in the oil and gas industry therefore extensive studies have been completed on the mechanism of CO_2 corrosion in order to improve the corrosion mitigation strategy [19].

2.2.1 CO_2 Corrosion Mechanism

The mechanism of general CO_2 corrosion, by carbonic acid direct reduction, was first published by C. de Waard in 1975 [20, 21]. More recent research by Nesic *et al.* [22-25] have proposed models to predict CO_2 corrosion mechanisms. Dugstad [26] stated that it is important to understand that the term "CO_2 corrosion" and the effect of CO_2 is not related to solely one mechanism, but a wide range of electrochemical, chemical and mass transport processes are occurring simultaneously at the interface of the corroding steel and the electrolyte. These reactions are sensitive to changes in the fluid properties (temperature, pressure, brine chemistry) and the flow conditions (velocity, flow regime), making the process incredibly complex in some instances, especially when localised attack or the precipitation of protective corrosion products occur in systems. The reactions associated with CO_2 corrosion are capable of being divided into both anodic and cathodic processes and are outlined in the following sections.

2.2.2 Cathodic and Anodic Reactions

The water chemistry of dissolved CO_2, evolves through the progressive dissociation of hydrated CO_2, and can be summarised by a set of system equilibria [27]. Figure 2.2 shows a schematic for the CO_2 corrosion mechanism of carbon steel, this mechanism has been called the 'buffering effect' in literature [28].

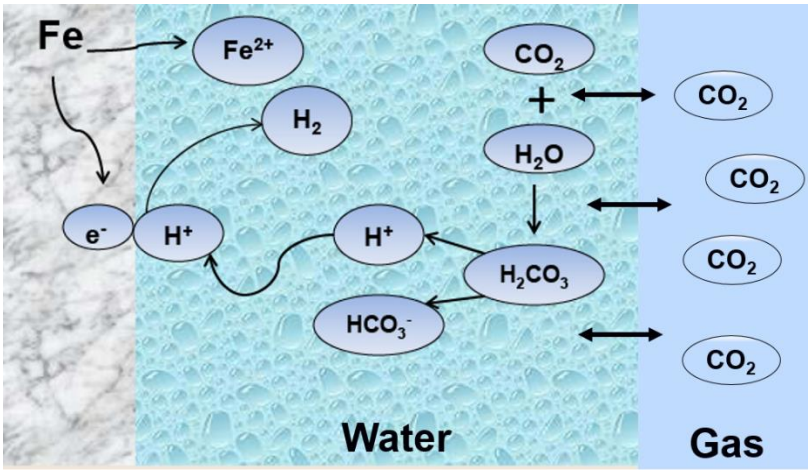

Figure 2.2. A schematic showing the aqueous CO_2 corrosion mechanism ("the buffering effect") of carbon steel (modified from [28]).

It is generally agreed that a given set of chemical reactions occurs in the aqueous solution in the CO_2 corrosion environment. The chemical reactions and their equilibrium constants that are involved in the overall CO_2 corrosion process can be seen in Table 2.2, where *K* represents the equilibrium constant for a given reaction and *c* the equilibrium concentration of a given species.

A large number of research papers have proposed and discussed various cathodic and anodic reactions on the steel surface in the presence of CO_2. Most of these reactions have recently been reviewed, discussed and summarized by Nesic *et al.* [29, 30, 31] and Garsany *et al.* [32]. The process begins when CO_2 dissolves in water (2.1), it is hydrated to produce carbonic acid (H_2CO_3) [33] (2.3), which partially dissociates in two steps releasing a proton (H^+) (2.5) and forms a bicarbonate ion (HCO_3^-) (2.7) [31, 33]. Then, the bicarbonate ion will dissociate once more and release a carbonate ion (CO_3^{2}) and one more proton (2.9). Because carbonic acid is a weak acid and it only dissociates partially, the CO_2 corrosion environment is deemed as a buffering effect and the equilibrium is dependent on temperature, the partial pressure of CO_2 and the ionic strength of the aqueous solution.

Table 2.2. Chemical reactions and their equilibrium constants in CO_2 aqueous environments.

Mechanism	Reaction	Equation	Equilibrium Constant	Equation
CO_2 dissolution	$CO_2 \overset{K_{sol}}{\longrightarrow} CO_2$	(2.1)	$K_{sol} = c_{CO_2}/pCO_2$	(2.2)
CO_2 hydration	$CO_2 + H_2O \overset{K_{hy}}{\longrightarrow} H_2CO_3$	(2.3)	$K_{hy} = c_{H_2CO_3}/c_{CO_2}$	(2.4)
H_2CO_3 dissociation	$H_2CO_3 \overset{K_{ca}}{\longrightarrow} H^+ + HCO_3^-$	(2.5)	$K_{ca} = c_{H^+}c_{HCO_3^-}/c_{H_2CO_3}$	(2.6)
HCO_3^- dissociation	$HCO_3^- \overset{K_{bi}}{\longrightarrow} H^+ + CO_3^{2-}$	(2.7)	$K_{bi} = c_{H^+}c_{CO_3^{2-}}/c_{HCO_3^-}$	(2.8)
H_2O dissociation	$H_2O \overset{K_{wa}}{\longrightarrow} H^+ + OH^-$	(2.9)	$K_{wa} = c_{H^+}c_{OH^-}$	(2.10)

The dissociation of carbonic acid and bicarbonate is a particularly fast reaction in comparison to CO_2 dissolution and hydration which are much slower and generally can become the rate-determining step, limiting the corrosion reaction rate or carbon steel and thus preserving chemical equilibrium [18]. However, the CO_2 dissolution reaction (2.1) and the hydration reaction (2.3) are much slower. When such chemical reactions proceed slowly, other faster processes (such as electrochemical reactions or diffusion) can lead to local non-equilibrium in the solution. Either way, the occurrence of chemical reactions can significantly alter the rate of electrochemical processes at the surface and the rate of corrosion. This is particularly true when, due to high local concentrations of species, the solubility limit of salts is exceeded and precipitation of a surface layer occurs. In a precipitation process, heterogeneous nucleation occurs first on the surface of the metal or within the pores of an existing layer since homogenous nucleation in the bulk requires a much higher concentration of species. Nucleation is followed by crystalline layer growth. Under certain conditions surface layers can become very protective and reduce the rate of corrosion [17, 19].

In water-CO_2 systems, the corrosion reaction is believed to proceed via two cathodic reactions and a single anodic reaction [29, 97, 98]. The mechanisms of the anodic and cathodic reactions have been investigated by many researchers. In terms of the heterogeneous reactions at the carbon steel

interface, the main cathodic and anodic half reactions (under oil and gas transportation conditions) are:

The cathodic half-reactions are,

$$2H^{+}_{(aq)} + 2e^{-} \leftrightarrow H_{2.(g)} \quad (2.11)$$

$$2H_2CO_{3.(aq)} + 2e^{-} \rightarrow H_{2.(g)} + 2HCO^{-}_{3.(aq)} \quad (2.12)$$

The anodic half-reaction is,

$$Fe_{(s)} \rightarrow Fe^{2+}_{(aq)} + 2e^{-} \quad (2.13)$$

Reaction (2.11) depends strongly on the solution pH. However, it is often limited by the rate at which H^+ ions can be transported to the steel surface by mass-transfer, making the reaction flow-dependant [34]. In CO_2 systems at low pH (< 4), the dominant process is the cathodic reduction of H^+ because of its high concentration. At intermediate concentrations and pH (4 < pH < 6), the limiting diffusion rate of H^+ is smaller because of its lower concentration. When CO_2 is hydrated to form H_2CO_3, hydrogen evolution can occur at a much faster rate compared to that found in a solution of a strong acid at the same pH, resulting in an increase in H^+ concentration and hence the corrosion rate [34]. This is attributed to the dissociation reactions of H_2CO_3 providing an additional source of H^+ ions which can readily be reduced at the steel surface [18]. In addition to hydrogen evolution, another cathodic reaction pathway, reaction (2.12), is also suggested to become important [21]. This is the direct reduction of H_2CO_3 where H^+ ions are directly reduced from H_2CO_3 molecules adsorbed on the steel surface [21]. This direct reduction of carbonic acid is believed to be a strong function of partial pressure, however, it should be noted that it has recently become subject to debate regarding as to whether it contributes significantly to the overall corrosion rate under oil and gas conditions [28, 35].

In terms of anodic reactions, the electrochemical dissolution of iron in acid solutions is associated with reaction (2.13), which has been studied extensively by researchers, with several multi-step mechanisms being used to explain experimental results. A detailed discussion of the proposed multi-step models can be found in the publication by Nesic *et al.* [22].

The overall electrochemical reaction that occurs on mild steel surface in the CO_2 corrosion environment can generally be expressed as Equation (2.14), which is composed of both the anodic and cathodic reactions when the solution does not become saturated with respect to $FeCO_3$ (Saturation Ratio (SR) <1). Under certain conditions, a layer of $FeCO_3$ can form on the steel surface when the solution is saturated with respect to $FeCO_3$ (SR >1).

For $SR < 1$, the overall reaction is,

$$Fe_{(s)} + 2H_2CO_{3.(aq)} \rightarrow Fe^{2+}_{(aq)} + 2HCO^{-}_{3.(aq)} + H_{2.(g)} \qquad (2.14)$$

For $SR > 1$, the overall reaction is,

$$Fe_{(s)} + 2H_2CO_{3.(aq)} \rightarrow FeCO_{3.(s)} + H_{2.(g)} \qquad (2.15)$$

It is the latter case which is of interest in this study when the solution is saturated with respect to $FeCO_3$.

2.2.3 Proposed Mechanisms for CO_2 Corrosion at 25-200 °C

Based on an experimental study by Tanupabrungsun *et al.* [36], four types of processes need to be considered as important for the CO_2 corrosion mechanism of carbon steel at high temperature.

1. <u>Chemical equilibria in a CO_2 system</u>

In a CO_2-H_2O-NaCl system, four homogeneous chemical reactions need to be considered. All of these reactions are relatively fast and can be considered to be in equilibrium. Since they are linked *via* common species, such as H^+, changing any one concentration will shift the equilibrium concentration for all the others.

2. <u>Corrosion processes</u>

As already mentioned, for CO_2 corrosion of carbon steel, the anodic reaction is iron oxidation and the cathodic reactions are the hydrogen evolution from H^+, H_2CO_3 and H_2O, as listed in Table 2.2. The kinetic rates of these reactions increase with temperature resulting in higher corrosion rate.

3. <u>$FeCO_3$ formation</u>

When steel corrodes, it releases Fe^{2+}. Once conditions for forming $FeCO_3$ are achieved, $FeCO_3$ will form and cover the steel surface, thereby lowering the

corrosion rate. The solubility constant, K_{sp} depends on temperature. For example, at 50-80°C, $FeCO_3$ precipitates only at elevated pH and/or high concentration of Fe^{2+}. As temperature is increased, $FeCO_3$ also precipitates at lower pH. For example, $FeCO_3$ was observed only at pH 6 at 80°C, whereas it was present at also at pH 4 at 120°C. Temperature accelerated the precipitation kinetics of $FeCO_3$, making it more protective.

4. $FeCO_3$ and Fe_3O_4 formation

At high temperatures (>100°C) and typical operating conditions, there are two types of corrosion products which can appear, $FeCO_3$ and Fe_3O_4. Which one will dominate depends on the thermodynamics and kinetics of their formation. For instance, at low pCO_2 (<1 bar) and 200°C, only Fe_3O_4 forms on the steel surface due to the very fast kinetics. However, at higher partial pressures of CO_2, (e.g. at pCO_2> 3 bars at 150°C), $FeCO_3$ and Fe_3O_4 may coexist on the steel surface.

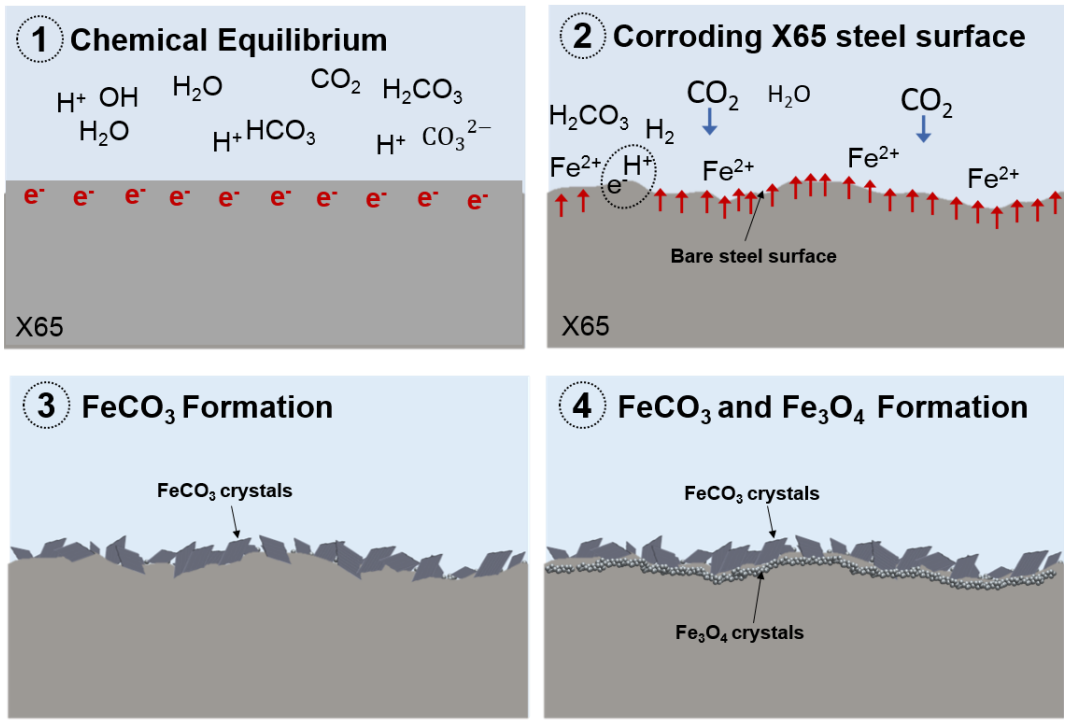

Figure 2.3. Schematic showing the proposed mechanisms for CO_2 Corrosion at 25-200°C

2.3 Aqueous CO_2 Corrosion of Carbon Steel: Failure Modes

CO_2 is harmless with respect to corrosion in gaseous form but becomes corrosive to carbon steel once it dissolves in water. Acidic CO_2 saturated water has been recognised as one of the most prevalent corrosive agents in upstream production and transport operations [37]. As mentioned previously, pipeline steels are known to be susceptible to CO_2 corrosion. CO_2 corrosion occurs primarily in the form of general (or uniform) corrosion and three variants of localised corrosion (pitting, mesa attack, and flow-induced localised corrosion) [37-39]. Uniform corrosion occurs at low pH and is not considered a threat to the integrity of carbon steel components and although not ideal, the corrosion rate values are generally within design corrosion allowance. The key factor contributing to localised CO_2 corrosion is the non-uniform formation of corrosion products on the carbon steel surface and localised destruction. Most studies covering localised CO_2 corrosion of carbon steels have been conducted in single-phase flow where the localised attack is always associated with the formation or breakdown of $FeCO_3$ films. Table 2.3 describes the severe forms of localised corrosion observed in CO_2 environments.

The form of localised corrosion observed in field pipelines is typically characterised by flat, film-free regions, separated by sharp steps from neighbouring areas which show significantly less damage [40, 41] and is typically referred to as ‘mesa’ attack [41, 42].

All of these forms of localised corrosion show very similar characteristics and can be linked with one and other. One of the most important features, is the formation of $FeCO_3$, which can be extremely complementary to the CO_2 corrosion of steel [1]. If an adherent $FeCO_3$ layer has attached to the carbon steel surface, such solids form a physical barrier that can reduce the corrosion rate of the underlying metal [54, 55]. Conversely, following breakdown, such surface layers are suspected to be involved in promoting localised corrosion [37–40] and is usually described as mesa corrosion attack. The initiation and growth of mesa corrosion attack was investigated by Nyborg, Dugstad and Nesic and presented in several publications [42, 51, 53-56]. One possible cause to promote mesa attack in CO_2 environments was proposed by Crolet *et al.* [57].

Table 2.3. The severe forms of localised corrosion observed in CO_2 environments.

Type of Corrosion	Description	References
Pitting Corrosion 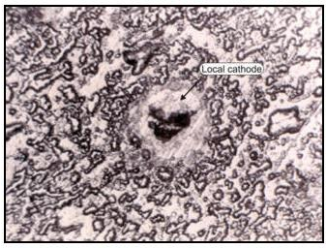	Pitting occurs at low velocities and around the dew-point temperatures in gas-producing wells. The controlling factor for pit initiation are local defects in the corrosion product layer due to non-uniform growth of the layer and/or local mechanical destruction by hydromechanics attack (high fluid shear stress, erosion, cavitation) or by scratching or mechanical stress.	[44-50]
Flow-induced localised corrosion 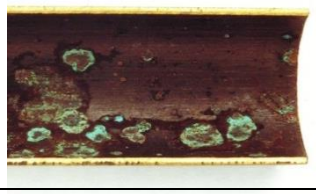	This form of corrosion starts from pits and/or sites of mesa attack above critical flow intensities. FILC occurs during turbulent flow when the protective $FeCO_3$ layer covering the pipe wall is stripped away, leaving small exposed steel for corrosion activities take place.	[43-45, 50]
Mesa-Type Attack 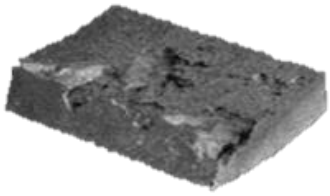	A type of localised corrosion and happens in low to medium conditions where the protective $FeCO_3$ film forms but it is unable to bear the operating flow regime and the breakdown of the protective layer creates a galvanic cell between the layer (cathode) and bare steel (anode) which results in severe localised corrosion.	[42, 48-53]

It was stated that the microstructurally formed galvanic coupling between steel (its ferrite phase) and the iron carbide (or cementite) (Fe_3C) layer was one possible cause to promote mesa attack. It was then shown that flow induced mesa-attack could occur in water saturated with $FeCO_3$ under turbulent flow conditions where film formation is prevented locally in work by Videm and Dugstad [58] which also demonstrated that the initiation of mesa attack was a result of the marginal film stability of $FeCO_3$. In addition to this work, Dugstad then discussed the relationship between $FeCO_3$ supersaturation of the aqueous environment and the initiation of mesa attack for CO_2 environments [59].

Dugstad [40] presented a schematic illustration (shown in Figure 2.4) to demonstrate the interaction between protective film formation, corrosion rate

and ferrous ion concentration in the process fluid in order to help explain the initiation of mesa-attack.

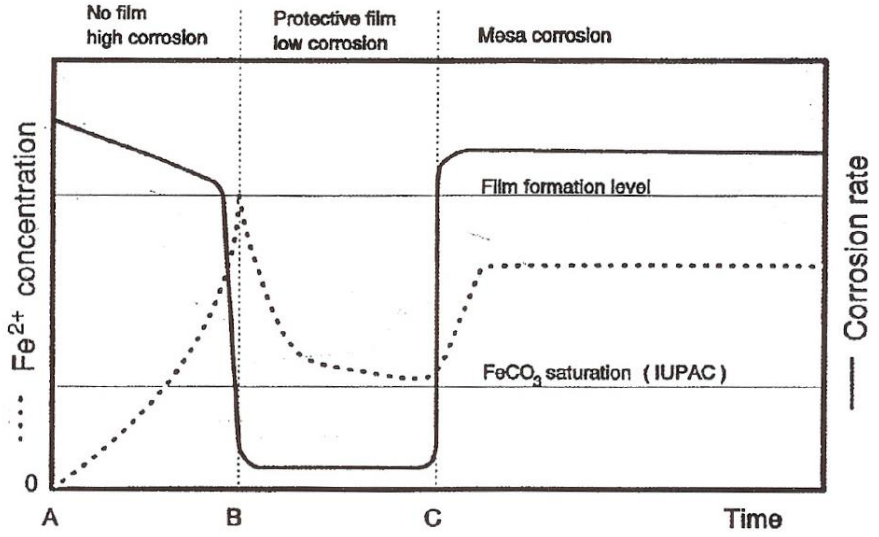

Figure 2.4. Schematic illustration of the interaction between protective $FeCO_3$ film formation, corrosion rate and ferrous ion concentration in the water – from Dugstad [40]

At time ‘A’, the steel becomes initially exposed to a solution without ferrous ions, resulting in high corrosion rates. Gradually, the solution becomes saturated with ferrous ions and ultimately, when supersaturation is reached, a protective $FeCO_3$ film forms (time ‘B’). Once the protective film is formed, the ferrous ion concentration in the bulk solution slowly reduces over a number of days. If the protective properties of the film are good, the ferrous ion concentration will decline towards the solubility limit. If the corrosion product layer becomes locally damaged (at time ‘C’ as a result of film dissolution or mechanical removal), healing of the film is very difficult as the iron ion concentration in the bulk solution does not increase sufficiently to enable the formation of a protective film. Dugstad [40] believed that a cyclic process such as this could result in multiple areas of mesa attack on a steel surface.

A proposed mechanism be Sun and Nesic *et al.* summarises the process of localised mesa-attack corrosion as follows [56].

Stage 1

In the initial stage, the steel is exposed to a corrosive environment. $FeCO_3$ film formation can proceed when its solubility limit is exceeded. This causes an increase in the local pH beneath the ferrous carbonate film.

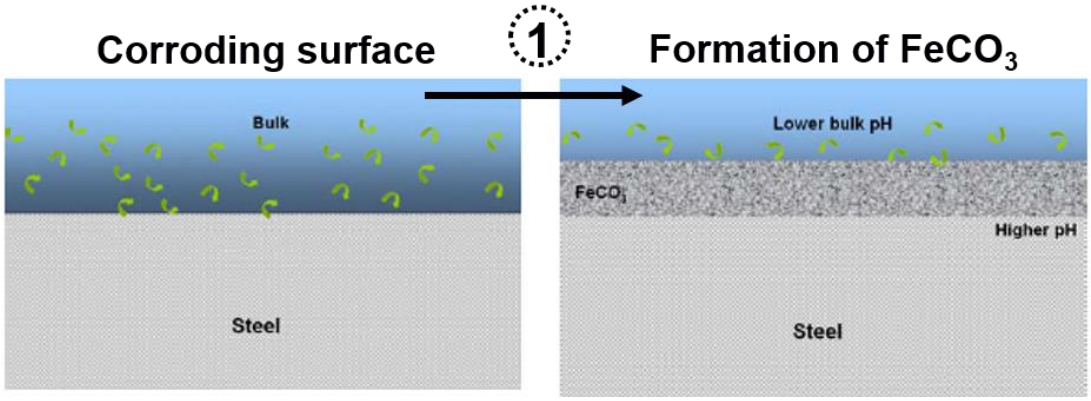

Figure 2.5. Schematic showing chemical equilibria in a CO_2 system followed by $FeCO_3$ film formation [from 56].

Stage 2

Consequently a ferrous hydroxide passive film can be formed, resulting in the potential increase. Localised corrosion may be initiated when the $FeCO_3$ film is locally damaged due to mechanical or chemical effects.

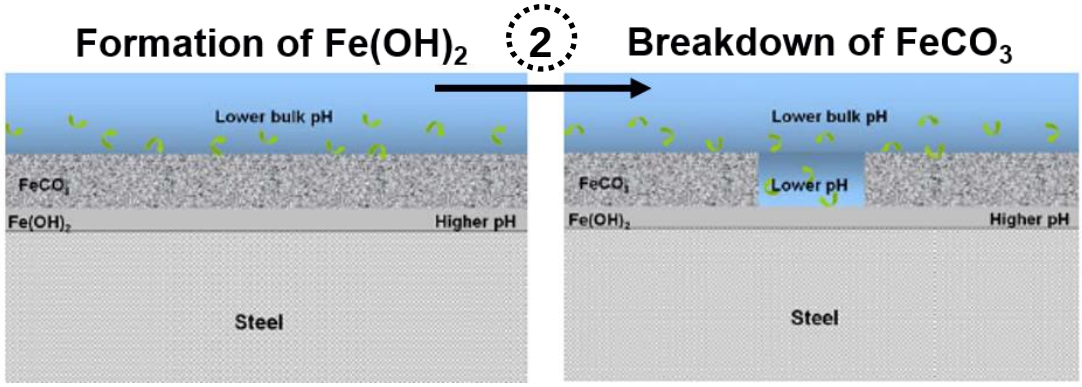

Figure 2.6. Schematic showing formation of $Fe(OH)_2$ and breakdown of $FeCO_3$ [from 56].

Stage 3

The ferrous hydroxide is then exposed to the bulk environment where the pH is lower. As a result, the ferrous hydroxide film dissolves and the steel is locally depassivated, leading to the exposure of its bare surface to bulk solution conditions. The potential of the large surrounding surface covered by passive ferrous hydroxide film and protective $FeCO_3$ film is higher than that of the bare metal surface. This results in the bare steel patch corroding at a very high rate due to the galvanic effect which is established when there is a local change in material potential. In this case, the bare still surface is acting as the anode and the film is acting as the cathode. When the film breaks down as illustrated in Figure 2.7, there will be a potential difference between two surfaces (bare

steel and film) in contact with the electrolyte – this is known as the galvanic effect.

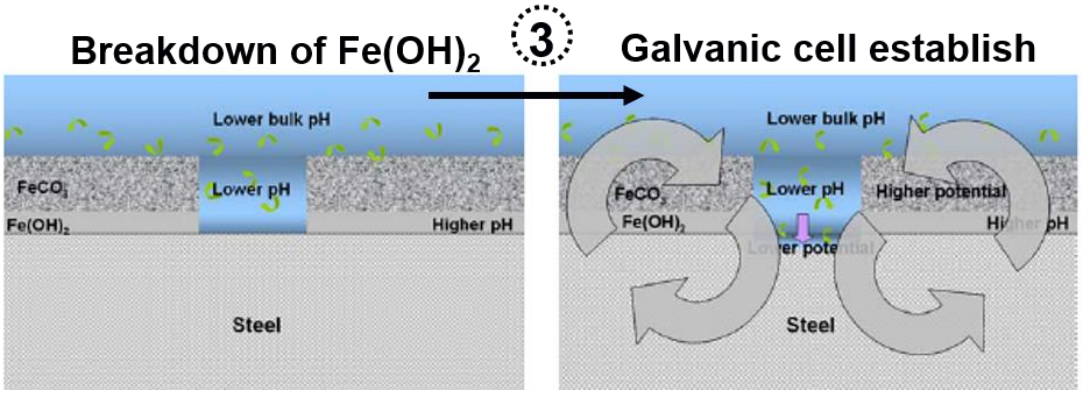

Figure 2.7. Schematic showing breakdown of $Fe(OH)_2$ and the established galvanic cell [from 56].

Stage 4

This is accompanied by corrosion and passive film dissolution in the lateral direction. Detachment of the $FeCO_3$ film occurs. The removal of the detached film causes the pit to grow wider.

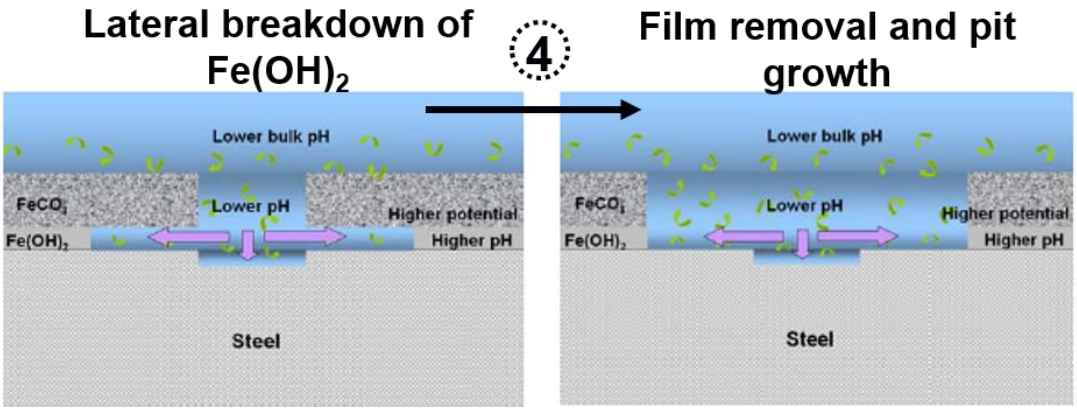

Figure 2.8. Schematic showing lateral breakdown of $Fe(OH)_2$ and film $FeCO_3$ film removal followed by pit growth [from 56].

The proposed mechanism has uncertainties with regard to the true nature and composition of the passive film beneath the $FeCO_3$ crystals which will be discussed in greater detail later within this thesis.

2.4 CO_2 Corrosion Products on Carbon Steel: Film Morphologies and Composition

Significant uncertainties present themselves in the formation process of corrosion products of the surface of carbon steel in CO_2-aqueous solutions. It is inevitable that $FeCO_3$ is the most common corrosion product found on the internal walls of pipeline steel and when compact layers of $FeCO_3$ crystals form, they can offer good corrosion resistance to the pipeline surface in many instances by forming a physical barrier (to the electrochemically active species involved in the charge-transfer process) and limiting electrolyte contact with the metal surface [60]. Although $FeCO_3$ is the most prevalent compound, it is not the only CO_2 corrosion product that can form in such environments. The following review therefore highlights the various corrosion product morphologies that can exist on carbon steels in CO_2-containing environments.

Recent studies have indicated that along with $FeCO_3$, Fe_3C (Cementite/Iron Carbide), Fe_3O_4 (magnetite) and $Fe_2(OH)_2CO_3$ (chukanovite) formation is possible [2,3, 61-65]. However, Fe_3C, is recognised to be a non-corroded remnant of the carbon steel matrix [38, 63] $Fe_2(OH)_2CO_3$ is yet to be observed in field in petroleum-carrying pipelines.

The following review considers literature on the formation of Fe_3C, $FeCO_3$, Fe_3O_4 and $Fe_2(OH)_2CO_3$ corrosion products.

2.4.1 Cementite/Iron Carbide (Fe_3C) Network

Fe_3C is commonly observed on carbon steel surfaces during CO_2 corrosion and the development of a porous network has been typically observed on steels with a carbon content in excess of 0.15% [63, 65]. A typical Fe_3C network is revealed on carbon steel surfaces as a result of the preferential dissolution of the α-ferrite phase within the steel microstructure when exposed to a corrosive media. Upon exposure of Fe_3C, it is believed to be able to act as an electronic conductor that is capable of accelerating the corrosion rate of carbon steel by inducing a galvanic effect on the steel surface and acting as a favourable cathodic site for hydrogen evolution [66]. Dugstad [67] identified that ferrite-pearlite microstructures can result in the evolution of a porous Fe_3C layer, which remains uncorroded when exposed to CO_2 environments. Farelas *et al.* [63, 65] attributed the significant increase in corrosion rate to the presence of Fe_3C, which generates cathodic sites with a lower overpotential for hydrogen evolution [66].

2.4.2 Iron Carbonate ($FeCO_3$) Corrosion Products

$FeCO_3$ is capable of dramatically influencing the corrosion kinetics of the underlying steel. $FeCO_3$ is structurally similar and is often considered as the scale counterpart of $CaCO_3$ (calcite), with both minerals being a soluble inorganic crystal salt. $FeCO_3$ is classified within the trigonal-hexagonal rhombohedral crystal system and has a density of ~3.96 g/cm^3 [69]. Within the $FeCO_3$ crystal structure (see Table 2.4) the carbonate (CO_3) remains approximately planar and iron atoms (Fe) occupy octahedral positions (where the iron atom replaces the calcium atom (Ca^{2+}) coordinating to six neighbouring oxygen (O) sites. $FeCO_3$ assigns rhombohedral/approximate cube shaped crystal morphology (Image reproduced from Pessu *et al*. [93] in Table 2.4) and when crystalline $FeCO_3$ has formed, it embraces the calcite structure $R\bar{3}c$. $FeCO_3$ is usually found on its own on carbon steel pipeline surfaces in CO_2 environments, but can also be incorporated into other compounds (e.g. $Ca(Fe,Mg)CO_3$ (ankerite)) [56]. After stable $FeCO_3$ crystals have formed on steel surfaces, upon exposure to dissolved oxygen, the crystal structure of $FeCO_3$ tends to transform into $Fe(OH)_2$ (goethite) [70]. The nature of or changes to micro-environment beneath $FeCO_3$ crystals which could promote localised corrosion as discussed previously, or that perhaps another semi-conductive or conductive component of the film, e.g. magnetite, could impart the proposed galvanic influence [10].

2.4.3 Magnetite (Fe_3O_4) Corrosion Products

It has been demonstrated that in addition to the generation of $FeCO_3$ corrosion product, the steel surface can enter into a pseudo-passive state, facilitating ultra-protective properties. The ‘pseudo-passivation’ process results in a signi ficant increase of the carbon steel open circuit potential (OCP) (by a magnitude ranging between 400 mV and 800 mV in some instances with a reduction in corrosion rate from ~0.1 mm/year to 0.01 mm/year). Fe_3O_4 is known to form as passivating layers on carbon steel surfaces and has therefore been concluded to be the reason for such corrosion resistance [4, 62, 71], instead of $FeCO_3$. Under corrosive CO_2-aqueous environments when contaminated with oxygen, Fe_3O_4 is proposed to form according to the Schikorr reaction [3]:

$$3Fe_{(s)} + 4H_2O_{(aq)} \rightarrow Fe_3O_{4.(s)} + 4H_{2.(g)} \qquad (2.16)$$

Fe_3O_4 is an iron oxide and belongs to the cubic crystal system and has a density of ~5.1 g/cm^3 [72]. Fe_3O_4 crystals have an octahedral morphology and the iron cations occupy two different sites in the crystal structure. All the Fe^{2+} and half the Fe^{3+} are octahedrally coordinated by O, while half the Fe^{3+} are tetrahedrally coordinated by O (see Table 2.4).

2.4.4 Chukanovite ($Fe_2(OH)_2CO_3$) Corrosion Products

$Fe_2(OH)_2CO_3$ forms in anaerobic and high pH (alkaline) CO_2-aqueous environments [62, 73, 74]. Al-Hassan *et al.* [61], and De Marco *et al.* [2], first detected its formation on carbon steel as a corrosion product under CO_2 conditions using *ex-situ* and *in-situ* X-ray diffraction techniques. $Fe_2(OH)_2CO_3$ appears as needle-like, plate-like or lath-like crystals [4,73], belongs to the prismatic class of the monoclinic crystal system [75] and has a density of ~ 3.6 g/cm^3 (see Table 2.4). The precipitation of $Fe_2(OH)_2CO_3$ may be in the form of:

$$2Fe^{2+}_{(aq)} + CO^{2-}_{3.(aq)} + 2H_2O_{(aq)} \rightarrow Fe_2(OH)_2CO_{2.(s)} + 2H^{+}_{(aq)} \quad (2.17)$$

$Fe_2(OH)_2CO_3$ is not reported in oil and gas failure analyses, or *often* in laboratory studies because it is has been suggested that the compound is metastable with respect to $FeCO_3$ or FeO(OH) [76, 77]. The needle/plate-like morphology of $Fe_2(OH)_2CO_3$ would suggest that it is not likely to be a phase that protects the carbon steel surfaces against corrosion. It would appear that $Fe_2(OH)_2CO_3$ crystallites are, perhaps, not always in intimate contact with the iron surface. The needle/plate-like morphology of $Fe_2(OH)_2CO_3$ crystals and their orientation on the surface shows that they still offer convenient electrolyte access to the underlying substrate and that it is not likely to be a phase that protects the carbon steel surfaces against corrosion.

Table 2.4 presents a summary of the common CO_2 corrosion products encountered in the oil and gas field (or not with respect to $Fe_2(OH)_2CO_3$) and their relative chemical composition, morphologies and structures.

The review that follows in Chapter 3 focuses only on one form of corrosion product formed on the internal walls of carbon steel pipelines: iron carbonate. The aim of Chapter 3 is to present a theoretical background on $FeCO_3$ formation. Firstly the basic principles of nucleation and growth kinetics and the factors that influence the formation of $FeCO_3$ are presented. Then, a review of the different *in-situ* synchrotron methods used to follow the evolution of corrosion products follows.

Table 2.4. Summary of the common CO_2 corrosion products encountered in the oil and gas field.

Crystal	**CO_2 Corrosion Products**		
Mineral	Iron carbonate	Magnetite	Chukanovite
Category	Carbonate	Iron oxide	Hydroxide
Composition	$FeCO_3$	Fe_3O_4	$Fe_2(OH)_2CO_3$
System	Trigonal	Cubic	Monoclinic
Morphology	Rhombohedral	Octahedral	Plate-like
	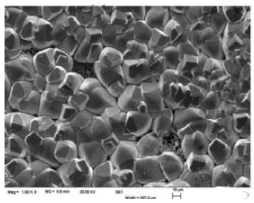	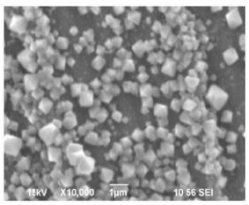	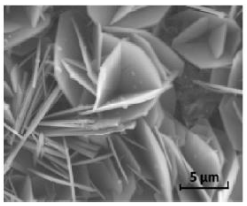
Structure	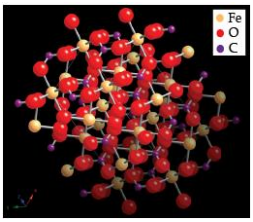	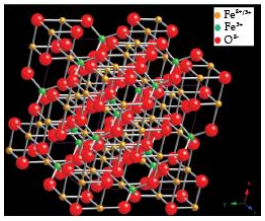	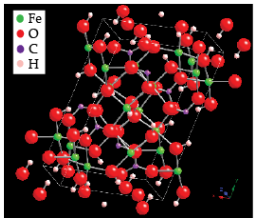
Density (kg/cm^3)	~3.69	~5.1	~3.6

Chapter 3
A Review of $FeCO_3$ Formation in the Oil and Gas Industry: Importance of $FeCO_3$ in Corrosion Mitigation

During oil and gas production and transportation, in CO_2 conditions, $FeCO_3$ is often the predominant corrosion product layer found in carbon steel pipelines and piping systems. Since the $FeCO_3$ formation process is one of the most important factors governing the corrosion rate, understanding the factors governing the rate of $FeCO_3$ precipitation is an important step in understanding the overall CO_2 corrosion process and this is detailed in this chapter. The CO_2 corrosion mechanism and the formation of $FeCO_3$ is an extremely complex process due to fluctuation operating conditions and environmental parameters during oil and gas production and transportation. Figure 3.1 outlines the complexity the parameters that will influence the kinetics of $FeCO_3$ formation and removal and the protectiveness offered which will be reviewed later in this chapter. Ultimately, the kinetics of $FeCO_3$ precipitation is driven by the supersaturation of the system which is a result of environmental factors and will be the starting point of the review following.

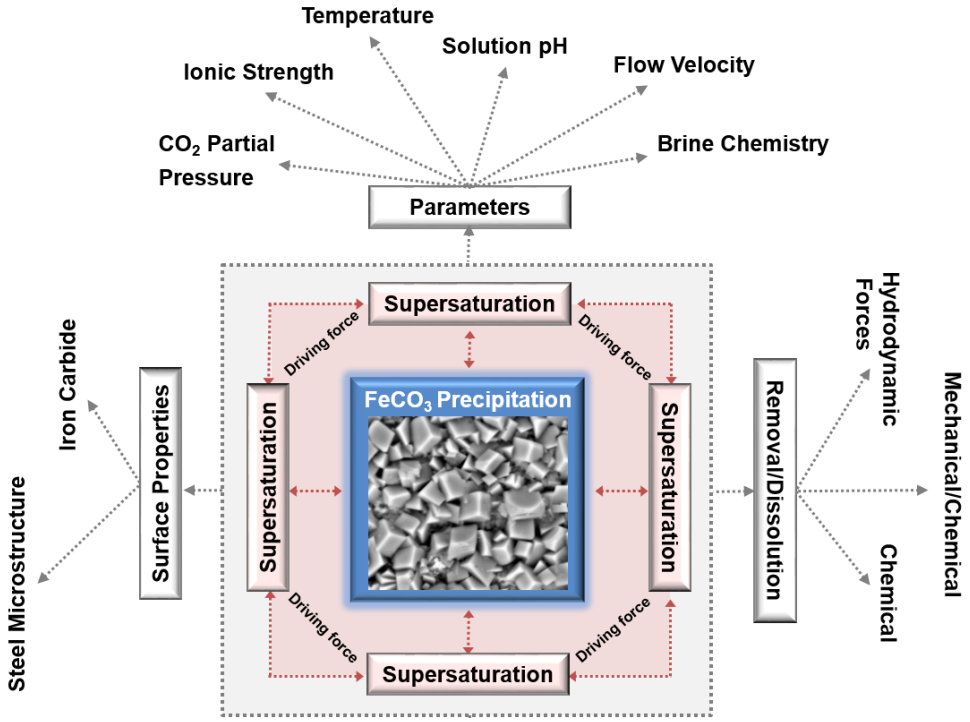

Figure 3.1. An outline illustrating the complexity and factors that will influence the kinetics and protective of $FeCO_3$ formation.

The magnitude of the corrosion rate and the occurrence or not of localized corrosion is determined by the nucleation, growth, morphology and stability of this corrosion product layer. The physical morphology of the $FeCO_3$ corrosion product is known to be detrimental in corrosion protection efficiency. As such, a compact, tight film usually protects the steel while a loose, poorly adherent film does not [76]. Moreover, the present review and research aims of elucidating on the mechanism and formation of $FeCO_3$ and taking advantage of this naturally forming film and rely on it in order to better protect the steel structure and will focus on some of the most influential parameters on the kinetics of $FeCO_3$ formation and the protectiveness offered.

3.1 $FeCO_3$ Formation Driving Force: Saturation Ratio and Relative Supersaturation

In CO_2 corrosive environments, the precipitation of $FeCO_3$ becomes thermodynamically possible when the concentration of $[Fe^{2+}]$ and $[CO_3^{2-}]$ ions exceed the solubility product (K_{sp}). $FeCO_3$ precipitates via the following reaction:

$$Fe^{2+}_{(aq)} + CO^{2-}_{3(aq)} \rightarrow FeCO_{3.(s)} \tag{3.1}$$

$FeCO_3$ film formation is a complex process, but when the system is saturated in respect to $FeCO_3$, the crystals can cover portions of the steel surface and make it unavailable for corrosion. $FeCO_3$ supersaturation (SS_{FeCO_3}) is found to be one of the key factors and the driving force that determines both the $FeCO_3$ precipitation process and the propagation of localised corrosion when a galvanic cell is established [79, 80]. A high degree of supersaturation is required in the bulk solution for the formation of protective $FeCO_3$ onto the steel surface. The saturation ratio SS_{FeCO_3} is defined as:

$$SS_{FeCO_3} = \frac{[Fe^{2+}][CO_3^{2-}]}{K_{sp}} > 1 \tag{3.2}$$

Where, K_{sp}, the solubility product for $FeCO_3$ is:

$$K_{sp} = [Fe^{2+}]_{eq}[CO_3^{2-}]_{eq} \tag{3.3}$$

$[Fe^{2+}]$ and $[CO_3^{2-}]$ (in mol/m^3) are the concentrations of ferrous and carbonate ions, respectively. $[Fe^{2+}]_{eq}$ and $[CO_3^{2-}]_{eq}$ are the concentrations of the species in equilibria. K_{sp} (in mol^2/m^6) is a function of ionic strength and temperature and the unified expression of K_{sp} is shown in Equation (3.3). This equation was developed by Sun, Nesic and Woollam based on their experimental data [81].

$$logK_{sp} = -59.3498 - 0.041377T_k - \frac{2.1963}{T_k} + 24.5724\log(T_k) + 2.518I^{0.5} - 0.657I \quad (3.4)$$

Where T_k is temperature in Kelvin and I is the ionic strength and can be calculated using Equation (3.5).

$$I = \frac{1}{2}\sum_i c_i z_i = \frac{1}{2}(c_1 z_1^2 + c_2 z_2^2 + \cdots) \quad (3.5)$$

Where c_i represents the concentration of each species in the solution (mol/m^3) and z_i is the charge of the species.

The supersaturation of $FeCO_3$, is an extremely important parameter influencing the precipitation. The nucleation of $FeCO_3$ is initiated onto the steel surface when the solubility limit has been exceeded ($SS_{FeCO_3} > 1$). When the solubility limit has been exceeded, a protective, dense, uniform layer of $FeCO_3$ will form on the steel surface and decreases the corrosion rate by acting as a diffusion barrier for the cathodic reactions and by blocking a portion of the steel and preventing electrochemical reactions from occurring. However, if conditions are not favourable of $FeCO_3$ formation and the system is under-saturated ($SS_{FeCO_3} < 1$), nuclei formation is possible but only a partially protective, porous film will form on the surface. This could result in localised removal of the film which could lead to localised attack or mesa attack [46]. These processes are summarised in Figure 3.2.

Crystalline $FeCO_3$ precipitates on to carbon steel surfaces via nucleation and crystal growth, similar to mineral scales (e.g. $CaCO_3$ formation from natural waters) [82]. Prior to growing into a crystal, it means that $FeCO_3$ complexes have to initially coagulate into a cluster, whilst orienting on to a crystal lattice when they have overcome the energy barrier for crystallisation.

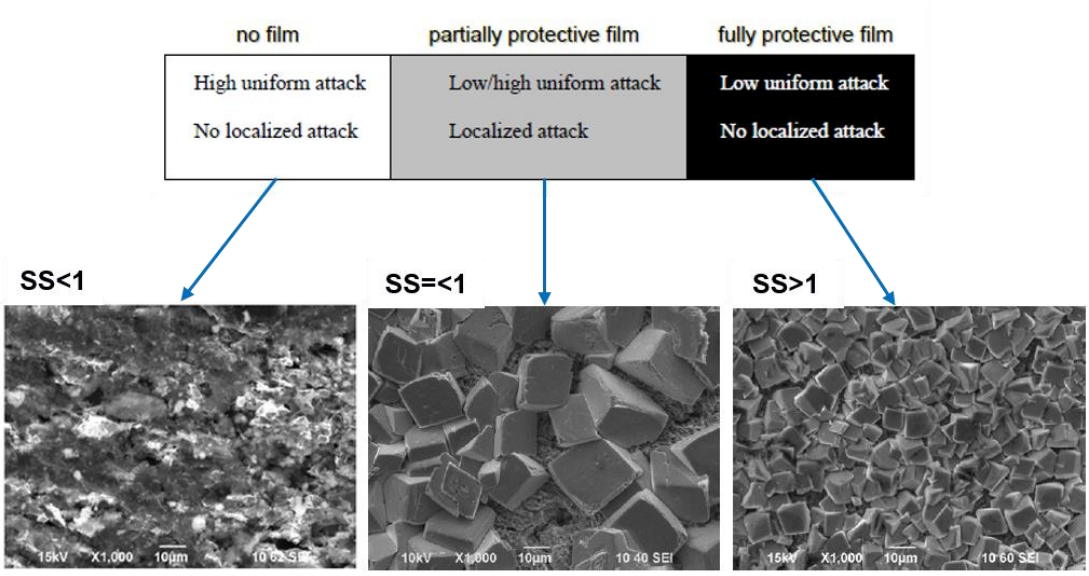

Figure 3.2. A schematic showing the influence of system saturation on the corrosion mechanism and morphology of $FeCO_3$.

Such a process is facilitated when there is an excess of Fe^{2+} and CO_3^{2-} and hence why precipitation is favourable only when SS_{FeCO_3} is much greater than one as previously mentioned [83]. The dominant step will therefore determine the final film morphology and ultimately the level of protection offered. The assumption is made that these two processes are related to the relative supersaturation (S_R):

$$S_R = \frac{Q - Q_{eq}}{K_{sp}} = SS_{FeCO_3} - 1 \tag{3.6}$$

Where Q is the concentration of the solute and Q_{eq} is the equilibrium solubility.

In practice, the process of $FeCO_3$ nucleation is observed more typically in the presence of impurity particles and foreign surfaces (heterogeneous nucleation) and the crystal growth should occur/dominate the overall kinetic process at low relative supersaturation [84]. The $FeCO_3$ precipitation process starts with heterogeneous nucleation, a process which is capable of occurring easily due to the numerous imperfections and adsorption sites to developing $FeCO_3$ nuclei, which decreases the interfacial tension term, and thus the overall Gibbs free energy of nucleation [83]. Nucleation is then followed by crystal growth which essentially limits the rate of precipitation. The nucleation rate is believed to increase exponentially with relative supersaturation, whilst crystal growth varies linearly with S_R. Conversely, when relative

supersaturation is high, nucleation dominates and a nano-crystalline or even amorphous film can develop [85]. Therefore, the nucleation rate of $FeCO_3$ increases rapidly only when a critical supersaturation is exceeded which obstructs the further growth of the crystals on the surface into larger crystals [85]. A simplified schematic (Figure 3.3) of the nucleation and crystal growth rate as a function of supersaturation on the same plot, the function of supersaturation on nucleation rate and crystal growth rate becomes clear [86].

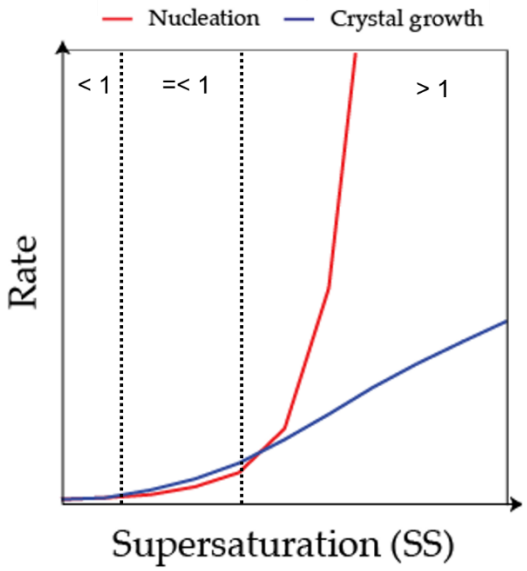

Figure 3.3. A schematic of nucleation rate and crystal growth rate as a function of supersaturation from [From 86].

The role of saturation on $FeCO_3$ precipitation was also described and demonstrated in the schematic produced by Lasaga in Figure 3.4 [87]. The different regions of crystal growth are shown in Figure 3.4 as a function of the concentrations of generic components [A+] and [B-] of the salt AB. The four regions were related to the crystal growth process associated with $FeCO_3$ by Yang [19] and the process of increasing in the level of saturation from region 1 to 4 is described.

As the concentration of Fe^{2+} and CO_3^{2-} increases, an originally undersaturated solution passes through the equilibrium saturation line (bold black line labelled SS=1). In the undersaturated solution (region 1), SS_{FeCO_3} < 1, it is thermodynamically unfavourable for new $FeCO_3$ crystals to form and there is the potential for dissolution existing crystals to dissolve away. Above SS_{FeCO_3} = 1, the solution is supersaturated, where SS_{FeCO_3} = 1, crystallisation of $FeCO_3$ is now favourable. However, in region 2, at low supersaturation values, some

crystallisation is possible but it can be difficult for nucleation events to take place (i.e. very long induction times) [83]. The growth $FeCO_3$ will only occur on seed crystals. In the absence of seed crystals, the system will remain supersaturated for a considerable period of time [87]. In region 3, Heterogeneous nucleation consists of nucleation induced by the presence of foreign particles, followed by crystal growth. Above some critical supersaturation (SS_{crit}), nucleation events are likely to proceed very fast ('spontaneously' or rapidly) (region 4).

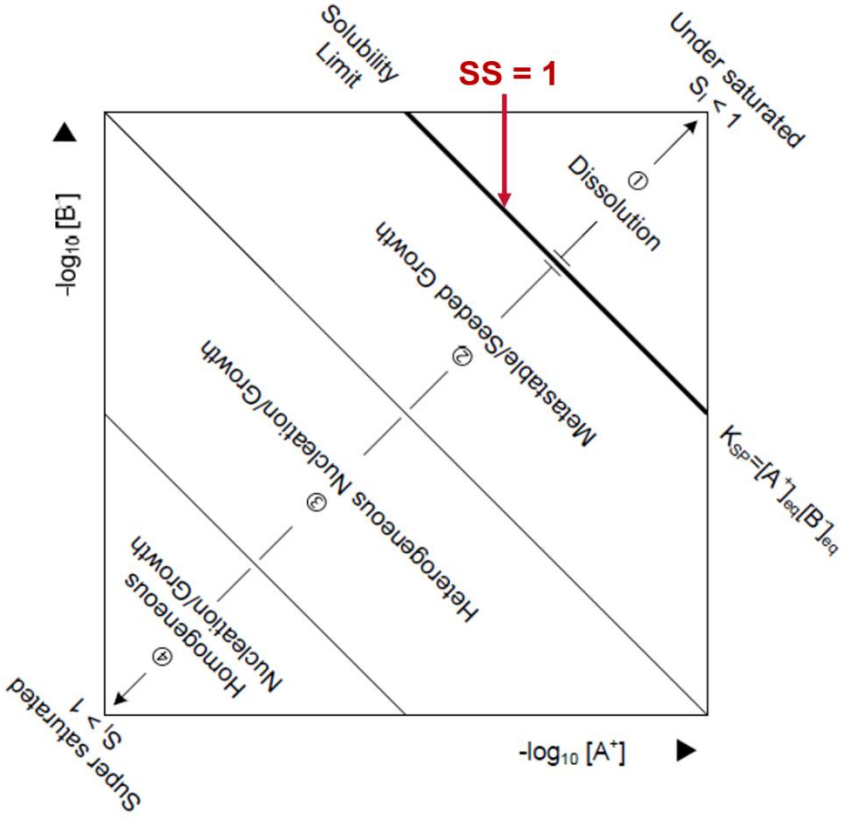

Figure 3.4. Regions of crystal growth, modified from [87].

Depending on the degree of supersaturation, precipitation of $FeCO_3$ can fall into region (2), (3) or (4) and corresponds to nucleation and/or crystal growth. In regions (3) and (4), both nucleation and growth can occur, whilst in Region (2), only growth of the crystals is possible. The key role of saturation level in $FeCO_3$ formation has long been identified, initially by Dugstad [59]. The importance of the saturation level near the steel surface was discussed by Nesic and Lee [89]. Moreover, an effort was also made to understand the role

of nucleation and crystal growth according to the saturation level of $FeCO_3$ close to the steel surface [90].

3.2 $FeCO_3$ Formation: Precipitation Kinetics

The growth of a protective $FeCO_3$ layer is heavily dependent upon the kinetics of the precipitation reaction and therefore understanding the factors governing the rate of precipitation and formation of $FeCO_3$ layer on the corroding surface is an important step in understanding the overall CO_2 corrosion process. Likewise, models of $FeCO_3$ precipitation kinetics are essential parts of broader CO_2 corrosion prediction models when evaluating the corrosion mechanisms under specific operating conditions. One of the simplest ways to account for a protectiveness of a $FeCO_3$ layer is to use the concept of the scaling tendency (ST), as introduced by van Hunnik *et al.* in 1996 [94]. Scaling tendency is defined as the ratio between $FeCO_3$ precipitation rate (PR_{FeCO_3}) and carbon steel corrosion rate (CR) expressed in the same units, as shown in Equation (3.7).

$$ST = \frac{PR_{FeCO_3}}{CR} \tag{3.7}$$

When the ST is much smaller than one, very porous and less protective $FeCO_3$ layers form due to the undermining effect of corrosion. Conversely, when ST is larger than one protective $FeCO_3$ layers form.

A number of corrosion prediction models are available in the literature; however, how to account for the effect of protective layers is a key component of successful corrosion rate prediction, since the presence of protective $FeCO_3$ layer can significantly slow down the corrosion rate [84]. The difficulty of modelling $FeCO_3$ layer growth is the main cause for the prediction deviations in the existing models. Different strategies have been proposed by various authors to account for the $FeCO_3$ effect. Most models incorporate an empirical factor into the corrosion calculations; some determine $FeCO_3$ effect based on thermodynamic criteria and others simulate $FeCO_3$ layer growth kinetics. Although no consensus has been reached as to the strategy for modelling the $FeCO_3$ layer effect, a satisfactory corrosion prediction can be achieved if the models are carefully calibrated with a good source of

experiment data. In the corrosion literature there are four models reported for calculating the rate of $FeCO_3$ precipitation, they are:

- Greenberg and Tomson [95, 96];
- Johnson and Tomson, [88, 91];
- Sun and Nesic, [81]; and
- van Hunnik *et al.* [94];

The experimental method used by Johnson and Tomson [88, 91], Greenberg and Tomson [95, 96] and van Hunnik *et al.* [100] to characterize precipitation rates was based on the measurement of the consumption of Fe^{2+} ion concentration in the bulk solution [84]. The study of Sun and Nesic [81] obtained precipitation rates by the weight change measurement of the precipitated $FeCO_3$ on the corroding steel specimen [88]. Semi-empirical equations for precipitation rate prediction were derived by all the researchers using the same general form:

$$PR_{FeCO_3} = k_r \frac{A}{V} \sigma(S_R) \tag{3.8}$$

where k_r is the kinetic constant, $\frac{A}{V}$ is the surface area to volume ratio, σ is termed as the driving force which, for $FeCO_3$ crystal growth, is described as a function of the saturation ratio (S_R).

3.3 $FeCO_3$ Formation: Nucleation and Crystal Growth Kinetics and Theories

During the process of precipitation of $FeCO_3$, from nucleation to crystal growth, the driving force is the supersaturation, which in turn has an influence on the overall Gibbs free energy. The overall Gibbs free energy is known to decrease in the negative direction during the formation of a new volume of material, in this case $FeCO_3$ aggregate. The formation of $FeCO_3$ aggregates is easier when there is a negative Gibbs free energy due to the energy barrier to overcome being less whereas creating a new phase boundary in solution (i.e. a surface layer of crystals) increases the positive free energy which is unfavourable for nucleation of $FeCO_3$ new crystals [82]. According to thermodynamics, $FeCO_3$ aggregates would only form a nucleus if they

exceeded a critical size, r_c (where total change in Gibbs free energy (ΔG) has peaked). Beyond this maximum peak in ΔG, the decreasing free energy means that it is favourable for the $FeCO_3$ aggregate to nucleate and eventually crystallise and grow. The height of the free energy barrier ΔG_c at the critical size of the $FeCO_3$ aggregate, is inversely proportional to the square of supersaturation [97]. Meaning that as the supersaturation is increased, the critical nucleus size and the critical free energy requirement decrease.

Figure 3.5 shows a schematic of how the degree of supersaturation increases the thermodynamic driving force for nucleation, by decreasing the height of the free energy barrier and the critical cluster size which has been modified from [86].

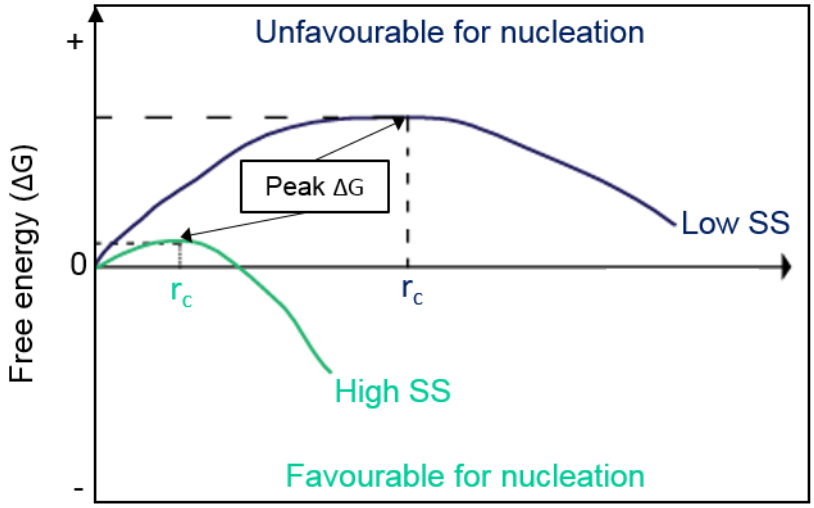

Figure 3.5. A schematic showing the free energy change during nucleation of a cluster, as a function of supersaturation, modified from [86].

It is energetically demanding for $FeCO_3$ crystals to nucleate in solution via homogenous nucleation. This is because the $FeCO_3$ aggregates would need to collide with each other in solution, overcome high interfacial tension during growth, and counteract intermolecular repulsion forces [86]. However, nucleation of $FeCO_3$ is considered to be heterogeneous nucleation in the presence of impurity particles and foreign surfaces. In this case, a carbon steel surface can offer adsorption sites to developing $FeCO_3$ nuclei. This process is less energetically demanding due to the decrease in the interfacial tension term [86]. Factors on a steel surface such as its structure, roughness,

composition and wettability, are important variables that influence crystal nucleation [83, 86].

Equation 3.9 and 3.10 provides a general expression for the free energy for homogeneous ($\Delta G_{c(\text{hom})}$) and heterogeneous ($\Delta G_{c(\text{het})}$) nucleation. The expression for heterogeneous nucleation is the free energy for homogeneous nucleation multiplied by a surface factor, $f(\theta)$:

Free energy for homogeneous nucleation:

$$\Delta G_{c(hom)} = \frac{16\pi\gamma^3 v^2}{3(-kTlnSS)^2} \tag{3.9}$$

Free energy for heterogeneous nucleation:

$$\Delta G_{c(het)} = \Delta G_{c(hom)} \times f(\theta) = \frac{16\pi\gamma^3 V^2}{3(-kTlnSS)^2} \times f(\theta) \tag{3.10}$$

Where SS is supersaturation, V is the volume of the aggregate, k is the Boltzmann constant (1.38 x10^{-23} $m^2kg/s^2/K$), T is temperature (K), γ is the interfacial tension and θ is contact/wetting angle between the nucleating phase and the foreign surface, i.e.

$$f(\theta) = \frac{(1 - cos\theta)^2 \times (2 + cos\theta)}{4} \tag{3.11}$$

$f(\theta)$ usually lies between 0 and 1, meaning that the Gibbs free energy for heterogeneous crystal nucleation is lower (and thus more favourable) compared to the required free energy for homogeneous nucleation [83].

If smaller critical cluster sizes, and lower ΔG_c are obtained at higher supersaturation, it implies that increasing supersaturation (SS) should make nucleation a more rapid process [83]. With this considered, at a high local supersaturation at the surface, $FeCO_3$ should be rapidly nucleating on to carbon steel surfaces [26, 86]. However, this phenomenon does not always happen for many reasons or this process can be delayed (e.g. surface structure, mass transfer effects etc.). The time that elapses between exceeding supersaturation to the creation of $FeCO_3$ aggregates and the onset of nucleation is known as induction time (T_{ind}).

Söhnel and Mullin [98] called induction time the time which elapses between the creation of the supersaturation and the first observable change in some physical property of the precipitating system (*i.e*. the appearance of crystals or turbidity change of solution conductivity change in solution composition etc.) [98]. A nuclei must grow to a detectable size therefore the induction time is composed of the nucleation time (T_n) and the time needed for a nucleus to grow until a detectable size (T_g) as shown in Equation 3.12 [99].

$$T_{ind} = T_n + T_g \tag{3.12}$$

The formation of a nucleus is a complex process: the constituents molecules have to coagulate in a stable manner (to avoid dissolution) and to be orientated into a fixed lattice. The collision of molecules usually starts the process of nucleation and then further molecules participates to the formation of the nucleus and so on [99]. Ion pairing and clusters are formed by electrostatic interactions between dissolved anions and cations. Then the clusters grow step by step by the addition of ions until a critical size [91]. The nucleation process occurs in very high supersaturated region and very rapidly [100]. In case of the formation of $FeCO_3$, the electrostatic interactions between the ferrous cations and the bicarbonate anions lead to the formation of the nucleus of $FeCO_3$.

The number of aggregates overcoming ΔG_c (or increasing to a size >> r_c) to form an $FeCO_3$ nucleus with time can defined as the rate of crystal nucleation (R_{Nuc}) as follows [86]:

$$R_{Nuc} = P[A]e^{\left(-\frac{16\pi\gamma^3 v^2}{3(kTlnSS)^2}\right)} \tag{3.13}$$

P is the probability that $[A]$ number of crystallising solute nuclei will grow into crystals [83, 97]. Once the nuclei are stable (when they are larger than the critical size), the growth process occurs to lead to the formation of a crystal of visible size. The growth is controlled by three general headings:

- the surface energy theory;
- the adsorption-layer theory; and
- the dislocation theory.

Precipitated nuclei demonstrate poor long-range order and are deemed to be nano-crystalline or ‘amorphous’. As the nucleated phase (infant crystal) begins to incorporate incoming $FeCO_3$ ‘growth units’ onto a lattice, it begins to

develop into a crystal. The growth of a crystal, then, must depend upon the frequency/positioning of the incoming growth units (determined by the environment), and the energetics associated with bonding to a particular site on the crystal surface. Defects on a crystal face in the form of dislocations (Figure 3.6 (b)), surface steps and kinks (Figure 3.6 (a)), for example, can provide energetically favourable binding sites [83, 86].

Several theories have been used to explain crystal growth over the decades, and some of the pertinent developments are summarised in [86, 100].

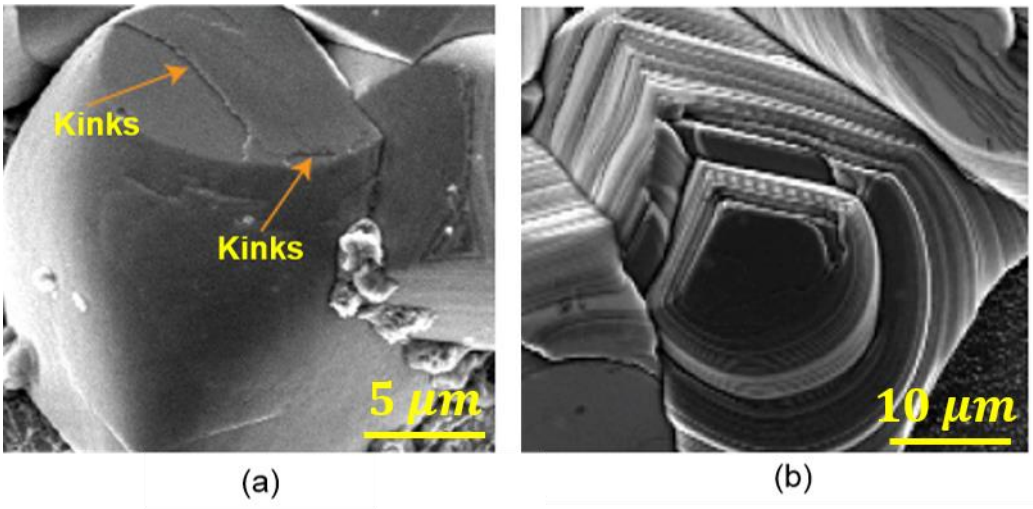

Figure 3.6. Different aspects of crystal growth in $FeCO_3$ revealed. (a) The orange arrows indicate a step on a growing face, and (b) a clear example of crystal spiral growth, taken and modified from [86].

3.4 $FeCO_3$ Formation Kinetics: Influencing Parameters

As a result of the $FeCO_3$ layer's ability to reduce the internal corrosion of carbon steel pipelines so significantly, understanding the factors which influence the rate of formation of this corrosion product are essential in developing a reliable corrosion prediction model and in enabling a robust corrosion management strategy for carbon steel pipelines. Regardless of advances made in both academia and industry, there still remains many questions and uncertainties (surrounding) the corrosion product layer formation in CO_2 corrosion of carbon steel. This ambiguity in the open literature indicates that more research needs to be done in order to elucidate the nature of corrosion products formed, as stated by Nesic [4]. This statement is true, particularly because $FeCO_3$ formation is an extremely complex

process which is influenced by subtle changes to a wide variety of natural, operational (physico-chemical) and metallurgical/material (surface) parameters throughout the oil and gas network during production and transportation of hydrocarbons. The following sections focus on the current understanding of the several environmental (such as temperature, pH, partial pressure, ferrous ion concentration other contaminants) and physical properties (such as fluid regime and velocity) which influence the rate of formation, morphology and protectiveness of $FeCO_3$ films.

3.4.1 Effect of Temperature and Ionic Strength

The formation of the $FeCO_3$ film is strongly dependent on the solubility and formation and one main factor that greatly affects the solubility of $FeCO_3$ the temperature and the solution ionic strength. The solubility of $FeCO_3$ is decreased as the temperature increases. $FeCO_3$ precipitation kinetics are accelerated at increased temperatures and the conditions for formation are favourable. This is due to the saturation level being higher at elevated temperatures. Films observed at higher temperatures have been identified as protective, dense, uniform and non-porous layers. At low temperatures, corrosion rates increase because of high solubility of the $FeCO_3$ film. As temperatures increase the $FeCO_3$ layer becomes more adherent to the metal surface and more protective in nature resulting in a decrease of the corrosion rate [43, 67, 101].

Several studies have examined the effect of temperature on the solubility product of $FeCO_3$ [81, 80, 95, 94, 96, 102, 103] and Table 3.1 lists some of the available models in literature which have been implemented to predict $FeCO_3$ solubility variation with temperature.

However, none of these models account for ionic strength. Sun and Nesic [81] developed a unified equation to cater for both temperature and ionic strength effects on $FeCO_3$ solubility. As part of their research, they initially reviewed the solubility models provided in Table 3.1. They found that the Greenberg and Tomson model was the most suitable model for describing the solubility limits as a function of temperatures ranging from 25 to 94°C. Although, it was noted that the model was generated under the belief that the ionic strength is 0. In reality, the ionic strength was actually 0.02 for their system because of the presence of H^+, HCO_3^-, CO_3^{2-}, OH^- and Fe^{2+} [104].

Table 3.1. Solubility product prediction models for $FeCO_3$ from various authors.

Author	Mathematical model
Greenberg and Tomson [84, 95]	$log(K_{sp}) = -59.2385 - 0.041377(T_K) - \frac{2.1963}{T_K} + 24.5724log(T_K)$
Marion *et al.* [80]	$log(K_{sp}) = -14.66 + \frac{1365.17}{T_K}$
Sun and Nesic [81]	$log(K_{sp}) = -10.13 - 0.0182(T_C)$
Braun [102]	$log(K_{sp}) = -10.2 - 0.0314(T_c)$
Benezeth *et al.* [103]	$log(K_{sp}) = 175.568 + 0.0139(T_K) - \frac{6738.483}{T_K} - 67.898\log(T_K)$

With this factor accounted for, a revised equation was obtained (which is valid for I=0):

$$log(K_{sp}) = -59.3498 - 0.041377(T_K) - \frac{2.1963}{T_K} + 24.5724log(T_K) \quad (3.14)$$

Introducing the effect of ionic strength from Silva *et al.* [105] produced the final unified equation which has been illustrated previously by Nesic *et al.* (Equation 3.4). The proposed unified equation by Sun and Nesic satisfies both the temperature and ionic strength fluctuations and the variation of the $FeCO_3$ solubility at various temperatures for different ionic strengths is shown in Figure 3.7.

From the results obtained using their modified equation, as the ionic strength increases, the solubility of $FeCO_3$ also increases. However, at higher values of ionic strength, the overall influence on K_{sp} reduces with each incremental change in the ionic strength of the solution. $FeCO_3$ precipitation becomes more favourable with a lower K_{sp} at higher temperatures.

De Waard and Milliams [20] studied the effect of temperature (up to 80°C) at pH 4.0 in CO_2 corrosion. They concluded that the corrosion rate increased

with temperature due to the kinetic rate of the electrochemical reactions being accelerated by temperature. Gray *et al.* [106, 107] also suggested that corrosion rate increased as temperature increased. However, at temperatures of 90-125°C, the corrosion rate did not change with temperature because there was protective $FeCO_3$ formation on the steel surface. It was suggested that $FeCO_3$ slowed down both anodic and cathodic reactions.

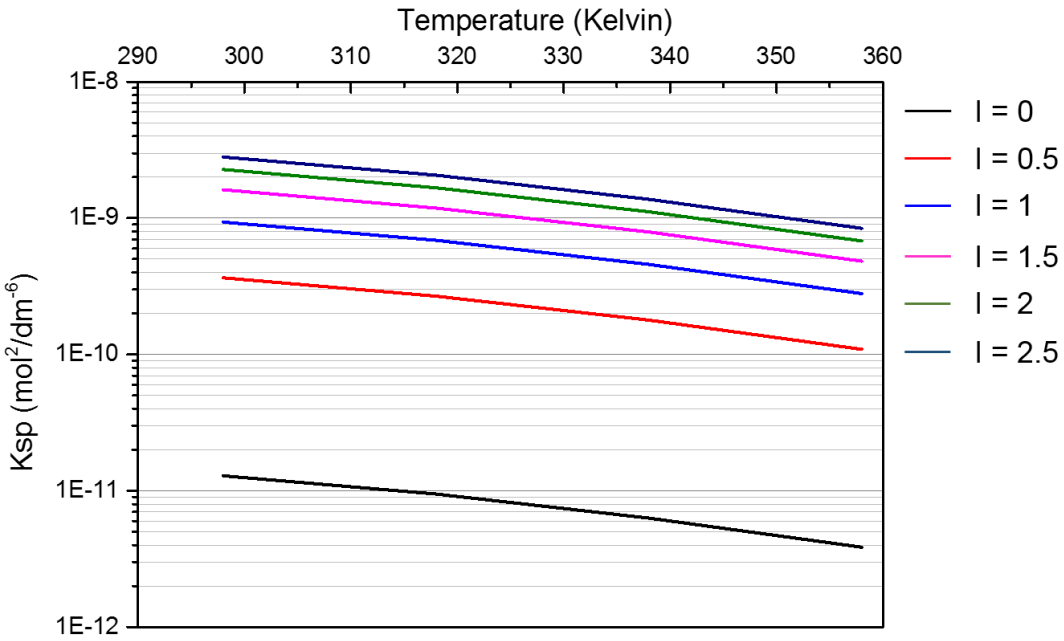

Figure 3.7. Plots of $FeCO_3$ solubility as a function of temperature for varying levels of ionic strength from 0 to 2.5 using the Sun and Nesic model [81].

Similarly, Ikeda *et al.* [108] and de Waard and Lotz [92] found that the corrosion rate increased with temperature until it reached maximum values around a temperature range of 60-120°C, depending on partial pressure of CO_2, then it decreased with temperature due to corrosion product formation.

A study by Tanupabrungsun *et al.* [36] focused on elevated temperatures. In all cases observed, the initial corrosion rates were much higher, releasing more corrosion products into the aqueous solution making the formation of $FeCO_3$ kinetically favourable. As expected, the initial corrosion rates are high at increased temperatures. However, the kinetics of $FeCO_3$ precipitation also increases with temperature which as discussed decreases the corrosion rate. At 80°C and pH 4.0, the condition was thermodynamically unfavourable for $FeCO_3$ formation, so there was no $FeCO_3$ found on the steel surface.

However, the equilibrium of $FeCO_3$ formation is shifted to lower pH when temperature increases. In other words, at higher temperature it is easier to reach saturation with respect to $FeCO_3$ even at lower pH. At temperatures above 150°C, Fe_3O_4 has been reported to be thermodynamically favoured [36]. Therefore, a mixture of $FeCO_3$ and Fe_3O_4 was observed. Enhanced corrosion $FeCO_3$ kinetics, and therefore $FeCO_3$ 'protectiveness', have been reported with increases in test solution temperature [90, 109, 110].

The physical structure and morphology of $FeCO_3$ (from 60°C – 90°C) has been determined using cross-sectional analysis under Scanning Electron Microscopy (SEM) [110]. The analysis indicates that thinner, denser films offering a greater degree of protection form with increasing solution temperature [90, 109, 110]. Figure 3.8, shows top view and cross-sectional SEM images of $FeCO_3$ films formed at different temperatures by Ingham *et al.* [110].

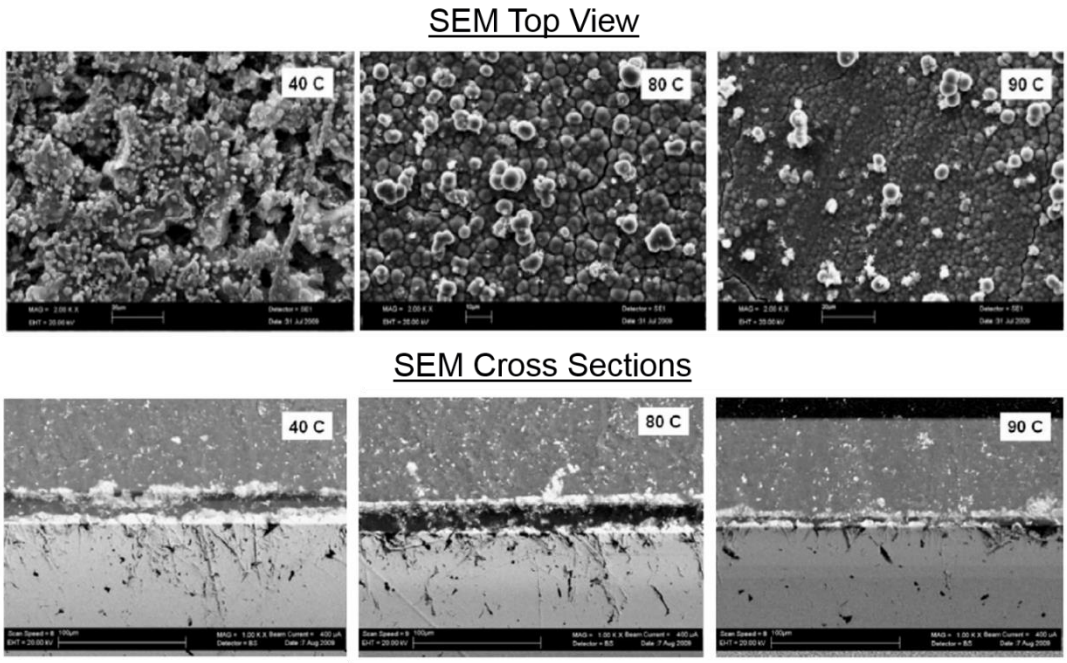

Figure 3.8. SEM images of $FeCO_3$ films (Top view morphologies and corresponding cross sections) formed at different temperatures at pH 6.8, pCO_2 = 0.54 bar under galvanostatic control at 12 mA/cm^2 by Ingham *et al.* [110].

The film formed at 40°C has a porous structure, while those formed at 80 and 90°C are more compact and comprised of spheres, with the individual spheres in the 90°C film being noticeably smaller (1–2 µm) than those in the 80°C film (5 µm). The spherical crystals in these images are notably different from the cubic/rhombohedra $FeCO_3$ crystals observed by Morshed [41] and Nazari *et*

al. [111] in similar test environments. This is most likely due to the faster formation of the crystals in tests performed by Ingham *et al.* [110] through the use of galvanostatic tests compared to the open-circuit tests carried out by Morshed and by Nazari [41, 111]. In the tests by Nazari *et al.* [111] at 65°C or higher appeared to be the threshold temperature for formation. Conversely, others suggest that $FeCO_3$ can develop and become thicker in CO_2 environments within a similar temperature range [57], although they might become thinner as temperatures increase to 160°C [100, 112]. It is too difficult to identify the source of such discrepancies because other variables (e.g. microstructure, substrate finish, Fe^{2+} concentration, solution flow, pH etc.) will affect the eventual $FeCO_3$ thickness/morphology.

All authors are in agreement that an increase in temperature improves the protectiveness of $FeCO_3$. However, there is no general consensus on the actual threshold temperature at which a protective $FeCO_3$ film can form. A number of authors have suggested that protective $FeCO_3$ films form only beyond a temperature of 60-70°C [114, 115]. However, research by Videm and Dugstad [54] and Pessu *et al.* [93] demonstrated that a protective $FeCO_3$ film is capable of forming at a temperature of 50°C under the right conditions (high enough pH in a Fe^{2+} saturated system). Nonetheless, there is consensus that higher temperature decreases the permeability in $FeCO_3$ layers at a faster rate, which is an important attribute regarding protection of the underlying carbon steel against corrosion.

3.4.2 Effect of Solution pH

The solution pH could potentially be regarded as one of the most important factors in influencing $FeCO_3$ formation, due to the fact that pH is directly related to CO_3^{2-} concentration and therefore affecting the saturation level. Increasing pH reduces $FeCO_3$ solubility (and increases the local supersaturation) because less Fe^{2+} ions are required to exceed the solubility limit and generate substantial levels of precipitation (as shown in Figure 3.9) and generally leads to a reduction of the corrosion rate by influencing the electrochemical mechanisms and the formation of protective $FeCO_3$ films [49, 99, 124]. Figure 3.9 is extracted from a publication by Dugstad *et al.* [26] and indicates the amount of Fe^{2+} required by a corroding surface to reach $FeCO_3$ saturation as a function of pH in a 1% NaCl solution at the start of the corrosion process. Referring to Figure 3.9, it can be observed that increasing pH from 4 to 5 reduces the solubility of Fe^{2+} by approximately a factor of 5. However, a further increase from 5 to 6 reduces the solubility 100 times. A lower solubility

can correspond to a higher level of supersaturation, which inevitably leads to an accelerated precipitation process [41].

Pessu *et al.* [93] demonstrated that pH not only influences precipitation kinetics, but that it can have a profound effect on the morphology and the level of protection offered by $FeCO_3$ films. Their test methodology involved exposing X65 steel samples to a 3.5 wt. % NaCl solution at 50°C for 168 hours at three different pH levels of 3.8, 6.6 and 7.5. Figure 3.10 shows the effect of pH change on the morphology of the corrosion films produced. At pH 3.8 (Figure 3.10 (a)) a non-protective, amorphous/nano-polycrystalline $FeCO_3$ film developed. Increasing pH to 6.6 resulted in a protective, cubic $FeCO_3$ film (Figure 3.10 (b)) which grew progressively on the steel surface, while at pH 7.5, film formation was rapid and produced rhombohedral $FeCO_3$ crystals with sharp, well defined edges (Figure 3.10 (c)) which were extremely protective. As pH was increased, there was a notable increase in the density and compactness of the corrosion product layer, which linked strongly to the level of protection offered to the steel substrate.

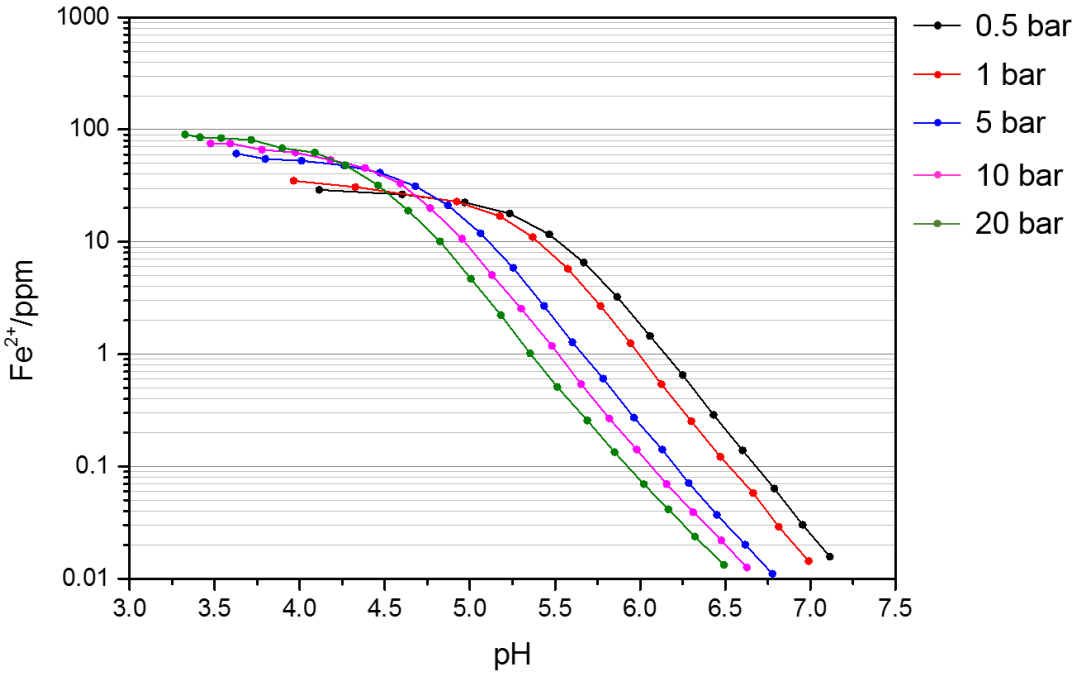

Figure 3.9. Amount of Fe^{2+} required to reach $FeCO_3$ saturation in a 1 wt.% NaCl solution as a function of pH for different CO_2 partial pressures - data extracted from Dugstad [26].

The effect of pH at temperatures up to 100°C has been described by Tanupabrungsun *et al.* [36]. The mechanisms of corrosion and the effect of

key parameters are less understood above 100°C. Although from the work of Tanupabrungsun *et al*. [36] it is clear to see that the $FeCO_3$ layer at higher pH values at the same temperature results in a crystalline layer pact full of smaller dense crystals resulting in a more protective layer in agreement with Pessu *et al.* [93]

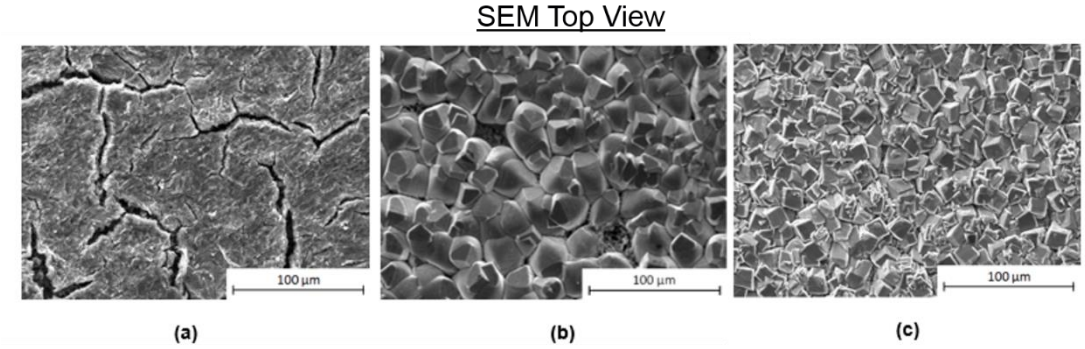

Figure 3.10. SEM images of X65 steel surface after exposure to a 3.5 wt.% NaCl solution at a temperature of 50°C for 168 hours ; (a) starting pH of 3.8 (b) pH 6.6 and (c) pH 7.5, taken from Pessu *et al.* [93].

In Figure 3.11 the calculated effect of pH on solubility of $FeCO_3$ is shown for a given set of operating conditions by Han [56]. The calculated effect of pH on the 'grey zone' is shown, where propagation of localised corrosion can be expected. Practical limits for 'grey zone' are taken to be $0.5 < SS_{FeCO_3} < 2$.

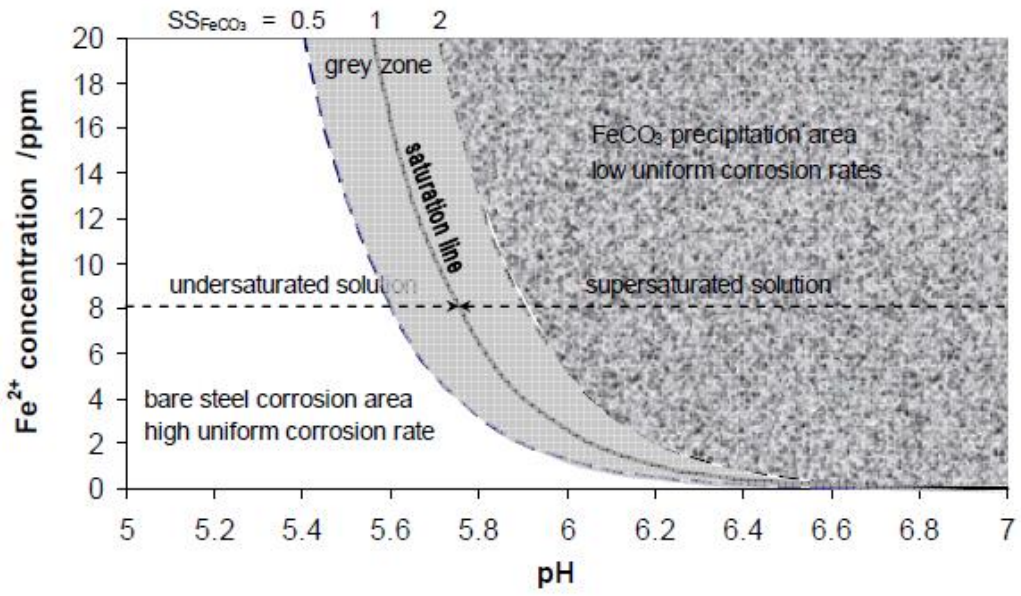

Figure 3.11. A schematic showing the calculated effect of pH on solubility of $FeCO_3$ is shown for a given set of operating conditions by Han [56].

If the range for Fe^{2+} concentration is 0 – 10 ppm in the field, then under these conditions the graph suggests that it is unlikely for $FeCO_3$ precipitation and

localised corrosion propagation to occur below pH 5.6. In this case, the localised attack is possible in the range of pH 5.7 to 6.4. Above pH 6.6 it appears that, for almost any Fe^{2+} concentration, $FeCO_3$ will precipitate resulting in lower corrosion rates.

3.4.3 Effect of CO_2 Partial Pressure

With regard to the gas partial pressure effect, it was shown that an increase in CO_2 partial pressure at a constant pH value will lead to an increase in the bicarbonate concentration which inevitably favours the supersaturation state thus accelerating the iron carbonate precipitation process if the pH value is high enough. The effect of the CO_2 partial pressure on the ferrous iron concentration is rather complex and evolve as per Figure 3.12.

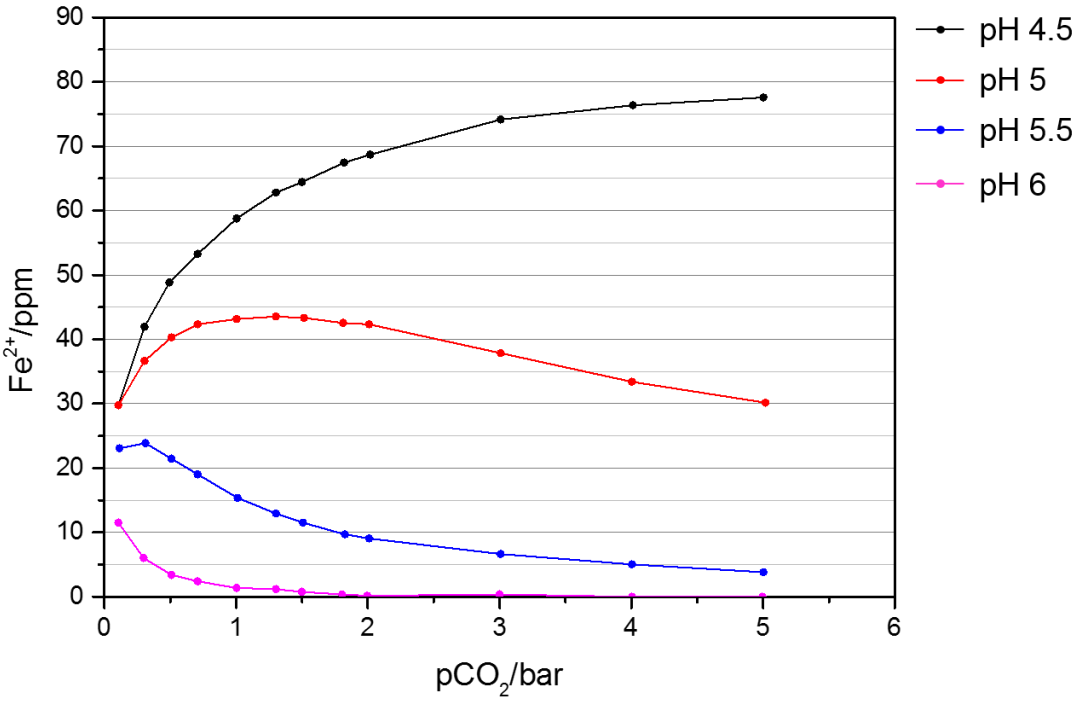

Figure 3.12. Concentration of Fe^{2+} required to reach $FeCO_3$ saturation, plotted as a function of pCO_2 at pH levels of 4, 5, 5.5 and 6 for a 3.5 wt.% NaCl solution at 60°C – data extracted from Dugstad [26].

Based on these plots it appears that for pH levels of 5 and 5.5, the solubility of Fe^{2+} exhibits goes through a maximum value as pressure is increased. At these lower values of pH the solubility increases with CO_2 partial pressure up to a certain point, while an opposite trend is observed at a pH of 6. These results suggest that in some instances, an increase in CO_2 partial pressure may reduce or increase the formation of a protective $FeCO_3$ film. Most

importantly, they reflect that pH alone cannot be used directly to predict the likelihood of $FeCO_3$ formation. In the absence of a protective film, an increase in CO_2 partial pressure generally leads to an increase in corrosion rate [117]. However, when conditions become favourable for the formation of $FeCO_3$, an increase in CO_2 partial pressure can enhance the precipitation process.

If other conditions remain the same (temperature, pH, etc.), the concentration of carbonate and bicarbonate can be increased due to the increase of CO_2 partial pressure, which consequently leads to an increase of saturation level with respect to $FeCO_3$ [19]. The CO_2 partial pressure plays an important role in CO_2 corrosion both for film-free conditions (formation of non-protective films) and for film-forming conditions. In most publications the authors established a relationship between CO_2 partial pressure and corrosion rate [8, 46, 108, 118-121]. Generally, under film-free conditions higher CO_2 partial pressures results in higher corrosion rates by reducing the pH and by increasing the rate of carbonic acid reduction [122]. This agrees with the finding [118, 123] that the anodic reaction is practically unaffected when the CO_2 partial pressure is increased from 3 to 20 bar while the cathodic limiting current density is strongly increased due to a higher reservoir of carbonic acid.

The effect of CO_2 partial pressure on solubility of $FeCO_3$ and indirectly on localised corrosion propagation likelihood has been studied by J. Han [56]. If all other conditions are the same, higher partial pressure of CO_2 leads to higher dissolved CO_2 concentration and eventually to higher concentrations of CO_3^{2-}. This means that the solubility of $FeCO_3$ decreases when the CO_2 partial pressure is increased as shown in Figure 3.13. From the conditions used in the work by Han [56], it can be seen in Figure 3.13 that $FeCO_3$ will easily form as the partial pressure of CO_2 exceeds 2 bar for any measurable Fe^{2+} concentration. The ‘grey zone’ conditions can be practically met only in the lower range of partial pressures of CO_2 which are most common for field conditions (< 2 bar). At higher partial pressures of CO_2 the ‘grey zone’ is possible only for very low Fe^{2+} concentration, allowing the formation of protective $FeCO_3$ films, suggesting a very low likelihood of both uniform and localised attack. Figure 3.14 shows the effect of CO_2 partial pressure on the morphology of $FeCO_3$ in a study by Gao *et al.* [124]. With increasing the CO_2 partial pressure, the layer became more compact together with a reduction in grain size of $FeCO_3$. At the same time, the corrosion product layer thickness increased.

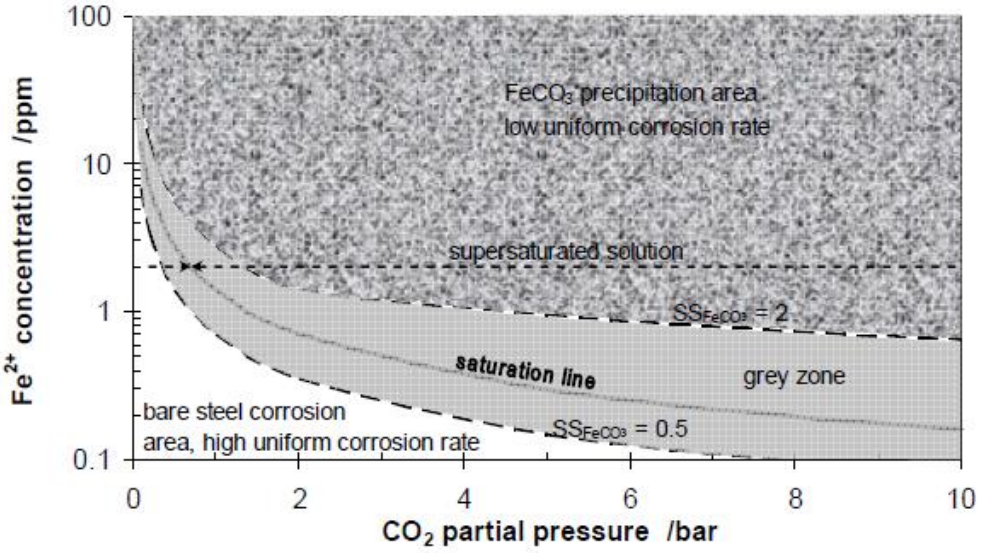

Figure 3.13. A schematic showing the calculated effect of CO_2 partial pressure on solubility of $FeCO_3$ is shown for a given set of operating conditions by Han [56].

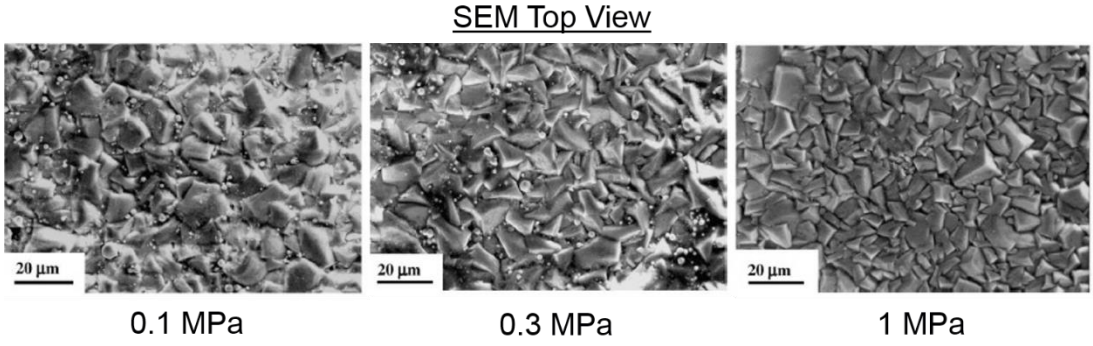

Figure 3.14. SEM images showing the effect of CO_2 partial pressure on the morphology of $FeCO_3$ in a study by Gao *et al.* [124].

3.4.4 Effect of Flow Velocity

Many researchers [125-129] investigated the effect of flow on CO_2 corrosion and the formation of $FeCO_3$. It was found that the corrosion rate increased as a function of flow in the absence of corrosion product layers. An increase of flow velocity leads to an enhanced mass transfer process, and the released Fe^{2+} ions due to corrosion can be more easily transported away from the steel surface, whilst H^+ ions are transported to the surface (decreasing the local pH and increasing the corrosion rate) [117, 130]. Figure 3.15 shows the species

in the system that will be influenced through the flow velocity of the system (through mass transfer).

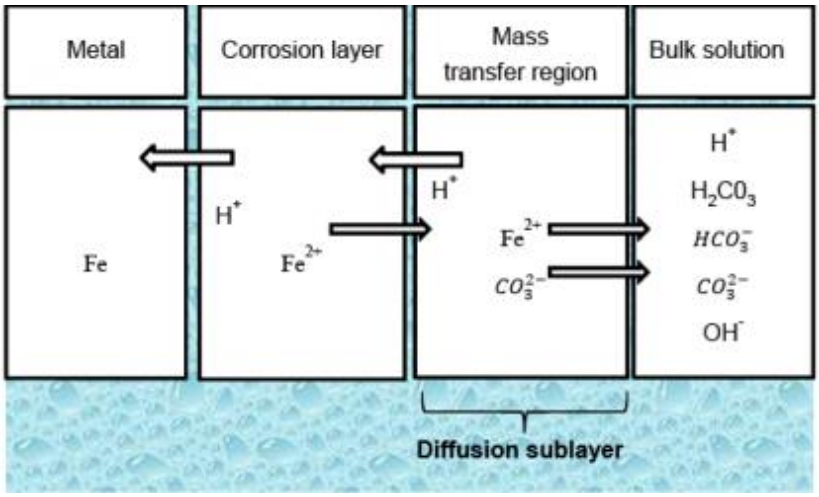

Figure 3.15. A schematic showing the species in the system that will be influenced through the flow velocity of the system (through mass transfer).

Below a critical flow intensity the corrosion rate increases only gradually with increasing flow intensity [29, 118]. Above the critical flow intensity the interaction between the fluid and the wall becomes so intense that protective films are difficult to form due to the near-wall turbulence elements which can damage the integrity of the already formed protective $FeCO_3$ film [131, 132]. In this case the dissolution of the unprotected (bare) metal surface is transport controlled. In the presence of protective $FeCO_3$ layer, the flow intensity can influence to a certain extent the transport of cathodic species towards the steel surface yielding an increase in corrosion rates at high flow velocities.

Consequently, although the mass flux of Fe^{2+} from the surface is increased (which would increase $FeCO_3$ saturation at the surface), the hydrodynamic conditions compete against this effect in an attempt to lower the surface saturation by transporting Fe^{2+} away from the surface more readily and slowing down the precipitation rate of $FeCO_3$ [43]. Considering the higher corrosion rate experienced under increased flow velocity, the scaling tendency becomes lower. Therefore under high flow velocity, it is more difficult to form a protective layer. Once a protective $FeCO_3$ layer is developed the question is whether it will remain protective. It was reported that under highly turbulent flow conditions, the protective $FeCO_3$ layer could be damaged and lead to severe localised corrosion [43].

A study by Nesic *et al*. [128] suggested that at higher temperatures (50-80°C), there is no flow sensitivity on the corrosion rate due to the rapid formation of $FeCO_3$ on the steel surface and its action as a mass transfer barrier. Within this study, Nesic also reported that the wall shear stresses generated at the interface of a pipeline during transportation are an order of magnitude lower than the forces needed to damage $FeCO_3$ layers [19].

However, through visual comparison of SEM images in a study by Tanupabrungsun [129], the author has suggested that the $FeCO_3$ crystals appear to be damaged after increasing the flow velocity of system, see Figure 3.16 (d). In the tests conducted in stagnant conditions (Figure 3.16 (a)), the concentration of Fe^{2+} will increase the pH. However, in the tests ran under flowing conditions (Figure 3.16 (b), (c) and (d)), the mass transfer of cathodic species reduces the local pH at the steel surface. In other words, a decrease in pH reduces the supersaturation to the point that in the local boundary layer, the solution becomes under-saturated with respect for $FeCO_3$ formation. Therefore, the $FeCO_3$ crystals that appear to be damaged in Figure 3.16 (d), is most likely a result of chemical dissolution rather than mechanical damage. The decrease in surface pH through increasing the flow velocity was also confirmed experimentally by Ning [133].

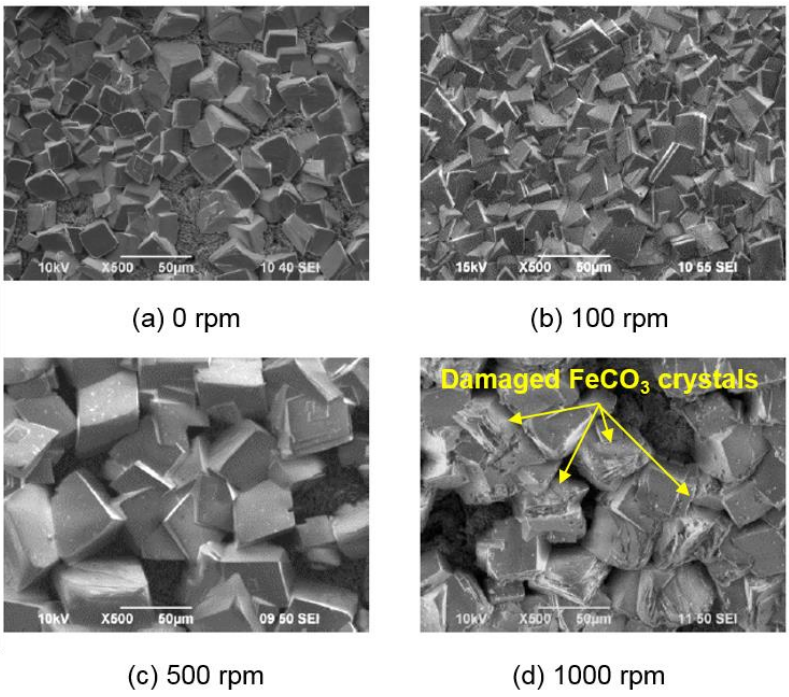

Figure 3.16. SEM images showing the effect of flow velocity on the morphology of $FeCO_3$ in a study by Tanupabrungsun [129].

3.4.5 Effect of Brine Chemistry

The brine chemistry of a system is one of the most influential parameters on the kinetics and formation of $FeCO_3$. The chemistry of the brine plays a key role in the protective characteristics of $FeCO_3$, yet, this area remains one the most unexplored avenues of research in CO_2 corrosion studies. The brine chemistry can influence the precipitation kinetics of $FeCO_3$ by:

- Influencing the ionic strength of the solution, which changes the solubility of $FeCO_3$
- Changing the corrosion rate (i.e. mass flux of Fe^{2+} from the steel surface)
- Competing with the $FeCO_3$ process through the formation of other scales (such as $CaCO_3$)

3.4.5.1 Addition of Mg^{2+} and Cr^{3+}

Shannon *et al.* [134] suggested that Mg^{2+} ions may be capable of improving the protection and adhesion of $FeCO_3$ crystals to the carbon steel surface. In a much more recent study, Ingham *et al.* [142] used *in-situ* synchrotron X-ray diffraction to follow the formation of $FeCO_3$ and suggested that the addition of $MgCl_2$ accelerated the onset of $FeCO_3$ precipitation, without any evidence of Mg incorporation within the crystalline corrosion product layer. Although these tests were performed using a potentiostatic method (with a resulting current of 12 mA/cm^2) to drive the corrosion reaction which could be regarded as being unrealistic when compared with a material corroding naturally at its free corrosion potential. In a separate study Ingham *et al.* [135] proposed that the addition of Cr^{3+} ions (10 to 20 µM) catalysed the nucleation and growth of $FeCO_3$ by decreasing the critical supersaturation for $FeCO_3$ precipitation

3.4.5.2 Addition of Ca^{2+}

In terms of the influence of Ca^{2+} ions on $FeCO_3$ formation, some attention has been directed towards mixed calcium-iron carbonate systems to understand their interaction and precipitation behaviour when present together. Al-Saiari *et al.* [137-139] utilised a continuous stirred tank reactor to observe the precipitation of $CaCO_3$ and $FeCO_3$. Although this method did not involve assessing the precipitation of these species onto a corroding surface, it did enable a better understanding of how the two cations interact in the bulk solution. They observed a fast rate of $FeCO_3$ precipitation at 65°C and a gradual rate of growth at 55°C. However, the introduction of Ca^{2+} ions reduced

and delayed the precipitation of $FeCO_3$ by increasing the solubility of Fe^{2+}. This increase in solubility also appeared to be proportional to the concentration of calcium present in the solution. In addition, Al-Saiari *et al.* [138] also compared the molar ratios in the precipitated salts relative to those in the solution. The results indicated that $CaCO_3$ possessed the greatest preference to precipitate within the system.

Esmaeely *et al.* [140] evaluated the effect of Ca^{2+} ions on the CO_2 corrosion of carbon steel in a 1 wt. % NaCl solution at 80°C and pH 6.6. Concentrations of 10, 100, 1000 and 10,000 ppm Ca^{2+} were added to the system and it was show that at low concentrations (10 and 100ppm) the precipitation of $FeCO_3$ remained unaffected. However, at higher concentrations of Ca^{2+}, $FeCO_3$ precipitation was prevented, and $CaCO_3$ precipitation was favoured, resulting in a non-protective film forming.

3.4.5.3 Fe^{2+} content – bulk vs surface concentrations

The concentration of Fe^{2+} within the bulk solution is important in the film formation process of $FeCO_3$. However, Fe^{2+} is also produced at the steel surface due to the corrosion process, while H^+ ions are consumed on the steel surface or the film surface (if the film is Fe_3C). The development of concentration gradients from the bulk solution to the steel surface may give rise to higher supersaturation in the film and/or at the metal surface, which will increase the level of precipitation at the surface [26]. Therefore, determining the bulk solution chemistry along with surface corrosion rates/reactions and how this influences the surface pH and concentration of Fe^{2+} is key to understanding the precipitation process and accurately predicting the rate of $FeCO_3$ growth.

3.4.6 Effect of Surface Properties – Iron Carbide and Steel Microstructure

The preferential dissolution of the ferrite phase within the carbon steel microstructure is capable of leaving behind an un-corroded iron carbide (Fe_3C) film which can accumulate at the steel surface and is known to increase the surface roughness of the surface [41]. There is limited literature focussing on the effect of surface roughness on CO_2 corrosion and will not be reviewed in this section. Depending upon the conditions under which Fe_3C forms, and the properties of the bulk steel, the Fe_3C remains can be porous and fragile, or be extremely tough [41].

Generally, the role of Fe_3C is quite contrasting in terms of influencing the corrosion behaviour of carbon steels and depends very much on the manner of formation and its dominance within the film structure. On one hand, the build-up of the porous network is capable of facilitating galvanic corrosion at the surface and generating local acidification at the interface which accentuates corrosion [41, 92]. From the other perspective, by preventing the diffusion of Fe^{2+} ions away from the surface, it is capable of promoting the formation of $FeCO_3$ within the film, lowering corrosion rate [25, 57].

The formation and adhesion of the $FeCO_3$ layer has been frequently related to the presence of Fe_3C and hence, the steel microstructure itself. The general consensus is that the presence of a carbide phase is able to strengthen the $FeCO_3$ film, anchoring it to the steel substrate [141, 152]. Palacios and Shadley [142] showed that the $FeCO_3$ crystals grown on normalised steels which possessed a ferritic/pearlitic structure were more adherent, more closely packed and thicker in comparison to quench and tempered steels which were formed under the same conditions. Invariably, the steel microstructure dictates the carbide distribution and this ultimately appears to influence the film stability or instability, as the case may be.

3.5 Mechanisms for $FeCO_3$ Removal Processes

The natural formation of $FeCO_3$ can be utilised as a form of protection for many oil and gas operators against corrosion when the system is favourable for $FeCO_3$ formation. However, if the protective film is damaged or removed in uninhibited conditions, severe uniform or localised corrosion could propagate which poses a significant threat to asset integrity [144, 145]. Therefore, understanding the removal process of protective $FeCO_3$ films is crucial for understanding and predicting the initiation and propagation of localised corrosion in the CO_2 corrosion environment.

Researchers have suggested that the protectiveness of $FeCO_3$ films formed on carbon steel surfaces may be compromised by one or a combination of the following mechanisms:

- mechanical removal by hydrodynamic forces (referred to here as flow-induced localised corrosion) [143, 144];
- chemical film dissolution, which is essentially believed to be governed by mass transfer [147];

- a combination of mechanical and chemical removal (chemo-mechanical removal) [152].

3.5.1 Mechanical Removal by Hydrodynamic Forces

The most significant contribution to understanding the mechanisms behind specifically $FeCO_3$ removal is the work of both Schmitt *et al*. [132, 148, 149] and Ruzic *et al*. [143, 147]. In the work presented by Schmitt *et al*. [132] a failure mode diagram for $FeCO_3$ crystals was constructed based on theoretical considerations for failure mechanism analysis, along with assumptions of $FeCO_3$ layer properties according to the data available for oxide scales. The critical value of fracture strains and stresses was evaluated based on the failure diagram of $FeCO_3$, and appeared to be in good agreement with experimental results. It was concluded that the flow induced localised corrosion (FILC) in the presence of $FeCO_3$ layer was due to the increase of intrinsic stress inside the layer as the layer formed, which could exceed the critical stresses for $FeCO_3$ layer fracture and spalling [19]. The authors also claimed that the contribution of flow turbulence was to prevent re-formation of the removed $FeCO_3$ layer, rather than directly removing the layer and they concluded that the wall shear stress was too small to remove the $FeCO_3$ layer.

Schmitt and Mueller [49, 131, 132] showed some experimental results obtained with a jet impingement setup. It was claimed that the “micro-turbulences” in the near-wall region caused pressure changes and led to cyclic loading on the layer, which was responsible for the “fatigue” cracking of the layer.

Gao *et al.* [124] conducted experiments to study the mechanical properties of the corrosion product layer formed under different flow velocities and CO_2 partial pressures. The uniform and localised corrosion rates were correlated with the interfacial fracture toughness of the layer, which was claimed as the parameter characterizing the resistance of the layer to mechanical flow damage [19].

Nesic *et al*. [143, 147] showed experimental work done in a glass cell with rotating cylinder electrode setup under single phase turbulent flow conditions. Protective $FeCO_3$ layer was formed before the increase of rotating speed. Partial breakdown of the layer was observed at high rotating speed.

Nesic and Lunde [122] also conducted a series of flow loop experiments to investigate CO_2 corrosion under severe flow condition. In their study,

protective $FeCO_3$ layer was formed in supersaturated solutions under single phase flow conditions with disturbance and gas-liquid two phase flow with slug flow regime. They claimed that the protective layer appeared to be very robust and resistive to severe flow condition. By establishing relationships between the experimental findings and various hydrodynamic parameters, a mechanism of mechanical removal can be proposed. This followed the subsequent steps:

1 Separation from the substrate

The wall shear stress was believed to be insufficient to be responsible for film removal. Instead, local fluctuations in velocity and wall shear stress imposes dynamic mechanical loading, which leads to fatigue damage. Ultimately, the adhesive strength of the film is exceeded and the film detaches from the substrate.

2 Vertical cracking

As a result of centrifugal forces or the negative relative pressure, the gap between the substrate and film increases. As internal stresses reach a critical value, vertical cracking occurs.

3 Crack propagation

The crack locations enhance local turbulence, promoting further film detachment, lifting the film from the metal surface.

4 Film detachment

The lifted film causes increased drag and the wall shear stress removes it from the surface.

3.5.2 Chemical Film Removal

As discussed already, protective $FeCO_3$ films are only capable of forming in environments when the solubility of the solution is exceeded ($SS > 1$). When the forward and backwards reaction rates are equal, the $FeCO_3$ film is in equilibrium with the Fe^{2+} and CO_3^{2-} ions in the solution. For a system in equilibrium, the saturation ratio would equal 1. Consequently, based on this notion of equilibrium, any disturbance to the system would cause a shift in the forward and backward reactions, resulting in precipitation or dissolution of the $FeCO_3$ film, depending upon the change in solubility. It is therefore theoretically possible for $FeCO_3$ films to be chemically dissolved if the solution

becomes under-saturated (S < 1). Considering that the pH values in the oil and gas industry are very wide ranging, favourable conditions for film dissolution can be easily reached at a low pH (i.e. pH = 4). This despite, very little work is available in literature relating to the dissolution of $FeCO_3$.

One of the very few studies which has considered the mechanisms of $FeCO_3$ film dissolution is the work of Ruzic *et al*. [147]. Their work consisted of forming $FeCO_3$ films in a controlled environment. Once a protective film had formed, the source of additional iron ions was discontinued. The dissolution of the film was initiated by decreasing the pH using hydrochloric acid. The study was divided into two parts; considering both the effect of pH and the effect of velocity on the chemical dissolution process.

In terms of considering the influence of solution acidity, $FeCO_3$ films were exposed to a series of solutions with a pH in the range of 5.5 to 6.1. These corresponded to saturation ratios of 0.03 to 0.46. Velocity was maintained at 10,000 rpm in all tests and dissolution was observed instantaneously after adjusting the pH. The results indicated that as pH reduced, the dissolution kinetics increased. SEM observations of the surface exposed to the highest pH (pH 6.1) produced little signs of damage to the $FeCO_3$ film, while significantly less crystals were observed at the lower pH value (pH 5.5). Based on these observation, Ruzic *et al.* [147] proposed a mechanism for the film removal process. The author believed the results supported the arguments that suggested the dissolution process is mass-transfer controlled. They suggested that while the film-dissolution kinetics dependence on pH can support both mass-transfer and chemical reaction theories, the strong effect of velocity was believed to provide a clear indication that the process is mass-transfer dependent.

A recent study by Yang *et al.* [150] has helped to provide more of an insight into the mechanism of $FeCO_3$ dissolution. In the SEM study, a C1018 carbon steel sample was exposed to a CO_2 solution supersaturated with respect to $FeCO_3$. Figure 3.17 shows SEM images of the film immediately before the dissolution process and then again after exposure to the under-saturated solution for 15 hours.

From the SEM images taken immediately after film formation (Figure 3.17 (a)) Yang *et al.* [150] identified that a relatively even coverage of $FeCO_3$ was obtained. A number of prismatic crystals were present, along with much

smaller plate-like crystals on the steel surface. After exposure to the under-saturated solution (Figure 3.17 (b)), a significant proportion of crystals had disappeared as a result of chemical dissolution. Interestingly, all the plate-like crystals had disappeared from the surface, suggesting that they dissolved preferentially.

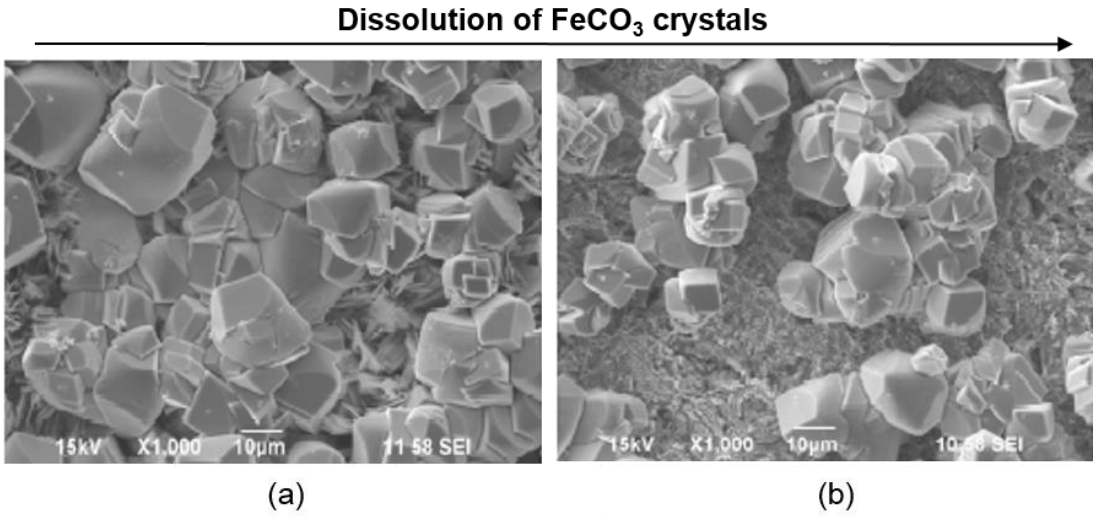

Figure 3.17. SEM images of the $FeCO_3$ layer present on the carbon steel surface (a) immediately before dissolution and (b) after dissolution by a pH 3.8 test solution after 15 hours, from Yang *et al.* [150].

Although the roles of chemical reaction and mass-transfer in the dissolution process are still debated in open literature as to which is the rate-determining step, there appears to be an overwhelming consensus that the process is mass-transfer controlled. However, the truth is that very few studies exist that consider the dissolution of $FeCO_3$ from steel surfaces in conditions typical of the oil and gas industry. Potentially the most common scenario observed in pipeline transportation would be a combination of both chemical and mechanical film removal. There is also a belief that the combined effect of mechanical and chemical processes acting together can be more damaging than if they were to act separately [151]. Some evidence for synergistic effects between mechanical removal and film dissolution can be found in the work of Han *et al.* [152]. A number of synergistic mechanisms involved in chemo-mechanical $FeCO_3$ removal have been proposed by Ruzic *et al.* [146]. This work determined the rate of $FeCO_3$ removal based on the gradient of the corrosion rate vs time graphs using a regression fit and found that the combined effect of chemical and mechanical removal was greater than the sum of the individual effects.

The change in surface topography as a result of film dissolution could result in the enhancement or abatement of the mechanical removal process in a chemo-mechanical removal system. For example, smoothening of the corrosion product top layer could potentially reduce turbulent intensity at the surface and therefore decreasing the mechanical forces acting on the $FeCO_3$ layer. Conversely, increased roughening of the crystalline surface due to dissolution could lead to enhanced mechanical removal by increasing local turbulence and the hydrodynamic forces acting on the corrosion product layer.

3.6 The Use of *In-situ* Synchrotron X-Ray Diffraction to Study CO_2 Corrosion of Carbon Steel: A Review

Additional to $FeCO_3$, previous studies have identified the presence of iron oxides/hydroxides in corrosion products of CO_2 corrosion, but this has usually been considered an artefact of *ex-situ* analysis, with the oxides/hydroxides believed to have formed after the sample was removed from the de-oxygenated CO_2 corrosion environment [62, 102-104]. Due to problems with the *ex-situ* surface analysis of the carbonate products of corrosion, the mechanism is still relatively unknown and many questions remain unanswered. As shown in previous studies [2, 136, 153-155], the surface analysis technique of grazing incidence X-ray diffraction (GIXRD) may be used to study *in-situ* the surface chemistry of solid–liquid interfaces. It has been demonstrated recently that *in-situ* GIXRD measurements may be undertaken using a laboratory-based diffractometer, but the signal-to noise ratio of the technique is relatively poor due to attenuation of the incident X-ray beam by the liquid in the experimental cell. However, the use of high brilliance synchrotron radiation (SR) will enhance significantly the signal-to-noise ratio of the *in-situ* SR-XRD (Synchrotron Radiation-Grazing Incidence X-Ray Diffraction) technique.

The use of SR-XRD in conjunction with electrochemical systems requires the design of a specific cell to carry out electrochemistry whilst also allowing the appropriate X-ray measurements to be made simultaneously. Many electrochemical-cell designs, each of which can carry out a wide variety of *in-situ* synchrotron studies exist in literature. As a general trend, each reported cell design differs slightly from the earliest reported designs ([155] and references within) in order to extend or improve the cell design to new SR experiments and/or provide enhanced electrochemistry. Each cell design will differ depending on intentions of the user. Despite this, each cell is intrinsically

based on one of two specific designs, which correspond to two different measurement geometries (i.e. reflection and transmission modes of measurement) as shown in Figure 3.18 [155].

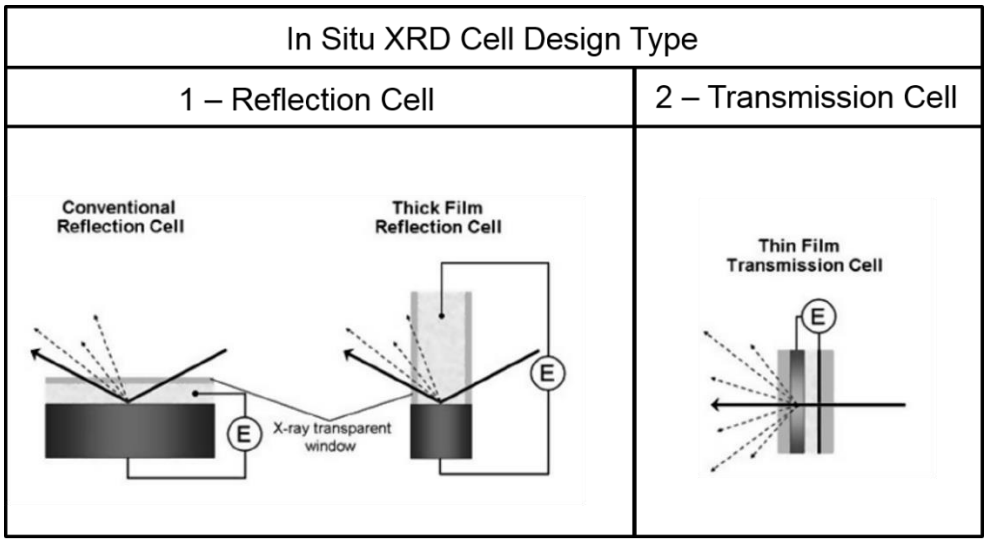

Figure 3.18. Different measurement geometries (1) reflection cell and (2) transmission cell, modified from [155].

Reflection cells generally comprise an X-ray transparent window (usually Kapton or Mylar) that is situated parallel [155], or sometimes perpendicular (as with thick-layer reflection cells) [155], to the working-electrode interface. The window is responsible for not only X-ray transmittance, but also for containing the electrolyte whilst not severely attenuating the X-ray beam itself, and therefore the thickness is kept minimal. On the other hand, transmission cells [155], are arranged such that the X-ray beam passes through the entire cell that incorporates a thin deposit of the electrode material under examination, these electrodes are usually in the order of microns. Each of these geometries comes with associated advantages and disadvantages, but the appropriate choice of *in-situ* cell requires careful consideration of the configuration of the synchrotron beam-line to be used, as well as the nature of the electrochemical system under scrutiny. Nagy *et al.* [156] discussed further comparisons between thick-layer and conventional reflectance cells in an early, but informative, review of the two configurations [155].

The composition and structure of the protective corrosion products such as $FeCO_3$ have been the subject of considerable research. In a study by De Marco *et al*. [153], the authors demonstrated that SR-XRD is a powerful

technique for elucidation of the mechanistic chemistry of electrochemical systems. The aim of this investigation was to identify the exact chemical nature of the corrosion products formed at the corroded surface, through the use of SR-XRD techniques for surface analysis. They studied the influence of the CO_2 corrosion of carbon steel. SR-XRD was employed in conjunction with the long-term monitoring of mixed potentials to examine the surface reactions occurring at the surface of the carbon steel working electrode. The study revealed that, during the initial stages of corrosion, $Fe_2O_2CO_3$ (iron-oxy carbonate) was formed due to preferential deposition of the reaction product at the cathodic sites of the electrode induced by the reaction between carbonic acid (formed from the dissolved CO_2 content in the solution) and the poorly crystalline native oxide film on the carbon steel surface (i.e. H_2CO_3 reacting with FeO(OH)). This reaction step was shown to be followed by the formation of the two reaction products of $Fe_2O_2CO_3$ and $Fe_2(OH)_2CO_3$ at anodic reaction sites over the electrode. This research was later extended [153] to study the influence of acetate on the carbon-dioxide corrosion of mild steel. It was shown, using SR-XRD and simultaneous electrochemical impedance spectroscopy (EIS), that acetate significantly alters the crystallisation behaviour of the corrosion products.

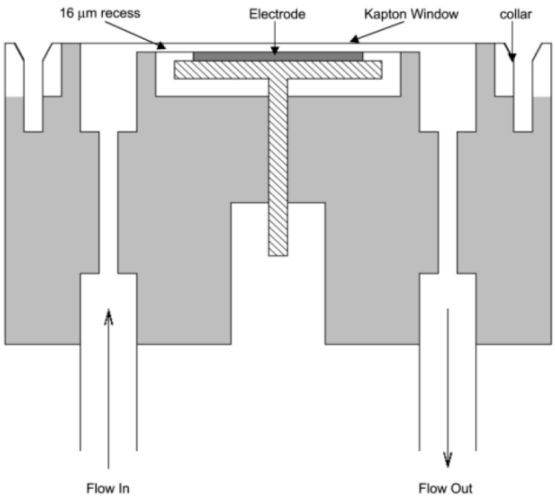

Figure 3.19. *In-situ* SR-XRD flow cell used by De Marco *et al.* in [2, 153, 155].

Figure 3.19 shows a schematic diagram of the flow cell design that was used for the study. The flow cell included a 20µm thick Kapton sheet which was used to act as a window such that the X-ray beam would be able to travel through the Kapton window. The study highlighted the need for combined and

simultaneous *in-situ* surface analyses and electrochemical measurements to obtain accurate data to implement into corrosion prediction models.

In more recent work [110], *in-situ* SR-XRD was used to investigate the structure and composition of the protective surface corrosion products formed at temperatures up to 90°C in CO_2 saturated sodium chloride solutions, under galvanostatic control at quite high applied current densities. This work showed that $FeCO_3$ was the primary phase formed, but that minor phases such as of iron-oxy carbonate ($Fe_2O_2CO_3$) and iron-hydroxy carbonate ($Fe_2(OH_2)CO_3$) could also be formed in some circumstances. Furthermore, *ex-situ* examination of the corrosion products shows an apparent difference in crystal morphology for the films formed under different circumstances: observations vary from tightly packed, well-formed cubic crystallites [111] to spherical particles showing crystalline facets [110]. As already mentioned, this could be due to the anodic current being used to promote Fe^{2+} concentration and hence supersaturation (to unrealistic values in comparison to the field) which is not a realistic approach for $FeCO_3$ layer formation.

Further work by Ingham *et al.* [154, 157] concluded that extremely stable, adherent and protective $FeCO_3$ crystals formed on carbon steel surfaces in presence of trace amounts of chromium additions (Cr^{3+}) to the steel and the solution. This study suggested that traces of Cr^{3+} in the solution significantly expedites the precipitation rate and crystallisation of $FeCO_3$ through its ability to act as a catalyst influence on the nucleation process by modulating the local pH level at the steel surface and thus reducing of the solubility of $FeCO_3$ and therefore increasing the precipitation rate.

In their most recent study, Ingham *et al.* [157] used *in-situ* synchrotron small- and wide-angle X-ray scattering (SAXS and WAXS). In this work, based on the early observations using SAXS, it was concluded that the formation of crystalline $FeCO_3$ during the corrosion of steel in CO_2-saturated brine is actually preceded by the formation of a colloidal precipitate and an amorphous surface layer, both assumed to be amorphous $FeCO_3$. Grazing incidence SAXS showed that upon the application of an anodic potential, the film forms instantaneously and then a separate population of particles develops in the later stage followed by the formation of crystalline $FeCO_3$. It was interpreted that nucleation crystalline $FeCO_3$ occurred within the amorphous surface layer. This observation was speculated to bear a significant consequence on the morphology of the corrosion product and hence its protectiveness.

All of the reviewed work that was conducted by Ingham *et al.* [110, 135, 154, 154, 157] was completed using the flow cell shown in Figure 3.20 to study the formation of corrosion products on carbon steel in CO_2 saturated brine in real time while the steel coupon was under electrochemical control. The design of the cell is comprised of a reservoir at the top (volume 50 mL) into which the counter and reference electrodes are placed, and a tapering neck down to the working electrode.

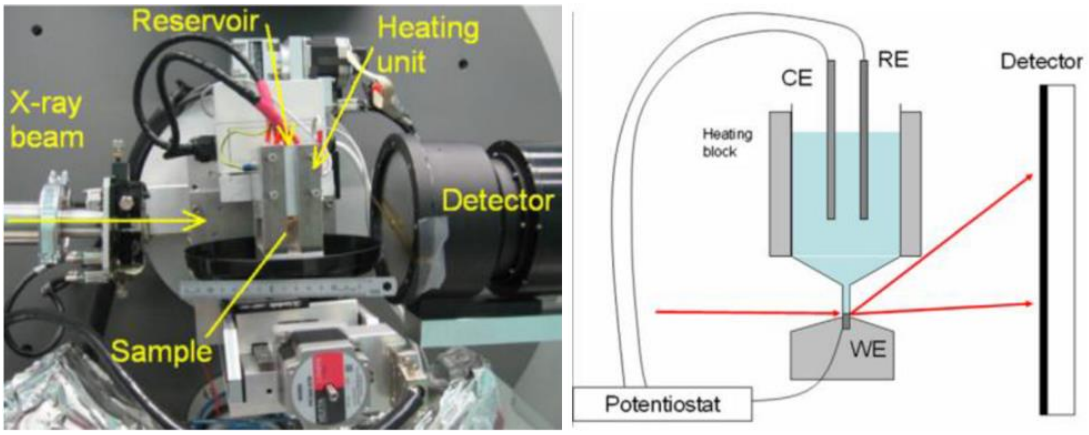

Figure 3.20. *In-situ* XRD flow cell used by Ingham *et al.* [110, 135, 154, 154, 157].

Joshi *et al.* [158] reported the design and implementation of an “E-cell” for *in-situ SR-XRD* to study CO_2 corrosion products. Regarding functionality, this cell was constructed to enable measurements from corroding substrates in solutions containing low concentrations of dissolved oxygen from room temperature up to ~ 80°C. An initial study of the corrosion of carbon steel immersed in CO_2-saturated aqueous NaCl solution (pH = 6.8, T = 80°C) demonstrated the performance of the cell. A number of different phases were observed in their study which was conducted for 24 hours, including iron carbonate, chukanovite, and most notably a so-called green rust carbonate; the latter is only apparent during the early period of immersion. In addition, features assigned to magnetite, wustite and goethite emerge, suggesting that dissolution of oxygen into the CO_2-saturated aqueous NaCl solution occurs with time. On this basis, they concluded that the cell design and experimental procedures require some further optimization to ensure complete data integrity. Figure 3.21 shows schematic diagrams of the E-cell used in [158].

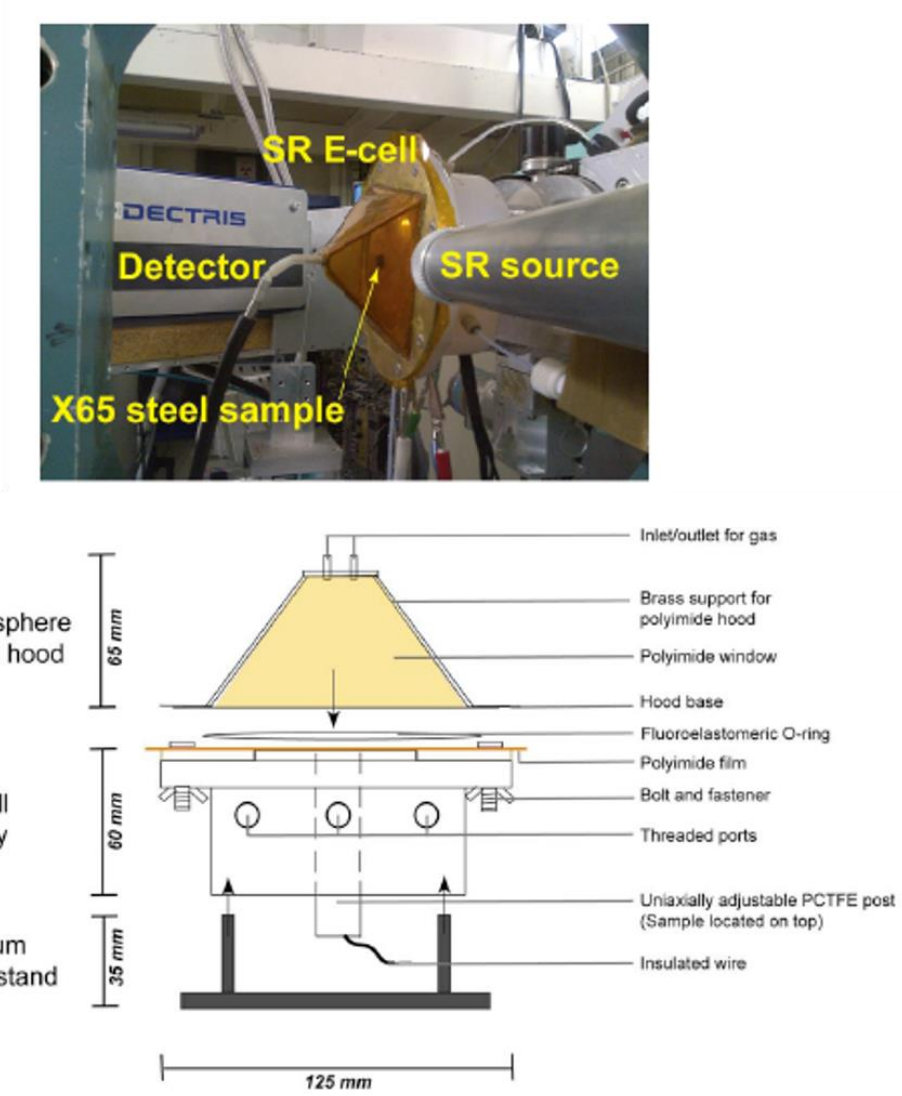

Figure 3.21. *In-situ* XRD flow cell used by Joshi *et al.* [158].

An insulated wire is attached to the back face of the sample to enable it to function as the working electrode in electrochemical measurements. Reference and counter electrodes (both Pt wires) are introduced through two threaded orifices machined into the side of the E-cell body. X-rays enter/exit the E-cell, and impinge on the sample, through a thin polymer film (x-ray transparent) located above the sample. The solution depth above the sample surface can be controlled by either extending/retracting the sample post or inflating/deflating the polymer film. Typically, a thin-film (thick-film) geometry is employed for acquisition of diffraction data (undertaking electrochemical measurements); the thin-film geometry reduces attenuation of x-ray intensity due to solution scattering.

3.7 Summary and Experimental Challenges when Determining $FeCO_3$ Kinetics

Carbon steel remains the material of choice in many oil and gas sectors such as production and transmission pipelines. This is mostly due to its low cost and adequate mechanical properties. The major drawback is that it can be subjected to severe corrosion in environments containing dissolved CO_2, which is believed to exist in most oil and gas resources especially with the implementation of the EOR (Enhanced Oil Recovery) techniques. Corrosion problems represent a large portion of the total costs for oil and gas producing companies every year worldwide.

CO_2 corrosion is the predominant form of attack and the major cause of incidents in the oil and gas industry. The mechanism of carbon steel corrosion in a CO_2-containing environment has been studied and debated for decades and progress has been made over the past two to three decades. The influence of a number of important electrochemical, hydrodynamic, chemical and metallurgical parameters have been investigated, but major challenges still exist in this field. The electrochemistry of steel dissolution in CO_2 solutions has been largely studied, along with the influence of various parameters on the corrosion rate and the kinetics of $FeCO_3$ precipitation. The influence of pH, temperature, CO_2 partial pressure, flow velocity and brine chemistry is generally well understood for general corrosion and the protectiveness of $FeCO_3$. However, the prediction of localised corrosion in CO_2 systems are areas requiring further attention.

Table 3.2 shows a matrix of environmental conditions, mainly pH and temperature with the resulting morphology and protectiveness within a certain range.

One of the main challenges experimentally is determining the early $FeCO_3$ precipitation kinetics and the composition and properties of the layer that offers ultra-protection and linking this into current CO_2 corrosion models. In this light, this research project sets out to provide a comprehensive understanding of the near surface region of a corroding steel and the early kinetics of $FeCO_3$ film formation on a carbon steel surface in a CO_2 corrosive environment and the protectiveness offered through the use of a new *in-situ* methodology. Explicitly, focusing on the growth kinetics and chemical composition $FeCO_3$ formation (and any other phases that may form) and the degree of protectiveness offered through a unique, custom made flow cell,

integrated with the ability to perform *in-situ* electrochemical measurements and collect real-time SR-XRD data simultaneously.

Table 3.2. A matrix of environmental conditions and their effect of the corrosion rate and $FeCO_3$ morphology.

Crystal	Undersaturated	Saturated	Supersaturated
Saturation	SS_{FeCO_3} < 1	SS_{FeCO_3} =< 1	SS_{FeCO_3} > 1
Corrosion Rate (mm/year)	1 - 10	1 - 3	0.1 - 1
Morphology	No $FeCO_3$	Partially protective $FeCO_3$	Protective $FeCO_3$
Structure	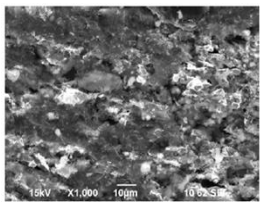 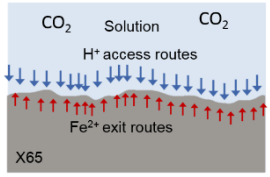	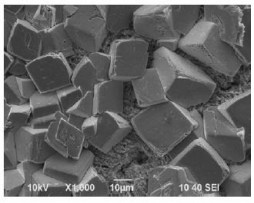 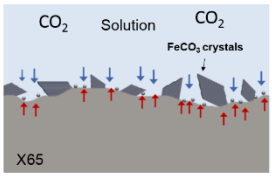	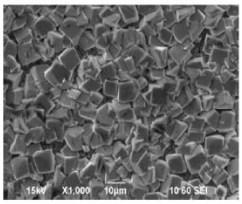 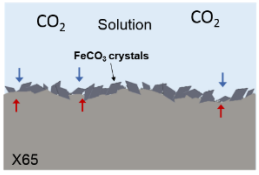
Type of corrosion	High general corrosion rate (No localised corrosion)	Low/high general corrosion rate (Localised corrosion can occur)	Low general corrosion rate (No localised corrosion)
pH	Low pH (<5)	Moderate pH (5-6)	High pH (>6)
Temperature	Low Temperature (<50°C)	Moderate Temperature (50-60°C)	High Temperature (>60°C)

The newly developed flow cell will be used to help understand how CO_2 corrosion products can be exploited and maintained to utilise their protective properties.

In the experiments performed within this work, the goal was to maintain the CO_2 partial pressure, temperature, and chloride ion concentration in the bulk solution, varying only the solution pH and flow velocity. This would enable identification of the role pH and flow velocity plays on the early kinetics of $FeCO_3$ precipitation. The succeeding chapters describe the experimental methodologies/theories and results from static immersion tests focusing on the development of ultra-protective $FeCO_3$ (Chapter 4 and 5), the design and development of the SR-XRD flow cell (Chapter 6), followed by the SR-XRD results chapters (Chapters 7 and 8). Whilst Chapter 9 brings the thesis together whilst identifying the key physical parameters of the $FeCO_3$ crystals that lead to enhanced corrosion protection. Chapter 10 then provides a summary and conclusions of the main findings from the individual chapters, and proposes possible future directions of research and the relevance and impact this research has on industry and future academic studies.

Part II:
Static Immersion Tests: Experimental Methodologies and Results

Chapter 4.
Experimental Methodology: Theory and Practice

4.1 Introduction

This chapter focuses on and describes the methodologies used during the experimental work and the related theory behind each of the techniques used. This chapter also discusses the material used throughout this research project. The techniques used to analyse the corrosion product morphology and the composition obtained from the sample testing procedures are also described. During this study, a number of practical techniques have been used to investigate CO_2 corrosion product growth on carbon steel substrates in CO_2-saturated solutions. Figure 4.1 provides an overview of the research programme and the analytical techniques that were used for the static immersion tests in Chapter 5.

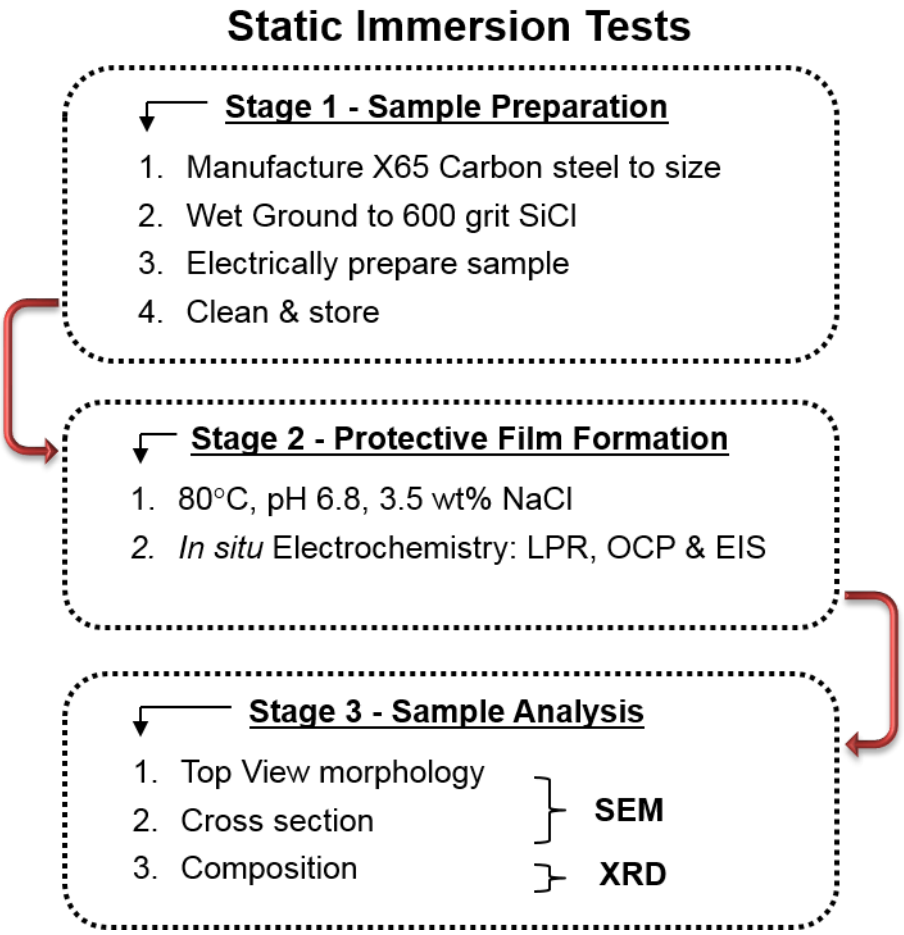

Figure 4.1. Outline of the experiment and analytical techniques that were used for the static immersion tests

The formation and composition of ultra-protective films is studied using a static glass cell which will be described in this chapter. The results obtained from undergoing such experimental methodologies presented provide an understanding of the different parameters that can cause an effect on the CO_2 corrosion rate of X65 carbon steel in a static environment emphasising the sensitivity of this process. The corrosion behaviour was monitored by electrochemical methods: Open Circuit Potential (OCP), Linear Polarisation Resistance (LPR), Tafel Polarisation and Electrochemical Impedance Spectroscopy (EIS). Samples from all experiments were characterized by X-ray diffraction (XRD), scanning electron microscopy (SEM) (and in some cases Focussed Ion Beam (FIB) and Transmission Electron Microscopy (TEM)) to investigate the morphology and composition of the corrosion product layer.

The following sections provide a theoretical understanding of the practical techniques used to investigate CO_2 corrosion of X65 carbon steel. This work contributes to furthering the understanding of the formation of $FeCO_3$.

4.2 Introduction to Aqueous Corrosion

4.2.1 Electrochemical Cell for Metal Corrosion

The most common form of corrosion related to metallic structures is aqueous corrosion. Aqueous corrosion occurs when an electrochemical reaction takes (reduction-oxidation (redox)) place on a metal-solution interface in an aqueous electrolyte [159]. This implies that two reactions occur; the anodic oxidation reaction of metal involving oxidation or the removal of electrons from metal atoms and the cathodic reaction, reduction of oxidising agents or consumption of electrons by an oxidizing agent [159]. The metal surface can be considered to be an ‘electrode’, formally defined as a site where electron/ionic charge transfer reactions can take place [159].

An electrochemical cell requires certain components to work together:

Anode (an electrode site where ‘electron releasing’ metal oxidation reactions take place);

Cathode (an electrode site where ’electron consuming’ reduction reactions take place);

Electron conductive path between the anode and cathode (for electron charge transfer between the anode and cathode);

Electrolyte (a medium that enables movement of participating species to/from the electrode surfaces and for ionic species charge transfer between anode and cathode).

At the anode, surface metal atoms (M_0) leave their crystal lattice, change their oxidation state and become solvated metal ions (M^{n+}). This is the anodic reaction or oxidation half-reaction, i.e.

$$M_{(s)} \rightarrow M_{(aq)}^{(n+)} + n(electrons) \tag{4.1}$$

At its simplest level, and regarding uniform corrosion, a real metal surface (such as steel, Fe) can be treated as an electrode that hosts dispersed anodic and cathodic sites [173]. Different regions of the same metal surface can represent the anodic and cathodic sites of an electrochemical cell. Anodes and cathodes on the metal surface are already in electrical contact, as part of the same structure, and only require a contacting electrolyte so as to complete an electrochemical cell as shown in Figure 4.2.

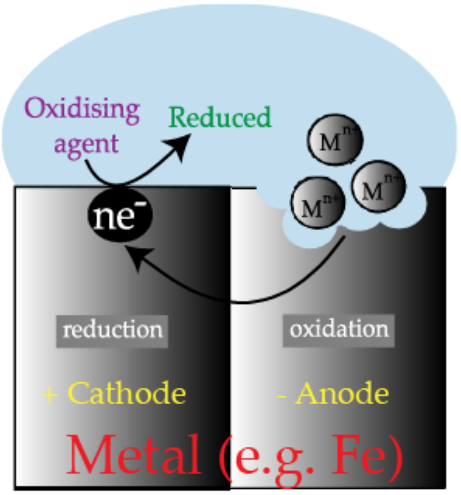

Figure 4.2. Schematic of an electrochemical cell at the metal-solution interface, from [86].

These electrochemical cells drive spontaneous electrochemical current and, thus, aqueous corrosion (i.e. anodic metal loss) [160, 161]. The relative sizes and locations of cathodic and anodic sites are important variables that affect the rate and type of corrosion. The cathodic reaction (Equation 4.2 to Equation 4.4), at which electrons are consumed, is demonstrated below. The precise

cathodic reaction will depend on the chemistry of the electrolyte. However some of the most common aqueous environments concern the following reaction:

Equation 4.2 - Cathodic half-cell reactions for hydrogen-evolution

$$2H^{+}_{(aq)} \rightarrow 2e^{-}_{(aq)} + H_{2(g)} \quad (4.2)$$

Equation 4.3 - Cathodic half-cell reactions for oxygen-reduction in acidic solutions

$$O_{2(g)} + 4H^{+}_{(aq)} \rightarrow 4e^{-}_{(aq)} + H_2O_{(aq)} \quad (4.3)$$

Equation 4.3 – Cathodic half-cell reactions for oxygen-reduction in base or alkali solutions

$$O_{2(g)} + H_2O_{(aq)} \rightarrow 4e^{-}_{(aq)} + 4OH^{-}_{(aq)} \quad (4.4)$$

A metal can be considered as an array of ions, with the valence electrons of each atom having been transferred to the crystal lattice as a whole. These “free” electrons account for the electrical conductivity of the metal and other electronic properties [161].

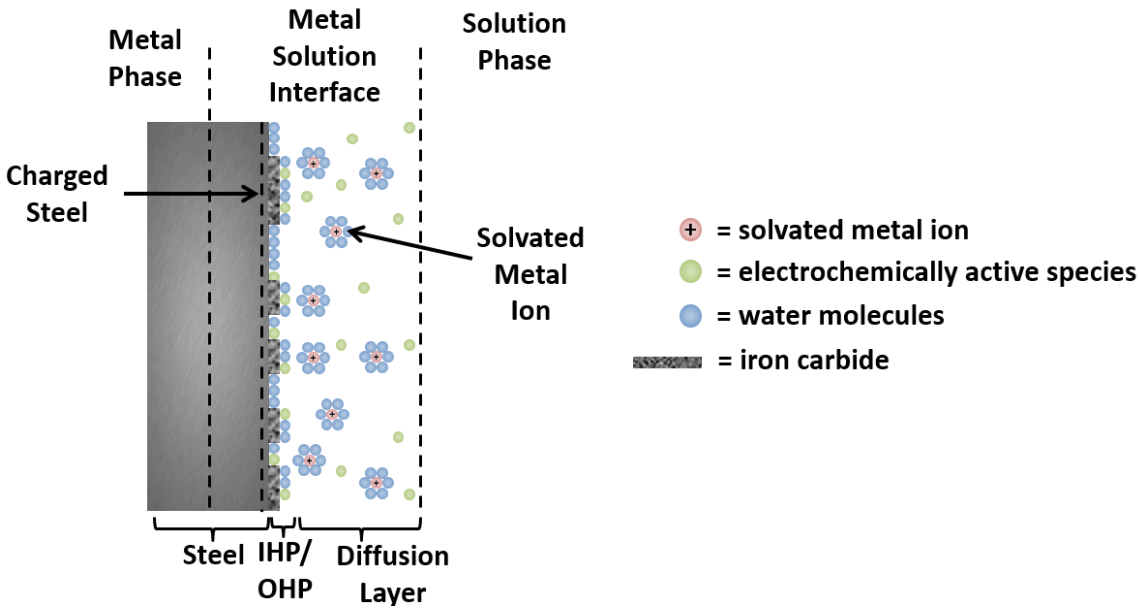

Figure 4.3. Schematic of the electrical double layer (EDL) at a metal-solution interface.

The metal in aqueous solution also exists as an ion and thus, the relative tendency for the ion to exist in the metal or in the solution depends, along with other factors such as the concentration, on the relative electrochemical free-energy of the ion in these two phases [161]. When a metal is immersed in a solution, hydration of the metal ions at the interface occurs resulting in a water layer on the metal releasing solvated metal ions into the solutions leaving the metal negatively charged. This results in an actual separation of charge at the electrode interface. By physically separating two planes of electrochemical charge an electrical capacitor and potential difference across metal-solution interface are established (Figure 4.3 demonstrates this schematically).

During corrosion, slow charge transfer reaction kinetics, diffusion effects and corrosion product deposits can impede electron flow in a manner similar to discrete passive electrical components in a circuit. Upon immersing a metal surface in solution, an electrical double layer (EDL) is expected to form at the metal-solution interface, as Figure 4.3 illustrates. The metal plane may have associated electron charge at the surface, which is balanced by a layer of specifically adsorbed ions within the inner Helmholtz plane (IHP). A layer of solvated ions, which are free to diffuse into the bulk solution, forms in the adjacent region known as the outer Helmholtz plane (OHP) [162]. The electric potential, in going from the metal surface (electrode) to the OHP (solution), changes in a manner analogous to the behaviour across two conductive plates of a parallel plate capacitor. Such capacitance has an impedance that changes with frequency of applied potential.

4.2.2 Aqueous Corrosion Kinetics and Thermodynamics

In order to evaluate a materials susceptibility to corrode the two half-cell reactions may be manipulated to occur at physically distinct surfaces by placing the electrode of interest in a solution relative to another material which is chemically inert. Due to charge separation, a potential difference will exist between the two electrodes. The existence of a measurable electrochemical potential is due to the chemical potential of the given species as well the partial free energy of the species. This can be described by the Nernst equation.

$$E = E^0 - \left(\frac{RT}{nF}\right) ln \left\{\frac{(a_{products})}{(a_{reactants})}\right\} \tag{4.5}$$

Where E is the measured cell potential (V), E^0 is the standard cell potential (V) for at a given electrode surface when all activity units equal unity, R is the ideal gas constant (JK/mol^{-1}), T is the temperature (K), 'n' is the valence number of the species in question, F is Faraday's constant (Cmol^{-1}) and 'a' is the chemical reactivity of the products or reactants at equilibrium. If the system is not at equilibrium (i.e. two electrode reactions) the final term can be replaced with the reaction quotient which is a measure of the relative amount of products and reactants present during a reaction at a particular point in time. The existence of a cell potential gives rise to the electrochemical series, from which the relative reactivity of metals is established. Depending on the direction of reaction, metal ion reduction or deposition can occur. In all corrosion processes, the rate of anodic reaction must equal the rate of the cathodic reaction to satisfy charge conservation [159]. Yang *et al.* [150] also stated that the formation of corrosion products, the solubility of corrosion products in the electrolyte and the formation of passive films all affect the overall rate of the anodic metal dissolution process. For passive materials, passive layers will distinguish themselves from corrosion products, in the sense that these films can provide a higher degree of protection from corrosive attack [159].

Corrosion only occurs if the reaction is energetically favourable; this is described by the thermodynamics of the corrosion reaction in which every element tries to minimize its energy state. Thermodynamics can be used to evaluate the theoretical activity of a given metal or alloy in a known corrosion environment [163]. The ability for any chemical reaction to occur, including the reaction of a metal within its environment is measured by the Gibbs free-energy change (*ΔG*) which describes the amount of energy available to perform work. The relationship between ΔG (Joules), cell potential and Faradays constant (F = 96500 C/mol) is defined as [163];

$$\Delta G = -nFE^0 \tag{4.6}$$

If the value for *ΔG* is negative, there is a greater tendency for reaction to occur as the electrode reaction has a greater amount of energy or electromotive force to complete the reaction or 'work'. If the free-energy is positive, the reaction will have no tendency to occur at all. Although the Gibbs free energy

change is a good indication of the materials susceptibility to corrosion, it cannot be used to measure the corrosion rate of a material. It has been found that materials with a large negative ΔG are sometimes not accompanied by a large corrosion rate. The tendency for metal to corrode can also be expressed in terms of electromotive force of the corrosion cell that is an integral part of the corrosion process.

The corrosion rate is usually described as a penetration rate in millimetres per year and is directly proportional to the rate of electron transfer thus to the correspondent current flow which is usually described as a corrosion current density where the surface of the corroding element is taken into account.

If the anodic current (i_a), from metal oxidation, is equal to the cathodic current (i_c), from metal ion reduction, and the 'net' electrode current passing is zero (when surface area is known), this becomes the electrode current density, known as the exchange current density (i_0). Faraday proposed that the magnitude of current density (i) indicates the rate of oxidation/reduction, i.e.

$$i = nFJ \tag{4.7}$$

The current density, i is measured in A/m^2 and J is the flux of material to/from the electrode surface. Through a range of electrochemical techniques, i can be measured and then the metal oxidation/reduction can be estimated. On the surface of a metal immersed in an aqueous phase, to drive oxidation (or reduction) reactions (current), additional potential (V) is required to overcome an energy barrier to enable charge transfer reactions to proceed [159]. This potential difference is known as overpotential (η) and is measured in volts. Such overpotential can be delivered to a metal surface from an external power source ($E_{applied}$) such as a potentiostat, but can also refer to the deviation in potential from a standard electrode potential (E^0) or at steady state (E).

$$\eta = E_{applied}(or\ E^0) - E \tag{4.7}$$

The measured current generated from the oxidation or a reduction reactions to increase when overpotential (or current) is applied. Therefore, it is common to apply an overpotential to study individual and overall electrochemical

reaction kinetics on electrode surfaces. This relationship between overpotential and current, is outlined in the Butler-Volmer Equation:

$$i = i_0 \underbrace{\left\{e^{\left(\frac{(\alpha)nF\eta)}{RT}\right)}\right\}}_{\text{Anodic}} - \underbrace{\left\{e^{\left(\frac{(1-\alpha)nF\eta)}{RT}\right)}\right\}}_{\text{Cathodic}} \tag{4.8}$$

The Butler-Volmer relation draws a theoretical model of the current and overvoltage reaction as shown in Equation 4.7 and can be related to the absolute reaction rate theory. The Butler-Volmer equation shows how electrode current density, i (A/m^2) depends upon the exchange current density, i_0 (A/m^2), the anodic and cathodic overpotentials, η and the charge transfer co-efficient, α. The first term in Butler-Volmer equation describes the forward, anodic (metal dissolution) reaction while the second term describes the backward, cathodic reaction [143].

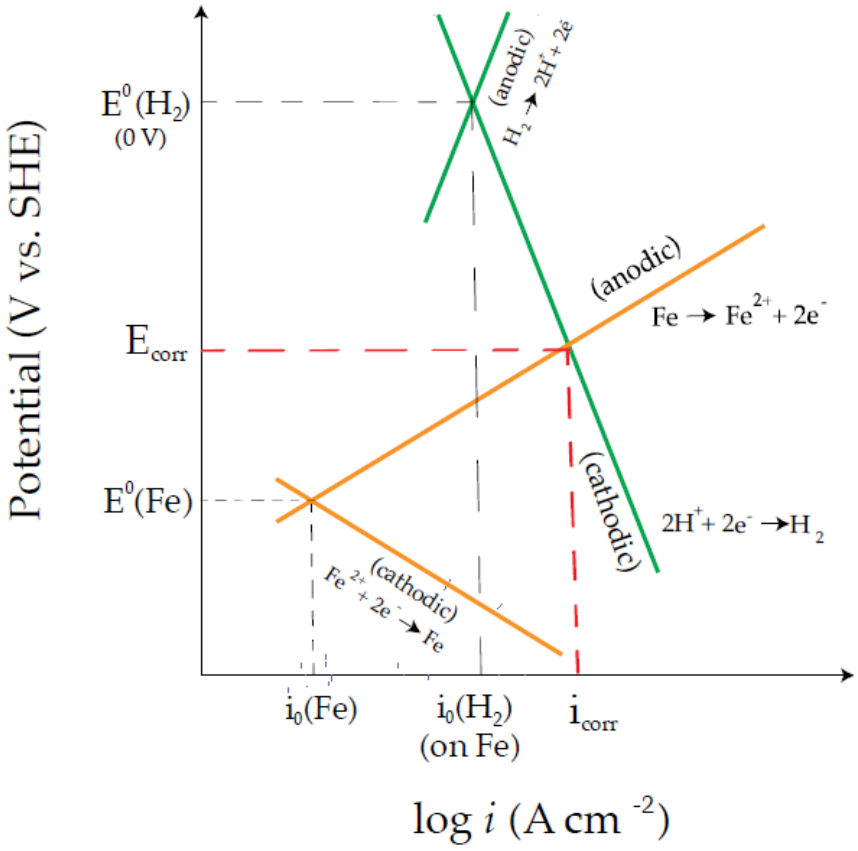

Figure 4.4. Schematic Evans plot for iron metal immersed in a deaerated acid. Yellow/green lines represent Fe oxidation/reduction and H_2 oxidation/evolution kinetics respectively, from [56].

The current flowing in a single electrode at E^0 is known as the exchange current density and Figure 4.4 shows those for both the hydrogen and iron electrode systems when combined in what's known as the Evans' diagram. In fact, when two elements are in solution, the potential of the metal will not be at the redox potential of either of them but rather around a value which is known as the corrosion potential of the system (E_{corr}). Only two reactions are of interest in that case since it is known that iron is the corroding specimen at steady state;

the iron dissolution at the anode;

$$Fe_{(s)} \rightarrow Fe^{2+}_{(aq)} + 2e^- \tag{4.9}$$

and the hydrogen-evolution at the cathode

$$2H^+_{(aq)} + 2e^- \rightarrow H_{2(g)} \tag{4.10}$$

Both of these reactions are known to intersect at the free corrosion potential. At this point, the charge conservation is maintained and the measured current is called the corrosion current (i_{corr}) and is directly proportional to the rate of corrosion rate of the iron [165].

Evans diagrams are useful because we consider the shapes of the anodic and cathodic reaction polarisation curves (kinetics), and the standard reversible potentials (E^0) (thermodynamics) at the same time. It is worth noting that the current densities and reaction kinetics shapes/gradients for cathodic reactions can be different, depending upon the catalytic activity of the metallic surface on which they take place which depends on the environmental conditions of the system [166]. Many environmental factors are also known to influence the corrosion rate (and hence the polarisation curves) such as flow, pressure, temperature, or the oil-gas-aqueous phase composition.

Figure 4.5 shows a simplified and theoretical, polarisation curve, for a single electrochemical reaction on a metal surface under standard conditions (e.g. Equation 4.9 – oxidation of Fe and reduction of Fe^{2+}(aq)) and illustrates how the current density varies as a function of applied overpotential.

The anodic oxidation and cathodic reduction half-reactions at E^0 take place at the same rate and net current cannot be measured because the system is expected to be at equilibrium.

Exchange current at equilibrium conditions:

$$i_0 = i_a = i_c \tag{4.11}$$

As the overpotential is increased further away from E^0, a electrochemical current flows as a result of a unidirectional charge transfer reaction. However, when a large anodic overpotential is applied (+ve), the contribution from anodic current density (i_a) is much higher than the cathodic current density (i_c).In this case, the cathodic exponential term in the Butler-Volmer equation can be ignored and the entire surface becomes a 'net' anode as the oxidation reaction dominates.

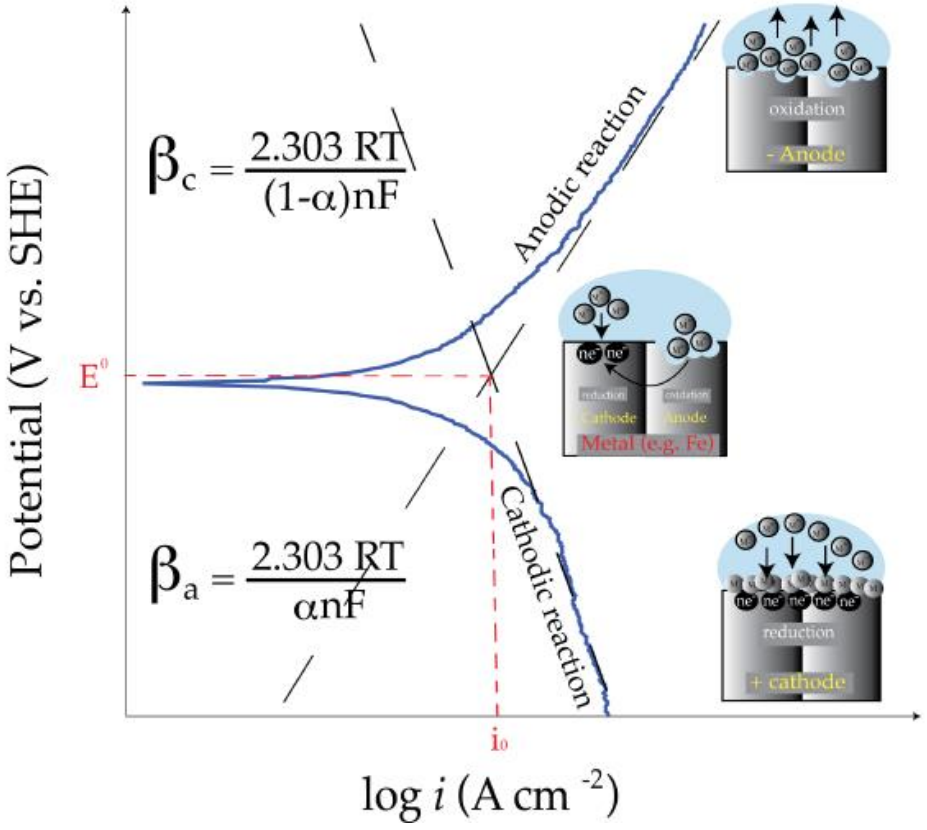

Figure 4.5. Theoretical potential-current density or polarisation curve (blue) for a single redox reaction on a metal surface (e.g. metal oxidation/reduction). Equations to calculate $\boldsymbol{\beta a}$ and $\boldsymbol{\beta c}$ gradients are provided, along with schematics of the surface at high anodic and cathodic overpotentials, From [56].

At a large negative overpotential, the surface performs as a ‘net’ cathode.

Net current in an anodic potential shift:

$$i_0 = i_a - i_c \tag{4.12}$$

Net current in an cathodic potential shift:

$$i_0 = i_c - i_a \tag{4.13}$$

Equations 4.14 and 4.15 represent the anodic and cathodic current densities at high anodic (η_a) or cathodic (η_c) overpotentials respectively.

$$i_a = i_0 \left\{ e^{\left(\frac{(\alpha)nF\eta)}{RT}\right)} \right\} \tag{4.14}$$

$$i_c = i_0 \left\{ e^{\left(\frac{(1-\alpha)nF\eta)}{RT}\right)} \right\} \tag{4.15}$$

Equations 4.14 and 4.15 can be rearranged for overpotential,

$$\eta_a = \frac{2.303RT}{\alpha nF} log \frac{i_a}{i_0} = \beta_a log \frac{i_a}{i_0} \tag{4.16}$$

$$\eta_c = \frac{2.303RT}{(1-\alpha)nF} log \frac{i_c}{i_0} = \beta_c log \frac{i_c}{i_0} \tag{4.17}$$

The pre-logarithm terms in Equations 4.16 and 4.17 are the anodic and cathodic reaction gradients (known as β_a and β_c respectively) [186] which is the point at which these gradients cross on a polarisation curve provides the value of the i_0. The anodic (β_a) and cathodic (β_c) gradients and are used to estimate material corrosion rates and is described later in this chapter.

4.3 Static Experimental Set-Up and Electrochemical Methods

The true mechanism behind corrosion is the actual atomic, molecular, or ionic transport process that occur at the material interface. These processes cannot be directly observed on an atomic scale, making it necessary to infer possible mechanisms based on indirect measurements and observations such as mass loss, rate of corrosion product formation or changes in surface appearance. When electrochemical corrosion is occurring, mechanisms can be identified through the implementation of an electrical potential and/ or current measurements [3]. The following sections will describe the set-up of the static immersion tests conducted during this work along with the operating conditions chosen (and why) and the electrochemical methods used. Practical corrosion science typically involves the study of electrochemical processes that are taking place at a metal electrode surface (solid metal phase) in an electrolyte (aqueous phase), using an instrument known as a potentiostat. Although there are a number of electrode setup configurations, the one used in this work is a 'three electrode configuration' which is described in more detail later in this chapter.

4.3.1 Static Glass Cell Configuration, Set Up and Operating Conditions

For all experiments, a glass cell was filled up with 1L of electrolyte that was prepared by dissolving 3.5 wt.% (35 grams) of NaCl in distilled water. To achieve de-aeration and minimise the dissolved oxygen concentration ($O_{2(aq)}$), the test solution was purged with high purity CO_2 for ~24 hours prior to each experiment. In addition, high purity CO_2 was continuously bubbled into the test solution throughout the duration of each experiment. The glass vessel was operating at atmospheric pressure and was sealed with one small outlet for CO_2 gas to prevent O_2 ingress and to maintain the total pressure of 1 bar. Based on colorimetric analysis of the test solution, this ensured that the concentration of O_2 was below 50 pbb to simulate oilfield conditions. Each test was conducted at a fixed temperature of 80 ± 1ºC and a fixed pH of 6.8. The temperature of the test solution was achieved by immersing a thermocouple probe connected to a heater controller, including of a hotplate and a magnetic stirrer. The solution pH which was varied and controlled through the addition of sodium bicarbonate ($NaHCO_3$) and was equal to ~8 grams in this case. A magnetic stirrer rotating at a speed of 200 rpm was used continuously

throughout the experiment to promote chemical consistency throughout the fluid. The working electrode was a carbon steel specimen with 4.9 cm^2 exposed surface area. A saturated Ag/AgCl reference redox electrode, which incorporated a platinum auxiliary electrode was immersed into the solution. Figure 4.6 shows a schematic and a 3D model of the experimental apparatus used to carry out the static immersion experiments.

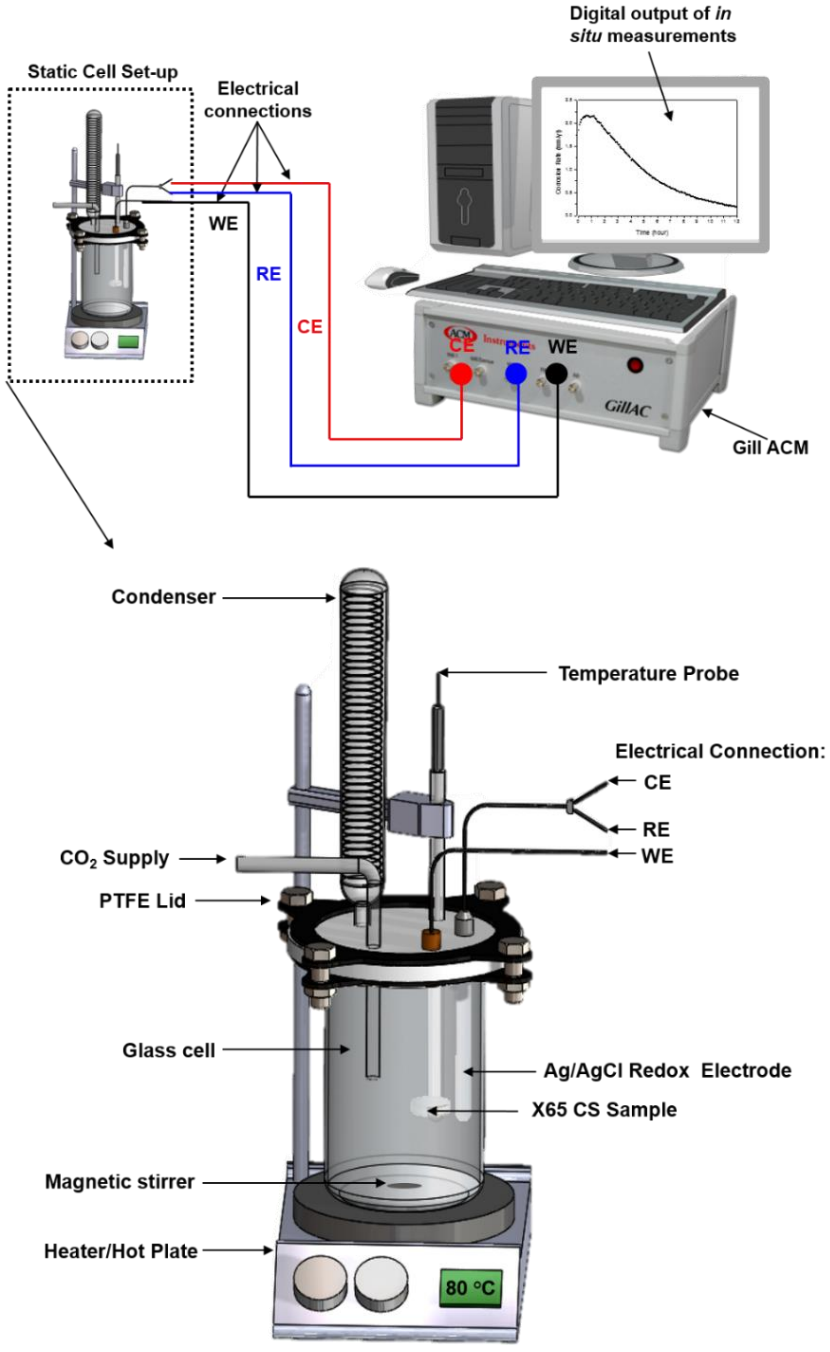

Figure 4.6. A schematic and 3D model of the experimental apparatus used to carry out the static immersion experiments.

The tests in Chapter 5 are designed to help understand the true nature, morphology and composition of the corrosion products offering ultra-protective properties and how the crystals develops over time.

After screening through a well-defined matrix of temperature (50 to 80°C) and pH (3.75 to 7), it was decided to run all tests in Chapter 5 at a pH of 6.8 and a temperature of 80°C. This is mainly due to the fact that these environmental conditions stimulate the formation of protective crystalline $FeCO_3$ (as shown in the potential-pH diagram for 80°C at atmospheric pressure in Figure 4.7) and is more likely to promote the formation any 'pseudo passive' corrosion product layers.

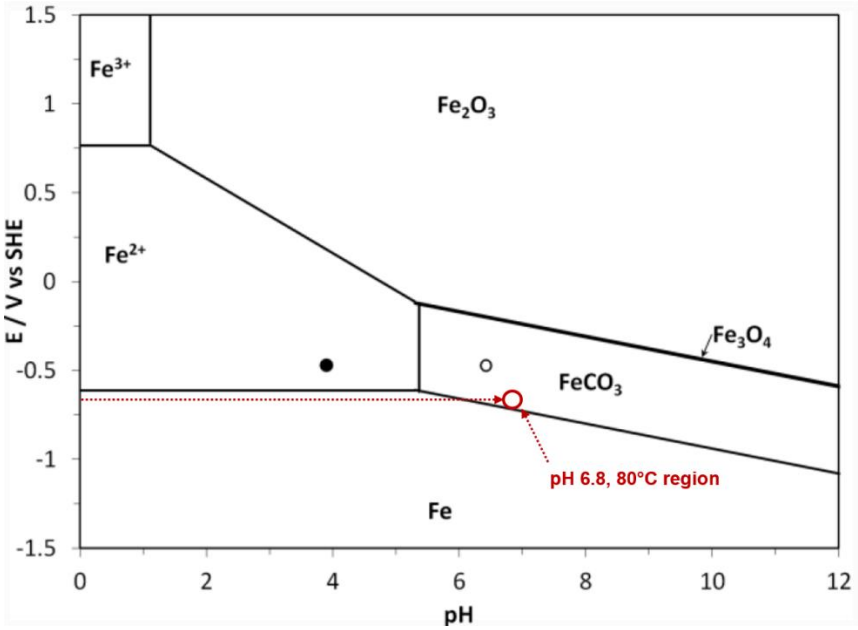

Figure 4.7. Potential-pH diagram for 80°C at atmospheric pressure, from [4].

All tests were conducted in a CO_2 saturated solution with a NaCl weight of 3.5%. The salinity is known to affect the solution resistance but also the solubility of gases such as CO_2. This value was chosen because it is the nearest to the sea water composition and the most widely abundant in the literature. It is also stated in ASTM G31 - 72(2004) entitled "Standard Practice for Laboratory Immersion Corrosion Testing of Metals" that the typical test solution to carry corrosion experiments corresponds to 0.6 mol/L of NaCl. At

atmospheric pressure, the CO_2 partial pressure is averaged to ~0.54 bar since at 80°C the water vapour pressure is ~ 0.46 bar.

Upon test completion, the samples are washed with distilled water, air dried, and carefully stored in a desiccator sample bag left in a deaerated chamber; this reduces the probability of oxidation of corrosion products prior to any planned surface analysis. All tests were ran in static conditions in a glass beaker having a volume equal to one litre. The only disturbances involved are the magnetic stirrers running at 200 rpm and the continual CO_2 bubbling at a flow rate of 0.1 litre per minute.

Once the setup was at the desired operating conditions, the electrodes were immersed into the test solution. They were then connected electrically to the potentiostat for electrochemical measurements to be taken. The corrosion process was monitored using a computer controlled Gill 12 ACM potentiostat to make electrochemical measurements during the test.

4.3.2 Study of Corrosion: Electrochemical Methods

Corrosion of metallic structures in aqueous systems is electrochemical in nature; for this reason studying such phenomena using electrochemistry techniques is the preferred methodology. The applications of electrochemistry are broad and could be described as the reduction of metal ions into atoms on an electrode surface by both chemical and electrochemical routes. Only the latter involves a flow of current and ultimately metal reduction initiates at the nanoscale and leads to atom agglomerates or nanoparticles [167].

Different techniques were implemented to record electrochemical responses in this study; open circuit potential (OCP), linear polarisation resistance (LPR), Tafel polarisation and electrochemical impedance spectroscopy (EIS). Corrosion rate and solution resistance measurements were conducted using both DC and AC measurements with an ACM GILL12 potentiostat.

4.3.2.1 Three Electrode Cell Setup

In the following study, as in most electrochemical techniques, a ‘three-electrode configuration’ is used. As Figure 4.8 illustrates, the setup comprises a working electrode (WE), the electrode under study; a reference electrode (RE), which has a reproducible interfacial potential to measure against the WE, and is calibrated by the manufacturer to the standard hydrogen electrode

(E = 0 V); and a counter electrode (CE), an inert electrode with a ‘current-carrying’ function, to study WE kinetics.

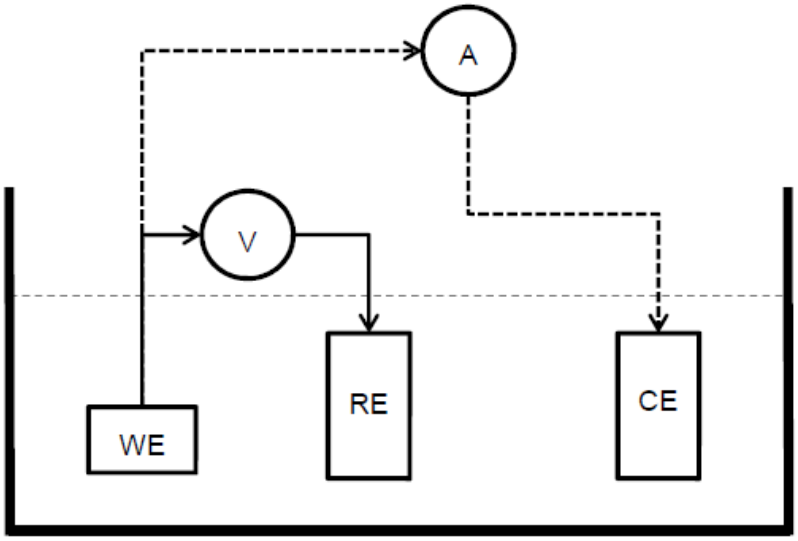

Figure 4.8. Schematic diagram of a 3 electrodes cell set up with (A) Ammeter, (V) Voltmeter, (WE) Working Electrode, (RE) Reference Electrode and (CE) Counter Electrode

In Figure 4.8, the potentiostat allows the measurement of the voltage between the WE and the RE through a high-impedance voltmeter and the ammeter computes the current flowing between the CE and WE. This setup tends to minimize the current that passes through the RE while the CE allows the application of the desired current or potential through the WE. The CE is usually made of an inert material and will always be polarised in the opposite direction in regards to the WE.

4.3.2.2 Working Electrode – X65 Carbon Steel

In the oil and gas industry, several metals and alloys are used throughout the entire network – from downstream to upstream processes. Carbon steel is an alloy in which the iron is the principle element, with a carbon content typically up to 2.5%. Carbon steel is the work-horse material in the oil and gas industry. At least 80% of all components in the oil and gas industry are made from carbon steel because it is in-expensive, readily available, and easily fabricated.

The working electrode terminology is used in relation to the electrochemical test setup used which is the three-electrode cell as described already. X65 (UNS K03014) pipeline carbon steel is the material used in this research as

the corroding specimen. The value showing after the X such as 65 denotes the yield strength of the specimen e.g. 65,000 psi for the selected X65 mild steel.

Table 4.1 details the nominal composition and as any carbon steel alloy, X65 shows iron as the principal element while the carbon content is below 0.25 wt.%.

Table 4.1. Composition of X65 pipeline carbon steel (wt.%)

C	Mn	Ni	Nb	Mo	Si	V	P	S	Fe
0.15	1.422	0.09	0.054	0.17	0.22	0.06	0.025	0.002	97.81

The X65 carbon steel specimens were cut to have surface area 0.64 cm^2 which was exposed to the electrolyte, with thickness of 1 cm which was isolated using epoxy resin, which is illustrated in Figure 4.9.

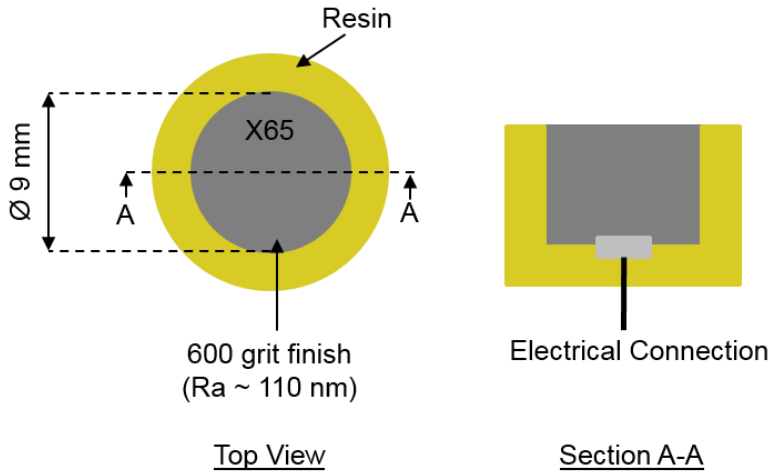

Figure 4.9. Schematic representation of the X65 carbon steel specimens used for the static immersion tests.

According to the ASTM G150 (2004) standard, the test volume should satisfy a minimum of 100 ml per cm^2 of the test area and therefore making the desired test area/volume ratio in these tests acceptable under these standards. A Cu-Sn wire was connected, to the face opposite to the surface of interest, using resistance spot solder. The WE segment was then mounted into a hollow poly-methyl methacrylate (PMMA) mould and half-filled with non-conductive epoxy resin and hardener (10:1 ratio by weight). Upon curing, the WE surface was sequentially ground using SiC paper (120, 320, 600 grit). Figure 4.10

illustrates SEM images of the X65 carbon steel surface finish after being wet ground with 600 grit SiC paper.

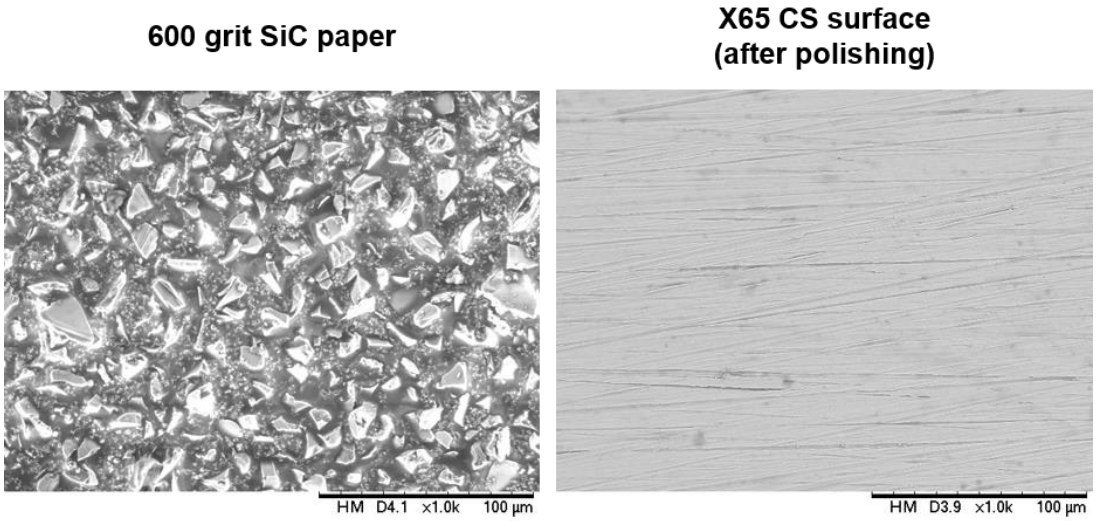

Figure 4.10. SEM images of an X65 carbon steel surface finish after being wet ground (right) with 600 grit SiC paper (left).

Samples were then degreased with ethanol and rinsed with distilled water to completely clean them of any leftover residue and then dried with compressed air. During the static immersion experiments, the isolated Cu-Sn wire emerges from the top of the glass cell to enable an electrical connection between the WE and the potentiostat.

4.3.2.3 Reference and Counter Electrode – Ag/AgCl Redox Electrode

The three-electrode cell used in this work also comprised of a silver/silver chloride InLab® Reference electrode; the reference system is an ARGENTHALTM with a silver ion tap bathing in a 3 mol/L potassium chloride solution. The reference electrode allows measurement of the working electrode potential without passing current through it while the counter (auxiliary) electrode is an inert electrode with a ‘current-carrying function’ (allows current to pass through WE) to study WE kinetics. The three electrodes are electrically connected to a potentiostat which controls the potential of the working electrode and measures the resulting current. The following sections highlight the procedure to collecting electrochemical and interpreting measurements.

4.3.3 Collection and Interpretation of Electrochemical Data

With regards to the electrochemical measurements, LPR and EIS were employed to determine the *in-situ* corrosion rate of the X65 carbon steel working electrode. The open circuit potential (OCP) was followed immediately after immersion and stabilised within 1-5 minutes. LPR measurements were performed by polarising the sample ±15 mV vs. the open circuit potential OCP at a scan rate of 0.25 mV/s (in accordance with ASTM-G102) to obtain a polarisation resistance (R_p) and were undertaken every approximately every 5-7 minutes. For such small potential perturbations, the WE surface is not altered/damaged [168, 169]. A typical plot obtained of current density vs. potential is shown in Figure 4.11 which shows that the measured current density is linearly proportional to the applied potential.

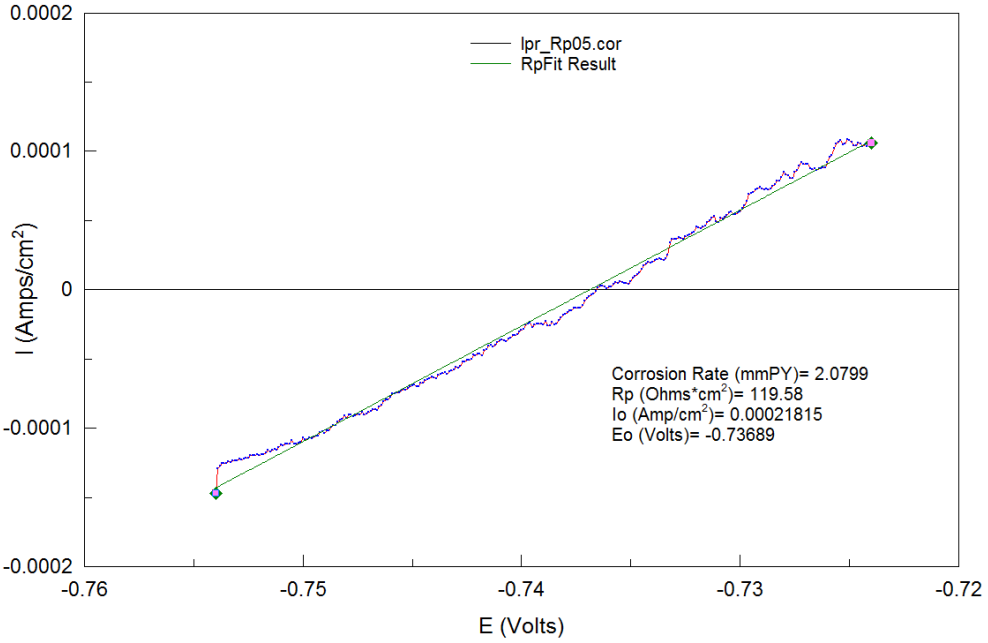

Figure 4.11 Typical LPR plot that demonstrates the linear potential-current relationship at low applied over potential. The gradient is used to obtain the polarisation resistance, $\boldsymbol{R_p}$.

The gradient of the linear section, attained from numerical fit of the curve, yields the value for, R_p of the electrode [86]. This potential-current gradient around OCP is uncompensated for the solution resistance (R_s) between the WE and RE. In all of the experiments, the solution resistance was measured using EIS. The carbon steel WE was polarised ±5 mV vs. the OCP using the frequency range from 20 kHz to 0.1 Hz. The value of R_s was subtracted from

R_p to produce a charge-transfer resistance (R_{ct}) which was used to determine the corrosion rate behaviour with time:

$$R_{ct} = R_p - R_s \tag{4.18}$$

Potentiodynamic measurements were also performed on freshly ground samples in separate experiments at each solution pH. This technique was used to generate Tafel polarisation curves to determine the anodic and cathodic Tafel constants (β_a and β_c respectively) and ultimately an appropriate Stern-Geary coefficient (B) to enable calculation of corrosion rates from the values of R_{ct} determined as a function of time in each experiment. Tafel polarisation curves were collected by performing individual anodic and cathodic sweeps starting at OCP and scanning to +150 mV or -500 mV vs. OCP, respectively at a scan rate of 0.5 mV/s. Freshly polished samples and new test solutions were used for each individual anodic and cathodic sweep. From the polarisation curves produced, it was possible to determine the anodic (β_a) and cathodic (β_c) Tafel constants in mV/decade by measuring their respective gradient over regions were linearity was observed between the applied voltage and the natural log of the measured current. Tafel extrapolation relies on the fact that the slope of the potential (Y-axis) versus the logarithm of the current density (X-axis) plot around the OCP is linear as shown in Figure 4.12 if sufficiently large potentials are applied in both anodic and cathodic directions.

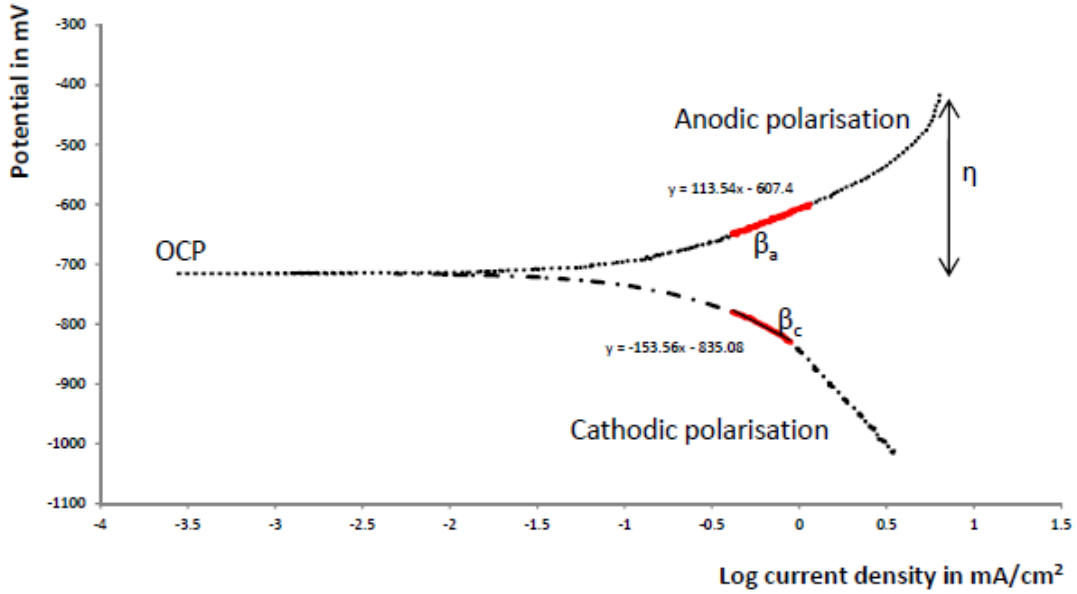

Figure 4.12. Anodic and cathodic Tafel slopes of the potential (Y-axis) versus the logarithm of the current density (X-axis) plot around the OCP, From [170].

The Tafel slope measurements were used in Equation 4.19 to determine the Stern-Geary coefficient, and the corrosion current density (i_{corr}) using Equation 4.20.

$$B = \frac{\beta_a \beta_c}{2.303(\beta_a + \beta_c)} \tag{4.19}$$

$$i_{corr} = \frac{\beta_a \beta_c}{2.303 R_{ct}(\beta_a + \beta_c)} \tag{4.20}$$

The i_{corr} value obtained through Equation 4.20 was then used in combination with Equation 4.21 (based on Faraday's Law) and the measured values of R_{ct} to determine the corrosion rate in mm/year:

$$CR\left(\frac{mm}{yr}\right) = 3.27 \frac{i_{corr}(A\ cm^{-2})\ x\ 55.847(g\ mol^{-1})}{2\ (e^{-})\ x\ 7.8\ (g\ cm^{-3})} \tag{4.21}$$

4.4 Post Experimental Surface Analysis

To supplement the *in-situ* electrochemical measurements in the experiments, the morphology and composition of the corrosion products formed during this study were analysed by a combination of scanning electron microscopy (SEM), focused ion beam and transmission electron microscopy (FIB-TEM) and X-ray diffraction (XRD).

The *ex-situ* data in the form of SEM images were used to assist in tracking crystal growth to develop a further understanding for the mechanism of corrosion product layer formation. The data obtained was then correlated with the recorded XRD patterns and electrochemistry data. The surface analysis techniques carried out are explained in the following sections.

4.4.1 Scanning Electron Microscopy (SEM)

SEM is a qualitative surface analysis technique used to observe the surface of the carbon steel sample exposed to a CO_2 environment under varying conditions. SEM was used throughout the project to examine and obtain

images of the surface morphology at different exposed time on samples of carbon steel. At the end of each experiment, the samples were rinsed with acetone, dried and retained in a desiccator prior to SEM analysis, which was performed using a Hitachi TM3030 bench top SEM in secondary electron mode with an operating voltage of 15 kV. The Hitachi TM3030 bench top SEM used during this study is shown in Figure 4.13.

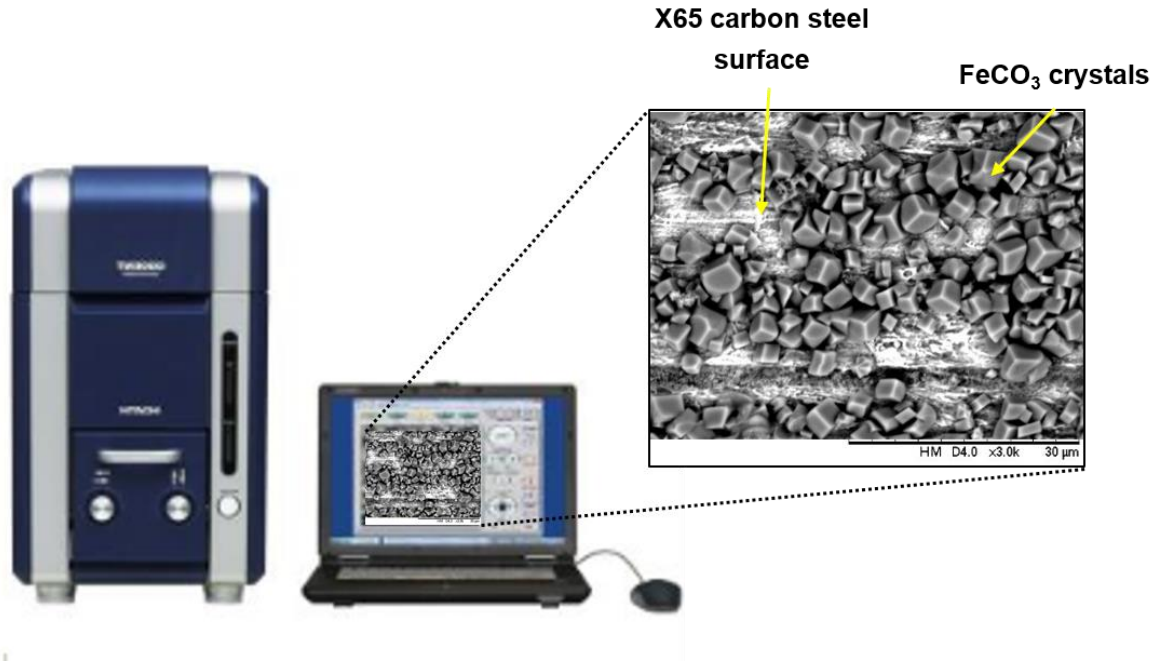

Figure 4.13. Image of the Hitachi TM3030 bench top SEM used in during this study.

The SEM images were carefully analysed to determine the crystal morphology, crystal size and the surface coverage. The surface coverage was obtained through processing numerous random images from across the same surface into a MATLAB programme that utilises the difference in contrast of the crystals formed against the bare steel surface to produce a binary output image in black and white. Surface coverage was determined through the determining the percentage of black pixels (crystals) against the white pixels (no crystals). This method of analysis surface coverage has been implemented and validated elsewhere through a previous publication [171].

4.4.2 Focused Ion Beam (FIB) and Transmission Electron Microscopy (TEM) Sample Preparation

In some cases, especially when investigating the ‘pseudo’-passive layer that offered ultra-protection to the carbon steel surface, FIB was used. FIB etching is a technique used to prepare thin samples from large specimens, allowing them to be analysed using TEM. The FIB-SEM is capable of milling segments from larger samples through the use of a gallium ion beam. The milled-out section can then be removed from the large sample and mounted onto a stage for further analysis in the TEM. The technique allows the user to select specific locations on the surface and analyse the interface between corrosion products and the steel substrate. Such an approach will allow a better understanding behind the corrosion process at the very interface between deposits and the steel surface. Sample preperation using FIB is shown in Figure 4.14.

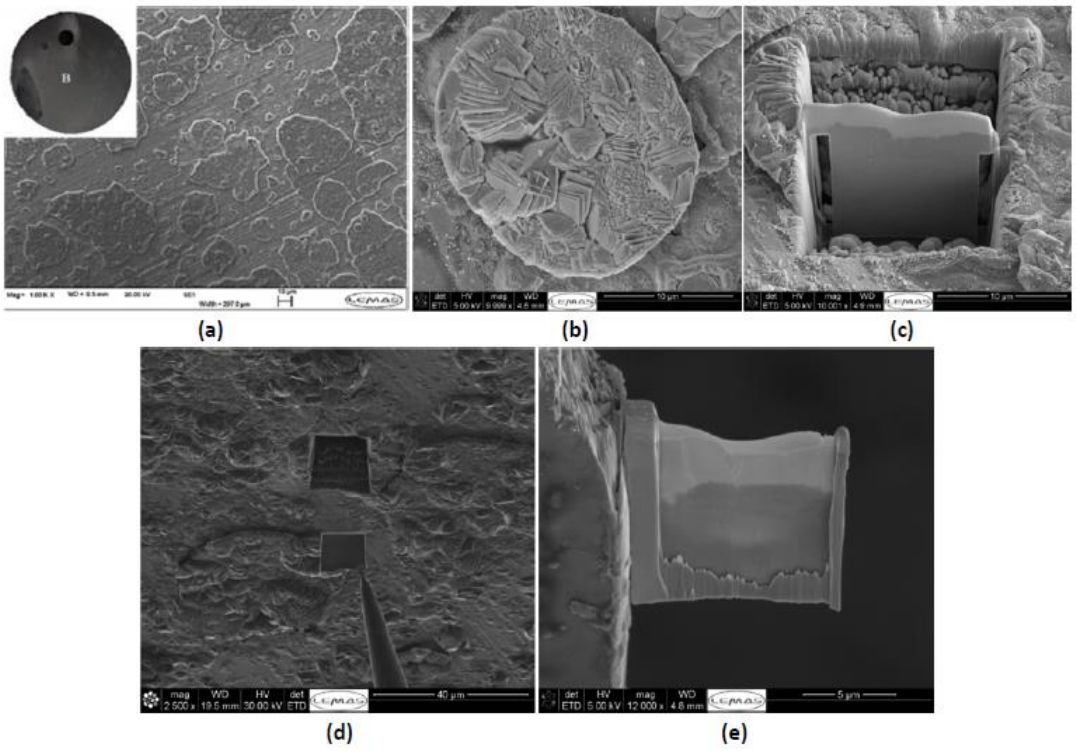

Figure 4.14. (a) SEM image of $FeCO_3$ corrosion deposits on steel surface at x1000 magnification (b) SEM image of surface at x10000 magnification, (c) milled out segment from the steel surface in same region, achieved using FIB, (d) removal of the thin segment from the surface and (e) positioning of the this segment onto the surface for TEM examination (the individual images in this figure have been provided by Dr Yong Hua, University of Leeds).

The instrument used was a FEI Nova200 dual beam SEM/FIB fitted with a Kleindiek micromanipulator for *in-situ* lift-out. The ion beam was operated at voltages between 30 and 5 kV, and with beam currents between 5 and 0.1 nA. Regions of interest were first coated with a protective layer of platinum before bulk removal of material was performed. Samples were then lifted out *in-situ*, attached to a Cu TEM grid, and then thinned to a final thickness of around 100 nm.

TEM is a technique capable of generating high resolution images (see Figure 4.15). Within the TEM, selected area electron diffraction (SAED) measurements can be taken. The patterns generated consist of dots in the case of a single crystal, or a series of rings in the case of a polycrystalline or amorphous material. The technique enables corrosion product morphology at very specific points to be analysed, to help relate the corrosion product to the extent of surface deterioration.

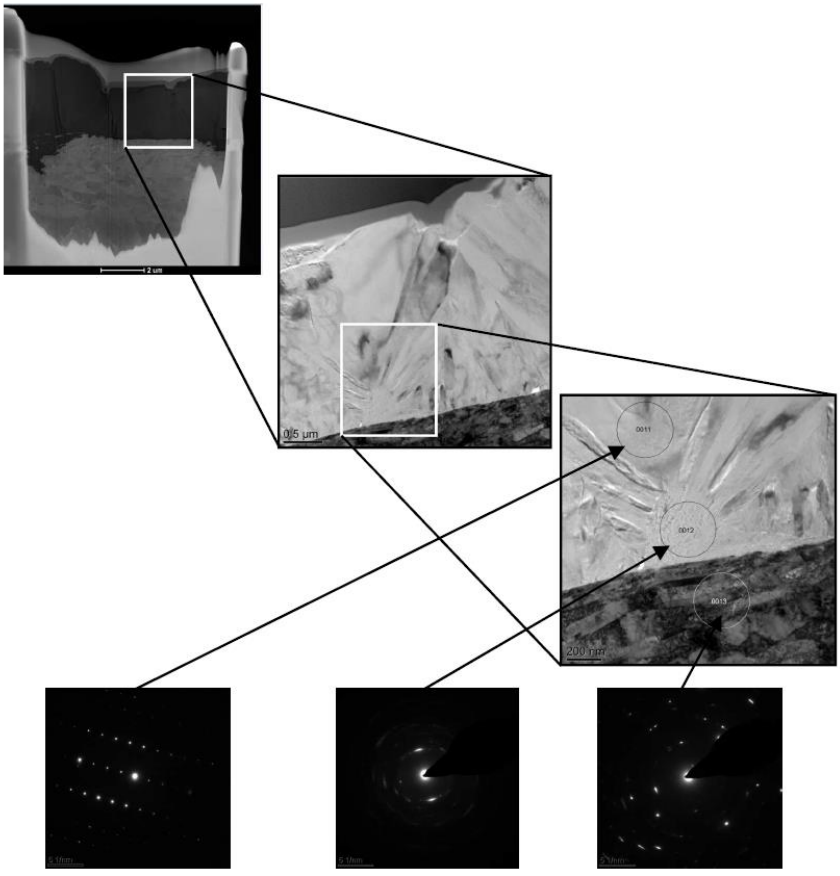

Figure 4.15. TEM images of thin segment extracted using the FIB-SEM and accompanying SAED patterns of the corrosion product and substrate (the individual images in this figure have been provided by Dr Yong Hua, University of Leeds).

TEM was performed using a FEI Tecnai F20 FEGTEM (200 kV) fitted with a high angle annular dark field (HAADF) detector and a Gatan Orius SC600 CCD camera. In a TEM, SAED used to measure a solid crystal.

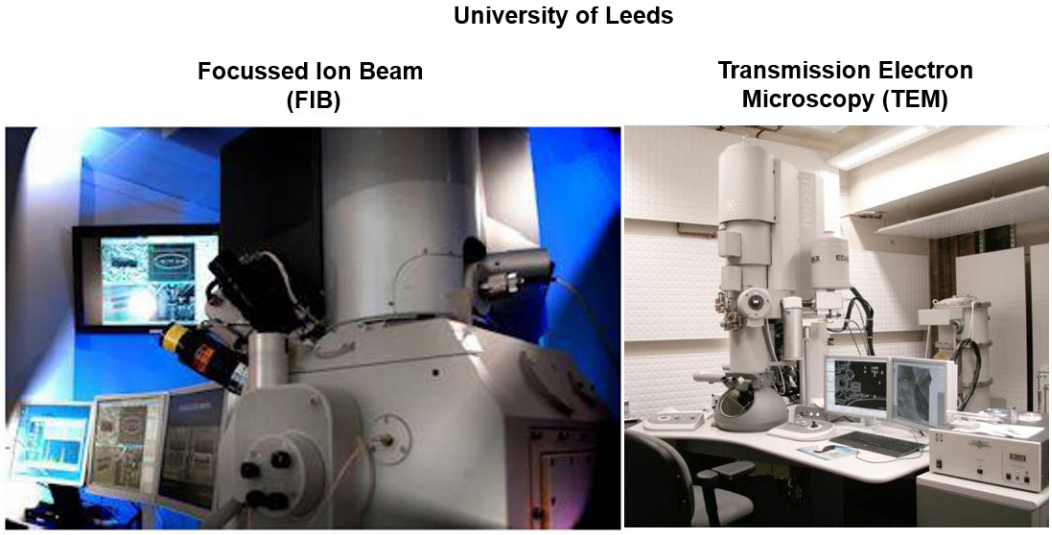

Figure 4.16. Images of the FIB and TEM facilities used at the University of Leeds, LEMAS (Leeds Electron Microscopy and Spectroscopy Centre)

4.4.3 X-ray Powder Diffraction Measurements

An important aspect of this research was to link the morphology of the corrosion products on the surface of the sample to their chemical composition. To determine the nature of the corrosion products formed on the steel surface in each environment, XRD measurements were conducted over the entire steel surface. Due to the crystallographic nature of the corrosion products formed, XRD is one of the most suitable techniques for this purpose.

XRD is a non-contact and non-destructive technique that can be used to obtain structural and physical information from a sample. This is achieved by irradiating the sample with monochromatic X-ray light and measuring the intensity of the diffracted X-rays as a function of the diffraction angle. When a crystalline sample is irradiated with monochromatic X-ray light, diffraction from lattice planes of the crystal will occur according to Bragg's Law:

$$2dsin\theta = n\lambda \tag{4.22}$$

Where d is the spacing between the diffracting planes or lattice, θ is the incident angle, n is any integer and λ is the wavelength of the beam [173, 174].

Figure 4.17 shows a schematic of Bragg's Law.

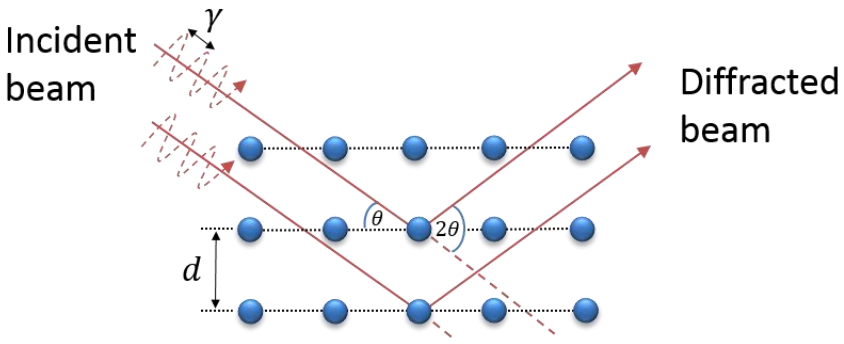

Figure 4.17. Schematic showing illustrated diagram of Bragg's Law.

A diffraction pattern is formed and the intensity of the diffracted X-ray as a function of the diffraction angle can provide both structural and physical information about the sample. Phase identification is done by comparing the measured d-spacings in the diffraction pattern and their integrated intensities with known standards (for example: powder diffraction data - International Centre for Diffraction Data (ICDD)). Note that the standard database contains diffraction patterns of materials with random orientation; thin films often have a preferred orientation and can cause the measured intensities to disagree with the ICDD powder diffraction data.

The XRD spectra for each sample was carry out using Siemens Bruker D8 Advance multipurpose diffractometer (see Figure 4.18), employing 40 kV (Kα1+2) Cu radiation with an active area of 10 x 10 mm programmable divergence slits. Scans were performed over a range 20° < 2θ < 70° using a step size of 0.033 per second, with a total scan time of approximately 50 minutes to capture the main $FeCO_3$ peaks. The diffracted X-ray beams are picked up by a detector scanning at this angle and the positions of these reflections inform the user about the inter-layer spacing of atoms in the crystal structure. Peak intensities give information about how much X-ray scattering is contributing to that reflection in terms of where particular atoms lie in the structure, or how much of a phase is present in a sample. The diffraction pattern is analysed using X-Pert Analysis software that allows the identification (through a search and match process using the ICDD) of the crystalline phases present on the samples surface.

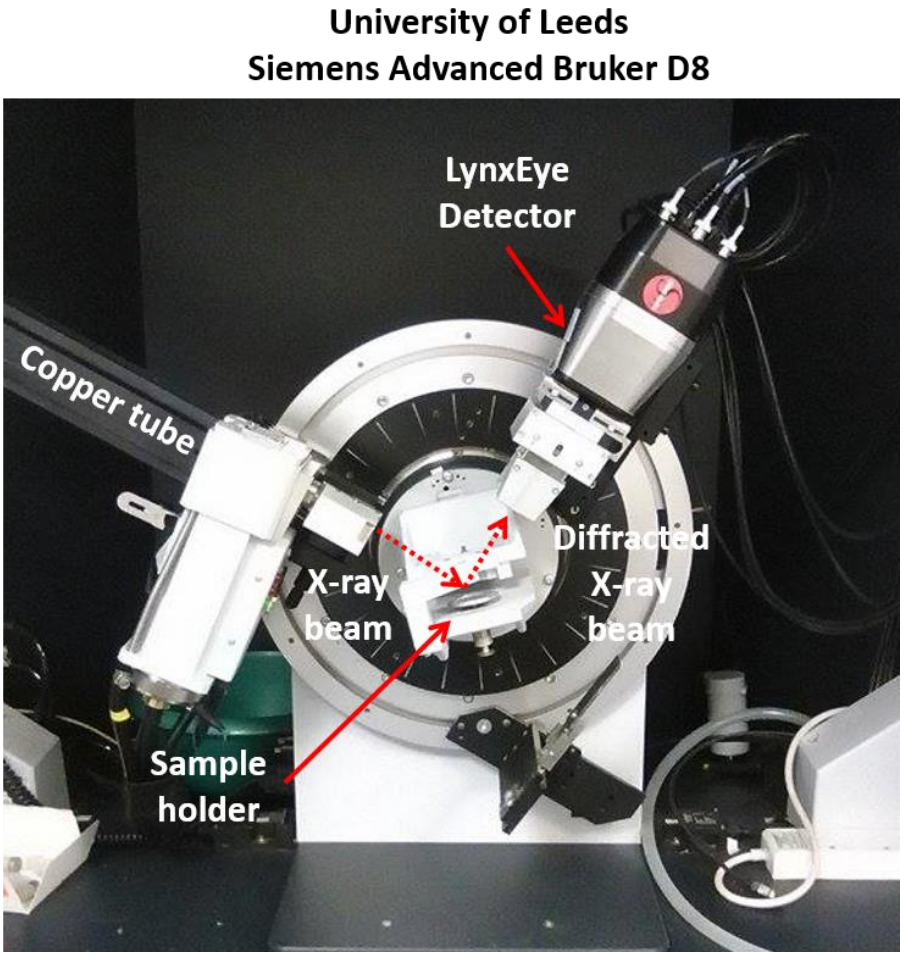

Figure 4.18. Image of in-house (University of Leeds) Siemens Advanced Bruker D8 diffractometer.

Chapter 5.
Understanding the Development of Protective $FeCO_3$ over Time

This chapter presents results from a study to gain a better understanding of the development of protective $FeCO_3$ on to X65 carbon steel over 144 hours of immersion time in a static glass cell set-up. The results show the growth of $FeCO_3$ on X65 carbon steel surfaces in a CO_2-saturated 3.5 wt.% NaCl brine at 80°C, pH 6.8 over a range of immersion times (24 hours, 72 hours, 106 hours and 144 hours) in the form of LPR, EIS, SEM and XRD.

5.1 Introduction

Aqueous CO_2-induced corrosion of carbon steel surfaces presents a significant problem during oil and gas production and $FeCO_3$ is one of the main corrosion products found on the internal walls carbon steel pipelines and piping systems. This growth of $FeCO_3$ is of importance in CO_2 corrosion due to its influence on the corrosion rate when covering the corroding surface [57, 41, 111]. Under specific operating conditions, a highly dense, protective $FeCO_3$ film is formed. The high degree of protection is attributed to a combination of a surface blocking effect from the precipitated crystals as well as $FeCO_3$ presenting itself as a diffusion barrier to electrochemically active species involved in the charge-transfer process as the layer becomes denser and less porous. The transient corrosion rate behaviour of carbon steel during $FeCO_3$ formation and the magnitude of the steady state corrosion rate after film formation is dictated by the crystal layer nucleation, growth, morphology and its stability/resistance against chemical/mechanical removal [2, 93, 153, 176].

The nucleation and growth of the $FeCO_3$ layer is heavily dependent upon the kinetics of the precipitation reaction which is governed by the surrounding environment. The precipitation of $FeCO_3$ onto the internal walls of pipelines becomes possible when the concentration of Fe^{2+} and CO_3^{2-} exceed the solubility product of $FeCO_3$ in a solution. $FeCO_3$ nucleation and growth is governed by the supersaturation, which is deemed to be the driving force behind the precipitation process [81]. The precipitation of protective $FeCO_3$ is favoured at higher supersaturation which is defined as:

$$S = \frac{[Fe^{2+}][CO_3^{2-}]}{K_{sp}} \quad (5.1)$$

Such a process is facilitated when SS_{FeCO_3} > 1 [6]. Although nuclei formation is possible at SS_{FeCO_3} < 1, its rate increases rapidly only when a critical supersaturation is exceeded [178] which is determined by the surrounding environment.

In addition to $FeCO_3$, field and laboratory based experiments in recent years have indicated that chukanovite ($Fe_2(OH)_2CO_3$) [4, 13, 73, 74] or magnetite (Fe_3O_4) [3, 6] are corrosion products that can form on steel in CO_2-saturated/carbonate rich solutions. The formation of $FeCO_3$ and/or any other CO_2 corrosion products to form on the walls of carbon steel pipelines is a complex process due to the fluctuation in operating conditions during production. Therefore, there are still unanswered questions and uncertainties in relation to the actual process during CO_2 corrosion. Questions on the presence of $Fe_2(OH)_2CO_3$ and Fe_3O_4 still remained unanswered, a pertinent one being what role, if any, these corrosion products play in determining the overall protectiveness of the corrosion products formed.

In this light, a fundamental study of the growth and development $FeCO_3$ is presented under a simple and well-defined solution conditions at a constant temperature. In the work reported in this chapter, electrochemical methods (LPR and EIS) are used to monitor the changes in the corrosion of X65 carbon steel immersed in CO_2-saturated distilled water at 80°C, pH = 6.8, P_{total} = 1 bar, p_{CO_2}= 0.54 bar. The work was carried out using a series of substrate immersion experiments for different periods of time (24, 72, 96 and 144 hours), which enabled the sequential development of $FeCO_3$ to be evaluated. The carbon steel surface analysis was performed using SEM and XRD.

5.2 Experimental Procedure

1 litre glass cell experiments where conducted by immersion of X65 carbon steel substrates in CO_2-saturated solution according to the procedure detailed in Chapter 4. For all experiments in this chapter, the test solution (pH 6.8, 3.5 wt.% NaCl) was maintained at a temperature of 80°C ± 1°C. The test solution was purged with high purity CO_2 for a minimum of 24 hours prior and throughout the duration of each experiment to minimise the dissolved oxygen

concentration ($O_{2(aq)}$). Table 5.1 summarises the operating conditions for the static immersion experiments that are presented in this work.

Table 5.1. Experimental test matrix for the static immersion tests.

Parameter	In-house laboratory tests
Material	X65 carbon steel – 9 mm Ø (exposed surface)
Test solution	3.5 wt.% NaCl, distilled water
Solution pH	6.8
Temperature	80 ºC
CO_2 partial pressure	0.54 bar
Flow velocity	0 m/s (static cell)
Sample removal interval (*ex-situ* analysis)	24, 72, 106, 144 hours

The carbon steel samples used for these tests were corroding at open circuit potential (OCP) for the entire immersion periods (24, 72, 106 or 144 hours) upon immersion of the samples into the static cell. With the exception of the electrochemical measurements, LPR (±15 mV vs. OCP, 0.25 mV/s (every 15 minutes)) and EIS (20 kHz – 0.1 Hz, ±5 mV peak vs. OCP (every 2 hours)) were employed to determine the *in-situ* corrosion behaviour of the X65 carbon steel working electrode. *Ex-situ* SEM analysis was used to assist in tracking crystal growth and development of $FeCO_3$ and the data was used to correlate with the recorded XRD patterns and electrochemistry data.

5.3 Results and Discussion

The results and discussion of the growth and development of $FeCO_3$ as a function of time is divided into three main parts including LPR (corrosion rate) and OCP analysis, surface/cross-section analysis and electrochemical impedance spectroscopy (EIS) analysis.

5.3.1 Interpretation of Electrochemical Observations

Figure 5.1 shows a plot of the corrosion rate profile over immersion time of X65 carbon steel in CO_2-saturated solution in the conditions described previously as a function of immersion time over 144 hours . The data is plotted on a $\log^{10}$ y-axis to reveal the corrosion rate profile more clearly.

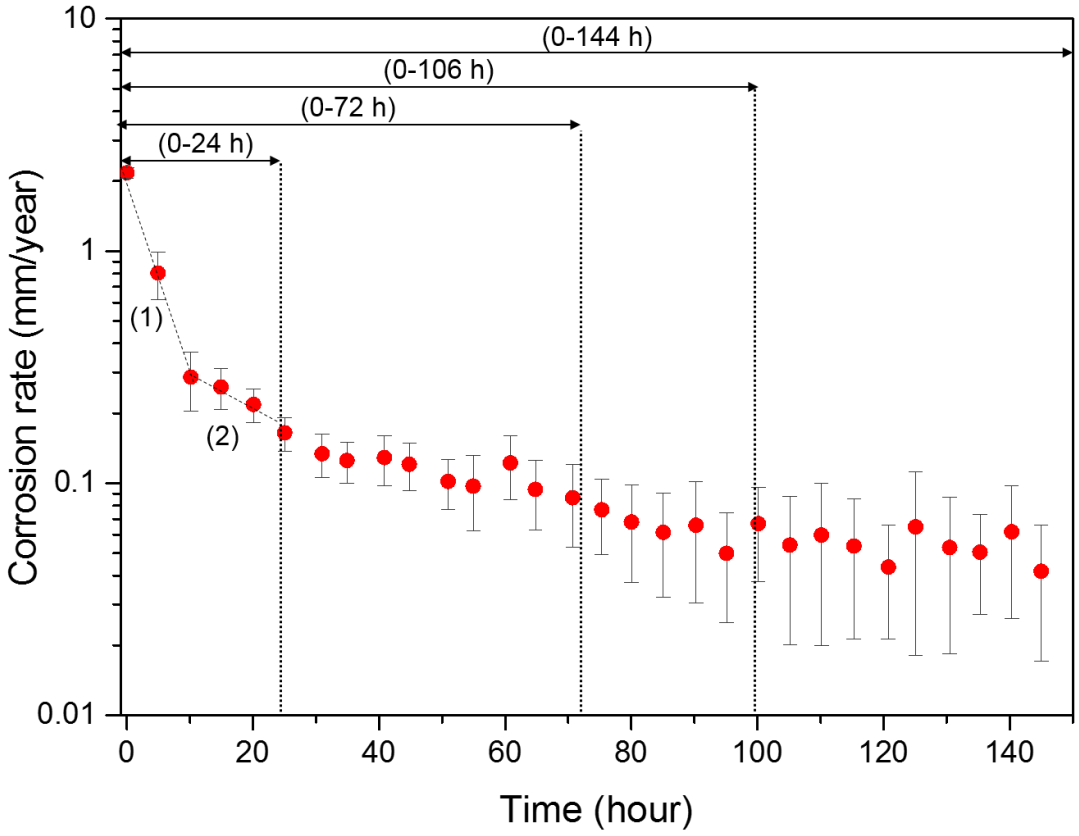

Figure 5.1. Average corrosion rate profile of X65 carbon steel in CO_2-saturated solution in the conditions over 144 hours at 80°C, pH 6.8, 3.5 wt.% NaCl and 0.54 bar p_{CO_2} (freely corroding).

The corrosion rates, plotted with error bars, have been determined using LPR measurements from 8 experiments in total, two x(24 hours, 72 hours, 100 hours and 144 hours) and the resulting corrosion rate values have been plotted every 5 hours for clarity. Figure 5.1 indicates that the corrosion rate of the carbon steel surface drops exponentially in the first 10 hours (region (1)), and then continues to decrease linearly with exposure time (region (2)). The corrosion rate of the system at the start of the test is ~2.2 mm/year and drops to a value of ~0.25 mm/year after 10 hours. This rapid drop in corrosion rate is assumed to be a result of $FeCO_3$ formation. The corrosion rate continues drop slowly for the remainder of the test to a value of 0.04 mm/year.

Figures 5.2 and 5.3 show the corrosion rate profiles and resulting OCP for each of the tests (run 1 and run 2) at different time intervals from 0-24 hours, 0-72 hours, 0-106 hours and 0-144 hours. Under these conditions, a well-developed $FeCO_3$ layer is expected to form offering protection to the steel surface against corrosion as shown in Chapter 3. Corrosion product layer characterisation was done to confirm this and will be discussed in the following section.

Looking at the corrosion rate data in Figure 5.2 and 5.3, it seems as if the profiles are extremely reproducible (especially within the first 24 hours of each test) with the exception of the observation of a sharp drop in corrosion rate in conjunction with a sharp rise in OCP in some of the tests. The drop in corrosion rate is a clear indication that protective crystals have formed. However, the physical mass, morphology, structure and precipitation rate of the corrosion products present cannot be dictated from LPR and OCP measurements alone. Therefore, suggesting that in this study, the drop in corrosion rate is a reliable means of concluding the formation of corrosion products and the protectiveness offered and gives reassurance to the reliability of the results presented.

In each of the tests conducted, the corrosion rate rapidly drops within the first 5 hours, and then continues drop exponentially for a further 10 hours to below 0.5 mm/year due to the formation of protective $FeCO_3$ crystals on the steel surface. Eventually decreasing to ~0.1 mm/year in all tests. Within this period, as the corrosion rate was decreasing (due to the build-up of $FeCO_3$ crystals), the OCP did not drastically change (~20 mV vs. Ag/AgCl). At this stage, the $FeCO_3$ crystals have formed a compact film reducing both anodic and cathodic reaction kinetics equally, offering protective properties similar to a mixed corrosion inhibitor [178, 179]. However, the degree of protectiveness varied marginally throughout the tests under the exact same conditions. This could be down to the initial surface roughness and boundary conditions at the steel interface. Another consideration is that these tests were performed in a static brine, which could result in the local surface concentration of the species present varying across the entire surface – making $FeCO_3$ precipitation more favourable at certain locations than at other locations across the sample.

An important observation up for discussion in these results is why a sharp rise in OCP (more than 200 mV), with an associated further drop in corrosion rate (with a final corrosion rate less than 0.02 mm/year) measured spontaneously at different time intervals during some of the tests as shown in Figure 5.2 (b)

(0-72 hours, Run 2), Figure 5.3 (a) (0-106 hours, Run 2) and Figure 5.3 (b) (0-144 hours, Run 1 and 2)).

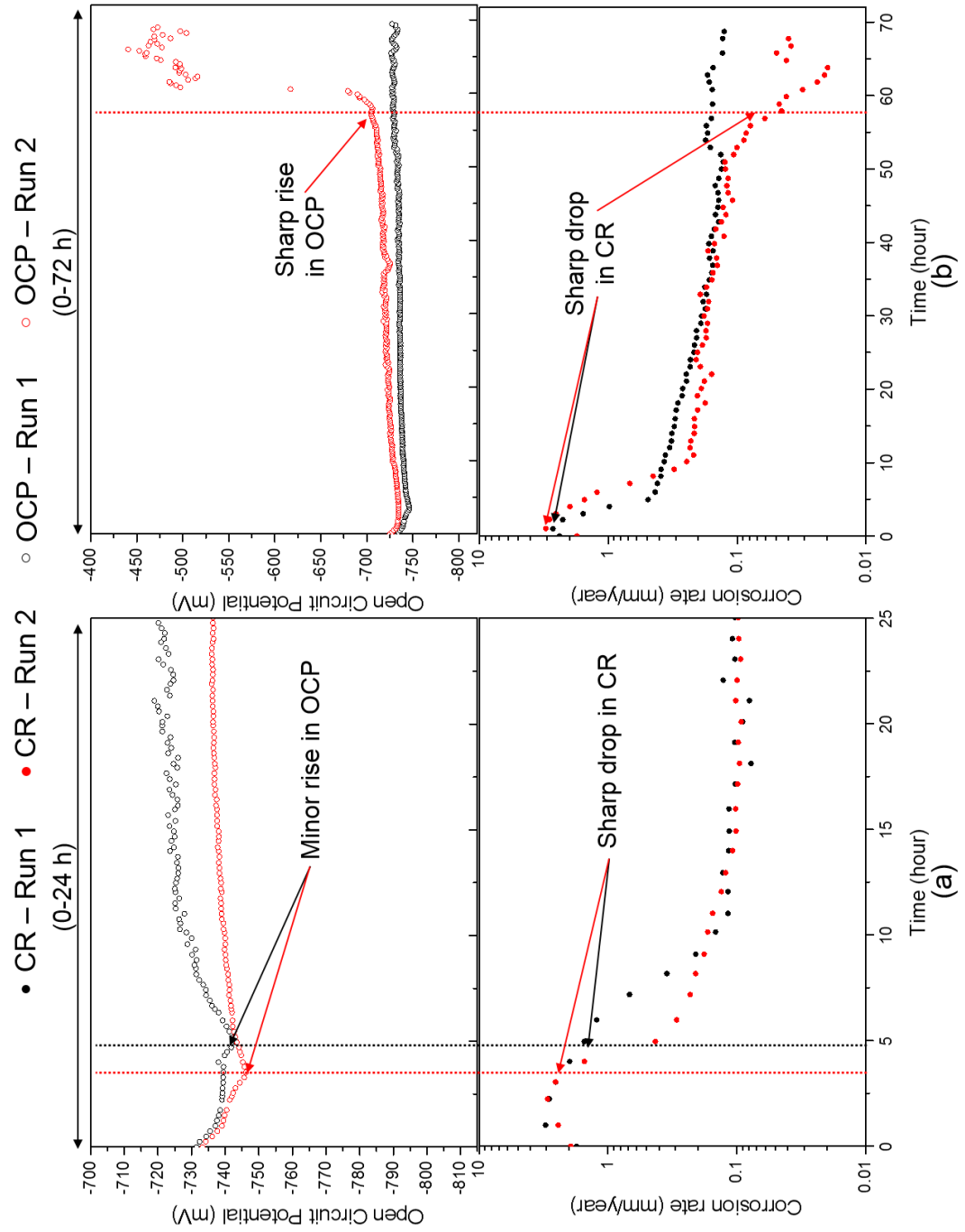

Figure 5.2. Corrosion rate and open circuit potential profiles at different immersion times in a CO_2 saturated brine at 80°C, pH 6.8, 3.5 wt.% NaCl and 0.54 bar $\boldsymbol{p_{CO_2}}$: (a) 0-24 hours; (b) 0-72 hours.

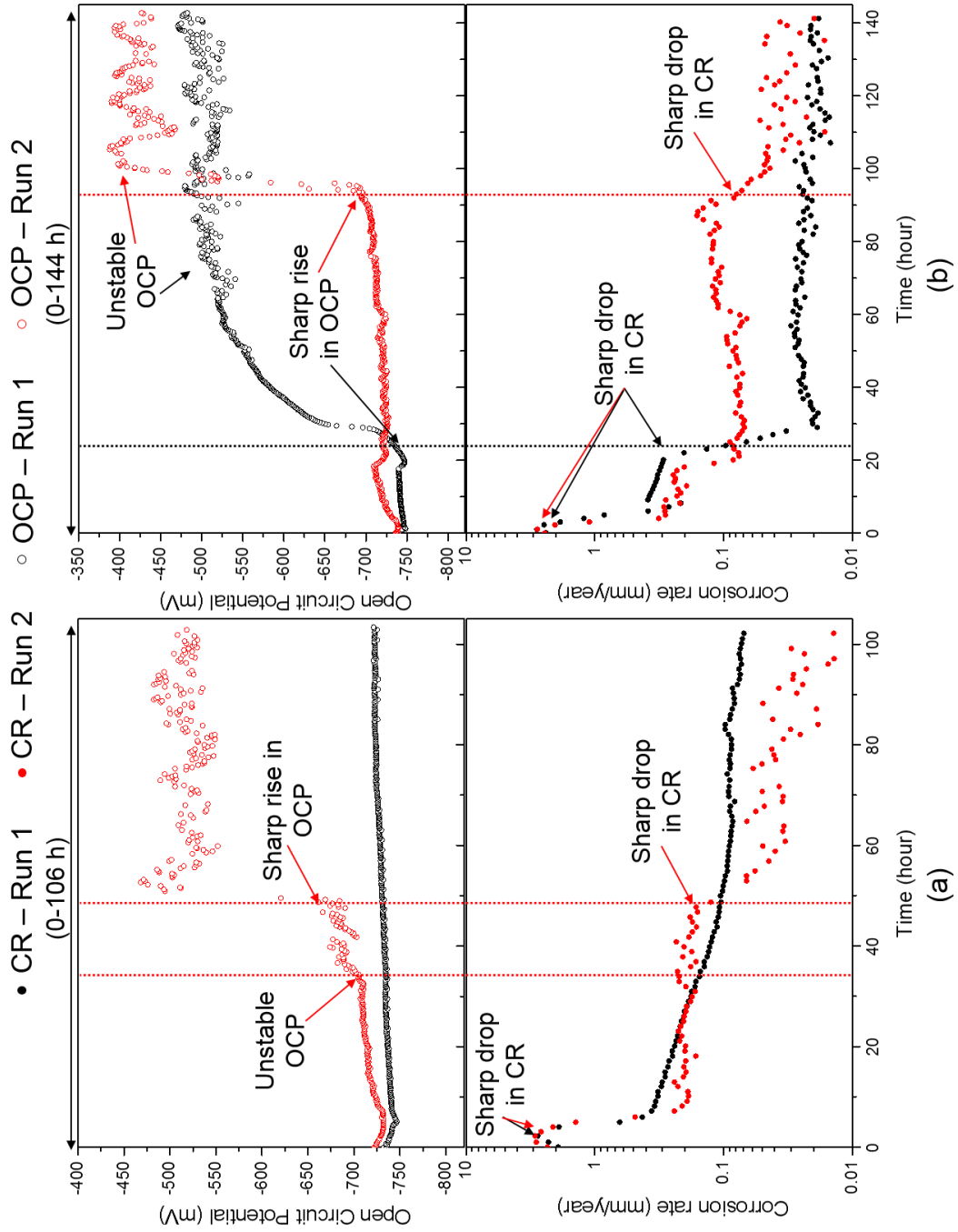

Figure 5.3. Corrosion rate and open circuit potential profiles at different immersion times in a CO_2 saturated brine at 80°C, pH 6.8, 3.5 wt.% NaCl and 0.54 bar $\boldsymbol{p_{CO_2}}$: (a) 0-106 hours; (b) 0-144 hours

This anodic shift in potential has been attributed to preferential suppression of the anodic half-reaction owing to the formation and build-up of $FeCO_3$, which retarded the diffusion of the cathodic species to the steel surface [21] performing more like an anodic corrosion inhibitor [178]. Table 5.2 summarises the initial and final measured corrosion rates and OCP from each of the tests. The tests where the rise in OCP and drop in corrosion rate are

highlighted for clearer clarification. Studies that have investigated CO_2 corrosion product development on carbon steel surfaces and have labelled such an OCP rise (with enhanced corrosion resistance) as 'passivation', 'spontaneous passivation' or 'pseudo-passivation' [5, 6, 63, 173]. The development of such a protective film is termed *pseudo*-passive because it can lose its superior protective properties once the local solution in the vicinity of the scaled surface becomes under-saturated with respect to $FeCO_3$ [6]. Li *et al.* [180] have suggested that a selective retardation of the anodic reaction, perhaps via direct site blocking of most/all active sites by a thin $FeCO_3$ layer, could be the reason behind the upward shift in OCP and drop in corrosion rate. The tests ran in Figure 5.2 (a) (0-24 hours, Run 1 and 2), Figure 5.2 (b) (0-72 hours, Run 1) and Figure 5.3 (a) (0-106 hours, Run 1) shows that pseudo-passive state could not be achieved. Neither an OCP increase nor a significant corrosion rate decline was observed. Table 5.2 provides a results summary from Figures 5.6 and 5.7 (the red highlighted text indicates the tests when 'pseudo-passivation' occurred).

Table 5.2. Summary of LPR and OCP results from the static immersion tests.

Time (hours)	Run	Initial CR (mm/year)	Final CR (mm/year)	Initial OCP (mV)	Final OCP (mV)	Time for rise in OCP (hours)
24	1	1.75	0.10	-731.52	-720.18	N/A
	2	1.94	0.10	-733.29	-729.26	N/A
72	1	2.39	0.13	-733.29	-727.33	N/A
	2	**1.75**	**0.04**	**-725.26**	**-472.81**	**58**
106	1	1.92	0.07	-732.64	-721.34	N/A
	2	**2.33**	**0.01**	**-722.16**	**-518.41**	**49**
144	**1**	**2.39**	**0.02**	**-739.27**	**-482.67**	**24**
	2	**2.45**	**0.02**	**-735.93**	**-426.77**	**93**

Highlighting and emphasising the fact that although this phenomena is taking place repeatedly, the time taken to happen varies and is less repeatable due

to uncontrollable factors such as surface roughness (after corrosion has taken place), defects and imperfections and rate of $FeCO_3$ formation.

5.3.2 Composition and Morphology

The XRD pattern (Figure 5.4 (a) and SEM image (Figure 5.4 (b) show a polished X65 carbon steel sample prior to immersion into the brine for testing. The XRD pattern which was scanned in the region of 20-60° 2θ (the range in which the strong $FeCO_3$ peaks would be present according to the ICDD) only provided one diffracted plane that can be attributed the α-Fe (110) plane, whilst the SEM image shows that the surface is lacking any addition crystal material other than the metal itself.

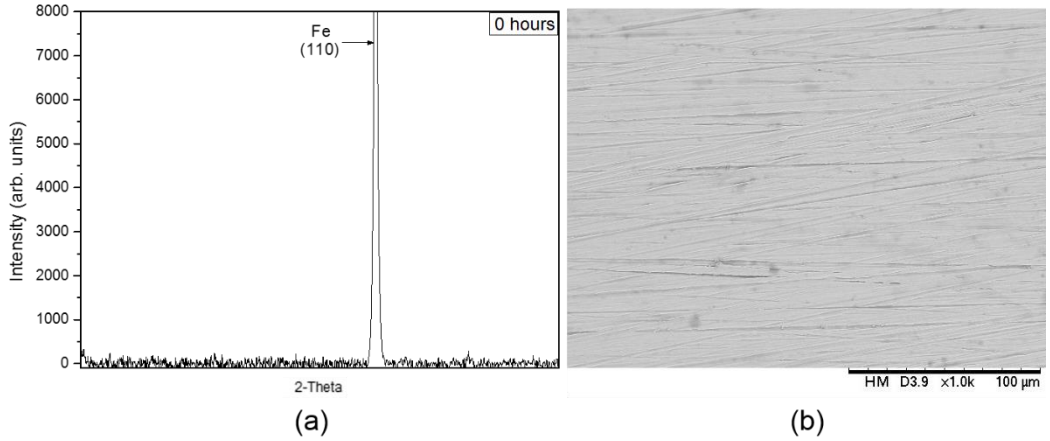

Figure 5.4. XRD pattern (a) and SEM image (b) of the X65 carbon steel surface prior to immersion into the solution.

In contrast, as Figure 5.5 shows, after immersion in CO_2-saturated solution (T = 80°C, pH = 6.8) for different periods of time (24, 72, 106 and 144 hours), the carbon steel surfaces are saturated with $FeCO_3$ covered with crystals. The XRD data in Figure 5.5 shows that the intensity of the major $FeCO_3$ (104) plane (2θ = ~32°) increases over time, whilst a reduction in the major Fe (110) plane (2θ = ~45°) intensity is observed. Whereas, from 106 hours to 144 hours, the major $FeCO_3$ plane has diminished slightly which is likely due to the dissolution of the $FeCO_3$ crystals which is discussed in greater detail later. A direct relationship between the major $FeCO_3$ plane (104) and the major Fe plane (110) could not be established in the tests due to the inconsistency in the alignment of the samples. This is a limitation of the set-up of technique and could not be avoided in this instance.

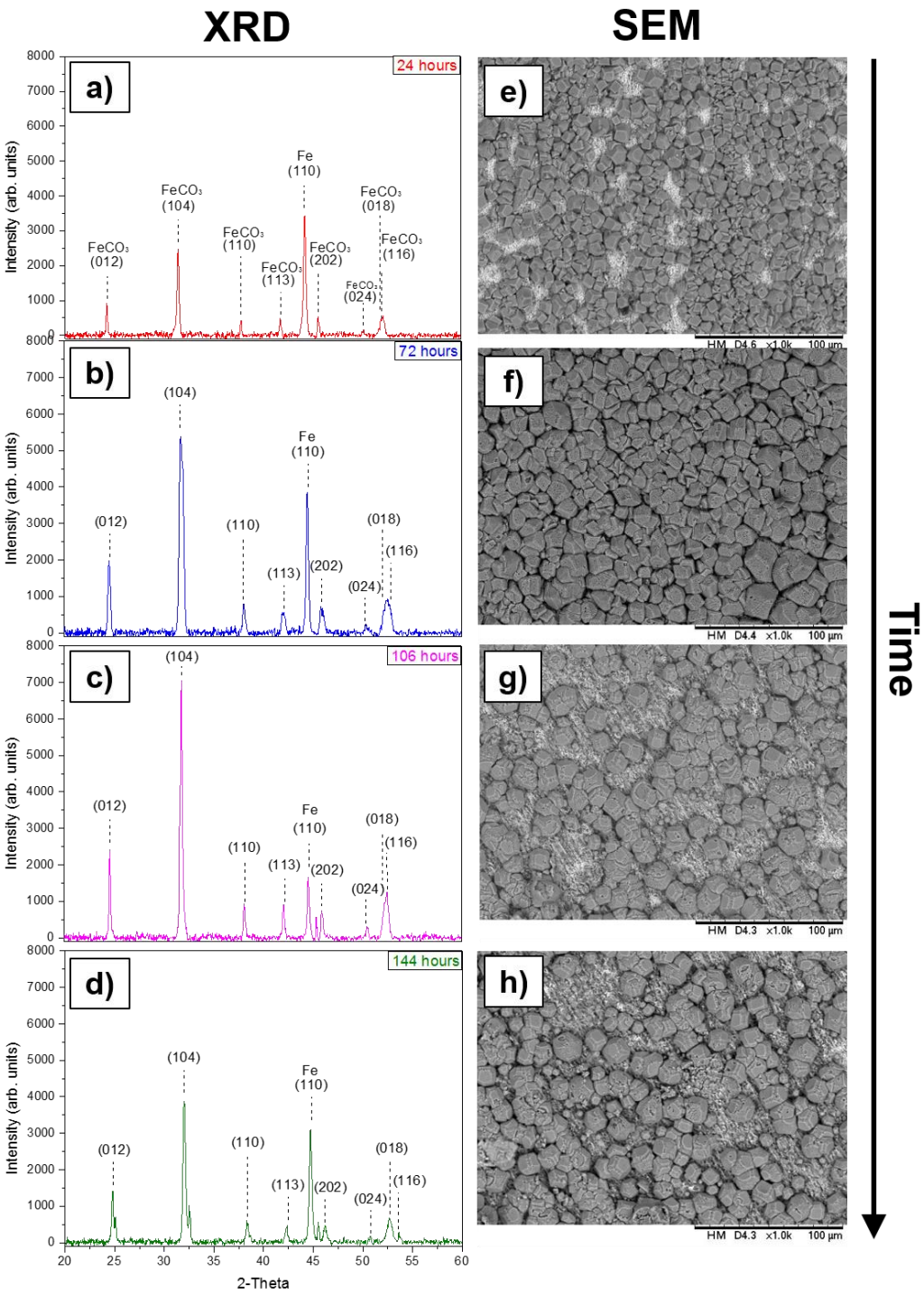

Figure 5.5. *Ex-situ* XRD patterns (a-d) and SEM images (e-h) from the samples as a function of immersion time of 144 hours at 80°C, pH 6.8, 3.5 wt.% NaCl and 0.54 bar p_{CO_2} (freely corroding).

5.3.3 EIS Observations in Relation to the Morphology of the $FeCO_3$ Film

To gain a further insight into the mechanism of $FeCO_3$ formation, EIS analysis was conducted and presented for each of the tests. Speculations on the phenomenon of the OCP rise/corrosion rate decrease are discussed further in the EIS investigation that follows. To facilitate the discussion, EIS and SEM results are divided into the different immersion periods.

5.3.3.1 Immersion Period: 0 to 24 hours

Figure 5.6 (a) and (b) shows a series of Nyquist plots taken during the first 24 hours immersion for run 1 and 2 respectively. Both runs show very similar characteristics with only single depressed arcs evident for almost all of the measurements. The increase in diameter of the Nyquist plots after 4 hours indicates the development of protective $FeCO_3$ crystals are covering the surface, hindering the production of Fe^{2+} and reducing the corrosion rate.

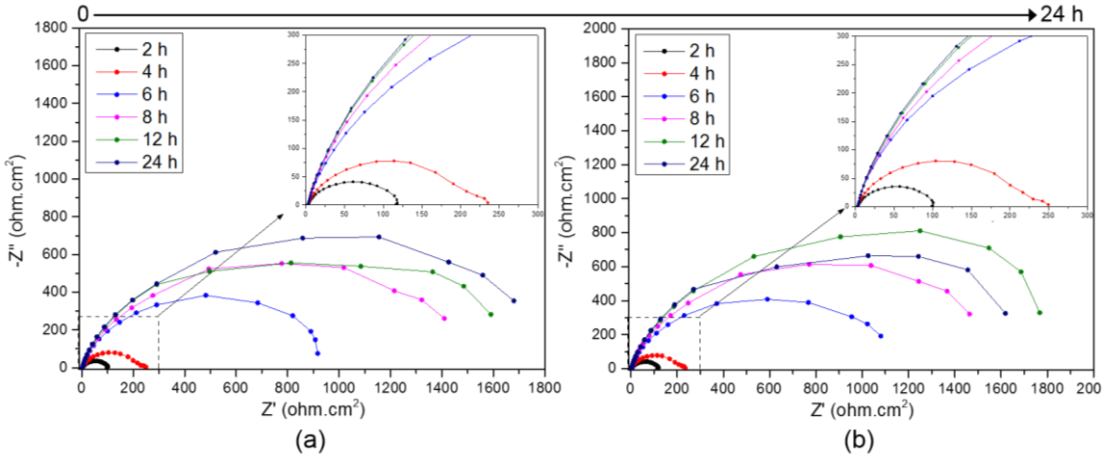

Figure 5.6. A series of EIS Nyquist plots over 24 hours at 80°C, pH 6.8, 3.5 wt.% NaCl and 0.54 bar p_{CO_2} (freely corroding): (a) Run 1; (b) Run 2.

To confirm the presence of $FeCO_3$ crystals on the steel surface, a comparison of the surface morphology captured at different magnifications and corresponding cross sections are presented in Figure 5.7 and 5.8 from the end of the tests after 24 hours of immersion. The $FeCO_3$ crystals cover the majority of the carbon steel surface in both tests consisting of well defined, compact rhombohedral/cubic crystals varying in size with a maximum crystal size of 16 μm.

The $FeCO_3$ crystals offer good corrosion protection (Figure 5.2 (a)) at this stage, acting as a partial mass-transfer barrier for the corrosive species. However, the $FeCO_3$ layer still shows permeability as areas of the steel surface are still in full contact with the electrolyte which is evident from the areas that change in contrast and the darks voids between the crystals in Figures 5.7 (a-d).

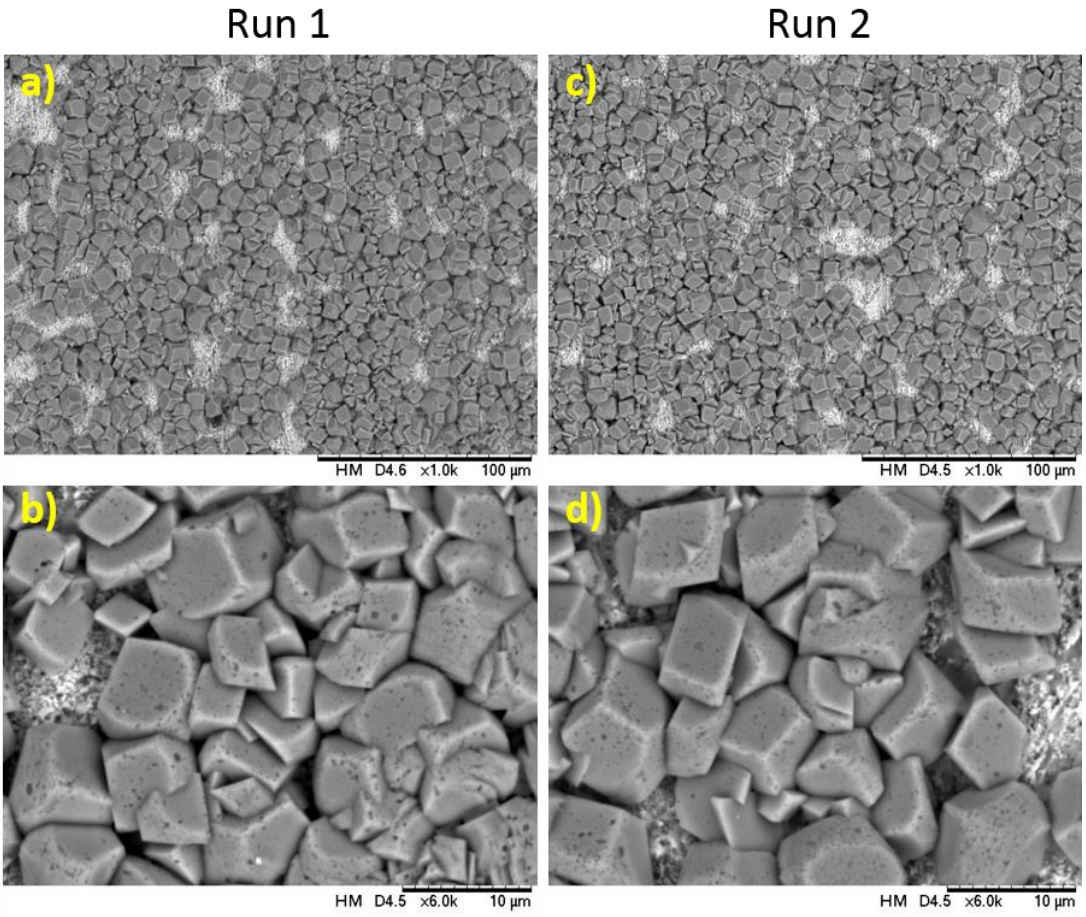

Figure 5.7. SEM images of the sample after 24 hours of immersion at 80°C, pH 6.8, 3.5 wt.% NaCl and 0.54 bar p_{CO_2} (freely corroding): (a) and (b) Run 1; (c) and (d) Run 2.

Furthermore, the cross sections (Figures 5.8 (a) and (b)) reveal the presence of small voids at the steel/crystal interface, allowing a pathway for the generated Fe^{2+} to diffuse away from the surface. The thickness of the layer is clearly dependent on the size of each of the crystals and varies across the surface between 3 to 8 µm.

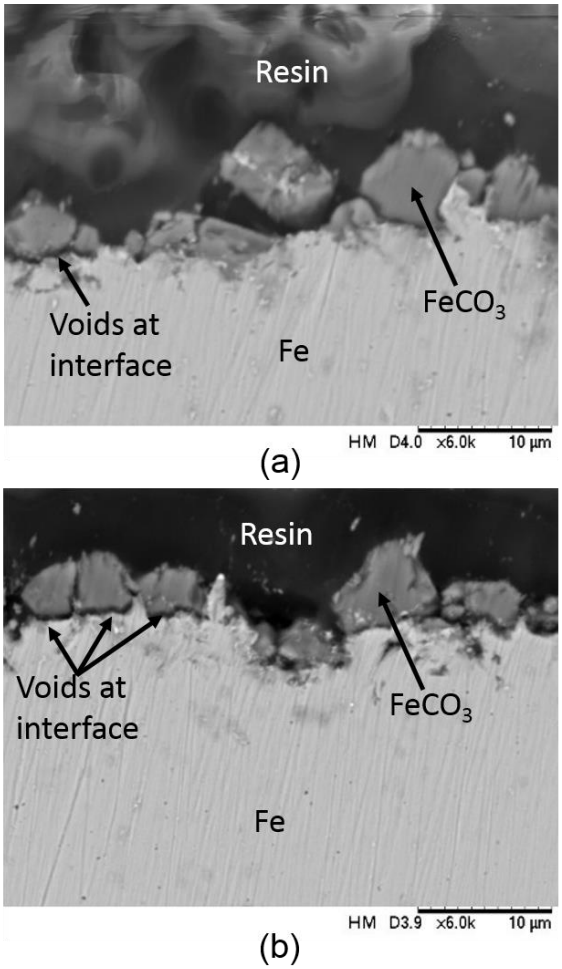

Figure 5.8. SEM cross sections of the surface after 24 hours of immersion at 80°C, pH 6.8, 3.5 wt.% NaCl and 0.54 bar p_{CO_2} (freely corroding): (a) Run 1; (b) Run 2.

5.3.3.2 Immersion Period: 0 to 72 hours, 0 to 106 hours and 0 to 144 hours

After 24 hours of immersion (Figure 5.6), an increase in the polarisation resistance at low frequencies indicated that a protective $FeCO_3$ film was formed reducing the corrosion rate (Figure 5.2 (a)), which was confirmed through XRD and SEM analysis (Figure 5.4 (a) and Figure 5.7). Observing the measurements over 72, 106 and 144 hours of immersion, the diameter of the Nyquist curves have elongated along the x-axis in Figure 5.9 (a-f) from 12 hours on wards, indicating that the corrosion rate is decreased far more rapidly. This change from, one semicircle to two semicircles, suggests a change in the metal-solution interface likely caused by considerable coverage of the carbon steel surface through the formation of a surface layer [181],

indicating a decrease in the porosity of the permeable $FeCO_3$ layer as well as increase in the corrosion resistance.

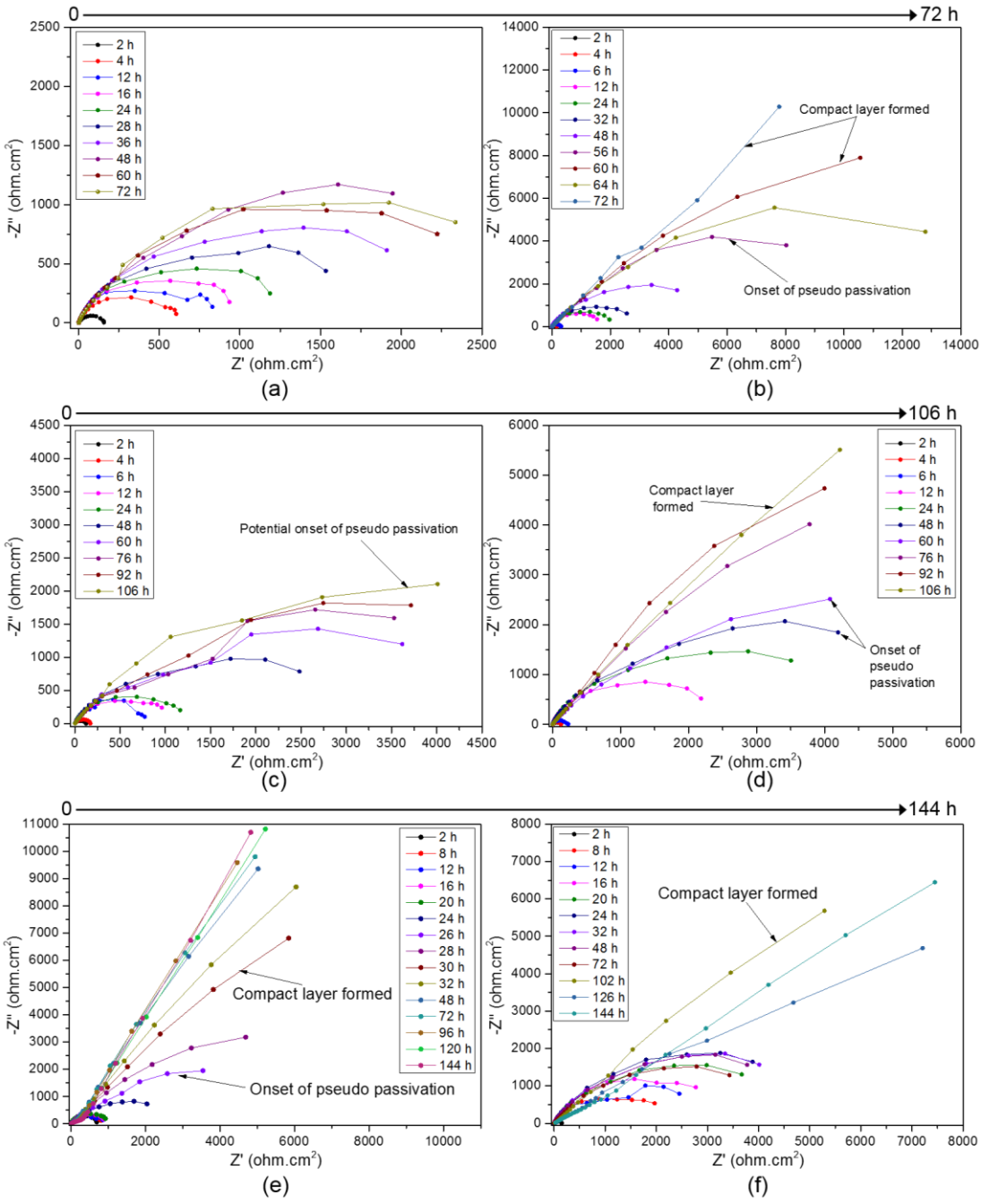

Figure 5.9. A series of EIS Nyquist plots over 144 hours at 80°C, pH 6.8, 3.5 wt.% NaCl and 0.54 bar p_{CO_2} (freely corroding): (a) 0-72 hours Run 1; (b) 0-72 hours Run 2; (c) 0-106 hours Run 1; (d) 0-106 hours Run 2; (e) 0-144 hours Run 1; (f) 0-144 hours Run 2.

This behaviour continues throughout the remainder of each of the tests until the shapes of Nyquist curves change quite significantly showing a linear tail

at lower applied frequencies. In four of the tests after the 48th hour in Figure 5.9 (b), the 60th hour in Figure 5.9(d), the 26th hour in Figure 5.9 (b) and finally the 126th hour in Figure 5.9 (b). This abrupt change coincided with the instantaneous rise in the OCP with the further drop in corrosion rates in Figure 5.2(b), Figure 5.3(a) and (b). This observation is expected only due to the further increase in resistance generated by the $FeCO_3$ crystals at the steel interface by decreasing permeability improving the insulating properties of the interface.

Authors have indicated that when such a linear tail at low frequency presents itself, it signifies the onset of diffusion impedance [182], where the diffusion of corrosive species to the crystal/substrate interface becomes difficult. As the permeability of the $FeCO_3$ crystals decreases, the previously described capacitive behaviour is quickly replaced by a diffusion-limited system where the diffusion of Fe^{2+} away from the interface and the diffusion of corrosive species towards the interface are both being restricted. Such switch is explained by a very fast nucleation and growth of protective $FeCO_3$ crystals restricting Fe^{2+} diffusion away from the interface giving rise to a diffusion impedance feature on the Nyquist curve. Furthermore, given that the linear tail is coincident with the sharp rise in OCP, and a higher degree of protection, that this observation represents ‘pseudo-passivation’ at the steel interface.

The top view SEM micrographs and cross-sections showing the morphology of the $FeCO_3$ crystals and the average $FeCO_3$ film thickness for tests ran at each of the time intervals (0-72 hours, 0-106 hours and 0-144 hours) are presented in Figure 5.10 (a-r). The cross sections in the bottom row of Figure 5.10 shows that the $FeCO_3$ crystals are not built up of layers of crystals but rather like a complete bigger single crystals that provide the thickness. Therefore, the $FeCO_3$ film thickness was difficult to determine using this technique due to the variation in crystal sizes across the surfaces of the tests. Focusing on the tests that did not show such ‘pseudo-passive’ behaviour (i.e. ultra-protective properties), the top view SEM images show a more homogeneous layer with smaller $FeCO_3$ crystals averaging ~5 to ~15 μm in width as observed in Figures 5.10 (a), (b), (g) and (h). These crystals appear to be a mixture of prisms and cubic in shape. The dense, $FeCO_3$ crystals packing on the steel surface offers good corrosion protection and is therefore reasonable to assume that this is because the dense $FeCO_3$ crystals acting as a mass-transfer barrier for the corrosive species.

However, for tests that did show the ‘pseudo-passive’ behaviour, the $FeCO_3$ crystals on the surface appear to be less compact with a larger crystal size distribution ranging from ~3 to ~28 μm in width (Figures (d), (e), (j), (k), (m), (n), (p) and (q)). Here, the $FeCO_3$ crystals do not seem very compact since some voids and apparent non-covered areas are visible on the top view SEM images and therefore it is difficult to imagine that such a layer can be a significant mass-transfer barrier, with ultra-protective properties which reduces the corrosion rate even further to low values of ~0.02 mm/yea. How a seemingly incomplete $FeCO_3$ layer can still provide significant protection against corrosion was in question. From the initial observations, it was assumed that the bare steel surface was on show and in contact with the surrounding electrolyte between the larger crystals on the surface. However, further analysis at higher magnification and cross-sectional (Figure 5.10 (f), (l), (o) and (r)) analysis gave a fundamental understanding as to why these $FeCO_3$ films offered further protection against corrosion. The cross sections (which can also be seen in Figure 5.11 (a-d) for further clarity) reveal a fine bilayer $FeCO_3$ crystals approximately 1 to 2 μm in thickness either beneath or between the large crystals and no bare steel surface can be seen to be exposed to the surrounding environment.

Further evidence of such finer bilayer of $FeCO_3$ layer can be seen in Figure 5.12 and Figure 5.13 after 144 hours of immersion. Figure 5.12 shows top views of the larger $FeCO_3$ crystals and finer $FeCO_3$ bilayer. Small cracks appear to have formed within the bilayer which is most likely due to the removal and drying process of the sample from the solution.

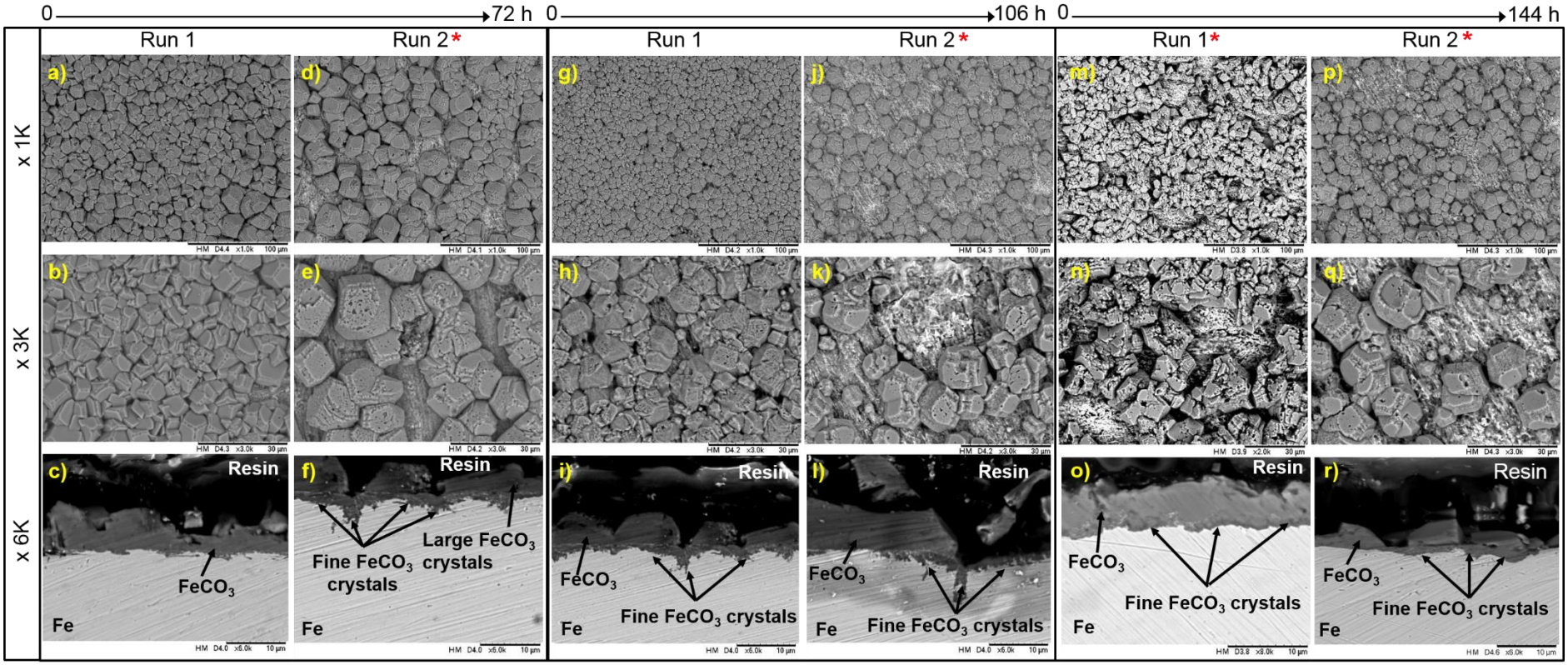

Figure 5.10. SEM images of the samples from the end of each tests at different time intervals at 80°C, pH 6.8, 3.5 wt.% NaCl and 0.54 bar p_{CO_2} (freely corroding): (a-c) 0-72 hours Run 1; (d-f) 0-72 hours Run 2; (g-i) 0-106 hours Run 1; (j-l) 0-106 hours Run 2; (m-o) 0-144 hours Run 1; (p-r) 0-144 hours Run 2

Note: Next to Run 1 or Run 2 in the figure the symbol '*****' indicates the tests that observed 'pseudo-passivation'.

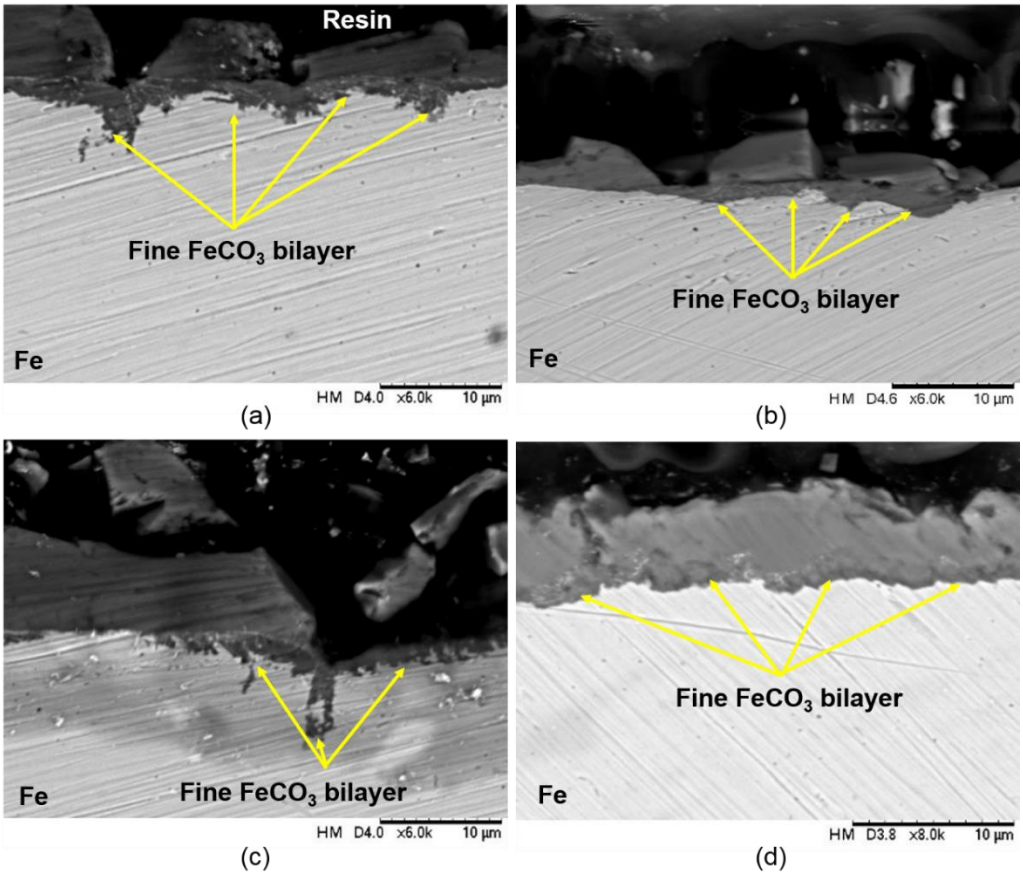

Figure 5.11. SEM cross sections of the surface at different time intervals dhowing $FeCO_3$ bilayer : (a) 106 hours Run 1; (b) 144 hours Run 1; (c) 106 hours Run 2; (d) 144 hours Run 2.

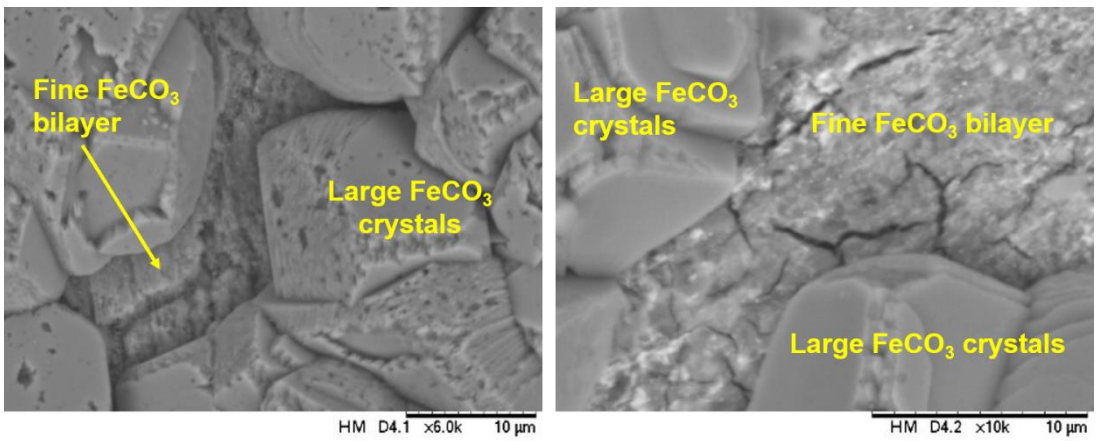

Figure 5.12. Increased magnification (x6k) SEM images showing the larger and finer bi-layer of $FeCO_3$ crystals.

Figure 5.13 shows two cross sections (Figure 5.13 (a) is the original image and Figure 5.13 (b) is the same image after changing the brightness and contrast settings) of the same surface and showing that changing the

brightness and contrast shows only the steel in Figure 5.13 (b), revealing the gaps at the interface that the finer $FeCO_3$ crystals have filled in.

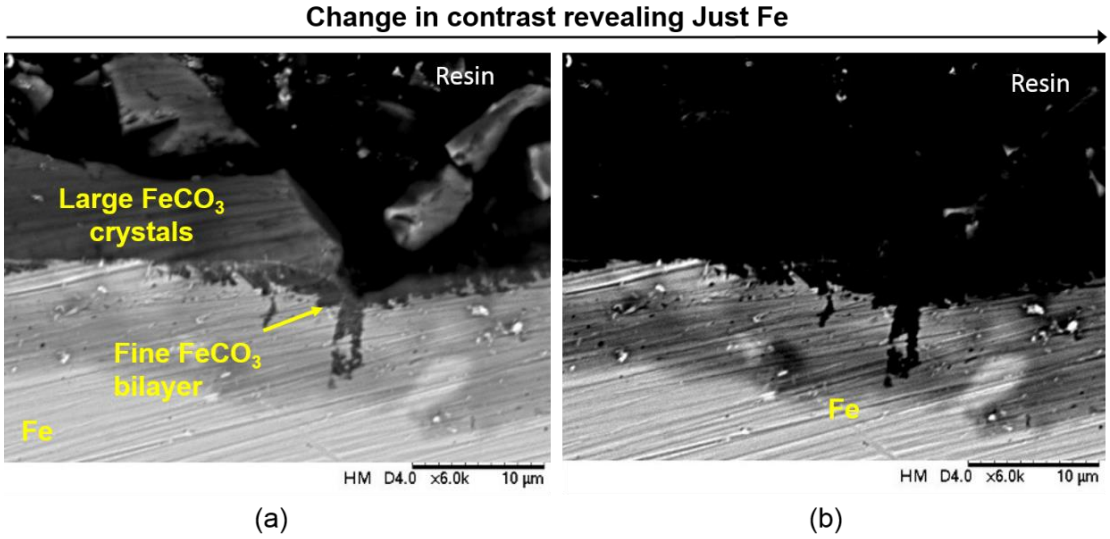

Figure 5.13. Cross section with changing contrast to reveal the presence of $FeCO_3$ bilayer.

The presence of this finer $FeCO_3$ bilayer means that the higher degree of protection against corrosion is not due to the larger $FeCO_3$ crystals observed from the top view, but rather to a finer $FeCO_3$ bilayer that is expected to have formed when the OCP showed a 'pseudo-passivation' response. Due to the decreased permeability, the diffusion of CO_2 towards the metal surface and the diffusion of Fe^{2+} away from the interface are both being restricted which is shifting the potential and reducing the corrosion rate through suppressing the anodic process. The depletion of Fe^{2+} production because of the $FeCO_3$ bilayer dramatically reduces the SR at the crystals faces which results in preferential dissolution of the larger $FeCO_3$ crystals in contact with the surrounding solution. This is evident in each of the tests that entailed the 'pseudo-passivation' process from the top view SEM images at higher magnitude in Figure 5.10 (e, k, n and q). A selection of images from these tests where the fine $FeCO_3$ bilayer was present are presented in Figure 5.14 at even higher magnification to show the dissolution of the larger $FeCO_3$ crystals.

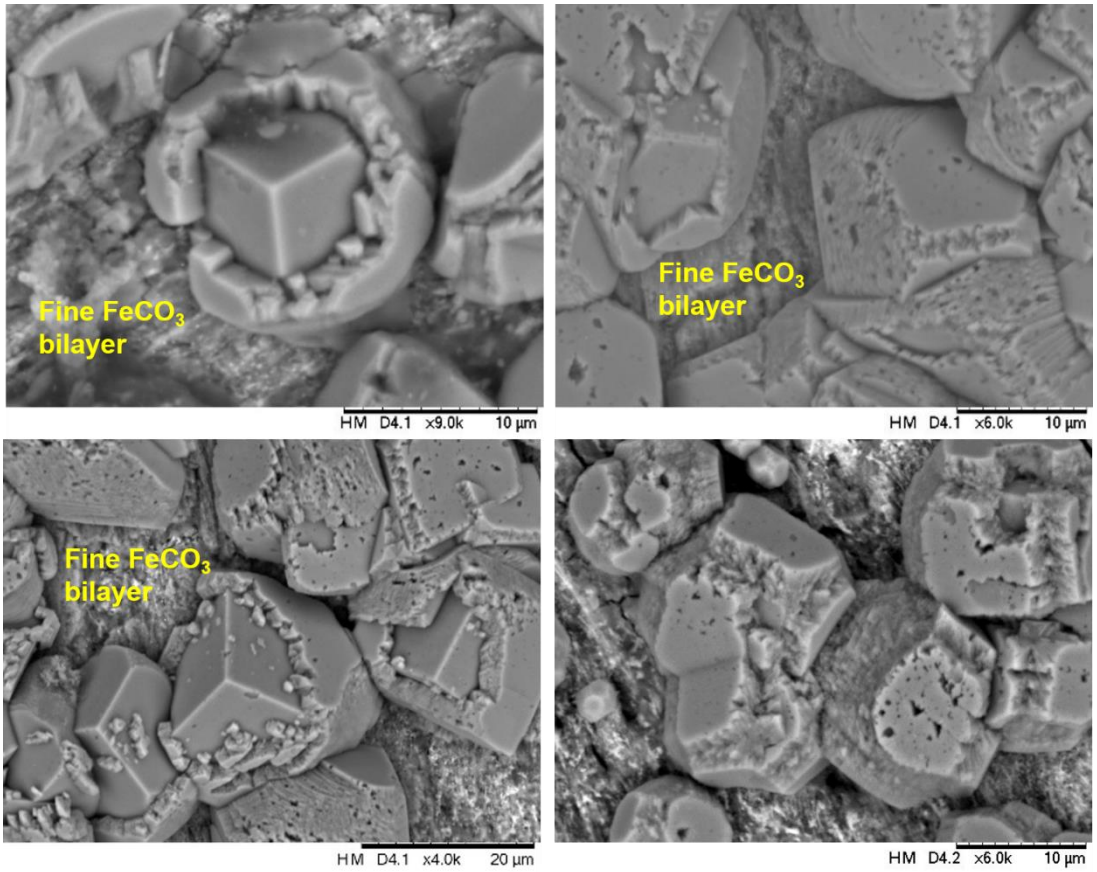

Figure 5.14. SEM images to show the dissolution of the $FeCO_3$ crystals (after 'pseudo-passivation').

These images show the deterioration of the larger $FeCO_3$ crystal faces in the presence of the finer $FeCO_3$ bilayer beneath. The dissolution of these $FeCO_3$ crystal faces appear to reveal more defined crystal faces underneath suggesting that the growth of the crystals build up layer by layer over time and increasing in size via Ostwald ripening similar to the Volmer-Weber mechanism of 3D island growth [83]. For the tests already discussed that did not show such 'pseudo-passive' properties, cross-sections were also prepared, as shown in Figure 5.8 (a) and (b) and Figure 5.10 (c) and (i). In Figures 5.8 (a) and (b) and Figure 5.10 (c), no fine $FeCO_3$ bilayer can be seen from the cross section, whereas in Figure 5.10 (i), the apparent fine $FeCO_3$ bilayer looks present at the crystal/steel interface. Yet, the corrosion rate (in Figure 5.3 (a)) remains stable at 0.07 mm/year with no rise in OCP. However, looking back at the EIS data in Figure 5.9 (c), the diameter of the Nyquist plot at the end of the test starts to rapidly increase which could be a sign of potential onset for 'pseudo-passivation'.

5.4 Summary and Limitations of Methodologies

Table 5.3 shows a summary of the results from the XRD, SEM and LPR analysis.

Table 5.3. Summary of the results from the XRD, SEM and LPR analysis.

	0-24 h	**0-72 h**	**0-106 h**	**0-144 h**
Run 1				
Crystal composition	$FeCO_3$	$FeCO_3$	$FeCO_3$	$FeCO_3$
Crystal morphology	Mixture of prisms and cubic crystals	Mixture of prisms and cubic crystals	Mixture of prisms and cubic crystals	Mixture of prisms and cubic crystals
Crystal size (μm)	1 ⇒ 8	1 ⇒ 10	3 ⇒ 15	3 ⇒ 28
Corrosion rate (mm/year)	1.75⇒0.10	2.39⇒0.13	1.92⇒0.07	2.39⇒0.02
'pseudo-passivation'	✗	✗	✗	✓
Dissolution of crystals	✗	✗	✓	✓
Run 2				
Crystal composition	$FeCO_3$	$FeCO_3$	$FeCO_3$	$FeCO_3$
Crystal morphology	Mixture of prisms and cubic crystals	Mixture of prisms and cubic crystals	Mixture of prisms and cubic crystals	Mixture of prisms and cubic crystals
Crystal size (μm)	3 ⇒ 8	9 ⇒ 21	2 ⇒ 18	3 ⇒ 28
Corrosion rate (mm/year)	1.93⇒0.10	1.75⇒0.04	2.33⇒0.01	2.45⇒0.02
'pseudo-passivation'	✗	✓	✓	✓
Dissolution of crystals	✗	✓	✓	✓

The only new crystalline phase detected during the tests in this study was $FeCO_3$ which comprised of a mixture of prismatic and cubic crystal morphologies ranging in size from 1 to 28 μm over 144 hours.

From the corrosion rate data presented, the profiles are extremely reproducible (especially within the first 24 hours of each test) with the exception of the observation of a sharp drop in corrosion rate in conjunction with a sharp rise in OCP in some of the tests. The drop in corrosion rate is attributed to the formation of a protective 'bi-layer' of $FeCO_3$ crystals. The corrosion rate profiles however cannot determine the physical mass, morphology, structure and precipitation rate of the corrosion products present on the carbon steel surface. Although the general corrosion rate and formation of crystal protective enough for the corrosion rate to reduce was repeatable, the formation of the ultra-protective $FeCO_3$ 'bi-layer' observed in the tests where 'pseudo-passivation' occurred was unpredictable and happened

spontaneously. This further emphasises the reasoning for this phenomena adopting the name ‘spontaneous ‘pseudo-passivation’.

Although this study was useful to elucidate on the formation of $FeCO_3$, especially when spontaneous ‘pseudo-passivation’ was observed, there were occasions that could have led to false conclusions and interpretation of the results due to the removal process of the sample from the solution. For example, two sets (one of 24 hours and one of 106 h) of results that were not included in the results and discussion and were repeated due to the presence of an unknown phase on the sample. Figure 5.15 shows the test results in question after 24 hours of immersion. Figure 5.15 (a) shows the XRD pattern from the end of the test revealing 3 unknown peaks at ~27°, ~45.5° and ~57° 2θ.

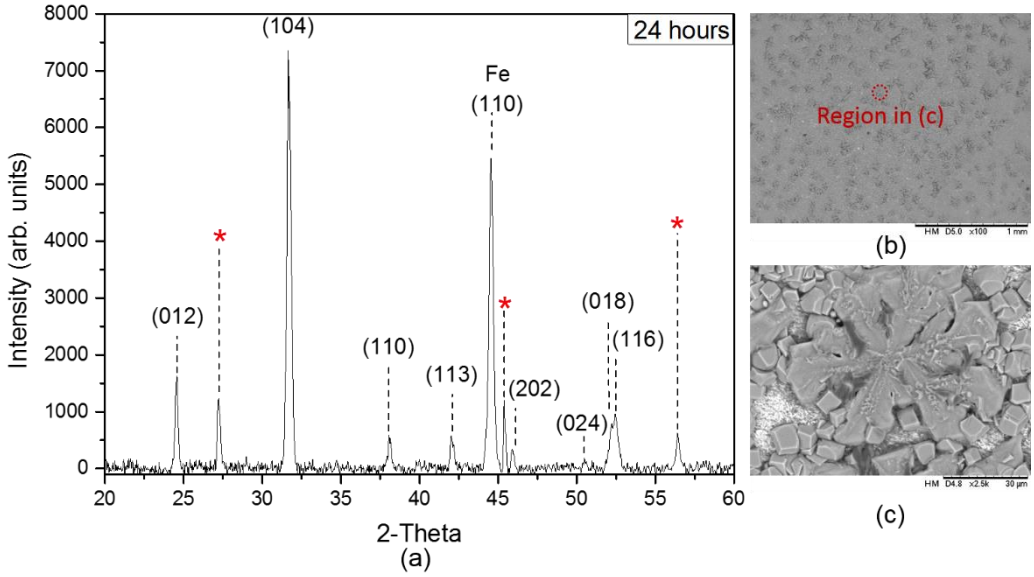

Figure 5.15. XRD and SEM images to reveal the presence of an unknown phase on the surface for one test conducted for 24 hours of immersion at 80°C, pH 6.8, 3.5 wt.% NaCl and 0.54 bar p_{CO_2} (freely corroding).

The rest of the peaks correspond to $FeCO_3$ crystal planes with the exception of the Fe (110) plane at ~45° 2θ. Figures 5.15 (b) and (c) show the SEM images from the end of the same test focusing on what could potentially be this unknown phase. When running the XRD pattern through the ICDD database, there was no confirmed match, but the most likely suspect from the possible candidates was FeOOH with a 25% match which could be due to the lack of peaks in this range of 2θ. Therefore, it has been assumed that this

artefact is a result of the removal and drying process which has transformed some of the $FeCO_3$ crystals into this iron hydrated oxide upon exposure to the outside atmosphere when removed from the solution.

Furthermore, evidence of surface contamination can be seen in Figure 5.16. This artefact on the surface is unlikely to be any form of corrosion product (of a crystalline nature anyway). This contamination was considered as a result of the removal process and cleaning.

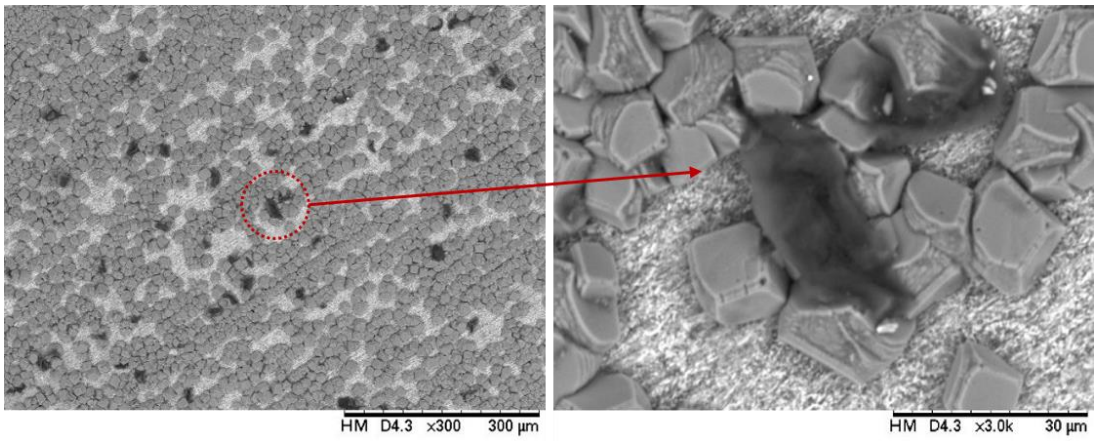

Figure 5.16. SEM images to show surface contamination after removing samples from the solution.

Another consideration is the formation of other phases such as $Fe_2(OH)_2CO_3$ or Fe_3O_4 in addition to $FeCO_3$ in similar operating conditions. Alternatively, a number of authors have proposed that Fe_3O_4 formation on carbon steel, beneath protective $FeCO_3$ layer, could be responsible for a higher level of corrosion resistance and a sudden increase in OCP [3, 5, 6, 180]. A study by Joshi [86], concluded that $Fe_2(OH)_2CO_3$ crystals were shown to be important with regards the ultimate protective property of the CO_2 corrosion products. Therefore, there are still unanswered questions and uncertainties in relation to the actual process during CO_2 corrosion. Questions on the presence of $Fe_2(OH)_2CO_3$ and Fe_3O_4 still remained unanswered, a pertinent one being what role, if any, these corrosion products play in determining the overall protectiveness of the corrosion products formed. This work did not show any evidence of any of these phases (or other phases) present during the development of protective $FeCO_3$.

However, laboratory source X-ray diffractometers can be restricted by factors such as weaker X-ray intensities, high noise-to-signal ratios, increased scanning times and difficult beam alignment procedures in comparison to high flux and high brilliance synchrotron light sources. These factors limit the possibilities of using in-house laboratory X-ray diffractometers. The kinetics and precipitation of corrosion products can occur extremely fast and these limitations could result in phases not being detected (due to the weakened intensities and signal-to-noise ratio in comparison to synchrotron radiation). With such clear disadvantages, using a synchrotron source is preferred to follow the kinetics of corrosion products *in-situ*. Also, removing the sample from its natural corroding environment clearly has disadvantages due to oxidation of the corrosion product or contamination of impurities onto the surface. Considering these factors combined, it is difficult to conclude with certainty that the formation of the bilayer causing a sudden rise in OCP and the sharp drop in corrosion rate are only $FeCO_3$, and therefore, there is a need for an *in-situ* methodology to follow the growth kinetics of $FeCO_3$ with confidence and reassurance. This gap in research is highlighted in Chapter 6, and a new *in-situ* methodology is presented.

5.4 Conclusions

This work aimed to gain a better understanding on the development of protective $FeCO_3$ on to X65 carbon steel over 144 hours of immersion time in a static glass cell set-up. Based on the results obtained, the following conclusions can be extracted:

- The phases of the corrosion products present are studied using standard in-house laboratory XRD and revealed only $FeCO_3$ in this study.
- In some instances, a spontaneous second drop in the corrosion rate profile with a corresponding rise in OCP occurred and was deemed as a ‘pseudo-passivation’ process resulting in an ultra-protective $FeCO_3$ layer (showing similar protective properties to mixed corrosion inhibitor) at the steel interface between/underneath larger $FeCO_3$ crystals with enhances diffusion limiting properties.
- The transition from protective $FeCO_3$ (limiting the corrosion rate to ~0.1 mm/year) to ultra-protective $FeCO_3$ (limiting the corrosion rate to ~0.02

mm/year) is related to significant direct blocking of the steel surface and restricting further production of Fe^{2+} through the formation of a bilayer.

- EIS methods, in conjunction with the LPR measurements deemed a valuable complementary technique towards interpreting the changing protective properties of the $FeCO_3$ layer.
- The change in Nyquist curves from well-defined capacitive semicircles to a capacitive semicircle with a linear tail at low frequencies is a good indicator of when the ‘pseudo-passivation’ process begins and an ultra-protective $FeCO_3$ begins to form.
- Through a combination of the results in this study, four stages were identified explaining the process resulting in the formation of an ultra-protective $FeCO_3$ bilayer: 1) An active corrosion stage (where the corrosion rate increased to Fe_3C exposure); 2) A nucleation and growth of $FeCO_3$ stage (where simultaneous nucleation and growth of $FeCO_3$ crystals occur); 3) Further $FeCO_3$ growth stage (where the growth of the $FeCO_3$ crystals dominate); 4) A ‘pseudo-passivation’ stage (where there is formation of an $FeCO_3$ bilayer).

Part III:
Synchrotron Radiation X-Ray Diffraction Tests: Flow Cell Development and Results

Chapter 6
Development of an electrochemically integrated SR-XRD flow cell to study $FeCO_3$ formation kinetics

This chapter describes the design and development of an electrochemically integrated Synchrotron Radiation-Grazing Incidence X-Ray Diffraction (SR-XRD) flow cell for studying corrosion product formation on carbon steel in carbon dioxide CO_2-containing brines. The design of the flow cell is presented. The flow cell is used to follow the nucleation and growth kinetics of $FeCO_3$ using SR-XRD linked to the simultaneous electrochemical response of the steel surface which were collected in the form of LPR measurements to decipher *in-situ* corrosion rates. The initial results along with the numerous capabilities of the flow cell are highlighted and presented in this chapter.

6.1 Introduction

The transient corrosion rate behaviour of carbon steel during $FeCO_3$ formation and the magnitude of the steady state corrosion rate after film formation is dictated by the crystal layer nucleation, growth, morphology and its stability/resistance against chemical/mechanical removal [2, 93, 153, 176]. Therefore, understanding the factors governing the rate of formation of $FeCO_3$ on the corroding surface of mild steel is an important step in understanding the overall CO_2 corrosion process. Accounting for $FeCO_3$ formation (and the formation of other corrosion products, for that matter) on the internal walls of carbon steel pipework is crucial when developing an accurate corrosion prediction model or when developing a robust corrosion management strategy. It is important to understand which corrosion products are formed and to what extent their rate of formation, morphology and protectiveness are influenced by changes in the operating conditions and the environment. However, two main challenges present themselves when analysing corrosion product film formation processes in oil and gas environments:

- It is difficult to determine $FeCO_3$ growth kinetics on the steel surface during formation without stopping experiments and performing mass gain measurements to identify the quantity of $FeCO_3$ on the steel surface.

- Due to the rapid formation of $FeCO_3$ in a supersaturated brine, is difficult to capture the very early nucleation and growth kinetics without using *in-situ* monitoring techniques that offer real-time kinetic information.

To overcome the limitations and challenges discussed, a new methodology and cell design is presented which enables corrosion rates and film formation/characteristics to be measured simultaneously without exposure of the sample to oxygen in a naturally corroding flowing cell. This section will focus on the development process of the flow cell. The work presented here describes the development of a new and unique SR-XRD flow cell integrated with *in-situ* electrochemical capabilities which is utilised to measure and understand the nucleation and growth of $FeCO_3$ as well as other species which may also form during the corrosion process on a naturally corroding surface. The early nucleation and growth kinetics of $FeCO_3$ of a naturally corroding surface in a flowing, deaerated system are characterised *in-situ* for the first time.

6.2 Development of SR-XRD Flow Cell

Figure 6.1 provides an outline of the key stages of development which helped improve the final product which was commissioned for the use of *in-situ* SR-XRD.

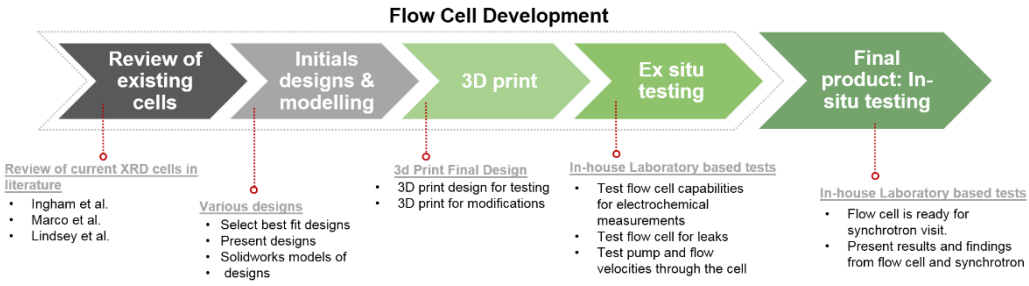

Figure 6.1 Key stages of *in-situ* SR-XRD flow cell development.

6.2.1 Review of Existing Cells and Methodologies Used to Study CO_2 Corrosion Using *In-situ* Synchrotron XRD

This section will focus on the limitations of the current designs in literature and how the design of the cell in this work overcomes these limitations. Future modifications of the flow cell and how it can be linked to industry related problems is exploited in greater detail in the discussion in Chapter 10.

There are a number of examples in the literature of *in-situ* SR-XRD studies using a variety of electrochemical cells designs [155], each of which can carry out a wide variety of *in-situ* X-ray studies which has already been reviewed in Chapter 4. To address the aforementioned challenges to study the formation of corrosion products in CO_2 conditions, several research groups have already exploited *in-situ* SR-XRD for determining the nature of corrosion products in CO_2 corrosive environments as discussed in Chapter 3. Researchers have reported that in simple CO_2-containing brine solutions a number of iron oxides/hydroxide phases to form in conjunction with $FeCO_3$. Such phases include magnetite (Fe_3O_4) [3, 6], chukanovite ($Fe_2(OH)_2CO_3$) [110, 135, 136, 153, 154, 155, 157, 158], wustite (FeO) [158] and goethite (FeO(OH)) [158]. However, these studies have either been performed in oxygen contaminated systems (as suggested by the authors themselves) [170], or the growth of the corrosion product was accelerated by applying excessive currents/voltages to the sample under study [110, 135, 136, 154, 157] which were not realistic of the actual corrosion kinetics encountered in the field. Although the conditions of accelerating the growth kinetics are not ideal in real world applications, they are good to monitor the very early stages of growth looking at what the effect of different parameters has on the very early kinetics.

Another factor is that the cells presented in literature are tested in static conditions which are good for stagnant areas in pipelines (during maintenance for example), but then in order to elucidate a deeper understanding on corrosion product formation in oil and gas production lines, dynamic regimes are of greater interest. Based on the review of the designs set out in the literature, the following improvements to a new system include:

- A system that can monitor the formation of corrosion products at open circuit potential without the need to force the corrosion rate.
- A system that can circulate a heated brine through the flow cell with a range of flow velocities.
- A system that can facilitate both *in-situ* SR-XRD and electrochemical measurements easily.
- A system that can maintain brine concentration without O_2 contamination.

6.2.2 Initial Design Concepts and 3D Modelling

To overcome the limitations of current cells previously discussed, a two new flow cell designs were considered for the use of *in-situ* SR-XRD whilst

facilitating X-ray measurements. The two distinctly different designs can be seen in the SolidWorks® model in Figure 6.2 (design 1) and Figure 6.3 (design 2).

In order to allow X-rays to penetrate into the working electrode within the cell design, an important design consideration is to implement a window made from a material that can transmit X-rays easily. Other important design considerations include the fluid flow profile through the cell and the positioning of the electrodes in order to complete the electrical circuit to monitor the electrochemistry on the working electrode (carbon steel) surface. These design features will be discussed in more detail later in this chapter. The first flow cell design is presented in Figure 6.2 and comprises two main components (the flow cell base (9) and a top plate (2)) that mount together with 10 x M3 countersunk screws (1) that thread into brass inserts (5) embedded within the bottom plate.

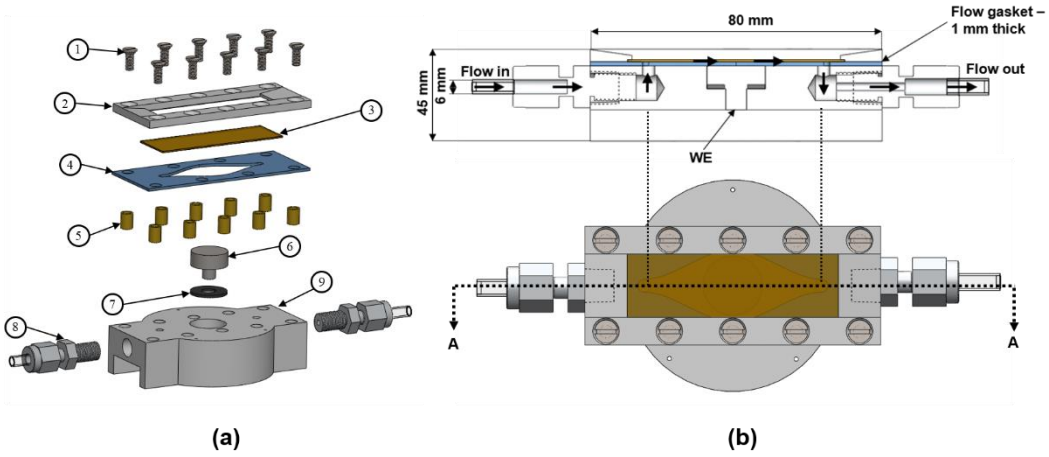

Figure 6.2 SolidWorks® model of flow cell design 1: a) Exploded view; b) flow profile schematic.

The top plate design has a section to accommodate a 50 µm thick Kapton® window (3) to allow for X-ray transmittance. A 9 mm diameter cylindrical X65 grade carbon steel sample (6) fits into the base of the flow cell and flush mounted with the top surface of the base plate. Stainless steel Swagelok male tube connecters (8) will provide the inlet and outlet for the brine as seen in Figure 6.2 (b). A 1 mm thick (thickness can vary) Teflon gasket (4) which acts as a flow path has been designed with a parametric curve (see Figure 6.3 that creates and ‘eye’ shape profile to achieve a smooth and uniform flow over the steel sample.

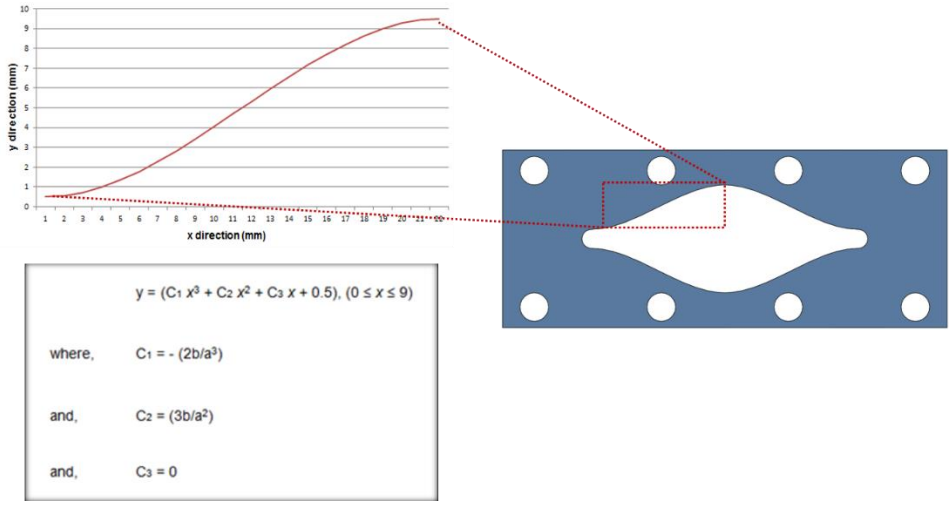

Figure 6.3. Parametric curve design for the flow gasket in design 1.

The second flow cell design is presented in Figure 6.4. Figure 6.4(a) shows an exploded view which entails two main components (the flow cell base (5) and a top plate (1)) that mount together with 8 x M5 bolts (7) that thread into the top plate into M5 x 0.8 mm helicoil threaded. The top plate design has a section to accommodate a 50 µm thick Kapton® window (3) to allow for X-ray transmittance. A 9 mm diameter cylindrical X65 grade carbon steel sample (6) fits into the base of the flow cell and flush mounted with the top surface of the base plate. Stainless steel Swagelok male tube connecters (2) will allow the flow through the cell through the inlet and outlet as seen in Figure 6.4(b). A custom made O-ring made from Viton will be implemented within the bottom plate of the cell to prevent leakage and oxygen contamination.

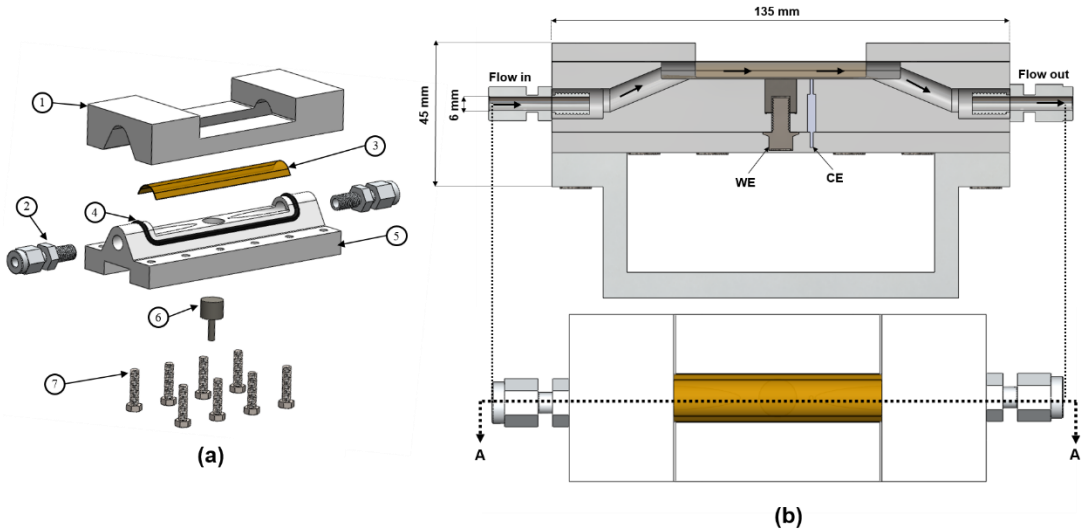

Figure 6.4. SolidWorks® model of Flow cell design 2: a) Exploded view; b) Flow profile schematic.

An essential consideration for deciding which flow cell design to go forward with for manufacture is to determine the flow profile across the sample for both configurations.

Basic Computational Fluid Dynamics (CFD) analysis of the flow through both designs has been conducted using SolidWorks®. Figure 6.5 shows the flow path through design 1, whilst Figure 6.6 shows the flow through design 2. In order to attempt to replicate the conditions of pipelines and to allow the unimpeded flow patterns (no stagnant regions) and electrochemical measurements, conventional flow cells (that have been reviewed previously) are not suitable for this work. Similarly, this is also the case for design 1 taking into account the flow across the steel sample which is observed in Figure 6.5.

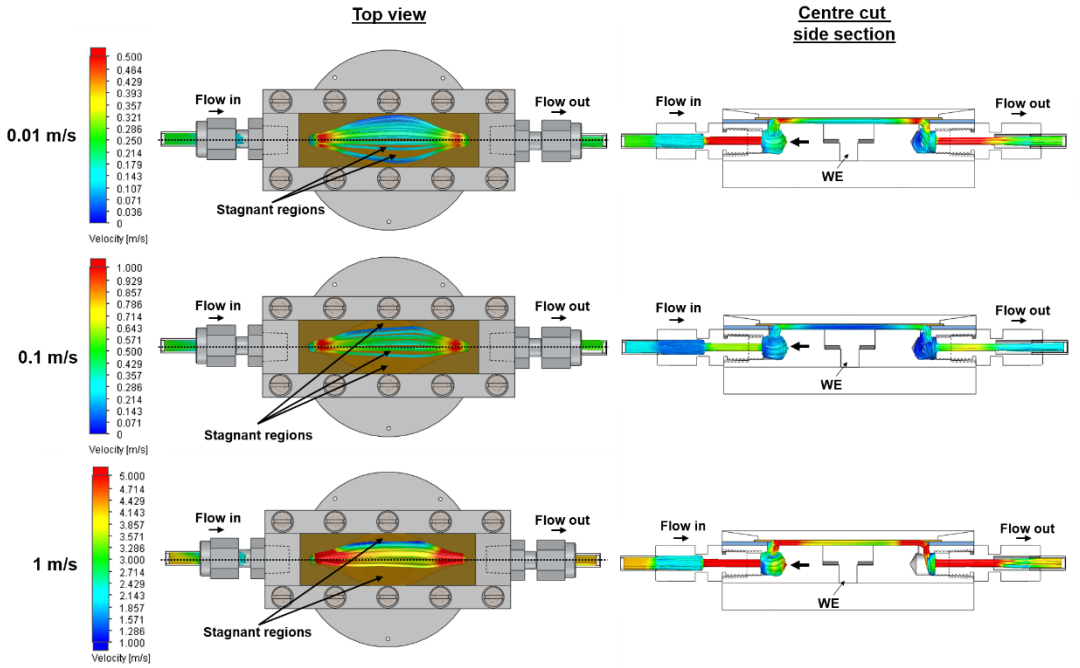

Figure 6.5. SolidWorks® CFD analysis of flow path at different flow rates for design 1: Left) Top view; Right) Side view cut through the centre plane.

Focusing on the top view for each flow inlet velocity analysed (0.01, 0.1, and 1 m/s), the flow across the sample is non-uniform and stagnant regions are clearly present, more so at 0.1 and 1 m/s. This limits the flow cell to function at flow velocities of <0.01 m/s which is too small to be considered for this study. In comparison to design 2, the CFD analysis of the flow pattern across the sample (Figure 6.6 top view and cross section) shows a uniform and unimpeded flow across the sample at both 0.1 and 1 m/s and therefore based on these observations, design 2 was chosen for the *in-situ* SR-XRD work. A more complete analysis of the fluid flow through the flow cell was studied with

COMSOL Multiphysics and will be presented later in this chapter. The software provides the ability to simulate a more accurate representation of the flow characteristics through the flow cell and determine the flow efficiency based on experimentally measured input parameters.

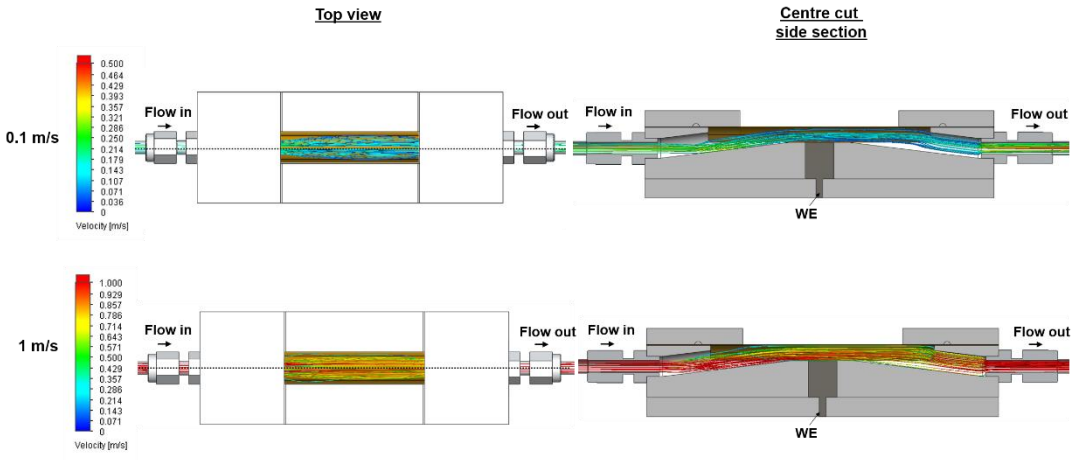

Figure 6.6. SolidWorks® CFD analysis of flow path at different flow rates for design 2: Left) Top view; Right) Side view cut through the centre plane.

Another crucial factor limited the use for the first design for *in-situ* SR-XRD and instantly excluding the first design for the SR-XRD work was the geometry of the cell. Each flow cell design is intrinsically based on one of two specific designs, which correspond to two different measurement geometries (i.e. reflection and transmission modes of measurement as discussed in Chapter 3). In this case, based on the nature of the experiments, the only possible geometry is the reflection cell. However, design 1 mimics the geometry of a conventional reflection cell whereas design 2 has more of a thick film reflection geometry. Reflection cells generally comprise an X-ray transparent window (Kapton® in this set-up) that is situated parallel, or sometimes perpendicular (as with thick-layer reflection cells), to the working-electrode interface, noting that this configuration is only utilised in surface analyses of substrates which is of interest in this work. This transmission window is not only responsible for transmitting X-rays but also containing the electrolyte whilst not severely attenuating the X-ray beam itself.

After carefully reviewing the geometry for both designs, design 2 was chosen for the *in-situ* SR-XRD work. This is based on the flow cell geometry in the first design masking out the majority of the reflected beam and regions of the detector due to the thickness of the top plate which is illustrated in Figure 6.7 (a). The second design will also mask portions of the reflected beam (Figure

6.7 (a)) but not quite as significant as the previous design and can provide enough data to radially integrate about the beam centre yielding 1D plots of intensity vs 2θ.

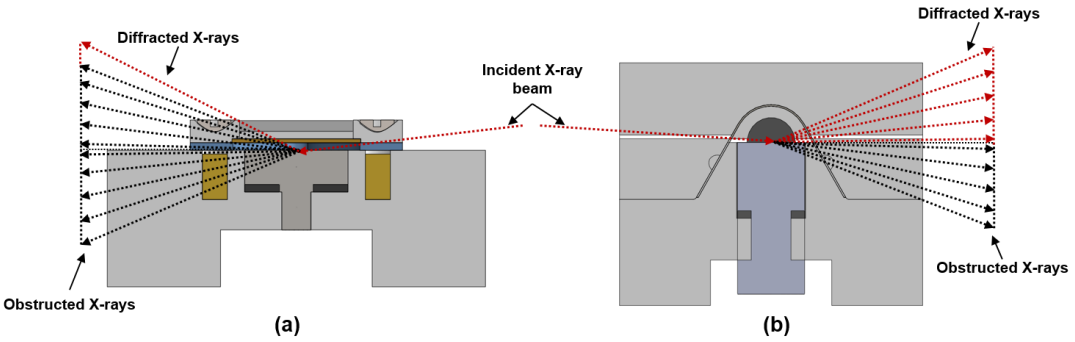

Figure 6.7. Flow cell configuration and X-ray reflection geometry: a) Design 1; b) Design 2.

6.2.3 Final design: 1st Prototype for Testing

The chosen flow cell design was 3D printed for initial testing and will be referred to as the SR-XRD flow cell. The 3D printed prototype is shown in Figure 6.8 (a-e).

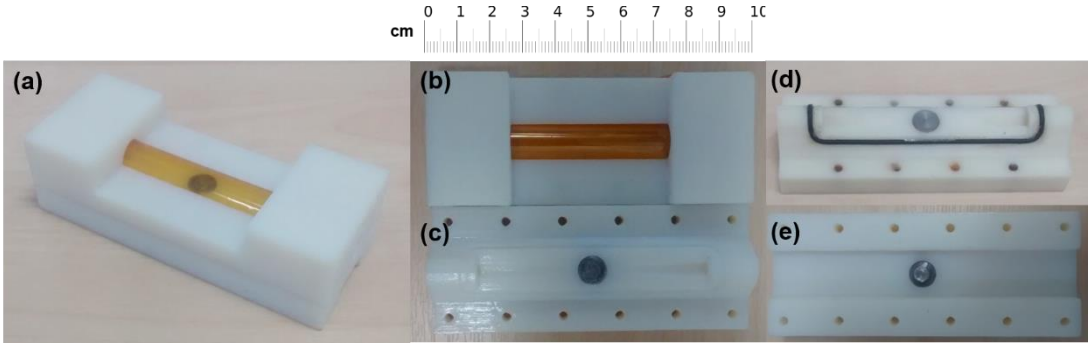

Figure 6.8. 3D printed prototype of SR-XRD final design: a) Assembled view; b) Top plate; c) Top view of base; d) Top view of base with O-ring; e) Bottom view of base.

The flow cell was 3D printed and assembled for preliminary testing before the final design was manufactured using Acetal due to the complex shape and difficulty to manufacture. The preliminary tests revealed some issues (listed below) within the design that needed improvement before the final product was manufactured.

1. Crevice corrosion on sample edges

Crevice corrosion is a localised form of corrosion usually associated with a stagnant solution on the micro-environmental level, this was observed in the early stages of testing on the edges of the sample. Figure 6.9(a) shows the electrochemistry and SEM results in which this phenomenon was observed at pH 6.8, 80°C and 0.1 m/s. The cause of crevice corrosion occurring on the sample edges was due to the tolerance between the sample holder slot in the base of the cell design and the sample itself. In order to stop sample from corroding around the edges of the sample, this tolerance was reduced and the sample edges where coated with corrosion resistant varnish. See Figure 6.9 (b) for the electrochemical observations after making these changes.

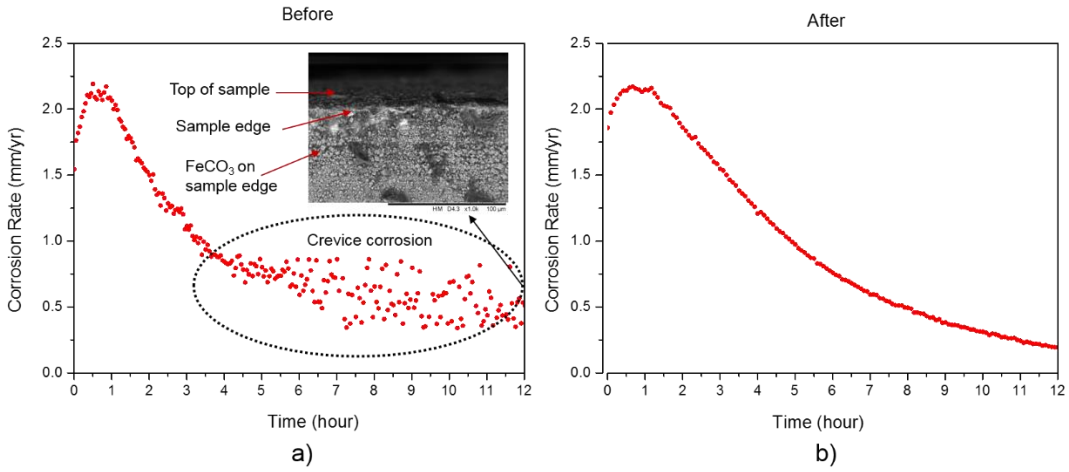

Figure 6.9. Corrosion rate analysis: a) Crevice corrosion on sample edges before adjustments; b) Steady corrosion rate measurements after adjustments.

2. Sample fixed into position using epoxy resin

The carbon steel sample was fixed into the flow cell base using epoxy resin. This was problematic when removing the sample and resulted in either ruining the sample surface, or the flow cell base. Instead, a thread was machined into the bottom of the sample and was mounted into position through an M5 bolt (which also provided the electrical contact for the work electrode) and an O-ring.

3. Fragile Kapton® window

Upon increasing the flow velocity, the 50 µm Kapton® sheet was extremely fragile and expanded extremely easily. The thickness of the Kapton® was increased to 125 µm which gave a robust solid fluid profile and solved this problem.

4. Solution leaking and oxygen contamination

During the early stages of testing before the flow cell was manufactured, leaks were observed from a number of locations randomly which made testing very problematic. One reason for the leaks was the poor thermal expansion properties of the ABS (Acrylonitrile Butadiene Styearene) plastic which was the material the flow cell was printed in. After the heated solution entered the cell, the material expanded slightly after some time reducing the air/water tight seal and allowing the solution to exit the cell, whilst oxygen entered the cell. For the final design, the potential leak zones and oxygen entry ports were examined and are numbered from 1 to 6 in Figure 6.10. Once the final design was machined, the thermal expansion would not be a problem and therefore each of the numbered zones in Figure 6.10 was fitted with Viton O-rings for further reassurance as seen in Figure 6.11.

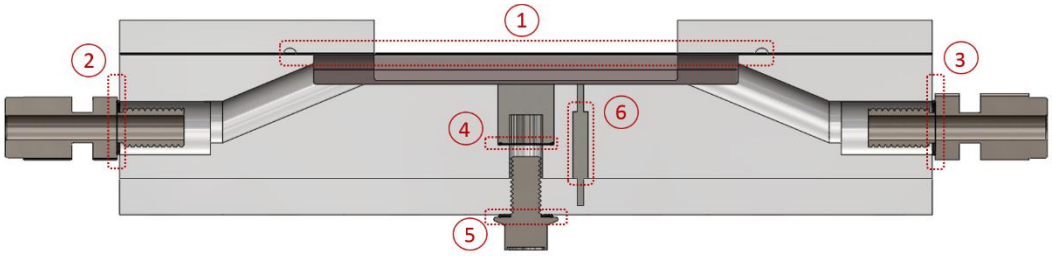

Figure 6.10. Potential oxygen entry ports and leak zones in the final flow cell design.

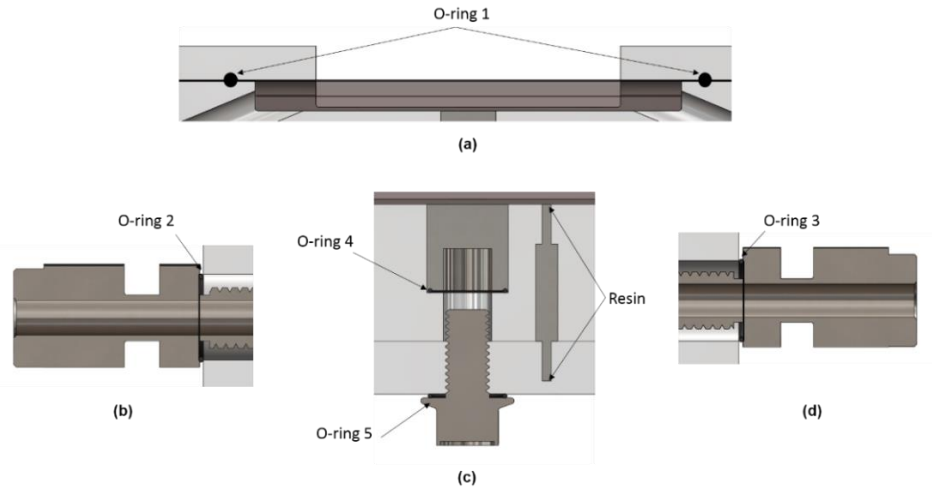

Figure 6.11. Image to show the locations of the implemented O-rings within the design.

O-rings were implemented into zones 1-5, whilst the platinum counter electrode in zone 6 was secured into the base of the flow cell using epoxy resin.

The flow cell was also designed to be longer to accommodate more bolts for a more secure seal and to allow bigger and more robust pipe fittings to be fitted for the solution inlet and outlet ports. The final design is described in Section 6.3.

6.2.4 SR-XRD Flow Cell Final Design

The SR-XRD flow cell is integrated with *in-situ* electrochemistry and is capable of generating flow velocities up to 2 m/s at temperatures in excess of 80˚C. Diffraction patterns can be collected through water, enabling the flow to be maintained over the course of the experiment while data is collected in real time and correlated with electrochemical measurements.

The design of the flow cell is shown in Figure 6.12 and comprises two main components (the flow cell base (4) and a top plate (1)) machined from Acetal that are mounted together with M5 socket cap stainless steel screws (8) that screw into M5 x 0.8 mm helicoil threaded inserts (manufactured as part of the top plate). The flow cell was then mounted and secured to a flow cell holder (7) designed to fit the stage in the experimental hutch at the Diamond Light Source synchrotron facility. A groove was machined into the base of the cell to accommodate a custom Viton O-ring (11) to facilitate an air-tight seal. The top plate has a section machined out to accommodate a 125 µm thick Kapton® window (2) to enable X-ray transmittance. A 9 mm diameter (and 9 mm in length) cylindrical X65 grade carbon steel sample (5) was embedded into the base of the flow cell and flush mounted with the top surface of the base plate. The steel sample acted as the working electrode (WE) in the three-electrode cell used to acquire electrochemical responses. The carbon steel sample was machined to allow a threaded M5 bolt (9) to be positioned into the base, providing both electrical contact but also acting with a Viton O-ring (6) to provide a compression seal when tightened, securing the sample into the base plate and preventing oxygen ingress. The substrate surface height position was highly reproducible between experiments minimising requirements for realignment between each experiment. This is an important design feature, which ensured that the maximum amount of beam time was used for data collection and not cell alignment. The tubing used to complete the flow loop was a ¼” stainless steel flexi-tube hose (9.14 mm outer diameter) with a PTFE inner bore (6 mm inner diameter) to minimise $FeCO_3$ precipitation elsewhere in the system. Stainless steel Swagelok male tube connecters (3) were used for the flow inlet and outlet. Images of the final flow cell design are shown in Figure 6.13 (a) and (b).

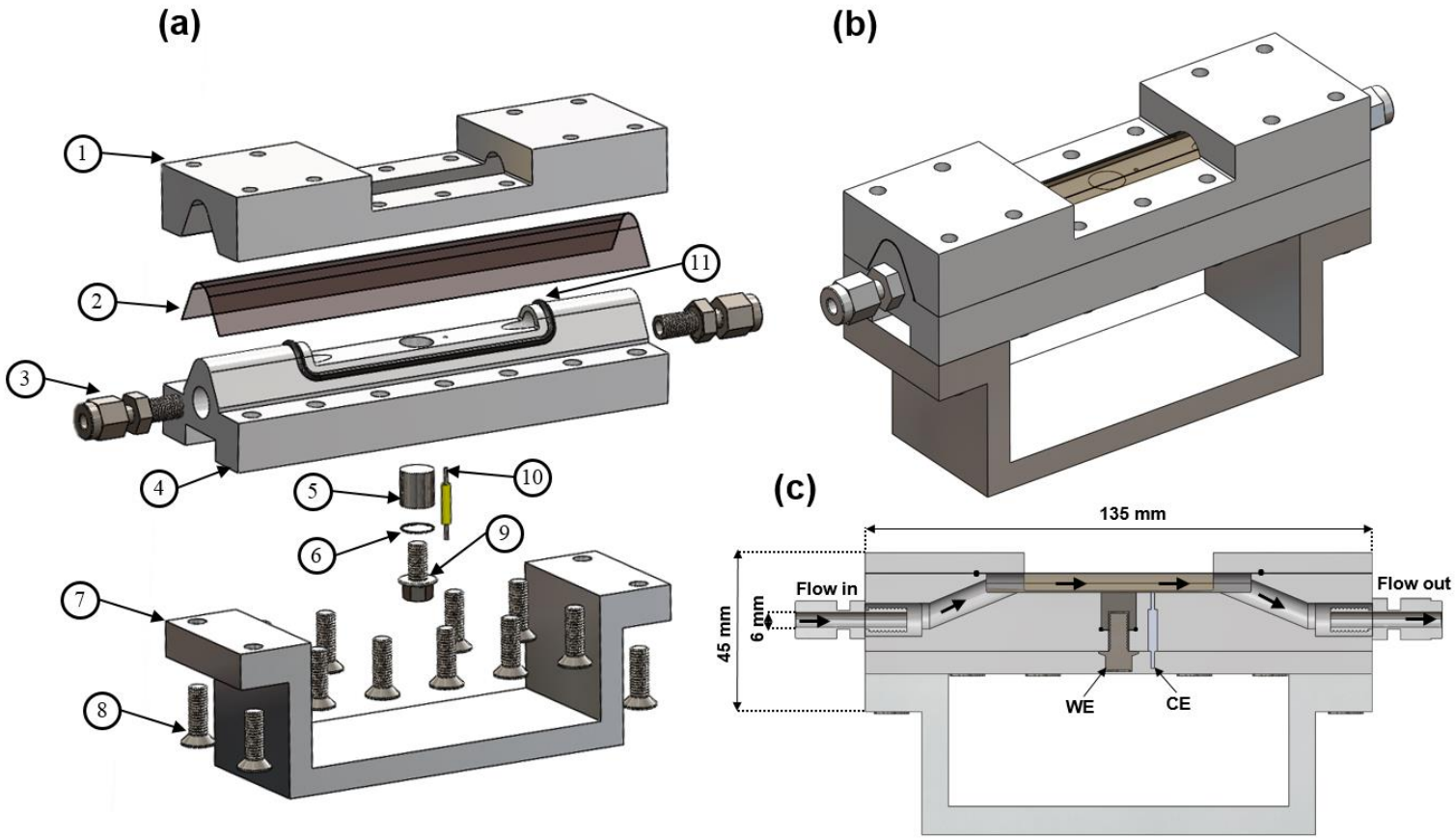

Figure 6.12. 3D schematic diagrams of the SR-XRD cell: (a) Exploded assembly of individual components; (b) Assembled view; (c) Schematic cross section; (WE = working electrode), (CE = counter electrode).

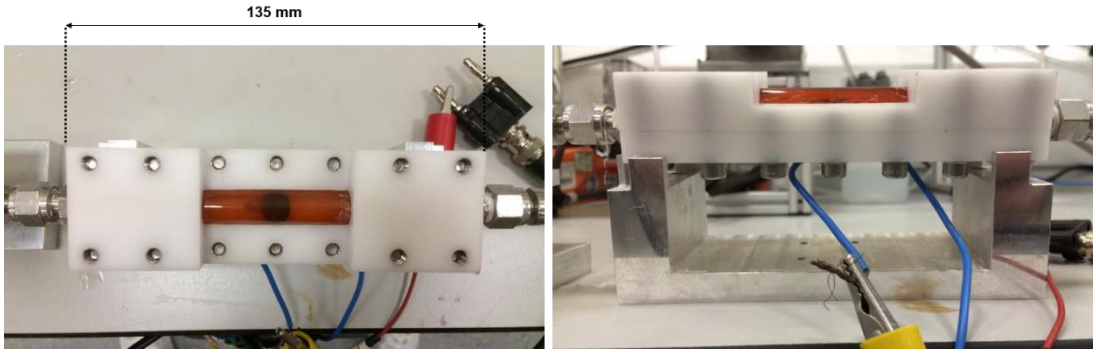

Figure 6.13. Images of final SR-XRD flow cell design.

The electrochemical set-up used for the flow cell design was a standard three-electrode cell (see Figure 6.14) which comprised of the X65 grade carbon steel sample as the WE, a 1 mm in diameter 99.9% pure platinum rod (10) as the counter electrode (CE) (which is also flush mounted with the surface 3 mm away from the WE) and a Ag/AgCl reference electrode (RE) positioned downstream in a separate port system.

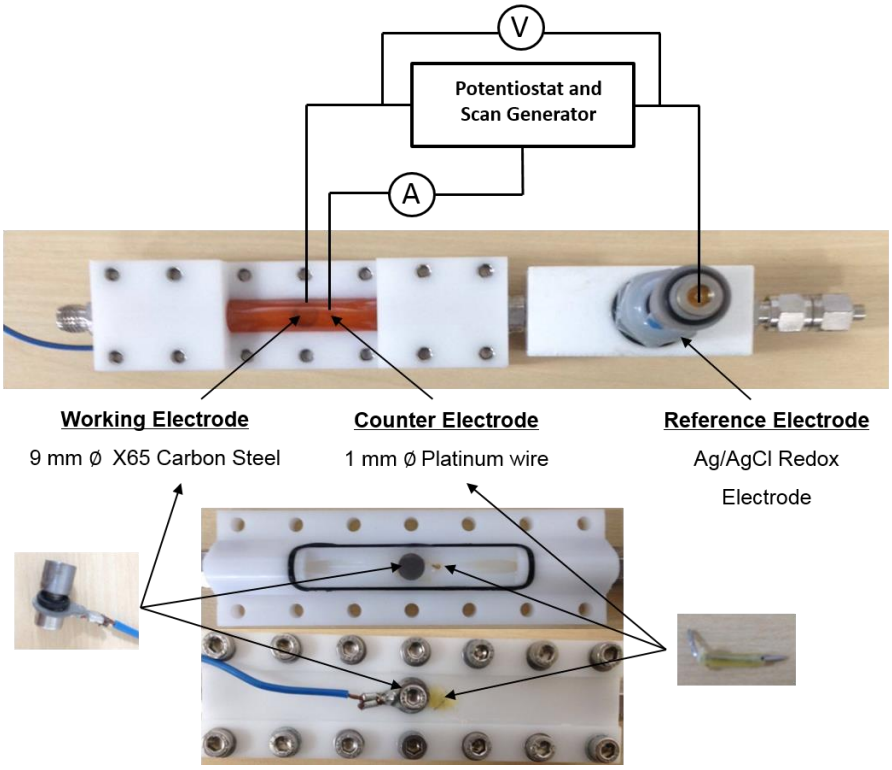

Figure 6.14. Flow cell electrochemical set-up used during SR-XRD tests: Three-electrode set-up.

The key design features for the SR-XRD flow cell are summarised highlighted in Figure 6.15.

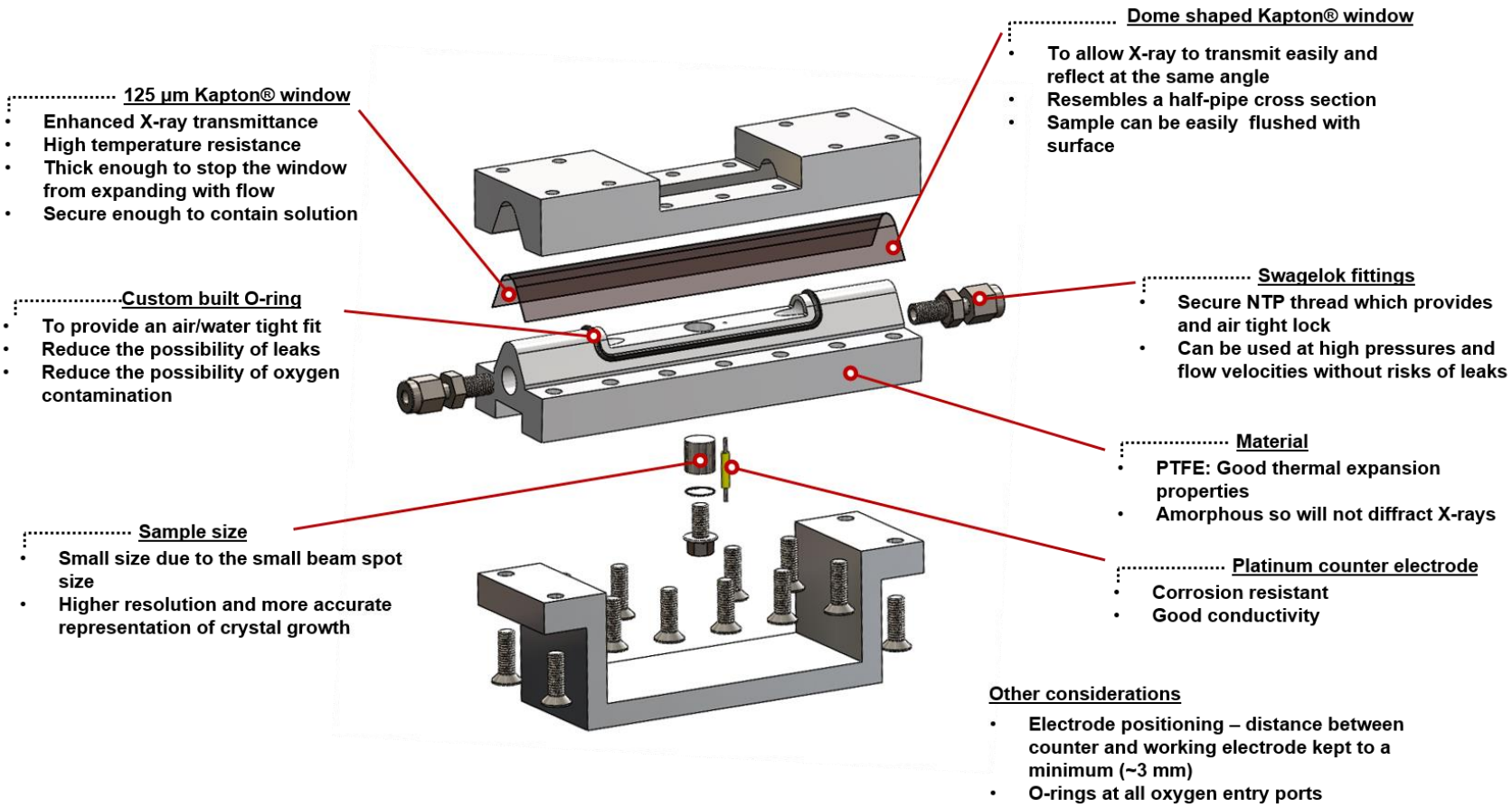

Figure 6.15. A schematic showing the key design features of the SR-XRD flow cell.

6.3 Introduction to Synchrotron Source Radiation

Modern Synchrotron Radiation (SR) sources produce high brilliance and highly collimated (small angular divergence) X-ray beams in comparison to those from standard laboratory based sources. Although *in-situ* GIXRD measurements can be undertaken using a normal laboratory-based diffractometer, the signal-to-noise ratio of the technique is relatively poor primarily due to attenuation of the incident X-ray beam by the liquid in the experimental cell. For *in-situ* assessment, laboratory source X-ray diffractometers can be restricted by factors such as weaker X-ray intensities, high noise-to-signal ratios, increased scanning times, confined working spaces and difficult beam alignment procedures. These factors limit the possibilities of using in-house laboratory X-ray diffractometers. The kinetics and precipitation of corrosion products can occur extremely fast and these limitations could result in phases either being missed (due to the time to complete the scan) or phases not being detected (due to the weakened intensities and signal-to-noise ratio in comparison to SR). With such clear disadvantages, using a synchrotron source is preferred to follow the kinetics of corrosion products *in-situ*. However, access to synchrotron facilities is rather difficult. It is approved on the perceived outcome and impact to science/industry based on merit of the submitted proposal to gain beam-time. Upon being granted time, the success of the experiments at a synchrotron facility depends upon attentive preparatory efforts and perfect execution during a small period of operational beam-time to fully utilise the opportunity to used such specialised equipment.

In this work, high brilliance SR has been utilised to substantially boost the signal-to-noise ratio of the recorded *in-situ* SR-XRD patterns to follow the evolution of corrosion products in real-time.

6.3.1 Diamond Light Source Synchrotron Radiation

The *in-situ* SR-XRD experiments detailed in Chapter 6, 7, 8 and 9 were conducted using the powder diffraction beamline (I15) at Diamond Light Source Synchrotron Facility (DLSSF) (Beamline I15) in Oxfordshire, United Kingdom over a total period of 3 days, see Figure 6.16 and Figure 6.17. The electrochemical flow cell previously outlined was designed to allow *in-situ* SR-XRD patterns to be recorded in real time while the sample was under electrochemical control. Therefore, relative kinetic information regarding the

formation and growth of corrosion products can be obtained without interrupting the electrochemistry, and then can be correlated with any changes observed via the electrochemical measurements. The SR-XRD technique allowed crystalline phases that were present to be determined as well as providing crystallographic information during the growth of the phases present.

Figure 6.16. Birds eye view of the Diamond Light Source Synchrotron Facility, Harlow, Oxfordshire, United Kingdom [189].

The Diamond Light Source (DLS) is a synchrotron; a huge scientific machine, half a kilometre in circumference, designed to produce very intense beams of X-rays, infrared and ultraviolet light. For centuries, scientists have used microscopes to study things that are too small to see with the naked eye. However, microscopes are limited by the visible light that they use. Optical microscopes can be used to study objects that are a few microns (0.001mm) in size, about the size of cells. However, to study smaller objects like molecules and atoms, scientists need to use the special light generated by the synchrotron.

A schematic of the DLS is shown in Figure 6.17. As a third generation synchrotron, the DLS is comprised of several components including the Electron Gun (1), Linear Accelerator (2), Booster Ring (3), and Storage Ring (4). Each of these sections contributes to producing a beam of synchrotron

light (5), which is then harnessed in a beamline (6), using an optics hutch (7), experimental hutch (8) and work stations (9).

Electron Gun: Bursts of electrons are injected into an ultra-high vacuum stainless steel tube. The energy of the electron beam is 0.22 MeV (million-electron volts). They are then fired out into the machine, where they are accelerated up to very high speeds through a series of three particle accelerators. These are called the linear accelerator (known as linac), the booster synchrotron and the large storage ring. The linac uses microwave energy to increase the energy of the electrons to 250 MeV. The electron beam is then transferred into the booster ring where the microwaves further accelerate the electrons to nearly the speed of light (increasing the energy from 250 MeV to 2900 MeV). The electron beam is transferred into the storage ring where insertion devices called wigglers and undalators can bend the beam many times over very short distances. The storage ring is what gives Diamond its iconic doughnut shape with a huge circumference (half a kilometre). The storage ring is, made of 48 straight sections angled together with 48 bending magnets, and this magnetism is used to steer the electrons around the ring. Third generation synchrotrons like Diamond also use special arrays of magnets called insertion devices.

When high-speed, high-energy electrons are accelerated, or their path is bent passing through powerful magnetic fields, a natural phenomenon occurs to produce an extremely brilliant, full spectrum beam of photons known as synchrotron light which can be 10 billion times brighter than the sun. When the path of the electron beam is bent by Diamond’s powerful magnets, the electrons lose energy in the form of light. Beams of synchrotron light are manipulated and channelled out of the storage ring and into the experimental stations, called beamlines.

It is inside these beamlines that scientists carry out their experiments. The beamline contains three different sections; the optics hutch, where the full spectrum beam of synchrotron light is segmented into portions of electromagnetic spectrum by equipment such as monochromators, then focused with specially curved mirror systems; the experimental hutch, where the selected wavelength of synchrotron light is directed onto the sample to and the experiment is carried out; and the control/work station, where the scientists control the experiment and the data is transferred to computers for storage and analysis. The beams of light are so strong that, in the case of

Diamond's X-ray beamlines, it is not safe to be in the same room whilst they are being directed at the sample.

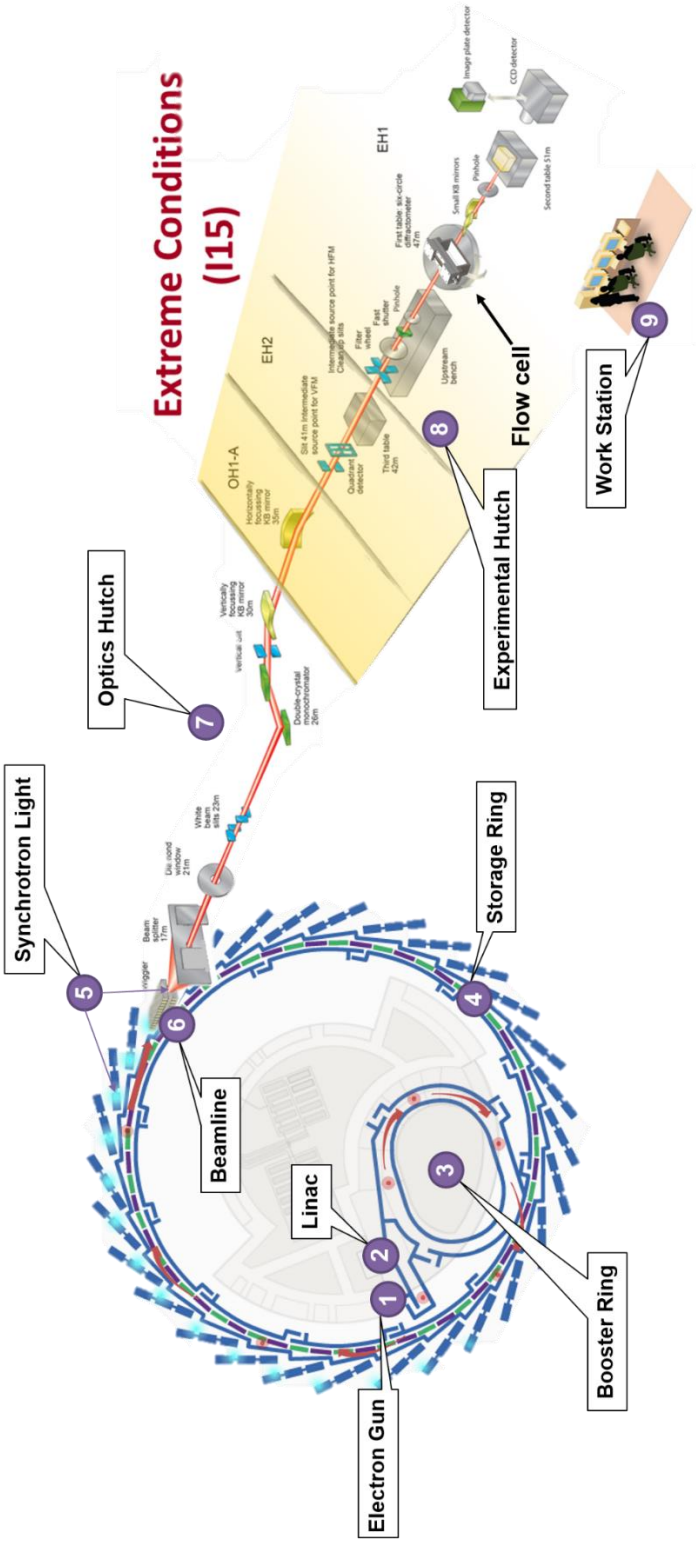

Figure 6.17. Diamond Light Source Synchrotron and I15 Beamline schematic (modified from [189]).

6.4 *In-situ* SR-XRD Flow Cell Synchrotron Experimental Procedure

To fully utilise the opportunity of having access to the Diamond Light Source synchrotron facility, a strategic test methodology was devised and the testing methodology is summarised in Figure 6.18 before the beam-time commenced.

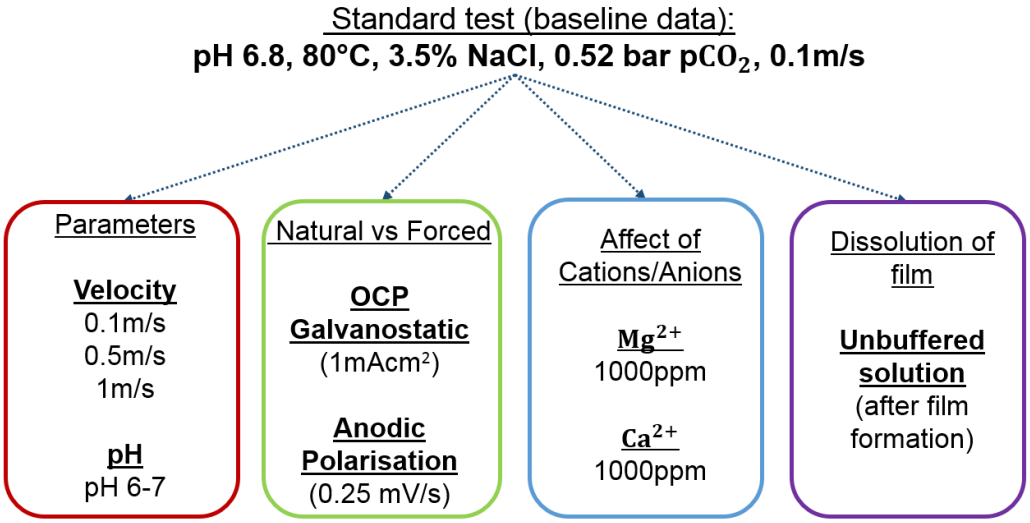

Figure 6.18. Summary of Synchrotron test methodology at the Diamond Light Source Synchrotron Facility.

The main aim of the synchrotron test methodology was to improve the understanding of the nature and kinetics of corrosion product formation in CO_2 corrosion of carbon steel. A range of short term tests were completed over the 3 days which gave an insight into the very early stages of $FeCO_3$ formation under a range of different parameters and will be the focus of the remaining chapters in this work.

6.4.1 Experimental Set-Up and Sample Preparation

Figure 6.19 and Figure 6.20 shows a schematic of the flow cell set-up at beamline I15, Diamond Light Source, Oxfordshire and an image taken in the experimental hutch respectively. To demonstrate the capabilities of the flow cell, one particular experiment is highlighted in this work. The following paragraphs provide information pertaining to the experimental approach and the test conditions evaluated. A formulated saline solution circulates within a closed loop between the flow cell and a locally heated 1 litre vessel via the use of a centrifugal micro-pump to provide precise flow rate control. The flow velocity of the test was maintained in a laminar flow regime at 0.1 m/s for the

experiment discussed here (although much higher velocities up to 2 m/s are possible which would prove advantageous in studies involving mechanical/chemical dissolution or mass-transfer controlled precipitation process) and was controlled using a customised magnetic drive gear micro-pump (Micropump® Series GJ-N23) which offers high precision control. The 1 litre vessel was continuously purged with CO_2 throughout the experiment to ensure the solution was completely saturated. Prior to the start of the experiment, the test sample was wet ground up to 600 silicon grit paper, degreased with acetone, rinsed with distilled water and dried with compressed air. The sample was then positioned into the base of the flow cell and electrical wires were connected to the steel samples prior to alignment. A sample surface area of 0.64 cm^2 was exposed to the electrolyte once fluid flow was initiated through the cell. The experiment considered here was performed for 4 hours with *in-situ* electrochemical measurement and SR-XRD measurements being collected throughout the duration of the test. The flow cell was bolted flat onto a specially designed stage that was attached to a kinematic mounting plate. This allowed the flow cell to be easily removed from the stage while fully assembled so that dismantling and cleaning parts and the removal of the sample could be performed in a laboratory away from the beamline. Once flow was initiated, electrochemical and X-ray diffraction measurements commenced after a period of no more than 3-4 minutes.

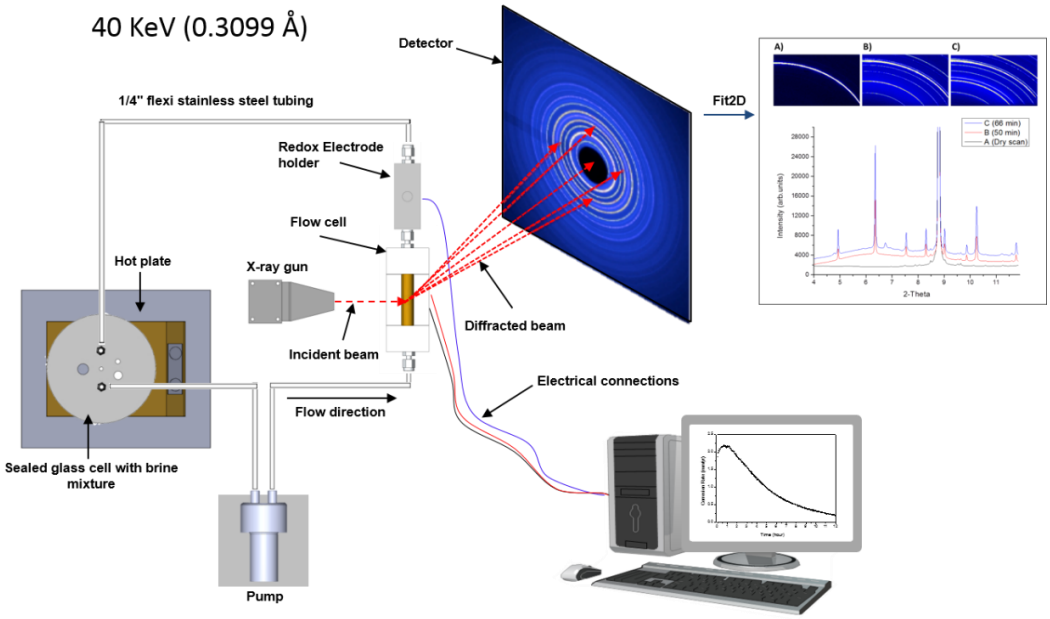

Figure 6.19. The cell set-up during Synchrotron tests: Schematic of the flow cell set-up used on the Diamond Light Source beamline (I15).

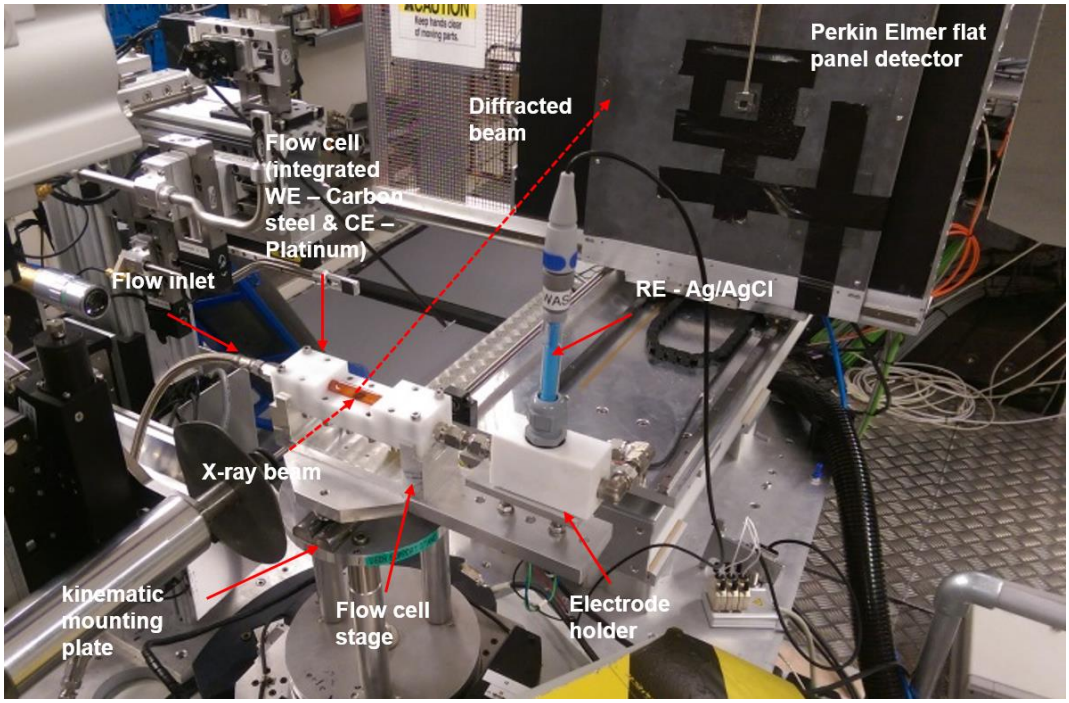

Figure 6.20. The cell set-up during Synchrotron tests: Photo of the flow cell set-up used on the Diamond Light Source beamline (I15).

6.4.2 Brine Preparation

The experiment was conducted in a de-aerated 3.5 wt. % NaCl brine saturated with CO_2, representing oil and gas production environments. CO_2 was bubbled into the system for at least 4 hours prior to the experiment and throughout the duration of the experiment which was conducted at atmospheric pressure. The temperature of the solution was maintained at 80°C using a high power Carousel Tech Stirring Hotplate with in integrated Pt1000 stainless steel temperature sensor that was immersed into the 1 litre vessel through an oil filled glass tube. The pH of the solution was adjusted to ~6.8 and was controlled by adding sodium bicarbonate (8g $NaHCO_3$ per 1 litre solution). The temperature drop between the hotplate and the flow cell was less than 1ºC.

6.4.3 *In-situ* Electrochemical Measurements

Electrochemical measurements were conducted using an ACM Gill AC potentiostat in order to determine the *in-situ* corrosion rate of the X65 carbon steel working electrode. Linear polarisation resistance (LPR) measurements were performed by polarising the sample ±15 mV vs. the open circuit potential (OCP) at a scan rate of 0.25 mV/s to obtain a polarisation resistance (R_p). LPR measurements were undertaken every 5 minutes, allowing the sample to remain at OCP between each reading. Tafel polarisation measurements were

completed using new and wet ground samples in separate experiments by performing anodic and cathodic sweeps starting at OCP and scanning to +150 mV or -500 mV vs. OCP, at a scan rate of 0.5 mV/s. Anodic and cathodic sweeps were performed separately in different experiments and the measured Tafel constants were used to determine an appropriate Stern-Geary coefficient to provide a more accurate calculation of corrosion rates. Solution resistance was measured using AC impedance and the polarisation resistance values were then corrected to give the charge-transfer resistance. Once the Stern-Geary coefficient was established, it was then used in combination with Faraday's Law and the measured values of charge transfer resistance to estimate the general corrosion rate of the system.

6.4.4 *In-situ* SR-XRD Measurements

The *in-situ* SR-XRD experiments were conducted at beamline I15 at the Diamond Light Source, UK. The beamline provides monochromatic high-energy X-rays from 20 to 80 keV in combination with a small beam spot size down to <20 μm which can penetrate into complex sample assemblies permitting detailed mapping of structural order or disorder and chemical composition [189]. High energies (compared to conventional XRD) are required to penetrate through the water (~15 mm path length) in the flow cell and the beam size allows scanning of the samples with appropriate spatial resolution. The X-ray beam energy in these experiments was 40 keV (i.e. λ = 0.3099 Å) and the beam size was 70 μm in diameter. The incident-beam to sample angle was set to 4º (through tilting the flow cell as shown in Figure 6.21) and *in-situ* SR-XRD measurements over the range of 2θ=0-12° were collected continuously during the experiments.

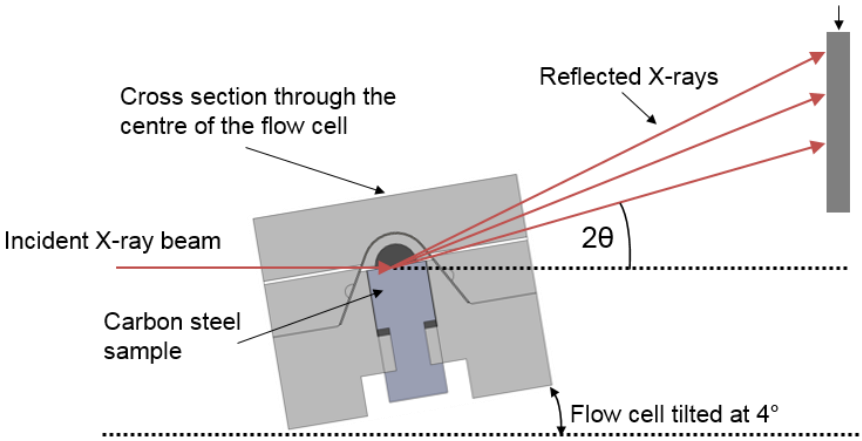

Figure 6.21. Schematic showing the incident X-ray beam to flow cell angle.

Using 40 keV radiation along with an incident angle of 4º, the penetration depth of the beam in to the steel sample was calculated using PANalytical's HighScore plus software. The estimated penetration depth using these values was 55 µm. Before switching the pump on, a dry scan of the steel sample was taken to use as baseline data relative to the *in-situ* data and to check the alignment of the beam. Data acquisition then began 3-4 minutes after the pump was switched on. This was the time taken to carry out the required safety checks and closure of the experimental hutch before the beamline shutter was opened. Individual data sets were collected for 60 seconds at any given location. In order to maximise the accuracy of the extent of crystal growth, a loop was devised to scan five measurements across a 2 mm path located at the centre of the sample to ensure more reliable statistics if the film formed was non-uniform across the steel surface. Therefore the overall scanning time to complete one cycle of the surface was 5 minutes. The diffraction results in this chapter show the average of the five scanned locations to represent a larger proportion of the overall surface as well as the individual transients themselves. The flux available at I15, together with the fast data collection times of 60 seconds enables intermediate phases (if any) to be measured. Diffraction images were recorded using a Perkin Elmer flat panel detector located 975 mm from the sample and conventional 2θ diffraction patterns were generated by radial integration of the Debye rings using the software Fit2D with subsequent data analysis performed by profile fitting and Rietveld analysis.

6.4.5 Post Test Synchrotron Data Analysis

The conversion of the raw data was not a simple task. Every test conducted during the visit to the DLS generated 2048 data points of intensity vs 2-Theta for just one scan across the surface of a sample in the format of a .tif file which was a 2D image produced from Fit2D. The beam-stop and regions of the detector occluded by the flow cell housing were masked out and the data was integrated radially about the beam centre through the conventional cake technique, yielding 1D plots of intensity vs. 2θ. A macro was devised to radially integrate every .tif files generated and to convert them into .chi files which was a 1D plot of intensity vs 2θ. One .tif file (with 2048 data points) is generated during each scan for every test completed. Putting this into perspective, one complete loop of the scanned area generated 10240 data points and each test consisted of at least 12 loops (122880 data points for a 60 minute test). The mass amount of raw data produced needed to be processed without having

to manually go through each scan individually. Therefore once the data had been obtained, the following stages in Figure 6.22 illustrates the process undertaken once the experimental data had been obtained from the visit to the Synchrotron.

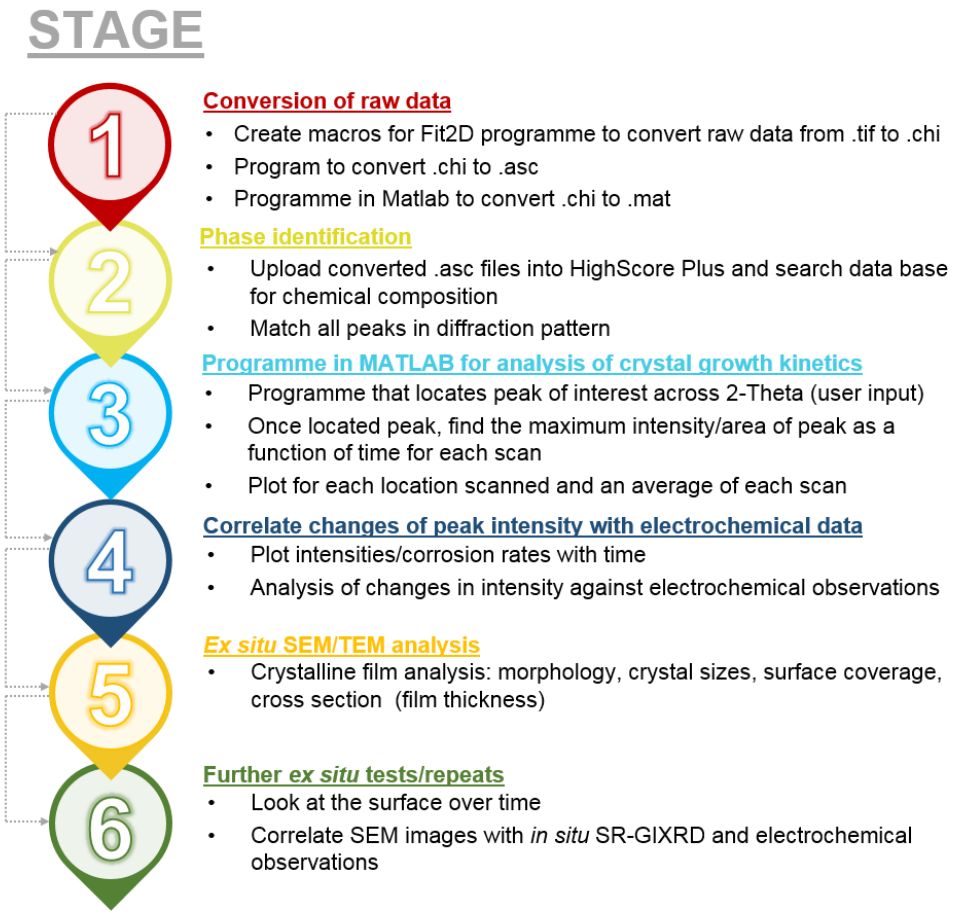

Figure 6.22. Stages of post synchrotron analysis

6.5 Selection of Synchrotron Results: Validation of the Flow Cell

The design and commissioning of the flow cell enabled corrosion kinetics and *in-situ* electrochemical responses to be related to diffraction measurements in a flowing cell in a naturally corroding CO_2 system. This section will focus on the performance of the flow cell with respect to the flow analysis through the cell, the *in-situ* electrochemical and SR-XRD observations.

6.5.1 Numerical and Experimental Validation of Flow

Once the final design has been manufactured, the flow rate across the surface of the sample was initially determined experimental and calibrated to

determine the flow velocity through the flow cell for each pump setting. The flow velocity was calculated using the measured flow rate in accordance with Equation 6.1.

$$v = \frac{Q}{A}\ (m/s) \tag{6.1}$$

Where, A is the inlet area in m^2, and Q is the flow rate in m^3/s. The calculated flow velocities are shown in Table 6.1 (the highlighted text in red indicates the velocities used throughout this study).

Table 6.1. Measured and calculated flow velocities.

Test	Pump Setting	Flow Rate (ml/min)			Velocity (m/s)
		Run 1	Run 2	Run 3	Average
1	**0.25**	229.87	219.75	217.22	**0.10**
2	0.5	456.55	442.94	451.06	0.21
3	0.75	686.97	685.87	682.44	0.32
4	1	953.59	968.68	953.29	0.45
5	1.25	1164.60	1152.52	1167.77	0.55
6	1.5	1483.68	1421.13	1392.76	0.68
7	1.75	1746.22	1736.11	1806.68	0.83
8	**2**	2052.69	2142.09	2212.39	**1.01**

Flow parameters within the flow cell were calculated by employing empirical relations based on the measured values for the velocity through the cell. The Reynolds number of the flow within the cell and flow shear stress across the carbon steel surface at different flow velocities can determined through the following equations. Dean's formula was used to calculate the friction factor (Equation 6.2),

$$C_f = 0.073 \times Re^{-0.25} \tag{6.2}$$

Where the Reynolds number is given by:

$$Re = \frac{D_h \times \upsilon \times \rho}{\mu} \tag{6.3}$$

Where D_h is the hydraulic diameter of the flow cell in m, υ is the flow velocity in m/s, ρ is the fluid density in kg/m^3 and μ is the fluid dynamic viscosity in kg/ms^{-1}.

The hydraulic diameter was calculated to be 6 x10^{-3} m based on a circular pipe section which is just the diameter of the inlet pipe section. The fluid density and dynamic viscosity at 80°C, 35 ppt (parts per thousand) salinity (35g in 1L solution) at atmospheric pressure are ρ = 997.375 kg/m^3 and μ = 0.387 x10^{-3} kg/ ms^{-1}.

This allows the wall shear stress to be calculated using:

$$\tau = \frac{C_f \times \upsilon^2 \times \rho}{2} \ (Pa) \tag{6.4}$$

The calculated Reynolds numbers and wall shear stress values at the different flow velocities are plotted in Figure 6.23.

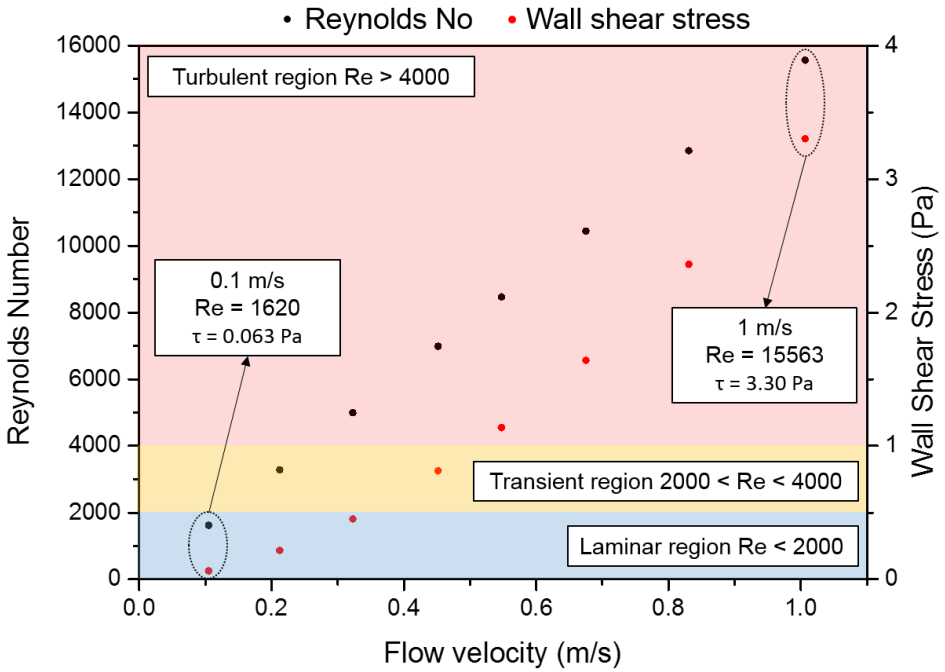

Figure 6.23. Calculated Reynolds numbers and wall shear stress values at the different flow velocities.

A flow velocity of 0.1 m/s will operate in a laminar flow regime, whereas a magnitude higher at 1 m/s, the system will operate under a turbulent flow

regime. Based on these observations, flow velocities of 0.1 and 1 m/s were chosen to study the corrosion kinetics under two distinctly different flow regimes. The fluid flow response of the flow cell was studied within ANSYS Fluent using the standard time-dependant advection-diffusion equation for an incompressible flow:

$$\frac{dc}{dt} = D\nabla^2 c - v \cdot \nabla c \qquad (6.5)$$

Where c is the concentration, t is the time, D is the diffusion coefficient of the species in question, v is the velocity field and ∇ is the del operator.

Initially, the steady state flow equations were solved subject to appropriate boundary conditions which consisted of a volumetric flow inlet boundary condition, a pressure boundary condition of 0 Pa at the flow cell outlet and a no-slip condition at the solid walls. The physical properties of the fluid were defined and are provided in Table 6.2.

Table 6.2. Physical properties of brine mixture defined for flow cell at 80ºC.

Property Name/Symbol	Expressions	Description
ρ	997.375 kg/m^3	Density of 3.5 wt.% NaCl solution at 80˚C
μ	0.387 kg/m^3	Viscosity of 3.5 wt.% NaCl solution at 80˚C
υ_{inlet}	0.1 and 1 m/s	Inlet flow velocity

An analysis of the velocity field and wall shear stress within the flow cell was performed to determine the uniformity of the fluid across the carbon steel sample. Flow velocities of 0.1 and 1 m/s were simulated and the results are provided in Figure 6.24. Figure 6.24(a) and (b) indicate the velocity field under the simulated flow velocities. The purpose of this is to be able to clearly identify regions within the cell where stagnation points could potentially exist. The carbon steel sample which is embedded into the base of the flow cell is provided in each of the images to show the distribution in fluid velocity over the surface of the sample.

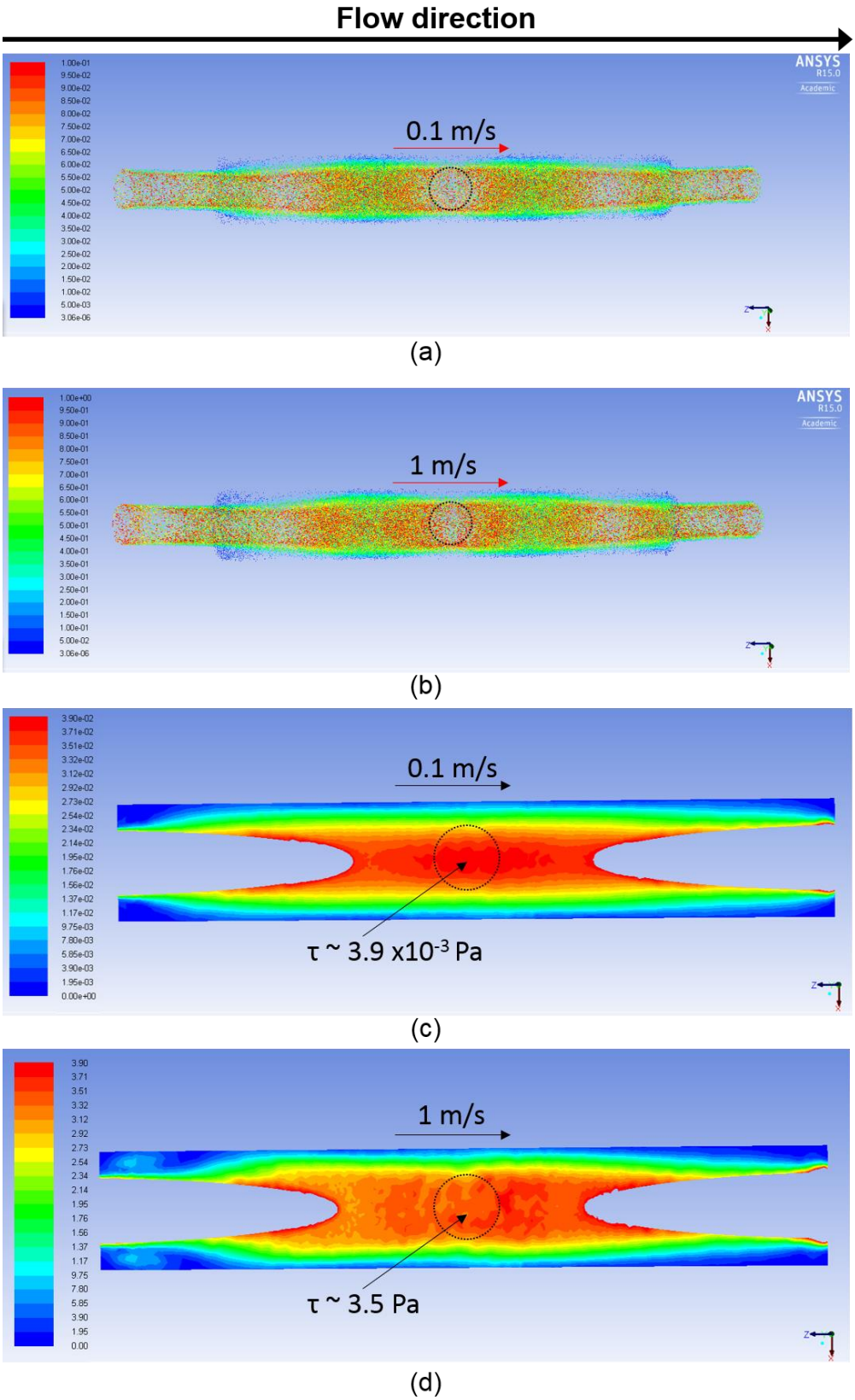

Figure 6.24. CFD results showing the velocity fields in m/s ((a) and (b)) and wall shear stress in Pa ((c) and (d)).

Over the flow range of 0.1-1 m/s, the stagnation points within the flow cell are minimal. The simulations indicated that the maximum flow velocity capable within the flow cell is around 2 m/s. At this point, recirculation within the cell begins to occur and the uniform velocity over the sample surface is disrupted. However, this velocity is beyond the capabilities of the pump and therefore is not including within this study. Similarly, the distribution of the wall shear stress is uniform across the surface of the sample under both simulated flow velocities and the results are in strong agreement with the calculations of wall shear stress using Equations 6.2-6.5.

6.5.2 Validation of Flow Cell Performance: Electrochemical Observations

Figure 6.25 shows the graph indicating the *in-situ* electrochemical measurements of the corrosion rate and OCP versus time for a 240 minute test conducted on a naturally corroding sample under the conditions described previously at 0.1 m/s.

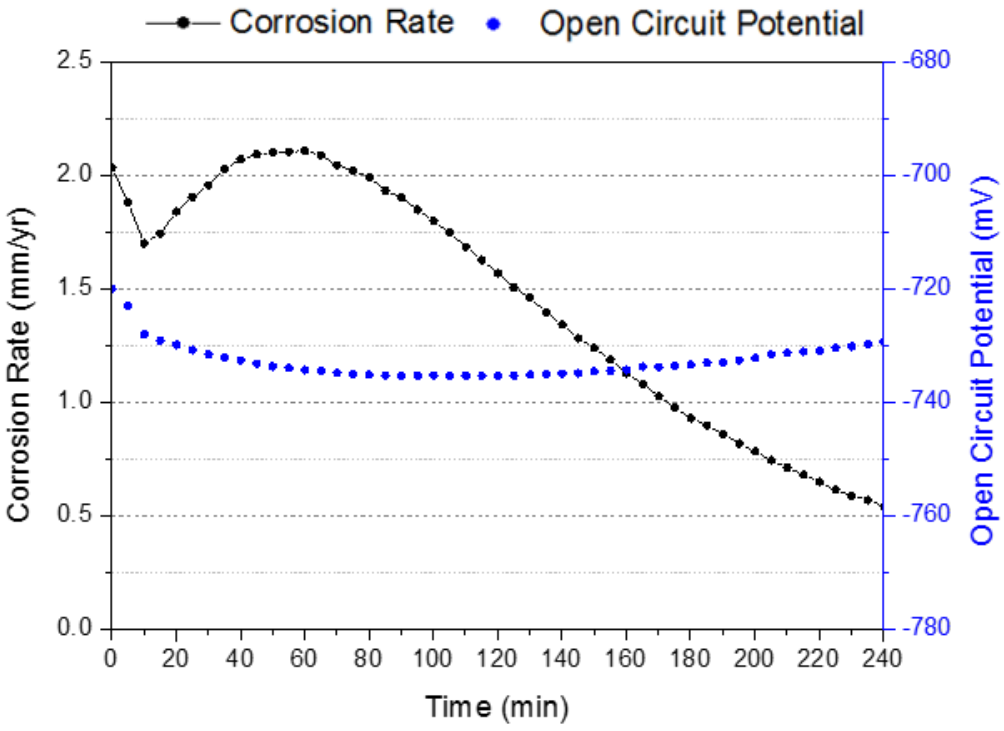

Figure 6.25. *In-situ* electrochemical data: Corrosion rate and open circuit potential data collected at Diamond Light Source beam line (I15).

The OCP remains stable throughout the duration of the test in the region between -720 and -740 mV which is in good agreement with literature [28,

153] and the static immersion tests in Chapter 5 of carbon steel in a CO_2 buffered solution at 80°C. The corrosion rate of the system at the start of the test is ~2 mm/year which increases to ~2.15 mm/year throughout the first 60 minutes of the test until a semi-protective $FeCO_3$ layer has formed, blocking active steel sites available for dissolution causing the corrosion rate to decrease with time. The corrosion rate drops to a value of ~0.54 mm/year after 240 mins as a result of $FeCO_3$ covering the majority of the steel surface. Figure 6.26 shows the Tafel plots obtained by performing separate anodic and cathodic sweeps once the corrosion rate had stabilised at 0.1 mm/year after 12 hours of testing during off beamline tests. The measured corrosion rate from the synchrotron test were calculated based on these measured Tafel constants. The anodic Tafel slope (βa) measured ~60 mV/decade which is in good agreement with literature at similar operating temperatures [29].

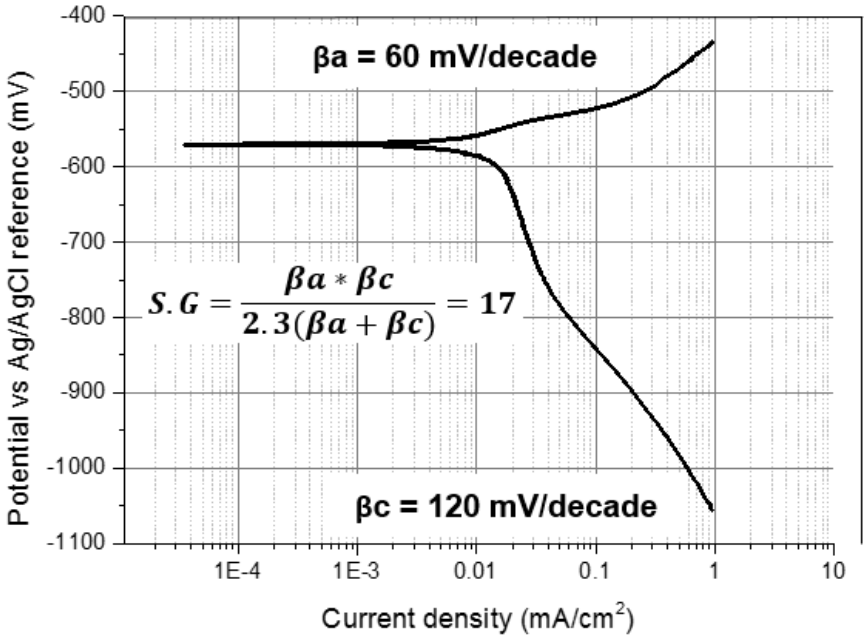

Figure 6.26. *In-situ* electrochemical data: Tafel plots for X65 carbon steel samples ran in-house under the identical conditions to SR-XRD tests after 12 hours (Note: Increase in potential is due to pseudo-polarisation of the sample [29]); (S.G = Stern-Geary coefficient), (βa = Anodic Tafel slope), (βc = Cathodic Tafel slope).

However, βc proved difficult to measure due to interference from high anodic currents at low negative overpotentials influencing the Tafel behaviour. However the cathodic Tafel slope (β_c) for CO_2-systems is well characterised

by Nesic *et al.* [29] to be ~120 mV/decade which was implemented to give Stern-Geary coefficient (S.G) of 17.

Figure 6.27 shows the error in corrosion rate after correcting the corrosion rate with the amended Stern-Geary coefficient based on measuring βa.

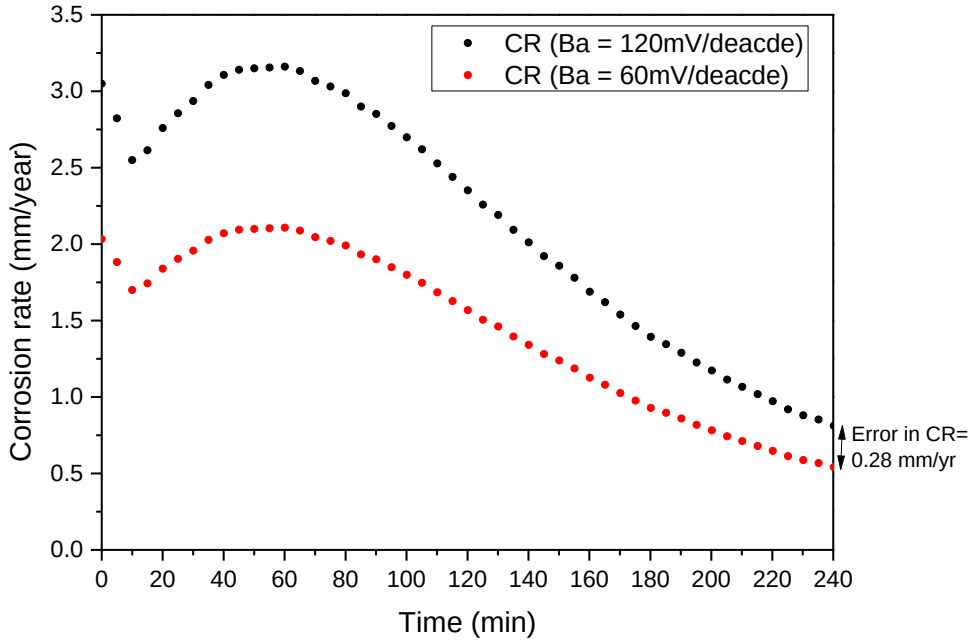

Figure 6.27. Error in corrosion rate after correcting for Stern-Geary coefficient based on measuring β_a.

The final error in corrosion rate without correction is 0.28 mm/year which is relatively substantial when analysing of the corrosion rate and the protectiveness of the corrosion product ($FeCO_3$ here) formed.

6.5.3 Validation of Flow Cell Performance: SR-XRD Observations

In-situ SR-XRD data over the range 2θ=0-12° was collected continuously for 240 minutes for this particular test which was conducted at pH 6.8, 80°C, 3.5 % wt. NaCl and 0.1 m/s. The results are outlined to validate the flow cell and will be discussed thoroughly in Chapter 7. Figure 6.28 shows a plot of multiple patterns representing the intensity against 2θ showing the growth of the phases present over time (patterns are offset for clarity).

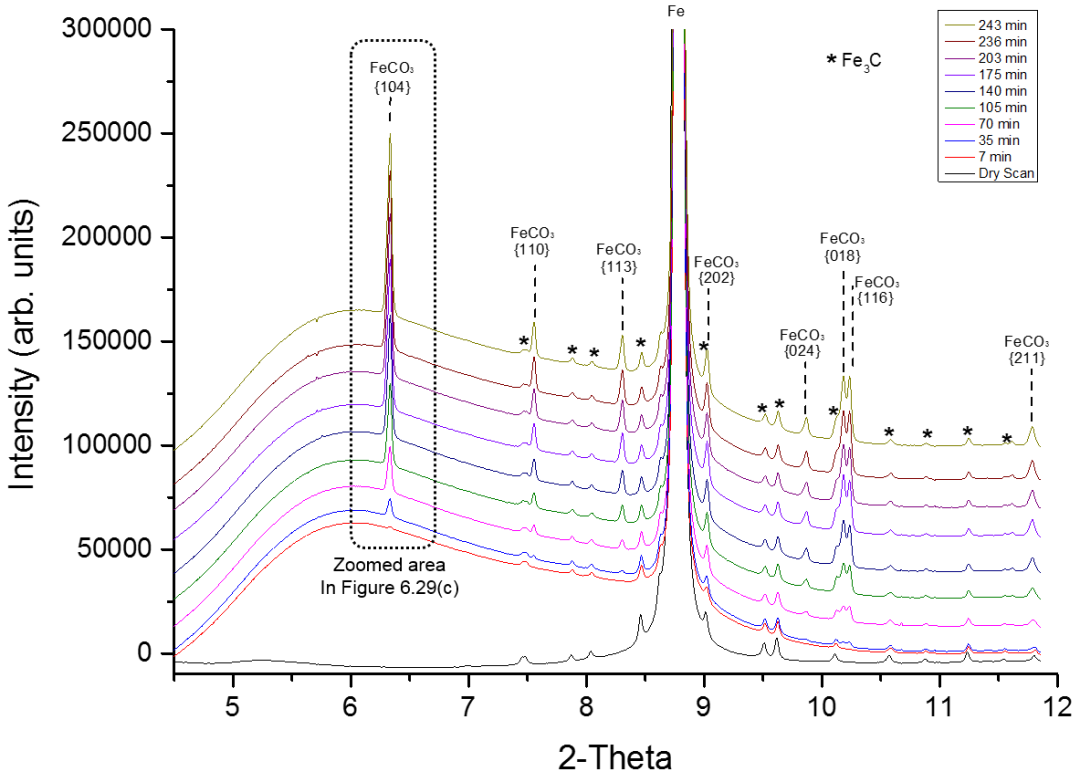

Figure 6.28. Selection of *in-situ* diffraction patterns recorded as a function of time at the Diamond Light Source powder diffraction beam line (I15). Each plot represents the phases present across a 2 mm path at the centre of the sample.

Phase identification of the *in-situ* SR-XRD patterns reveals that the only crystalline phase detected on the steel surface during the test was $FeCO_3$. Whilst iron carbide (Fe_3C) was present prior to running the tests and was a part of the steel composition. Throughout the duration of the entire experiment, the growth of the crystals was dominated by the growth of the plane observed at 2θ=~6.35º (Miller Index – (104)). Each pattern represents the cumulative sum of all five scans across the sample at each time interval reflecting the intensity of the phases present across a 2 mm linear region as indicted in the schematic in Figure 6.29 (a). The growth and shape of the major $FeCO_3$ plane is illustrated by the boxed area in Figure (6.28) and in the magnified image provided in Figure 6.29 (c). Figure 6.29 (b) shows the growth of the major $FeCO_3$ plane (104) at each location scanned across the sample and shows that crystalline $FeCO_3$ was detected at each location on the sample within 7-15 minutes of scanning.

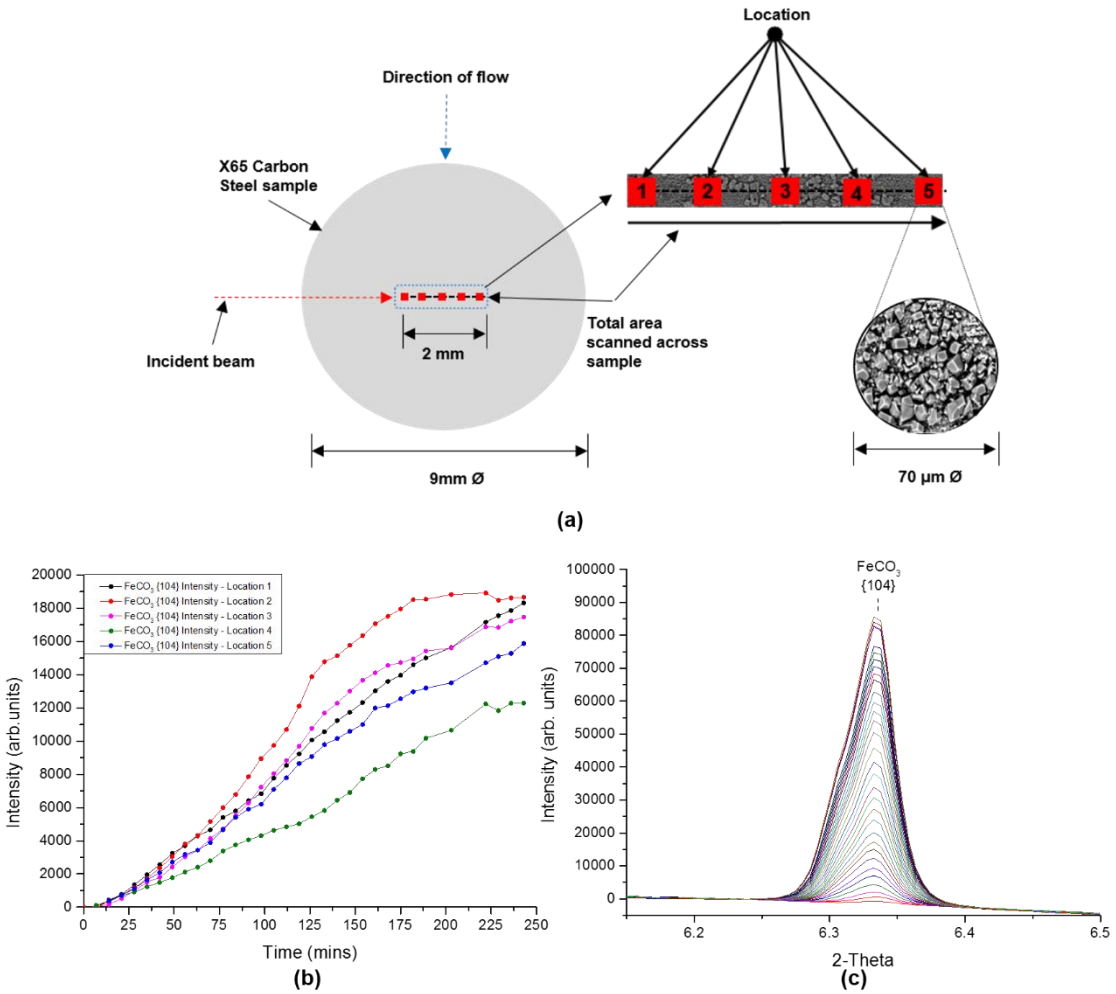

Figure 6.29. a) Schematic showing the regions of the sample scanned; b) $FeCO_3$ (104) intensity at each location; c) A plot of the accumulated intensities in (b).

The conversion of the diffraction angles between the standard laboratory diffractometer radiation source (dual copper Cu Kα1+2) is calculated in accordance with Bragg's Law which is illustrated in Figure 6.30. The values obtained from the conversion are shown in Table 6.3. It should be noted that the 2θ values are in degrees while the θ values are in radians. As such, the SR-XRD results shown in this chapter and every chapter going forward are relying on the strongest $FeCO_3$ peak (104) Miller indices and strongest Fe (110) Miller indices that show a 40 kV (K 1+2) diffraction angle of ~32° and ~45° respectively. Using 40 KeV SR, these angles correspond to diffraction angle of ~6.35° ($FeCO_3$ (104)) and ~8.75° (Fe (110)) which agrees with the diffraction data in Figure 6.28.

$\gamma = 2dsin\theta$

γ = X-ray wavelength

d = distance between lattice planes

θ = angle of incidence with lattice plane

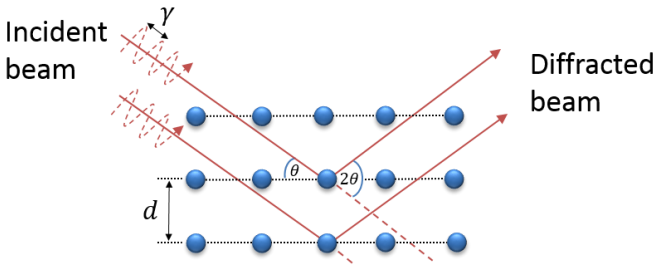

Figure 6.30. Schematic showing Bragg's Law: Bragg equation (left); Illustrated diagram of Bragg's Law (right).

Table 6.3. Conversion between 40 kV (Kα1+2) Cu and 40 KeV for $FeCO_3$ diffraction angles.

2θ (°)	λ_{Cu} (Å)	θ_{Cu} (rad)	d-spacing (Å)	λ_{40KeV} (Å)	$2\theta_{40KeV}$ (°)
24	1.541	0.209	3.7049	0.31	4.79
32	**1.541**	**0.279**	**2.7946**	**0.31**	**6.35**
38	1.541	0.332	2.366	0.31	7.51
42	1.541	0.367	2.1495	0.31	8.27
46	1.541	0.401	1.9714	0.31	9.02
50.5	1.541	0.441	1.8058	0.31	9.85
52.5	1.541	0.458	1.7416	0.31	10.21
52.8	1.541	0.461	1.7324	0.31	10.26
61	1.541	0.532	1.5177	0.31	11.72

The wavelength corresponding to 35 KeV or 40 KeV was converted by using the Plank-Einstein relation shown in Equation 6 where h is the Plank's constant equal to 4.135667662(25)x10^{-15} eV/s and c is the speed of light approximately equal to 3.00×10^{8} m/s.

$$E = \frac{h \cdot c}{\lambda} \tag{6.6}$$

6.6 Summary and Conclusions

Based on the lack of consistency and certainty in the literature and the results in Chapter 5 on the true nature of the phases to form during the CO_2 corrosion process expresses the need for a new *in-situ* methodology to determine the

CO_2 corrosion mechanism and the kinetics of corrosion product formation. In order to fill this major gap, this work has demonstrated that a newly designed flow cell can be used for *in-situ* SR-XRD studies of corrosion product formation on carbon steel surfaces that are naturally corroding in a corrosive and flowing system.

This Chapter has presented a new system and methodology comprising of a flow cell with integrated *in-situ* electrochemistry and SR-XRD capabilities which has been developed to facilitate corrosion measurements under a variety of experimental conditions. Some of the first data obtained for *in-situ* analysis has been presented to show the capabilities of the cell. Using *in-situ* SR-XRD, the formation of corrosion products on a naturally corroding carbon steel sample in a CO_2 saturated brine has been followed as a function of time in a newly designed flowing cell.

The design and development of a unique flow cell for *in-situ* corrosion studies has enabled the following conclusions to be drawn:

- The *in-situ* electrochemical and SR-XRD observations validate the use of the flow cell to monitor the corrosion rate and growth kinetics of $FeCO_3$ (and/or any other corrosion products) formation.
- The flow cell can be used to evaluate the effect of flow velocities on the rate of corrosion product formation and the corrosion rate of the system with the ability to operate from 0.1 m/s (under a laminar flow regime) to 2 m/s (under a turbulent flow regime).
- Under the specific conditions evaluated, $FeCO_3$ was the only crystalline phase to form in the system, with no crystalline precursors being apparent prior to or during its formation.
- $FeCO_3$ nucleation could be detected consistently and well before its inhibitive effect on general corrosion rate was recorded from electrochemical responses.
- The $FeCO_3$ intensity plots of the most prominent peak at each of the locations scanned shows a nucleation period, followed by a growth stage.
- The major $FeCO_3$ crystal plane at each of the five locations scanned shows surface growth is heterogeneous (i.e. non-uniform), highlighting

the importance of multiple scans to accumulate a clear interpretation of the growth kinetics across the steel surface.

- A cumulative intensity relationship with corrosion rate and film formation is apparent.

The system opens up several avenues of research where real-time corrosion measurements might enable some mechanisms to be determined. The flow cell will be used in future investigations into the effect of different environmental parameters on the formation of $FeCO_3$.

Chapter 7
In-situ SR-XRD Study of $FeCO_3$ Precipitation Kinetics onto Carbon Steel in CO_2-containing Environments: The Influence of Brine Chemistry and Operating Conditions

This chapter presents results from an *in-situ* SR-XRD flow cell integrated with electrochemistry for corrosion measurement at the Diamond Light Source Synchrotron facility. The cell was used to follow the nucleation and growth kinetics of corrosion products on X65 carbon steel surfaces in a CO_2-saturated 3.5 wt.% NaCl brine at 80°C and a flow rate of 0.1 and 1 m/s over a range of solution pH values (6.3, 6.8 and 7). The purpose of the work was to determine the effect of the brine chemistry on the early kinetics of $FeCO_3$ nucleation and growth.

7.1 Introduction

The nucleation and growth of the $FeCO_3$ layer is heavily dependent upon the kinetics of the precipitation reaction which is governed by the surrounding environment. The process of nucleation starts with heterogeneous nucleation, a process which is capable of occurring easily due to the numerous imperfections on the steel surface such as defects, change in roughness, different grain structures and pearlite/ferrite ratios etc. Nucleation is then followed by crystal growth which essentially limits the rate of precipitation because it less energetically demanding for the ions (Fe^{2+} and CO_3^{2-}) to incorporate into the growing crystal lattice rather than forming a new nuclei.

As previously stated, the protectiveness of the $FeCO_3$ is influenced by several environmental factors such as temperature, pH, CO_2 partial pressure and Fe^{2+} concentration. From all the parameters, solution pH can be regarded as one of the most important factors. Chokshi *et al.* [183] demonstrated that for the corrosion of carbon steel in a pH 6 at 80°C in a 1 wt.% NaCl brine with an addition of 50 ppm Fe^{2+}, a lower bulk supersaturation was obtained resulting in formation of a porous, detached and less protective $FeCO_3$ film forming on to the steel surface resulting in a final corrosion rate of 1.8 mm/year after 45 hours . Higher pH values of pH 6.6 under the same operating conditions (80°C, 1% wt. NaCl, 50 ppm Fe^{2+}) resulted in a higher bulk supersaturation, faster precipitation kinetics and formation of a more protective $FeCO_3$ film resulting in a final corrosion rate of 0.1 mm/year after 45 hours.

As well as influencing the precipitation kinetics of $FeCO_3$, pH can also have a profound effect on the size and morphology of the crystals by influencing supersaturation and hence, crystal nucleation and growth, which in turn influences the level of protection offered by the $FeCO_3$ film. Pessu *et al*. [93] exposed X65 steel samples to a 3.5 wt.% NaCl solution at 50°C for 168 hours at three different pH levels of 3.8, 6.6 and 7.5. At pH 3.8 a porous, amorphous/nano-polycrystalline $FeCO_3$ film developed that offered minimal protection to the steel surface. Increasing pH to 6.6 resulted in a protective $FeCO_3$ film consisting of cubic crystals which grew progressively on the steel surface. The crystals were observed to be loosely packed on the steel surface. At pH 7.5, film formation was rapid and produced rhombohedral $FeCO_3$ crystals with sharp, well defined edges which were extremely protective and compact. As the pH was increased, there was a notable increase in the density and compactness of the corrosion product layer, which linked strongly to the level of protection offered to the steel substrate. Similarly, Tanupabrungsun *et al.* [36] and Li *et al.* [95] demonstrate that protective $FeCO_3$ formation is accelerated/enhanced at higher solution pH, corroborating the observations of Pessu *et al.* [93].

Considering that pH plays a critical role in influencing both the kinetics of corrosion reactions as well as the morphology and composition of corrosion products, the present chapter focuses on examining the influence of solution acidity/alkalinity on the early stages of film development. However, one key challenge in studying $FeCO_3$ precipitation is following the growth kinetics and relating this to the corrosion rate of the steel substrate either in a quantitative or qualitative manner. Therefore, in this work, we demonstrate the capabilities of *in-situ* Synchrotron Radiation-Grazing Incidence X-Ray Diffraction (SR-XRD) to study the film growth processes with a custom designed flow cell which is described in Chapter 6 and our previous publication [184]. The flow cell enables the kinetics of film formation to be followed and correlated with the corrosion rate of the steel substrate in real-time.

7.2 Experimental Procedure

For all experiments in this chapter, the test solution used was a CO_2-saturated 3.5 wt.% NaCl brine. To achieve de-aeration and minimise the dissolved oxygen concentration ($O_{2(aq)}$), the test solution test was purged with high purity CO_2 for a minimum of 4 hours prior to each experiment. In addition, high purity CO_2 was continuously bubbled into the test solution throughout the duration

of each experiment. The flow cell and brine vessel were also sealed with one small outlet for CO_2 gas to prevent O_2 ingress. Based on colorimetric analysis of the test solution, this ensured that the concentration of O_2 was below 50 ppb to simulate oilfield conditions. The operating conditions for tests completed at the Diamond Light Source Synchrotron facility (DLSSF) and in-house are outlined in Table 7.1.

Table 7.1. Experimental test matrix used for *in-house* laboratory tests (at the University of Leeds) and *in-situ* SR-XRD tests.

Parameter	**In-house laboratory tests**	**SR-XRD tests**
Material	X65 carbon steel – 9 mm Ø (exposed surface)	
Brine chemistry	3.5 wt.% NaCl, distilled water	3.5 wt.% NaCl, distilled water, 0 and 1000 ppm Ca^{2+}
Solution pH	6.3, 6.8, 7	
Temperature	80 ºC	
CO_2 partial pressure	0.54 bar (1 bar total pressure in system)	
Flow velocity	0.1 m/s	0.1 and 1 m/s
Test duration	24 hours	4 hours
Sample removal interval (*ex-situ* analysis)	24 hours	0.5, 1, 2, 4 hours (tests repeated in-house)

Each test was conducted at a fixed temperature of 80$\pm$1ºC and flow velocity of 0.1 m/s. The only parameter changed between each test was the solution pH which was varied for each experiment and controlled through the addition of sodium bicarbonate ($NaHCO_3$). Three pH values of 6.3, 6.8 and 7.0 were assessed within this study in an effort to create three distinctly different corrosion films on the steel surface which would all theoretically offer varying levels of protection to the substrate.

7.2.1 Data acquisition: XRD and Electrochemistry

7.2.1.1 Collection and Interpretation of XRD Data

The *in-situ* SR-XRD experiments were conducted at beamline I15 at the Diamond Light Source, UK. Synchrotron radiation was adjusted and focused into a monochromatic beam (70 µm in diameter) with well-defined energy of 40 keV and a corresponding wavelength (λ) of 0.3099 Å. The incident-beam to sample angle was set to 4º. In order to maximise the accuracy and the ability of the XRD patterns to be correlated with the extent of crystal growth, a loop was devised to scan five measurements across a 2 mm path length across the centre of the sample for each experiment. Individual data scans at each location took 60 seconds to acquire an XRD pattern (including the time taken for movement to each point) and the time taken for the detector shutters to open and close was 2 minutes, therefore the overall scanning time to complete the 5 scans over a 2 mm path length was 7 minutes. The diffraction results in this chapter show the accumulated average of the five scanned locations to provide information which represented the crystal growth characteristics of the overall surface.

7.2.1.2 Collection and Interpretation of Electrochemical Data

LPR measurements were performed by polarising the sample ±15 mV vs. the open circuit potential (OCP) at a scan rate of 0.25 mV/s to obtain a polarisation resistance, R_p and were undertaken every 5 minutes. In all of the experiments, the solution resistance (R_s) was measured independently in laboratory tests away from the synchrotron beam using EIS. For these specific measurements, the sample was polarised ±5 mV vs. OCP using the frequency range from 20 kHz to 0.1 Hz. The value of R_s was subtracted from R_p to produce a charge-transfer resistance (R_{ct}) which was used to determine the corrosion rate behaviour with time. Potentiodynamic measurements were also performed within the flow cell on freshly ground samples in separate experiments at each solution pH. This technique was used to generate Tafel polarisation curves to determine the anodic and cathodic Tafel constants and ultimately an appropriate Stern-Geary coefficient (B) to enable calculation of corrosion rates from the values of R_{ct} determined as a function of time in each experiment. From the polarisation curves produced, it was possible to determine the anodic (β_a) and cathodic (β_c) Tafel constants in mV/decade by measuring their respective gradient over regions were linearity was observed between the applied voltage and the natural log of the measured current.

7.2.1.3 *Ex-situ* Surface Analysis

To supplement the synchrotron experiments, laboratory tests were performed away from the beamline to enable *ex-situ* data to be collected in the form of SEM images to assist in tracking crystal growth and correlating with the recorded XRD patterns and electrochemistry data. These experiments varied in duration from 30 mins to 4 hours.

7.3. Solution Equilibrium Chemistry at Varying pH Values

As mentioned previously, the precipitation of $FeCO_3$ onto the internal walls of pipelines becomes thermodynamically possible via the following equation when the concentration of Fe^{2+} and CO_3^{2-} exceed the solubility product (K_{sp}) of $FeCO_3$ in a solution:

$$\mathrm{Fe}^{2+}_{(\mathrm{aq})} + \mathrm{CO}^{2-}_{3\,(\mathrm{aq})} \rightarrow \mathrm{FeCO}_{3(\mathrm{s})} \tag{7.1}$$

$FeCO_3$ nucleation and growth is governed by the supersaturation, which is deemed to be the driving force behind the precipitation process. The supersaturation is defined as:

$$S_{FeCO_3} = \frac{[Fe^{2+}][CO_3^{2-}]}{K_{sp}} \tag{7.2}$$

where $[\mathrm{Fe}^{2+}]$ and $[\mathrm{CO}_3^{2-}]$ (in mol/m^3) are the concentrations of ferrous and carbonate ions, respectively. K_{sp} (mol^2/m^6) is the solubility product for $FeCO_3$, which is a function of ionic strength and temperature. At higher solution pH, higher concentrations of HCO_3^- and CO_3^{2-} result in fewer Fe^{2+} ions being required to exceed the solubility product of $FeCO_3$, and generate significant levels of precipitation [41].

The pH has a significant effect on the rate of corrosion rate reduction as a result of $FeCO_3$ formation. At higher pH, the solubility of $FeCO_3$ is reduced, meaning less Fe^{2+} ions are required to exceed the solubility limit and generate substantial levels of precipitation onto the steel surface, resulting in corrosion rates declining earlier and faster as pH increases. Through consideration of the equilibrium and dissociation reactions and their corresponding equilibrium constants (Equations (7.3) to (7.12) in Table 7.2) it is possible to determine

the bicarbonate concentration (and concentration of other ions in the system) as a function of pH at 80°C, pCO_2= 0.54 bar in a 3.5 w.t % NaCl solution.

Table 7.2. Homogenous H_2O-CO_2 equilibrium chemical reactions and their equilibrium constants.

Reaction		Equilibrium Constant	Equation
Dissolution of carbon dioxide	$CO_2 \overset{K_{sol}}{\Longleftrightarrow} CO_2$	$K_{sol} = c_{CO_2}/pCO_2$	(7.3),(7.4)
Water dissociation	$H_2O \overset{K_{wa}}{\Longleftrightarrow} H^+ + OH^-$	$K_{wa} = c_{H^+}c_{OH^-}$	(7.5),(7.6)
Carbon dioxide hydration	$CO_2 + H_2O \overset{K_{hy}}{\Longleftrightarrow} H_2CO_3$	$K_{hy} = c_{H_2CO_3}/c_{CO_2}$	(7.7),(7.8)
Carbonic acid dissociation	$H_2CO_3 \overset{K_{ca}}{\Longleftrightarrow} H^+ + {HCO_3}^-$	$K_{ca} = c_{H^+}c_{HCO_3^-}/c_{H_2CO_3}$	(7.9),(7.10)
Bicarbonate anion dissociation	${HCO_3}^- \overset{K_{bi}}{\Longleftrightarrow} H^+ + {CO_3}^{2-}$	$K_{bi} = c_{H^+}c_{CO_3^{2-}}/c_{HCO_3^-}$	(7.11),(7.12)

The exact equilibrium constant values included in the model are listed elsewhere (K_{sol} [15], K_{wa} [16], K_{hy} [17], K_{ca} [15], K_{bi} [15]), but the concentration of species over the pH range of 6.3 to 7 are provided in Figure 7.1.

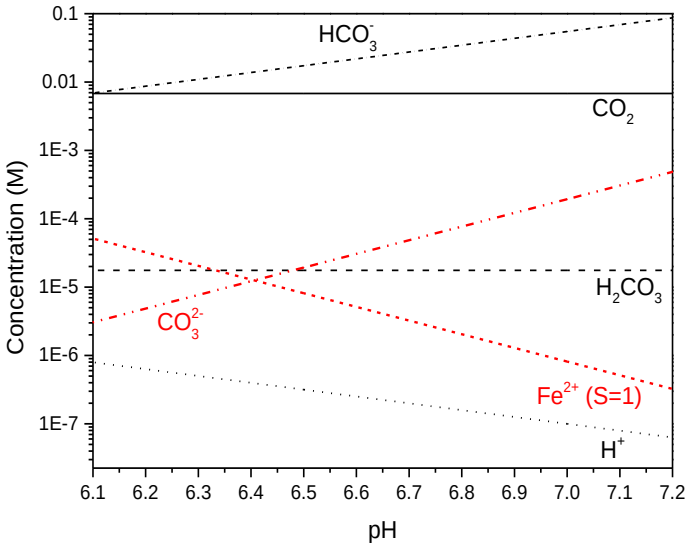

Figure 7.1. Equilibrium distribution of species concentration in bulk solution as a function of pH at 80°C, pCO_2 = 0.54 bar, 3.5 w.t % NaCl and 0.1 m/s.

The solubility limit for $FeCO_3$ is determined based on the knowledge of solution temperature and ionic strength using the empirical expression proposed by Sun *et al.* [81] discussed previously.

$$\log K_{sp} = -59.3498 - 0.041377T_k - \frac{2.1963}{T_K} + 24.5724\log_{10}(T_K) + 2.518I^{0.5} - 0.657I \quad (7.13)$$

Where T_K is the temperature in degrees Kelvin (K), and I is the solution ionic strength. For a system of CO_2 saturated distilled water at 80°C and 3.5 wt.% NaCl, the K_{sp} ($FeCO_3$) can be calculated to be 1.57×10^{-10}, where I is 5.99×10^{-1} moles. Through the use of the solubility product, from Sun *et al.* [81] (Equation 7.13) and the definition of saturation ratio in Equation 7.2, the Fe^{2+} concentration required for saturation of the $FeCO_3$ in the bulk solution can be determined, and this has also been included in Figure 7.1. Based on Figure 7.1 the amount of Fe^{2+} required to reach saturation is reduced as the pH increases due to the increase in CO_3^{2-}. The concentration of the species from the chemical reactions that were considered in the model are presented in Table 7.3 and the concentrations of Fe^{2+} and CO_3^{2-} are highlighted.

Table 7.3. Concentration of the species from the chemical reactions at pH 6.3, 6.8 and 7

pH	CO_2	H_2CO_3	HCO_3^-	H^+	CO_3^{2-}	Fe^{2+}
6.3	6.80×10^{-3}	1.76×10^{-5}	1.09×10^{-2}	5.01×10^{-7}	7.70×10^{-6}	2.04×10^{-5}
6.8	6.80×10^{-3}	1.76×10^{-5}	3.46×10^{-2}	1.58×10^{-7}	7.70×10^{-5}	2.04×10^{-6}
7	6.80×10^{-3}	1.76×10^{-5}	5.48×10^{-2}	1.00×10^{-7}	1.93×10^{-4}	8.13×10^{-7}

Increasing solution pH therefore results in greater nucleation of crystals which are smaller and more densely packed. The interpretation of these observations is supported through *in-situ* SR-XRD and *ex-situ* FIB-SEM analysis later in the results.

7.4. In-house Laboratory Tests: Effect of pH on Electrochemical Observations and Film Morphology

In-house laboratory experiments were performed over 20 hours to understand the long-term behaviour and corrosion rate transient response of carbon steel as a result of changing bulk solution pH within the flow cell. These experiments formed the basis for comparison with shorter duration tests conducted over 4 hours under the exact same conditions using an identical setup at the synchrotron facility. Figure 7.2 shows the Tafel plots obtained by performing separate anodic and cathodic polarisation sweeps around the OCP of X65 steel after 20 hours of immersion in the test solution. The Tafel constants (βa = anodic Tafel constant; βc = cathodic Tafel constant), obtained as a function of pH, were measured based on the anodic and cathodic curves in Figure 7.2 and resulted in an S-G of approximately 17 mV/decade with βa = 60 and βc = 120 mV/decade. Figure 7.3 shows the EIS Nyquist plots depicting the solution resistance (R_s) and the charge transfer resistance (R_{ct}) at the start of each test on the bare steel surface. The iR drop (potential drop due to solution resistance) measurement was conducted using the AC impedance technique and for all conditions, the solution resistance was measured to be around 5 Ω.

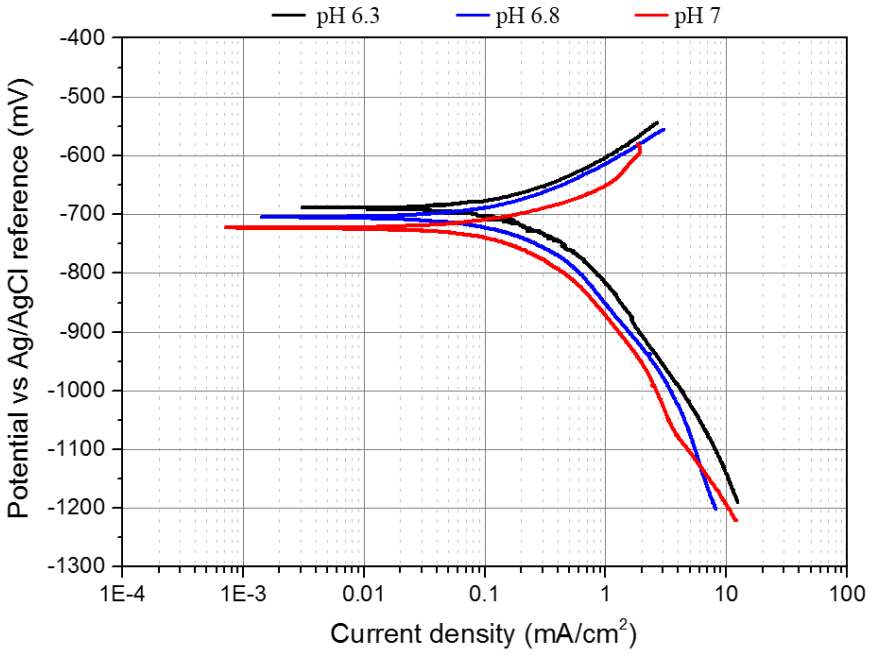

Figure 7.2. Tafel plots for X65 carbon steel conducted at 80°C, 3.5 wt.% NaCl and 0.54 bar p_{CO_2} and 0.1 m/s at different pH values of pH 6.3, 6.8 and 7 in a freely corroding system.

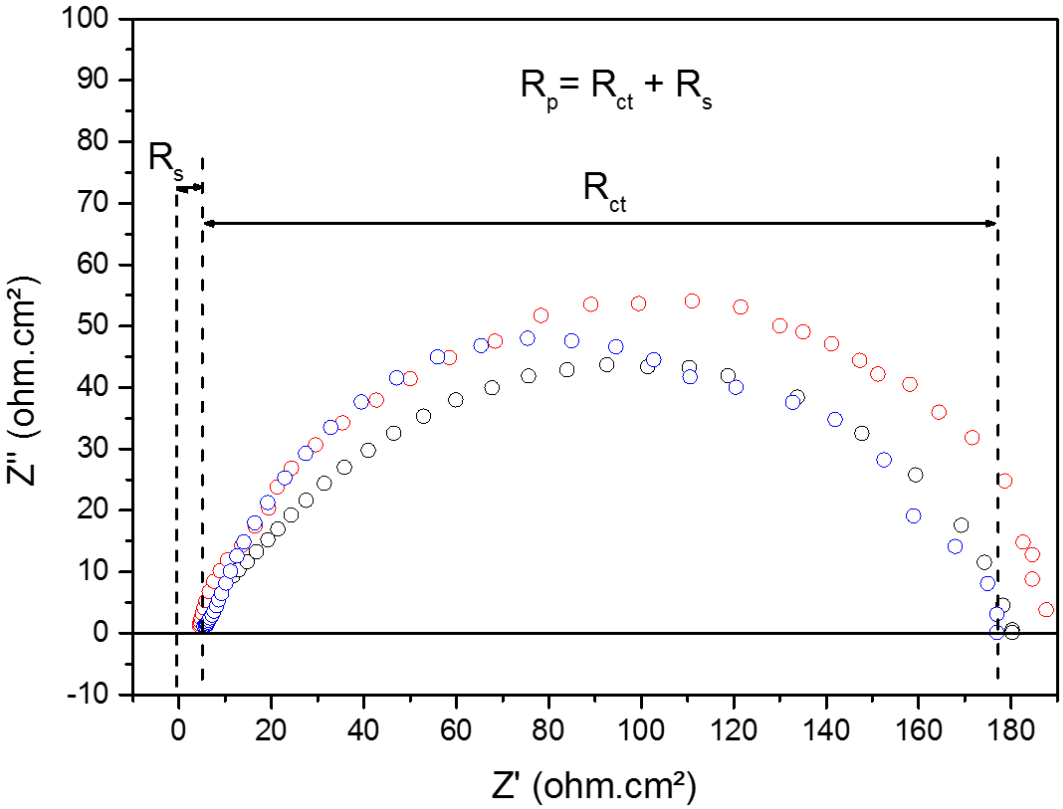

Figure 7.3. EIS Nyquist plots showing the solution resistance (R_s) and the charge transfer resistance (R_{ct}) for X65 carbon steel conducted at 80°C, 3.5 wt.% NaCl and 0.54 bar p_{CO_2} and 0.1 m/s at different pH values of pH 6.3, 6.8 and 7 in a freely corroding system.

The Tafel plots and EIS plots in Figures 7.2 and 7.3 respectively indicates that initial corrosion rate at each pH is very similar. The effect of pH on the corrosion behaviour of carbon over the 20 hour laboratory tests (away from the beamline) are shown in Figures 7.4. In acidic conditions, as the pH increases, the corrosivity of the solution generally decreases in CO_2 conditions due to the reduction in H^+ ions available for the cathodic hydrogen evolution reaction. This difference can be observed in the initial stages prior to film growth, but due to the high pH of the three systems, there is only small sensitivity in initial corrosion rate to the change in pH under these conditions. Keeping the temperature and CO_2 pressure constant, while increasing the pH generally resulted in more protective film formation and a decrease in the rate of corrosion. The formation of a protective surface film at pH values of 6.8 and 7 lowered the corrosion rates to ~0.2 mm/year after 20 hours, whereas at the lower pH of 6.3, the final corrosion rate reached 1 mm/year but was still continuing to reduce. In addition to the electrochemical observations, SEM

micrographs provided in Figures 7.5 (a), (b) and (c) indicate the difference in crystal morphology for the three tests; namely the size of the crystals and how densely packed they are.

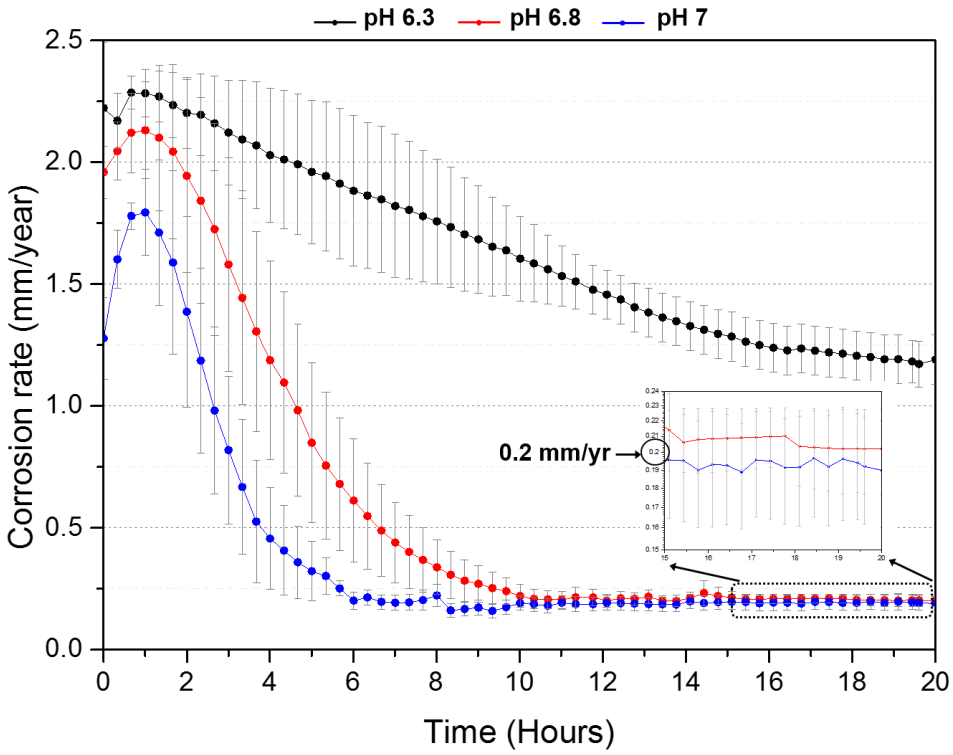

Figure 7.4. *In-situ* corrosion rate data over 20 hours conducted at 80°C, 3.5 wt.% NaCl and 0.54 bar p_{CO_2} and 0.1 m/s at different pH values of pH 6.3, 6.8 and 7 in a freely corroding system.

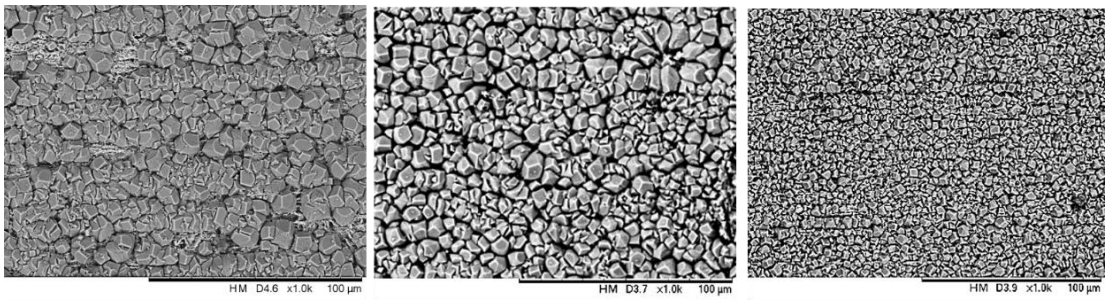

Figure 7.5. *Ex-situ* SEM data after 20 hours conducted at 80°C, 3.5 wt.% NaCl and 0.54 bar p_{CO_2} and 0.1 m/s in a freely corroding system: (a) pH 6.3; (b) pH 6.8; (c) pH 7.

The most obvious change in the morphology of the individual $FeCO_3$ crystals at increasing pH is the size of the crystals. The higher the pH, the smaller and more compact the crystals appear to be. This is simply due to the rate of nucleation and growth in the early stages of formation. Higher pH results in a faster nucleation and growth across the entire surface and the growth of more crystals in close proximity blocks the growth rate due the collision of the crystals with one and other. At the lower pH, the rate of formation is slower which allows the crystals to grow into larger crystals. This phenomenon will be explored further later in this chapter.

7.5 Kinetics of $FeCO_3$ Film Formation: *In-situ* SR-XRD and *ex-situ* SEM Analysis

In-situ SR-XRD patterns between the values 2θ=0-12° were collected continuously over the first 240 minutes for the three tests described previously. The experiments were then repeated away from the beamline for further extensive *ex-situ* SEM analysis of the films formed over a range of time intervals between 0 and 240 minutes. The results are reviewed over the ranges of pH in the following sections.

7.5.1 Composition and Orientation of the Corrosion Products Formed at varying pH Values

7.5.1.1 Observations at pH 6.3

The *in-situ* SR-XRD patterns over time at pH 6.3 reveal that the only crystalline phase detected on the steel surface during the experiment was $FeCO_3$. In fact, no other phases were detected at any point during the experiment, with the exception of iron carbide (Fe_3C) and iron (Fe), which already existed as part of the steel microstructure. The diffraction patterns at pH 6.3 showed that 4 lattice planes of $FeCO_3$ ((104), (110), (018), (116)) were detected, see Figure 7.6. Among the formed $FeCO_3$ crystal planes, the most intense reflection was observed at 2θ=~6.35º corresponding to the (104) plane which is evident from Figure 7.6 and 7.7.

Figure 7.7 shows the growth of the $FeCO_3$ crystal planes over time at each of the locations scanned across the surface during the test.

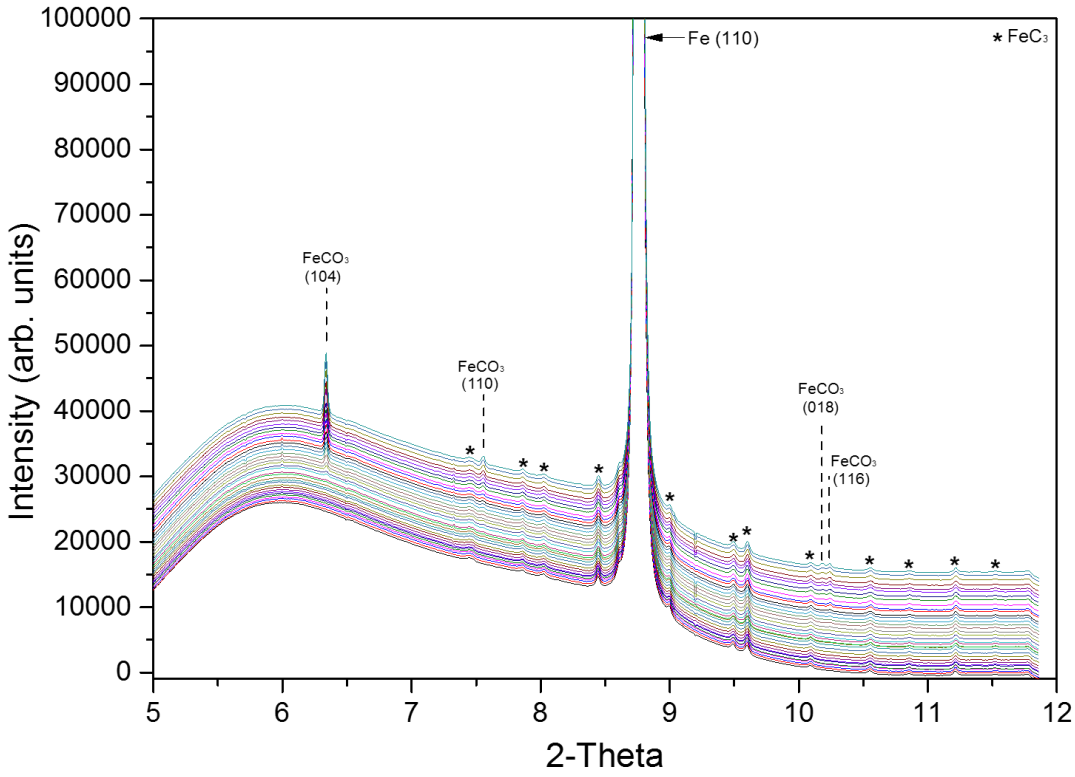

Figure 7.6. *In-situ* diffraction patterns recorded as a function of time conducted at 80°C, 3.5 wt.% NaCl, 0.54 bar p_{CO_2} and 0.1 m/s at pH 6.3 in a freely corroding system.

It is evident that the (104) crystal plane was the most dominant during the nucleation and crystal growth stage with the exception of Location 4. The $FeCO_3$ crystal plane (116) was the most dominant plane at this location which inhibited the growth of the (104) crystal plane in this instance, and any other plane in fact. This shows that at a low pH, in the very early stages of crystal growth that $FeCO_3$ crystals are extremely unstable and assorted across the surface. Further support of this observation is the substantial difference in $FeCO_3$ induction time at each location scanned.

Figure 7.8 shows the growth of the most dominant $FeCO_3$ crystal plane (104) across the surface. The Figure shows that the induction time varies considerably across the surface. The term 'induction time' is referred to as the time taken until the onset of the crystal nucleation and growth (i.e. when the nuclei has become measurable through X-ray interception). The induction time for the (104) plane was measured to be ~110 minutes at location 1 and 3, shortly followed by location 5 after ~125 minutes. Then towards the end of the experiment $FeCO_3$ was detected at locations 2 (~205 minutes) and 4 (225 minutes).

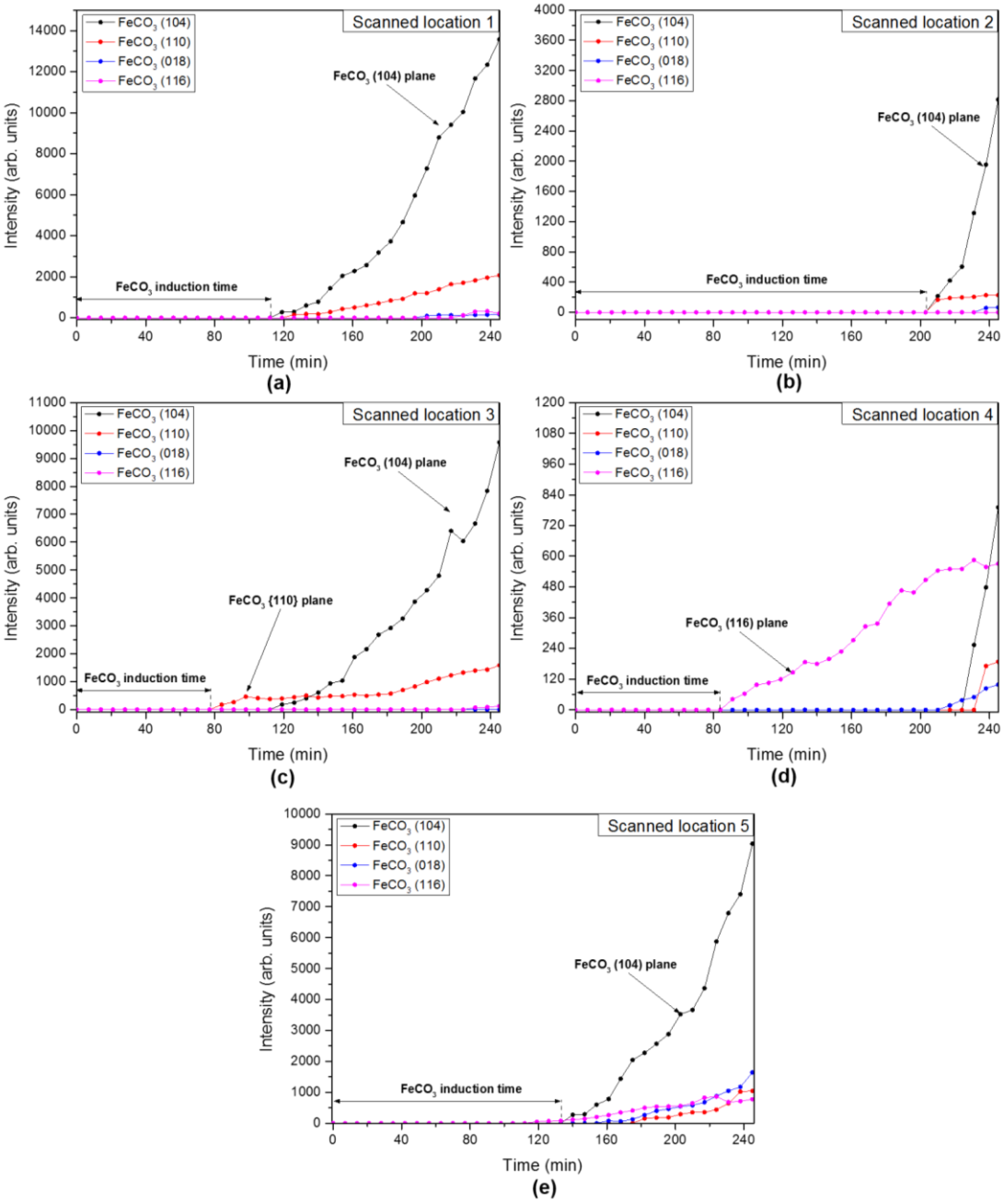

Figure 7.7. Growth of the $FeCO_3$ crystal planes intensities over time at each of the locations scanned across the surface conducted conducted at 80°C, 3.5 wt.% NaCl, 0.54 bar p_{CO_2} and 0.1 m/s at pH 6.3 in a freely corroding system.

Although the $FeCO_3$ crystal plane (116) was most dominant at location 4, this plane remained virtually undetected at locations 2 and 3, was very minor at location 1 with slight increase in intensity at location 5 (although still minor in comparison to the (104) plane). This shows that the lower solubility in $FeCO_3$ due to the decreased amounts of carbonate ions in the system (see Figure

7.1 and Table 7.3 in section 7.3) affects the stability of the $FeCO_3$ nuclei to overcome the energy barrier for nucleation and crystal growth. This in turn affects the orientation of crystal growth (the most thermodynamically favourable plane), the induction time and also the protectiveness offered from the crystals present on the steel surface.

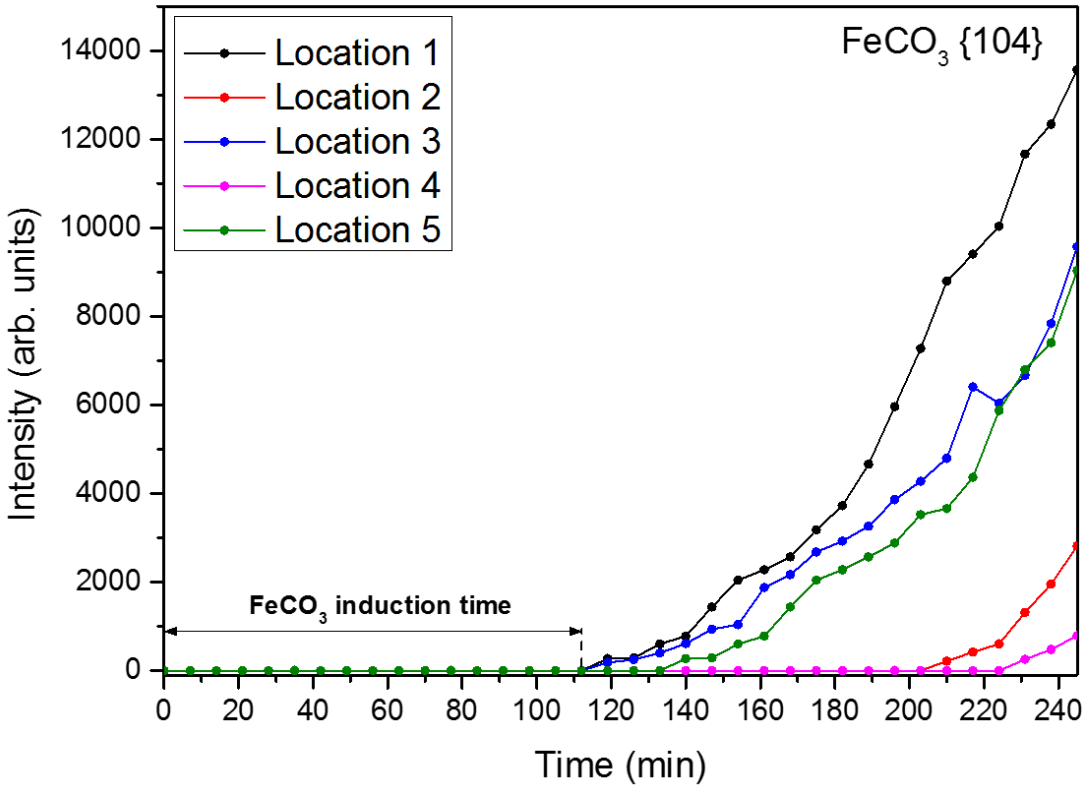

Figure 7.8. Growth of the most dominant $FeCO_3$ crystal plane (104) across the surface conducted at 80°C, 3.5 wt.% NaCl, 0.54 bar p_{CO_2} and 0.1 m/s at pH 6.3 in a freely corroding system.

7.5.1.2 Observations at pH 6.8

The *in-situ* SR-XRD patterns over time at pH 6.8 reveal that the only crystalline phase detected on the steel surface during all three experiments was $FeCO_3$, similarly, with respect of Fe_3C and Fe, which already existed as part of the steel microstructure. The diffraction patterns at pH 6.8 showed that 8 lattice planes of $FeCO_3$ ((104), (110), (113), (202), (024), (018), (116), (122)) were detected, see Figure 7.9.

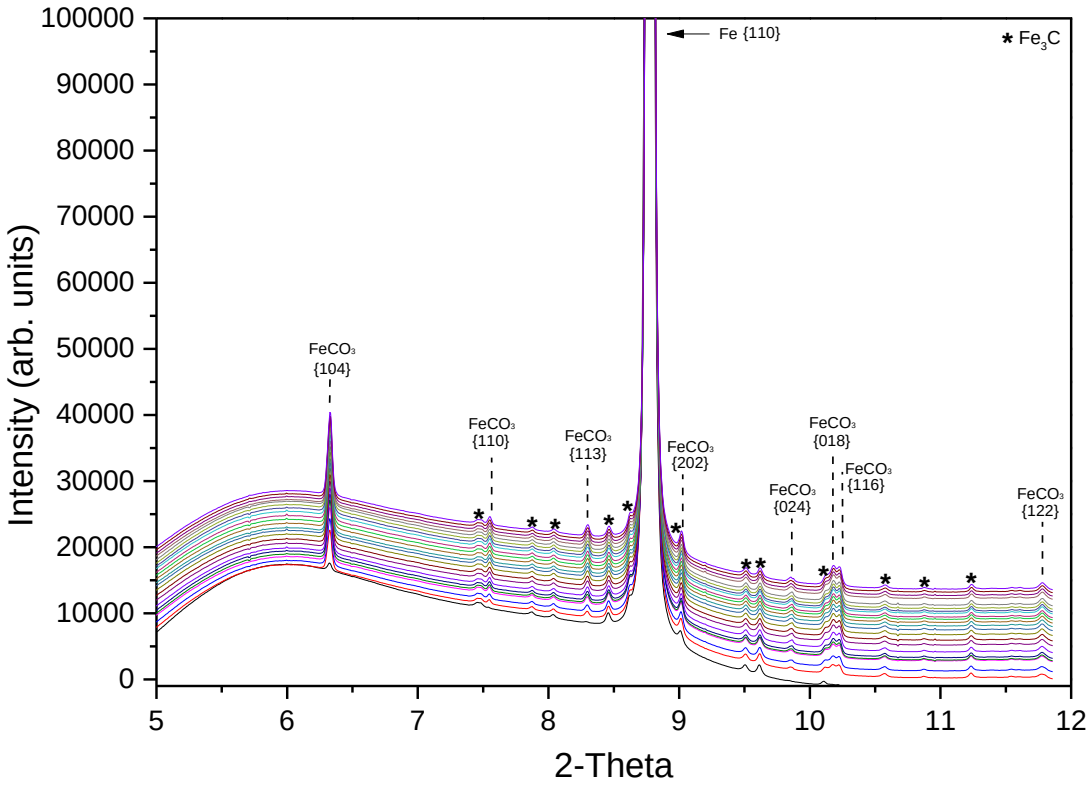

Figure 7.9. *In-situ* diffraction patterns recorded as a function of time conducted at 80°C, 3.5 wt.% NaCl, 0.54 bar p_{CO_2} and 0.1 m/s at pH 6.8 in a freely corroding system.

Similarly at pH 6.8, the most intense peak was observed at 2θ=~6.35º corresponding to the (104) plane which is evident from Figure 7.9 and 7.10. Figure 7.10 shows the growth of the $FeCO_3$ crystal planes over time at each of the locations scanned across the surface during the test.

Similar to at pH 6.3, the $FeCO_3$ crystal plane (104) was the most dominant plane at all locations in great fashion which inhibited the any substantial growth of the remaining 7 crystal planes detected with the exception of the (018) and (116) $FeCO_3$ planes. The growth of both of these planes are identical to one and other and are detected after ~40 minutes. The growth rate of crystals present appear to be extremely stable and uniform across the majority of the surface. However, at location 4, the growth rate of the (140) plane is slower and seems to have dampened which has encouraged the growth of other planes ((110) and (113) planes). Although the major $FeCO_3$ (104) crystal plane at each of the five locations scanned shows a similar (but not identical) growth trend with marginally different characteristics such as

emergence time, growth rate and final intensity indicates heterogeneous growth across the surface of the sample.

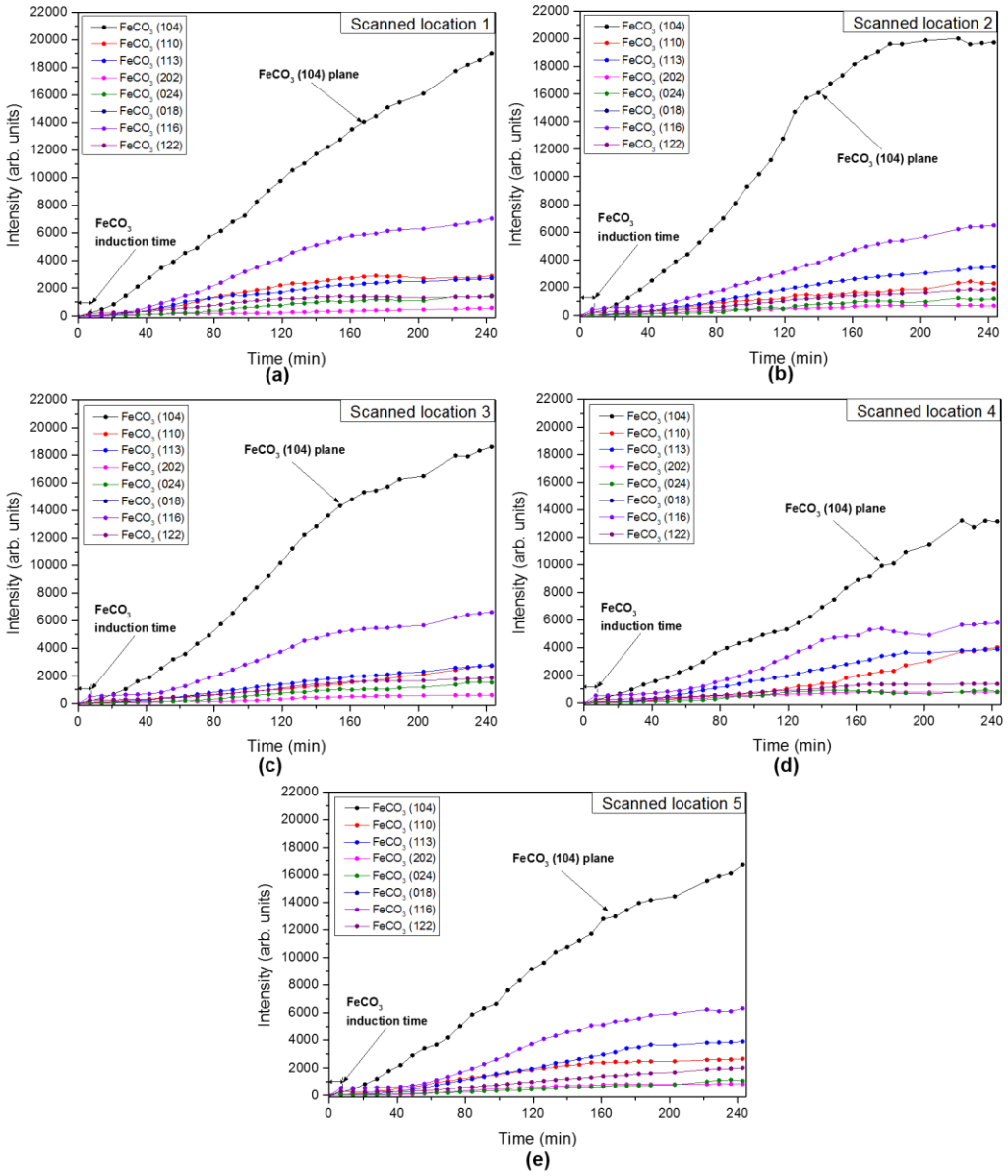

Figure 7.10. Growth of the $FeCO_3$ crystal planes intensities over time at each of the locations scanned across the surface conducted at 80°C, 3.5 wt.% NaCl, 0.54 bar p_{CO_2} and 0.1 m/s at pH 6.8 in a freely corroding system.

Figure 7.11 shows the growth of the most dominant $FeCO_3$ crystal plane (104) across the surface. The Figure shows that the induction time for $FeCO_3$ is instantaneous upon applying the X-rays to the surface with crystalline $FeCO_3$

being detected during the first scan of the surface. The induction time for the (104) plane was measured to be essentially ~1 minute at location 1 upon running the X-ray beam. Each location scanned within the first loop of scans across the 5 locations of the surface detected $FeCO_3$ and therefore the induction time will be considered as 7 minutes here (the time taken to complete each location, including the detector open/close time).

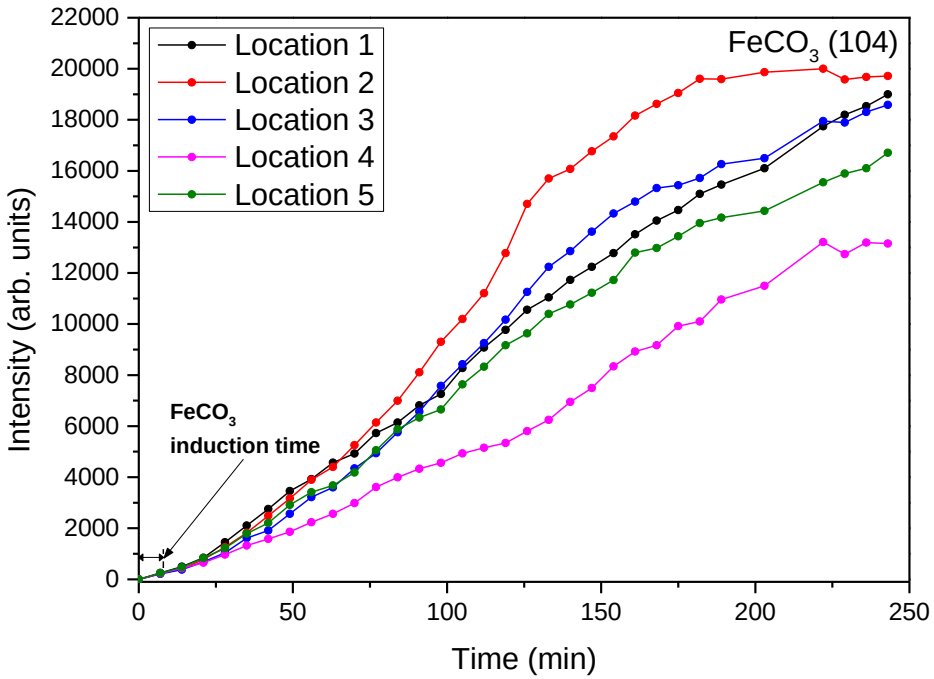

Figure 7.11. Growth of the most dominant $FeCO_3$ crystal plane (104) across the surface conducted at 80°C, 3.5 wt.% NaCl, 0.54 bar p_{CO_2} and 0.1 m/s at pH 6.8 in a freely corroding system.

7.5.1.3 Observations at pH 7

The *in-situ* SR-XRD patterns over time at pH 7 reveal that the only crystalline phase detected on the steel surface during all three experiments was $FeCO_3$, again Fe_3C was present prior to running the brine through the flow cell. Likewise, the diffraction patterns at pH 7 showed that 8 lattice planes of $FeCO_3$ ((104), (110), (113), (202), (024), (018), (116), (122)) were detected, see Figure 7.12.

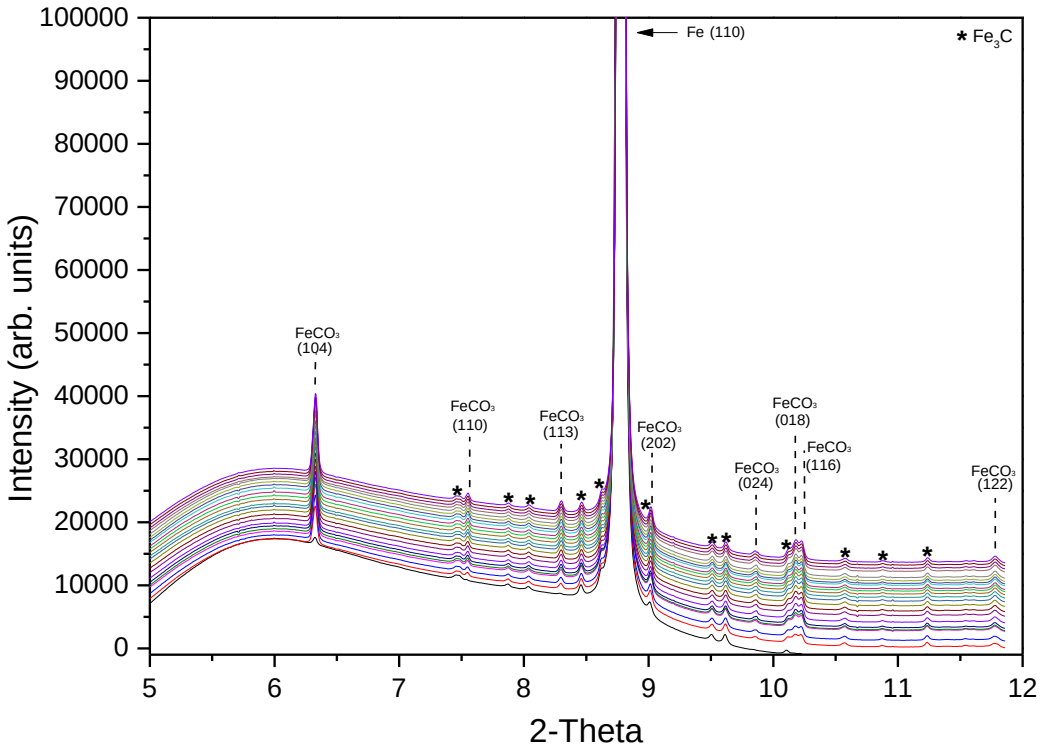

Figure 7.12. *In-situ* diffraction patterns recorded as a function of time conducted at 80°C, 3.5 wt.% NaCl, 0.54 bar p_{CO_2} and 0.1 m/s at pH 7 in a freely corroding system.

Similarly two the previous two tests the most prominent $FeCO_3$ plane was the (104) plane. Figure 7.13 shows the growth of the $FeCO_3$ crystal planes over time at each of the locations scanned across the surface during the test. Yet again, it is evident that the crystal plane (104) was the most dominant during the nucleation and crystal growth of $FeCO_3$.

The $FeCO_3$ crystal plane (104) was the most dominant plane across the surface which repressed any substantial growth of the remaining 7 crystal planes detected. The major $FeCO_3$ (104) crystal plane at each location shows an even more encouraging growth trend with very similar characteristics, once again indicating heterogeneous growth across the surface of the sample at a higher system pH. The growth rate of the crystals are extremely stable and uniform across the majority of the surface.

Figure 7.14 shows the growth of the most dominant $FeCO_3$ crystal plane (104) across the surface. The Figure shows that the induction time for $FeCO_3$ is yet again instantaneous upon applying the X-rays to the surface with all of the

$FeCO_3$ planes being detected during the initial loop of scanning across the surface.

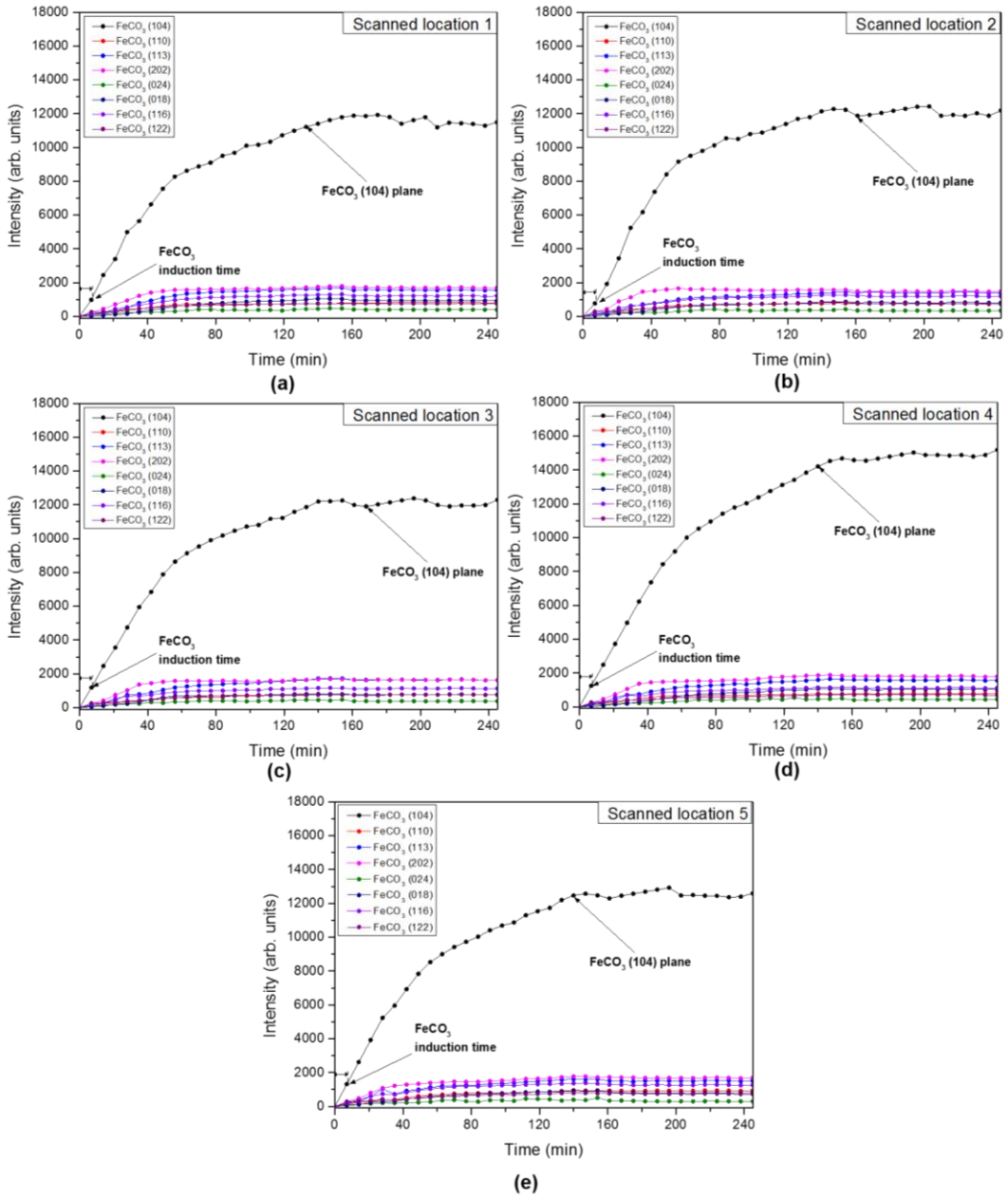

Figure 7.13. Growth of the $FeCO_3$ crystal planes intensities over time at each of the locations scanned across the surface conducted at 80°C, 3.5 wt.% NaCl, 0.54 bar p_{CO_2} and 0.1 m/s at pH 7 in a freely corroding system.

The induction time for the each of the $FeCO_3$ planes detected was ~1 minute at all locations. The intensity and hence the growth rate of the $FeCO_3$ (104)

plane then increased exponentially across the surface for the first 60 minutes until slowing down and reaching a plateau after ~140 minutes. After an early increase in intensity for the remaining 7 planes, the rapid growth and domination of the (104) plane seems to have hindered further growth of these planes with a plateau in the measured intensity being reached after ~40 minutes.

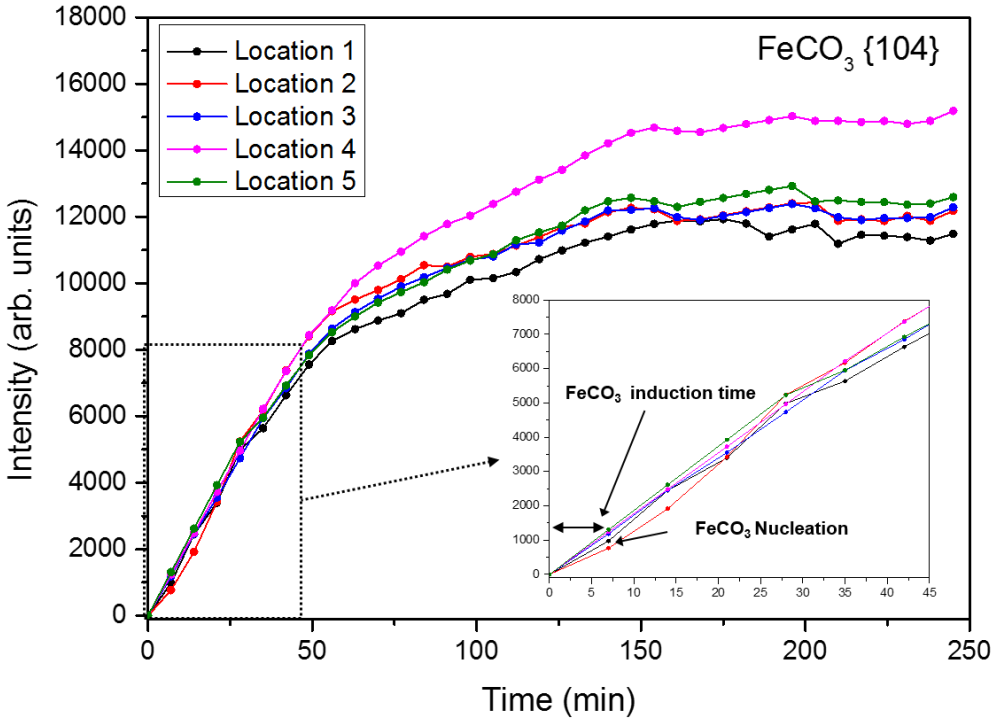

Figure 7.14. Growth of the most dominant $FeCO_3$ crystal plane (104) across the surface conducted at 80°C, 3.5 wt.% NaCl, 0.54 bar p_{CO_2} and 0.1 m/s at pH 7 in a freely corroding system.

7.6 Kinetics of $FeCO_3$ Film Formation: Comparison and Summary of the Tests at Different pH Values

Figure 7.15 shows XRD patterns representing the signal intensity against 2θ collected from the carbon steel surface at the end of each 240 minute experiment for the three pH values (patterns are offset for clarity). Each pattern represents the cumulative sum of five scans across the sample surface across a 2 mm linear region at the centre of each sample. The *in-situ* SR-XRD patterns reveal that the only crystalline phase detected on the steel surface during all three experiments was $FeCO_3$. In fact, no other phases were detected at any point during the experiments, with the exception of iron

carbide (Fe_3C) and iron (Fe), which already existed as part of the steel microstructure. The diffraction patterns at pH 6.3 showed that 5 lattice planes of $FeCO_3$ ((104), (110), (018), (116), (211)) were detected. While at pH 6.8 and 7, 8 lattice planes present were ((104), (110), (113), (202), (024), (018), (116), (211)). Among the formed $FeCO_3$ crystal faces, the most intense peak was observed at 2θ=~6.35º corresponding to the (104) plane.

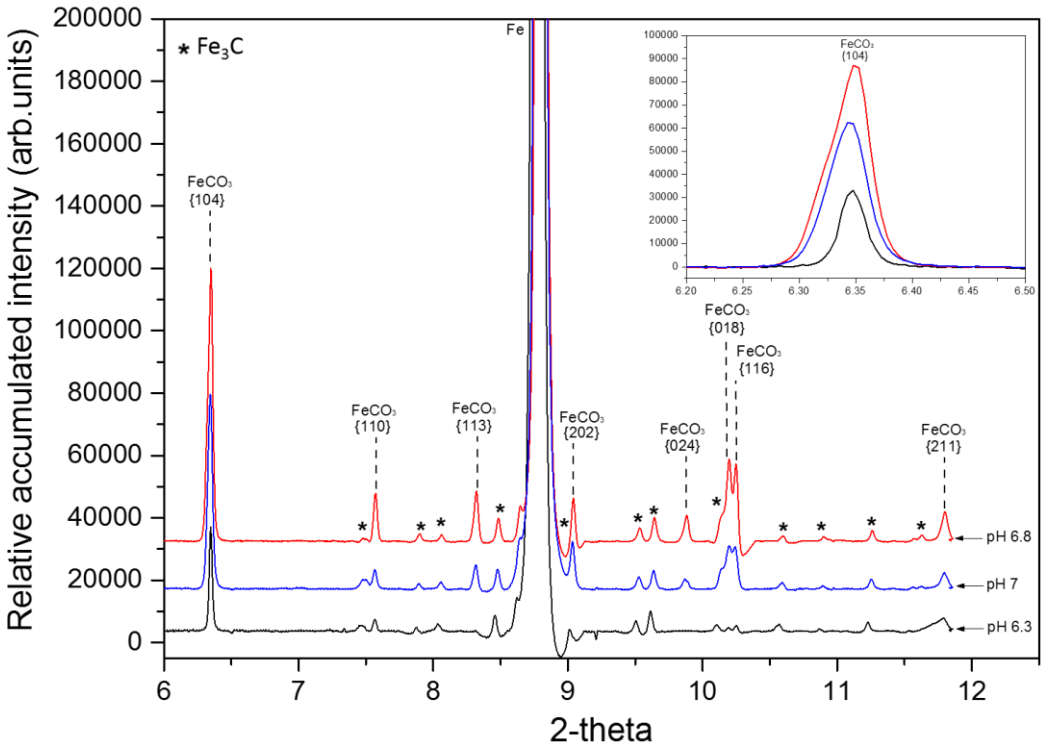

Figure 7.15. Selection of *in-situ* diffraction patterns recorded after 240 minutes conducted at 80°C, 3.5 wt.% NaCl and 0.54 bar p_{CO_2} and 0.1 m/s at different pH values of pH 6.3, 6.8 and 7 in a freely corroding system.

The $FeCO_3$ (104) crystal plane is visibly the most dominant plane across the surface under all conditions and therefore will be used to study the kinetics of crystal growth in comparison to the corrosion rate within the system. Figure 7.16 (a) shows the *in-situ* electrochemical LPR measurements (in the form of corrosion rates). The growth mechanism is depicted more clearly from the average accumulative intensity of all five points over the steel surface and Figure 7.16 (b) shows a direct comparison with the growth of the most intense $FeCO_3$ (104) peak over time in the form of integrated diffraction intensities (peak area) for the different pH values studied. Theoretically, the peak area

for a specific crystal plane in a diffraction pattern is proportional to the crystal volume formed in the areas scanned across the samples and so the intensity as a function of time represents a suitable technique to follow the evolution of $FeCO_3$ formation kinetics in real-time.

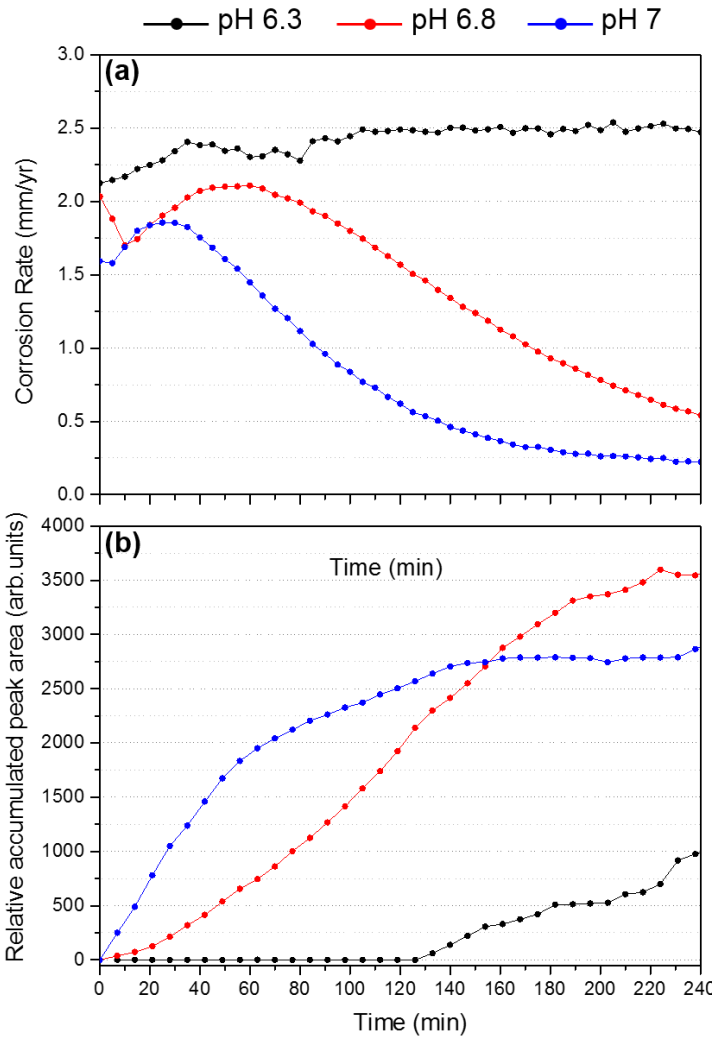

Figure 7.16. *In-situ* data recorded over time for each test conducted at 80°C, 3.5 wt.% NaCl and 0.54 bar p_{CO_2} and 0.1 m/s at different pH values of pH 6.3, 6.8 and 7 in a freely corroding system: (a) Corrosion rates; (b) Integrated diffraction intensities for $FeCO_3$ (104) plane for each of the 5 scans performed over a 2 mm line scan on each sample.

Referring to Figure 7.16 (a), at a starting pH of 6.3, the corrosion rate increases with time before stabilising at ~2.5 mm/year from 120 minutes onwards. In this experiment, the corrosion rate does not change throughout the remainder of the test, although interestingly, $FeCO_3$ precipitation is detected after 130 mins as shown in Figure 7.16 (b), reflecting the fact that the XRD is capable of detecting the very early stages of crystal growth, prior

to it having any substantial effect on general corrosion rate. At pH 6.8, the corrosion rate increases with time before reducing continuously over the test duration, reaching a final corrosion rate of ~0.55 mm/year after 240 minutes.

Similarly, at pH 7, the initial corrosion rate increases yet again but reduces rapidly to values of approximately ~0.22 mm/year after 240 minutes. The higher pH values of 6.8 and 7 results in higher supersaturation, faster precipitation and formation of a more protective $FeCO_3$ film due to the increase in CO_3^{2-}, which is reflected by a rapid decrease in the corrosion rate with time. The faster film formation at pH values of 6.8 and 7 observed with the *in-situ* corrosion data is further reinforced by the *in-situ* SR-GRXRD data, as it is clear from Figure 7.16 (b) that the induction time changes with pH, becoming shorter with increasing pH. The induction time of $FeCO_3$ is significantly longer at pH 6.3 (~110 minutes), but is instantaneous at pH 6.8 and 7 (~7 minutes, under both circumstances). The induction time, and hence the growth kinetics of $FeCO_3$ is faster at the higher pH in comparison with the system at pH 6.3. This shows that at a higher pH, in the very early stages of crystal growth that $FeCO_3$ crystals overcome the energy barrier required to nucleate and grow more easily due to the local critical supersaturation at the surface. Another interesting observation here is that at the end of the test at pH 6.3, the corrosion rate is still stable with no indications of dropping. At this point, the measured relative area is 1000. However, when the area measures 1000 in the tests at pH 6.8 and 7, the amount of $FeCO_3$ crystals on the surface is enough to reduce the production of Fe^{2+}. Theoretically, the same amount (in mass) of $FeCO_3$ on the surface in all tests are the same when the measured intensity measures the same suggesting that despite the amount of $FeCO_3$ present on the carbon steel surface, this is not necessarily a good indication of how protective the crystals are. Clearly, at this stage, the $FeCO_3$ crystals are less permeable and more protective at higher pH. This will be discussed further in Chapter 9.

When comparing the two systems operating at pH 6.8 and 7 (where protective $FeCO_3$ crystals formed on the surface), assuming a direct relationship between crystal mass and peak area extracted from the XRD patterns, the growth kinetics are noticeably different. The initial nucleation and crystal growth rate is faster at pH 7, but the primary difference is that the growth rate decreases until a plateau is approached after ~125 minutes (blue graph in Figure 7.16 (b)) and remains constant until the end of the experiment. Here, the crystal growth rate decreases due to larger proportions of the surface are

being covered with crystals and ultimately reducing the production of Fe^{2+} from the steel surface which has a direct impact on the formation of $FeCO_3$, reducing the precipitation rate. These observations are consistent with the electrochemical data. In comparison, at a pH of 6.8, the induction time for $FeCO_3$ nucleation is also extremely fast, but the crystal growth rate is relatively constant throughout the majority of the experiment, slowing down towards the final hour. Importantly, the integrated peak intensity at the end of the experiment ran at pH 7 is lower than the experiment conducted at pH 6.8 indicating that the film formed at the higher pH is not as substantial, yet offers more protection to the steel substrate.

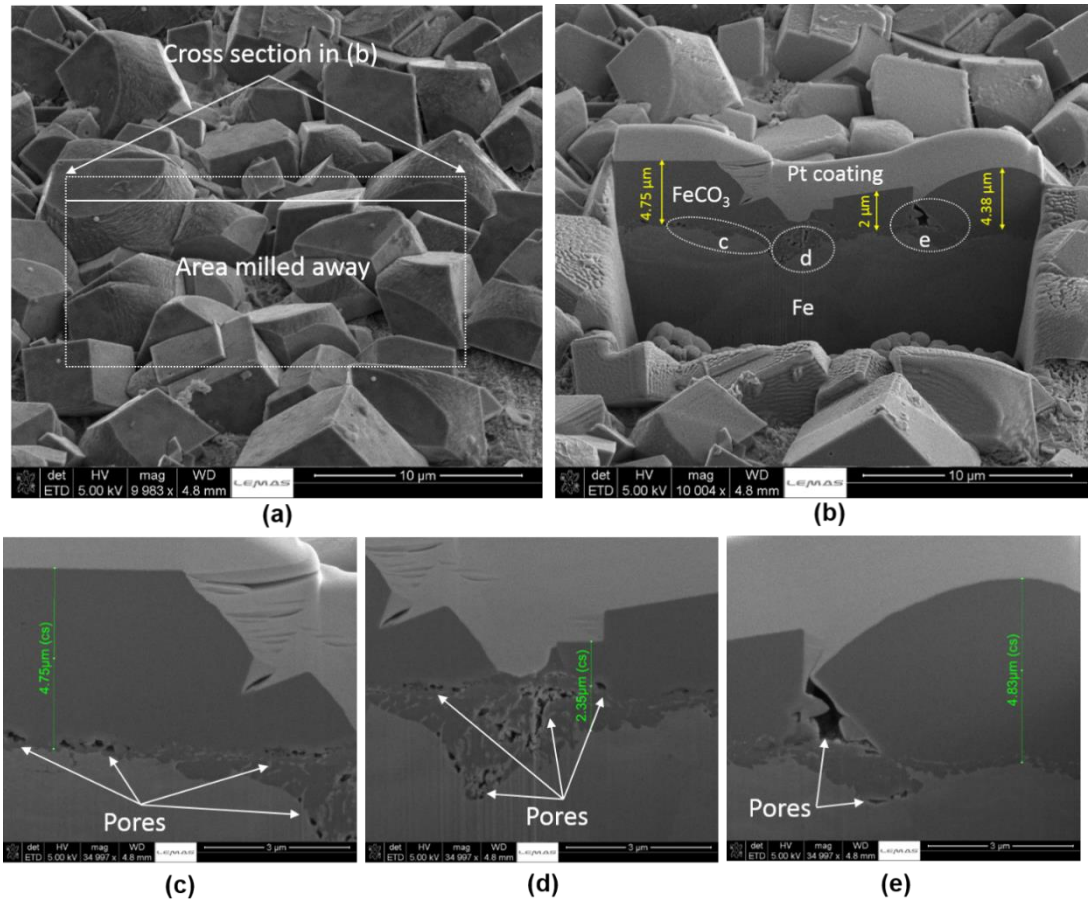

Figure 7.17. *Ex-situ* SEM images of the X65 carbon steel surface at the end of the test showing the cross-sections of the films formed at 80°C, 3.5 wt.% NaCl, 0.54 bar p_{CO_2} and 0.1 m/s at pH 6.8 in a freely corroding system.

SEM images later in this chapter indicate that very high surface coverage of $FeCO_3$ crystals is achieved at both pH 6.8 and 7, and that the key difference for the higher intensity measured at pH 6.8 after 4 hours is the difference in

thickness of the corrosion product film. The difference in film thickness is highlighted in Figures 7.17 (a) and (b) which are SEM images where a focused ion beam (FIB) has been used to mill away part of the protective $FeCO_3$ film to reveal the layer thickness. Figure 7.17 (a) shows the area milled away revealing the cross section of the $FeCO_3$ film formed at pH 6.8 (Figure 7.17 (b)). The film ranges from 2 to 4.75 µm in thickness. Figures 7.17 (c) and (d) exposes the pores at the steel and $FeCO_3$ crystal interface allowing a clear pathway for species to diffuse through the $FeCO_3$ layer which are not noticeable from SEM images of the top view of the morphology of the crystals. Figure 7.18 (a) shows the area milled away revealing the cross section of the $FeCO_3$ film formed at pH 7 (Figure 7.18 (b)).

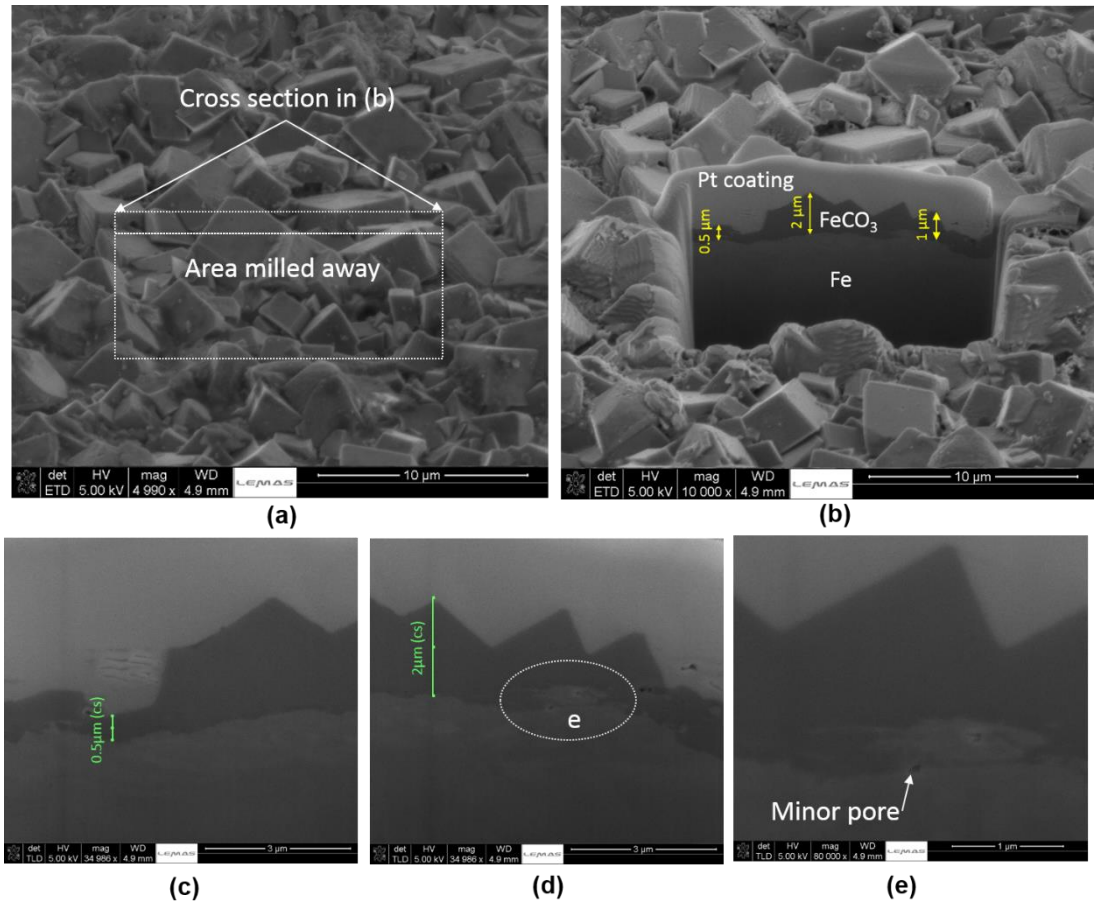

Figure 7.18. *Ex-situ* SEM images of the X65 carbon steel surface at the end of the test showing the cross-sections of the films formed at 80°C, 3.5 wt.% NaCl, 0.54 bar p_{CO_2} and 0.1 m/s at pH 7 in a freely corroding system.

The film ranges from 0.5 to 2 µm in thickness. Unlike the crystals formed at pH 6.8, Figures 7.18(c) and (d) show crystals that are well anchored to the

steel surface interface which will clearly block the diffusion of species to and from the surface. The images show that the film formed at pH 6.8 is considerable thicker and consists of much larger crystals than those at pH 7, agreeing with the measured XRD peak area intensities. This is an important observation which suggests that the application of XRD may be able to provide quantitative data for a specific fixed incident angle if the system were to be calibrated appropriately. As a final point in Figure 7.18, there is a clear difference in the level of compactness of crystal and their interaction with the substrate. Crystals formed at pH 7 (Figure 7.18 (b)) produced a less porous layer which conforms better to the steel substrate compared to crystals precipitated at pH 6.8 (Figure 7.18 (a)) which aids in explaining why corrosion rates were noticeably lower after 4 hours at pH 7.

7.7 Early stages of $FeCO_3$ film formation over time: Development of film through *in-situ* and *ex-situ* observations

In-situ SR-XRD and corrosion rate measurements are compared with *ex-situ* SEM observations showing the visual appearance of the corroding steel surface and $FeCO_3$ crystals in Figures 7.19, 7.20 and 7.21(a-e). The SEM images within the figures are analysed at a magnification of x3000 to project an area of ~70x70 µm to represent the size of the beam and to illustrate the area of the surface being scanned at each location. Additionally, Figures 7.19, 7.20 and 7.21 (e) show the kinetics of the $FeCO_3$ crystal growth in the form of the average of the accumulative intensity from all five locations providing an average over the steel surface and can be compared with the electrochemical response which is also an average corrosion rate over the steel surface.

Figure 7.19 refers to the kinetics of $FeCO_3$ formation for pH 6.3. The SEM images agree with the data obtained *in-situ* as the average intensity increases after ~110 minutes which has already been illustrated. In Figures 7.19 (a) and (b), no crystals are observed until minute crystals of <1 µm are observed in the frame taken after 120 minutes (Figure 7.19 (c)). At this point, it can be assumed that the system has reached the critical supersaturation required for not only $FeCO_3$ nucleation but also further crystal growth because in the following 120 minutes, the $FeCO_3$ intensity rapidly increases and more crystals are captured in Figure 7.19 (d) with a slight increase in overall size to ~1.5 µm covering approximately 23% of the surface. An interesting observation here is that despite the growth of $FeCO_3$ crystals on the surface,

the corrosion rate remains stable at 2.4 mm/year with only a small indication of a potential decrease after 230 minutes.

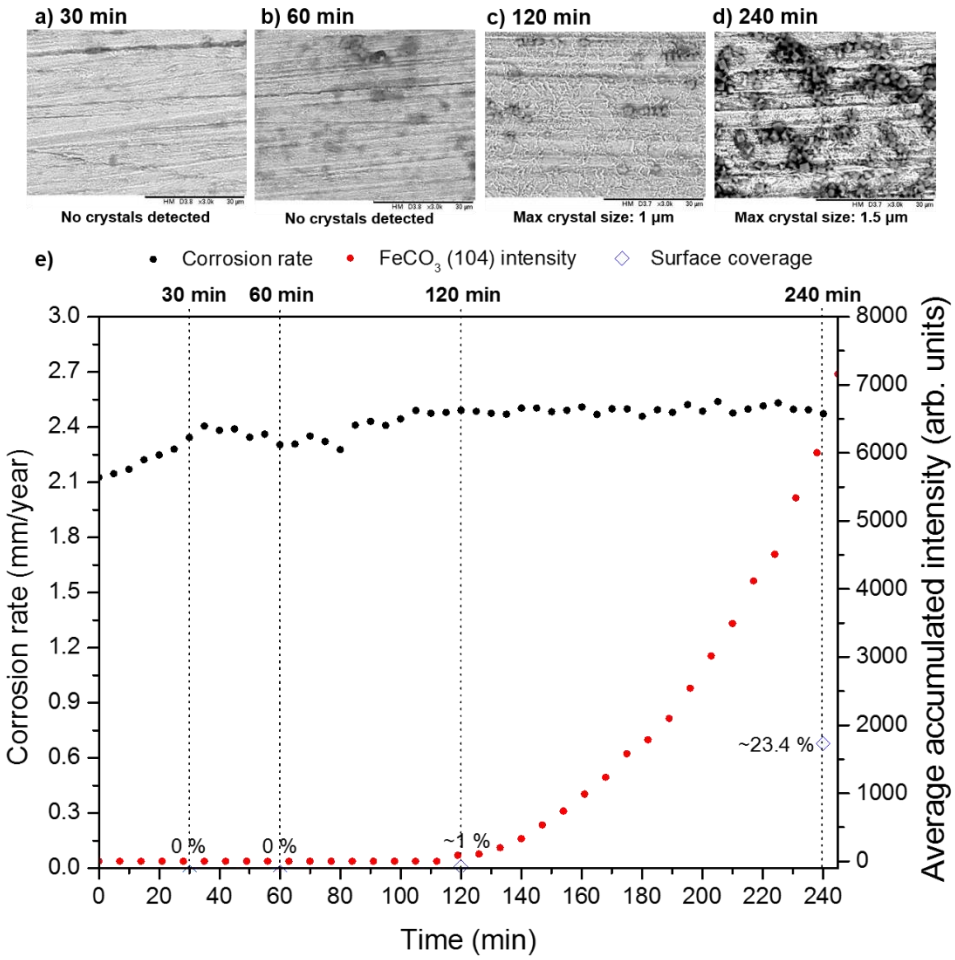

Figure 7.19. Development of the $FeCO_3$ crystals (a)-(d) SEM images over time; (e) *In-situ* corrosion rate and major $FeCO_3$ plane intensity versus time conducted at 80°C, 3.5 wt.% NaCl, 0.54 bar p_{CO_2} and 0.1 m/s at pH 6.3 in a freely corroding system.

Although $FeCO_3$ crystals are present, at this point in time they offer no protection to the steel surface against corrosion. The crystals have already been shown to be random and unstable, which could suggest that the local supersaturation is insufficient to promote further growth at this stage in time and could even lead to the dissolution of less stable crystal planes $FeCO_3$ whilst other crystals are nucleating and growing on the surface.

An increase in system pH from 6.3 to 6.8 results in an increased growth rate of $FeCO_3$ crystals offering protection against corrosion to the steel surface. The *in-situ* SR-XRD and corrosion rate measures and coupled with the *ex-situ*

SEM observations in Figures 7.20. From the average accumulated measured intensity in Figure 7.20, three steps characterise the growth mechanism: (1) An induction time when the measured intensity is zero (from 0 to the 7th minute); (2) Nucleation of the $FeCO_3$ crystals (between the 7th and 14th minute); (3) Nucleation-growth stage which is characterised by an increase of the growth according two different regimes; the growth rate first linearly increases (between the 14th and 175th minute) and then slows down towards the end of the experiment (240th minute). After the induction time (7 minutes), the major $FeCO_3$ peak intensity begins to increase due to the crystals forming on the steel surface through heterogeneous nucleation.

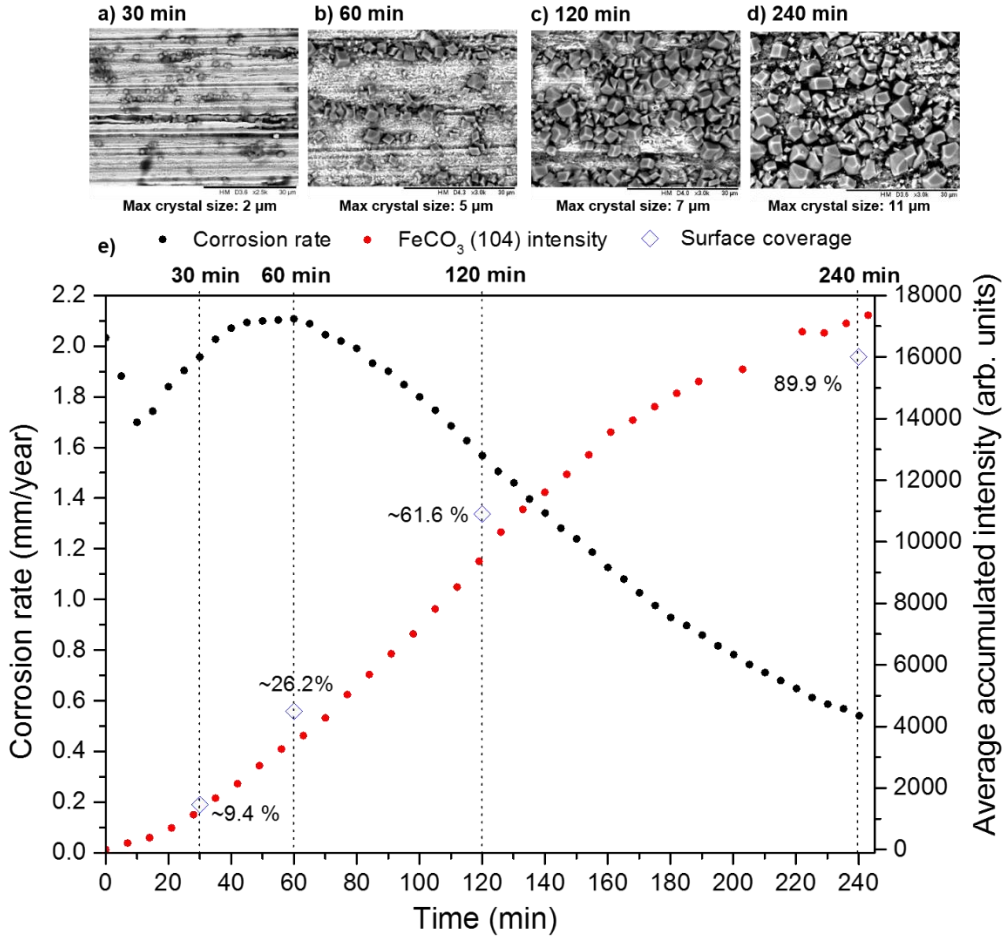

Figure 7.20. Development of the $FeCO_3$ crystals (a)-(d) SEM images over time; (e) *In-situ* corrosion rate and major $FeCO_3$ plane intensity versus time conducted at 80°C, 3.5 wt.% NaCl, 0.54 bar p_{CO_2} and 0.1 m/s at pH 6.8 in a freely corroding system.

After 30 minutes, following nucleation, discrete crystals on the surface begin to grow with crystal sizes varying from <1 µm to 2 µm in width (Figure 7.20(a))

covering ~9.4% of the surface. At this stage the crystals offer little or no protection against corrosion. After 60 minutes, the nucleated crystals have grown with an average size from 1 µm to 5 µm in width (Figure 7.20(b)) whilst new crystals continue to nucleate on to the steel surface. In conjunction with this behaviour, the corrosion rate begins to decrease as a result of the $FeCO_3$ crystals blocking active sites on the steel surface with ~26.2% of the surface covered with $FeCO_3$ crystals. From 60 minutes onwards, the combined *in-situ* observations and *ex-situ* SEM images exemplify that this process of nucleation and growth continues until the $FeCO_3$ film has the ability to reduce the corrosion rate significantly. This sequence of nucleation and growth illustrates that as the $FeCO_3$ layer develops, larger proportions of the surface are being covered with crystals and ultimately reducing the reaction rate of species across the entire surface (i.e. production of Fe^{2+}) which has a direct impact on the formation of $FeCO_3$, reducing the precipitation rate and therefore less $FeCO_3$ is formed. Therefore, as the $FeCO_3$ layer builds up, the precipitation kinetics slow down which is captured by the SR-XRD measurements after 175 minutes. After 240 minutes, further nucleation and growth then contributed to a subsequent build-up of the $FeCO_3$ layer with crystals ranging from 1 µm to 10 µm.

A further increase in system pH to 7 resulted in even more substantial levels of $FeCO_3$ precipitation occurring earlier in the experiment with an increased nucleation and crystal growth rate. This was attributed the solubility of $FeCO_3$ being further reduced due to the increased pH. No significant change in the morphology of the film was observed between this test and the previous test (pH 6.8) other than the size of $FeCO_3$ crystals (Figure 7.21 (a)-(d)). After just 30 minutes of exposure (Figure 7.21(a)), a significant proportion of the steel surface was covered in small $FeCO_3$ crystals varying from <1 µm to 2 µm in width that possessed a very similar structure to those observed at pH 6.8. After just 60 minutes of exposure, ~50% of the surface is covered with $FeCO_3$ crystals which is observed in Figure 7.21(b). In conjunction with these observations, the corrosion rate is rapidly reducing at this stage suggesting the crystals are very well adhered to the surface. After 120 minutes of exposure, a very large portion of the surface was covered by $FeCO_3$ crystals varying from 1 µm to 5 µm in width. At this point, the rate of reduction in corrosion rate has slowed down due to the reduction in Fe^{2+} production from the surface, hindering iron carbonate formation.

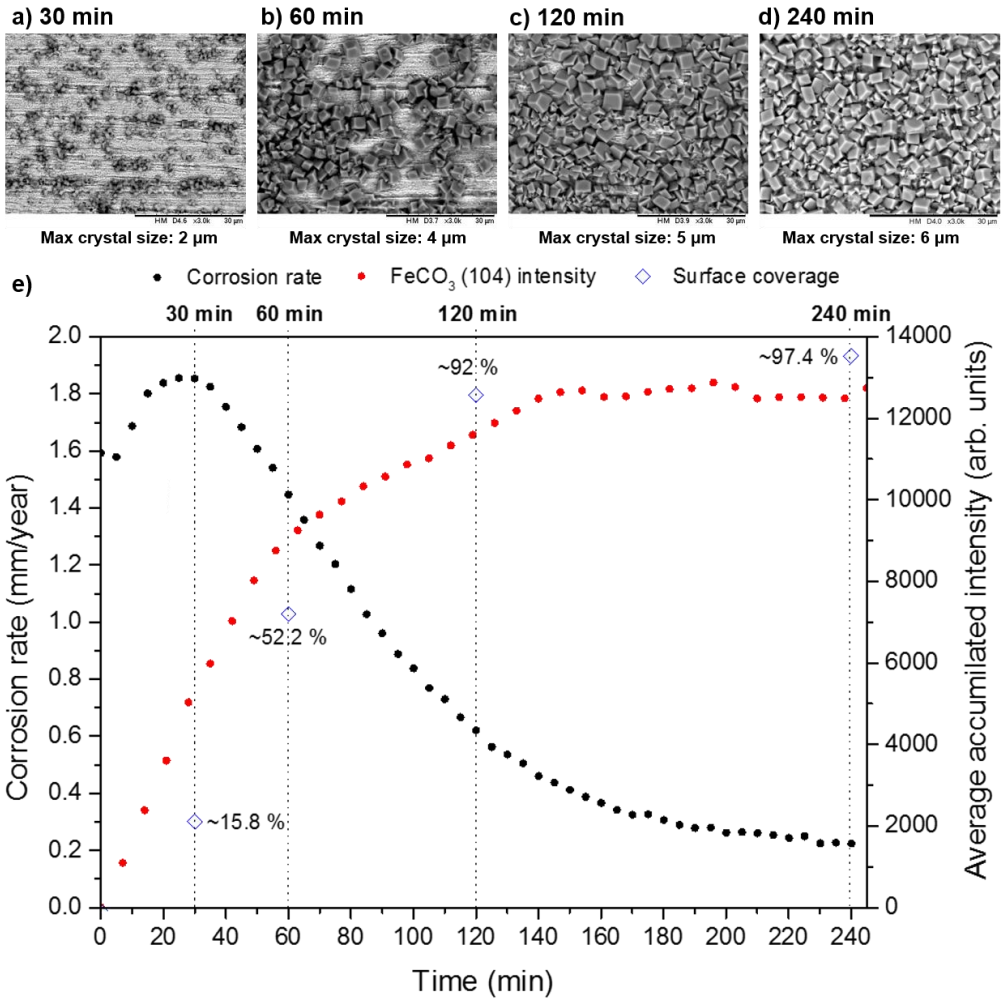

Figure 7.21. Development of the $FeCO_3$ crystals (a)-(d) SEM images over time; (e) *In-situ* corrosion rate and major $FeCO_3$ plane intensity verses time conducted at 80°C, 3.5 wt.% NaCl, 0.54 bar p_{CO_2} and 0.1 m/s at pH 7 in a freely corroding system.

The corrosion rate gradually continues to drop until the end of the test (corrosion rate = 0.25 mm/year) were almost an entire surface coverage is achieved. Very few changes were observed from the SEM images from 120 minutes onward with the only noticeable change being a minor increase in crystal size. Comparing this to the previous test, the maximum crystal size here is almost half the size of the largest crystal found at pH 6.8 through SEM observations. It has to be noticed that the surface coverage at pH 7 continued to increase marginally even though a plateau in $FeCO_3$ intensity has occurred. It can therefore be considered that after a plateau in intensity has been reached, no more nucleation occurs and the crystals are agglomerating. This could explain the fact that no more $FeCO_3$ is detected whereas the surface coverage still increases. The $FeCO_3$ crystals formed in each of the three

experiments consisted of a rhombohedral/cubic structure. Figure 7.22 summarises the effect of pH on the development and morphology of the $FeCO_3$ crystals over time.

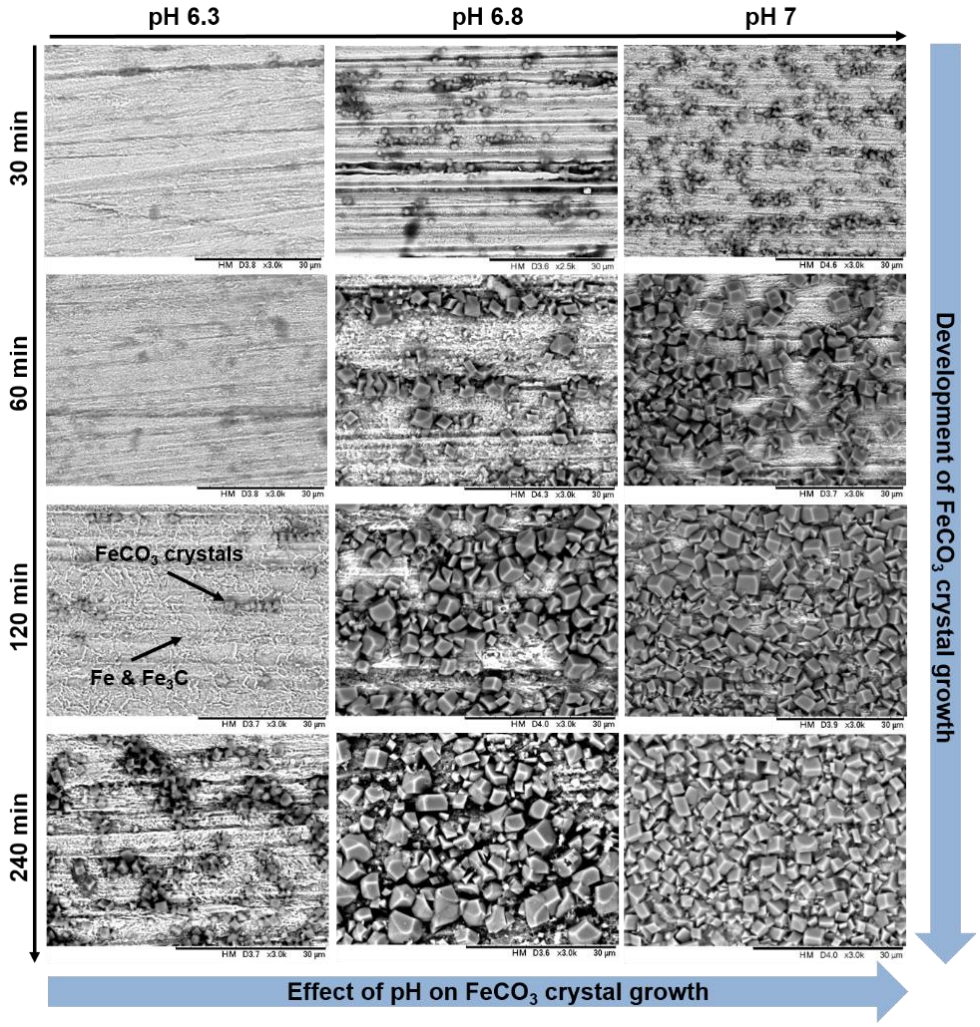

Figure 7.22. The effect of pH on the development and morphology of $FeCO_3$ crystals over time conducted at 80°C, 3.5 wt.% NaCl, 0.54 bar p_{CO_2} and 0.1 m/s at pH 6.3, 6.8 and 7 in a freely corroding system.

The only major difference throughout the tests were the sizes (see Figure 7.23(b) which is a plot of the maximum crystal size observed as function of time at each pH) and growth rate of the crystals. Although the crystals formed at pH 7 appeared to have sharper and more defined edges which is most likely due to the dominance of the (104) plane. Whereas at pH 6.8, the crystals on the surface appear to be a mixture of well-defined cubic crystals with sharp edges (as seen at pH 7) and disorientated crystals with random shapes and faces with fine edges. The crystals at pH 6.8 also seem to vary in size considerably in comparison to the $FeCO_3$ at pH 7. Figure 7.23 shows a

summary of the surface coverage (Figure 7.23 (a)) and the crystal size (Figure 7.23 (b)) at the corresponding system pH. The increase in pH significantly decreases the solubility of $FeCO_3$, resulting in faster precipitation and hence increased surface coverage. Consequently, $FeCO_3$ precipitation is far more favourable at the higher pH and has resulted in the formation of a smaller, compact and more protective crystals covering larger portions of the steel surface. Decreased pH shows the predominance of growth over nucleation which results in larger crystals that are less dense and less protective.

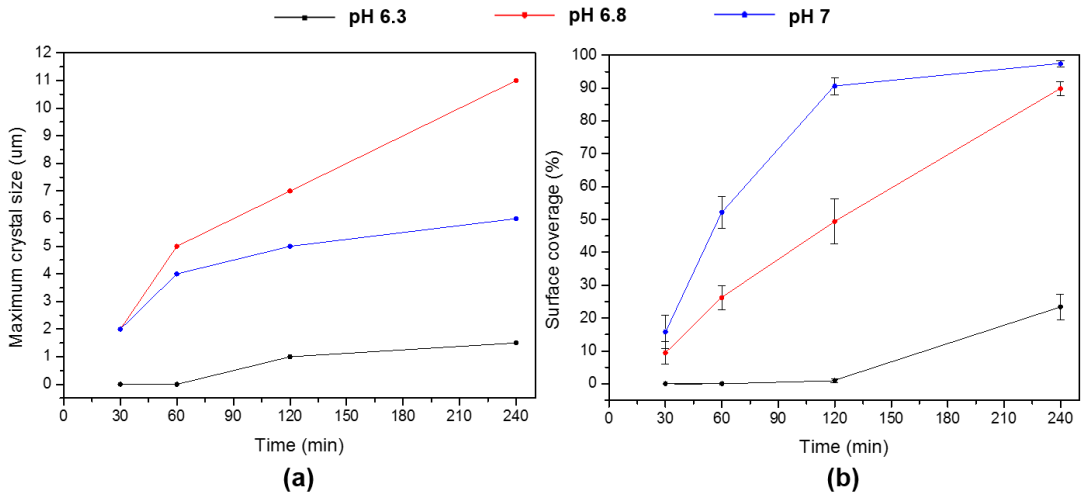

Figure 7.23. *Ex-situ* SEM image analysis data conducted at 80°C, 3.5 wt.% NaCl, 0.54 bar p_{CO_2} and 0.1 m/s at pH 6.3, 6.8 and 7 in a freely corroding system: (a) Maximum crystal size; (b) Surface coverage.

7.8 Growth Kinetics and Morphology of the $FeCO_3$ Films Formed at Different Flow Velocities

The results presented in this section report the effect flow velocity has on the corrosion rate of the system and the initial precipitation of $FeCO_3$. The only difference in the tests was the flow velocity of the system. Two distinctly different flow regimes were assessed: Laminar flow (0.1 m/s, Re<2000) and turbulent flow (1 m/s, Re>4000). The effect of flow velocity on the corrosion rate of carbon steel is generally well understood. The corrosion rate rises with increasing velocity due to the effect of mass transfer on the species movement to/from the mass transfer boundary layer. An increase in flow velocity of the system can increase the transport of the cathodic reaction species H^+ from the bulk solution to the surface**.** Higher velocities increases the mass transfer of H^+ ions to the surface for the reduction reaction to take place. Buffering H^+

ion concentration at the surface reduces the local pH at the surface interface resulting in increased corrosion rate which is evident from Figure 7.24 for 1 m/s.

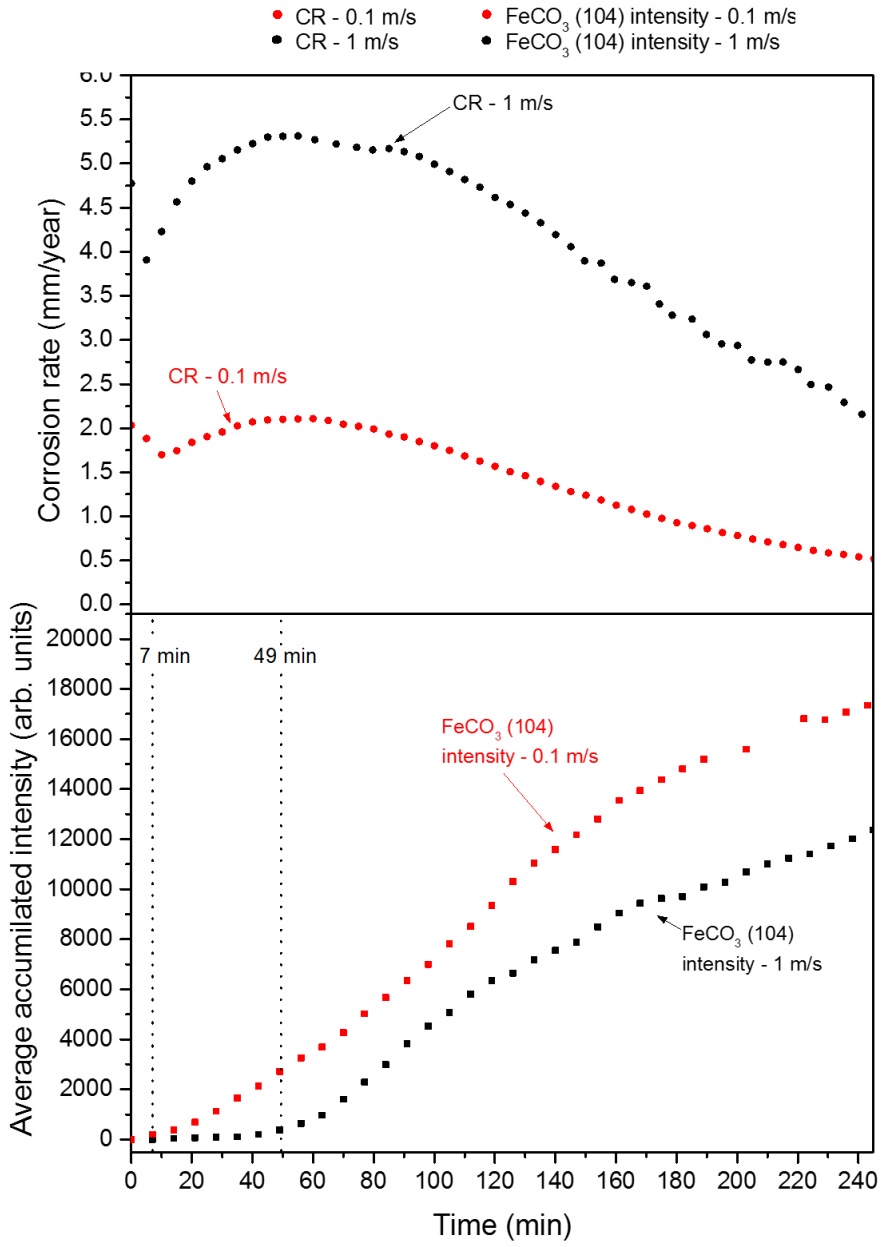

Figure 7.24. *In-situ* data recorded over time for each test conducted at 80°C, 3.5 wt.% NaCl and 0.54 bar p_{CO_2} and pH 6.8 at different flow velocities of 0.1 and 1 m/s in a freely corroding system: (a) Corrosion rates; (b) Integrated diffraction intensities for $FeCO_3$ (104) plane for each of the 5 scans performed over a 2 mm line scan on each sample.

An increase of flow velocity leads to an enhanced mass transfer process, and the released Fe^{2+} ions due to corrosion can be more easily carried away from

the steel surface. During the first 50 minutes of the test at 1 m/s, the corrosion rate increases from ~ 4 mm/year to ~5.4 mm/year as a result of this process. The corrosion rate then starts to reduce once sufficient $FeCO_3$ has precipitated on the surface to act as a diffusion barrier.

A combination of the mass transfer of H^+ ions to the surface, and Fe^{2+} away from the surface lowers the local saturation ratio in the diffusion boundary layer and slows down $FeCO_3$ precipitation at higher flow velocity. The induction time $FeCO_3$ at 0.1 m/s is instantaneous across all locations of the sample which has been shown previously. This is extremely rapid, especially in comparison to the exact same system with the only different parameter being the flow velocity. At 1 m/s, the induction time for $FeCO_3$ is ~45 minutes. Such delay in $FeCO_3$ formation at higher flow velocity is a result of a number of processes combined. Due to the difference in flow regimes of the two tests, the physical properties of the flow across the steel sample influences the formation of $FeCO_3$ because of the mass transfer coefficient and the electrochemical reactions at the surface. Increasing the flow velocity by a magnitude from 0.1 to 1 m/s results in mass transfer coefficient approximately 7 times higher at 1 m/s (which is primarily a result of such a difference in Reynolds number from 1620 at 0.1 m/s to 15563 at 1 m/s). As seen in Equation 7.13, the diffusion boundary (δ) layer is proportional to the mass transfer coefficient (K_m).

$$\delta = \frac{D}{K_m} \tag{7.13}$$

Where D is the diffusion coefficient at 80°C (2.90 x10^{-8} m^2/s). The mass transfer coefficient (m/s) can be calculated from mass transfer correlation via:

$$K_m = \frac{1}{L_c} \times D(5 + 0.15 \times Re^a \times Sc^b) \tag{7.14}$$

Where (L_c) is the characteristic length (m) and the Schmitt number (Sc) is dimensionless and given by:

$$Sc = \frac{\mu}{\rho \times D} \tag{7.15}$$

Parameters a and b are dimensionless empirical constants and can be calculated by:

$$a = 0.88 - \frac{0.24}{4 \times Sc} \quad (7.16)$$

$$b = \frac{1}{3} + 0.5 \times e^{-0.6Sc} \quad (7.17)$$

Based on this relationship between the diffusion boundary layer and mass transfer coefficient, the diffusion boundary layer is approximately 7 times thinner at 1 m/s, compared to at 0.1 m/s making it easier for species to diffuse in (CO_3^{2-} and H^+ via the buffering affect from the bulk) and out (Fe^{2+} due to corrosion) and increasing the rate of anodic/cathodic reactions at the surface. Considering the higher corrosion rate experienced under increased flow velocity, the scaling tendency becomes lower.

Table 7.4. A summary of the important flow-related parameters and their effect on $FeCO_3$ precipitation.

Turbulent flow regime (1 m/s)	**Laminar flow regime (0.1 m/s)**
High mass transfer coefficient	Low mass transfer coefficient
Thinner diffusion boundary layer	Thicker diffusion boundary layer
Higher H^+ at the surface	Lower H^+ at the surface
Lower Fe^{2+} at the surface	Higher Fe^{2+} at the surface
Lower SR	Higher SR
Higher energy barrier to overcome	Lower energy barrier to overcome
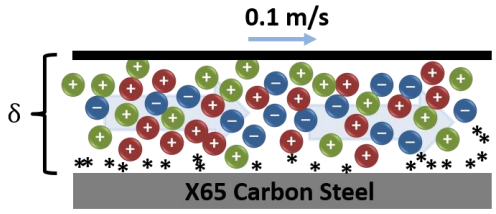	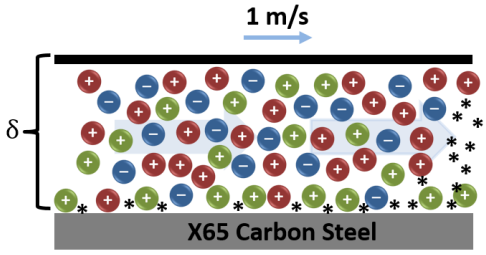
	

Therefore under high flow velocity, it is more difficult to form a protective $FeCO_3$ layer as opposed to lower flow rates. Not only are the electrochemical

reactions at the surface affected at higher flow velocities, the physical nucleation and growth of $FeCO_3$ crystals is more difficult. The energy required to form a nuclei and then to nucleate on to the surface must overcome the viscous energy from the flow across the surface. Table 7.4 summarises the important parameters that the flow affects (in relation to $FeCO_3$ precipitation) and the reasons behind the increased induction times for $FeCO_3$ precipitation at higher flow velocities.

Once this energy barrier has been achieved and crystals nucleate, this will in turn increase the local turbulence caused by the crystal faces and therefore it is likely that the crystals that are not well adhered to the surface will be flushed away and then dissolve in the bulk. However, once the stable $FeCO_3$ crystals start to grow after ~45 minutes, the growth rate of the crystals is extremely uniform across the surface which is illustrated in Figure 7.25.

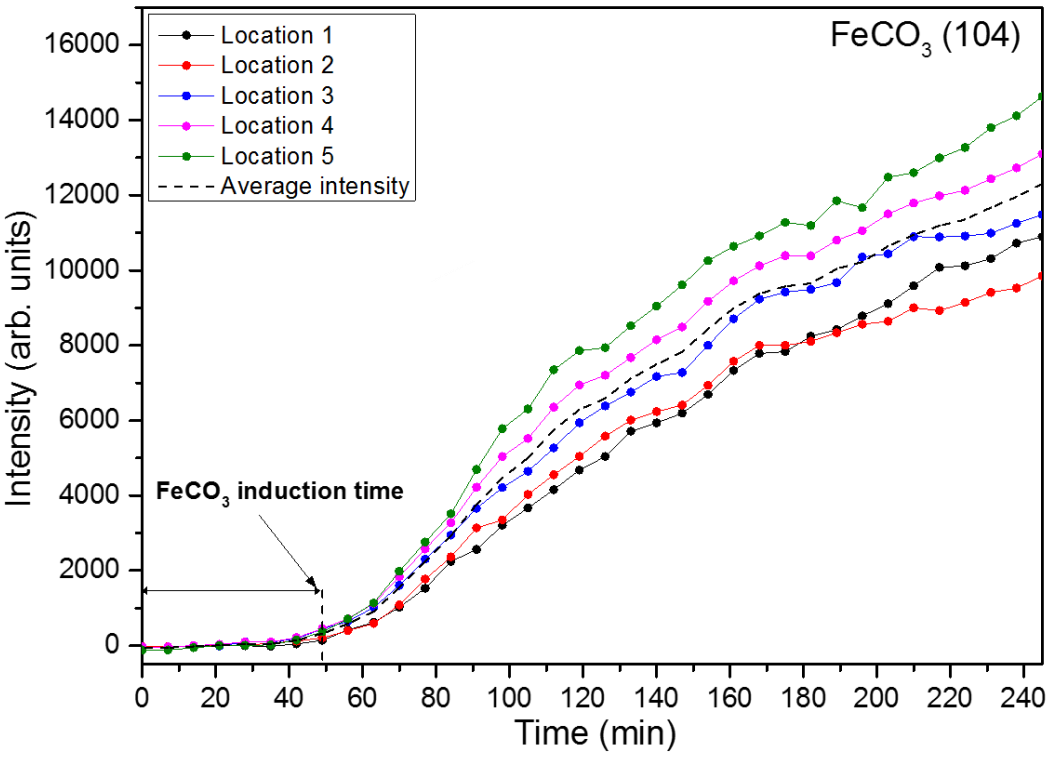

Figure 7.25. Growth of the most dominant $FeCO_3$ crystal plane (104) across the surface conducted at 80°C, 3.5 wt.% NaCl, 0.54 bar p_{CO_2} and pH 6.8 at 1 m/s in a freely corroding system.

The induction time of $FeCO_3$ is consistent across the surface of the carbon steel surface and then the growth rate varies slightly with respect to the measured intensity, but the overall trend is very similar. The $FeCO_3$ growth

rate increase continuously for the remainder of the test until a final average accumulated intensity of ~12000 (arb.units) is reached. The $FeCO_3$ crystals formed on the surface at 0.1 m/s offer more protection against corrosion. The final corrosion rate at 1 m/s is ~2.3 mm/year, yet the reduction in corrosion rate is faster than at 0.1 m/s. This is most likely due to the local pH in the boundary layer and the turbulence at the $FeCO_3$ crystal and steel interface. Figure 7.26 shows a comparison of the $FeCO_3$ crystals morphology at the end of each tests. Upon reviewing the surfaces from the SEM images, it is hard to believe that the quantity of $FeCO_3$ is as low as the measured *in-situ* SR-XRD data suggests at 1 m/s in comparison to 0.1 m/s in Figure 7.24. This could be due to the top view SEM not being an accurate indication of the mass of $FeCO_3$ on the surface and it is difficult to determine the thickness of the layer. Alternatively, the crystals internal structures are a lot more permeable at 1 m/s allowing the Fe^{2+} to diffuse through and therefore the actual quantity of $FeCO_3$ is less than suggested by the SEM images.

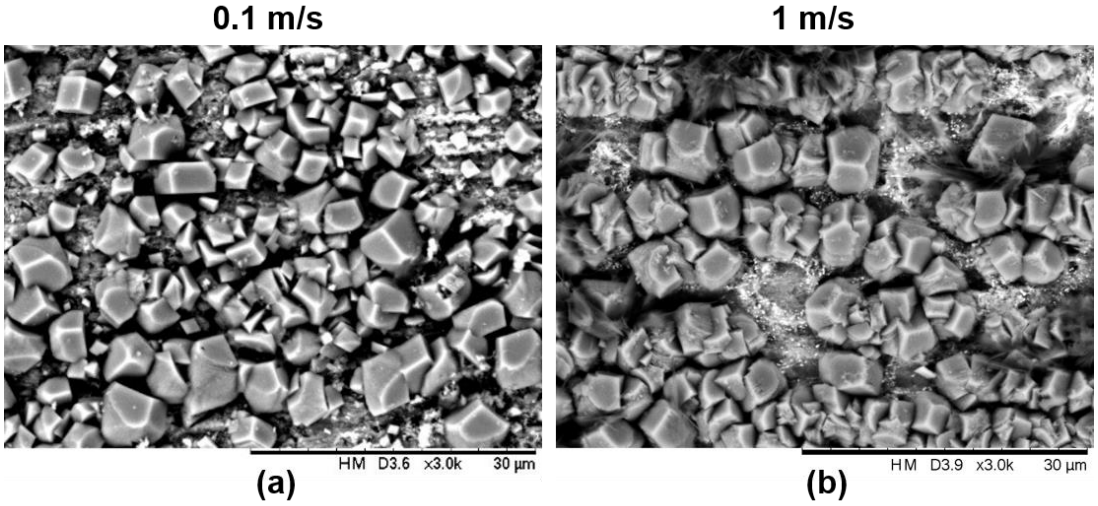

Figure 7.26. *Ex-situ* SEM data at the end of each test conducted at 80°C, 3.5 wt.% NaCl and 0.54 bar p_{CO_2} and pH 6.8 in a freely corroding system: (a) 0.1 m/s; (b) 1 m/s.

These tests have shown that in the early stages of $FeCO_3$ precipitation, that the nucleation of $FeCO_3$ crystals is delayed at higher flow velocities. However, once a protective $FeCO_3$ layer is developed the question is whether it will remain protective under such turbulent flow conditions and therefore future

studies using the designed flow cell should build on this work with higher flow velocities and for longer exposure times.

7.9 Growth Kinetics and Morphology of the $FeCO_3$: Effect of Ca^{2+} addition before and after $FeCO_3$ Formation

This section looks at the variations of OCP and corrosion rate with time for each test in a CO_2-saturated 3.5 wt.% NaCl brine at pH 6.8 and 0.1 m/s when 1000 ppm of Ca^{2+} was added to the solution before $FeCO_3$ film formation (start of the test) and after film formation (after 4 hours) and the effect Ca^{2+} has on $FeCO_3$ precipitation and growth.

7.9.1 1000 ppm Ca^{2+} added after $FeCO_3$ Film Formation

As shown in Figure 7.27, the corrosion rate decreased with time for the test with zero Ca^{2+} concentration conditions for the first 4 hours of the test.

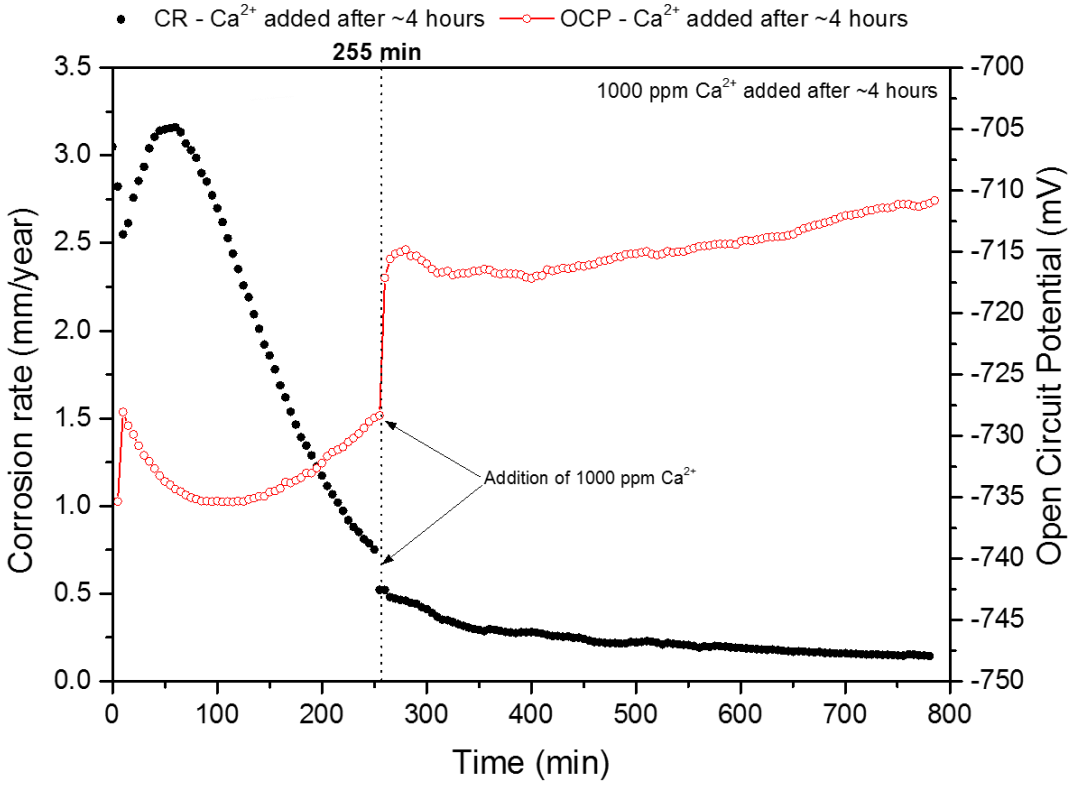

Figure 7.27. Corrosion rate and open circuit potential profiles after ~13 hours in a CO_2 saturated brine at 80°C, pH 6.8, 3.5 wt.% NaCl and 0.54 bar p_{CO_2}, 0.1 m/s and addition of 1000 ppm Ca^{2+} after $FeCO_3$ film formation (after 4 hours) in a freely corroding system.

This was due to protective $FeCO_3$ crystals that have formed on the steel surface. Under these initial conditions before Ca^{2+} was added to the system, the formation of a protective $FeCO_3$ crystals occurred without any interference. Once 1000 ppm of Ca^{2+} was added to the system, the corrosion behaviour of the carbon steel continued to decrease until eventually stabilising at ~ 0.15 mm/year. The OCP increased from ~ -730 mV to ~ -715 mV when the Ca^{2+} was added to the system due to the $CaCO_3$ crystals forming instantly onto the $FeCO_3$ crystals already present on the surface. The corrosion rate continued to drop due to the $CaCO_3$ crystals adding an extra layer of crystals acting as a denser diffusion barrier against the corrosive species which precipitates via:

$$\mathrm{Ca}^{2+}_{(\mathrm{aq})} + \mathrm{CO}^{2-}_{3\,(\mathrm{aq})} \rightarrow \mathrm{CaCO}_{3(\mathrm{s})} \tag{7.17}$$

The saturation degree with respect to $CaCO_3$ was calculated according to:

$$S_{CaCO_3} = \frac{[Ca^{2+}][CO_3^{2-}]}{K_{sp,\mathrm{CaCO_3}}} \tag{7.18}$$

Where $K_{sp,\mathrm{CaCO_3}}$ is the solubility product of $CaCO_3$ which can be calculated as:

$$K_{sp,\mathrm{CaCO_3}} = -1228.732 - 0.294T_k + \frac{35512.75}{T_K} + 485.818\log_{10}(T_K) \tag{7.13}$$

Figure 7.28 shows the *in-situ* SR-XRD data from before and after the addition of 1000 ppm into the solution. Before the addition of Ca^{2+}, the only new crystalline phase to form on the surface was $FeCO_3$ which reveals that 8 lattice planes ((104), (110), (113), (202), (024), (018), (116), (122)) were detected. Upon adding the Ca^{2+} into the solution, a 26 new planes were detected during the first scan across the surface along with the $FeCO_3$ crystals planes already present due to such a high concentration and hence saturation ratio in respect to $CaCO_3$. Among the new planes detected, were three polymorphs of $CaCO_3$ (Aragonite, Vaterite and Calcite). Calcite is the most stable form of $CaCO_3$, and because of its internal crystal structure similarities with $FeCO_3$, the most dominant plane will be assessed and compared with the $FeCO_3$ (104) to assess the growth of the crystals. Embedded within Figure 7.28, is a table

showing the different planes of $FeCO_3$ and $CaCO_3$ and their corresponding position along the 2θ x-axis which shows the similarities in the crystal structures. The graph reveals that 8 lattice planes of calcite were detected ((104), (110), (113), (202), (024), (018), (119), (122)). The only difference in the planes detected was the substitute from the (116) $FeCO_3$ plane with the (119) $CaCO_3$ plane. Similarly, the most intense calcite plane is also the (104) plane.

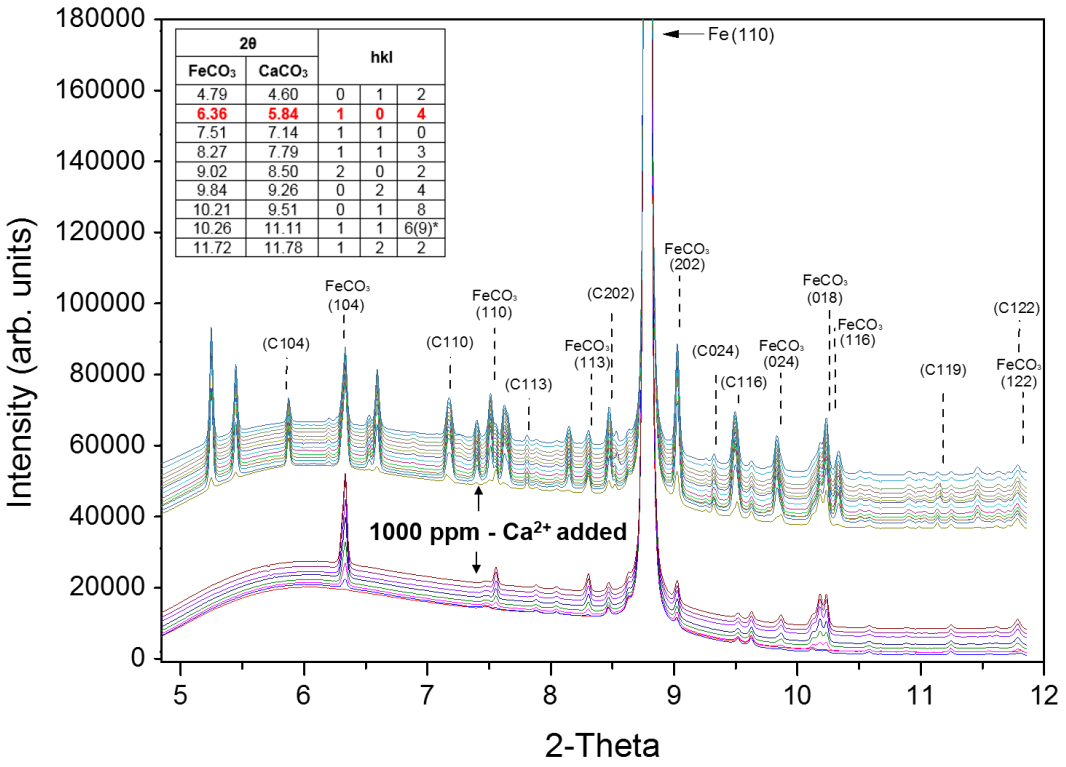

Figure 7.28. *In-situ* diffraction patterns recorded as a function of time conducted at 80°C, pH 6.8, 3.5 wt.% NaCl and 0.54 bar $\boldsymbol{p_{CO_2}}$, 0.1 m/s and addition of 1000 ppm Ca^{2+} after $FeCO_3$ film formation (after 4 hours) in a freely corroding system.

The rest of the 18 $CaCO_3$ planes detected were a mixture of aragonite and vaterite. However, the most stable $CaCO_3$ plane is the calicite (104) plane and therefore the kinetics of growth of the $FeCO_3$ and $CaCO_3$ (104) planes are assessed in Figure 7.29. Upon adding the Ca^{2+} in to the solution, the growth of $FeCO_3$ is instantly hindered and the growth rate hits a plateau at all locations scanned. This is assumed to be that the system is now saturated in the favour for $CaCO_3$ formation. Initially, the calcite (104) crystal plane is unstable at location 1 and 5 until eventually stabilising. However, after the

immediate formation of $CaCO_3$, there is no further growth of either $CaCO_3$ or $FeCO_3$ for the remainder of the test.

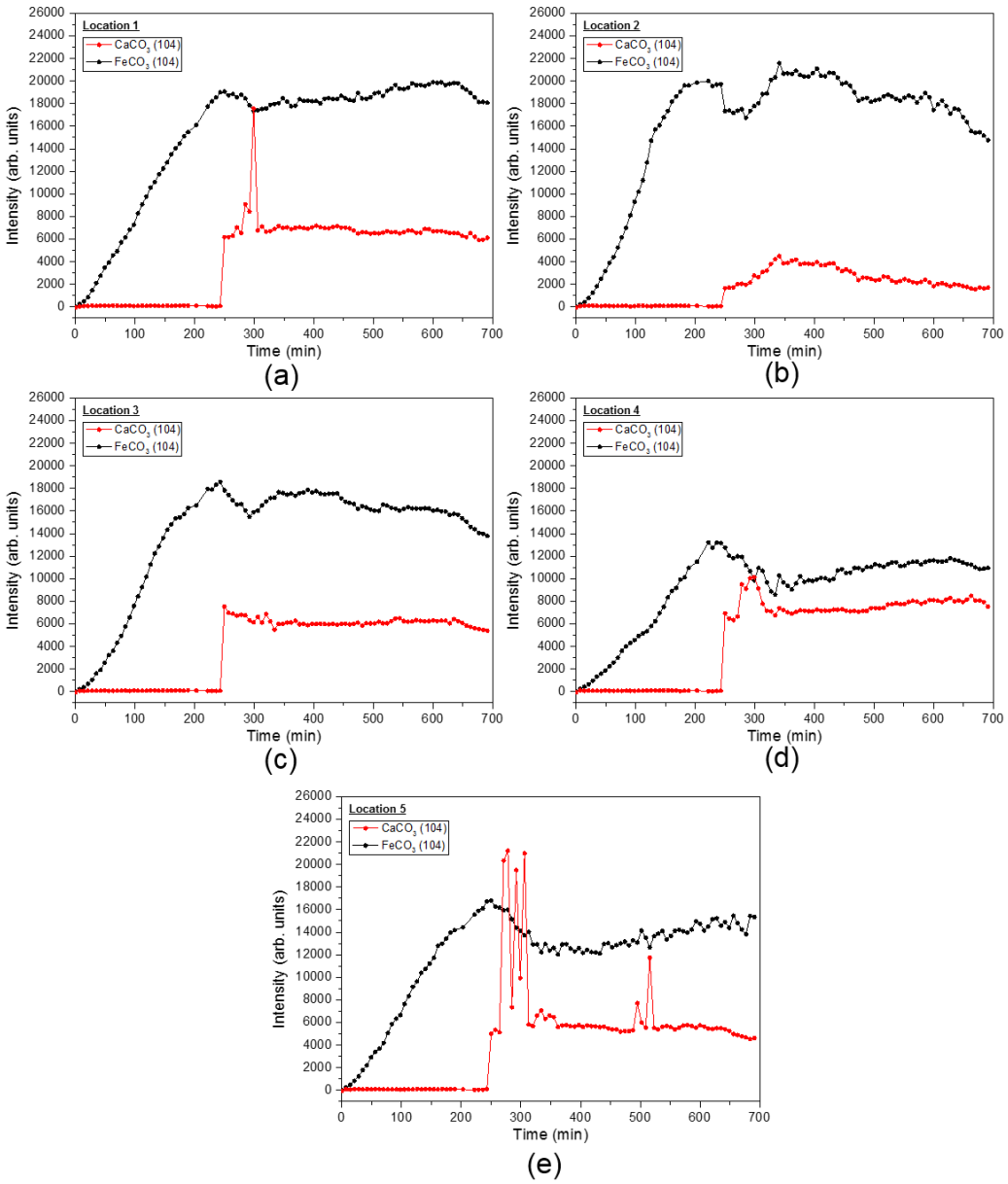

Figure 7.29. Growth of the $FeCO_3$ and $CaCO_3$ crystal planes intensities over time at each of the locations scanned across the surface conducted conducted at 80°C, pH 6.8, 3.5 wt.% NaCl and 0.54 bar $\boldsymbol{p_{CO_2}}$, 0.1 m/s and addition of 1000 ppm Ca^{2+} after $FeCO_3$ film formation (after 4 hours) in a freely corroding system.

In fact, the intensity of $FeCO_3$ decreases slightly due to the reduction in the saturation ratio of the system. Nesic *et al.* [140] reported that the precipitation

of $CaCO_3$ in aqueous CO_2 solutions will lead to local acidification and therefore a reduction in local pH which is mostly likely the cause of the dissolution of $FeCO_3$. Despite this process, the mixture of $FeCO_3$ and $CaCO_3$ crystals on the steel surface still offered good protection against corrosion.

7.9.2 1000 ppm Ca^{2+} added before $FeCO_3$ film formation

Figure 7.30, shows the corrosion rate and OCP as a function of time when 1000 ppm Ca^{2+} is added to the system from the start of the test. The corrosion rate only marginally decreased with time, which is most likely due to the lack of formation of a protective $FeCO_3$ layer on the steel surface which is shown in Figure 7.31. At the initial Ca^{2+} concentration of 1000 ppm (which was added to the bulk solution), the rapid precipitation of $CaCO_3$ made the solution under-saturated with respect to $FeCO_3$, making it impossible for protective $FeCO_3$ crystals to form.

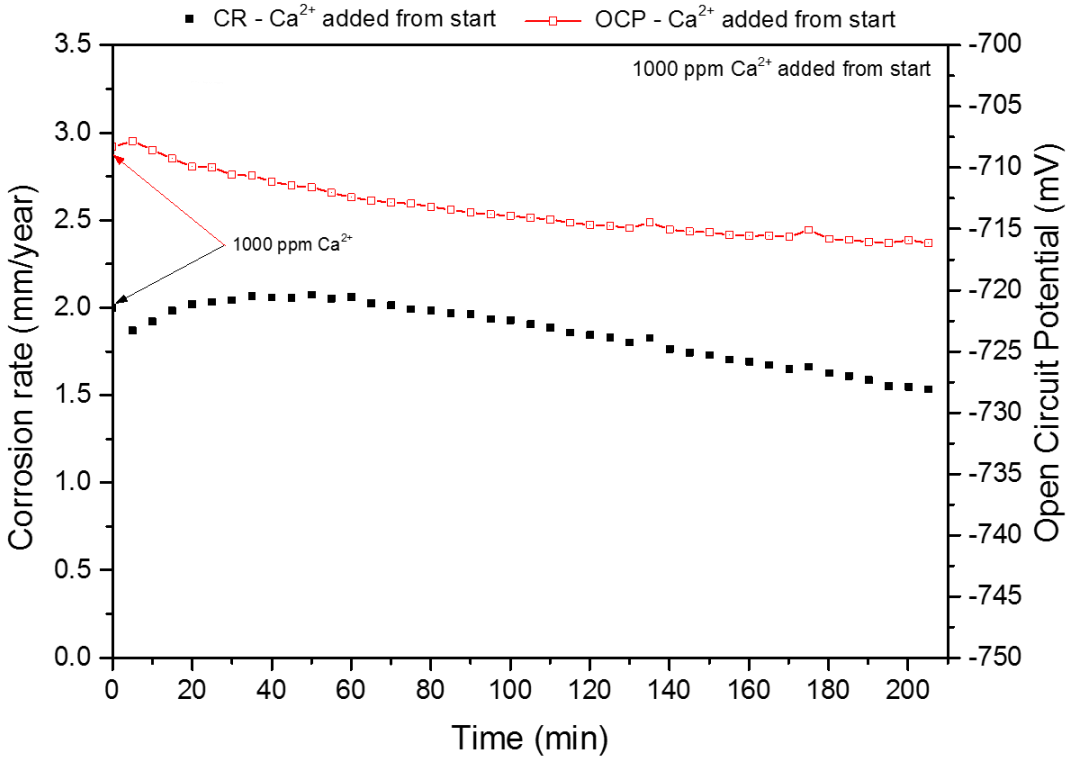

Figure 7.30. Corrosion rate and open circuit potential profiles after ~3.5 **hours** in a CO_2 saturated brine at 80°C, pH 6.8, 3.5 wt.% NaCl and 0.54 bar p_{CO_2}, 0.1 m/s and addition of 1000 ppm Ca^{2+} before $FeCO_3$ film formation (at start of test) in a freely corroding system.

The *in-situ* SR-XRD patterns over time when 1000 ppm Ca^{2+} was added before $FeCO_3$ formation at the start of the test reveal that the only new crystalline phase detected on the steel surface during the experiment was $CaCO_3$. The diffraction patterns showed that 29 lattice planes of $CaCO_3$ were detected, 9 of which were calcite ((012), (104), (110), (113), (202), (024), (018), (119), (122)), see Figure 7.30.

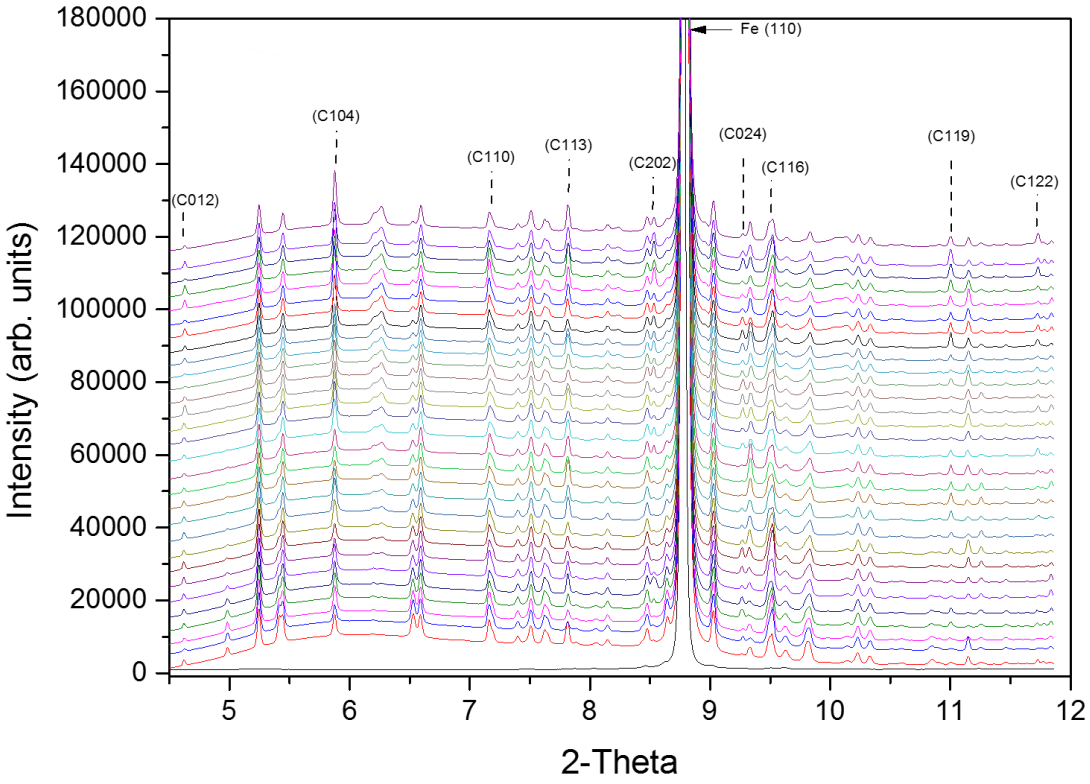

Figure 7.31. *In-situ* diffraction patterns recorded as a function of time conducted at 80°C, pH 6.8, 3.5 wt.% NaCl and 0.54 bar p_{CO_2}, 0.1 m/s and addition of 1000 ppm Ca^{2+} before $FeCO_3$ film formation (at start of test) in a freely corroding system.

Similarly in this test, the most intense calcite plane was observed at 2θ=~5.84º corresponding to the (104) plane. $CaCO_3$ was detected instantaneously across the surface, although there was no presence of $FeCO_3$ in this instance which clearly indicates that the system was saturated with respect to $CaCO_3$ instead of $FeCO_3$. At this stage it can be hypothesized that this was caused by a lower pH due to the high Ca^{2+} concentration in comparison to the Fe^{2+}. The immediate formation of $CaCO_3$ on to the surface of the carbon steel surface has dampened the production of Fe^{2+}. However, the initial crystals on the surface are permeable allowing the surface to corrode beneath, but at a slower rate than a bare steel surface would corrode. Eventually (after 60

minutes) the corrosion rate begins to reduce due to the increase in surface coverage of the $CaCO_3$ crystals.

Figure 7.32 shows the growth of the most dominant $CaCO_3$ (calcite (104)) crystal plane over time at each of the locations scanned across the surface during the test. The graph shows that the amount of $CaCO_3$ detected is extremely high from the first scan, more so at location 3 (where I = ~15000), then at location 4 after 180 minutes where the measured intensity was close to 60000. Conversely, the $CaCO_3$ crystals on the surface are clearly unstable indicated by the noisy intensity plots across the entire surface of the sample. This indicates that the crystals are either dissolving and then precipitating again or being flushed downstream through the flow in the system. It is assumed that there is an 'inner' layer of $CaCO_3$ crystals that are well adhered to the steel surface, with larger loose crystals forming on top of this layer.

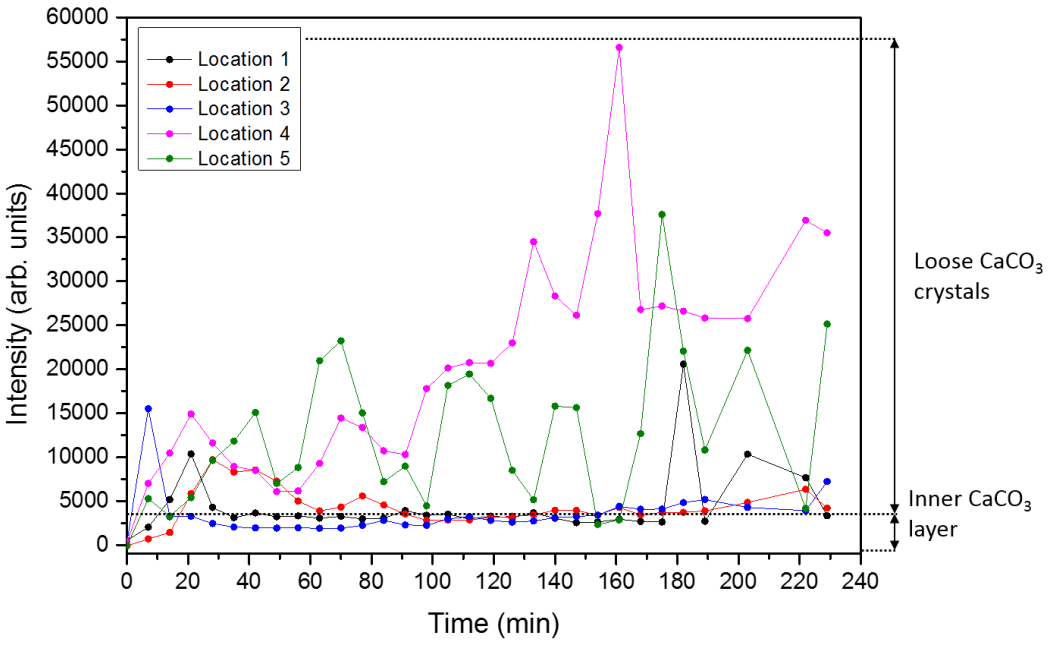

Figure 7.32. Growth of the most dominant $CaCO_3$ crystal plane (104) across the surface conducted at 80°C, pH 6.8, 3.5 wt.% NaCl and 0.54 bar p_{CO_2}, 0.1 m/s and addition of 1000 ppm Ca^{2+} before $FeCO_3$ film formation (at start of test) in a freely corroding system.

7.9.3 Morphology of the Crystals at 1000 ppm Ca^{2+} Added before and after $FeCO_3$ Film Formation

Figure 7.33 shows the effect of 1000 ppm of Ca^{2+} on the morphology of the $FeCO_3$ crystals corresponding to the accumulated growth rates (Figure 7.33 (a)) of $FeCO_3$ and $CaCO_3$ when Ca^{2+} was added after $FeCO_3$ film formation and $CaCO_3$ before $FeCO_3$ film formation. Figure 7.33 (b) shows the $FeCO_3$ crystals on the surface before Ca^{2+} was added to the system after 4 hours. After adding 1000 ppm of Ca^{2+} to the system, Figure 7.33 (c) shows the crystal morphology at the end of the test. The figure shows smaller $FeCO_3$ crystals along with the presence of $CaCO_3$ which agrees with the *in-situ* SR-XRD data which suggests the dissolution of $FeCO_3$.

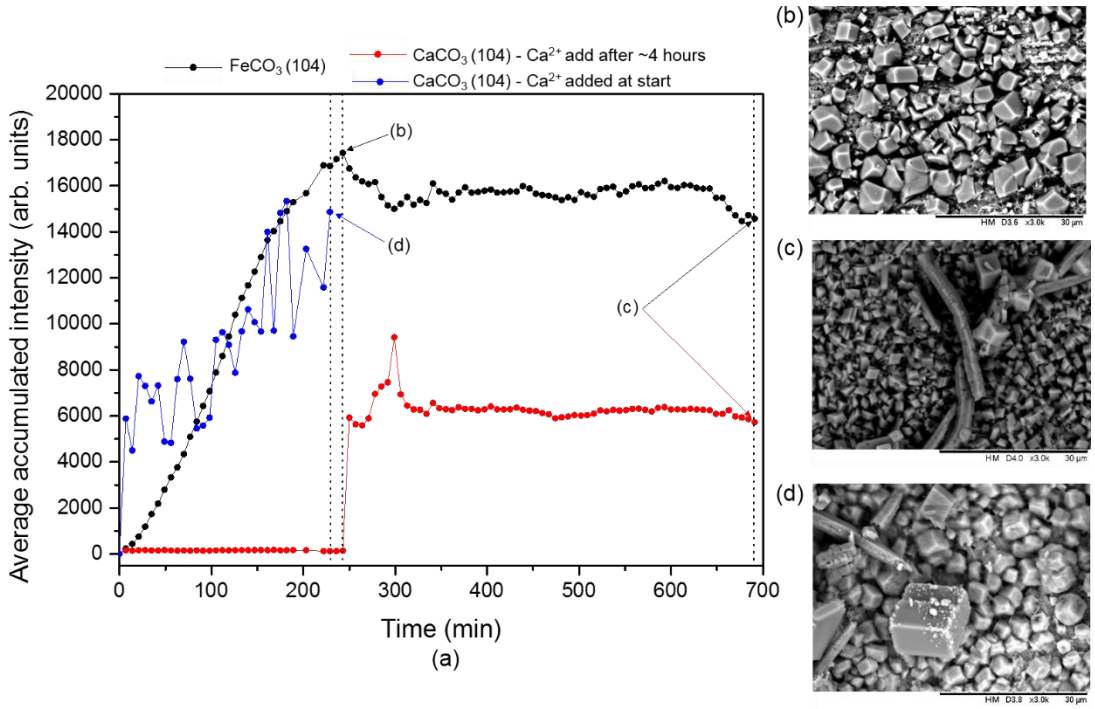

Figure 7.33. *In-situ* and *ex-situ* data conducted at 80°C, pH 6.8, 3.5 wt.% NaCl and 0.54 bar p_{CO_2}, 0.1 m/s and addition of 1000 ppm Ca^{2+} before and after $FeCO_3$ film formation in a freely corroding system.

In Figure 7.33 (d), where no $FeCO_3$ was detected, it is clear to see a denser, more compact inner layer which is mostly likely built up of the crystals that are contributing to the reduction in the corrosion rate of the system. It is unlikely that the larger crystals observed are stable and well attached to the crystals beneath which will explain the measured intensities showing crystals disappearing and reappearing. Figure 7.34 summarises the effect of 1000 ppm Ca^{2+} on the morphology of the $FeCO_3$ crystals.

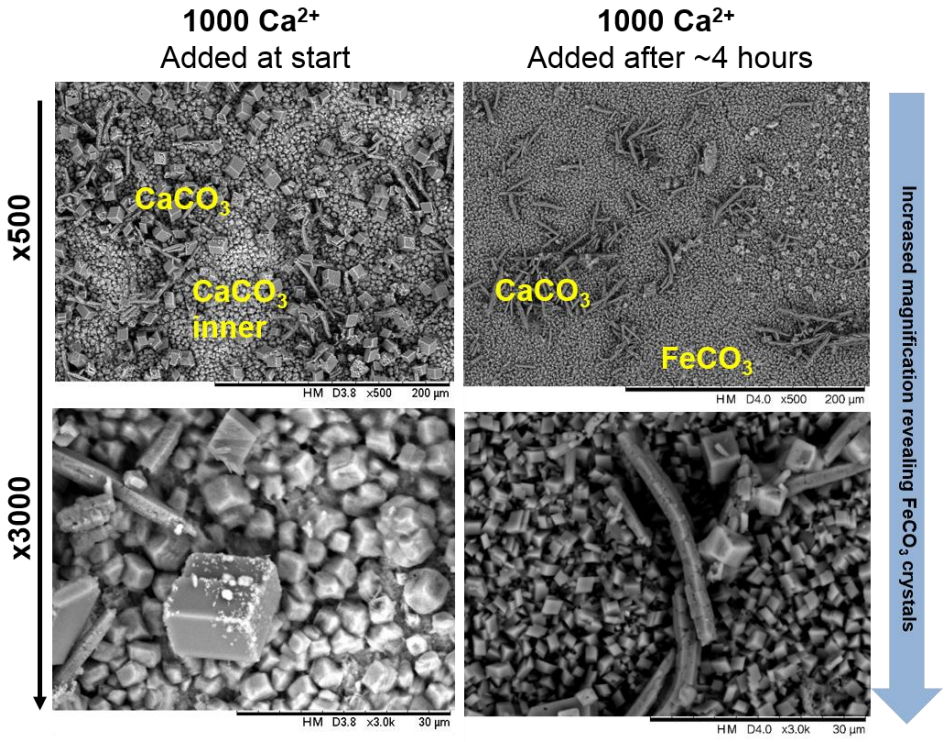

Figure 7.34. The effect of Ca^{2+} addition on the morphology of $FeCO_3$ crystals over time conducted at 80°C, 3.5 wt.% NaCl, 0.54 bar p_{CO_2} and 0.1 m/s at pH 6.8 in a freely corroding system.

7.10 Summary and Conclusions

A new system comprising of a flow cell with integrated *in-situ* electrochemistry and SR-XRD capabilities has been used to follow the corrosion kinetics of X65 carbon steel in real-time in a CO_2 saturated brine at different pH values of 6.3, 6.8, and 7 when subjected to a flow rate of 0.1 m/s. The following conclusions can be extracted from the results presented in this work:

- $FeCO_3$ nucleation could be detected consistently and well before its inhibitive effect on general corrosion rate was recorded from electrochemical responses, indicating that *in-situ* SR-GXRD is able to detect the very early stages of crystal nucleation on surfaces in a flowing cell.
- Under the specific conditions evaluated, $FeCO_3$ was the only crystalline phase to form in the system, with no crystalline precursors being apparent prior to or during its formation and being the sole phase

responsible for the observed reduction in corrosion rate, predominantly through the blocking of active sites on the steel surface.

- The growth and the morphology of the $FeCO_3$ crystals recorded using *in-situ* diffraction patterns can be well described by the most dominant (104) crystal plane which is the most predominant during the nucleation and growth of $FeCO_3$.
- From the accumulated integrated peak intensities, four steps characterised the growth mechanism of the $FeCO_3$ layer: (1) An induction time when the measured intensity is zero; (2) Nucleation of the $FeCO_3$ crystals when the measured intensity initially increases; (3) Nucleation-growth stage which is characterised by an increase in crystal growth with nucleation occurring simultaneously; (4) Growth stage when the integrated intensity slows down and near full surface coverage is achieved, limiting nucleation.
- The induction time for $FeCO_3$ formation significantly reduces with increased pH, which also causes increase in crystal nucleation rate resulting in the formation of a smaller, compact and more protective crystals in the early stages of growth.
- An increase in flow velocity leads to an enhanced mass transfer process, and the released Fe^{2+} ions due to a higher corrosion rate can be easily flushed away from the steel surface, reducing the local supersaturation and increasing the induction time for $FeCO_3$ precipitation.
- The presence of 1000 ppm Ca^{2+} affected the corrosion mechanism by changing the water chemistry, which in turn resulted in the precipitation of less-protective $CaCO_3$ which interfered with the continued formation and growth of protective $FeCO_3$ crystals when added after $FeCO_3$ film formation.
- The presence of 1000 ppm Ca^{2+} in the same conditions but before $FeCO_3$ formation resulted in the solution being saturated for only $CaCO_3$ and no $FeCO_3$ was detected.
- When $CaCO_3$ was the only new crystalline phase to form, an inner layer rapidly precipitated on to the steel surface which offered some

protection against corrosion and unstable/non-protective larger crystals were continuously being flushed away from the surface.

- The growth and the morphology of the $CaCO_3$ crystals recorded *in-situ* was dominated by the (104) calcite crystal plane which is the most predominant during the precipitation of $CaCO_3$.

Chapter 8.
Investigation into the Kinetics and Composition of the Protective Layer Formed during '*Pseudo Passivation'* of Carbon Steel: An *In-situ* and *Ex-situ* Approach

This chapter presents results from an *in-situ* SR-XRD flow cell integrated with electrochemistry for corrosion measurement at the Diamond Light Source Synchrotron facility. The cell was used to follow the nucleation and growth kinetics of corrosion products on X65 carbon steel surfaces in a CO_2-saturated 3.5 wt.% NaCl brine at 80°C over a range of solution pH values (6.3, 6.8 and 7) and flow rates of 0.1, 0.5 and 1 m/s under anodic polarisation through potentiostatic and galvanostatic control methods to accelerate the corrosion kinetics to monitor the composition and growth of corrosion products during 'pseudo-passivation'.

8.1 Introduction

$FeCO_3$ is consistently found as the major corrosion product phase found on the internal walls carbon steel pipelines and piping systems. The importance of $FeCO_3$ in terms of protecting carbon steel pipelines during transportation of hydrocarbons has already been discussed previously. Under specific operating conditions, a highly dense $FeCO_3$ film is formed which is known to protect the steel from further corrosion. However, if the $FeCO_3$ crystals are only partially covering the steel surface, the initiation of localised corrosion may proceed due to a galvanic effect caused be the bare steel areas (the anodic regions) and the film covered areas (the cathodic regions). A "grey zone" criterion was determined through experiments and theory to explain localised CO_2 corrosion propagation by Han *et al.* [6] It was concluded that localised corrosion propagates when the conditions that are not favourable for protective $FeCO_3$ formation. In the so called "grey zone" the conditions are described as highly supersaturated nor undersaturated with respect to $FeCO_3$.

In addition to $FeCO_3$, field and laboratory based experiments in recent years have indicated that chukanovite ($Fe_2(OH)_2CO_3$) or magnetite (Fe_3O_4) are corrosion products that can form on steel in CO_2-saturated/carbonate rich solutions. Questions on the presence of $Fe_2(OH)_2CO_3$ and Fe_3O_4 still remained unanswered, a pertinent one being what role, if any, these corrosion products play in determining the overall protectiveness of the corrosion products formed. Han *et al.* [9] reported that $FeCO_3$ was the major phase, but that trace

amounts of Fe_3O_4 were also present at the interface beneath the $FeCO_3$ crystals. Based on these results, they proposed that the protectiveness properties were specifically due to the formation of a thin Fe_3O_4 film beneath the $FeCO_3$ layer. However, the identification of Fe_3O_4 in these studies was attributed to the presence of a single peak at 18° 2θ (using Cu+kα1 radiation source), with three other peaks being unaccounted for (at 27.5, 34.2 and 36°). Other studies have investigated the formation of $FeCO_3$ during CO_2 corrosion on carbon steel during the observed phenomenon labelled as 'spontaneous passivation' or 'pseudo-passivation' on active metals. Similarly, these authors have proposed that Fe_3O_4 formed at the interface of the carbon steel, beneath the $FeCO_3$ crystals. They have suggested that this phase (Fe_3O_4) could be responsible for the ultra-protective properties against corrosion and a sudden increase in OCP. However, there still remains uncertainties on these observations and conclusions based on the limitations in analysis techniques. For such 'pseudo-passive' film to form (whether it be purely $FeCO_3$ or Fe_3O_4) at the carbon steel interface among the $FeCO_3$ crystals already present on the surface, it can be suggested that the crystals are permeable allowing the electrolyte a pathway to steel surface, or at least pockets of solution remain trapped between the pores that exists between the steel surface the $FeCO_3$ crystals or within the $FeCO_3$ crystals themselves. The local solution chemistry beneath the $FeCO_3$ crystals might change, resulting in a higher supersaturation due to the further production of Fe^{2+} at the exposed regions to the solution.

Although the true nature and purpose of the corrosion products that offer protection against corrosion, many oil and gas production companies utilise the protective properties of the natural corrosion products in the field through the use of pH control (or pH stabilisation). This deems to be a popular management strategy to control levels of corrosion to provide a more neutral environment and/or to stimulate formation of protective corrosion products. However, such corrosion products can leave the carbon steel pipeline more vulnerable to localised corrosion attack during internal CO_2 corrosion. Despite the fact that the general CO_2 corrosion mechanisms are well understood, the role of the protective corrosion product layer and its potential to lead to localised CO_2 corrosion remains unclear and therefore understanding the nature, composition and mechanism of the corrosion products present could help to prevent this form of severe corrosion in pipelines during production and transportation of hydrocarbons.

Although this phenomenon was studied in Chapter 5, the composition of the ultra-protective film that formed at the carbon steel interface was believed to be purely $FeCO_3$, but was difficult to conclude with certainty. In the present study, 'pseudo-passivation' was investigated over range pH and flow velocities using *in-situ* SR-XRD. Questions about the mechanism of the formation of the corrosion product layer leading to 'pseudo-passivation', as well as its morphology and chemical composition, are addressed in this chapter using anodic polarisation through controlling the corrosion process through potentiostatic or galvanostatic control.

8.2 Experimental Procedure

For all experiments in this chapter, the tests were performed in the newly designed SR-XRD flow cell both at the Diamond Light Source Synchrotron facility (DLSSF) (Beamline I15) and away from the beamline in the in-house laboratory. The test solution used was a CO_2-saturated (keeping dissolved $O_{2(aq)}$ to a minimum) 3.5 wt.% NaCl brine maintained at 80°C. The operating conditions for tests completed at the DLSSF facility and in-house are outlined in Table 8.1.

Table 8.1. Experimental test matrix used for *in-house* laboratory tests (at the University of Leeds) and *in-situ* SR-XRD tests.

Parameter	**In-house laboratory tests**	**SR-XRD tests**
Material	X65 carbon steel – 9 mm Ø (exposed surface)	
Test solution	3.5 wt.% NaCl, distilled water	
Solution pH	6.8	6.3, 6.8, 7
Temperature	80 ºC	
CO_2 partial pressure	0.54 bar	
Flow velocity	0.1 m/s	0.1, 0.5, 1 m/s
Test duration	72, 144 hours	60 – 90 minutes

8.2.1 Collection and Interpretation of Electrochemical Data

Three different electrochemical methods were used in this chapter to either monitor the corrosion rate at OCP or to control and accelerate the corrosion process:

- In-house (away from beamline) tests operated at OCP: For these tests ran away from the beamline under a freely corroding system at OCP, LPR measurements were performed by polarising the sample ±15 mV vs. the OCP at a scan rate of 0.25 mV/s and were undertaken every 5 minutes.
- SR-XRD potentiostatic controlled tests: In these tests, the carbon steel working electrode was anodically polarised from -15 mV below the steady state OCP to +700 mV, and the resulting current density was recorded until the end of each test.
- SR-XRD galvanostatic controlled tests: In these tests, the carbon steel working electrode was subject to a constant current of 1 mA/cm^2 throughout the duration of test. The OCP was then monitored throughout the test.

In comparison with open-circuit conditions, both the potentiostatic and the galvanostatic polarisation methods are intended to accelerate the formation process of $FeCO_3$ (and any other phases for that matter) to a timescale that makes it feasible to perform *in-situ* SR-XRD observations of the 'pseudo-passivation' process. This constant replenishment of Fe^{2+} production at the steel interface in the controlled/accelerated tests will dramatically increase the local supersaturation and the surface will essentially be a 'net' anode, resulting a faster process of the spontaneous 'pseudo-passivation' observed at OCP under certain conditions. Therefore, the *in-situ* SR-XRD experiments were conducted under anodic polarisation to monitor the formation of ultra-protective $FeCO_3$ on a reasonable timescale.

8.2.2 Collection and Interpretation of *In-situ* SR-XRD Data

Collection and interpretation of the *in-situ* SR-XRD experimental data is in accordance with Chapter 7. The only difference in the scanning procedure was the amount of areas scanned across the sample. As elaborated already, a loop was devised to scan five measurements across a 2 mm path length across the centre of the sample for each experiment in order to maximise the

accuracy and the ability of the XRD patterns to be correlated with the extent of crystal growth. In these, tests the loop was amended to scan three areas across a 1 mm to reduce the scanning time for one full loop due to the faster kinetics of $FeCO_3$ crystal growth. Therefore the overall scanning time to complete the three scans over a 1 mm path length was ~2 minutes.

8.2.3 *Ex-situ* Surface Analysis

To supplement the experiments in this chapter, SEM was used to generate images to assist in observing the morphology of the crystals formed on the surface at the end of each test.

8.3 Results and Discussion

8.3.1 Long Term *Ex-Situ* SR-XRD Flow Cell Tests: Spontaneous 'pseudo-passivation'

The corrosion rate profiles have been determined using LPR measurements from experiments conducted in the SR-XRD flow over 72 and 144 hours and the resulting corrosion rate and OCP values of X65 carbon steel with a 3.5 wt. % NaCl CO_2-saturated brine flowing at a velocity of 0.1 m/s, pH 6.8, 80°C have been plotted on a $\log^{10}$ y-axis to reveal the corrosion rate profile more clearly and is presented in Figure 8.1.

Under these conditions, based on the review in Chapter 3, a well-developed $FeCO_3$ layer is expected to form offering protection to the steel surface against corrosion. The corrosion rate profile from both tests shows a repeatable trend over 72 hours and shows that the corrosion rate of the carbon steel surface drops exponentially approximately 2 hours of exposure to the flowing solution. Similar to the tests static immersion tests with the same solution chemistry in Chapter 5, the corrosion rate decreases extremely fast due to the formation of protective $FeCO_3$ (confirmed with XRD/SEM later) in the first 20 hours , and then continues to decrease with exposure time. Within this period, as the corrosion rate was decreasing (due to the build-up of $FeCO_3$ crystals), the OCP did not drastically change (~20 mV vs. Ag/AgCl). At this stage, the $FeCO_3$ crystals have formed a compact film reducing both anodic and cathodic reaction kinetics equally, offering protective properties similar to a mixed corrosion inhibitor [77].

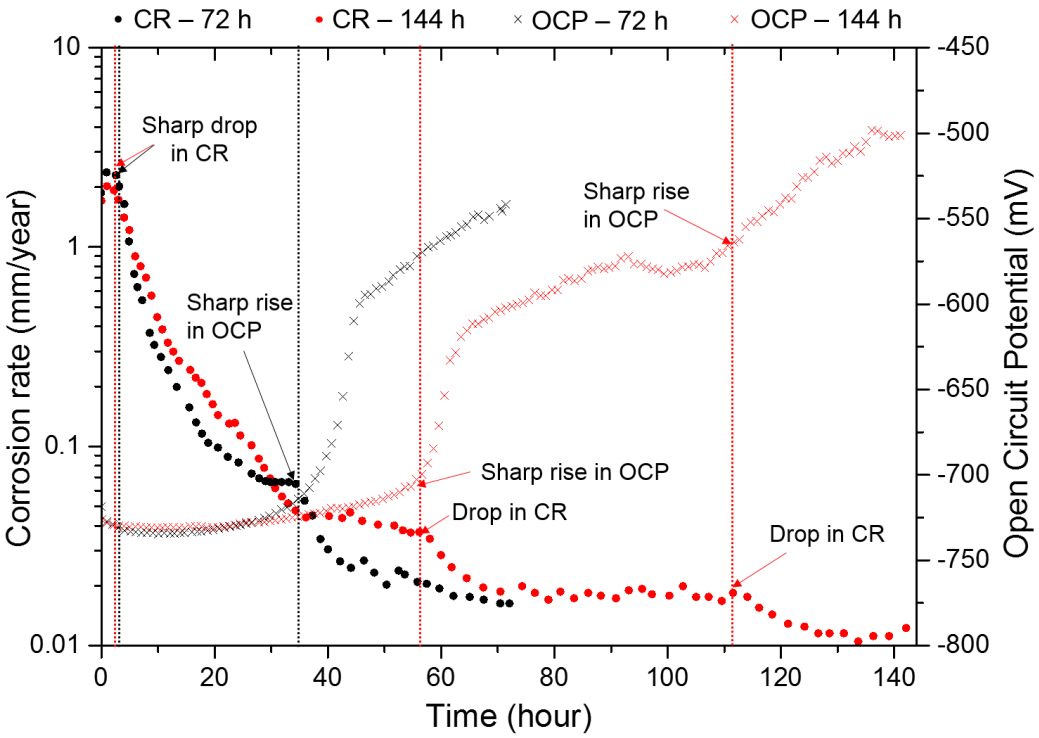

Figure 8.1. Corrosion rate and open circuit potential profiles at different immersion times in a CO_2 saturated brine at 80°C, pH 6.8, 3.5 wt.% NaCl, 0.54 bar $\boldsymbol{p_{CO_2}}$, 0.1 m/s over 72 and 144 hours (freely corroding).

The corrosion rate of the system at the start of the test is ~2mm/year in both cases, then drops to a value of ~0.07 mm/year after ~28 hours in the test ran for 72 hours in total. There is a short plateau observed in the corrosion rate for a further 6 hours until another sharp drop in the corrosion rate is observed after 34 hours and continues drop for the remainder of the test to a value of 0.016 mm/year. Again, similar to the tests conducted in Chapter 5, 'pseudo-passivation' is observed and the second drop in corrosion rate to an extremely low value is associated with a sharp rise in OCP (from -700 mV to -540 mV). The same observation is witnessed in the test ran for a total of 144 hours after 56 hours, where the corrosion rate drops to 0.017 mm/year and the OCP increases from -730mV to -577 mV. However, this phenomenon happens again in the same test after 114 hours with a further third drop in corrosion rate to 0.011 mm/year and a further rise in OCP from -577 mV to 501 mV.

The XRD patterns from both of the tests described are show in Figure 8.2 and reveals that once again, only $FeCO_3$ is detected on the surface. The XRD data in Figures 8.2 (a) and (b) shows that the intensity of the major $FeCO_3$ (104) plane (2θ = ~32°) is higher after 144 hours, relative to a reduction in the major

Fe (110) plane (2θ = ~45°) intensity suggesting that more $FeCO_3$ is present on the surface.

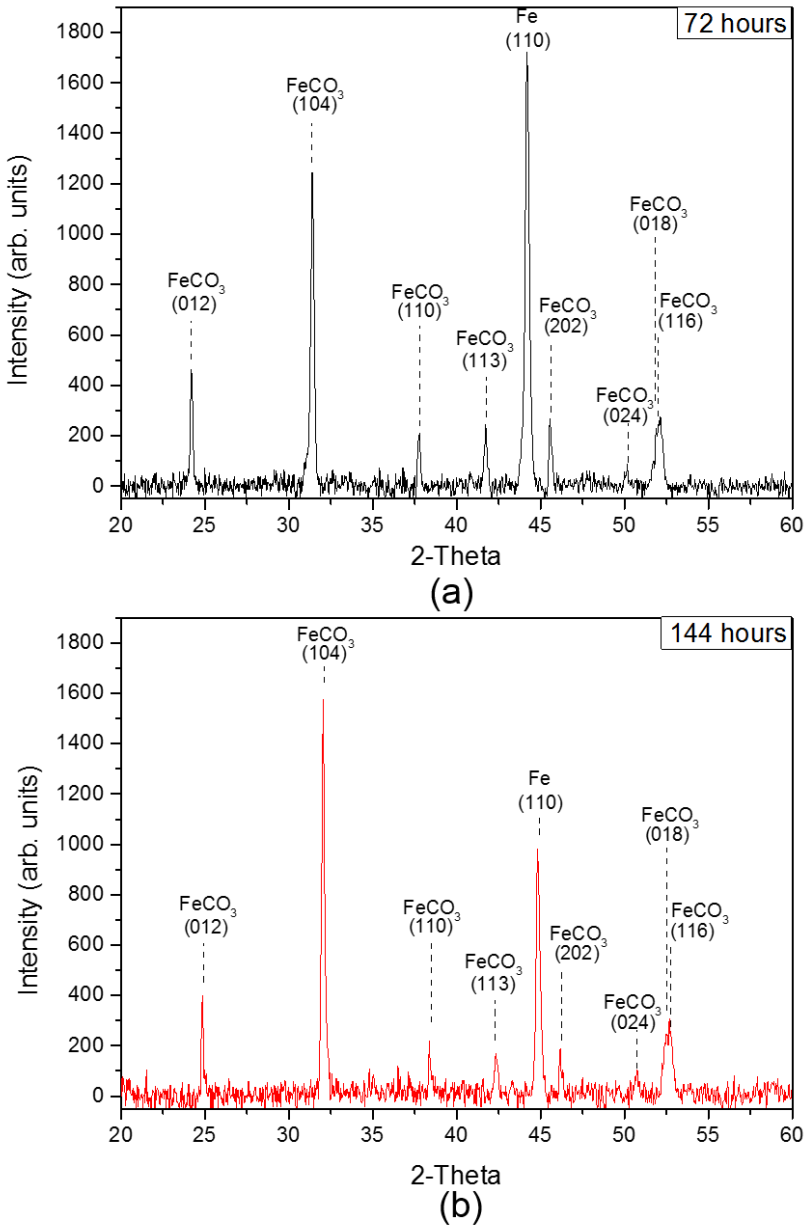

Figure 8.2. *Ex-situ* XRD patterns from the samples as a function of immersion time of 72 hours (a) and 144 hours (b) at 80°C, pH 6.8, 3.5 wt.% NaCl, 0.54 bar p_{CO_2} and 0.1 m/s (freely corroding).

The top view SEM micrographs and cross-sections showing the morphology of the $FeCO_3$ crystals for tests ran at each of the time intervals (0-72 hours, and 0-144 h) are presented in Figure 8.3 (a-f). From the SEM images within, it is clear to see that the surface is saturated with $FeCO_3$ crystals offering good

protection against corrosion, acting as a partial mass-transfer barrier for the corrosive species.

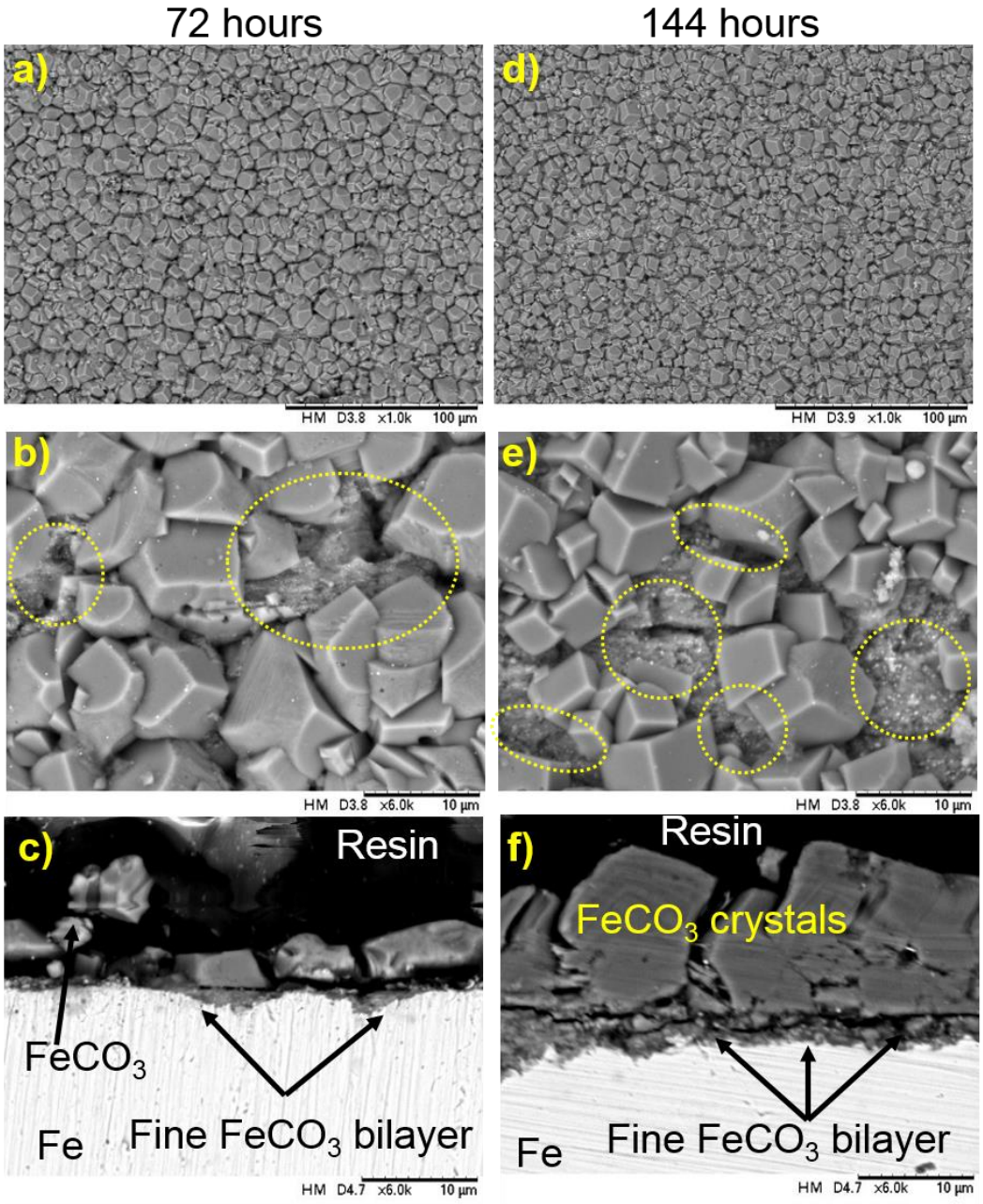

Figure 8.3. SEM micrographs (a), (b), (d) and (e) and cross-sections (c) and (f) showing the morphology of the $FeCO_3$ crystals for tests ran at each of the time intervals (0-72 hours, and 0-144 h) at 80°C, pH 6.8, 3.5 wt.% NaCl, 0.54 bar p_{CO_2} and 0.1 m/s (freely corroding).

The top view of the $FeCO_3$ layer still shows areas of permeability between the crystal faces in Figures 8.3 (a) and (d). However, increased magnification (x6k) in the top views in Figures 8.3 (b) and (e) (highlighted by the circled areas within the images) and the cross sections (shown in Figure 8.3 (c) and

(f)) reveal the same fine bilayer of $FeCO_3$ crystals approximately 1 to 2 µm in thickness either beneath or between the large crystals and no bare steel surface can be seen to be exposed to the surrounding environment – showing the same characteristics as the static immersion tests in Chapter 5.

The larger top-layer of $FeCO_3$ crystals in cross sections after 144 hours in Figure 8.3 (e) are considerably larger than after 72 hours (Figure 8.3 (c)) which agrees with the XRD observations. Similarly, the presence of this finer $FeCO_3$ bilayer means that the higher degree of protection against corrosion is not due to the larger $FeCO_3$ crystals observed from the top view, but rather to a finer $FeCO_3$ bilayer that is expected to have formed when the OCP showed a 'pseudo-passivation' response. As already described previously in this thesis, this anodic shift in potential was ascribable to preferential suppression of the anodic half-reaction owing to the formation and build-up of ultra-protective $FeCO_3$, which retarded the diffusion of the reductive species to the steel surface.

As previously addressed, many studies have investigated the composition of the corrosion products and the mechanism behind the cause of the ultra-protection against corrosion on carbon steel surfaces in CO_2 environments. However, despite such efforts and theories, the underlying fact is that it is still not clear (with confidence anyway), whether the protection offered is a result of purely $FeCO_3$, or whether Fe_3O_4/$Fe_2(OH)_2CO_3$ play a role in the formation of this ultra-protective corrosion product. Therefore, the remainder of this chapter aims to fill these gaps through the use of *in-situ* SR-XRD studies on the phases to form in conjunction with this 'pseudo-passive' behaviour.

8.3.2 *In-situ* SR-XRD Potentiostatic Driven Anodic Polarisation Tests: Effect of Brine pH on 'pseudo-passivation'

In this section, the results will focus on a range of *in-situ* SR-XRD results under anodic polarisation where 'pseudo-passivation' is likely to arise.

The results in Chapter 7 concluded that higher pH values promote the formation of a protective $FeCO_3$ crystals and therefore should also promote the formation of an ultra-protective pseudo-passive layer under anodic polarisation. Such 'pseudo-passivation' process plays an important role in the protection of carbon steel, reducing the corrosion rate values to <0.02 mm/year as seen in Chapter 5 in the static immersion tests and the results already presented in this chapter at OCP. The remarkable nature of the

'pseudo-passivation' effect is shown most clearly by polarisation curves (i-V plots) in the active-passive transition region which can be generated through the electrochemical control methods already described.

The current density responses to the potentiostatic polarisation at pH conditions of low, standard and high pH (pH 6.3, 6.8 and 7 respectively) at 80°C are shown in Figure 8.4.

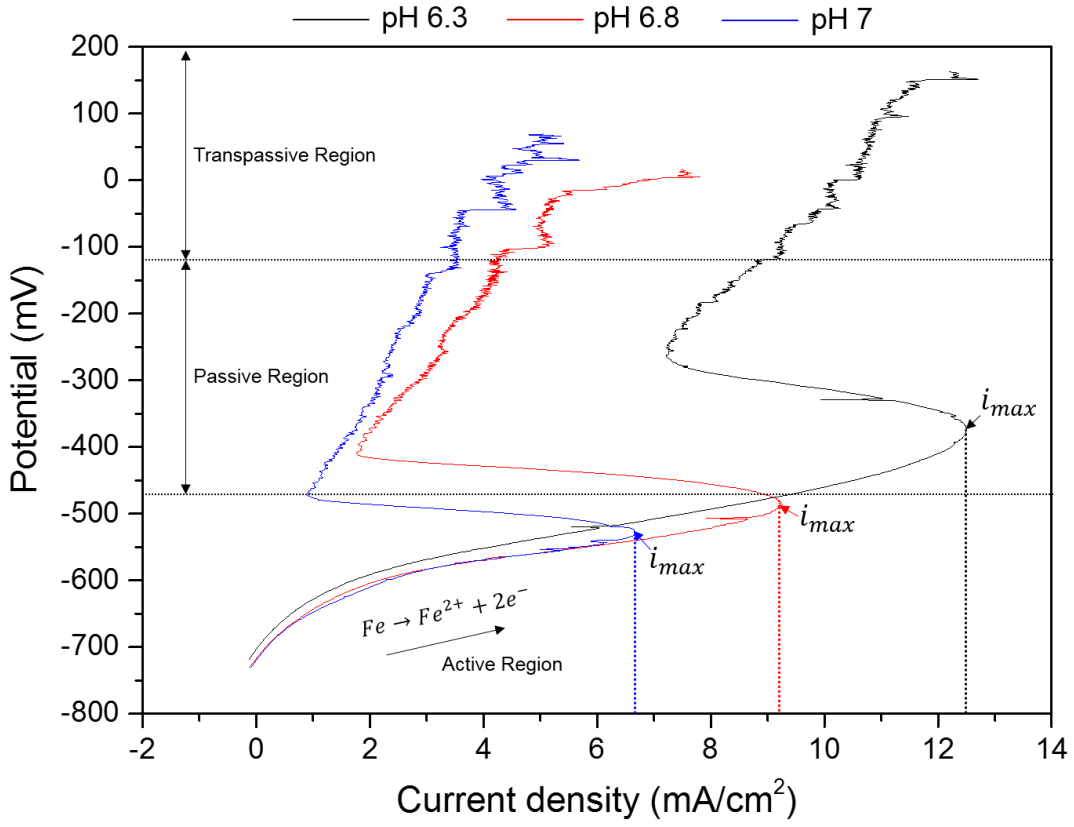

Figure 8.4. Current density profiles versus OCP for three tests under potentiostatic control at 80°C, 3.5 wt.% NaCl, 0.54 bar p_{CO_2}, 0.1 m/s at pH 6.3, 6.8 and 7 (anodic polarisation).

The local pH under an $FeCO_3$ film can be high enough (7 < pH < 9) to initiate 'pseudo-passivation' even if the bulk pH is acidic (e.g. pH 4 to 6) which has been demonstrated by Han *et al.* [56]. The overall shape of a curves in Figure 8.4 is an indication of the corrosion behaviour of the carbon steel in the CO_2 saturated test solution for the different pH values tested. The potential and current values at critical points of the potentiodynamic curves can reveal an insight into the 'pseudo-passivation' tendencies of the carbon steel samples. Consider the peak-shaped active-to-passive transition of the curves, the lower the critical anodic current (i_{max}) at the peak of this curve indicates that

'pseudo-passivation' happens faster. The degree of 'pseudo-passivation' and the stability of the passive layer can be assessed by observing the passive region current. The lower currents in the passive region indicate a higher degree of 'pseudo-passivation' and therefore a more protective $FeCO_3$ film. The closer the primary passive potential is to OCP suggests the prospect of the mechanism to show the spontaneous pseudo-passive behaviour. As the pH increased, the current density peaks became sharper, followed by a slow decay as 'protective' crystals covered the surface resulting in less total charge to be passed in the experiment, indicating more efficient formation of the protective crystals. The initially active surface at pH 7 showed an exponential rise in potential at lower OCP and current density indicating that 'pseudo-passivation' preferably occurs at a higher pH, as expected. The time to reach spontaneous 'pseudo-passivation' was longer at lower pH. This is not surprising as more time is required to accumulate sufficient Fe^{2+} for $FeCO_3$ precipitation.

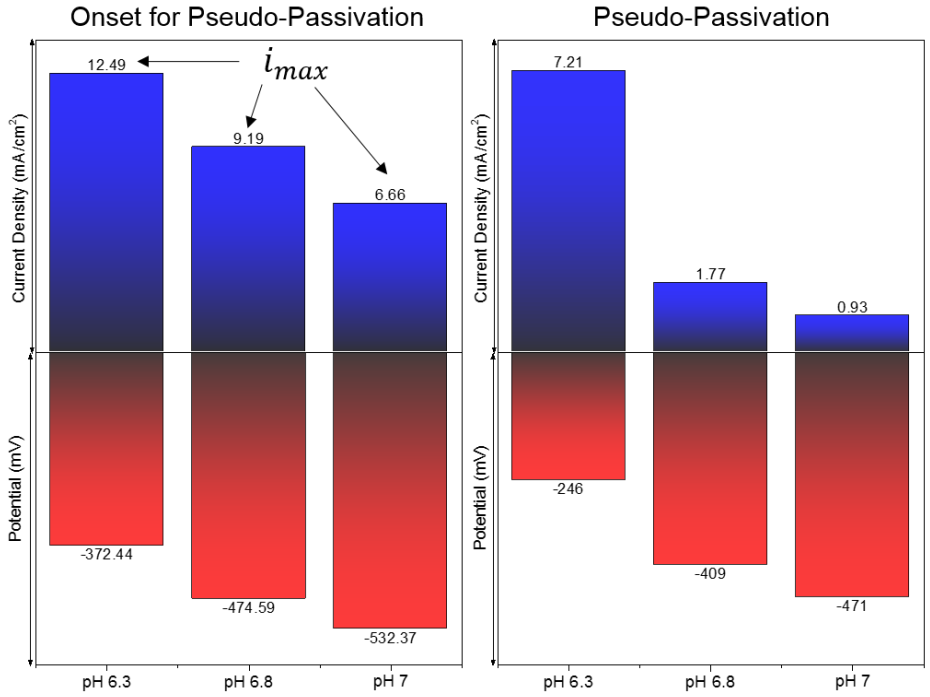

Figure 8.5. A comparison between the current density values and OCP values at each pH tested at different time intervals under potentiostatic control at 80°C, 3.5 wt.% NaCl, 0.54 bar p_{CO_2}, 0.1 m/s at pH 6.3, 6.8 and 7 (anodic polarisation): Onset for 'pseudo-passivation' and during 'pseudo-passivation'.

Figure 8.5 shows the critical values of OCP and current density at the critical stages of the process and illustrates the change of these values for varying system pH with applied voltage. From Figure 8.5, a clear trend is observed as a function of pH, showing more characteristics for spontaneous 'pseudo-passivation' and more protective/stable $FeCO_3$ film.

8.3.2.1 Composition of the Films Formed Using *In-situ* SR-XRD at Different pH Values

SR-XRD patterns recorded *in-situ* over time during the experiments are shown in Figures 8.6 to 8.9. These images show that $FeCO_3$ was the primary phase formed in all conditions. However, similar to the composition of the tests ran in Chapter 7, a minor phase was present prior to running each experiment (identified as Fe_3C) at each pH and another minor phase (identified as $Fe_2(OH)_2CO_3$) was present at pH 7 towards the end of the experiment. At least one minor un-identified phase is present at pH 6.8 also.

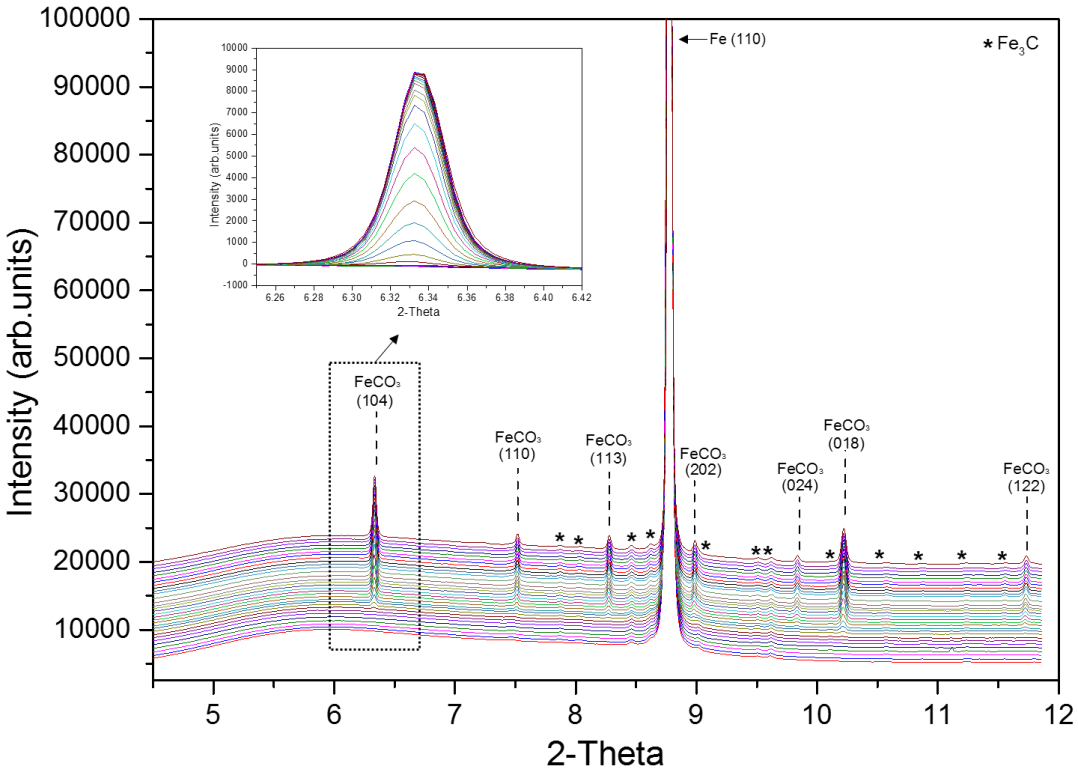

Figure 8.6. *In-situ* diffraction patterns recorded as a function of time conducted at 80°C, 3.5 wt.% NaCl, 0.54 bar p_{CO_2} and 0.1 m/s at pH 6.3 under potentiostatic control.

The *in-situ* SR-XRD patterns over time at pH 6.3 reveal that the only new crystalline phase detected on the steel surface during the experiment was $FeCO_3$ displaying 7 lattice planes of $FeCO_3$ ((104), (110), (113), (202), (204), (018) and (122)) were detected, see Figure 8.6.

The *in-situ* SR-XRD patterns over the duration of the test at pH 6.8 reveal the same 7 lattice planes of $FeCO_3$ ((104), (110), (113), (202), (204), (018) and (122)) as shown in Figure 8.7(a-c). Each of the diffraction patterns at the three locations scanned have been illustrated because the different locations reveal different phases. The growth of the $FeCO_3$ peaks have been dampened in comparison to the test at pH 6.3. This is most likely due to the presence of this unknown crystalline phase (or phases) inhibiting the growth rate of the $FeCO_3$ crystals. This phase has not been conclusively identified, as the peaks observed are of low intensity.

Conversely, the most intense peaks expected for possible phases to precipitate under CO_2 corrosive conditions using carbon steel (specifically $Fe_2(OH)_2CO_3$, Fe_3O_4 and a number of other iron oxides/hydroxides) are absent. After an extensive investigation and reviewing a number of possibilities, it was concluded that this un-identified phase is likely to be $CaCO_3$ at location 3 in Figure 8.7(c). Four of the unknown peaks match with one of the well-known polymorphs of $CaCO_3$ in the form of calcite located at (5.84° (104), 8.50° (202), 9.25° (024) and 11.11° (122) 2θ with the corresponding lattice planes), which is most likely due to left over residue following the test where Ca^{2+} was added to the system in Chapter 7 as this test was performed after. Vast amounts of $CaCO_3$ had precipitated into the bulk solution via homogeneous nucleation and had attached on to the walls of the pipes, beaker, fittings, pump etc and everything was replaced fresh equipment. Then the pump was flushed out with ethanol, but it seems as if $CaCO_3$ particles have still progressed into the system (most likely from the inner walls of the pump) and effected the growth of $FeCO_3$. $FeCO_3$ was still the major phase however, which suggests that only very low concentrations of $CaCO_3$ species have infiltrated into the system (but enough to have a profound effect on the growth kinetics of $FeCO_3$). Calcite has rhombohedral crystal lattice structure very much similar to $FeCO_3$. In fact, so similar, the crystal planes detected of the two phases are the same with the (104) lattice plane both being the most dominant plane.

The growth kinetics of these planes will be discussed in the next section of this chapter.

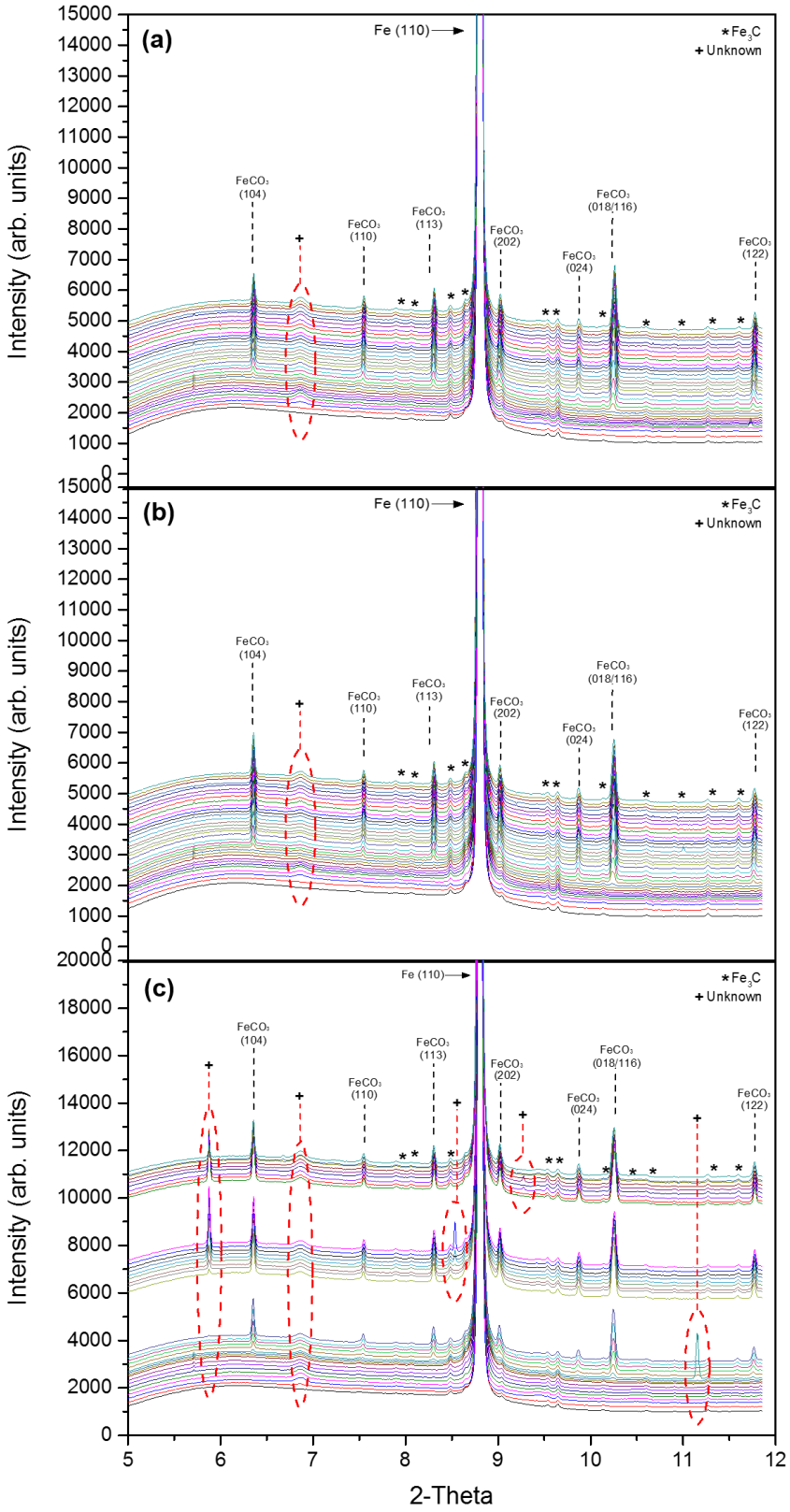

Figure 8.7. *In-situ* diffraction patterns recorded as a function of time conducted at 80°C, 3.5 wt.% NaCl, 0.54 bar p_{CO_2} and 0.1 m/s at pH 6.8 under potentiostatic control: a) scanned location 1; b) scanned location 2; and c) scanned location 3.

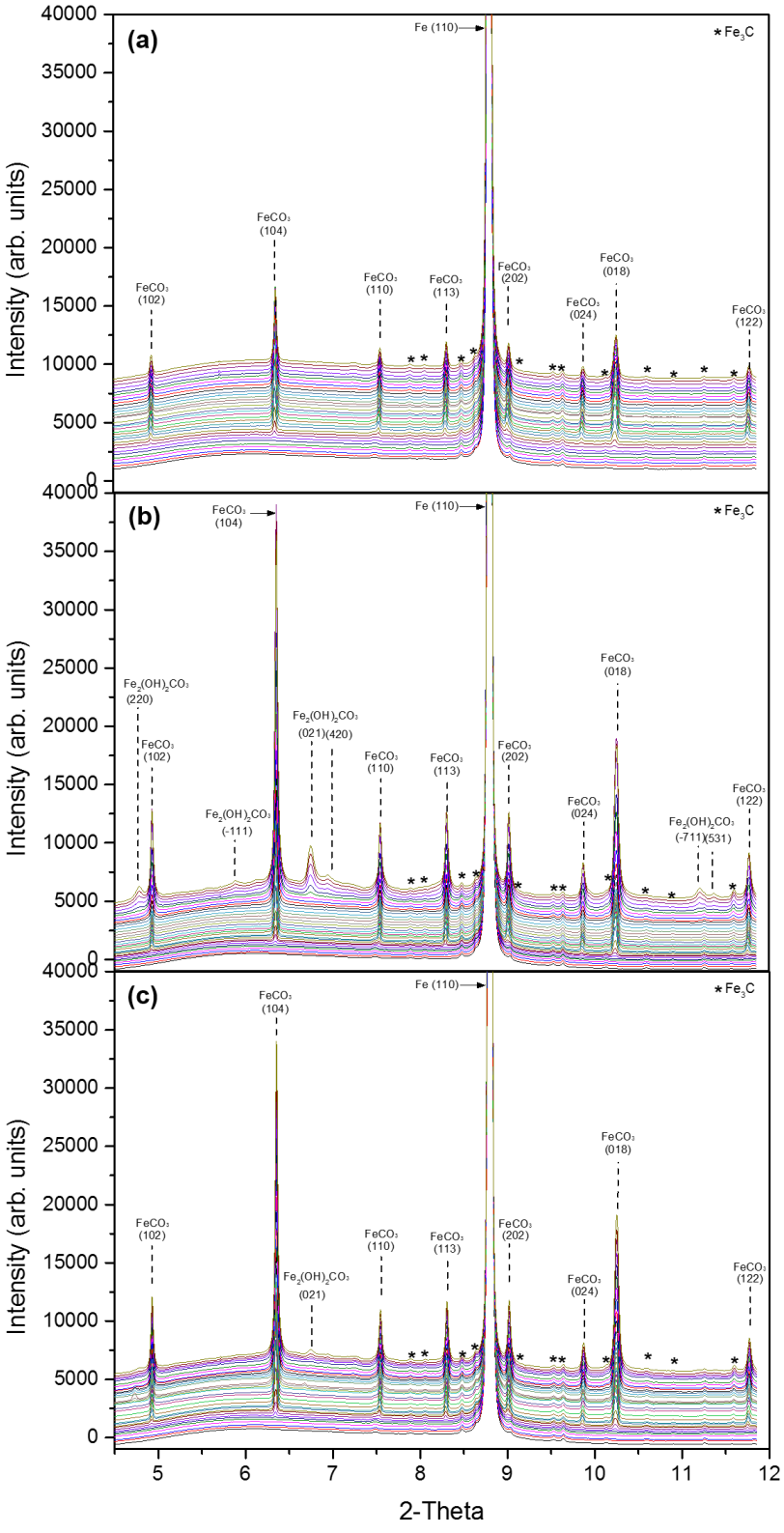

Figure 8.8. *In-situ* diffraction patterns recorded as a function of time conducted at 80°C, 3.5 wt.% NaCl, 0.54 bar p_{CO_2} and 0.1 m/s at pH 7 under potentiostatic control: a) scanned location 1; b) scanned location 2; and c) scanned location 3.

Another minor un-identified phase was detected at each of the locations and was detected early on in the tests and was present for the remainder of the test. Due to the lack of peaks present, the composition of this phase remains unclear. The peak could correlate to a combination of two $Fe_2(OH)_2CO_3$ planes ((021) and (420)) or a combination of the remaining two $CaCO_3$ polymorphs (aragonite and vaterite – lattice planes (111) and (110) respectively). Although this scenario is less likely because the expected locations for these peaks using 40 KeV radiation would be ~6.55° (aragonite (111)) and ~6.51° (vaterite (110)) 2θ.

The *in-situ* SR-XRD patterns over the duration of the test at pH 7 reveal the same 7 lattice planes of $FeCO_3$ ((104), (110), (113), (202), (204), (018) and (122)) with an additional plane located at 4.80° (012) 2θ as shown in Figure 8.8(a-c). All of the three locations scanned in this test also exhibit different phases to have formed. $Fe_2(OH)_2CO_3$ was detected to form towards the end of the experiments at locations 2 Figure 8.8(b) and 3 Figure 8.8(c), whilst only $FeCO_3$ was detected at location 1 Figure 8.8(a).

8.3.2.2 Growth Kinetics of the Films Formed under Potentiostatic Control at Different pH Values

The growth kinetics and orientation of the $FeCO_3$ crystals varied throughout the tests and Figures 8.9, 8.10 and 8.11 shows the growth kinetics of each crystalline phase to nucleate and grow and the preferred orientation of the crystals (the most dominant crystal plane). Each test shows diversity for a number of reasons, with different phases/planes dominating the process and different times across the scanned regions of the samples. At pH 6.3 (Figure 8.9), among the formed $FeCO_3$ crystal planes to emerge across the sample, the most intense was observed at 2θ=~6.35º corresponding to the (104) plane.

It is evident that the crystal plane (104) had the fastest induction time and was the most dominant face during the nucleation and crystal growth stage at each of the scanned locations. The $FeCO_3$ crystal plane (018/116) which seems to be a combination of the (018) and (116) planes was the second most dominant plane at this location which inhibited the growth of the (104) crystal plane in this instance, and any other plane in fact.

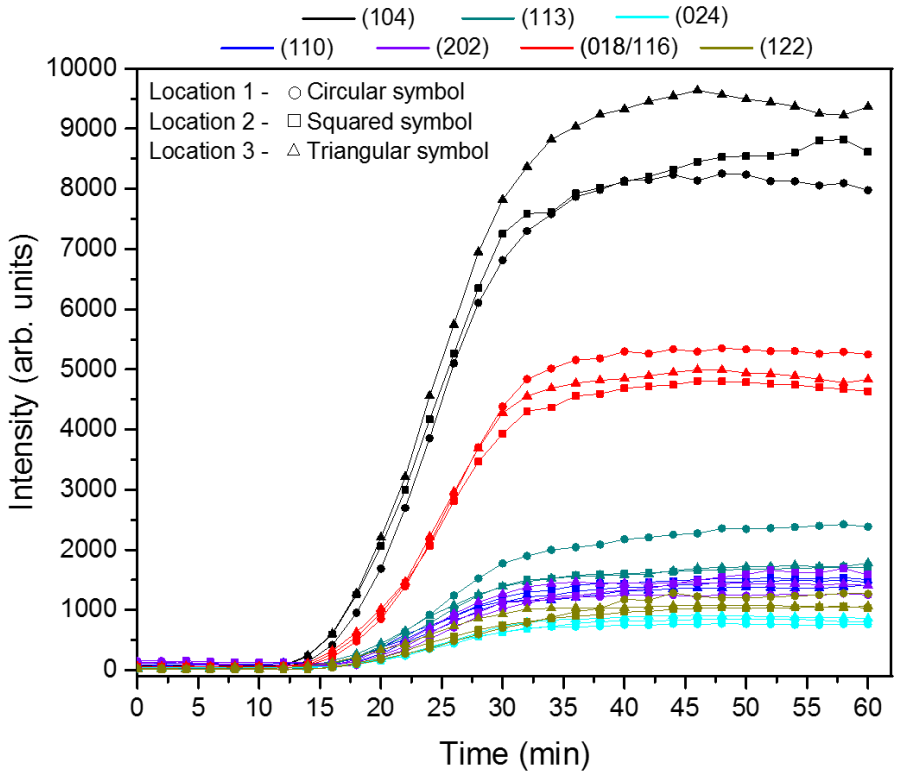

Figure 8.9. Growth of the $FeCO_3$ crystal planes intensities over time at each of the locations scanned across the surface conducted at 80°C, 3.5 wt.% NaCl, 0.54 bar p_{CO_2} and 0.1 m/s at pH 6.3 under potentiostatic control.

The $FeCO_3$ crystal plane (018/116) which seems to be a combination of the (018) and (116) planes was the second most dominant. Following these two planes, the remaining planes that emerged shows extremely uniform growth characteristics across the sample which is ultimately a result of such a high local supersaturation in the boundary layer at the interface due constant replenishment of Fe^{2+} production.

At pH 6.8, the most intense $FeCO_3$ peak was observed at 2θ=~10.25º corresponding to the (018) and (116) planes as shown in Figure 8.10(a). This is unlike anything else observed in the SR-XRD tests, and the $FeCO_3$ (104) plane would be expected to dominate the growth rate of the crystals, especially at such a high local saturation ratios. This unexpected preferred orientation of $FeCO_3$ is most likely due to the system being contaminated with $CaCO_3$. The most intense $CaCO_3$ plane is also the (104) and the crystal system is very similar to $FeCO_3$.

The growth kinetics of the detected calcite planes are shown in Figure 8.10(b) (calcite planes are only observed at location 3).

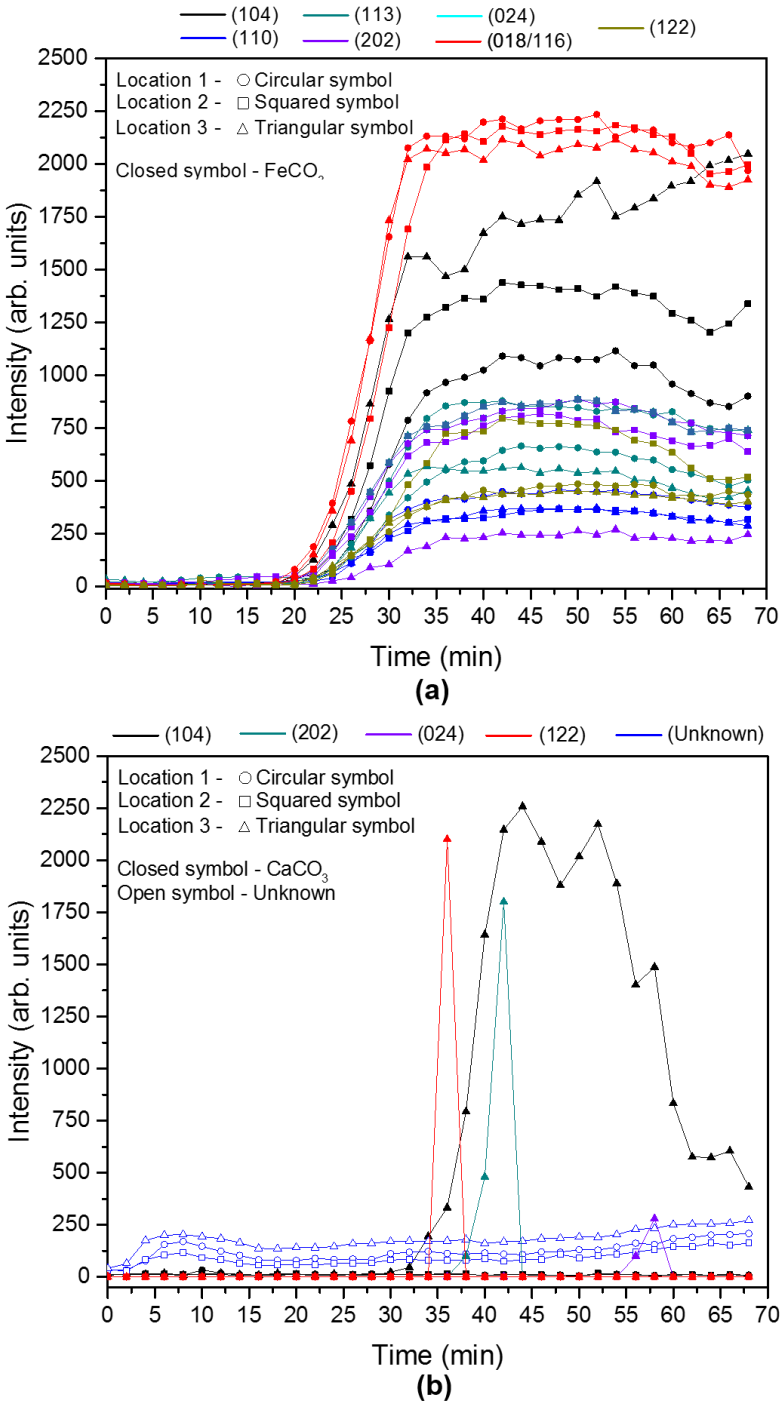

Figure 8.10. Growth of the $FeCO_3$ (a) and $CaCO_3$/unknown (b) crystal planes intensities over time at each of the locations scanned across the surface conducted at 80°C, 3.5 wt.% NaCl, 0.54 bar p_{CO_2} and 0.1 m/s at pH 6.8 under potentiostatic control.

The growth of the calcite crystals are clearly very unstable with three of the detected planes ((202), (024) and (122)) appearing for a short intervals and then disappearing within one or two scans. Also, the most intense calcite plane (104) is showing unstable characteristics with the intensity initially increasing exponentially after 32 minutes, then deceasing slightly followed by another increase and then finally dropping rapidly after 52 minutes.

In conjunction with this behaviour, the $FeCO_3$ (104) plane at location 3 (Figure 8.10(a)) is showing very similar unstable characteristics. This could be an indication that these planes are competing with one and other which at the same time, hinders the growth of each plane. However, the system is influenced to favour the formation of $FeCO_3$ and the presence of Ca^{2+} is an artefact and therefore the supersaturation is greater in respect to $FeCO_3$. After 52 minutes when the $CaCO_3$ (104) plane diminishes, the $FeCO_3$ (104) plane eventually dominates the growth which is observed by a more steady increase in intensity (also after 52 minutes).

At this point, the supersaturation is far greater for $FeCO_3$ resulting in either of the possible two outcomes:

1) The dissolution of the $CaCO_3$ crystals; or

2) The Ca^{2+} atoms have integrated in the $FeCO_3$ crystal lattice system creating a new $Fe_2Ca_xCO_3$ phase [140].

Both of these possible outcomes could also explain the short appearance of the other $CaCO_3$ planes that were detected. This competition between the major $FeCO_3$ and $CaCO_3$ crystal planes has given rise to other planes which now dominate the growth. The presence of another unknown phase at all three of the scanned locations could also hinder the formation of the $FeCO_3$ crystal planes.

Figure 8.11 shows the growth of the $FeCO_3$ crystal planes over time at each of the locations scanned across the surface during the test at pH 7. Yet again, it is evident that the $FecO_3$ crystal plane (104) was the most dominant face during the nucleation and crystal growth of $FeCO_3$.

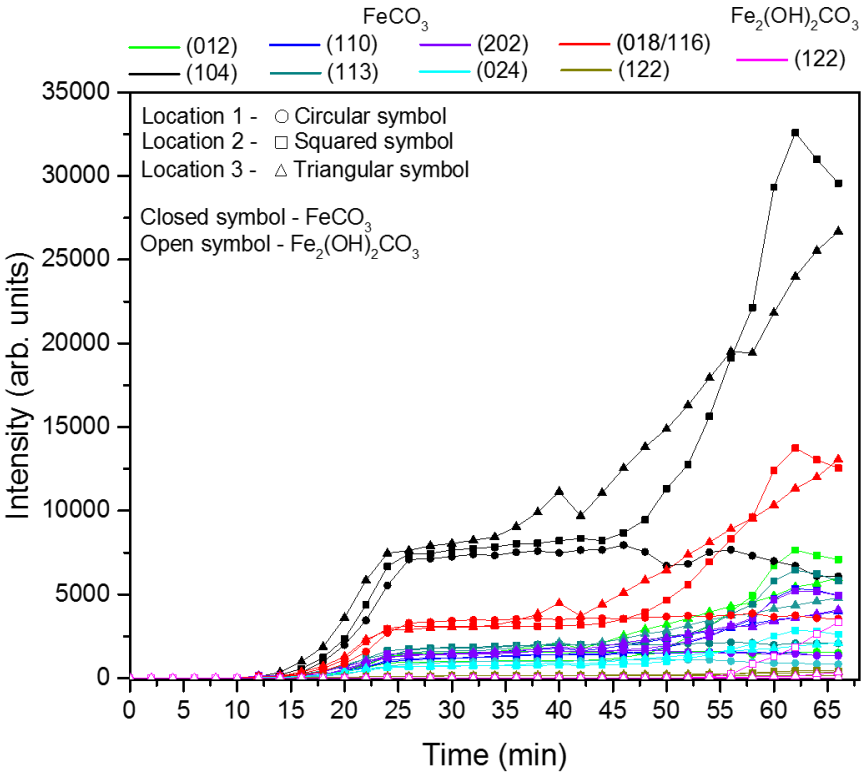

Figure 8.11. Growth of the $FeCO_3$ and $Fe_2(OH)_2CO_3$ crystal planes intensities over time at each of the locations scanned across the surface conducted at 80°C, 3.5 wt.% NaCl, 0.54 bar p_{CO_2} and 0.1 m/s at pH 7 under potentiostatic control.

The $FeCO_3$ crystal plane (104) repressed any substantial growth of the remaining 7 crystal planes detected throughout the test and shows an encouraging growth trend with very similar characteristics indicating heterogeneous growth across the surface for the first 25 minutes where a plateau in the intensity (and growth) is reached. The growth rate of the crystals are extremely stable and uniform across the majority of the surface at this stage. However, at locations 2 and 3, a further substantial increase in the growth rate is observed after some time. This is most likely due to a build-up of Fe^{2+} beneath the ultra-protective $FeCO_3$ crystals. This constantly production of Fe^{2+} at the steel interface will eventually be too much for the $FeCO_3$ film to withstand resulting in the film detaching from the steel surface and cracks propagating providing an exit route for the vast amount of Fe^{2+} generated. This was confirmed by SEM analysis and will be discussed further in the following section of this chapter. After some time, traces of $Fe_2(OH)_2CO_3$ was detected which could be a result of the excess of Fe^{2+} generated at the interface which are now being released through cracks in the $FeCO_3$ film. At this point, at

location one, the growth of $FeCO_3$ is now retarded once again but most likely due to the conditions being in favour of $Fe_2(OH)_2CO_3$ formation.

8.3.2.3 Growth Kinetics Coupled with Electrochemical Observations of the Films Formed under Potentiostatic Control at Different pH Values

In-situ SR-XRD and current density measurements over time are plotted for each pH in Figure 8.12 (a-c) showing the kinetics of the $FeCO_3$ crystal growth in the form of the average of the accumulative intensity from all three locations providing an average over the steel surface and can be compared with the electrochemical response from steel surface.

Figure 8.12 (a) refers to the kinetics of $FeCO_3$ formation for pH 6.3. The induction time for $FeCO_3$ is 14 minutes, which corresponds with a rapid increase in current density to ~ 12.5 mA/cm^2 (at this point, the accumulated measured $FeCO_3$ (104) intensity was ~ 4000 (arb.units)) which then dropped again to ~7 mA/cm^2 after 32 minutes. This drop in current density was in line with a decrease in $FeCO_3$ crystal growth until the growth eventually stopped completely at ~9000 (arb.units).The current density began to increase gradually in the transpassive region (after 'pseudo-passivation') due to the local breakdown and $FeCO_3$ film and the separation of such film from the steel interface. At this point, it can be assumed that the system has reached the critical supersaturation required for further $FeCO_3$ nucleation and growth.

A further increase in system pH to 7 resulted in even more substantial levels of $FeCO_3$ precipitation occurring earlier in the experiment with an increased nucleation and crystal growth rate. This was attributed the solubility of $FeCO_3$ being further reduced due to the increased pH. This increase in growth rate of $FeCO_3$ crystals offered enhanced protection against corrosion to the steel surface. The *in-situ* SR-XRD and current density measurements are shown in Figures 8.12 (b). After the induction time (12 minutes), the major $FeCO_3$ peak intensity begins to increase due to the crystals forming on the steel surface through heterogeneous nucleation which similarly resulted in a further increase in current density to ~6.6 mA/cm^2 and an average measured $FeCO_3$ intensity of ~1000 (arb.units). after 17 minutes.

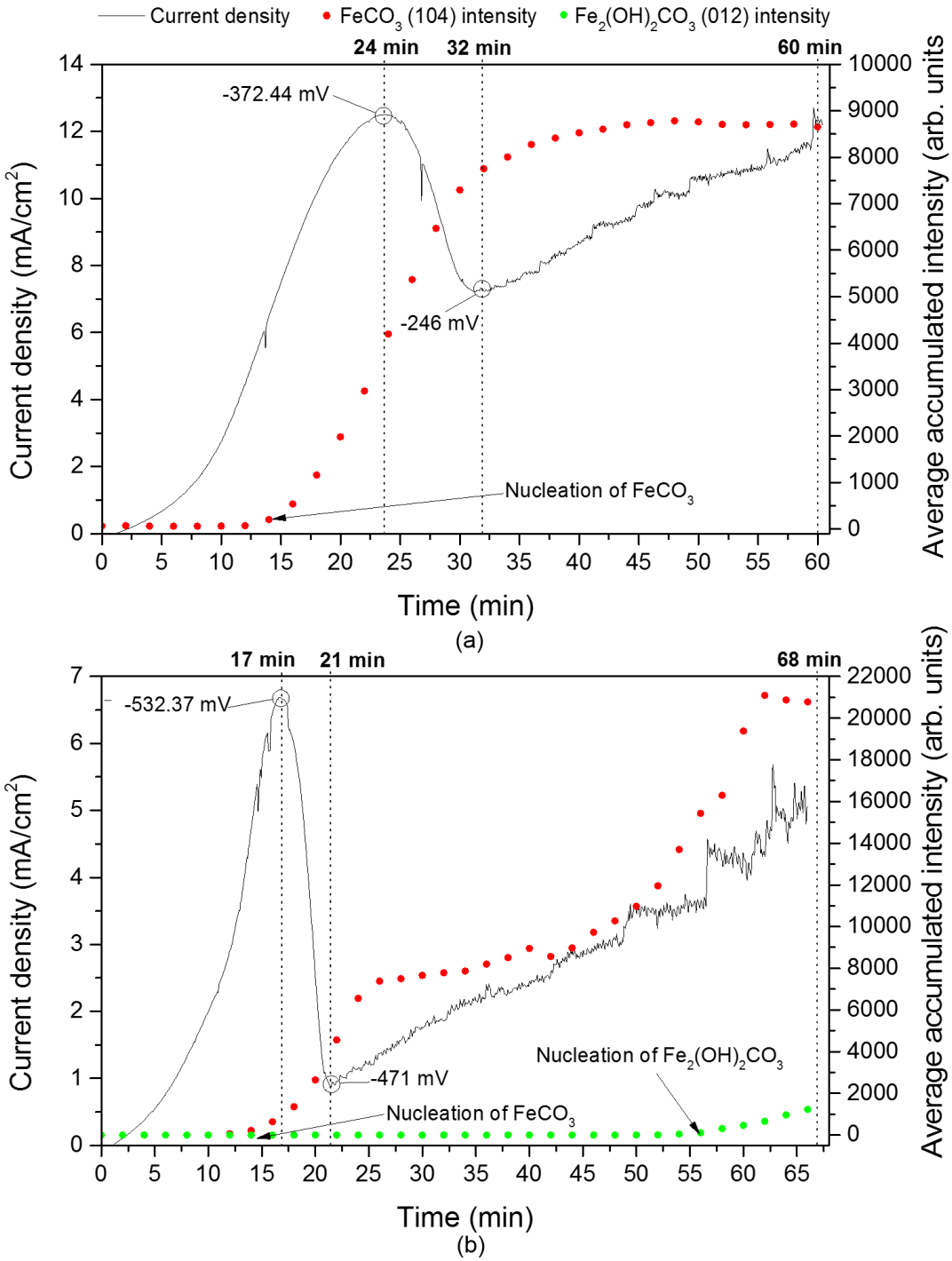

Figure 8.12. *In-situ* data recorded over time for each test showing current density and integrated diffraction intensities for the most dominant $FeCO_3$ and $Fe_2(OH)_2CO_3$ crystal planes for each of the 3 scans performed over a 2 mm line scan on each sample conducted at 80°C, 3.5 wt.% NaCl, 0.54 bar p_{CO_2} and 0.1 m/s at pH 7 under potentiostatic control: a) pH 6.3; and (b) pH 7.

The current density then rapidly dropped to <1 mA/cm^2 after a further 4 minutes of $FeCO_3$ crystal growth which effectively doubled in this time which indicates that a layer of extremely small crystals are offering such enhanced protection to the steel surface. However, the constant production of Fe^{2+} beneath the $FeCO_3$ layer makes it difficult for the crystals to fully adhere to steel surface allowing more $FeCO_3$ to precipitate which is indicated by the further growth. Then, after 25 minutes the growth rate of $FeCO_3$ reaches a plateau (with a measure intensity of ~7000 (arb.units)) until the layer gives way to cracks and the growth rate increases rapidly again after 45 minutes to a measured intensity of ~20000 (arb.units). The electrochemical response in this transpassive region is now very noisy which can be a result of pitting or most likely an unstable film (which could also result in pitting). Due to such high amounts of Fe^{2+} now leaving the surface interface (due to cracks in the $FeCO_3$ layer), the kinetics become more favourable for $Fe_2(OH)_2CO_3$ and the resulting growth of $FeCO_3$ reduces again. This will be explored in greater detail in Chapter 9.

From the average accumulated measured intensity in Figure 8.12, from both tests, three steps characterise the growth mechanism: (1) An induction time when the measured intensity is zero; (2) Nucleation of the $FeCO_3$ crystals; (3) Nucleation-growth stage which is characterised by an increase of the growth according two different regimes; the growth rate first linearly increases and then slows down towards the end of the experiment.

8.3.2.4 Morphology of the Crystals under Potentiostatic Control at Different pH Values

Figure 8.13 shows a comparison of the *ex-situ* SEM images of the top surface of the crystals formed following the synchrotron potentiostatic controlled tests at each pH. Under potentiostatic control, the crystals consisted of extremely compact nano-crystals that appear to look like large prisms (at pH 6.3 and 6.8 x3000) or spheres (at pH 7 x3000) before magnifying the images to reveal the true nature of the morphologies. Observation of the crystal morphologies at a higher magnification reveal the larger prism and sphere shapes are actually made up of high quantities of nano-sized crystals. The SEM images across the surface also revealed an inner layer of highly compact tiny crystals and a diffuse outer layer of much larger bundles of the same crystals.

The morphologies in these images are notably different from the cubic/rhombohedral crystals observed at OCP in previously (Chapter 7) in the same test environments. This is most likely due to the faster formation of the $FeCO_3$ crystals under potentiostatic control compared to the open-circuit tests. The crystals formed at higher pH generally look smaller and more compact, with the exception of pH 6.8 (due to contamination of the system), which also supports the earlier notion that the crystals formed at higher pH are more protective than those formed at lower pH.

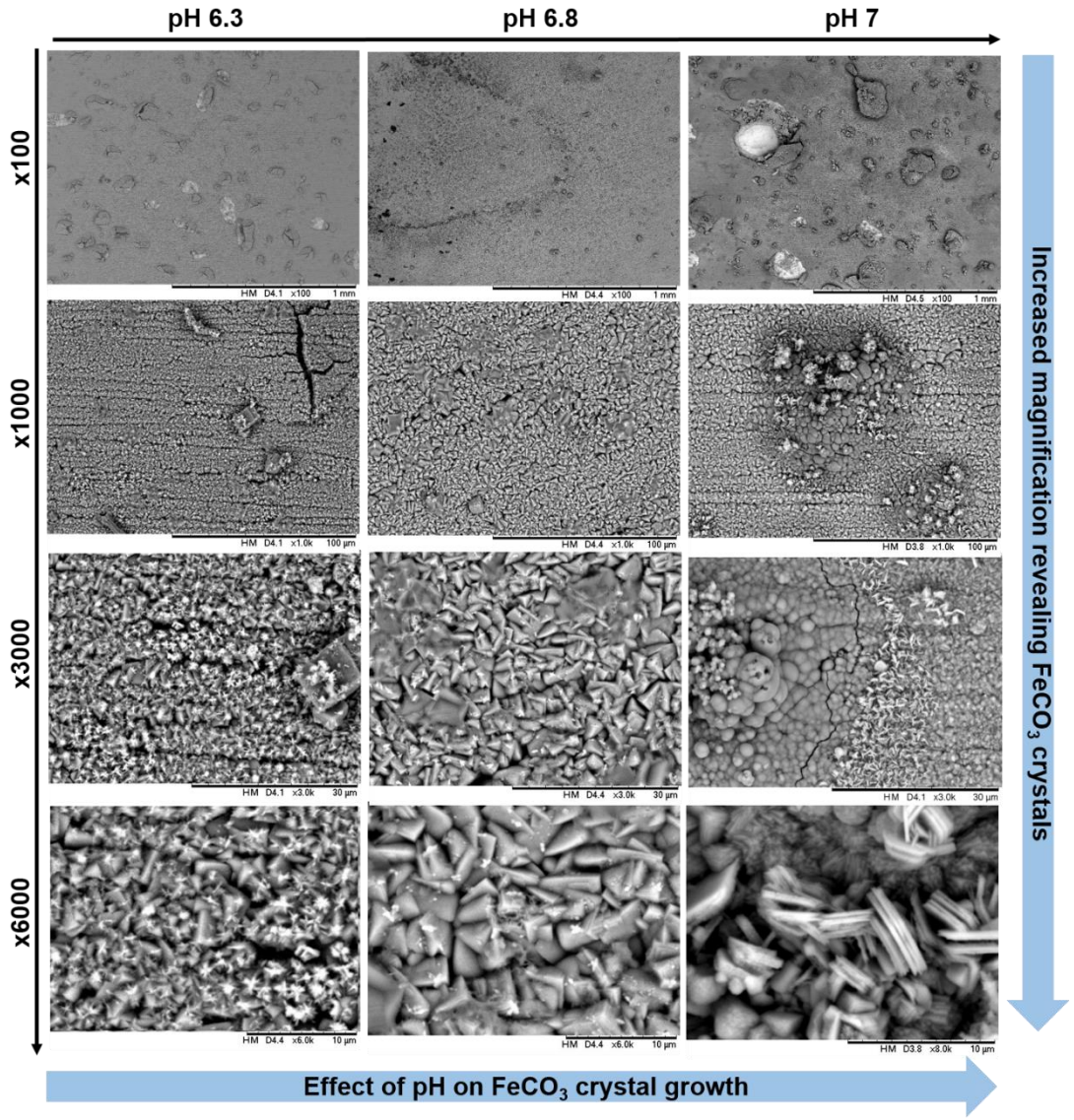

Figure 8.13. The effect of pH on the development and morphology of $FeCO_3$ crystals over time conducted at 80°C, 3.5 wt.% NaCl, 0.54 bar p_{CO_2} and 0.1 m/s at pH 6.3, 6.8 and 7 under potentiostatic control.

There are also some cracks in the film, which seem to be a result of an overload in Fe^{2+} production at the steel interface beneath the protective $FeCO_3$ layers. At pH 7, the SEM image at a magnification of x3000 and x6000 also reveal a number type of crystal morphology consisting of larger plate-like crystals which exhibit a change in contrast in comparison to the $FeCO_3$ crystals. This new crystal morphology is consistent with the *in-situ* SR-XRD data as it appears to have formed on top of the $FeCO_3$ crystals and therefore has been concluded to be $Fe_2(OH)_2CO_3$. The presence of $Fe_2(OH)_2CO_3$ and the crystals morphology was further investigated *ex-situ* through SEM/FIB analysis shown in Figure 8.14 (a-d).

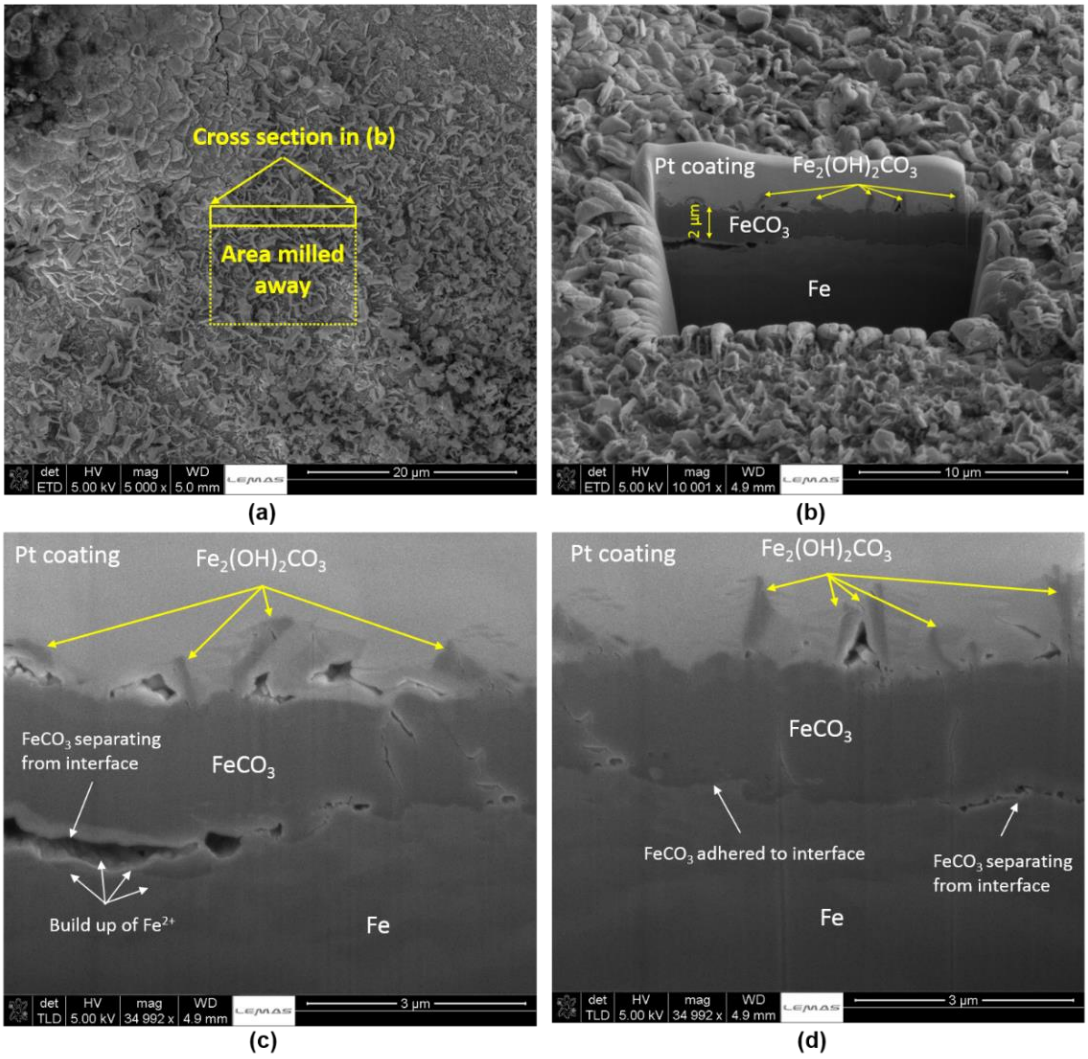

Figure 8.14. *Ex-situ* SEM images of the X65 carbon steel surface at the end of the test showing the cross-sections of the films formed at 80°C, 3.5 wt.% NaCl, 0.54 bar p_{CO_2} and 0.1 m/s at pH 7 under potentiostatic control.

The crystals associated with the plate-like morphology $Fe_2(OH)_2CO_3$ which is consistent with microscopy of the authentic mineral [4, 73]. From the cross sections in Figures 8.14 (b), (c) and (d), the $Fe_2(OH)_2CO_3$ crystals appear to be standing vertically on top of the $FeCO_3$ layer assuming no added protection is offered through the presence of this phase. Therefore, the overall protection of the system is solely down to formation of $FeCO_3$. In this case, from Figure 8.14 (d), the $FeCO_3$ layer seems to be extremely well attached to the steel interface, however, the layer seems to have separated considerably with voids being present between the steel surface and the $FeCO_3$ layer in both Figures 8.14 (c) and (d). This is most likely, a result of the continued production of Fe^{2+} at the interface. Hence, from the results in this work, it is suggested that an excess Fe^{2+} ions in the boundary layer, though increasing the applied potentials, promoted the formation of $Fe_2(OH)_2CO_3$ which could be a result of the excess of Fe^{2+} generated at the interface which are now being released through cracks in the $FeCO_3$ film.

Further evidence of such theory is shown in Figure 8.14 which is the same sample shown in Figure 8.15 taken from a different location on the surface. Focusing on the top view of the morphology in Figure 8.15 (a) of the whole sample at x32 magnification, there appears to be raised islands built of nano-$FeCO_3$ crystals randomly scattered across the surface. However, after cutting into the sample, through one of these islands as shown in Figure 8.15 (b), interestingly, the raised crystals appeared to be a result of the film entirely separating from the carbon steel substrate which is most likely a result of the shear force generated from high flux concentrations of Fe^{2+} building up causing such voids as shown in Figures 8.15 (c) and (d).

The cross section was later removed for FIB analysis which confirmed the presence of only $FeCO_3$ here (again agreeing that $FeCO_3$ alone was responsible for the pseudo-passive behaviour). After thinning the cross section, the TEM images (Figures 8.15 (e) and (f)) reveal further cracks within the film. These images also show that the overall thickness (of up to 5 μm) is made up of finer nano-crystalline layers.

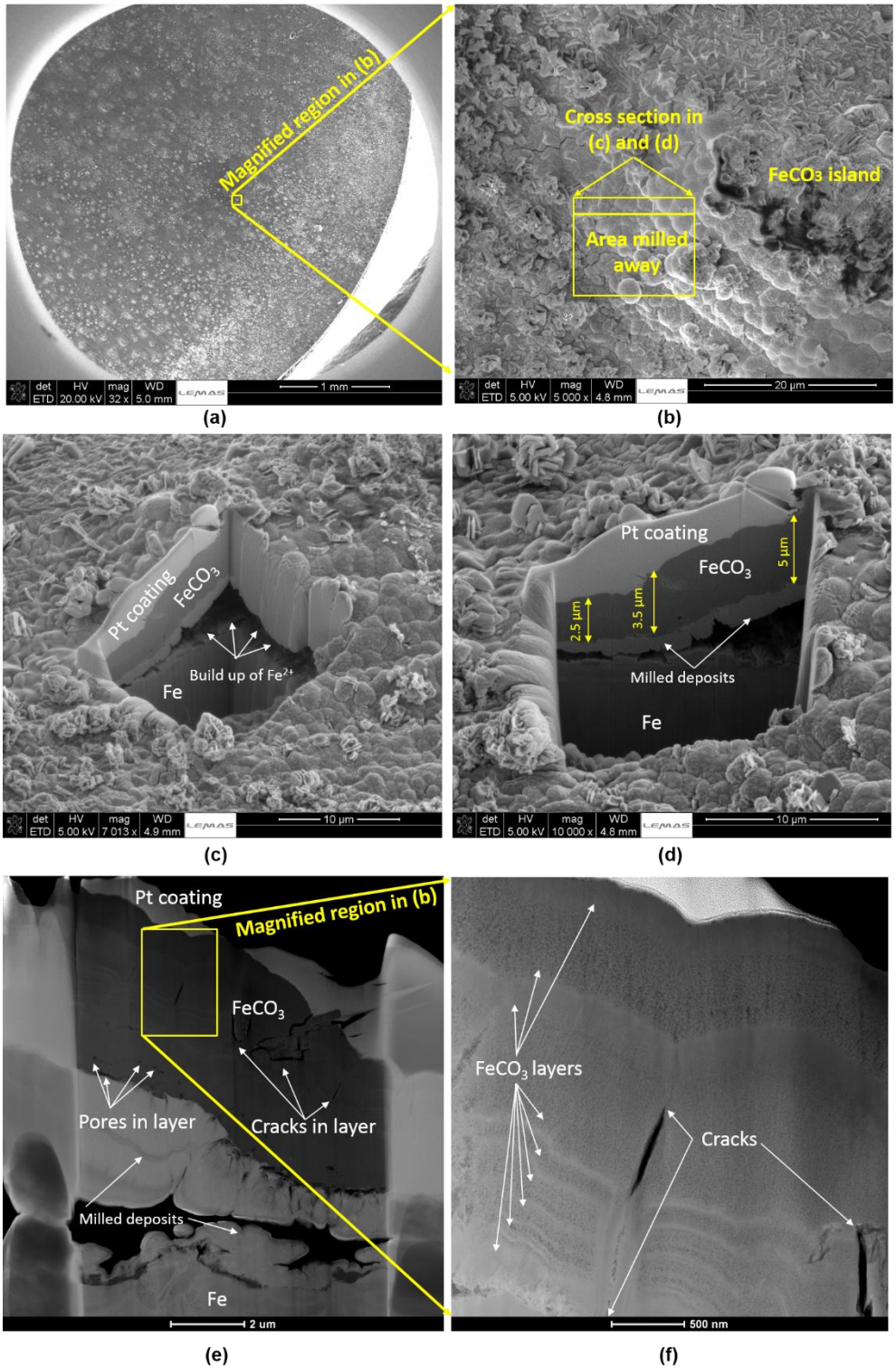

Figure 8.15. *Ex-situ* SEM images of the X65 carbon steel surface at the end of the test showing the cross-sections of the films formed at 80°C, 3.5 wt.% NaCl, 0.54 bar p_{CO_2} and 0.1 m/s at pH 7 under potentiostatic control.

8.3.4. *In-situ* SR-XRD Potentiostatic Driven Anodic Polarisation Tests: Effect of Flow Velocity on 'pseudo-passivation'

The kinetics of $FeCO_3$ crystal growth are assessed at different flow velocities at pH 6.8, 80°C and in a 3.5 wt. % NaCl brine saturated with CO_2. The flow velocities evaluated in this section are 0.5 and 1 m/s. Originally, the test at 0.1 m/s was to be compared also, but due to the contamination of Ca^{2+} in to the system, the results in that test are inconclusive and the true nature of $FeCO_3$ crystal growth was not determined and therefore will not be included in this section.

The results in Chapter 7 concluded that higher flow velocities delay the formation of a protective $FeCO_3$ crystals and therefore should also delay the formation of an ultra-protective pseudo-passive layer under anodic polarisation.

8.4.2.1 Composition of the Films Formed using *In-Situ* SR-XRD

SR-XRD patterns recorded *in-situ* over time during the experiments at different flow velocities are shown in Figure 8.16 (a) and (b). These images show that $FeCO_3$ was the primary phase formed in all conditions and the only new crystalline phase detected on the steel surface with the addition of Fe and Fe_3C prior to running the tests. At 0.5 m/s (Figure 8.16 (a)), the pattern reveals 7 detected lattice planes of $FeCO_3$ ((104), (110), (113), (202), (204), (018) and (122)), whilst at 1 m/s (Figure 8.16 (b), the pattern reveals 8 detected lattice planes of $FeCO_3$ ((104), (110), (113), (202), (204), (018) and (122)) with the addition of the (012) plane.

The results in these tests revealed that the growth rate across the sample was extremely uniform showing heterogeneous characteristics throughout with the $FeCO_3$ (104) plane dominating the growth kinetics at all three locations scanned and therefore only this plane will be displayed when assessing the growth kinetics at different flow velocities.

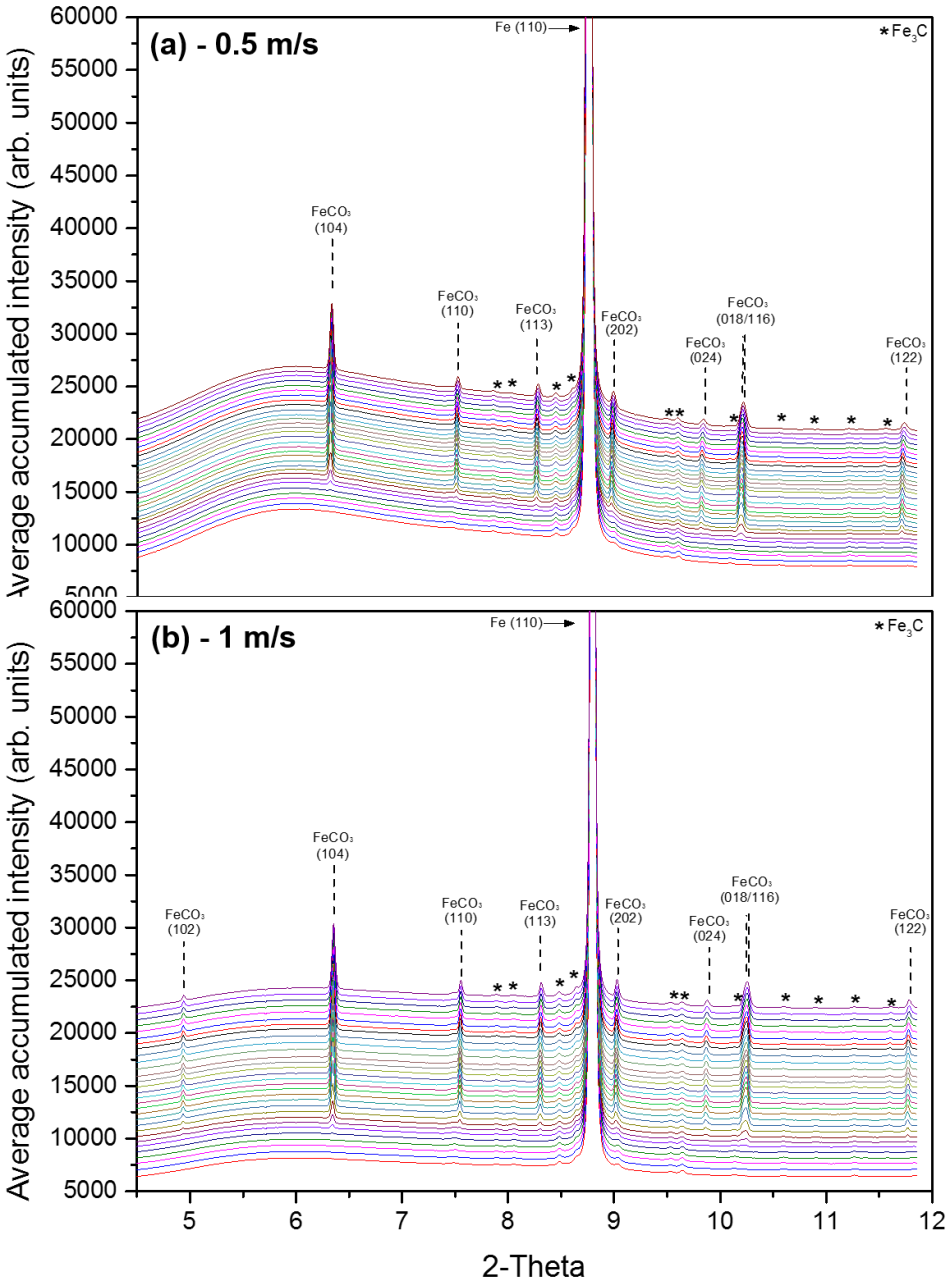

Figure 8.16. *In-situ* diffraction patterns recorded as a function of time at pH 6.8: a) 0.5 m/s 1; b) 1 m/s conducted at 80°C, 3.5 wt.% NaCl, 0.54 bar p_{CO_2} and 0.1 m/s at pH 7 under potentiostatic control.

8.4.2.2 Growth Kinetics and Morphology of the Films Formed Under Potentiostatic Control at Different Flow Velocities

The current density responses to the potentiostatic polarisation and corresponding $FeCO_3$ growth kinetics at flow velocities of 0.5 and 1 m/s at a pH 6.8 and 80°C are shown in Figure 8.17.

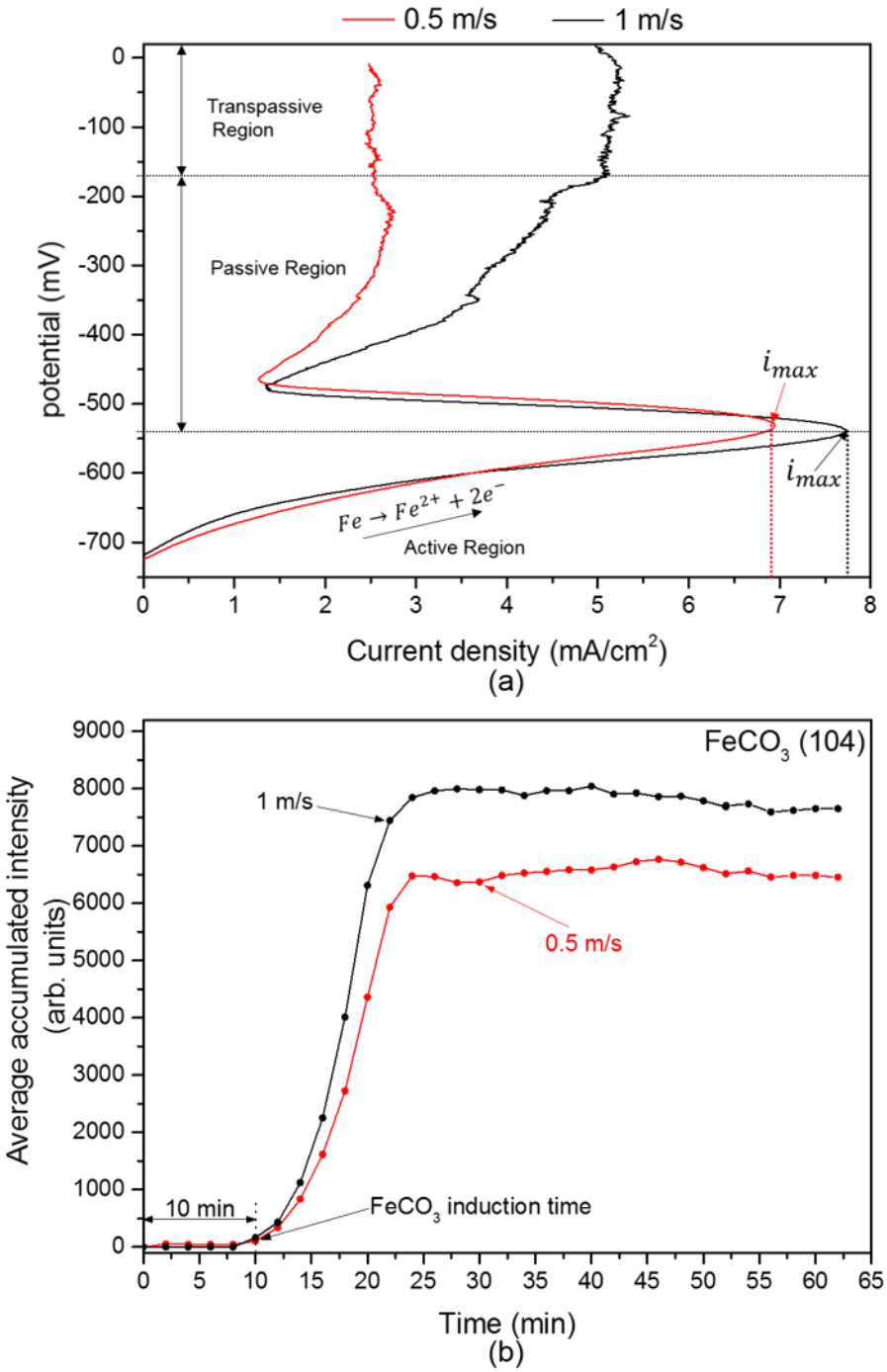

Figure 8.17. *In-situ* data recorded over time for each test conducted at 80°C, 3.5 wt.% NaCl and 0.54 bar p_{CO_2} and pH 6.8 at different flow velocity of 0.5 and 1 m/s under potentiostatic control: (a) Current density vs OCP; (b) Integrated diffraction intensities for $FeCO_3$ (104) plane for each of the 3 scans performed over a 2 mm line scan on each sample.

As the flow velocity increased, the current density peak was slightly higher at 1 m/s during the active corrosion stage as the local flux of Fe^{2+} concentration in the boundary layer exceeds the amounts needed for supersaturation and

eventually resulting in the nucleation of $FeCO_3$ crystals after 10 minutes in both tests (Figure 8.17 (a)). Such higher current is most likely due to the impact of mass transfer influencing the species movement to/from the mass transfer boundary layer. As previously explained, an increase in fluid velocity can increase the transport of the cathodic reaction species H^+ from the bulk solution to the surface**.** The increase in fluid velocity increases the mass transfer of H^+ ions to the surface to proceed the reduction reaction, and buffering H^+ ion concentration at the surface leading to a reduced local pH at the surface interface and an increased corrosion rate**.**

Upon the observed peak in current density, once the $FeCO_3$ crystals are protective enough to reduce the current passing through (and therefore corrosion rate) the current density begins to drop as the protective layer continues to grow as 'protective' crystals covered the surface resulting in less total charge to be passed in the experiment, indicating more efficient formation of the protective crystals. The $FeCO_3$ growth rate reaches a plateau after 24 minutes in both experiments indicating that the layer is dense enough to resist the current passing through it. The initially active surface at both flow velocities showed an exponential rise in potential at similar OCP and current density values showing that flow did not have a huge influence on the 'pseudo-passivation' of the carbon steel due to such high concentrations of Fe^{2+}. The growth rate of the $FeCO_3$ crystals was faster at 1 m/s, despite the induction time being ~ 10 minutes in both cases. The plateau seen in the growth rate of $FeCO_3$ was also observed at similar times but the intensity was lower at 0.5 m/s which indicates that less $FeCO_3$ has formed which also suggests (from the results presented previously) that the $FeCO_3$ crystals are more protective.

Figure 8.18 shows a comparison of the *ex-situ* SEM images of the top surface of the crystals formed following the synchrotron potentiostatic controlled tests at each flow velocity. The top morphology of the crystals appear to look prismatic with smaller and compact crystals integrating between the bigger crystals.

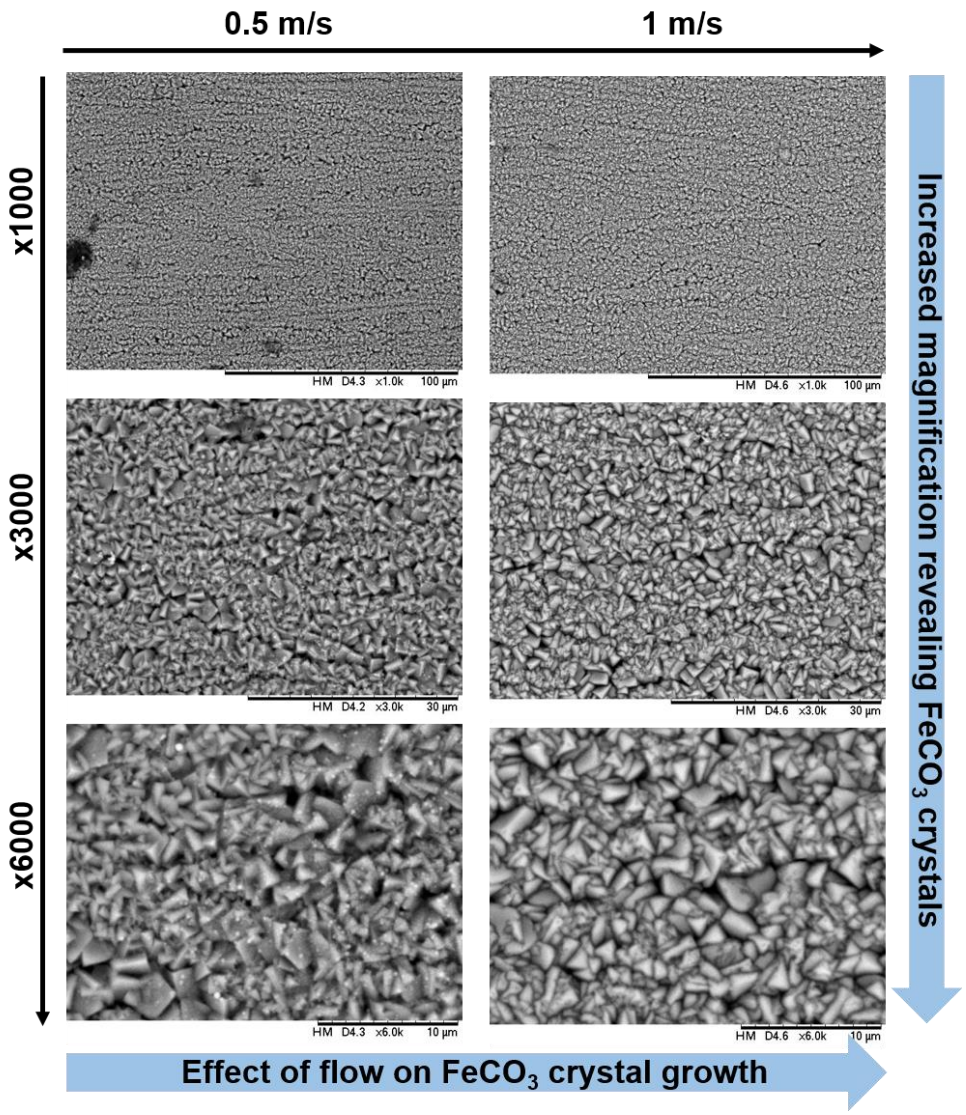

Figure 8.18. The effect of flow velocity on the development and morphology of $FeCO_3$ crystals over time conducted at 80°C, 3.5 wt.% NaCl, 0.54 bar p_{CO_2} and pH 6.8 and flow velocities of 0.5 and 1 m/s under potentiostatic control.

8.4.2.1 Composition and Growth Kinetics of the Films Formed Using *In-situ* SR-XRD: Anodic Polarisation through Galvanostatic Control

A series of anodic polarisation experiments were also conducted under galvanostatic control at 1 mA/cm^2. SR-XRD patterns recorded *in-situ* over time during the experiments at 0.1 and 1 m/s at pH 6.8 and 80°C under the controlled conditions are shown in Figure 8.19 (a) and (b), respectively. These images show that $FeCO_3$ was the primary phase formed in all conditions and the only new crystalline phase detected on the steel surface with the addition of Fe and Fe_3C prior to running the tests. At 0.1 m/s (Figure 8.19 (a)), the pattern reveals 8 detected lattice planes of $FeCO_3$ ((012), (104), (110), (113),

(202), (204), (018) and (122)), whilst at 1 m/s (Figure 8.19 (b), the pattern reveals 7 detected lattice planes of $FeCO_3$ ((104), (110), (113), (202), (204), (018) and (122)).

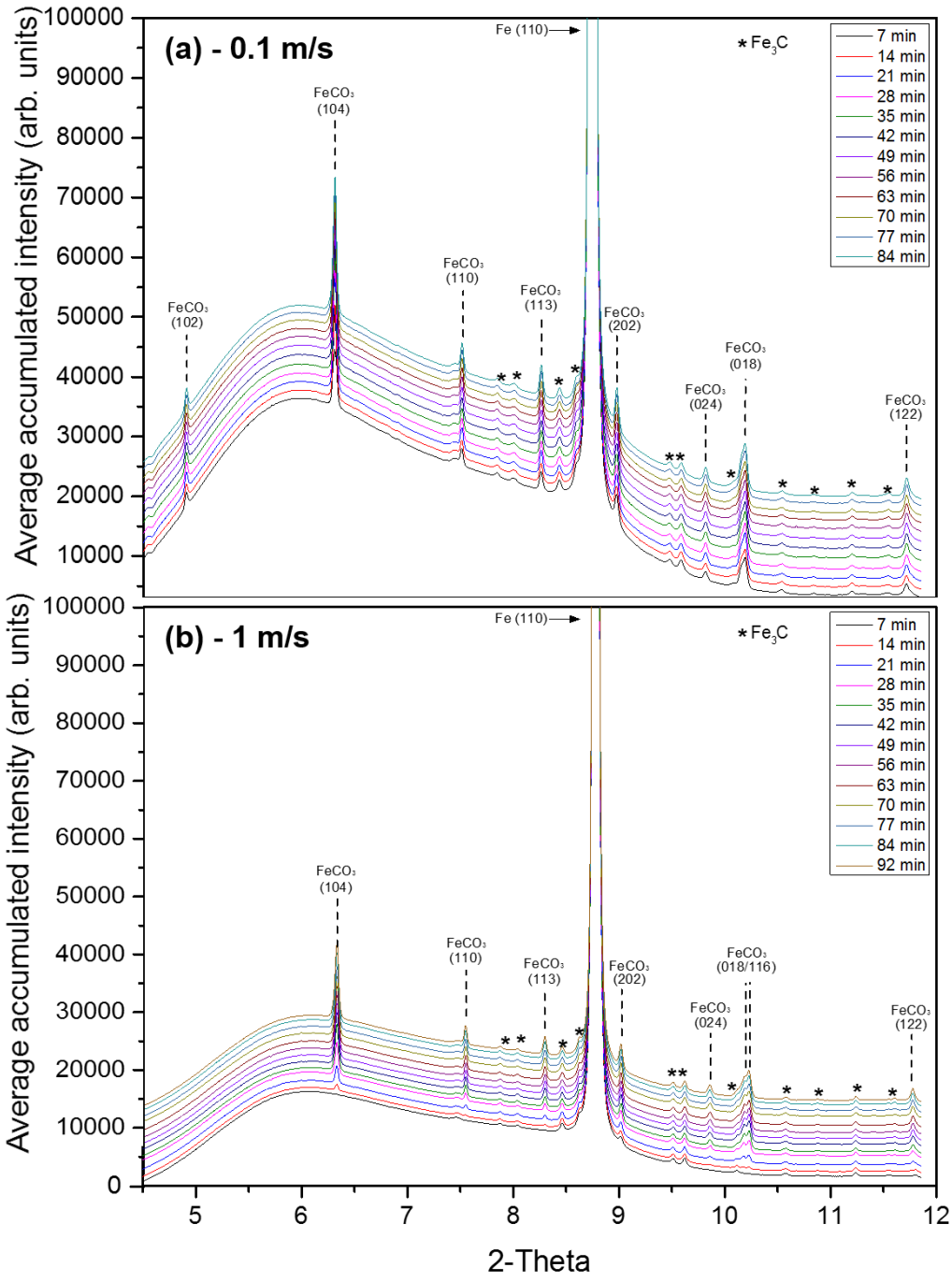

Figure 8.19. *In-situ* diffraction patterns recorded as a function of time at conducted at 80°C, 3.5 wt.% NaCl, 0.54 bar p_{CO_2} and pH 6.8 under galvanostatic control.: a) 0.1 m/s 1; b) 1 m/s.

The results in these tests, yet again revealed that the growth rate across the sample was extremely uniform throughout with the $FeCO_3$ (104) plane dominating the growth kinetics at all locations scanned and therefore only this plane will be displayed when assessing the growth kinetics at different flow velocities.

Figure 8.20 and 8.21 show the growth of the most dominant $FeCO_3$ crystal plane (104) across the surface during both tests at 0.1 and 1 m/s flow velocity. Figure 8.20, at 0.1 m/s flow velocity shows that the induction time for $FeCO_3$ is instantaneous upon applying the X-rays to the surface with $FeCO_3$ being detected at every location during the initial loop of scanning across the surface, other than location 3.

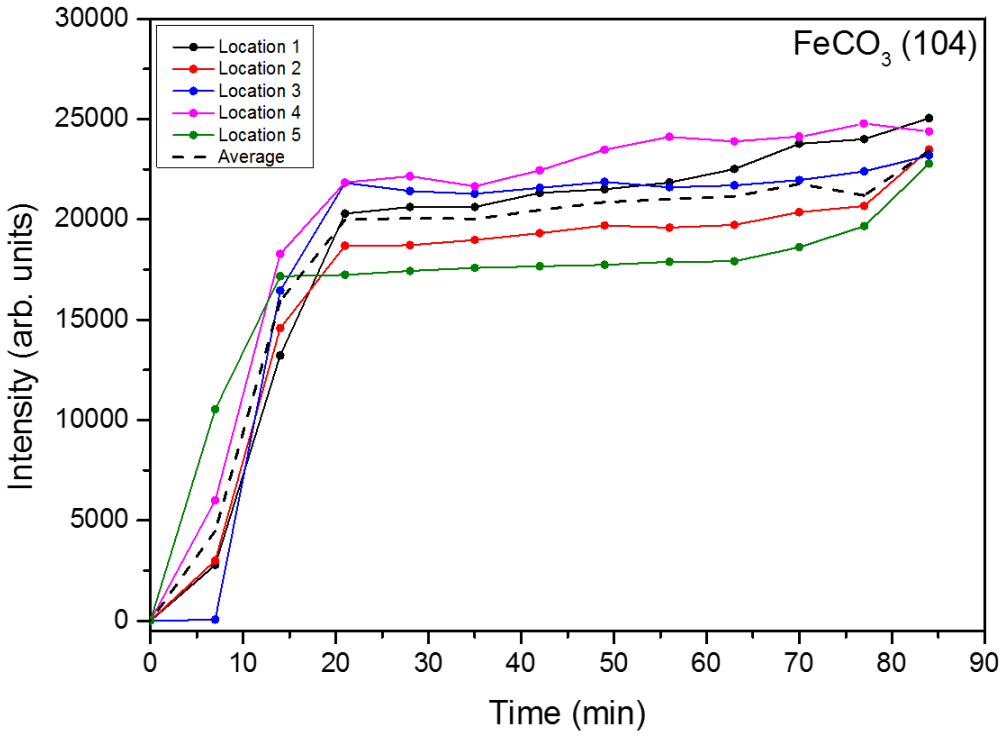

Figure 8.20. Growth of the $FeCO_3$ crystal planes intensities over time at each of the locations scanned across the surface conducted at 80°C, 3.5 wt.% NaCl, 0.54 bar p_{CO_2} and 0.1 m/s at pH 6.8 under galvanostatic control.

The induction time for $FeCO_3$ was within the first 7 minutes with the intensity (and growth rate) rapidly increases by the time the next scan was complete which again shows the importance of scanning multiple locations to better represent the growth kinetics of $FeCO_3$. The intensity and hence the growth rate of the $FeCO_3$ (104) plane then increased exponentially across the surface

for the first 20 minutes until slowing down and reaching a plateau at an intensity of 22000 (arb.units).

Figure 8.21, at 1 m/s flow velocity shows that the induction time for $FeCO_3$ is slightly delayed in comparison to at 0.1 m/s with the induction time for $FeCO_3$ between 7-14 minutes. The growth rate is also slower in comparison to the test at 0.1 m/s, reaching a plateau in $FeCO_3$ intensity after ~35 minutes (with a measured intensity of ~10000 (arb.units)). This growth of $FeCO_3$ is repressed for a further 35 minutes until slowly increasing again after 70 minutes until the end of the test.

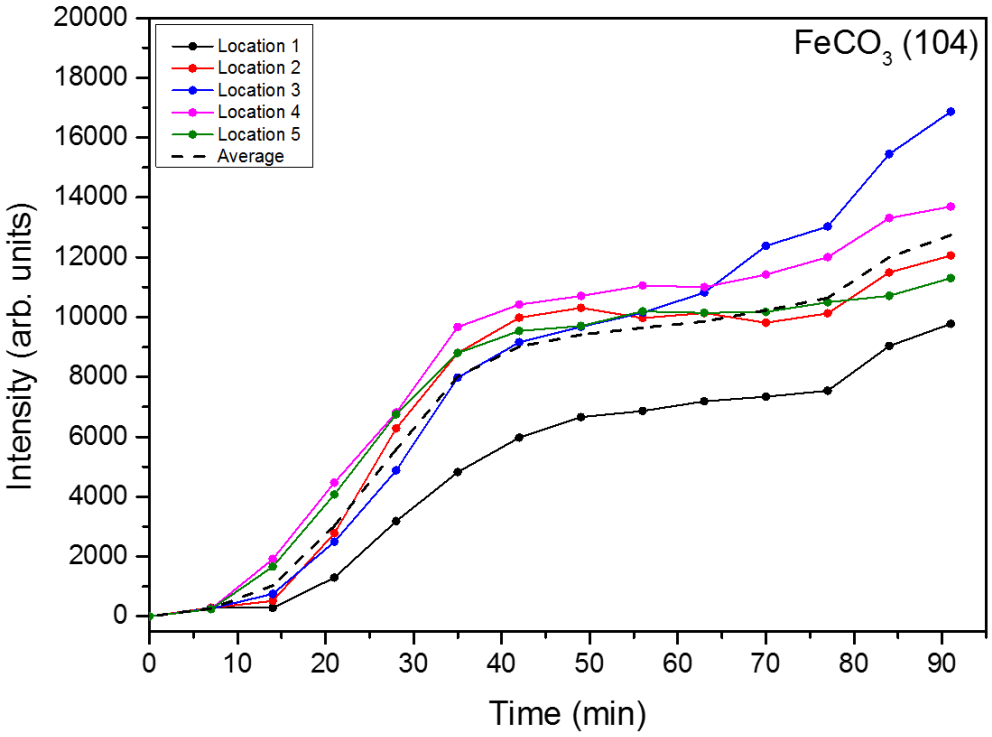

Figure 8.21. Growth of the $FeCO_3$ crystal planes intensities over time at each of the locations scanned across the surface conducted at 80°C, 3.5 wt.% NaCl, 0.54 bar p_{CO_2} and 1 m/s at pH 6.8 under galvanostatic control.

Figures 8.22 (a) and (b) show the plot of the average accumulated $FeCO_3$ (104) plane across the surface of the samples in each of the tests at 0.1 and 1 m/s in conjunction with the electrochemical response of the resulting potential of the system. The potential vs time data in Figures 8.22 (a) and (b) show the same trends as the current-time data from the potentiostatic tests shown previously where the U-shape in the potential trace is the equivalent of the anodic current peak seen in the potentiostatic data. As the external current

of 1 mA/cm^2 was applied, the potential immediately increased to a value governed by the anodic kinetics of the bare steel surface. The potential then decreased relatively slowly due to activation of the anodic reaction taking place simultaneously across the surface releasing a constant flux of Fe^{2+} at the interface for the duration of tests. This constant flux of Fe^{2+} changes the local chemistry and the supersaturation in the boundary layer leading to a rapid $FeCO_3$ induction time with an instant rise in OCP at 0.1 m/s.

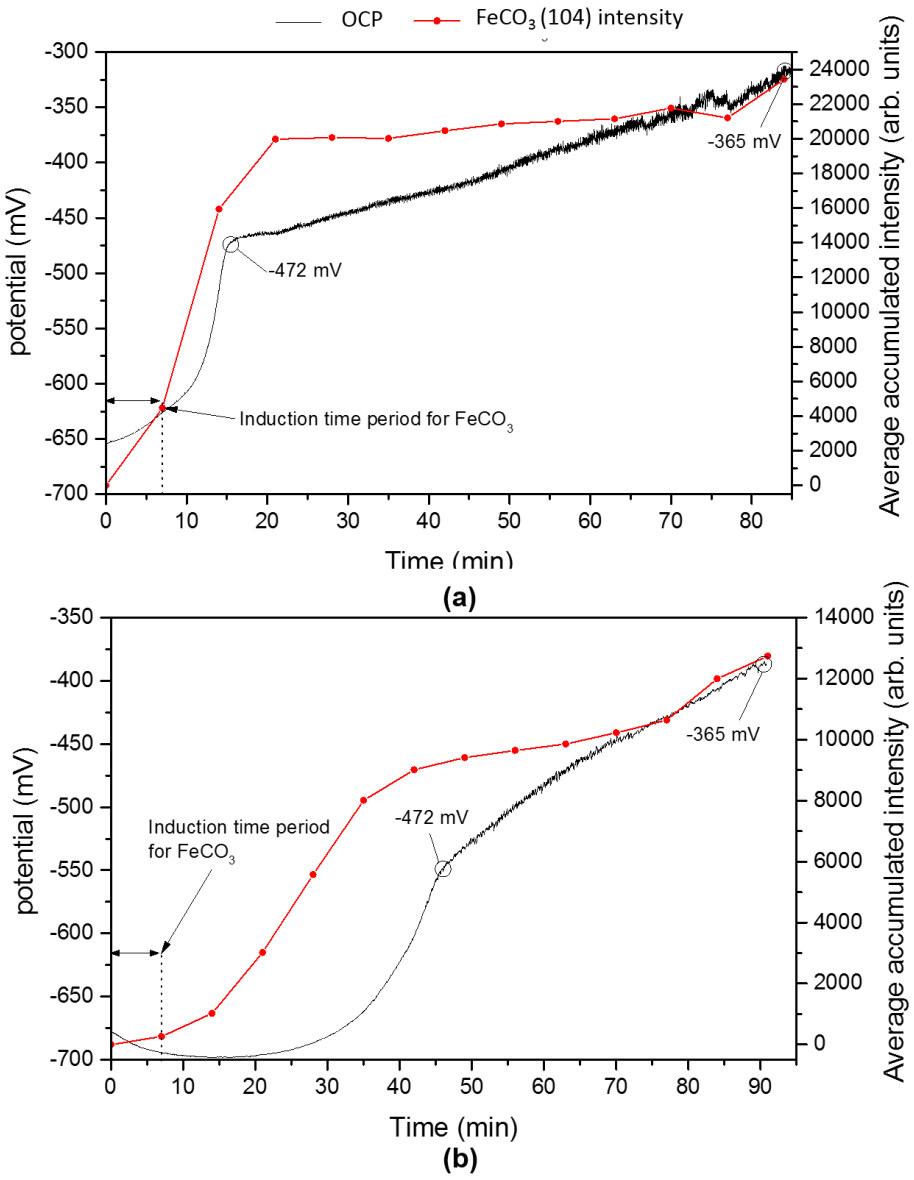

Figure 8.22. Growth of the $FeCO_3$ crystal planes intensities and OCP response over time conducted at 80°C, 3.5 wt.% NaCl, 0.54 bar p_{CO_2} and pH 6.8 under galvanostatic control: a) 0.1 m/s 1; b) 1 m/s.

Once $FeCO_3$ had nucleated, and protective crystals propagated across the surface (indicated through the exponential rise in measured $FeCO_3$ intensity), the polarisation resistance of the carbon steel surface increased such that the over potential required to generate the fixed anodic current must also increase. As the rate of increase in measured potential started to slow down, this indicates that steady-state was approaching. In conjunction with this behaviour, the growth rate of $FeCO_3$ has slowed down as the measured intensity reaches a plateau. At this point, the majority of the anodic current was restricted by the protective $FeCO_3$ crystals and the current was presumed to be passing through cracks formed in the crystals due to the constant overload of Fe^{2+} beneath the $FeCO_3$ layer.

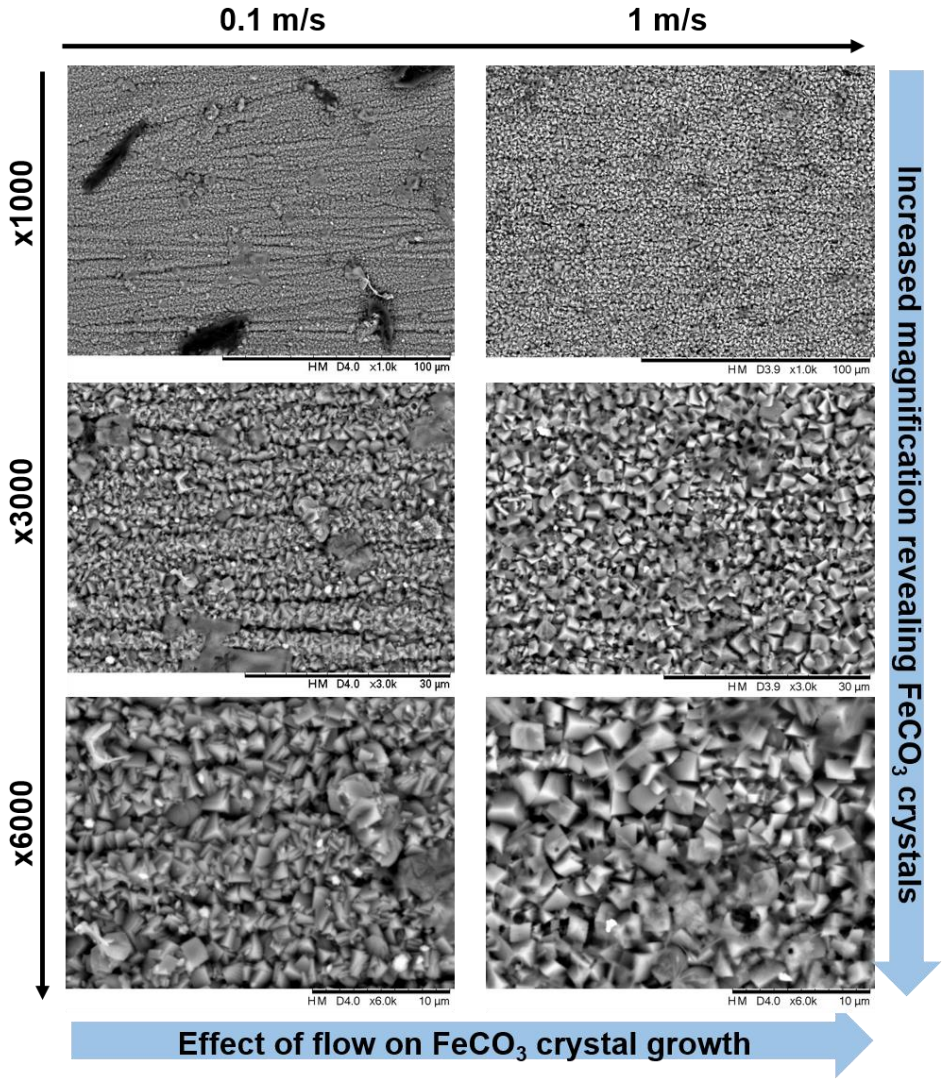

Figure 8.23. The effect of flow velocity on the development and morphology of $FeCO_3$ crystals over time conducted at 80°C, 3.5 wt.% NaCl, 0.54 bar p_{CO_2} and pH 6.8 and flow velocities of 0.1 and 1 m/s under galvanostatic control.

Figure 8.23 shows a comparison of the *ex-situ* SEM images of the top surface of the crystals formed following the synchrotron potentiostatic controlled tests at each flow velocity.

The top morphology of the crystals appear to have formed into a number of different morphologies including prismatic, cubic and rhombohedral crystals which very well defined edges. The crystals are a range of extremely small and compact crystals of <1 µm in size integrating between the bigger crystals of no greater than 2 µm. It is difficult to observe from these top view images, but smaller and more compact crystals are likely to present themselves at the interface of the carbon steel which is giving rise to the potential with ultra-protective properties.

8.5 Summary and Conclusions

Minor anodic polarisation of carbon steel in the form of potentiostatic and galvanostatic control at the DLSSF resulted in the rapid formation of protective crystalline $FeCO_3$ when exposed to the flowing brine, resulting in an artificial form of 'pseudo-passivation' within two hours. Increasing the solution pH and decreasing the flow velocity of the system generally resulted in a reduced induction period and an increase in crystalline $FeCO_3$ growth rate which was concluded from the *in-situ* SR-XRD and electrochemical observations. Increasing the brine pH had significant effects on not only the growth kinetics of $FeCO_3$, but the morphology of the observable crystals also. Whereas changing the flow velocity had less of an impact on both the kinetics and morphology of the $FeCO_3$ crystals, with both flow velocities showing similar characteristics. The results from the tests in this chapter imply that the critical supersaturation required for the nucleation of crystalline $FeCO_3$, and then the growth rate following nucleation into an ultra-protective pseudo-passive layer is more dependent on the local pH, rather than the flow velocity.

The crystals formed became increasingly protective at higher pH and lower flow velocity to some extent which was indicated by the electrochemical response. The tests under potentiostatic and galvanostatic control and at pH values between 6.3 and 7, and flow velocities of 0.1 and 1 m/s showed that $FeCO_3$ was the primary phase formed in all tests with the $FeCO_3$ (104) plane dominating the growth kinetics and orientation. Fe_3C was observed before the $FeCO_3$ was detected in all cases along with Fe. However, two minor phases were observed in addition to $FeCO_3$ at pH 6.8 under potentiostatic control,

which was assumed to be a result of Ca^{2+} contamination into the system and therefore the results in this test can be deemed inconclusive. $Fe_2(OH)_2CO_3$ was observed at pH 7 under potentiostatic control and formed after the $FeCO_3$ was detected and then grew at a slower rate, but became the dominant phase as the growth rate of $FeCO_3$ had diminished for the remainder of the test. The formation of this phase will be explored in greater detail in Chapter 9.

The $FeCO_3$ (104) plane growth curves in each condition showed a nucleation stage, followed by a growth stage. The results in Chapter 7 completed under the same brine conditions in a freely corroding system (where the corrosion kinetics were not accelerated via potentiostatic/galvanostatic control) showed the growth kinetics of $FeCO_3$ through four steps. In those tests, the nucleation stage showed a clear trend versus pH: higher pH resulted in shorter $FeCO_3$ induction times. However, the tests in the current chapter showed that the nucleation stage, and the induction period was slightly delayed in comparison to the same tests ran at OCP in Chapter 7. This observation is mostly likely due to the carbon steel working electrode acting as a 'net' anode where the ratio between anodic and cathodic reactions is far in favour of the anodic reaction. The possible causes for this observation will be explored in more detail in Chapter 9.

During the induction period, there was no significant detectable diffraction signal for any species other than the already present Fe and Fe_3C. Following the induction period, the current began to rise which could be due to the local acidification accelerating the electrochemical dissolution rate of the carbon steel (positive anodic reaction order with respect to $[H^+]$). In conjunction with this behaviour, the *in-situ* SR-XRD results show that the onset of the current rise corresponded with the formation of a crystalline $FeCO_3$ crystals, followed by a rapid increase in the growth rate. Then, once the anodic current had peaked, it began to decrease until eventually being restricted by the $FeCO_3$ crystals. At this point, the rate of $FeCO_3$ formation rapidly slowed and approaching a plateau, indicating that the ultra-protective pseudo-passive layer had formed.

SEM images of the $FeCO_3$ crystals formed under at different pH and flow velocities showed significantly different surface morphology. The results suggest that the $FeCO_3$ crystal morphologies vary and are dependent on the growth rate, which is in turn determined by the local critical supersaturation required to form $FeCO_3$ nuclei's during the induction period. Therefore, higher

supersaturation of the solution would lead to a more rapid crystal growth rate (leading to smaller and more compact nano-size $FeCO_3$ crystals), and is a rate determining factor on the crystal morphology. The plate-like structure observed on the surface (on top of the $FeCO_3$ crystals) at pH 7 under potentiostatic control was deemed to be $Fe_2(OH)_2CO_3$ due to this phase forming after $FeCO_3$ in the SR-XRD results.

A thorough review and discussion in Chapter 9 compares the kinetics, composition and morphology of $FeCO_3$ from the tests presented in Chapter 7 and the current chapter at OCP and under anodic polarisation. The formation of $Fe_2(OH)_2CO_3$ and the possible mechanisms leading to the phases formation are also discussed. Before Chapter 9 is presented, the results from the current chapter can be qualitatively interpreted as follows:

- $FeCO_3$ was the primary phase to form under all testing conditions which precipitated when a critical local supersaturation near the surface was achieved and was solely responsible for the ultra-protective properties during 'pseudo-passivation' of carbon steel in CO_2 corrosive environments.
- In the test that $Fe_2(OH)_2CO_3$ was also observed, it did not form until after the $FeCO_3$ later on in the test and did not seem to offer any protection to the carbon steel surface.
- The crystalline $FeCO_3$ growth curves for each *in-situ* SR-XRD test showed an induction period (before crystalline $FeCO_3$ was detected), followed by a growth stage where crystalline $FeCO_3$ precipitation was directly correlated with a rise in the current density, which then fell when the growth rate had reached a plateau once a protective pseudo-passive layer had formed.
- Once this pseudo-passive layer had formed in all tests, the film was protective enough to resist the current passing through which lead to an increase in the measured potential.
- The crystal morphology depends on the growth rate of the crystals, which is in turn determined by the supersaturation required to form $FeCO_3$.
- Higher supersaturation (through increasing the system pH) of the solution leads to a more rapid crystal growth rate with smaller, compact and protective crystals formed by the continuous nucleation of small crystals which explains the observation of extremely small crystals in comparison to the OCP tests.

- An increase in flow velocity leads to an enhanced mass transfer process, and the released Fe^{2+} ions due to a higher corrosion rate can be easily flushed away from the steel surface, reducing the local supersaturation and increasing the induction time for $FeCO_3$ precipitation and the time taken for ‘pseudo-passivation’ to take place.
- In the long term OCP tests where spontaneous ‘pseudo-passivation’ occurred, corrosion currents for Fe^{2+} production at the steel interface was much lower. This would mean that there is no continuous nucleation of new crystals and that crystal growth would dominate the process in comparison to the anodically polarised SR-XRD tests.
- The morphology of the crystals in these tests comprised of larger, well-formed crystals which can therefore be explained. Until the build-up of Fe^{2+} between and within the pores of the larger crystals and at the steel interface increased the local supersaturation resulting in further nucleation of $FeCO_3$ which resulting in a rise in OCP and a further drop in the corrosion rate.
- No significant difference was observed between the potentiostatic and galvanostatic controlled tests. Although the induction time was reduced under galvanostatic control but the crystals under potentiostatic control appeared to be smaller, more compact and more protective.

Part IV:
Discussion and Conclusions

Chapter 9.
A discussion on the development and mechanisms of $FeCO_3$ formation under different operating conditions

9.1 Introduction

$FeCO_3$ is a naturally-occurring protective corrosion product that forms on the surface of X65 carbon steel pipelines. During oil and gas production in CO_2 environments, the precipitation of $FeCO_3$ is extremely important. Two of the key aspects to consider when predicting pipeline corrosion rates in CO_2 environments are the kinetics of film formation and level of protection afforded by the film under different operating conditions. Solution pH can be considered to be one of the most influential factors with regards to the kinetics, morphology and protection of the $FeCO_3$ film. As discussed previously, in addition to $FeCO_3$, $Fe_2(OH)_2CO_3$ and Fe_3O_4 are corrosion products that can form on steel in CO_2-saturated/carbonate rich solutions. However, this work aims to answer some questions on the presence of these phases that still remained unanswered, a pertinent one being what role, if any, these corrosion products play in determining the overall protectiveness of the corrosion products formed.

The objectives of the work presented in this thesis were to provide a further understanding of protective $FeCO_3$ formation directly onto a carbon steel surface by combining *in-situ* and *ex-situ* methodologies. To utilise the natural formation of $FeCO_3$ and to gain confidence in using $FeCO_3$ as a natural inhibitor against corrosion, it is important to understand the mechanisms of $FeCO_3$ formation under a range of operating conditions. The use of different methodologies meant that several aspects of their mechanisms could be explored and understood. Each methodology had its own specificity and some important conclusions were raised from these results. In this chapter, some key points are discussed in a way to present the main aspects of the inhibitor mechanisms. The main contribution of this work to the corrosion community is therefore able to be extracted from the following discussion.

From the results presented in Chapter 5, 7 and 8, the effect of varying parameters on the kinetics and development and the protectiveness of the $FeCO_3$ have been studied. Understanding the true nature of nucleation and growth of $FeCO_3$ crystals, the factors that govern the rate of precipitation, and the characteristics of the developed film is essential in assessing the practical

use of $FeCO_3$ in the protection of pipelines. In the following chapter, the early kinetics, development, morphology and protectiveness of $FeCO_3$ are discussed. Questions about the mechanism of the formation of $FeCO_3$ leading to 'pseudo-passivation', as well as its morphology and chemical composition, are addressed in this chapter. The results show that the composition of the ultra-protective film that formed at the carbon steel interface was believed to be purely $FeCO_3$ and was the dominant phase during every test conducted.

The discussion is divided into six key areas:

1. The early kinetics (inductions times, growth rates and orientation) of $FeCO_3$ film formation are compared and discussed.

2. The morphologies and characteristics of the distinctly different $FeCO_3$ films formed that contribute to its protectiveness are discussed.

3. The effect of accelerating the kinetics of $FeCO_3$ film formation is discussed when $Fe_2(OH)_2CO_3$ was observed.

4. The mechanisms of $FeCO_3$ film formation over time under different operating conditions are discussed.

5. Rationality and key role of $FeCO_3$ as a corrosion mitigator is discussed.

6. The usefulness of the *in-situ* SR-XRD methodology to follow the evolution of $FeCO_3$ formation is discussed.

9.2 Early Kinetics and Orientation of $FeCO_3$ Crystal Growth: OCP vs Anodic Polarisation

Table 9.1 summarises the main crystal planes of $FeCO_3$ formed when the electrochemical charge transfer is not controlled at the surface (the surface is freely corroding) and when Fe^{2+} formation at the surface is stimulated by application of a positive potential or galvanostatically.

The diffraction patterns throughout the SR-XRD tests at Diamond showed that 9 lattice planes of $FeCO_3$ ((012), (104), (110), (113), (202), (024), (018), (116), (211)) were present in total. The different crystal planes grow at different rates during each test of identical operating conditions, however, among the formed $FeCO_3$ crystal faces, the most dominant plane across the surface under all conditions was observed at 2θ=~6.35º corresponding to the (104) plane.

Table 9.1. A summary of the main crystal planes of $FeCO_3$ formed during the SR-XRD tests conducted at 80°C, 3.5 wt.% NaCl and 0.54 bar p_{CO_2} and a range of pH values (pH 6.3, 6.8 and 7) and flow velocities (0.1, 0.5 and 1 m/s) in both freely and controlled corroding systems.

		Open Circuit Potential tests (80°C, 3.5 wt. % NaCl, CO_2 saturated)				Potentiostatic controlled tests (0.25 mV/s, 80°C, 3.5 wt. % NaCl, CO_2 saturated)					Galvanostatic controlled tests (1 mA/cm2, 80°C, 3.5 wt. % NaCl, CO2 saturated)	
		pH 6.3, 0.1 m/s	pH 6.8, 0.1 m/s	pH 7, 0.1 m/s	pH 6.8, 1 m/s	pH 6.3, 0.1 m/s	pH 6.8, 0.1 m/s	pH 7, 0.1 m/s	pH 6.8, 0.5 m/s	pH 6.8, 1 m/s	pH 6.8, 0.5 m/s	pH 6.8, 1 m/s
Crystal plane ($FeCO_3$)	(012)	✗	✗	✓	✓	✗	✗	✓	✗	✓	✓	✗
	(104)	✓	✓	✓	✓	✓	✓	✓	✓	✓	✓	✓
	(110)	✓	✓	✓	✓	✓	✓	✓	✓	✓	✓	✓
	(113)	✗	✓	✓	✓	✓	✓	✓	✓	✓	✓	✓
	(202)	✗	✓	✓	✓	✓	✓	✓	✓	✓	✓	✓
	(024)	✗	✓	✓	✓	✓	✓	✓	✓	✓	✓	✓
	(018)	✓	✓	✓	✓	✓	✓	✓	✓	✓	✓	✓
	(116)	✓	✓	✓	✓	✓	✓	✓	✓	✓	✓	✓
	(122)	✗	✓	✓	✓	✓	✓	✓	✓	✓	✓	✓
Crystal composition		$FeCO_3$	$FeCO_3$	$FeCO_3$	$FeCO_3$	$FeCO_3$	$FeCO_3$	$FeCO_3$	$FeCO_3$	$FeCO_3$	$FeCO_3$	$FeCO_3$
Most dominant plane		104	104	104	104	104	104	104	104	104	104	104
Total intensity		35788	87166	63730	27848	25960	3730	62333	18469	19080	117697	63701

The kinetics of $FeCO_3$ growth (from the induction time to the overall growth rate of the crystals) varied considerably through changing not only the physical environmental parameters, but whilst changing the way in which the Fe^{2+} was generated. When the surface is anodically polarised, the production of Fe^{2+} is far greater than that of a freely corroding surface. This remainder of this section will elucidate on the nature of $FeCO_3$ growth kinetics when formed naturally and when formed artificially, and the differences in growth kinetics will be discussed.

Figure 9.1 shows the growth of the most dominant $FeCO_3$ crystal plane (104) across the surface from each of the major *in-situ* SR-XRD experiments discussed in this work.

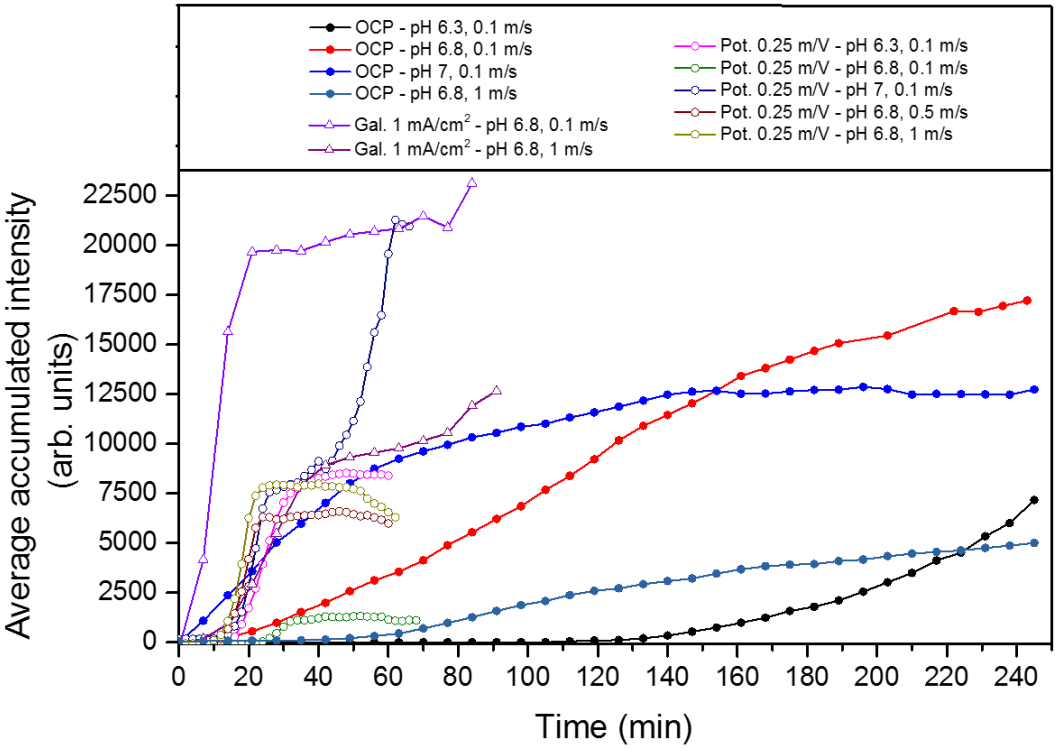

Figure 9.1. Growth of the most dominant $FeCO_3$ crystal plane (104) across the surface during the SR-XRD tests conducted at 80°C, 3.5 wt.% NaCl and 0.54 bar p_{CO_2} and a range of pH values (pH 6.3, 6.8 and 7) and flow velocities (0.1, 0.5 and 1 m/s) in both freely and controlled corroding systems.

Upon nucleation of $FeCO_3$, the most noticeable difference between the tests conducted at OCP and under anodic polarisation was the growth rate of the crystals and the final intensities. The intensity and hence the growth rate of the $FeCO_3$ increased exponentially within the first 30 minutes until slowing

down and reaching a plateau in all of the experiments that were anodically polarised. The remaining tests under OCP had a much more linear growth trend over a longer time period and often resulted in more $FeCO_3$ being detected on the surface. This confirms the previous statement that the growth of $FeCO_3$ dominates at lower supersaturations instead of nucleation of new crystals.

An interesting observation in these tests showed that the nucleation stage, and the induction period was slightly delayed under anodic polarisation in comparison to the same tests ran at OCP. Crystalline $FeCO_3$ was precipitated when a critical local supersaturation near the surface was achieved and the induction time has been regarded as the time required to achieve this critical supersaturation (once $FeCO_3$ had been detected). Figure 9.2 shows a summary of the induction time for every $FeCO_3$ crystal plane detected on the carbon steel surface from each of the major *in-situ* SR-XRD experiments discussed in this work.

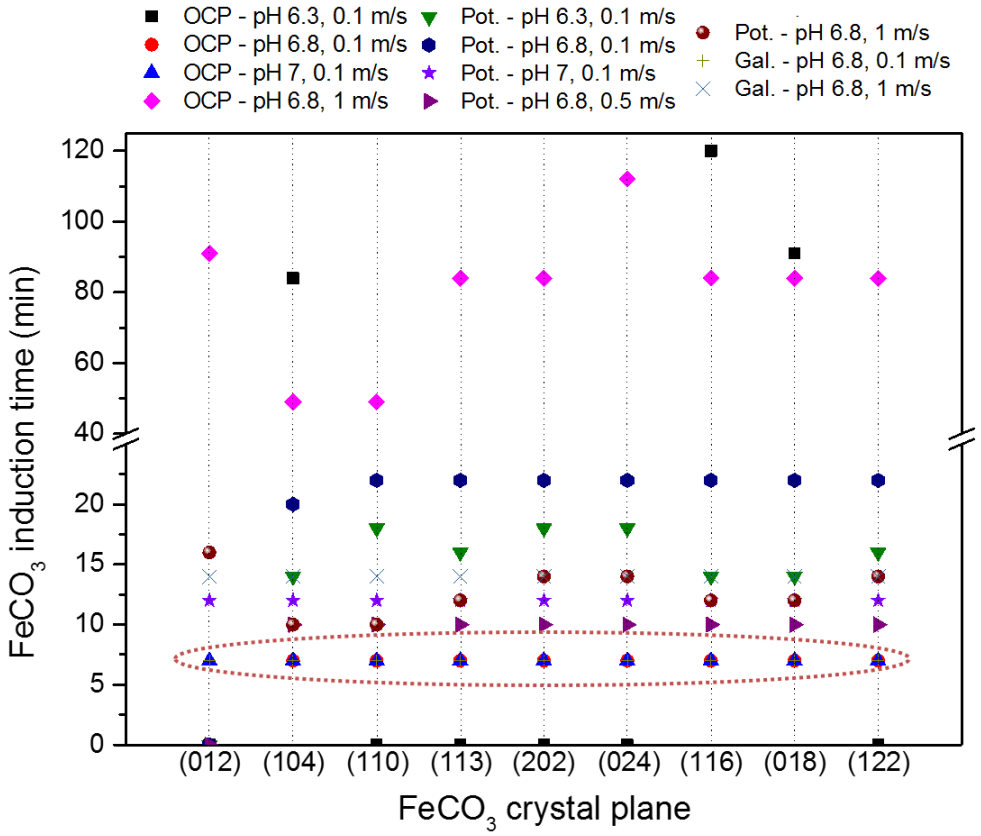

Figure 9.2. A summary of $FeCO_3$ induction times during the SR-XRD tests conducted at 80°C, 3.5 wt.% NaCl and 0.54 bar p_{CO_2} and a range of pH values (pH 6.3, 6.8 and 7) and flow velocities (0.1, 0.5 and 1 m/s) in both freely and controlled corroding systems.

For each of the tests conducted, Figure 9.2 shows that the induction time for every $FeCO_3$ plane detected varied considerably from test to test and some planes are far more stable than others in the early stages of crystal growth. The induction time for $FeCO_3$ during the freely corroding tests at OCP (at pH 6.8 and 7) was faster and instantaneous upon applying the X-rays to the surface with all of the $FeCO_3$ planes being detected during the initial loop of scanning across the surface in comparison to all tests under anodic polarisation.

This observation is mostly likely due to the carbon steel working electrode acting as a 'net' anode (when anodically polarised) where the ratio between anodic and cathodic reactions is far in favour of the anodic reaction which is illustrated in the schematic in Figure 9.3.

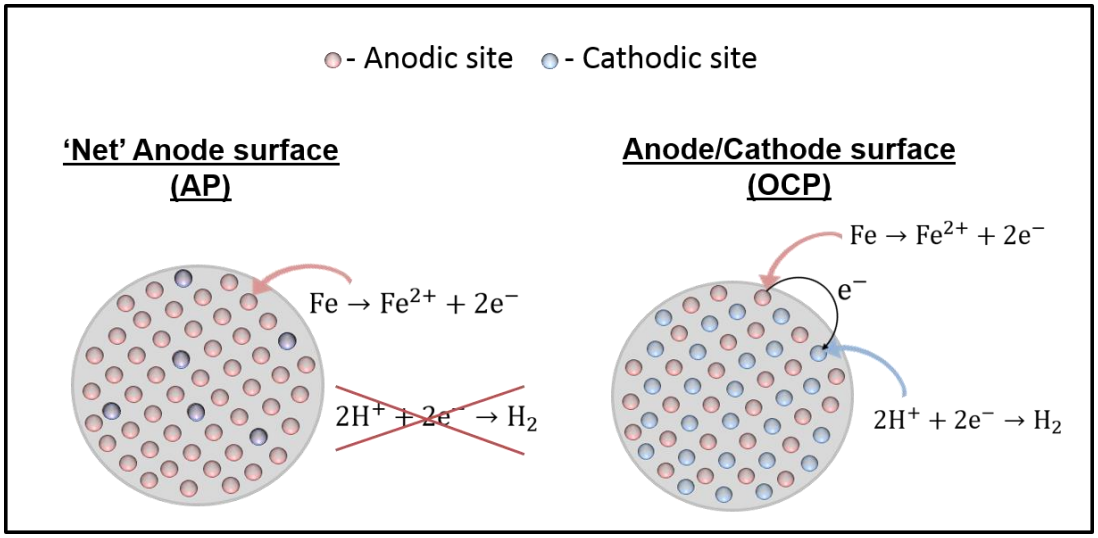

Figure 9.3. A schematic representation illustrating the surface as a 'Net' Anode surface (anodic polarisation) and as an Anode/Cathode surface (freely corroding).

The possible causes for this delay in induction could be due to such high local supersaturation at the interface. Especially as the rate of $FeCO_3$ growth is far greater once this induction time has been overcome. The exact explanation for this observation is unclear. However, two possibilities are outlined for the surface that represents a 'net' anode surface that results in the delay in $FeCO_3$ nucleation:

1. The negative electrons generated from the anodic reactions are not being consumed by the limited cathodic reactions taking place and therefore the surface boundary layer becomes saturated with these negative electrons, and hence, repelling the incoming carbonate ions. However, after some

time, due to the 'buffering effect' which is illustrated in Figure 9.4 (reproduced from Chapter 2), the boundary layer will become saturated with H^+ and CO_3^{2-} initiating $FeCO_3$ precipitation.

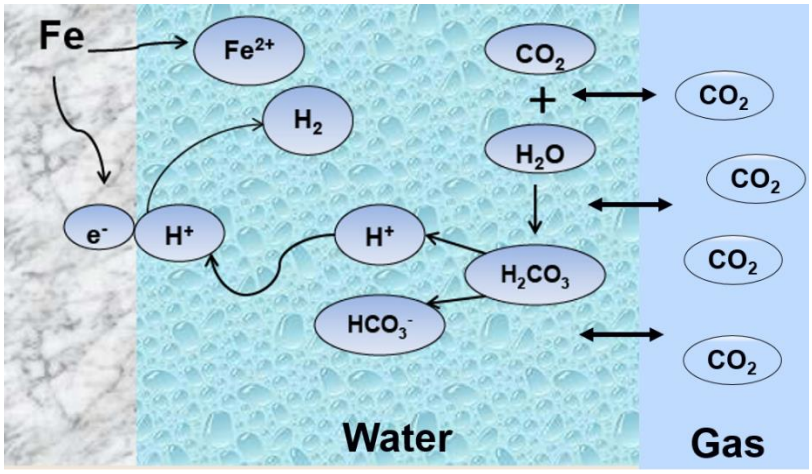

Figure 9.4. A schematic showing the aqueous CO_2 corrosion mechanism ("the buffering effect") of carbon steel (also shown in Chapter 2 as 'Figure 2.2' which is modified from [28]).

2. Due to such a high flux on Fe^{2+} production at the steel interface, local acidification and decrease in pH could occur due to hydrolysis of Fe^{2+} via:

$$Fe^{2+}_{(aq)} + H_2O_{(aq)} \rightarrow FeOH^{+}_{(aq)} + H^{+}_{(aq)} \qquad (9.1)$$

9.3 Morphology of $FeCO_3$ Layer

$FeCO_3$ assigns rhombohedral/approximate cube shaped crystal morphology. Crystal morphology depends on the growth rate of the crystals, which is in turn determined by the supersaturation required to form the first crystal nuclei. Therefore, higher supersaturation of the solution would lead to a more rapid crystal growth rate. The results in this work suggest that the local supersaturation is the determining factor on the resulting crystal morphology. The final morphology of the $FeCO_3$ crystals depends on the local supersaturation within the diffusion boundary layer and the surface roughness of the steel. The supersaturation for crystalline $FeCO_3$ precipitation, combined with the growth rate of the crystals has important consequences for the final morphology.

SEM images of the $FeCO_3$ crystals formed at different pH values under a freely corroding system and under a controlled/forced showed significantly different surface morphology which will be discussed. The major difference throughout the tests ran at OCP were the sizes and growth rate of the crystals. The crystals formed at pH 7 (Figure 9.5 (a)) appeared to be cubic in structure with sharper and more defined edges which is most likely due to the dominance of the (104) plane which inhibited the growth of other crystal faces. Whereas the $FeCO_3$ crystals that formed on the surface at pH 6.8 (Figure 9.5 (b)) are made up of a mixture of well-defined cubic crystals with sharp edges (as seen at pH 7) and disorientated rhombohedral crystals with random shapes and faces with fine edges. The slower growth rate of the crystals in comparison to the growth of the crystals at pH 7, allowed other crystal faces to develop which is illustrated by the observed crystal morphologies.

The crystals at pH 6.8 also seem to vary in size considerably in comparison to the $FeCO_3$ crystals at pH 7 which is due to the lower supersaturation in the system and therefore crystal growth dominating the process reducing the rate of nucleation of new crystals. The increase in pH significantly decreases the solubility of $FeCO_3$, resulting in faster precipitation and hence increased surface coverage resulting in the formation of a smaller, compact and more protective crystals covering larger portions of the steel surface. The smaller crystals are a result of increased nucleation sites and therefore an increased number of crystals which essentially block the growth rate of their counterpart crystals. Decreased pH shows the predominance of growth over nucleation which results in larger crystals that are less dense and less protective.

In the tests conducted at OCP, the relatively low corrosion current to generate ferrous ions at the surface (in comparison to the forced tests) would mean that the crystal growth process would dominate due to the lower supersaturation. This ultimately resulted in the formation $FeCO_3$ comprising of larger, well-formed crystals. In the electrochemically controlled experiments, where the current density sustains the critical supersaturation, the formation and final morphology of $FeCO_3$ would develop through the continuous nucleation of new, small crystals which explains the observation of friable morphologies with small crystallite size.

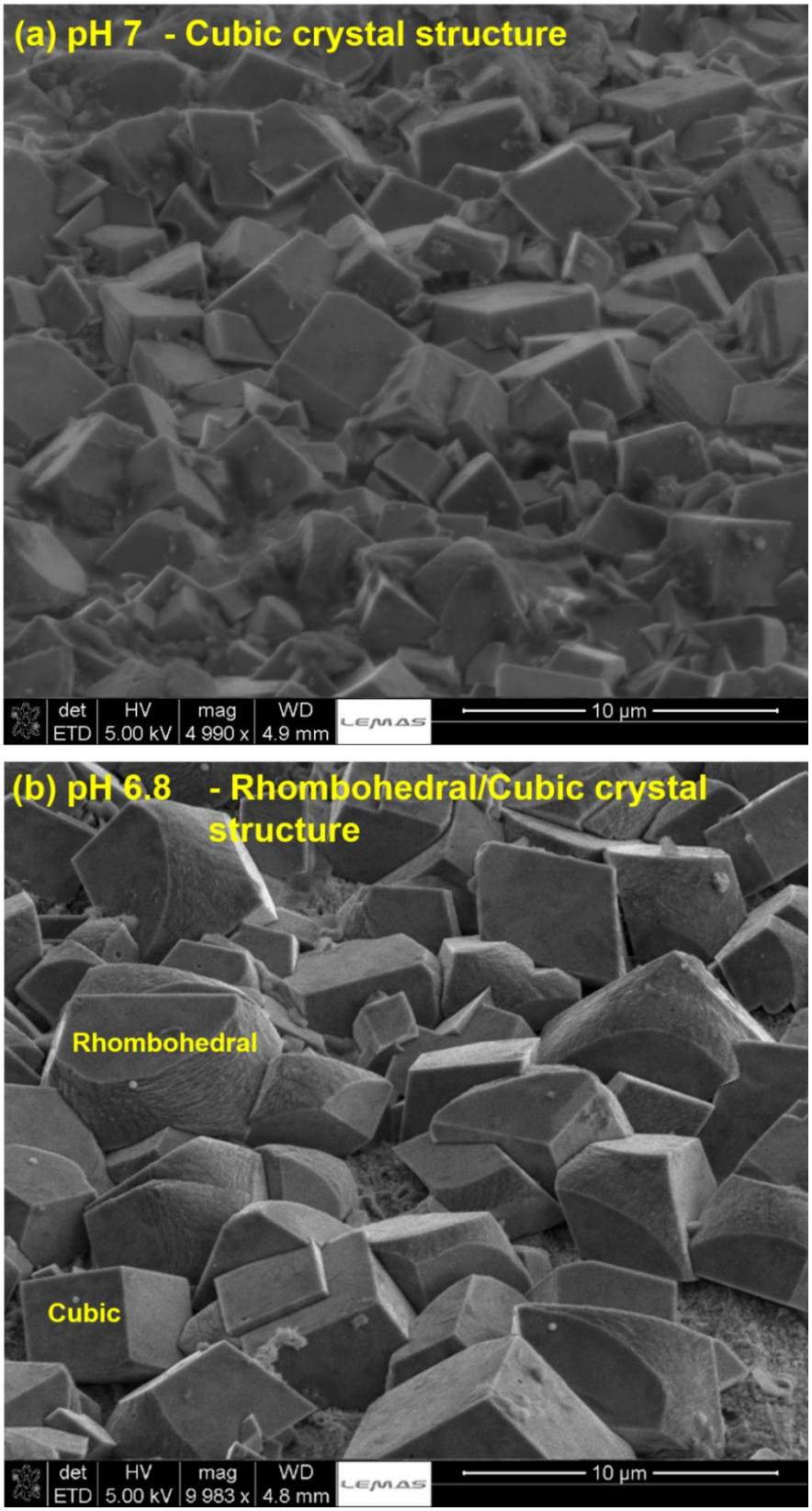

Figure 9.5. *Ex-situ* SEM images of the X65 carbon steel surface at the end of the test showing the cross-sections of the films formed at 80°C, 3.5 wt.% NaCl, 0.54 bar p_{CO_2} and 0.1 m/s in a freely corroding system: (a) pH 7; (b) at pH 6.8.

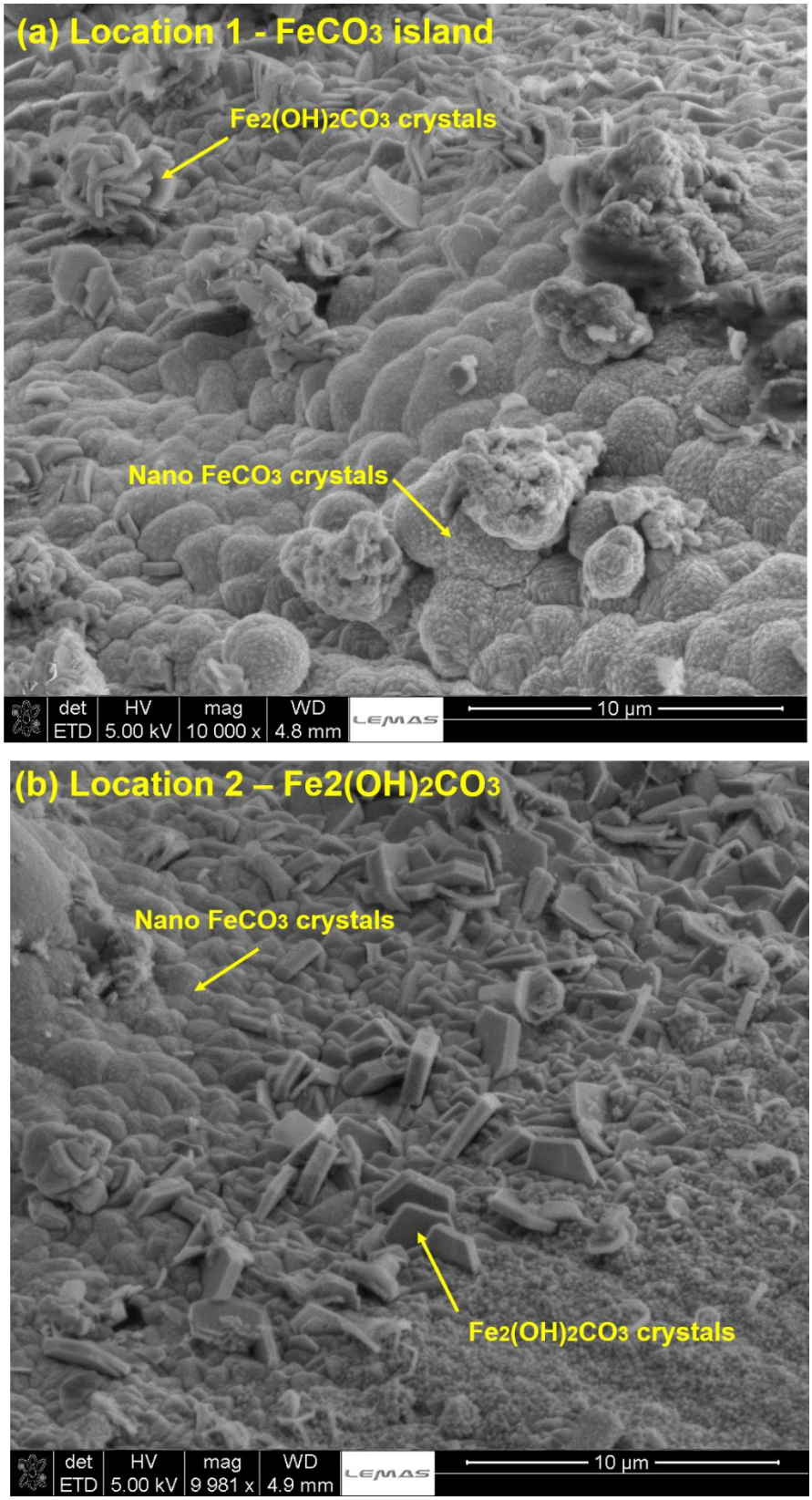

Figure 9.6. *Ex-situ* SEM images of the X65 carbon steel surface at the end of the test showing the cross-sections of the films formed at 80°C, 3.5 wt.% NaCl, 0.54 bar p_{CO_2}, pH 7 and 0.1 m/s under potentiostatic control.

Figure 9.6 shows the crystal morphology under potentiostatic control at 80°C, pH 7 and 0.1 m/s at two distinctly different locations across the steel surface. In Figure 9.6 (a), the $FeCO_3$ layer consisted of extremely compact nano-sized crystals. The morphologies of the crystals formed in the controlled corrosion tests are notably different from the cubic/rhombohedral crystals observed at OCP in the same test environments which is due to the faster formation of the $FeCO_3$ crystals under potentiostatic control and increased nucleation rate of crystals.

Figure 9.6 (b) shows the crystal morphology at a different location on the same sample and reveals a different type of crystal morphology consisting of larger plate-like crystals which are distinctly different to the $FeCO_3$ crystals. The increase of $Fe_2(OH)_2CO_3$ phase in the *in-situ* SR-XRD corresponds to the formation of this plate-like structure observe. The results show that $Fe_2(OH)_2CO_3$ crystals are not in intimate contact with the carbon steel surface. The morphology of $Fe_2(OH)_2CO_3$ crystals and their orientation on top of the $FeCO_3$ suggests that they still offer convenient electrolyte access to the underlying crystals/substrate concluding that this phase does not provide as good a resistance against corrosion to the surface relative to a $FeCO_3$ crystals. Thus, it appears that the overall corrosion protection comes predominantly from a $FeCO_3$, rather than a combination $FeCO_3$/ $Fe_2(OH)_2CO_3$.

9.4 Accelerating the Kinetics of $FeCO_3$ Film Formation with the Presence of $Fe_2(OH)_2CO_3$

Figure 9.7 shows the *in-situ* SR-XRD shows three distinctly different XRD diffraction patterns with their corresponding one-dimensional Debye rings recorded on a bare carbon steel surface (before film formation), the carbon steel surface after $FeCO_3$ film formation (OCP, pH 7, 80°C, 0.1 m/s) and the carbon steel surface after $FeCO_3$ and $Fe_2(OH)_2CO_3$ formation (anodic polarisation, pH 7, 80°C, 0.1 m/s).

The diffraction rings were observed from the bare steel surface and the film phases, indicating both phases were isotropic. The diffraction ring from the steel ((110) plane) was smooth at the start of each experiment and became less distinct as the $FeCO_3$ peaks appeared. The reduction in intensity was indicates that there are less diffracting crystals being intersected by the beam.

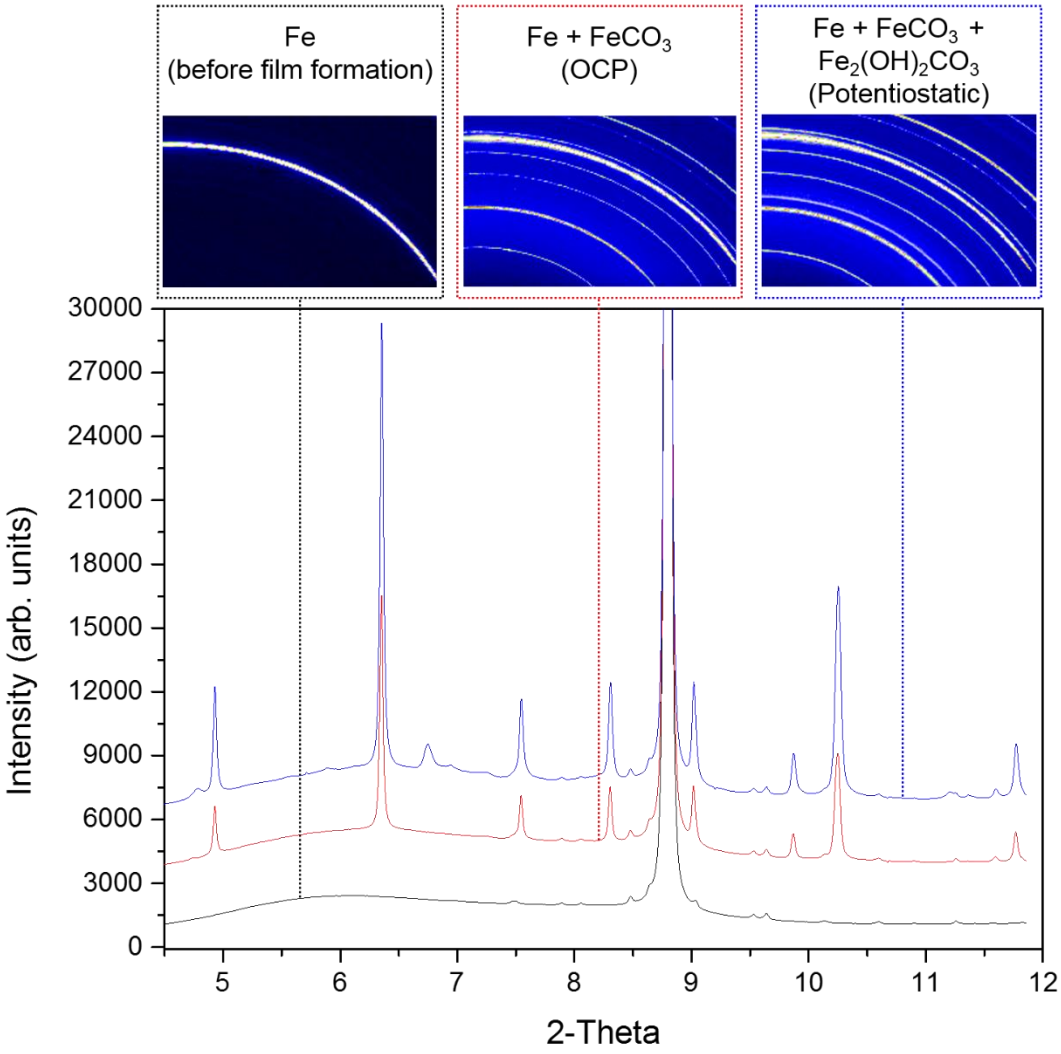

Figure 9.7. Selection of *in-situ* diffraction patterns recorded on bare steel (black line) and after the tests conducted at 80°C, 3.5 wt.% NaCl and 0.54 bar $\boldsymbol{p_{CO_2}}$, pH 7 and 0.1 m/s in a freely corroding system (red line) and under potentiostatic control (blue line).

Thus there appeared to be a decrease in the number of diffracting Fe crystals in the beam as the experiment proceeded which can be explained by the preferential dissolution of certain steel grains exposing particular faces, while the diffraction from the remaining grains was concentrated in small spots. Given that the steel grains were initially of random orientation with respect to the X-ray beam and that each crystallite gave a diffraction peak for a given plane, then the number of diffraction peaks corresponds to the number of crystallites intersecting the beam.

Initially, the number of crystallites intersecting the beam was sufficient to give a smooth diffraction ring. However there is evidence that different crystal facets have slightly different dissolution rates [110], in which case corrosion would gradually lead to selective dissolution of grains with the worst orientation (which would cause the diffraction rings to become patchy) suggesting that significant surface roughening is taking place during the early stages of these experiments as the steel corrodes [110]. After some time, traces of $Fe_2(OH)_2CO_3$ was detected which can be seen from both the diffraction peaks and new rings observed in Figure 9.7. The $Fe_2(OH)_2CO_3$ phase formed later than $FeCO_3$ and then ultimately became the dominant phase. As mentioned previously in Chapter 3 (section 2.4.4), the precipitation of $Fe_2(OH)_2CO_3$ may be in the form of:

$$2Fe^{2+}_{(aq)} + CO^{2-}_{3.(aq)} + 2H_2O_{(aq)} \rightarrow Fe_2(OH)_2CO_{2.(s)} + 2H^{+}_{(aq)} \quad (9.2)$$

The precipitation of crystalline $FeCO_3$ is proposed to have an effect on the local pH. The initial crystalline phase formed was $FeCO_3$ in all experiments: this would reflect the stable phase expected at the solution pH perturbed only by the solution equilibria of Fe^{2+} within the boundary layer. However, the number, size and precipitation rate of the nuclei formed would then determine the evolution of the local pH and thus the identity of phases subsequently formed. $FeCO_3$ microcrystals could act as nuclei for a different phase (in this case: $Fe_2(OH)_2CO_3$) that reflected the perturbation of pH within the boundary layer. Both $FeCO_3$ and $Fe_2(OH)_2CO_3$ will have different critical supersaturation for formation of the crystalline phases, and once this is exceeded, crystals will continue to grow even when the supersaturation decreases. The precipitation of the crystalline $Fe_2(OH)_2CO_3$ phase formed was considered to be critically dependent on the local solution pH within the boundary layer and not that within the bulk solution. These results suggest that the formation of $Fe_2(OH)_2CO_3$ is highly dependent on the concentration and ratio of Fe^{2+} (through the applied potential) and CO_3^{2-} in the boundary layer as well as the local pH. In support of this possibility, it was noted that for very high bicarbonate concentrations (0.1 to 0.2 mol/L) at 25°C and pH of around 8.3, Dong *et al.* [186] have shown the formation of corrosion products consisting entirely of $Fe_2(OH)_2CO_3$ and $Fe_6(OH)_{12}CO_3$ instead of $FeCO_3$. The $Fe_2(OH)_2CO_3$ phase was also observed at lower temperatures by De Marco *et al.* [2]. Ingham *et al.* [135] also shown that $Fe_2(OH)_2CO_3$ became the

dominant phase (after the formation of $FeCO_3$) at pH values of 6.8 and above, 80°C under high anodic potentials. However, excessive currents were generated during these tests (12 mA/cm^2) which would have flooded the boundary layer with high concentrations of Fe^{2+}. This is most likely the reason that in their tests, $Fe_2(OH)_2CO_3$ was detected consistently due to the high pH values generated in the surface boundary layer. Consistent with the *in-situ* SR-XRD data, the presence of $Fe_2(OH)_2CO_3$ was observed *ex-situ* through SEM analysis in Figure 9.8 (a) and (b) (image reproduced from Chapter 8). The crystals associated with the plate-like morphology $Fe_2(OH)_2CO_3$ which is consistent with microscopy of the authentic mineral [4, 73].

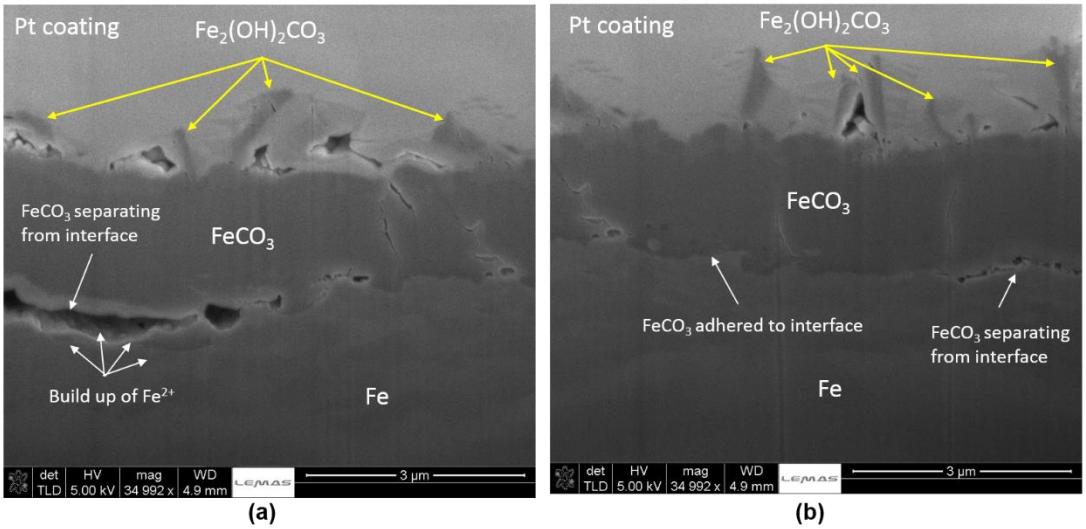

Figure 9.8. *Ex-situ* SEM images of the X65 carbon steel surface at the end of the test showing the cross-sections of the films formed at 80°C, 3.5 wt.% NaCl, 0.54 bar p_{CO_2} and 0.1 m/s at pH 7 under potentiostatic control.

From the cross sections in Figures 9.8 (a) and (b), the $Fe_2(OH)_2CO_3$ crystals appear to be standing vertically on top of the $FeCO_3$ layer assuming no added protection is offered through the presence of this phase. Therefore, the overall protection of the system is solely down to formation of $FeCO_3$

9.5 Mechanisms of $FeCO_3$ Crystal Growth

9.5.1 Mechanism of the Early Kinetics of $FeCO_3$ Film Formation on a Freely Corroding Surface

With consideration of *in-situ* electrochemical, *in-situ* SR-XRD and *ex-situ* SEM data combined in Chapter 7, it can be interpreted that the formation of the $FeCO_3$ crystals have caused the drop in corrosion rate. The combined *in-situ*

observations and *ex-situ* SEM images illustrates that the process of nucleation and growth continues until the $FeCO_3$ film is protective enough to reduce the corrosion rate significantly. However, this sequence of nucleation and growth illustrates that as the $FeCO_3$ layer develops, larger proportions of the surface are being covered with crystals and ultimately reducing the reaction rate of Fe^{2+} production across the surface which has a direct impact on the formation of $FeCO_3$, reducing the precipitation rate and limiting $FeCO_3$ precipitation. Therefore, as the $FeCO_3$ layer builds up, the kinetics slow down which is captured by the SR-XRD measurements. From the accumulated measured peak areas and intensities from the tests, four steps characterise the growth mechanism of the $FeCO_3$ layer. During each step, either the nucleation rate or the crystal growth rate dominates the kinetics of the layer build up. The steps, based on the work in this thesis are characterised as followed:

(1) An induction time when the measured intensity is zero and no nucleation or crystal growth rate occurs (high Fe^{2+} production rate and therefore higher SR);

(2) Nucleation of the $FeCO_3$ crystals when the measured intensity starts to increase (nucleation rate dominates as new crystals initially form). At this point, the production of Fe^{2+} is still rising (high SR);

(3) Nucleation-growth stage which is characterised by an increase in crystal growth, but also the nucleation and growth of new crystals. Here, the Fe^{2+} production rate will begin reduce at some time along with the SR, whilst crystals continue to grow;

(4) Growth stage when the integrated intensity slows down or reaches a plateau (crystal growth dominates the kinetics due to formation of a protective $FeCO_3$ film and hence a reduction in supersaturation and Fe^{2+} production, while nucleation of new crystals reduces). Larger $FeCO_3$ crystals present on the surface.

A schematic showing the different steps of $FeCO_3$ crystal growth mechanism is provided in Figure 9.9.

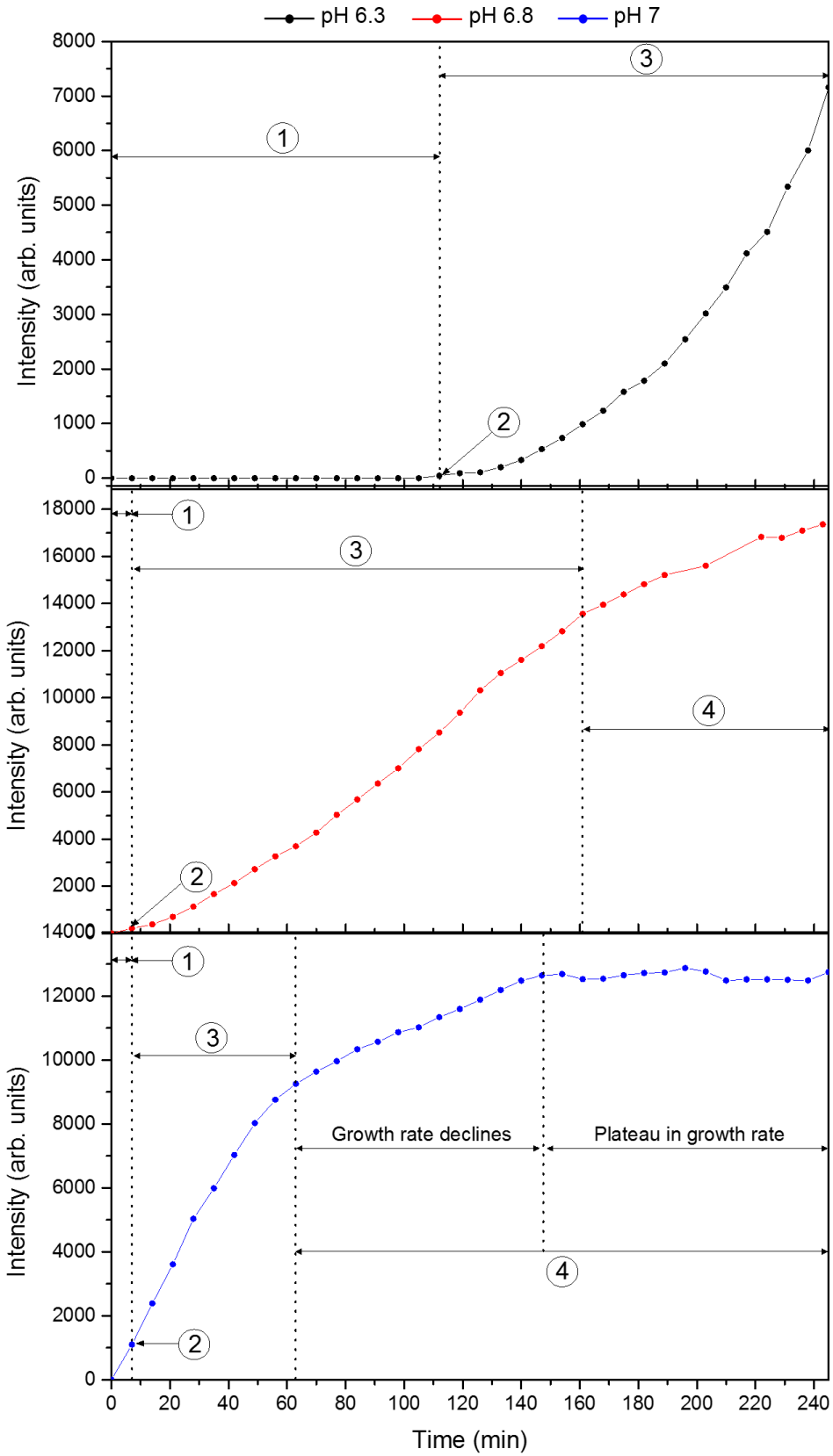

Figure 9.9. Mechanism of $FeCO_3$ crystal growth over time for varying pH conducted at 80°C, 3.5 wt.% NaCl, 0.54 bar p_{CO_2} and 0.1 m/s in a freely corroding system.

The nucleation rate is believed to increase exponentially with the relative supersaturation, whilst the crystal growth rate varies linearly with SR (agreeing with what has been mentioned previously and the work by Dugstad [40]). Consequently, crystal growth should occur/dominate at lower relative supersaturation. Conversely, when the relative supersaturation is high, simultaneous nucleation and growth dominates which is evident from the intensity measurements in Figures 9.9 (a-c) and illustrated in the schematic in Figure 9.10.

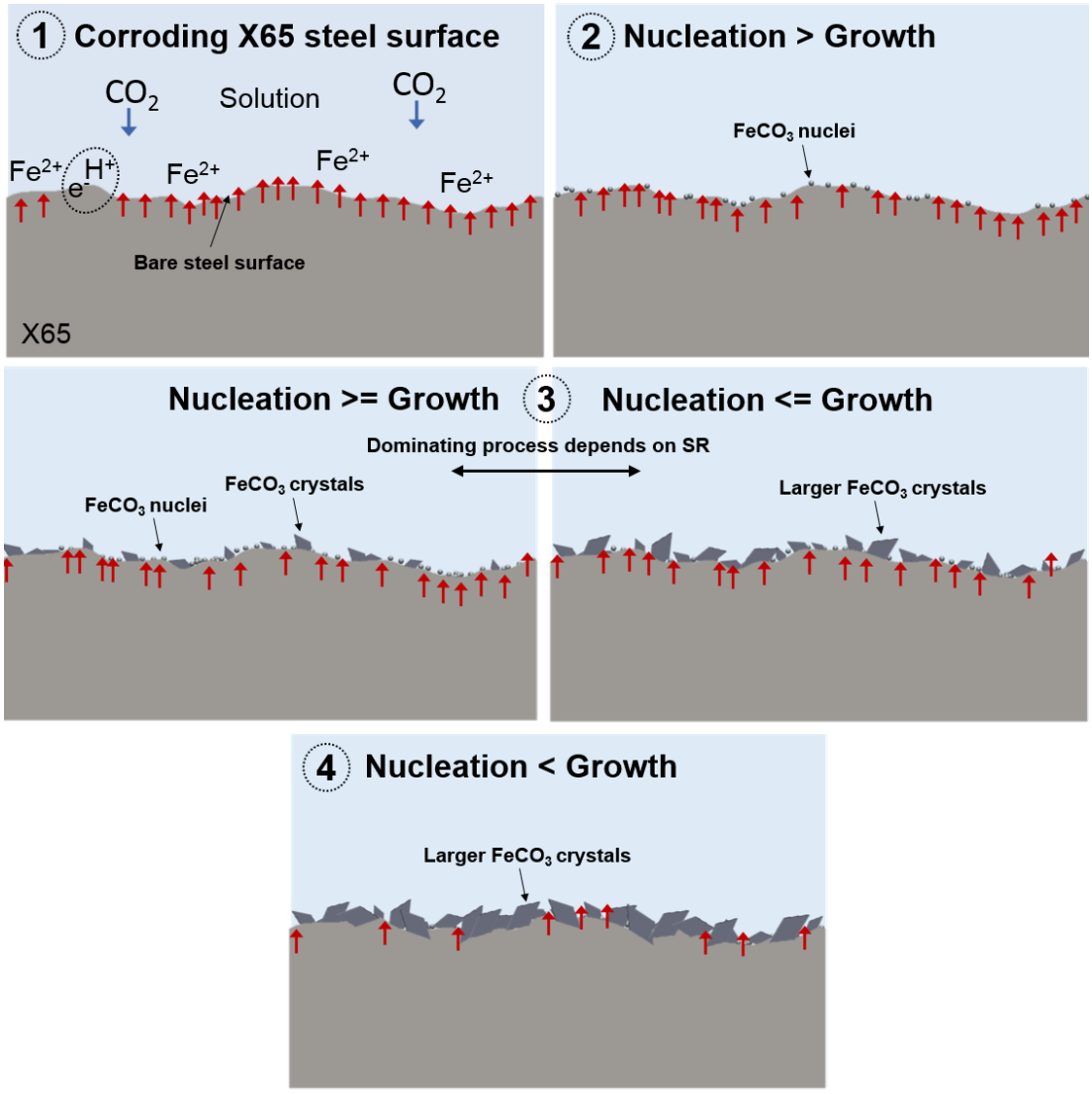

Figure 9.10. Mechanism of early kinetics $FeCO_3$ crystal growth at OCP.

The system pH will then evidently result in different time frames for the steps that outline the early stages of growth and will determine whether nucleation or crystal growth dominates the process at each step.

9.5.2 Development of Ultra-Protective $FeCO_3$: Spontaneous 'pseudo-passivation'

From interpretation of the results in Chapter 5, the corrosion rate profile and corresponding OCP can be divided into four regions and a schematic describing the behaviour is shown in Figure 9.11. Schematic depictions of the surface, proposed Randles electrochemical equivalent circuit (EEC) models and corresponding Nyquist plots are displayed in Figure 9.12 that describes the four regions discussed and shown in Figure 9.11.

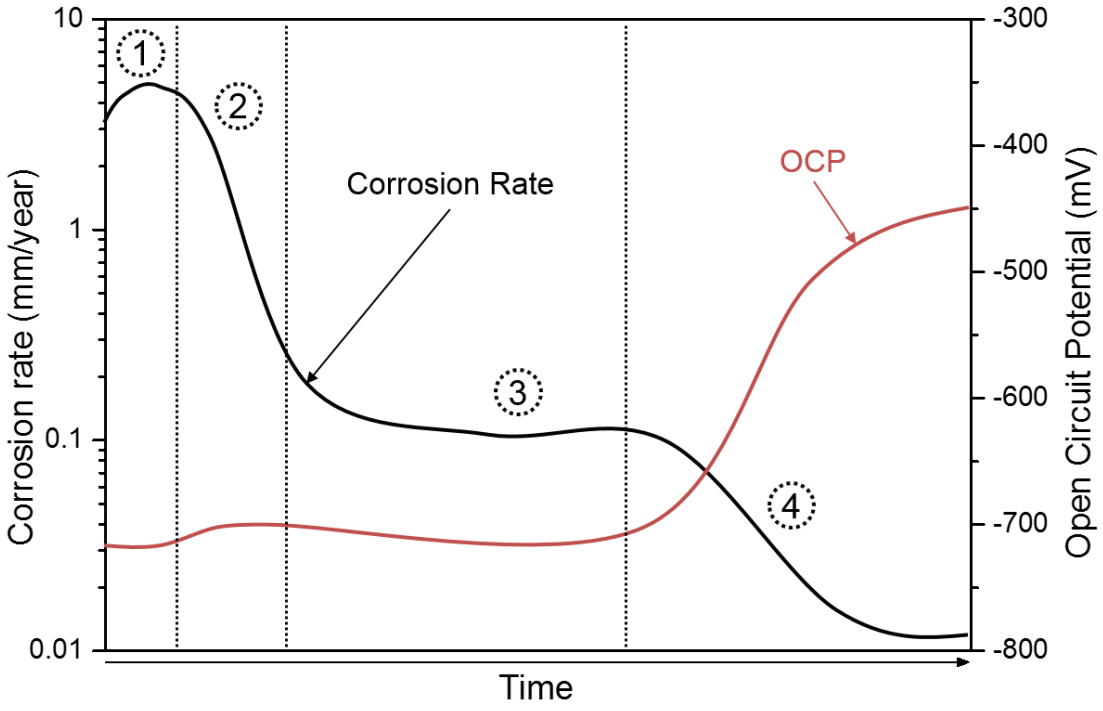

Figure 9.11. A schematic showing the corrosion rate and open circuit potential profiles divided into four regions.

Region 1 – Active stage

In region 1, the active stage is characterised by an initial increase in the corrosion rate upon exposure (for ~2 hours) of the carbon steel surface into

the solution. The increase in corrosion rate can be attributed to presence of ferrite and pearlite (Fe_3C) in the steel. It has been reported that Fe_3C can accelerate the corrosion rate since it is possible for Fe_3C to adopt the role of a cathodic sites while ferrite corrodes [63]. As the corrosion process proceeds, more carbides are exposed, increasing the overall cathodic surface area and therefore the corrosion rate. During this region, nucleation of $FeCO_3$ is likely but has could not be confirmed in these tests. The EIS data in this region can be represented using a Randles EEC model because only a single semicircle is evident on the Nyquist curve. This is illustrated in Figure 9.12 (region 1).

Region 2 – Nucleation and growth (of $FeCO_3$) stage

In region 2, the corrosion rate decreases exponentially after the current maximum (peak corrosion rate) is reached due to the high saturation ratio at the surface via production of Fe^{2+} resulting in precipitation of $FeCO_3$ crystals onto the steel surface (in the form of heterogeneous nucleation and then growth of the crystals). Here, it is assumed nucleation-growth stage of $FeCO_3$ is characterised by an increase in crystal growth (via Ostwald ripening in the form of the Volmer-Weber mechanism of 3D island growth [83]), but also the continued nucleation and growth of new crystals simultaneously resulting in a further drop in corrosion rate. In this region, the system is best represented by a mixture of Randles EEC and the ‘layer-covered metal’ EEC model. EIS has been used to characterise CO_2 corrosion product growth and suggests that the ‘layer-covered metal’ EEC model is appropriate [86] in areas of the surface covered with crystals. At the start of this region, Randles EEC model will dominate the system, but over time, as the crystals continue to nucleate and grow, the ‘layer-covered metal’ EEC model will eventually dominate and best describe the electrical circuit at the interface. This is illustrated in Figure 9.12 (region 2).

Region 3 – $FeCO_3$ growth stage

In region 3, the corrosion rate has dropped and stabilised to ~0.1 mm/year in all tests between 10 and 20 hours. Within this period, as the corrosion rate was decreasing (due to the build-up of $FeCO_3$ crystals), the OCP did not drastically change (~20 mV vs. Ag/AgCl). At this stage, the $FeCO_3$ crystals have formed a compact film reducing both anodic and cathodic reaction kinetics equally, offering protective properties similar to a mixed corrosion

inhibitor. During this period, it is assumed that the growth of the $FeCO_3$ crystals dominates the process. However, SEM analysis suggests that the layer of $FeCO_3$ is still permeable between the crystal faces allowing the production and diffusion of Fe^{2+} from the surface and the mass transport of CO_3^{2-} to the interface. In these regions, at the remaining areas of the interface, there is a local build-up of such ions which rapidly increases the supersaturation resulting in extremely high rates of nucleation of $FeCO_3$ at the interface, between the gaps observed and beneath the larger crystals were voids exist. The 'layer-covered metal' EEC model will dominate the system and best describe the electrical circuit at the interface. This is illustrated in Figure 9.12 (region 3).

Region 4 – 'pseudo-passivation' stage

In region 4, the formation of an ultra-protective bilayer of $FeCO_3$ is observed, specifically in the tests that formed considerably larger crystals (higher porosity) in the earlier stages of growth which essentially invited the nucleation and growth of minute $FeCO_3$ crystals to fill the pores in the latter stages as discussed in 'Region 3'. It can be suggested that extremely high rates of nucleation occur within the voids at the interface (where there is an increased local supersaturation) but the further growth of the crystals is supressed by the larger crystals which forms such bilayer made up of nano-$FeCO_3$ crystals. In this region, the formation of the $FeCO_3$ bilayer results in a further spontaneous drop in corrosion rate (with a final corrosion rate less than 0.02 mm/year) with an associated exponential increase in OCP. This anodic shift in potential was ascribable to preferential suppression of the anodic half-reaction owing to the formation and build-up of $FeCO_3$, which retarded the diffusion of the reductive species to the steel surface performing more like an anodic corrosion inhibitor.

In this region, due to protective $FeCO_3$ formation the corrosion current is diminished and less likely to pass through that part of the equivalent circuit due to the resistance (R_{ct}) being so high and therefore the EEC model representing EIS data after 'pseudo-passivation' has occurred can collapse into one shown in Figure 9.12 (region 4). See [86] for a description of how EEC model was depicted for such system.

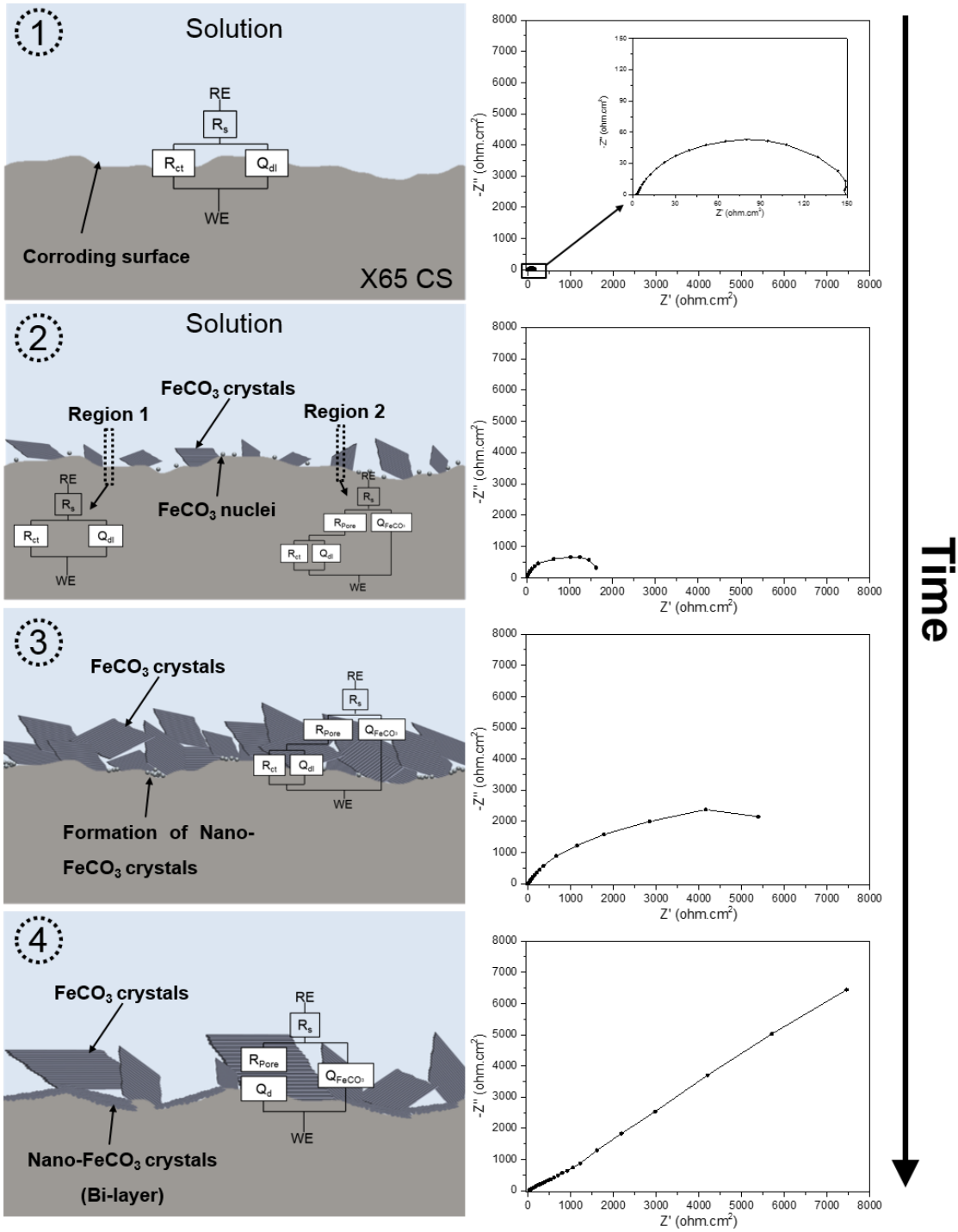

Figure 9.12. Schematic depictions of the surface, proposed EEC models and corresponding Nyquist plots at each of the four regions in Figure 9.14.

9.5.3 Mechanism of the Early Kinetics of $FeCO_3$ Film Formation on a Controlled Corroding Surface

From interpretation of the results in Chapter 8, the current density profile over time and corresponding growth kinetics can be divided into six regions and a schematic describing the behaviour is shown in Figure 9.13.

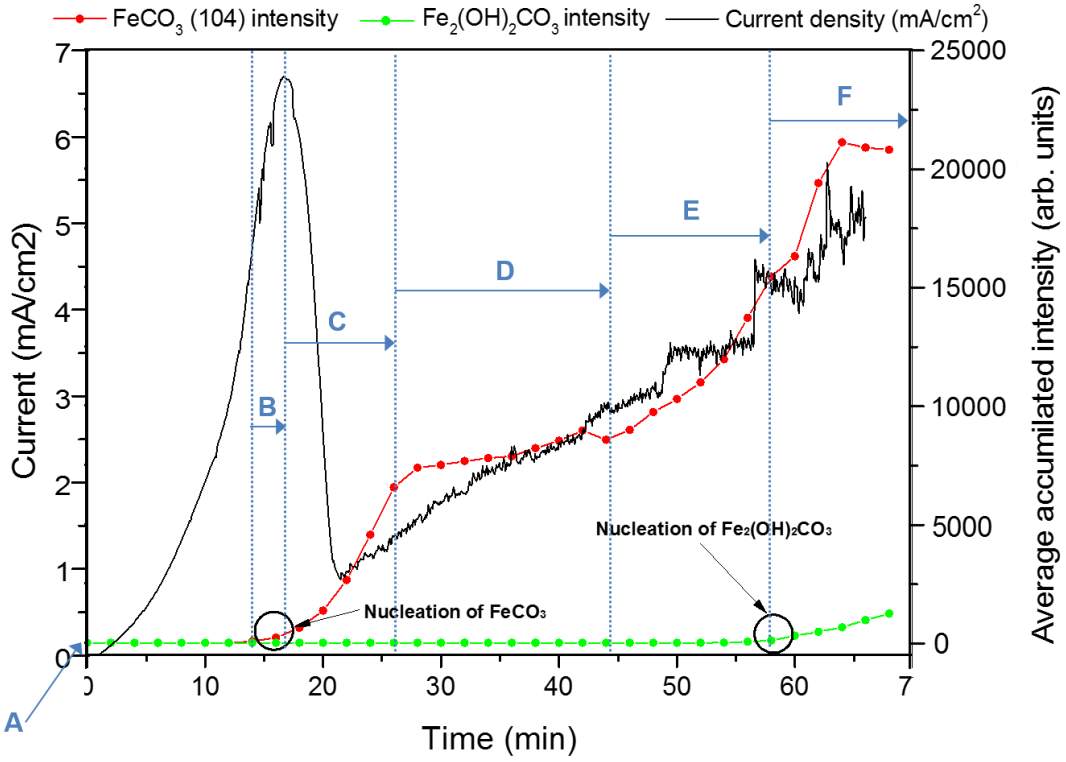

Figure 9.13. Mechanism of $FeCO_3$ crystal growth and current response over time conducted at 80°C, 3.5 wt.% NaCl, 0.54 bar p_{CO_2}, pH 7 and 0.1 m/s under anodic polarisation.

Region A. Start of corrosion process and the induction period for $FeCO_3$. During the induction period, there was no significant detectable diffraction signal for any species other than the already present Fe and Fe_3C. In this region, there is a local excess in Fe^{2+} concentration in the boundary layer when the voltage supply is generated.

Region B. Following the induction period, the current began to rise which could be due to the local acidification accelerating the electrochemical dissolution rate of the carbon steel (positive anodic reaction order with respect to $[H^+]$). In conjunction with this behaviour, the *in-situ* SR-XRD results show

that the onset of the current rise corresponded with the formation of a crystalline $FeCO_3$ crystals, followed by a rapid increase in the growth rate through continued nucleation of new $FeCO_3$ crystals.

Region C. Once the anodic current had peaked (i_{max}), it began to decrease until eventually being restricted by the $FeCO_3$ crystals. At this point, the rate of $FeCO_3$ formation rapidly slowed and approaching a plateau, indicating that the ultra-protective pseudo-passive layer had formed.

Region D. $FeCO_3$ growth reaches a plateau. In this region of growth, the $FeCO_3$ layer is dense and protective enough to resist the current passing through it as seen in the cross section in.

Region E. Possible $FeCO_3$ layer breakdown/removal (in the transpassive regime in Figure 9.13) due to the local build-up of Fe^{2+} beneath the surface resulting in an supersaturation and further growth of $FeCO_3$ (see Figure 9.14 showing the breakdown of the $FeCO_3$ layer).

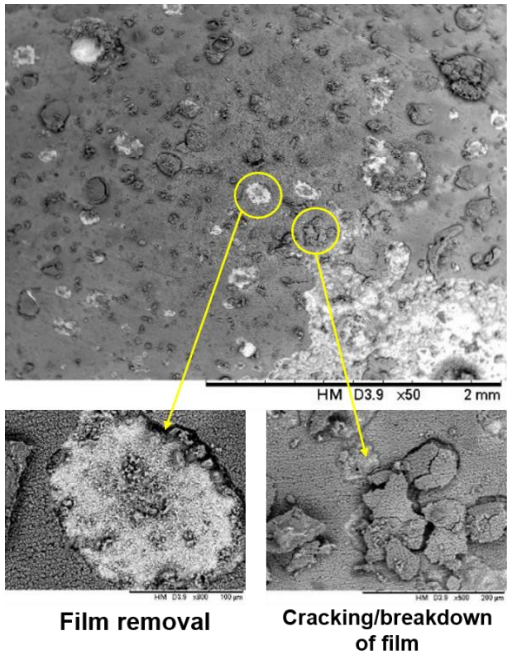

Figure 9.14. *Ex-situ* SEM images of the X65 carbon steel surface at the end of the test showing the breakdown and removal (in the transpassive region) of the films formed at 80°C, 3.5 wt.% NaCl, 0.54 bar p_{CO_2} and 0.1 m/s at pH 7 under potentiostatic control.

Region F. The sudden exponential rise in $FeCO_3$ could be a result of further growth or could be due to the $FeCO_3$ layer separating from the surface and

therefore more $FeCO_3$ is being intercepted by the beam. The nucleation of $Fe_2(OH)_2CO_3$ also occurs in this region to the increase in Fe^{2+}.

A schematic showing the different stages of $FeCO_3$ crystal growth mechanism under anodic polarisation is provided in Figure 9.15.

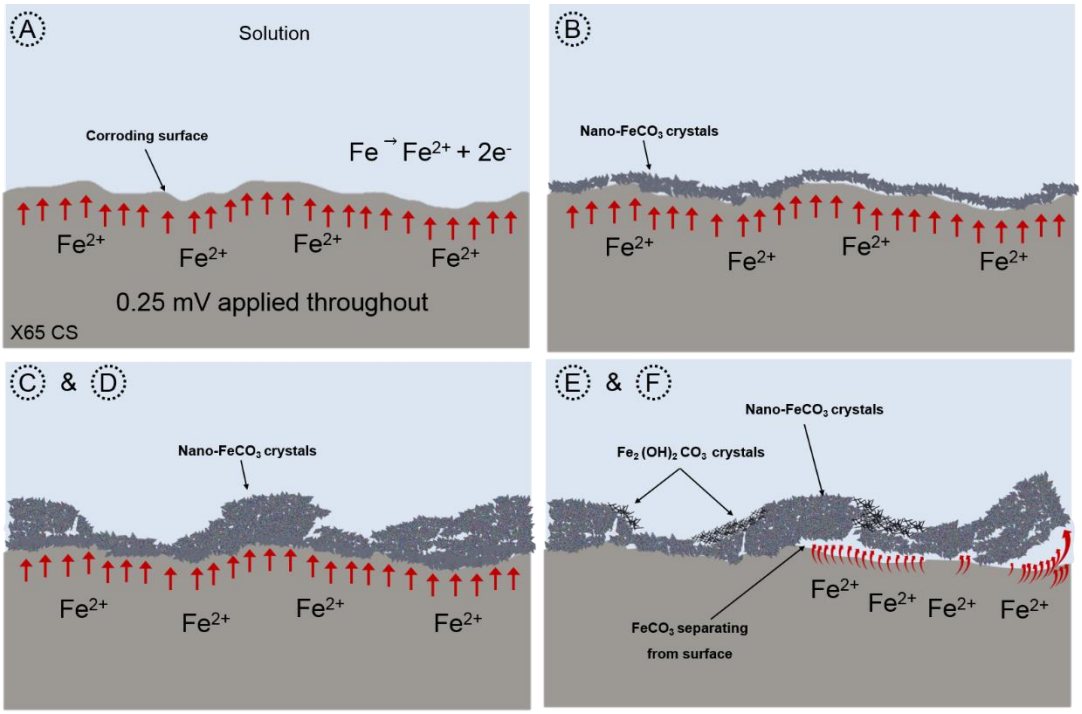

Figure 9.15. Mechanism of early kinetics $FeCO_3$ crystal growth under potentiostatic control.

9.6 Usefulness of *In-situ* SR-XRD for Quantitative and Qualitative Analysis of Precipitation Kinetics

A new system comprising of a flow cell with integrated *in-situ* electrochemistry and SR-XRD capabilities has been developed to facilitate corrosion measurements under a variety of experimental conditions. Some of the first data obtained for *in-situ* analysis has been presented to show the capabilities of the cell. The results have shown that $FeCO_3$ nucleation could be detected consistently and well before its inhibitive effect on general corrosion rate was recorded from electrochemical responses. The $FeCO_3$ intensity plots of the most prominent peak at each of the locations scanned shows a nucleation

period, followed by a growth stage. The major $FeCO_3$ crystal plane (104) at each of the five locations scanned for all of the *in-situ* SR-XRD experiments are shown in Figures 9.16, 9.17 and 9.18. These images show that the rate of $FeCO_3$ growth can be either uniform, or non-uniform, highlighting the importance of multiple scans to accumulate a clear interpretation of the growth kinetics across the steel surface. The growth rate appeared to be very similar across the sample when the relative supersaturation in the system was high and therefore this was observed more so during the anodic polarisation tests (Figures 9.17 and 9.18).

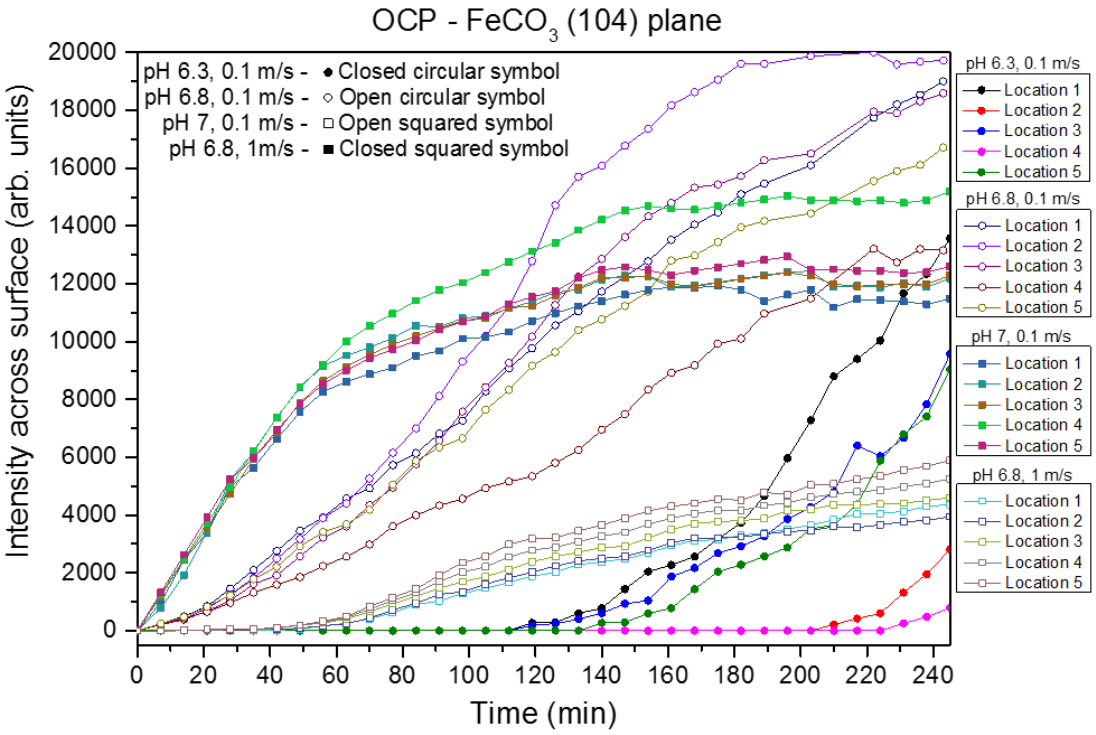

Figure 9.16. Growth of the most dominant $FeCO_3$ crystal plane (104) across the surface conducted at 80°C, 3.5 wt.% NaCl, 0.54 bar p_{CO_2} and 0.1 and 1 m/s at pH 6.3, 6.8 and 7 in a freely corroding system.

The major $FeCO_3$ crystal plane at each of the locations scanned shows a similar (but not identical) growth trend with marginally different characteristics (emergence time, growth rate, final intensity).

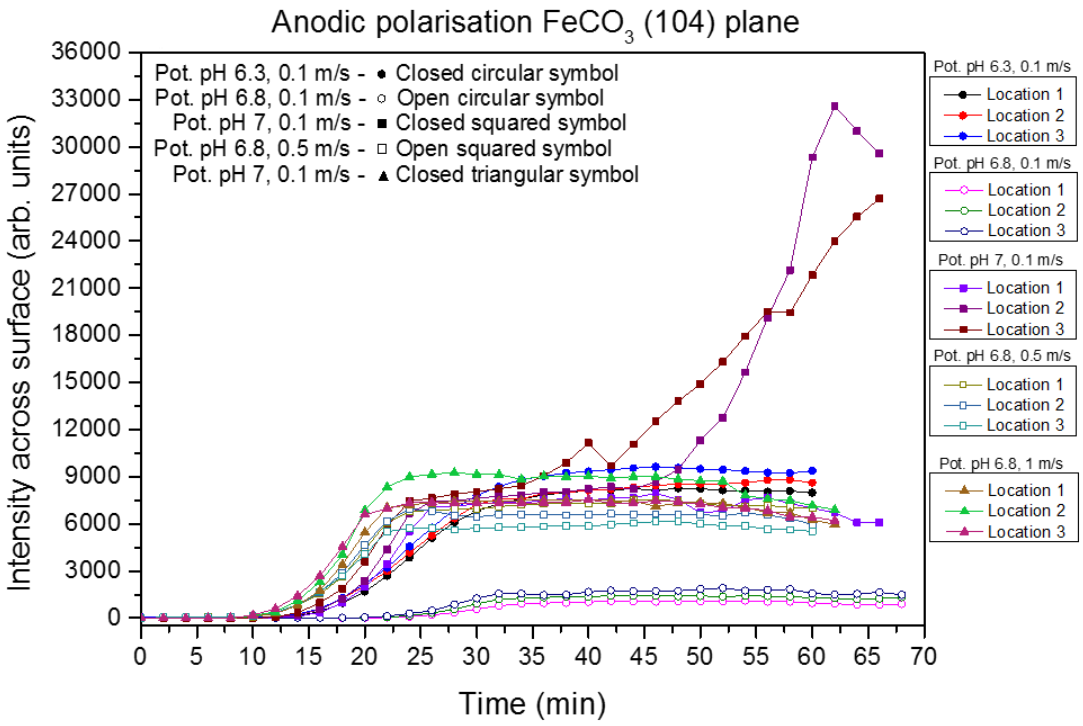

Figure 9.17. Growth of the most dominant $FeCO_3$ crystal plane (104) across the surface conducted at 80°C, 3.5 wt.% NaCl, 0.54 bar p_{CO_2} and 0.1, 0.5 and 1 m/s at pH 6.3, 6.8 and 7 under potentiostatic control.

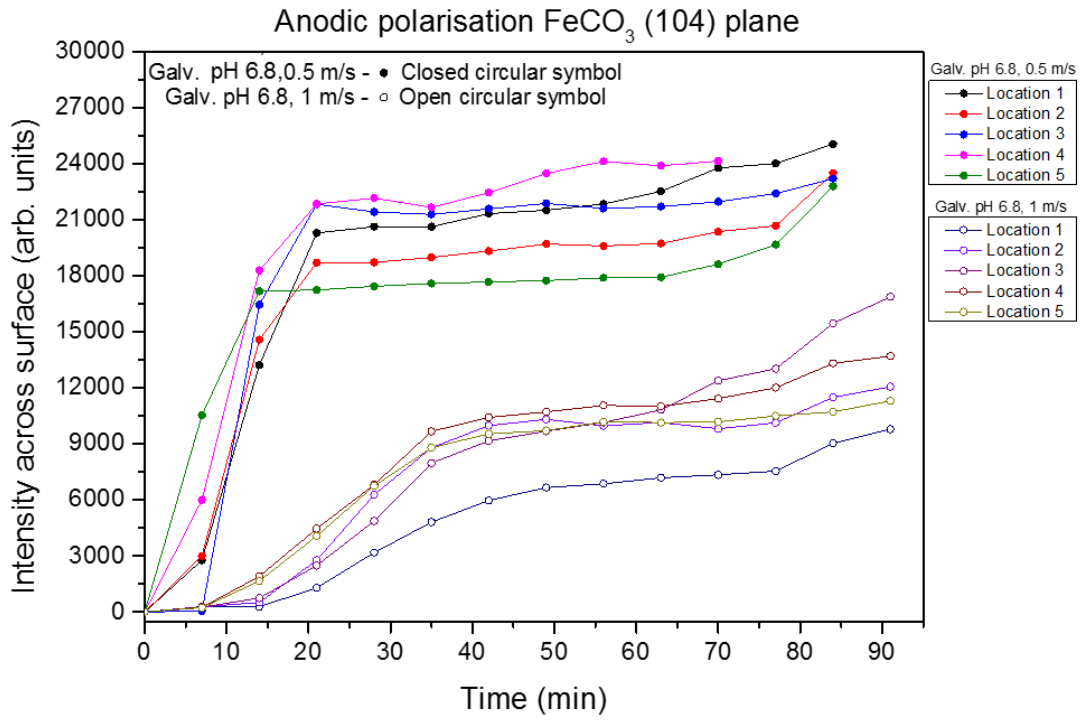

Figure 9.18. Growth of the most dominant $FeCO_3$ crystal plane (104) across the surface conducted at 80°C, 3.5 wt.% NaCl, 0.54 bar p_{CO_2} and 0.5, 0.5 and 1 m/s at pH 6.8 under galvanostatic control.

A particular focus of this study was to identify whether a quantitative link could be established between the intensity of the *in-situ* SR-XRD patterns and the mass of $FeCO_3$ on the steel surface. Accurately quantifying the kinetics of $FeCO_3$ and other corrosion products (such as iron sulphide) on the internal walls of carbon steel pipeline is of huge importance to the oil and gas industry and has been the subject of significant research attention in recent years as addressed throughout this thesis. The ability to monitor film precipitation kinetics in real time and relate this to the protectiveness of the various films capable of forming on the steel surface enables more robust corrosion management strategies and corrosion prediction tools/models to be developed which account for the presence of such films.

A vast amount of research has been conducted focusing on evaluating precipitation kinetics of corrosion products in oilfield environments as reviewed in Chapter 2, particularly in terms of $FeCO_3$ as reviewed in Chapter 3. However, the main challenges in determining precipitation kinetics of $FeCO_3$ relate to the suitability and accuracy of the methodologies applied to determine growth rates. For example, previous studies by Johnson and Thompson [88, 91] and Greenberg and Thompson [95, 96] have typically involved inferring precipitation rates through the measurement of Fe^{2+} ion concentration drop within the bulk solution. Based on this methodology, the assumption is made that all precipitation in the system occurs on the steel surface, something which was shown to be invalid through work performed by Sun and Nesic [81]. In fact, in this work [81], Sun and Nesic showed that the original models developed for $FeCO_3$ precipitation overestimated the film growth by orders of magnitude. Such conclusion were based on result obtained using the ‘weight gain’ method in which the sample is weighed before and after removal of the corrosion product through the use of an inhibited acid known as Clarke’s solution. Although this method was shown to be much more robust and to provide a more accurate measurement of $FeCO_3$ precipitation rates, the approach (just as with mass loss measurement) provides an integral value over a particular time frame. Hence, as well as being time consuming, the approach does not provide real-time precipitation kinetics and measurements of small mass gains can be challenging.

Consequently, from this study the interest was in examining if there was a relationship between film mass and peak area intensity from the produced diffraction patterns. However, although using *in-situ* SR-XRD theoretically is

an ideal means of determining the growth kinetics and composition of corrosion products in conjunction with the electrochemical behaviour, the measurement of such small crystal masses to correlate with the peak intensities is challenging and proved impractical for the early stages of film growth in each of the tests conducted within this work. This was mostly attributed to the small sample size required to minimise water path length through the flow cell. As a result of this, only the final mass gain could be correlated with the XRD patterns with any certainty.

Figure 9.19 shows the relationship between the mass of the corrosion product film on the steel surface with the cumulative intensity of peak area and total $FeCO_3$ calculated volume (calculated using surface coverage and average crystal size) under each pH condition. Based on Figure 9.19, there is evidence to suggest that the technique may hold promise in terms of providing quantitative analysis of film mass for a fixed incident angle and a calibrated system.

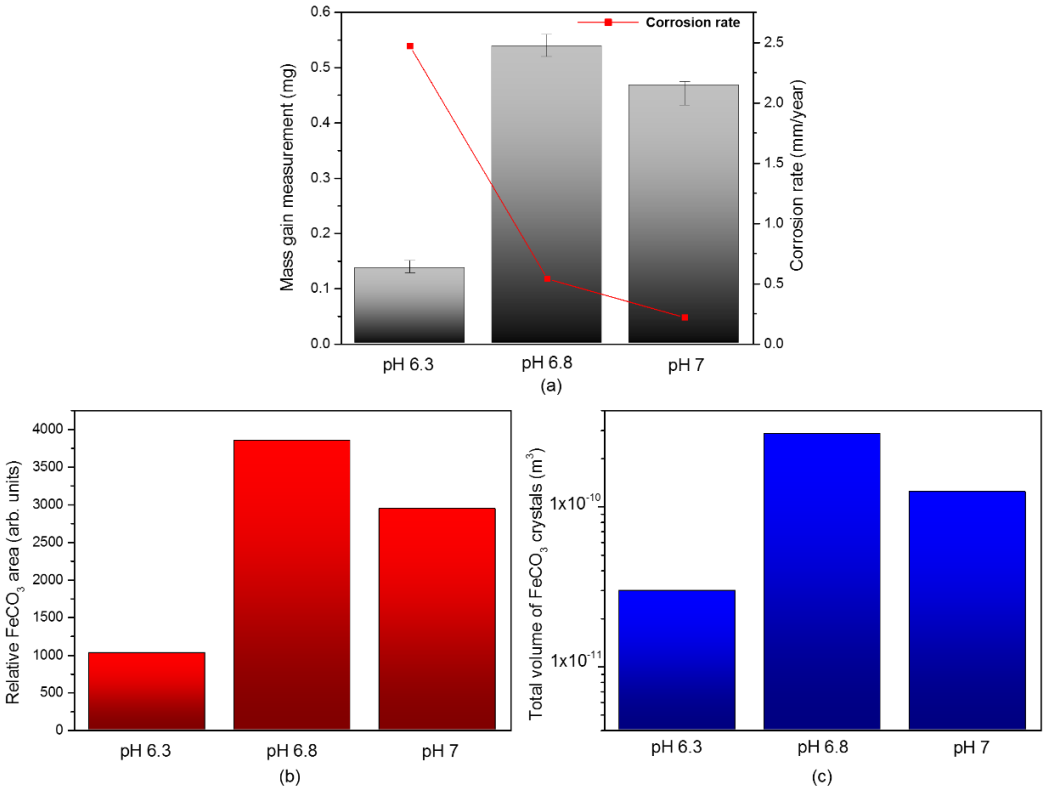

Figure 9.19. Relationship between the mass of the $FeCO_3$ film (a) on the steel surface with the cumulative intensity of peak area (b) and total calculated $FeCO_3$ volume (c) conducted at 80°C, 3.5 wt.% NaCl, 0.54 bar p_{CO_2} and 0.1 and 1 m/s at pH 6.3, 6.8 and 7 in a freely corroding system.

To achieve a better understanding of capabilities of XRD to infer precipitation kinetics and overcome limitations of being able measure earlier levels of mass gain, the surface coverage was correlated with peak area intensity. Although a direct comparison across all pH values could not be performed due to different film thicknesses, it would be possible to see if the peak area intensity correlated with the quantity of film for each individual pH separately as more of the surface became occupied by crystals. Considering that the spot size scanned on the surface was significantly greater than thickness of the film (i.e. five 70 x 70 µm scanned areas vs. a <5 µm thick film), it would be expected that a good correlation could be achieved between the two values, particularly at higher levels of surface coverage.

Figure 9.20 shows the correlation between surface coverage and cumulative peak area intensity over five different scanned areas of the steel surface. Considering the small areas processed from images and XRD, the agreement is very strong.

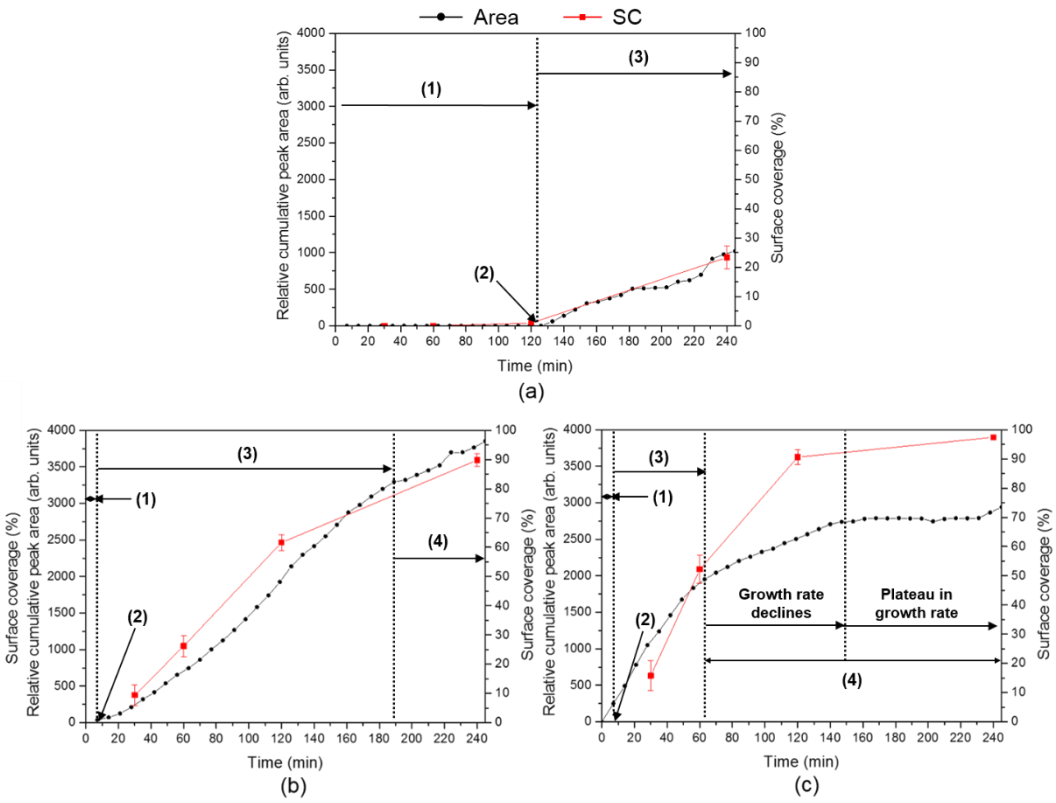

Figure 9.20. *In-situ* integrated diffraction intensities for $FeCO_3$ (104) plane compared with the surface coverage for each test conducted at 80°C, 3.5 wt.% NaCl, 0.54 bar p_{CO_2} and 0.1 and 1 m/s in a freely corroding system: (a) pH 6.3; (b) pH 6.8; (c) pH 7.

Again, these observations reinforce the capability of XRD to help understand and quantify precipitation kinetics. At the very least, these results indicate that XRD and processing of the (104) peak intensity can provide qualitative data on the film growth kinetics, but strong potential exists to develop this into a quantitative technique. Due to the true nature of the corroding surface and it's forever changing profile (i.e. surface roughness) and the precipitation of $FeCO_3$ (i.e. porosity, thickness), it is difficult to acquire an accurate quantitative measure of $FeCO_3$ on the surface (in terms of mass, surface coverage and volume). The intensity itself can be a measurable quantity but it cannot be used as a measurement and determination of how protective a layer is. For instance, lower intensities at the end of the tests generally resulted in higher protection.

The overall intensity of $FeCO_3$ is always lower for more protective systems. The greatest amount of $FeCO_3$ detected during the anodic polarisation tests was still ~ 1/3 the amount of the most protective case at OCP at the end of the test. During the forced corrosion tests, formation of ultra-protective nano-crystals was consistent. However, the true nature of the protection offered is difficult to determine due to the constant flux of Fe^{2+} being generated at the surface through the voltage supply. This being the case, further work on this is required and it is suggested that the system should remain at OCP for the initial period of testing (before film formation), then the voltage/current supply to the working electrode is introduced until a protective layer has formed, then the voltage/current supply should be cut and the system should remain at OCP for the remainder of the test whilst monitoring the corrosion rate. This will give an appreciation of how protective the layer is that is observed under these conditions. Although the intensity in these tests can not directly inform quantitatively on how much $FeCO_3$ is present, a plateau in the growth rate usually complied with the formation of a protective layer. Further studies in a range of conditions could indicate that this plateau in growth could be a direct relationship with the corrosion rate of the system.

9.7 Rationale and Key Role of $FeCO_3$ as a Corrosion Mitigator

When iron carbonate films are well adherent to the underlying steel and compact, they offer a corrosion protection which is similar to the one achieved by applying common carbon dioxide corrosion inhibitors as shown in Figure 9.21.

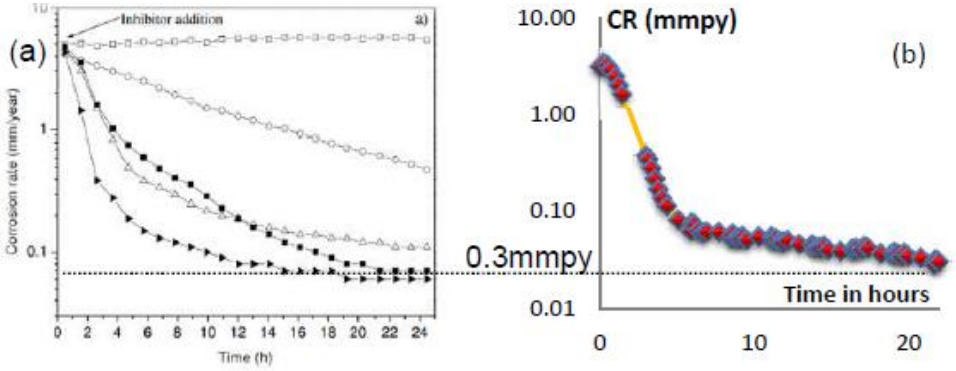

Figure 9.21. Comparison between the corrosion rate variations when (a) bis-imidazoline CI is added [187] and when (b) an $FeCO_3$ corrosion layer has developed.

As such, corrosion rates as low as 0.3 mm/year are observed when 50ppm of the CI is added or a protective $FeCO_3$ has grown as represented by the dotted line. Moreover, a thorough examination of the literature shows that in general, corrosion inhibitors achieve a corrosion rate drop up to 0.1 mm/year while a protective iron carbonate layer brings the corrosion rate to values ten times lower as shown in this work when a 'bi-layer' of $FeCO_3$ forms (pseudo-passive layer).The protective properties offered from the natural formation of $FeCO_3$ has recently been implemented in environments where an $FeCO_3$ coating process toward the corrosion protection of carbon steel in a post combustion CO_2 capture system was utilised [188]. As such, Zheng *et al.* [188] showed that a sodium bicarbonate solution is a practical flushing solution in a real capture system because of its fast implementation as a coating process in order to build a protective $FeCO_3$ layer, environmentally friendly nature, lower cost, and easy process control. This method can be utilised during oil and gas production when the carbon steel pipelines are subject to conditions where $FeCO_3$ may form, but is later removed through chemical dissolution or mechanical damage. Similarly, pipelines are often inspected through the use of a 'smart-pig' (piping inspection gauge) which can physically damage/remove any films formed on the carbon steel surface.

The analysis of the results in this thesis have shown the overall process of $FeCO_3$ precipitation to be a complex process and is dependent on a number of combined factors. $FeCO_3$ precipitation is seen when the saturation level of the solution is exceeded. Therefore, it is well known that supersaturation of the system is an important aspect and the driving force for $FeCO_3$ precipitation but there a number of other physical kinetic parameters that play an extremely

important role when determining the protectiveness of the crystals. At high supersaturation levels, the nucleation phase prevails and $FeCO_3$ forms primarily by coagulation, whereas the crystal growth mechanism predominates at low relative supersaturation. This can very well account for inconstancy of the $FeCO_3$ films often seen in the field where supersaturation levels may considerably vary due to fluctuating water chemistry conditions [40].

The degree of $FeCO_3$ film protection seems to be strongly correlated with a number film morphological characteristics. The protectiveness of the $FeCO_3$ layer is usually associated with its thickness and porosity. It is common to assume that the protectiveness of a layer is due to the mass-transfer resistance, which, in this case, a dense and thick $FeCO_3$ layer offers protection against inward diffusion of corrosive species. However, the experiments in this work have shown that this is only partially correct. For example, better protective properties were observed in experiments where the $FeCO_3$ layer was thin, well anchored to the steel interface with minimum pores in comparison to a thicker film with such porosities as shown in the cross sections in Figure 9.22 (images taken from Chapter 7) showing the $FeCO_3$ films at pH 6.8 and 7.

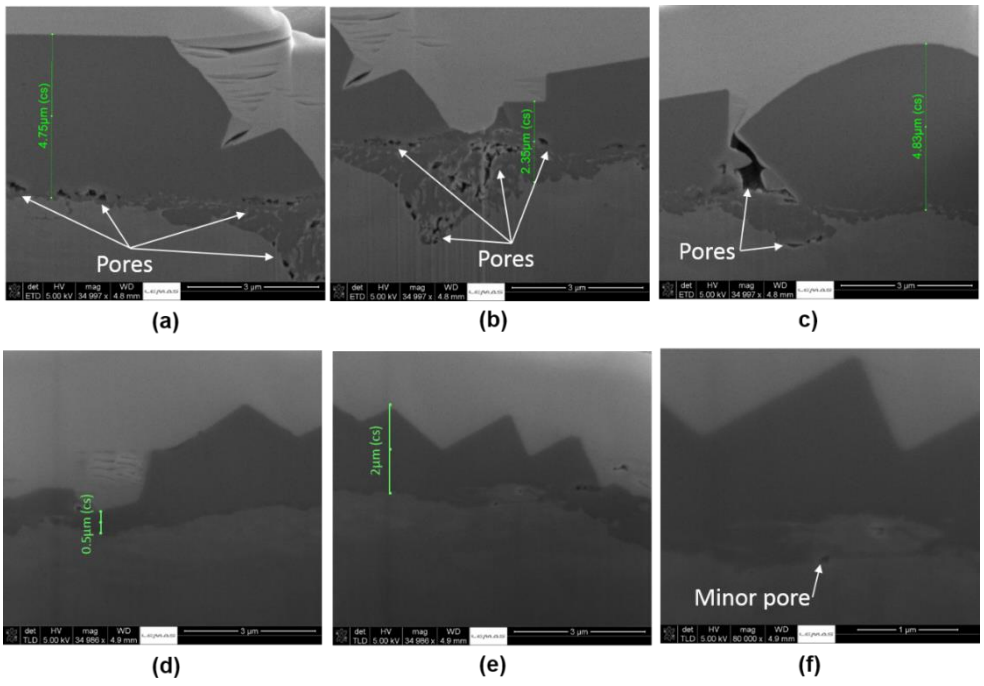

Figure 9.22. *Ex-situ* SEM images of the X65 carbon steel surface at the end of the test showing the cross-sections of the films formed at 80°C, 3.5 wt.% NaCl, 0.54 bar p_{CO_2} and 0.1 m/s at pH 6.8 (a-c) and pH 7 (d-f) in a freely corroding system.

Therefore, the thickness of the $FeCO_3$ does not show a direct relationship with protective properties. Following this, it can be suggested that the surface coverage (blockage) effect which retards dissolution of the metal surface has far more importance than the diffusion barrier effect which impedes the transport of the corrosion species. This demonstrates that, in contrast to irrelevant film thickness, film density/porosity and how well the crystals adhere to the surface is essential to film protectiveness.

This work has also shown that an extremely compact, impermeable and adherent $FeCO_3$ "'bi-layer'" can form spontaneously at times offering excellent corrosion resistance (~0.01 mm/year), which seems to be the key to corrosion protection. The protectiveness of this thin $FeCO_3$ 'bi-layer' seemed to be associated with its adherence to the steel surface as much as it was related to its permeability. Given the rise in OCP when protective corrosion product layers form in CO_2 corrosion, it was deduced that the protection comes from the retardation of the anodic reaction more than the cathodic reaction. The "outer", more porous $FeCO_3$ layer, which forms first, does retard the diffusion of corrosive species to the surface but also the diffusion of ferrous ions away from it.

For such 'pseudo-passive' film to form at the carbon steel interface among the $FeCO_3$ crystals already present on the surface, it can be suggested that the crystals are permeable allowing the electrolyte a pathway to steel surface, or at least pockets of solution remain trapped between the pores that exists between the steel surface the $FeCO_3$ crystals or within the $FeCO_3$ crystals themselves. The local solution chemistry beneath the $FeCO_3$ crystals might change, resulting in a higher supersaturation due to the further production of Fe^{2+} at the exposed regions to the solution. There seems to be an optimum operating window for this layer to form which is controlled by the crystals size, porosity and growth rate which are all influenced by the local supersaturation. Future work should focus more attention on this optimum operating window to decipher empirical data which could help predict exactly when this spontaneous behaviour is likely to occur to fully utilise the protective properties that are established once this 'bi-layer' of $FeCO_3$ forms.

The results in this work have suggested that an increase in supersaturation, surface coverage and a decrease in porosity and crystal size, along with how well the crystals adhere to the surface are the driving forces behind the reduction in the corrosion rate and govern the overall protectiveness of the system. This work has helped in understanding the most important factors

governing the rate of $FeCO_3$ formation and the overall protectiveness offered. It is suggested that four *key* parameters are the biggest contributors to how much protection an $FeCO_3$ layer can offer to the carbon steel surface: (1) Porosity; (2) adherence; (3) surface coverage and (4) crystal size. Each of these parameters are linked and dependent on each other, but are essentially all driven by the supersaturation. Ultimately, an increase/decrease in these parameters are what controls the protection against further Fe^{2+} production at the steel interface. This is illustrated in Figure 9.23 which shows the most important factors governing the rate of $FeCO_3$ formation and the overall protectiveness offered.

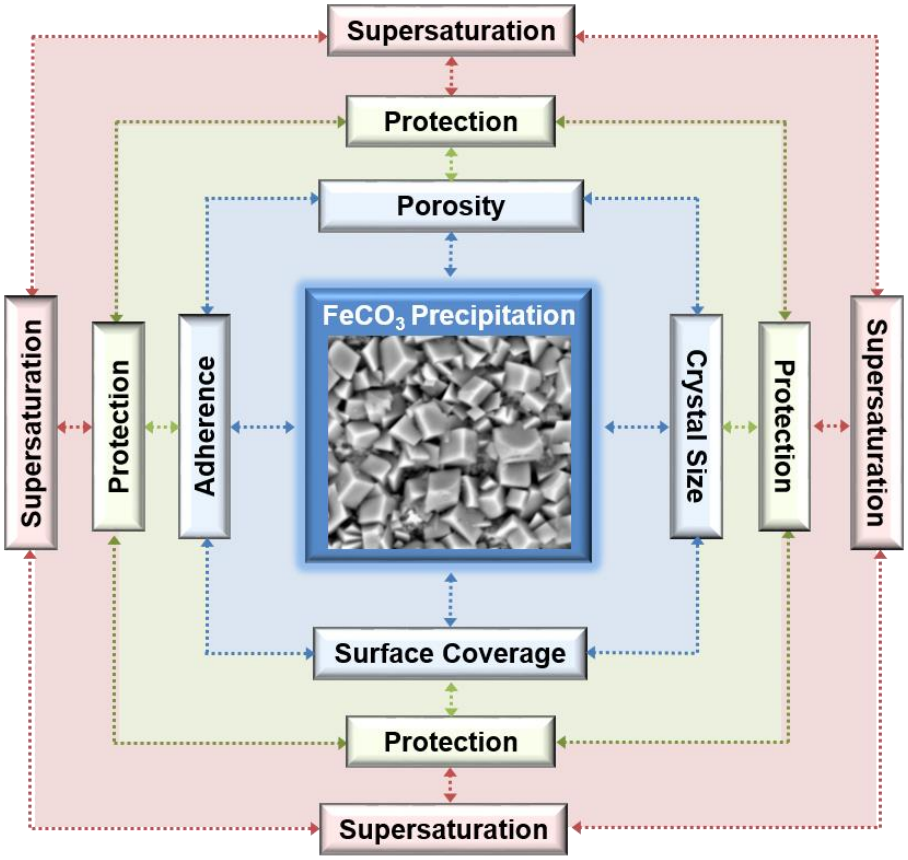

Figure 9.23. A schematic showing the most important factors governing the rate of $FeCO_3$ formation and the overall protectiveness offered.

Chapter 10.
Conclusions: Final Conclusions and Major Findings, Relevance to Industry, Future Considerations

This chapter presents the major findings and conclusions from the work undertaken during the project whilst showing the relevance to industry practicalities. The chapter ends on ideas for relevant future work within the wider picture in the fight against corrosion in oil and gas production and transportation.

10.1 Conclusions

Understanding the factors governing the rate of formation of $FeCO_3$ on the corroding surface of carbon steel and the protection offered is an important step in understanding the overall CO_2 corrosion mechanism. It is crucial for researchers and oil and gas operators to account for $FeCO_3$ formation when developing an accurate corrosion prediction model or when developing a robust corrosion management strategy. It is important to understand which corrosion products are formed and to what extent their rate of formation, morphology and protectiveness are influenced by changes in the operating conditions and the environment.

Based on the lack of consistency and certainty in the literature and the results in Chapter 5 on the true nature of the phases to form during the CO_2 corrosion process expresses the need for a new *in-situ* methodology to determine the CO_2 corrosion mechanism and the kinetics of corrosion product formation. Two main challenges presented themselves when analysing corrosion product film formation processes in oil and gas environments which this work has addressed. To overcome the limitations and challenges and what can been viewed as a major gap, this work has presented a new system and methodology comprising of a flow cell with integrated *in-situ* electrochemistry and SR-XRD capabilities which has been developed to facilitate corrosion measurements under a variety of experimental conditions in a flowing system. Some of the first data obtained for *in-situ* analysis has been presented to show the capabilities of the cell. Using *in-situ* SR-XRD, the formation of corrosion products on a naturally corroding carbon steel sample in a CO_2 saturated brine has been followed as a function of time in the newly designed flowing cell. The early nucleation and growth kinetics of $FeCO_3$ of a naturally corroding surface in a flowing, deaerated system are characterised *in-situ* and presented for the

first time. This work aimed to gain a better understanding on the development of protective $FeCO_3$ on to X65 carbon steel. Based on the results obtained, the following conclusions can be extracted which have been taken from each of the chapters presented.

In Chapter 5, the development of ultra-protective $FeCO_3$ has shown that;

- A spontaneous second drop in the corrosion rate profile with a corresponding rise in OCP occurred and was deemed as a 'pseudo-passivation' process resulting in an ultra-protective $FeCO_3$ layer (showing similar protective properties to mixed corrosion inhibitor) at the steel interface between/underneath larger $FeCO_3$ crystals with enhanced diffusion limiting properties.
- The transition from protective $FeCO_3$ (limiting the corrosion rate to ~0.1 mm/year) to ultra-protective $FeCO_3$ (limiting the corrosion rate to ~0.02 mm/year) is related to significant direct blocking of the steel surface and restricting further production of Fe^{2+} through the formation of a bilayer.
- EIS methods, in conjunction with the LPR measurements deemed a valuable complementary technique towards interpreting the changing protective properties of the $FeCO_3$ layer.
- The change in Nyquist curves from well-defined capacitive semicircles to a capacitive semicircle with a linear tail at low frequencies is a good indicator of when the 'pseudo-passivation' process begins and an ultra-protective $FeCO_3$ begins to form.
- For such 'pseudo-passive' film to form at the carbon steel interface among the $FeCO_3$ crystals already present on the surface, it can be suggested that the crystals are permeable allowing the electrolyte a pathway to steel surface, or at least pockets of solution remain trapped between the pores that exists between the steel surface the $FeCO_3$ crystals or within the $FeCO_3$ crystals themselves. The local solution chemistry beneath the $FeCO_3$ crystals might change, resulting in a higher supersaturation due to the further production of Fe^{2+} at the exposed regions to the solution.

- Through a combination of the results in this study, four stages were identified explaining the process resulting in the formation of an ultra-protective $FeCO_3$ bilayer: 1) An active corrosion stage (where the corrosion rate increased to Fe_3C exposure); 2) A nucleation and growth of $FeCO_3$ stage (where simultaneous nucleation and growth of $FeCO_3$ crystals occur); 3) Further $FeCO_3$ growth stage (where the growth of the $FeCO_3$ crystals dominate); 4) A 'pseudo-passivation' stage (where there is formation of an $FeCO_3$ bilayer).

In Chapter 6, the design and development of a unique flow cell for *in-situ* corrosion studies was presented. The initial *in-situ* electrochemical and SR-XRD observations validates the use the flow cell to monitor the corrosion rate and growth kinetics of $FeCO_3$ (and/or any other corrosion products) formation with confidence and reassurance. The results have shown that a cumulative intensity relationship with corrosion rate and film formation exists. The results have also shown that $FeCO_3$ nucleation could be detected consistently and well before its inhibitive effect on general corrosion rate was recorded from electrochemical responses, indicating that *in-situ* SR-GXRD is able to detect the very early stages of crystal nucleation on surfaces in a flowing cell. The flow cell can be used to evaluate the effect of flow velocities on the rate of corrosion product formation and the corrosion rate of the system with the ability to operate from 0.1 m/s (under a laminar flow regime) to 2 m/s (under a turbulent flow regime). The design, development and implantation of such system opens up several avenues of research where real-time corrosion measurements might enable some mechanisms to be determined. The flow cell will be used in future investigations into the effect of different environmental parameters on the formation of $FeCO_3$.

In Chapter 7 and 8, this new system comprising of a flow cell with integrated *in-situ* electrochemistry and SR-XRD capabilities was used to follow the corrosion kinetics of X65 carbon steel in real-time in a CO_2 saturated brine at varying brine and surface conditions (through adjusting the pH and adding Ca^{2+} to the solution) when subjected to a flow rate of 0.1 m/s. The effects of the flow velocity under the same brine conditions was also assessed. The following conclusions can be extracted from the results presented in these chapters:

Phase composition and relevance in the protection against corrosion:

- Under the specific conditions evaluated in this entire thesis, $FeCO_3$ was the major crystalline phase to form in the system, with no crystalline precursors being apparent prior to or during its formation and being the sole phase responsible for the observed reduction in corrosion rate, predominantly through the blocking of active sites on the steel surface.
- It is also concluded that $FeCO_3$ is solely responsible for the ultra-protective properties during 'pseudo-passivation' of carbon steel in CO_2 corrosive environments.
- In the test that $Fe_2(OH)_2CO_3$ was also observed, it did not form until after the $FeCO_3$ later on in the test and did not seem to offer any protection to the carbon steel surface.

$FeCO_3$ growth kinetics:

- The major $FeCO_3$ crystal plane at each of the five locations scanned shows surface growth is heterogeneous (i.e. non-uniform) at times under different operating conditions, highlighting the importance of multiple scans to accumulate a clear interpretation of the growth kinetics across the steel surface.
- The growth and the morphology of the $FeCO_3$ crystals recorded using *in-situ* diffraction patterns can be well described by the most dominant (104) crystal plane which is the most predominant during the nucleation and growth of $FeCO_3$ and the final crystal morphology depends on the growth rate of the crystals, which is in turn determined by the supersaturation required to form $FeCO_3$.
- From the accumulated integrated peak intensities in the tests conducted in a freely corroding system, four steps characterised the growth mechanism of the $FeCO_3$ layer: (1) An induction time when the measured intensity is zero; (2) Nucleation of the $FeCO_3$ crystals when

the measured intensity initially increases; (3) Nucleation-growth stage which is characterised by an increase in crystal growth with nucleation occurring simultaneously; (4) Growth stage when the integrated intensity slows down and near full surface coverage is achieved, limiting nucleation.

- From the accumulated integrated peak intensities in the tests conducted in a controlled corroding system, the $FeCO_3$ growth curves for each *in-situ* SR-XRD test showed an induction period (before crystalline $FeCO_3$ was detected), followed by a growth stage where crystalline $FeCO_3$ precipitation and was directly correlated with a rise in the current density, which then fell when the growth rate had reached a plateau once a protective pseudo-passive layer had formed.
- Once this pseudo-passive layer had formed, the film was protective enough to resist the current passing through which lead to an increase in the measured potential.

Environmental factors affecting $FeCO_3$ formation:

- The induction time for $FeCO_3$ formation significantly reduces with increased pH, which also causes increase in crystal nucleation rate resulting in the formation of a smaller, compact and more protective crystals in the early stages of growth.
- An increase in flow velocity leads to an enhanced mass transfer process, and the released Fe^{2+} ions due to a higher corrosion rate can be easily flushed away from the steel surface, reducing the local supersaturation and increasing the induction time for $FeCO_3$ precipitation.
- The presence of 1000 ppm Ca^{2+} affected the corrosion mechanism by changing the water chemistry, which in turn resulted in the precipitation of less-protective $CaCO_3$ which interfered with the continued formation and growth of protective $FeCO_3$ crystals when added after $FeCO_3$ film formation.

- The presence of 1000 ppm Ca^{2+} in the same conditions but before $FeCO_3$ formation resulted in the solution being saturated for only $CaCO_3$ and no $FeCO_3$ was detected.
- When $CaCO_3$ was the only new crystalline phase to form, an inner layer rapidly precipitated on to the steel surface which offered some protection against corrosion and unstable/non-protective larger crystals were continuously being flushed away from the surface.

In summary, this work has shown that a continual decrease in the corrosion rate of carbon steel (evaluated from LPR measurements *in-situ*), has shown that the evolving $FeCO_3$ layer always offers an improving degree of corrosion resistance to the underlying surface. However, $FeCO_3$ precipitation is an extremely complex process of simultaneous nucleation and growth that determines the overall protectiveness of the layer. The characteristics and protective properties offered of the $FeCO_3$ film significantly changes under varying operating conditions.

A more protective $FeCO_3$ film is made up of compact and dense crystals offering a higher degree of surface coverage. A less protective film consists of larger, more discrete crystals not effectively blocking active corrosive sites. The results in this work have suggested that an increase in supersaturation, surface coverage and a decrease in porosity and crystal size, along with how well the crystals adhere to the surface are the driving forces behind the reduction in the corrosion rate.

10.2 Novel Aspects and Relevance to Future Work and Industry

Within the development of the new unique flow cell designed to follow the evolution of corrosion products in real time to the physical results and findings in this work, some of the novelties are outlined with their relevance to industry and future studies in this field.

Novelty 1: *The findings from the naturally corroding long term tests (static immersion tests and flow cell tests) reveal a very fine, dense and compact 'bi-layer' of $FeCO_3$ that offers ultra-protection to the carbon steel beneath.*

Relevance/Importance/Future work: The protection offered from this 'bi-layer' of $FeCO_3$ is in the range of the most advanced inhibitors available on

the market. Further work in this area could help improve the knowledge of exactly when this layer forms (which is a result of the very early growth and morphology of the crystals when the system SR is high) and identifying an optimum window with accurate experimental values. This layer can be exploited and utilized to protect pipelines (with precaution because any damage to this layer can result in extremely severe localized corrosion). However, work can be done on improving the mechanical properties of the $FeCO_3$ layer which is currently being attempted in work at the University of Leeds by Wassim Taleb (see reference 170) through try two methodologies: 1) the use of silicon based nano-particles; 2) the use of bacteria. Method 1 has shown to increase the mechanical properties through embedding itself into the $FeCO_3$ crystal lattice and also acts as nucleating agent to increase the nucleation rate of $FeCO_3$. Alternatively, if the conditions of the pipeline can be maintained throughout the system for the duration of service then this work has shown that $FeCO_3$ will form extremely fast under the correct conditions. If the natural formation of such protective $FeCO_3$ can be exploited and utilized to protect pipelines, this will reduce the need for costly inhibitors, saving oil and gas operators money whilst being environmentally friendly.

Novelty 2: *The development and implantation of the in-situ SR-XRD flow cell to follow the very early kinetics, growth and composition (and longer term changes in film chemistry) of corrosion products in real time.*

Relevance/Importance/Future work: The capabilities of the flow cell alone are novel and a good addition to literature with the ability to: facilitate both *in-situ* electrochemistry and SR-XRD simultaneously allowing the early kinetics of nucleation, growth and phase transitions to be followed in real time; and operate under high temperatures, flow velocities and a range of other operating conditions. Utilising the capabilities of this new methodology can allow other researchers to gain an even further understand to $FeCO_3$ formation (beyond what this work has added to the literature) and can allow early mechanisms and kinetics of $FeCO_3$ formation to be implemented into industry standard CO_2 corrosion models. Improved corrosion product precipitation models can be used to support material selection and risk assessment.

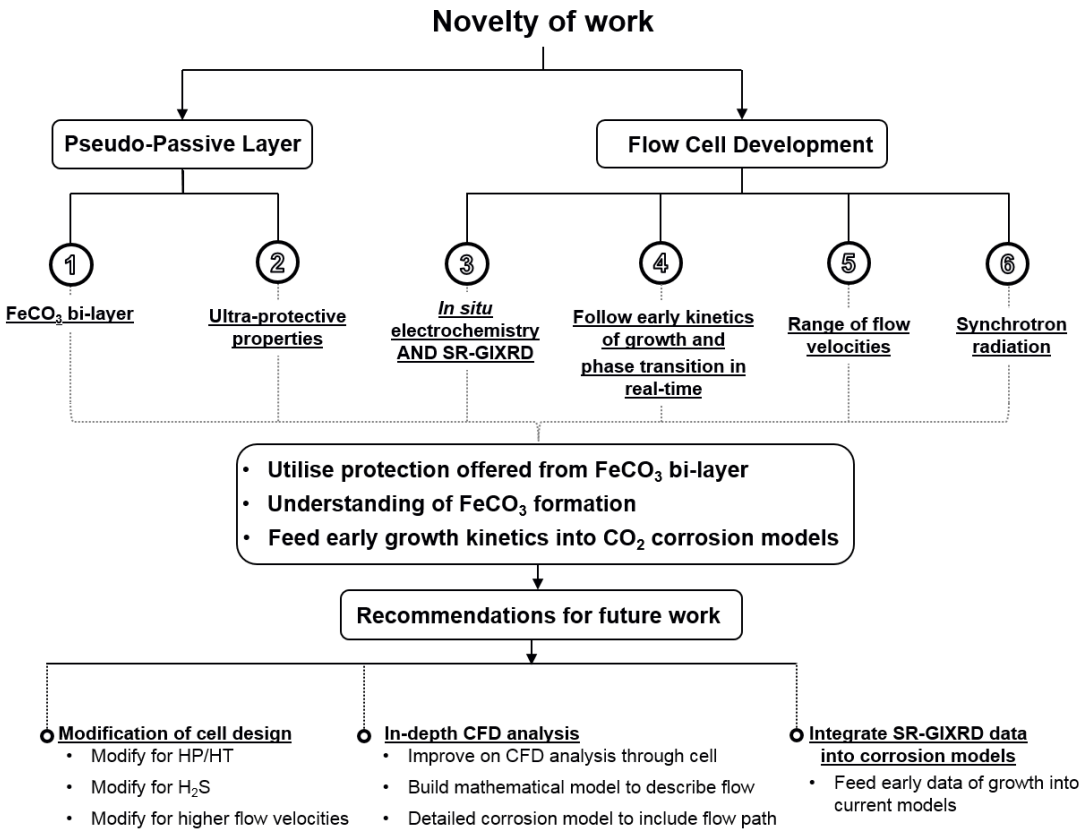

Figure 10.1. A schematic showing the novelties of the work with recommendations for future studies.

10.3 Recommendations for Future: Building on Synchrotron Methodology

This research has successfully proven the capability of a combined electrochemical and SR-XRD methodology to elucidate the growth kinetics of $FeCO_3$ formation *in-situ*. The results give further insight on the mechanism and controlling factors of $FeCO_3$ formation during CO_2 corrosion. However, there many other aspects of corrosion that can be explored using the flow cell and synchrotron radiation.

Extension of work and future studies are recommended:

Recommendation 1: Building upon initial $FeCO_3$ experiments – brine chemistry

There exists considerable controversy in the literature regarding the formation of $FeCO_3$, the initial experiments in the work have gone someway to

disproving these theories. The studies in this work have shown that $FeCO_3$ forms directly on the steel surface without any crystalline pre-cursors, and that the $FeCO_3$ phase remains stable on the steel surface with no formation of $Fe_2(OH)_2CO_3$ apparent when compared to unrealistic static, current-driven processes, or systems where oxygen contamination was reported to have occurred. The observed variations in $FeCO_3$ mechanisms and the associated possibility of significant variations in corrosion rate also have potential implications for corrosion testing and corrosion control methods. Therefore, further experiments mapping the effect of system pH and temperature are required in order to clarify these observations and fully understand the formation of FeCO3. The majority of scientific studies on CO_2 corrosion are conducted in NaCl-based solutions, without the inclusion of additional cations such as Ca^{2+} and Mg^{2+}, and many industrial testing regimes are based on standardised test conditions focused on chloride concentration, pH and CO_2 partial pressure, without consideration of the cation mix. In contrast, the results of this study suggest that even very small variations in the cationic make-up could have significant effects on protective $FeCO_3$ film formation and should be studied in greater detail. It is therefore recommended that future work should intend to build upon the initial research by evaluating the effect of Mg^{2+} and Ca^{2+} ions on the early kinetics of $FeCO_3$ formation. It is perhaps worth noting that research into the formation of other carbonate species on steel surfaces ($CaCO_3$ for example) has indicated that specific cations (Mg^{2+} in particular) within the process fluid can have a dramatic influence.

Recommendation 2: Building upon $FeCO_3$ experiments – higher temperatures and pressures

The next proposed stage of work is to consider the stability of $FeCO_3$ and the potential of other corrosion products to form at higher temperatures and pressures. At temperatures above 100ºC, the formation of $FeCO_3$ and magnetite (Fe_3O_4) are both possible when considering Pourbaix diagrams. However, the type of films formed depend on both thermodynamics and kinetics of formation; something which cannot be determined from thermodynamic equilibria. Additionally, the influence of Fe_3O_4 formation on the corrosion rate of the substrate is largely unknown. With autoclaves typically being used for such corrosion experiments, to this date no *in-situ* techniques have been applied to CO_2-saturated systems where the temperature is in excess of 100ºC and 100 bar in a flowing environment. Understanding the nature of the films formed at higher temperatures/pressures and how these

relate to the corrosion rate of carbon steel is a key step in determining appropriate chemical inhibition and material selection strategies, as well as quantifying and predicting the risk of pipeline failure.

Recommendation 3: Understanding the conditions conducive to $FeCO_3$ removal

One of the main concerns in the oil and gas industry are the conditions conducive to removal of protective $FeCO_3$ layers as this can induce galvanic effects, resulting in localised corrosion and unpredictable failures. A concerted effort should be devoted towards evaluating $FeCO_3$ film stability when subjected to changes in system pH and fluid velocity. Once film formation is substantial and protective, the conditions within the cell will be changed to generate dissolution or mechanical removal of the film. Understanding the likely stability of $FeCO_3$ will be of paramount importance to industry, influencing their corrosion management strategy.

Recommendation 4: New frontiers in corrosion inhibition treatment

Inhibitors are generally used when carbon steel is the preferred pipework material of choice. It is therefore not uncommon for $FeCO_3$ and chemical inhibitors to compete to protect the steel substrate. Very few studies have examined the influence of inhibitors on $FeCO_3$ formation and its crystallographic nature, although it is likely these compound will have a dramatic effect on their structure. It is recommended that future work is based on evaluating two common corrosion inhibitors (an amine and imidazoline derivative) and their influence on $FeCO_3$ kinetics. Furthermore, research at Leeds has been directed towards the development of nanoparticles to promote and strengthen $FeCO_3$ films. Future beam-time should be used to evaluate and demonstrate the potential of these nanoparticles (specifically, functionalised polyhedral oligomeric silsesquioxanes) to increase the film precipitation kinetics and improve the films mechanical properties. The ability to modify $FeCO_3$ and its mechanical properties is state of the art and of significant value to industry in terms of minimising the risk of pipeline failures.

Recommendation 5: Understanding film formation and film transitions in simulated H_2S environments

One of the main concerns in the oil and gas industry is the presence of dissolved H_2S in the process fluid as this can result in localised corrosion and unpredictable failures. It has been well established that the formation of iron sulphide films leads to localised corrosion. What is unclear currently is which

specific morphologies of iron sulphide are conducive to such attack, given that around four different crystalline structures of films are possible under typical oil and gas conditions, each with very different physical properties. The flow cell can be used to shed new light on the kinetics of iron sulphide formation and determine whether the formation and transitions in films structure can be identified *in-situ*, whilst also being linked to the corrosion of the underlying substrate. There is currently no literature where *in-situ* film formation of iron sulphide has been recorded, let alone where this has been simultaneously been linked to corrosion rates.

Recommendation 6: The use of alternative synchrotron techniques

The use of other synchrotron radiation techniques to elucidate even further on the currently hypothesised $FeCO_3$ formation process. It is suggested that further work could implement the use of other synchrotron radiation techniques such as grazing incidence small angle x-ray scattering (GISAXS) with the aim of monitoring the nucleation and growth of any potential amorphous precursors near to the steel surface (that could be present during the induction time for crystalline $FeCO_3$) and to characterise the kinetics of its transformation to crystalline phases. This would improve the understanding of the $FeCO_3$ nucleation and growth process. It is also proposed that *in-situ* techniques where electrochemical tests are coupled to *in-situ* synchrotron tomography techniques could help achieve such aims.

This technique could prove useful to attempt a systematic determination of all $FeCO_3$ layers (and the crystals porosities) formed in CO_2 saturated environments. This technique is known to have lower resolution than FIB/SEM but is non-destructive and does not require impregnation and vacuum. It allows for the determination of many parameters such as the porosity, its pore connectivity, tortuosity, structural diffusivity coefficient and the mean pore size. This technique could play a vital role in determining the mechanism prior and during localised corrosion and pitting which could effectively change the whole dynamics of how oil and gas pipelines are operated.

References

1. Garverick, L. ed., 1994. *Corrosion in the petrochemical industry*. ASM international.
2. De Marco, R., Jiang, Z.T., Pejcic, B. and Poinen, E., 2005. An *in situ* synchrotron radiation grazing incidence X-ray diffraction study of carbon dioxide corrosion. *Journal of The Electrochemical Society*, *152*(10), pp.B389-B392.
3. Chan, E.W.L., 2011. *Magnetite and its galvanic effect on the corrosion of carbon steel under carbon dioxide environments.* (Doctoral dissertation).
4. Tanupabrungsun, T., Young, D., Brown, B. and Nesic, S., 2012, January. Construction and verification of pourbaix diagrams for CO_2 corrosion of mild steel valid up to 250˚C. In *CORROSION 2012*. NACE International.
5. Gulbrandsen, E. and Morard, J.H., 1999, January. Study of the possible mechanisms of steel passivation in CO_2 corrosion. In *CORROSION 1999*. NACE International.
6. Han, J., Nesic, S., Yang, Y. and Brown, B.N., 2011. Spontaneous passivation observations during scale formation on mild steel in CO_2 brines. *Electrochimica Acta*, *56*(15), pp.5396-5404.
7. Schlumberger Oilfield Glossary, available at http://www.glossary.oilfield.slb.com/,(last accessed on 07/04/2017).
8. Fosbøl, P., 2008. *Carbon Dioxide Corrosion: Modelling and Experimental Work Applied to Natural Gas Pipelines.* (Doctoral dissertation).
9. Abduh, M., The 50 Major Engineering Failures. 2008.
10. Kermani, M.B. and Harr, D., 2008, June. The impact of corrosion on oil and gas industry. In *Giornata di studio IGF S. Donato Milanese 1996*.
11. I. Borthwick, F. Balkau, T. Read, J. Monopolis, Overview of the oil and gas exploration and production process, in: UNEP IE/PAC Tech. Rep. 37, 1997: pp. 411.
12. Elboujdaini, M., 2011. Hydrogen-induced cracking and sulfide stress cracking. *Uhlig's Corrosion Handbook*, *3*, pp.183-194.
13. Reffass, M., Sabot, R., Savall, C., Jeannin, M., Creus, J. and Refait, P., 2006. Localised corrosion of carbon steel in $NaHCO_3$/NaCl electrolytes: role of Fe (II)-containing compounds. *Corrosion Science*, *48*(3), pp.709-726.
14. Yereth, R., Greater Prudhoe Bay. BP, 2012.
15. Roberge, P.R., 2000. *Handbook of corrosion engineering*. McGraw-Hill.
16. Popoola, L.T., Grema, A.S., Latinwo, G.K., Gutti, B. and Balogun, A.S., 2013. Corrosion problems during oil and gas production and its mitigation. *International Journal of Industrial Chemistry*, *4*(1), p.35.
17. Ossai, C.I., 2012. Advances in asset management techniques: an overview of corrosion mechanisms and mitigation strategies for oil and gas pipelines. *ISRN Corrosion*, *2012*.
18. Carneiro, R.A., Ratnapuli, R.C. and Lins, V.D.F.C., 2003. The influence of chemical composition and microstructure of API linepipe steels on

hydrogen induced cracking and sulfide stress corrosion cracking. *Materials Science and Engineering: A*, *357*(1), pp.104-110.
19. Yang, Y., 2012. *Removal mechanisms of protective iron carbonate layer in flowing solutions*. (Doctoral dissertation).
20. De Waard, C. and Williams, D.E., 1976. Prediction of carbonic acid corrosion in natural gas pipelines. *Ind. Finish. Surf. Coatings*, *28*(340), pp.24-26.
21. De Waard, C. and Milliams, D.E., 1975. Carbonic acid corrosion of steel. *Corrosion*, *31*(5), pp.177-181.
22. Nesic, S., 2007. Key issues related to modelling of internal corrosion of oil and gas pipelines–A review. *Corrosion Science*, *49*(12), pp.4308-4338.
23. Nesic, S., Nordsveen, M. and Stangel, A., 2001. A Mechanistic Model for CO_2 Corrosion with Protective Iron Carbonate Films. In *CORROSION 2001*. NACE International. (1040).
24. Nesic, S., Postlethwaite, J. and Olsen, S., 1995. An electrochemical model for prediction of CO_2 corrosion. In *CORROSION 1995*. NACE International. (131).
25. Nesic, S., Nordsveen, M. and Stangel, A., 2001. A Mechanistic Model for CO_2 Corrosion with Protective Iron Carbonate Films. In *CORROSION 2001*. NACE International.
26. Dugstad, A., 2006, January. Fundamental aspects of CO_2 metal loss corrosion-part 1: mechanism. In *CORROSION 2006*. NACE International.
27. Butler, J.N., 1991. *Carbon dioxide equilibria and their applications*. CRC Press.
28. Tanupabrungsun, T., Brown, B. and Nesic, S., 2015. Corrosion of mild steel in an aqueous CO_2 environment - basic electrochemical mechanisms revisited. In *CORROSION 2015*. NACE International. (671).
29. Nesic, S., Postlethwaite, J. and Olsen, S., 1996. An electrochemical model for prediction of corrosion of mild steel in aqueous carbon dioxide solutions. *Corrosion*, *52*(4), pp.280-294.
30. Nesic, S., 2004, March. A Critical Review of CO_2 Corrosion Modelling in the Oil and GAS Industry. In *10th Middle East Corrosion Conference* (pp. 7-10).
31. Nesic, S., Nordsveen, M. and Stangel, A., 2001. A Mechanistic Model for CO_2 Corrosion with Protective Iron Carbonate Films. In *CORROSION 2001*. NACE International.
32. Garsany, Y., Pletcher, D. and Hedges, B.M., 2003. The Role of Acetate in CO_2 Corrosion of Carbon Steel: Studies Related to Oilfield Conditions.
33. Seewald, J.S. and Seyfried, W.E., 1991. Experimental determination of portlandite solubility in H_2O and acetate solutions at 100–350˚C and 500 bars: constraints on calcium hydroxide and calcium acetate complex stability. *Geochimica et Cosmochimica Acta*, *55*(3), pp.659-669.
34. Nesic, S., 2012. Effects of multiphase flow on internal CO_2 corrosion of mild steel pipelines. *Energy & Fuels*, *26*(7), pp.4098-4111.

35. Singer, M. Li, C. Achour, M. Jenkins A. and Hernandez, S., 2014. Top of the line corrosion – Part 1: Review of the mechanism and laboratory experience. In *CORROSION 2014*. NACE International.
36. Tanupabrungsun, T., Brown, B. and Nesic, S., 2013. Effect of pH on CO_2 corrosion of mild steel at elevated temperatures. In *CORROSION 2013*. NACE International. (48).
37. Moiseeva, L.S., 2005. Carbon dioxide corrosion of oil and gas field equipment. *Protection of metals*, *41*(1), pp.76-83.
38. Manuel, R.W., 1947. Effect of Carbide Structure on the Corrosion Resistance of Steel. *Corrosion*, *3*(9), pp.415-431.
39. Lange, K.H. and Popperling, R.K., 1980, January. Control of CO_2 Corrosion by Special Production Tubulars in Offshore Operation. In *Offshore Technology Conference*. Offshore Technology Conference.
40. Dugstad, A., 1992. The importance of $FeCO_3$ supersaturation on the CO_2 corrosion of carbon steels. In *CORROSION 1992*. NACE International. (14).
41. Kermani, M.B. and Morshed, A., 2003. Carbon dioxide corrosion in oil and gas production—a compendium. *Corrosion*, *59*(8), pp.659-683.
42. Nyborg, R. and Dugstad, A., 1998. *Mesa corrosion attack in carbon steel and 0.5% chromium steel*. In *CORROSION 1998*. NACE International.
43. Schmitt, G. and Horstemeier, M., 2006, January. Fundamental aspects of CO_2 metal loss corrosion-Part II: Influence of different parameters on CO_2 corrosion mechanisms. In *CORROSION 2006*. NACE International.
44. Schmitt, G. and Engels, D., 1988. SEM/EDX Analysis of Corrosion Products for Investigations on Metallurgy and Solution Effects in CO_2 Corrosion. *G. Schmitt and D. Engels.* In *CORROSION 1998*. NACE International.
45. Schmitt, G. and Feinen, S., 2000, January. Effect of anions and cations on the pit initiation in CO_2 corrosion of iron and steel. In *CORROSION 2000*. NACE International.
46. Sun, Y. and Nesic, S., 2004. A parametric study and modeling on localized CO_2 corrosion in horizontal wet gas flow. In *CORROSION 2004*. NACE International. (380).
47. Tebbal, S. and Hackerman, N., 1999, January. Effect of buffer capacity on the CO_2 pitting of steel. In *CORROSION 1999*. NACE International.
48. Crolet, J.L., Thevenot, N. and Nesic, S., 1996. *Role of conductive corrosion products on the protectiveness of corrosion layers*. In *CORROSION 1996*. NACE International.
49. Schmitt, G., Mueller, M., Papenfuss, M. and Sttrobel-Effertz, E., 1999. Understanding Localized CO_2 Corrosion of Mild steel from Physical Properties of Iron Carbonate Scales. In *CORROSION 1999*. NACE International.
50. Kermani, B. and Smith, L.M. eds., 1997. CO_2 Corrosion Control in Oil and Gas Production: Design Considerations. (Vol. 688).

51. Nyborg, R., 1998. Initiation and growth of mesa corrosion attack during CO_2 corrosion of carbon steel. In *CORROSION 1998*. NACE International.
52. Nyborg, R. and Dugstad, A., 2003. Understanding and prediction of mesa corrosion attack. In *CORROSION 2003*. NACE International.
53. Nyborg, R. and Dugstad, A., 1997. Effect of chromium on mesa corrosion attack of carbon steel. *Drdegreesnen(Inst. for Energy Technology, Norway)*, pp.9-14.
54. Videm, K. and Dugstad, A., 1989. Corrosion of carbon steel in an aqueous carbon dioxide environment. *Mater. Performance; (United States)*, *28*(4).
55. Dugstad, A. Mechanism of Protective Film Formation during CO_2 Corrosion of Carbon Steel. In *CORROSION 1989*. NACE International.
56. Han, J., Yang, Y., Nesic, S. and Brown, B.N., 2008. Roles of passivation and galvanic effects in localized CO_2 corrosion of mild steel. In *CORROSION 2008*. NACE International. (08332).
57. Crolet, J.L., Thevenot, N. and Nesic, S., 1998. Role of conductive corrosion products in the protectiveness of corrosion layers. *Corrosion*, *54*(3), pp.194-203.
58. Videm, K. and Dugstad, A., 1987. Effect of flow rate, pH, Fe^{2+} concentration and steel quality on the CO_2 corrosion of carbon steels. In *CORROSION 1987*. NACE International.
59. Dugstad, A., 1992. The importance of $FeCO_3$ supersaturation on the CO_2 corrosion of carbon steels. In *CORROSION 1992*. NACE International. (14).
60. Dugstad, A., Lunde, L. and Nesic, S., 1994, October. Control of internal corrosion in multi-phase oil and gas pipelines. In *Proceedings of the conference Prevention of Pipeline Corrosion, Gulf Publishing Co*.
61. Al-Hassan, S., Mishra, B., Olson, D.L. and Salama, M.M., 1998. Effect of microstructure on corrosion of steels in aqueous solutions containing carbon dioxide. *Corrosion*, *54*(6), pp.480-491.
62. Refait, P., Bourdoiseau, J.A., Jeannin, M., Nguyen, D.D., Romaine, A. and Sabot, R., 2012. Electrochemical formation of carbonated corrosion products on carbon steel in deaerated solutions. *Electrochimica Acta*, *79*, pp.210-217.
63. Farelas, F., Brown, B. and Nesic, S., 2013. Iron carbide and its influence on the formation of protective iron carbonate in CO_2 corrosion of mild steel. In *CORROSION 2013*. NACE International. (2291).
64. Cabrini, M., Hoxha, G., Kopliku, A. and Lazzari, L., 1998. Prediction of CO_2 Corrosion in Oil and Gas Wells. Analysis of Some Case Histories. In *CORROSION 1998*. NACE International. (24).
65. Farelas, F., Choi, Y.S. and Nešić, S., 2012. Corrosion behavior of API 5L X65 carbon steel under supercritical and liquid carbon dioxide phases in the presence of water and sulfur dioxide. *Corrosion*, *69*(3), pp.243-250.
66. Crolet, J.L., Thevenot, N. and Nesic, S., 1998. Role of conductive corrosion products in the protectiveness of corrosion layers. *Corrosion*, *54*(3), pp.194-203.

67. Dugstad, A. Mechanism of Protective Film Formation during CO_2 Corrosion of Carbon Steel. In *CORROSION 1989*. NACE International.
68. Figueiredo, C.M.S., Junior, A.G.B., Flaten, E.M., Beck, R. and Seiersten, M., 2015. Crystal growth of $FeCO_3$ in mixed monoethylene glycol and water solvent. *Crystal Research and Technology*, *50*(5), pp.354-361.
69. Ramachandran, S., Jovancicevic, V. and Ward, M.B., 1999. *Understanding interactions between corrosion inhibitors and iron carbonate films using molecular modeling*. In *CORROSION 1999*. NACE International.
70. Kim, J.D., Yee, N., Nanda, V. and Falkowski, P.G., 2013. Anoxic photochemical oxidation of siderite generates molecular hydrogen and iron oxides. *Proceedings of the National Academy of Sciences*, *110*(25), pp.10073-10077.
71. Saheb, M., Neff, D., Dillmann, P., Matthiesen, H. and Foy, E., 2008. Long-term corrosion behaviour of low-carbon steel in anoxic environment: characterisation of archaeological artefacts. *Journal of Nuclear Materials*, *379*(1), pp.118-123.
72. Magnetite Mineral Data, available at: http://webmineral.com/data/Magnetite.shtml#.VVYUJGa3eHk, (last accessed on (07/04/2017).
73. Pandarinathan, V., Lepková, K. and Van Bronswijk, W., 2014. Chukanovite ($Fe_2(OH)_2CO_3$) identified as a corrosion product at sand-deposited carbon steel in CO_2-saturated brine. *Corrosion Science*, *85*, pp.26-32.
74. Schlegel, M.L., Bataillon, C., Blanc, C., Prêt, D. and Foy, E., 2010. Anodic activation of iron corrosion in clay media under water-saturated conditions at 90 C: characterization of the corrosion interface. *Environmental Science & Technology*, *44*(4), pp.1503-1508.
75. Pekov, I.V., Perchiazzi, N., Merlino, S., Kalachev, V.N., Merlini, M. and Zadov, A.E., 2007. Chukanovite, $Fe_2(CO_3)(OH)_2$, a new mineral from the weathered iron meteorite Dronino. *European Journal of Mineralogy*, *19*(6), pp.891-898.
76. Azoulay, I., Rémazeilles, C. and Refait, P., 2012. Determination of standard Gibbs free energy of formation of chukanovite and Pourbaix diagrams of iron in carbonated media. *Corrosion science*, *58*, pp.229-236.
77. Azoulay, I., Rémazeilles, C. and Refait, P., 2014. Corrosion of steel in carbonated media: The oxidation processes of chukanovite ($Fe_2(OH)_2CO_3$). *Corrosion Science*, *85*, pp.101-108.
78. Mc Cafferty, E. and Brodd, R.J., 1986. *Surfaces, inhibition and passivation* (No. CONF-861068-). The Electrochemical Society, Pennington, NJ.
79. Garside, J., 1984. Advances in the characterization of crystal growth. In *AIChE symposium series* (Vol. 80, No. 240, pp. 23-38). American institute of chemical engineers.

80. Marion, G.M., Catling, D.C. and Kargel, J.S., 2003. Modeling aqueous ferrous iron chemistry at low temperatures with application to Mars. *Geochimica et cosmochimica Acta*, *67*(22), pp.4251-4266.
81. Sun, W., Nesic, S. and Woollam, R.C., 2009. The effect of temperature and ionic strength on iron carbonate ($FeCO_3$) solubility limit. *Corrosion Science*, *51*(6), pp.1273-1276.
82. Lyon, S.B., 2009. Corrosion in natural waters. *Shreir's Corros*, *2*, pp.1094-1106.
83. Garside, J. and Davey, R.J., 2000. From Molecules to Crystallizers—An Introduction to Crystallization. Oxford University Press.
84. Sun, W. and Nesic, S., 2008. Kinetics of corrosion layer formation: part 1—iron carbonate layers in carbon dioxide corrosion. *Corrosion*, *64*(4), pp.334-346.
85. Linter, B.R. and Burstein, G.T., 1999. Reactions of pipeline steels in carbon dioxide solutions. *Corrosion science*, *41*(1), pp.117-139.
86. Joshi, G.R., 2015. Elucidating Sweet Corrosion Scales. (Doctoral dissertation).
87. Lasaga, A.C., 2014. *Kinetic theory in the earth sciences*. Princeton University Press.
88. Johnson, M.L., 1991. *Ferrous carbonate precipitation kinetics: A temperature ramped approach* (Doctoral dissertation).
89. Nesic, S. and Lee, K.L., 2003. A mechanistic model for carbon dioxide corrosion of mild steel in the presence of protective iron carbonate films—part 3: film growth model. *Corrosion*, *59*(7), pp.616-628.
90. Gao, M., Pang, X. and Gao, K., 2011. The growth mechanism of CO_2 corrosion product films. *Corrosion Science*, *53*(2), pp.557-568.
91. Johnson, M.L. and Tomson, M.B., 1991. Ferrous carbonate precipitation kinetics and its impact CO_2 corrosion. In *CORROSION 1991*. NACE International. (628).
92. de Waard, C. Lotz, U. Prediction of CO_2 Corrosion of Carbon Steel. In *CORROSION 1991*. NACE International. (69).
93. Pessu, F., Barker, R. and Neville, A., 2015. The influence of pH on localized corrosion behavior of X65 carbon steel in CO_2-saturated brines. *Corrosion*, *71*(12), pp.1452-1466.
94. Hunnik, Van. Hendriksen, E. Pots, B.F. Formation of Protective $FeCO_3$ Corrosion Product Layers in CO_2 Corrosion. In *CORROSION 1996*. NACE International.
95. Greenberg, J. and Tomson, M., 1992. Precipitation and dissolution kinetics and equilibria of aqueous ferrous carbonate vs temperature. *Applied Geochemistry*, *7*(2), pp.185-190.
96. Greenberg, J.L., 1987. *High temperature kinetics of precipitation and dissolution of ferrous-carbonate* (Doctoral dissertation).
97. Markov, I.V., 2003. *Crystal growth for beginners: fundamentals of nucleation, crystal growth and epitaxy*. World scientific.
98. Söhnel, O. and Mullin, J.W., 1982. Precipitation of calcium carbonate. *Journal of Crystal Growth*, *60*(2), pp.239-250.

99. Söhnel, O. and Mullin, J.W., 1988. Interpretation of crystallization induction periods. *Journal of colloid and interface science*, *123*(1), pp.43-50.
100. Mullin, J.W., 2001. *Crystallization*. Butterworth-Heinemann.
101. Llongueras, J.G., Hernandez, J., Munoz, A., Flores, J.M. and Duran-Romero, R., 2005. Mechanism of $FeCO_3$ formation on API X70 pipeline steel in brine solutions containing CO_2. In *CORROSION 2005*. NACE International.
102. Braun, R.D., 1991. Solubility of iron (II) carbonate at temperatures between 30 and 80˚C. *Talanta*, *38*(2), pp.205-211.
103. Bénézeth, P., Dandurand, J.L. and Harrichoury, J.C., 2009. Solubility product of siderite ($FeCO_3$) as a function of temperature (25–250˚C). *Chemical Geology*, *265*(1), pp.3-12.
104. Sun, W., 2006. *Kinetics of iron carbonate and iron sulfide scale formation in CO_2/H_2S corrosion* (Doctoral dissertation).
105. Silva, C.A., Liu, X. and Millero, F.J., 2002. Solubility of siderite ($FeCO_3$) in NaCl solutions. *Journal of solution chemistry*, *31*(2), pp.97-108.
106. Gray, L.G., Anderson, B.G., Danysh, M.J. and Tremaine, P.R., 1990. Effect of pH and temperature on the mechanism of carbon steel corrosion by aqueous carbon dioxide. In *CORROSION 1990.* NACE International. (40).
107. Gray, L.G., Anderson, B.G., Danysh, M.J. and Tremaine, P.G., 1989. Mechanism of carbon steel corrosion in brines containing dissolved carbon dioxide at pH 4. In *CORROSION 1989.* NACE International. (464).
108. Ikeda, A. Mukai, S. 1983. CO_2 corrosion behavior and mechanism of carbon steel and alloy steel. In *CORROSION 1983.* NACE International. (45).
109. Zhang, Y., Pang, X., Qu, S., Li, X. and Gao, K., 2012. Discussion of the CO_2 corrosion mechanism between low partial pressure and supercritical condition. *Corrosion Science*, *59*, pp.186-197.
110. Ingham, B., Ko, M., Kear, G., Kappen, P., Laycock, N., Kimpton, J.A. and Williams, D.E., 2010. *In situ* synchrotron X-ray diffraction study of surface scale formation during CO_2 corrosion of carbon steel at temperatures up to 90˚C. *Corrosion Science*, *52*(9), pp.3052-3061.
111. Nazari, M.H., Allahkaram, S.R. and Kermani, M.B., 2010. The effects of temperature and pH on the characteristics of corrosion product in CO_2 corrosion of grade X70 steel. *Materials & Design*, *31*(7), pp.3559-3563.
112. Lin, G., Zheng, M., Bai, Z. and Zhao, X., 2006. Effect of temperature and pressure on the morphology of carbon dioxide corrosion scales. *Corrosion*, *62*(6), pp.501-507.
113. Yin, Z., Zhao, W., Bai, Z. and Feng, Y., 2008. Characteristics of CO_2 corrosion scale formed on P110 steel in simulant solution with saturated CO_2. *Surface and Interface Analysis*, *40*(9), pp.1231-1236.
114. Heuer, J.K. and Stubbins, J.F., 1998. Microstructure analysis of coupons exposed to carbon dioxide corrosion in multiphase flow. *Corrosion*, *54*(7), pp.566-575.

115. Rajappa, S., Zhang, R. and Gopal, M., 1998. Modeling the diffusion effects through the iron carbonate layer in the carbon dioxide corrosion of carbon steel. In *CORROSION 1998.* NACE International.
116. Videm, K., 1993., The influence of pH and concentration of bicarbonate and ferrous ions on the CO_2 corrosion of carbon steels. In *CORROSION 1993.* NACE International. (83).
117. Nesic, S. Lee, J. and V. Ruzic, V. 2002. A mechanistic model of iron carbonate film growth and the effect on CO_2 corrosion of mild steel. In *CORROSION 2002.* NACE International. (2237).
118. Videm, K., Dugstad, A. and Lunde, L. 1994. Parametric study of CO_2 corrosion of carbon steel. In *CORROSION 1994.* NACE International. (14).
119. Kinsella, B., Tan, Y.J. and Bailey, S., 1998. Electrochemical impedance spectroscopy and surface characterization techniques to study carbon dioxide corrosion product scales. *Corrosion*, *54*(10), pp.835-842.
120. Hesjevik, S.M., Olsen, S. and Seiersten, M., 2003. Corrosion at high CO_2 pressure. In *CORROSION 2003*. NACE International.
121. de Moraes, F., Shadley, J.R., Chen, J. and Rybicki, E.F., 2000. Characterization of CO_2 corrosion product scales related to environmental conditions. In *CORROSION 2000*. NACE International.
122. Nesic, S. and Lunde, L., 1994. Carbon dioxide corrosion of carbon steel in two-phase flow. *Corrosion*, *50*(9), pp.717-727.
123. Nesic, S. and Wang, S., High Pressure CO_2 Corrosion Electrochemistry. In *CORROSION 2004*. NACE International.
124. Gao, K., Yu, F., Pang, X., Zhang, G., Qiao, L., Chu, W. and Lu, M., 2008. Mechanical properties of CO_2 corrosion product scales and their relationship to corrosion rates. *Corrosion Science*, *50*(10), pp.2796-2803.
125. Nesic, S., Wang, S., Cai, J. and Xiao, Y., 2004, January. Integrated CO_2 corrosion-multiphase flow model. In *SPE International Symposium on Oilfield Corrosion*. Society of Petroleum Engineers.
126. Pots, B.F.M., 1995. Mechanistic models for the prediction of CO_2 corrosion rates under multi-phase flow conditions. In *CORROSION 1995*. NACE International.
127. De Waard, C., Lotz, U. and Dugstad, A., 1995. Influence of Liquid Flow Velocity on CO_2 Corrosion: A Semi-Empirical Model. In *CORROSION 1995*. NACE International.
128. Nesic, S., Solvi, G.T. and Enerhaug, J., 1995. Comparison of the rotating cylinder and pipe flow tests for flow-sensitive carbon dioxide corrosion. *Corrosion*, *51*(10), pp.773-787.
129. Tanupabrungsun, T., 2012. *Thermodynamics and kinetics of carbon dioxide corrosion of mild steel at elevated temperatures* (Doctoral dissertation).
130. Nordsveen, M., Nesic, S., Nyborg, R. and Stangeland, A., 2003. A mechanistic model for carbon dioxide corrosion of mild steel in the presence of protective iron carbonate films—part 1: theory and verification. *Corrosion*, *59*(5), pp.443-456.

131. Schmitt, G., Bosch, C., Mueller, M. and Siegmund, G., 2000, January. A probabilistic model for flow induced localized corrosion. In *CORROSION 2000*. NACE International.
132. Schmitt, G.A. and Mueller, M., 1999. Critical wall shear stresses in CO_2 corrosion of carbon steel. In *CORROSION 1999*. NACE International. (44).
133. Ning, J., Brown, B. and Nesic, S., 2012. Verification of Pourbaix Diagrams for the H_2S-H_2O-Fe System at 25˚C. In *ICMT Ohio University Advisory Board Meeting,(March, 2012)*.
134. Shannon, D.W., 1978. The Role of Chemical Components in Geothermal Brines on Corrosion. In *CORROSION 1978*. NACE International. (57).
135. Ingham, B., Ko, M., Laycock, N., Burnell, J., Kappen, P., Kimpton, J.A. and Williams, D.E., 2012. *In situ* synchrotron X-ray diffraction study of scale formation during CO_2 corrosion of carbon steel in sodium and magnesium chloride solutions. *Corrosion Science*, *56*, pp.96-104.
136. Ko, M., Laycock, N.J., Ingham, B. and Williams, D.E., 2012. *In Situ* Synchrotron X-Ray Diffraction Studies of CO_2 Corrosion of Carbon Steel with Scale Inhibitors ATMPA and PEI at 80° C. *Corrosion*, *68*(12), pp.1085-1093.
137. Alsaiari, H.A., Yean, S., Tomson, M.B. and Kan, A.T., 2008, January. Iron Calcium Carbonate: Precipitation Interaction. In *SPE International Oilfield Scale Conference*. Society of Petroleum Engineers.
138. Alsaiari, H.A., Kan, A. and Tomson, M., 2010. Effect of Calcium and Iron (II) Ions on the Precipitation of Calcium Carbonate and Ferrous Carbonate. *SPE Journal*, *15*(02), pp.294-300.
139. Alsaiari, H.A., Tomson, M.B. and Kan, A.T., 2010, January. Constant Composition Study of Crystal Growth of Mixed Calcium-Ferrous Carbonate Salt. In *CORROSION 2010*. NACE International.
140. Navabzadeh Esmaeely, S., Choi, Y.S., Young, D. and Nešić, S., 2013. Effect of calcium on the formation and protectiveness of iron carbonate layer in CO_2 corrosion. *Corrosion*, *69*(9), pp.912-920.
141. Dugstad, A., Hemmer, H. and Seiersten, M., 2001. Effect of steel microstructure on corrosion rate and protective iron carbonate film formation. *Corrosion*, *57*(4), pp.369-378.
142. Palacios, C.A. and Shadley, J.R., 1991. Characteristics of corrosion scales on steels in a CO_2-saturated NaCl brine. *Corrosion*, *47*(2), pp.122-127.
143. Ruzic, V., Veidt, M. and Nesic, S., 2006. Protective Iron Carbonate Films—Part 1: Mechanical removal in single-phase aqueous flow. *Corrosion*, *62*(5), pp.419-432.
144. Crolet, J. L., 1994. Protectiveness of corrosion layers, in Modelling Aqueous Corrosion. 1994, Springer. p. 1-28.
145. Shadley, J.R., Shirazi, S.A., Dayalan, E., Ismail, M. and Rybicki, E.F., 1996. Erosion-corrosion of a carbon steel elbow in a carbon dioxide environment. *Corrosion*, *52*(9), pp.714-723.

146. Ruzic, V., Veidt, M. and Nesic, S., 2007. Protective iron carbonate films—part 3: simultaneous chemo-mechanical removal in single-phase aqueous flow. *Corrosion*, *63*(8), pp.758-769.
147. Ruzic, V., Veidt, M. and Nešsic, S., 2006. Protective iron carbonate films—Part 2: Chemical removal by dissolution in single-phase aqueous flow. *Corrosion*, *62*(7), pp.598-611.
148. Schmitt, G., Bosch, C., Bruckhoff, W. and Siegmund, G., 1998. Evaluation of critical flow intensities for FILC in sour gas production. In *CORROSION 1998*. NACE International.
149. Schmitt, G., Gudde, T. and Strobel-Effertz, E., 1996. Fracture mechanical properties of CO_2 corrosion product scales and their relation to localized corrosion. In *CORROSION 1996*. NACE International.
150. Yang, Y., Brown, B. and Nesic, S., 2012. Study of Protective Iron Carbonate Layer Dissolution in a CO_2 Corrosion Environment. In *CORROSION 2012*. NACE International.
151. Vyas, B., 1978. *Erosion--Corrosion* (No. BNL-24884). Brookhaven National Lab., Upton, NY (USA).
152. Han, J., Yang, Y., Brown, B. and Nesic, S., 2007. Electrochemical investigation of localized CO_2 corrosion on mild steel. In *CORROSION 2007*. NACE International. (7323).
153. De Marco, R., Jiang, Z.T., John, D., Sercombe, M. and Kinsella, B., 2007. An in situ electrochemical impedance spectroscopy/synchrotron radiation grazing incidence X-ray diffraction study of the influence of acetate on the carbon dioxide corrosion of mild steel. *Electrochimica acta*, *52*(11), pp.3746-3750.
154. Ingham, B., Ko, M., Laycock, N., Burnell, J., Kappen, P., Kimpton, J.A. and Williams, D.E., 2012. *In situ* synchrotron X-ray diffraction study of scale formation during CO_2 corrosion of carbon steel in sodium and magnesium chloride solutions. *Corrosion Science*, *56*, pp.96-104.
155. De Marco, R., Veder, J, *In situ* structural characterization of electrochemical systems using synchrotron-radiation techniques, Anal. Chem, 2010. 29(6).
156. Nagy, Z., You, H., Yonco, R.M., Melendres, C.A., Yun, W. and Maroni, V.A., 1991. Cell design for in—situ X-ray scattering study of electrodes in transmission geometry. *Electrochimica acta*, *36*(1), pp.209-212.
157. Ingham, B., Ko, M., Laycock, N., Kirby, N.M. and Williams, D.E., 2015. First stages of siderite crystallisation during CO_2 corrosion of steel evaluated using *in situ* synchrotron small-and wide-angle X-ray scattering. *Faraday discussions*, *180*, pp.171-190.
158. Joshi, G.R., Cooper, K., Lapinski, J., Engelberg, D.L., Bikondoa, O., Dowsett, M.G. and Lindsay, R., 2015, May. In Situ Grazing Incidence X-ray Diffraction of Sweet Corrosion Scaling on Carbon Steel. In *CORROSION 2015*. NACE International.
159. Fontana, M.G., 2005. *Corrosion engineering*. Tata McGraw-Hill Education.

160. Atkins, P.W. and De Paula, J., 2005. *The elements of physical chemistry* (Vol. 3). New York, NY, USA:: Oxford University Press.
161. Stansbury, E.E. and Buchanan, R.A., 2000. *Fundamentals of electrochemical corrosion*. ASM international.
162. Orazem, M.E. and Tribollet, B., 2011. *Electrochemical impedance spectroscopy* (Vol. 48). John Wiley & Sons.
163. Revie, R.W. and Uhlig, H.H., 2000. Thermodynamics: Corrosion Tendency and Electrode Potentials. *Corrosion and Corrosion Control: An Introduction to Corrosion Science and Engineering, Fourth Edition*, pp.21-41.
164. Barker, R.J., 2012. *Erosion-corrosion of carbon steel pipework on an offshore oil and gas facility*. (Doctoral dissertation).
165. Bockris, J.O.M. and Reddy, A.K., 2000. *Modern Electrochemistry 2B: Electrodics in Chemistry, Engineering, Biology and Environmental Science* (Vol. 2). Springer Science & Business Media.
166. Trethewey, K.R. and Chamberlain, J., 1995. Corrosion for science and engineering.
167. Barnes, C.E., 2000. Chemistry of Advanced Materials: An Overview (ed. s Interrante, Leonard V.; Hampden-Smith, Mark J.).
168. Scully, J.R., 2000. Polarization resistance method for determination of instantaneous corrosion rates. *Corrosion*, *56*(2), pp.199-218.
169. Stern, M., 1958. A method for determining corrosion rates from linear polarization data. *Corrosion*, *14*(9), pp.60-64.
170. Taleb, W., 2017, *Nanotechnology for corrosion control*. (Doctoral dissertation).
171. Sanni, O., Charpentier, T., Kapur, N. and Neville, A., 2015, January. Study of surface deposition and bulk scaling kinetics in oilfield conditions using an in-situ flow rig. In *CORROSION 2015*. NACE International.
172. Krawitz, A.D., 2001. Introduction to diffraction in materials science and engineering. *Introduction to Diffraction in Materials Science and Engineering, by Aaron D. Krawitz, pp. 424. ISBN 0-471-24724-3. Wiley-VCH, April 2001.* p.424.
173. Robinson, I.K. and Tweet, D.J., 1992. Surface X-ray diffraction. *Reports on Progress in Physics*, *55*(5), p.599.
174. Palacios, C.A. and Shadley, J.R., 1991. Characteristics of corrosion scales on steels in a CO_2-saturated NaCl brine. *Corrosion*, *47*(2), pp.122-127.
175. Sun, W., Nesic, S. and Papavinasam, S., 2006. Kinetics of iron sulfide and mixed iron sulfide/carbonate scale precipitation in CO_2/H_2S corrosion. In *CORROSION 2006*. NACE International. (6644).
176. Barker, R., Hua, Y. and Neville, A., 2017. Internal corrosion of carbon steel pipelines for dense-phase CO_2 transport in carbon capture and storage (CCS)–a review. *International Materials Reviews*, *62*(1), pp.1-31.
177. Hassani, S. Roberts, K.P. Shirazi, S.A. Shadley, J.R. Rybicki, E.F. and Joia C. 2012. Flow Loop Study of NaCl Concentration Effect on Erosion,

Corrosion, and Erosion-Corrosion of Carbon Steel in CO_2-Saturated Systems. *Corrosion, 68(2).*

178. He, Y., Zhou, Y., Yang, R., Ma, L. and Chen, Z., 2015. Imidazoline derivative with four imidazole reaction centers as an efficient corrosion inhibitor for anti-CO_2 corrosion. *Russian Journal of Applied Chemistry*, *88*(7), pp.1192-1200.
179. Jaal, R.A., Ismail, M.C. and Ariwahjoedi, B., 2014. A Review of CO_2 Corrosion Inhibition by Imidazoline-based Inhibitor. In *MATEC Web of Conferences* (Vol. 13, p. 05012). EDP Sciences.
180. Li, W., Brown, B., Young, D. and Nešić, S., 2013. Investigation of pseudo-passivation of mild steel in CO_2 corrosion. *Corrosion*, *70*(3), pp.294-302.
181. Silverman, D.C. and Carrico, J.E., 1988. Electrochemical impedance technique—a practical tool for corrosion prediction. *Corrosion*, *44*(5), pp.280-287.
182. Zhang, G.A., Lu, M.X., Qiu, Y.B., Guo, X.P. and Chen, Z.Y., 2012. The Relationship between the Formation Process of Corrosion Scales and the Electrochemical Mechanism of Carbon Steel in High Pressure CO_2-Containing Formation Water. *Journal of The Electrochemical Society*, *159*(9), pp.C393-C402.
183. Sun, W. Chokshi, K. and Nesic, S. 2005 Iron Carbonate Scale Growth and the Effect of Inhibition in CO_2 Corrosion of Mild Steel. In *CORROSION 2005*. NACE International.
184. Burkle, D., De Motte, R., Taleb, W., Kleppe, A., Comyn, T., Vargas, S.M., Neville, A. and Barker, R., 2016. Development of an electrochemically integrated SR-XRD flow cell to study $FeCO_3$ formation kinetics. *Review of Scientific Instruments*, *87*(10), p.105125.
185. Janik-Czachor, M. and Szklarska-Smialowska, Z., 1968. Pitting corrosion of single crystals of the Fe-16 Cr alloy in solutions containing Cl−ions. *Corrosion Science*, *8*(4), pp.215IN1217-216IN6220.
186. Dong, J., Nishimura, T. and Kodama, T., 2002. Corrosion behavior of carbon steel in bicarbonate (HCO_3) solutions. In *MRS Proceedings* (Vol. 713, pp. JJ11-8). Cambridge University Press.
187. Farelas, F. and Ramirez, A., 2010. Carbon dioxide corrosion inhibition of carbon steels through bis-imidazoline and imidazoline compounds studied by EIS. *Int. J. Electrochem. Sci*, *5*(1).
188. Zheng, L., Landon, J., Matin, N.S. and Liu, K., 2016. $FeCO_3$ Coating Process toward the Corrosion Protection of Carbon Steel in a Postcombustion CO_2 Capture System. *Industrial & Engineering Chemistry Research*, *55*(14), pp.3939-3948.
189. Diamond Light Source, Beamline I15. Available at: http://www.diamond.ac.uk/Beamlines/Engineering-and-Environment/I15-Extreme.html. (Last accessed on 07/04/2017)